

Cavités diélectriques
Formalisme de diffusion et applications

Thèse

Guillaume Painchaud-April

Doctorat en physique
Philosophiæ Doctor (Ph. D.)

Québec, Canada

© Guillaume Painchaud-April, 2014

Résumé

Les cavités diélectriques résonantes quasi-bidimensionnelles présentent un important potentiel pour des domaines aussi variés que la biodétection et la production de rayonnement laser. Leur faible taille - typiquement quelques dizaines de micromètres sur leur plus grand axe - conjuguée à une forte capacité de rétention du rayonnement électromagnétique - facteurs de qualité pouvant atteindre 10^9 - en font d'excellentes candidates à un grand nombre d'applications de haute technologie où la gestion de l'énergie, la précision des mesures, et le volume occupé sont des paramètres critiques. À cela s'ajoute une facilité d'implantation accrue grâce à l'utilisation de principes de microgravure bien connus.

Un des défis importants relié à l'utilisation des microcavités demeure la conciliation des hauts facteurs de qualité, la caractéristique fondamentale des microcavités, et de la capacité à produire une émission de radiation directionnelle. C'est sous ce thème général que s'articule cette thèse.

Dans un premier temps, l'accent est porté au développement d'un formalisme encadrant la caractérisation des cavités diélectriques. Une méthode originale utilisant la matrice de diffusion comme pierre d'assise est présentée à cette fin. Ensuite, une étude perturbative de la cavité diélectrique la plus simple, le disque, est réalisée. Les observations résultantes sont utilisées comme lignes directrices dans la suite du travail.

Dans un second temps, le formalisme développé est appliqué à une cavité présentant une déformation d'indice de réfraction simple, la cavité annulaire. Certaines 'règles' de transition vers l'émission directionnelle sont obtenues. Aussi, une discussion sur un modèle de couplage entre un guide d'onde et une microcavité est présentée.

Finalement, un concept de cavité découlant de résultats obtenus tout au long de la thèse est présenté. La principe de fonctionnement demande le couplage d'un anneau diélectrique, servant de réservoir de champ électromagnétique à une seconde cavité 'parasite' fortement directionnelle.

Ce document est rédigé en majeure partie en Anglais pour faciliter sa diffusion autant pour fins d'évaluation que pour consultation ultérieure par la Communauté.

Summary

Two-dimensional resonant dielectric microcavities present an important potential in various domains ranging from bio-detection to production of laser radiation. Their small footprint - typically tens of microns over their longest axis - conjugated to a strong capacity to retain the electromagnetic field - quality factors reaching values of 10^9 - make them excellent candidates for a large number of high-tech applications where tight energy management, high precision and low volumes are critical parameters. Moreover, the implantation of microcavities benefit from well-mastered micro-etching techniques.

One of the the most challenging issues related to microcavities remains the merging of high quality factors, the fundamental characteristic of microcavities, and the capacity to produce highly directional radiation emission. This thematic forms the leitmotiv of this thesis.

First, attention is focused on the development of a formalism framing the characterisation of dielectric cavities. An original method using the scattering matrix is presented for this purpose. Then, a perturbation study of the dielectric disc cavity is carried out. The results gathered from this investigation are used as guidelines for further applications.

Second, the scattering formalism is applied to the simplest refractive index deformation of the disc cavity, the annular cavity. Some transition 'rules' from non-directional emission to directional emission are obtained. Also, a discussion about the waveguide-cavity coupling is presented. This type of configuration is often found in experimental setups using microcavities.

Finally, a proposal derived from results obtained throughout the thesis is presented. The operation principle exploits the coupling from a dielectric ring used as an electromagnetic field reservoir to a second strongly directional 'parasitic' cavity.

This document is written in English to ease its distribution both for evaluation purposes and consultation by the Community.

Pour mes filles, Clara et Gabrielle,
et leur maman, Mylène

Avant-propos

Je suis entré dans le groupe de recherche du Pr Louis J. Dubé à l'automne 2004. Le Pr. Dubé est le catalyseur de cet ultime document résumant de façon partielle ces nombreuses années de travail au sein de cette petite section de recherche en physique sur les systèmes dynamiques. Je tiens à souligner la confiance qu'il m'a porté au cours de ces années, son support financier et moral continu et, particulièrement depuis ces deux dernières années, sa grande patience à mon égard. Ce fut un grand honneur de travailler sous sa direction, et l'inestimable expérience acquise me suivra tout au long de ma vie.

Plusieurs personnages croisés au long du périple ont marqué l'avancement de mon travail d'étudiant gradué. Tout d'abord, je souligne la contribution du Dr Samir Saïdi à qui je dois une importante collaboration scientifique, des lectures patientes et des discussions critiques, ainsi qu'une grande confiance en mes capacités. Dans la même lignée, j'aimerais remercier Julien Poirier pour ces nombreuses années de travail à mes côtés, son sens critique et son intuition furent grandement appréciés. Aussi, je tiens à remercier particulièrement Denis Gagnon, un étudiant au jugement vif mais sensé, avec qui j'ai passé les dernières années de ma vie d'étudiant gradué.

Il y a aussi Pierre-Yves St-Louis, avec qui j'ai débuté mes études gradués; Dr Pierre-André Noël, un individu créatif et plein de ressources qui fera un jour un excellent professeur-chercheur; Antoine Allard, attentionné et brillant; puis Laurent Hébert-Dufresne, sensible et créatif, et Vincent Marceau, dont l'humilité n'a d'égal que le talent. Finalement, j'aimerais souligner l'intérêt d'un nouvel étudiant, Joey Dumont, pour mes travaux: ce fut une source de motivation lors de la rédaction des derniers chapitres de cette thèse. La présence de ces gens dans le groupe de recherche a contribué à un climat de travail permettant des échanges scientifiques (et autres!) créatifs mais réfléchis (presque toujours) qui ont à leur tour influencé de près ou de loin le cours de mes études.

Finalement, il y a tous ces gens à l'extérieur du microcosme du groupe de recherche,

parents et amis, pour qui mon insistence à poursuivre des études devait paraître difficile à comprendre. Je profite de ces quelques lignes pour les remercier de leur respect, mais aussi de leurs nombreux encouragements qui furent nécessaires à plusieurs moments.

Cette liste serait gravement incomplète sans mentionner le support, les encouragements et l'amour de ma compagne Mylène Arsenault durant l'ensemble de ces longues années d'étude. Les épreuves des dernières années n'ont jamais émoussé son soutien alors que ma volonté de poursuivre le travail s'amenuissait. Elle m'a permis de compléter tout ceci en prenant sur elle la charge de nos petites. Je lui en serai toujours reconnaissant. Merci.

Contents

Résumé iii

Summary v

Avant-propos ix

Contents xi

List of Figures xv

List of Tables xxxv

Notation xxxvii

1 Introduction 1
- 1.1 Summary of content . . . 3
- 1.2 Preliminary considerations . . . 6
  - 1.2.1 A short discussion of cavities . . . 7
  - 1.2.2 Definition of the physical content . . . 13
- 1.3 A solvable case: The homogeneous cavity . . . 24
  - 1.3.1 The effective potential description . . . 29
  - 1.3.2 The semi-classical limit . . . 30

2 Formalism I: Theoretical and numerical approach 41
- 2.1 An energy description of the modes . . . 42
  - 2.1.1 Main derivation . . . 42
  - 2.1.2 Energy modes as stationary scattering states . . . 45
  - 2.1.3 Some properties of the **Q** matrix . . . 47
- 2.2 Numerical calculation of the **S** matrix . . . 61
  - 2.2.1 A transfer matrix algorithm . . . 61
  - 2.2.2 Testing the main approximation . . . 67
  - 2.2.3 Testing a non-diagonal case . . . 67
- 2.3 Wavefunction reconstruction . . . 71

2.3.1 Early and failed attempts . . . 71
2.3.2 The adopted procedure: A hybrid finite element approach . . . 73
2.4 Numerical calculation of the **Q** matrix . . . 75

3 Formalism II: Perturbation series 81
3.1 Small deformations of the disc cavity . . . 82
3.1.1 Perturbation correction of the **S** matrix . . . 84
3.1.2 Perturbation treatment of the corrected delay matrix modes . . . 87
3.1.3 Phase perturbation and time delay . . . 88
3.2 Two illustrative examples: Presentation . . . 93
3.2.1 Small amplitude boundary deformation . . . 93
3.2.2 Small circular inclusion . . . 100
3.2.3 Perspectives for other systems . . . 102
3.3 Two illustrative examples: Further analysis... . . . 103
3.3.1 Global behaviour of the scattering matrix . . . 103
3.3.2 Results from perturbation theory . . . 106
3.3.3 Inhomogeneous versus Deformed disc cavity . . . 115

4 Application I: The annular cavity 117
4.1 The non-uniform emission from WGMs... . . . 120
4.1.1 Effect of the displacement of the inclusion on the far-field of a WGM . . . 121
4.1.2 An iterative model of the annular cavity: Highlighting two escape mechanisms . . . 126
4.2 Control of the annular cavity emission output . . . 133
4.2.1 Dominant structures of phase space . . . 135
4.2.2 Husimi distribution . . . 140
4.2.3 Initial conditions for ray optics simulations . . . 142
4.2.4 Wave and classical simulations in phase space . . . 144
4.3 Notes on coupled resonances . . . 150
4.4 Notes on boundary roughness . . . 158

5 Application II: Cavity-waveguide coupling model 165
5.1 Evanescent field and cylindrical harmonics . . . 167
5.2 Coupling theory . . . 171
5.3 Solution of the model . . . 174
5.3.1 General solution . . . 174
5.3.2 Evaluation of the elements of $\mathbf{G}^0$ . . . 177
5.4 Alternative development of the model . . . 182
5.4.1 Description of the electromagnetic field in the guide . . . 182
5.4.2 Solution of the alternative model . . . 185

5.5 Results for the disc cavity . . . 185
5.5.1 Validity of the assumptions (5.34) - (5.36) and (5.97) - (5.98) . 186
5.5.2 Transmission coefficient . . . 188

6 Conclusions and perspectives **193**
6.1 Summary of observations and results . . . 193
6.2 Perspectives on mode quality *vs* directionality tradeoff... . . . 200

A Fonctions de Bessel... **211**
A.1 Relations exactes de fonctions de Bessel . . . 211
A.2 Développements des fonctions de Bessel . . . 213
A.2.1 Développements pour m fixe et $x \ll m$ . . . 213
A.2.2 Développements pour m fixe et $x \gg m$ . . . 214
A.2.3 Développements pour m grand . . . 215

B Oscillateurs, états comprimés... **221**
B.1 Oscillateur harmonique classique: Rappels . . . 221
B.2 Oscillateur harmonique ondulatoire: Rappels . . . 222
B.3 États cohérents . . . 223
B.3.1 Représentation des états cohérents sur la base $\{\big| n \big\rangle\}$ . . . 223
B.3.2 L'état cohérent comme état quasi classique . . . 225
B.3.3 États comprimés . . . 227
B.4 Distribution de Husimi . . . 228
B.4.1 Distributions quantiques . . . 228
B.4.2 Une distribution particulière: La distribution de Husimi . . . 228
B.4.3 Exemple: Application à l'oscillateur harmonique . . . 230

C Calcul numérique de la matrice S **235**
C.1 Développement de l'équation angulaire locale sur une base de Fourier . 235
C.2 Définition des matrices intermédiaires . . . 237
C.2.1 Domaine intérieur et couplage au premier anneau ($j = 0$) . . . 237
C.2.2 Anneaux intermédiaires ($j = 1, 2, 3, ... N - 1$) . . . 239
C.2.3 Dernier anneau et couplage au domaine extérieur ($j = N$) . . . 240

D Forme analytique de la matrice S... **243**
D.1 Matrice de déplacement $\mathbf{T}$ et... . . . 244
D.1.1 Cas $r > d$ . . . 244
D.1.2 Cas $r < d$ . . . 245
D.2 Effet du déplacement de l'origine sur... . . . 246
D.2.1 Calcul de $\mathbf{T}^{\dagger}(nkd, \phi_0)\frac{\partial}{\partial k}\mathbf{T}(nkd, \phi_0)$ . . . 247
D.2.2 Matrice des délais déplacée $\mathbf{Q}$ . . . 248
D.3 Matrice de diffusion $\mathbf{S}$ de la cavité annulaire . . . 250

E Modes d'un guide d'onde plan **253**
E.1 Modes d'un guide d'onde plan 253
E.2 Modèle de couplage cavité-guide d'onde: Analyse 256
E.2.1 Représentation en ondes planes de $H_m^{(1)}(z)\mathrm{e}^{im\phi}$ 256
E.2.2 Résultat asymptotique de l'intégrale $\int_{x_0}^{+\infty} dx\ H_m^{(1)}(n_o kr)\mathrm{e}^{im\phi}\mathrm{e}^{\mp i\beta x}$ pour $x_0/y \gg |m|$ 259
E.2.3 Intégration de $\int_{-\infty}^{+\infty} dx\ H_m^{(1)}(n_o kr)\mathrm{e}^{im\phi}\mathrm{e}^{\mp i\beta x}$ 263
E.2.4 Calcul de $\int_{\tilde{x}}^{+\infty} dx\ \mathrm{e}^{-\alpha x}H_m^{(1)}(\kappa x)$ pour $\tilde{x} \gg |m|/\kappa$ 268
E.2.5 Calcul de $\int dx'\ \chi(x')\mathrm{e}^{+i2\beta x'}$ pour le disque homogène et la cavité annulaire 272

F Fonctions de Green **275**
F.1 Fonction de Green libre en 2D 275
F.2 Fonctions de Green du disque homogène 277

Bibliography **281**

List of Figures

1 Description of the field display. The far-field is depicted as a ring surrounding the near field of the cavity. The amplitude increases with the color scale from light yellow to dark brown. xxxix

1.1 Flow chart of the thesis. 5

1.2 (a) Left: Principle of action of a tunable VCSEL (Thor Labs www.thorlabs.com); Upper right: Scanning Electron Microscope (SEM) rendition of a VCSEL (Ferdinand-Braun Institut www.fbh-berlin.com); Lower right: Array of VCSELs on a single wafer (Thor Labs). (b) SEM rendition of silica micro-discs on their support pilar, S. Saïdi and Y.-A. Peter, École Polytechnique de Montréal 2009. Right inset: The trapped light field is reflected at the media discontinuity. (c) Left: A laser microsphere makes the front cover of the Nature issue of February 2002, S. M. Spillane *et al.* [137]. Right: The laser microsphere spectrum. 8

1.3 Left: Some eigenfunctions $\psi_j(\mathbf{r})$ that solve problem (1.1) for a quadripolar deformation of the disc. The boundary of this specific cavity is defined by the radial function $r_{\mathrm{bnd}}(\phi) = R_0(1 + \epsilon \cos 2\phi)$ with respect to polar angle ϕ and numerical values $R_0 = 1$ and $\epsilon = 0.1$. The labels 'regular' and 'irregular' attributed to each modes refer to trajectories found in the classical billiard picture, Fig. 1.4. The eigenfunctions shown here have eigen-wavenumber values pertaining to the discrete spectrum $k = \{k_j\}$ presented to the right. The non-dimensional abscissa of the spectrum is in kl units where l is the mean radius of the cavity ($l = R_0 = 1$). 9

1.4 Classical trajectories of the quadripole billiard. The cavity geometry is the same as the one of Fig. 1.3. Typical regular and irregular 'chaotic' trajectories are shown in configuration space on the left and in phase space on the right. The correspondence between configuration space and phase space is schematically represented on the right. The phase space itself summarizes the overall dynamical properties of a given billiard geometry: regular trajectories appear as 'stable islands', and irregular trajectories quickly fill (part of) the 'chaotic sea'. 10

1.5 Differences between (a) the scattering experiment and (b) the emission experiment. While the scattering experiment may be solved for all real wavenumbers and all incoming fields ψ_{inc} solving Eq. (1.2), the emission experiment seeks to obtain singular solutions of Eq. (1.2) that result solely in an outgoing wave ψ_{out}. These singular solutions lie in the complex k-plane in the form of poles of the scattering matrix $\mathbf{S}(k)$. 11

1.6 Left: Some modes of the open quadripole cavity solving Eq. (1.2). The cavity geometry is the same as the one of Fig. 1.3, supplemented with a cavity refractive index $n_c = 1.5$ and an outside medium refractive index $n_o = 1$. Notice the far-field intensity distribution (*i.e.* $|\psi(\mathbf{r})|^2$ as $|\mathbf{r}| \to \infty$) represented by a color-scaled ring encircling the cavity. Right: 'Energy' spectrum of the quadripole cavity and some of its poles located in the complex k-plane. 13

1.7 The optical thinness hypothesis for the dielectric cavity. This hypothesis asserts that the amplitude $|A|$ of the electromagnetic field along the z axis resembles that the fundamental mode of a planar waveguide (see Appendix E). It is assumed that any z dependency may be factored out of the electromagnetic field. 16

1.8 Two-dimensional cavity and assumed TM and TE polarization states with details on the boundary including the unit normal vector $\hat{\nu}$. 18

1.9 A continuous wave scattering event with a finite-sized dielectric cavity with proper radiation condition at infinity. With regards to incoming and outgoing waves, the presence of the cavity inside the circular domain of radius R_{max} is expressed by the scattering matrix $\mathbf{S}$. 20

1.10 Definition of the PDE problem for the two-dimensional dielectric cavity. 23

1.11 Representation of $|\psi(\mathbf{r})|^2$ for one of the modes of the disc cavity $n_c = 1.5$, $n_o = 1.0$ and $R_0 = 1$; dark = high amplitude, white = low amplitude. This (resonant) mode is labeled $(21, 3)$ because it possesses angular momentum $|m| = 21$ and presents 3 maxima along its radial line inside the cavity. We arbitrarily choose to set the incoming coefficients $A_{+21} = A_{-21} = 1/\sqrt{2}$ to select the odd symmetry mode with respect to the horizontal axis of this picture. Accordingly, this mode has a degenerate (orthogonal) companion with even symmetry obtained by setting $A_{+21} = +1/\sqrt{2}$ and $A_{-21} = -1/\sqrt{2}$. 26

1.12 Complex k-plane amplitude of $\Delta_m(k)$ Eq. (1.59) for a homogeneous disc cavity of radius $R_0 = 1$ and refractive index $n_c = 1.5$ immersed in an environment $n_o = 1.0$. The (logarithmic) color scale ranges from dark near zero values (largely negative on a logarithmic scale) to bright for high $|\Delta_m(k)|$ values. The poles of the $\mathbf{S}$ matrix (1.60) for the two angular momenta presented are indicated by white crosses. 27

1.13 Non-dimensional delay $c\tau/R_0$ (c is the speed of light in vacuum) as computed by Eq. (1.63) for the homogeneous disc cavity defined by the same parameters as those used for Fig. 1.12, and the same two angular momenta. The labeling (m, j) of the different resonant peaks refers to the angular momenta m, and the number j of in-cavity radial extrema of the field. For instance, $(31, 1)$ is the first - and largest lifetime - resonance of the $|m| = 31$ series; no other $|m| = 31$ resonances exist at smaller wavenumber values. 28

1.14 Effective potential representation of the homogeneous disc cavity with $n_c = 1.5$, $n_o = 1.0$ and $R_0 = 1$ for $|m| = 21$. The 'classically forbidden' regions of the potential are colored in gray, and the energy level $(n_o k)^2$ is represented by the dashed green line with the wavefunction $|\psi(r, \phi)|^2 = |\mathcal{R}(r)|^2$ in plain blue trace standing upon it. (a) Below barrier regime (off-resonance); (b) In-barrier regime, off-resonance; (c) In-barrier regime, on-resonance $(21, 1)$; (d) Above barrier regime, on-resonance $(21, 4)$. . 31

1.15 Phases $\theta^-(r, \phi)$ (blue) and $\theta^+(r, \phi)$ (red) according to Eq. (1.89) evaluated at evenly spaced constant values. A geometrical trajectory 'optical ray' perpendicular to the constant phase levels Eq. (1.88) is also shown with emphasis on the changeover at the caustic from the incoming wave in blue to the outgoing wave in red. The scattering by the caustic curve causes a phase offset of $-\pi/2$ between the two wave types. 35

1.16 Application of Eq. (1.89) to the disc cavity of radius R_0 in a no loss scenario. A trajectory perpendicular to constant phase levels is reflected at the boundary of the cavity and undergoes a phase shift as it moves from an outgoing wave to an incoming wave. 36

1.17 Graphical solution to problem (1.101) for $m = 21$ and $n_c = 1.5$, $n_o = 1.0$ and $R_0 = 1$. The black line is the left hand side of (1.101) and green curves correspond to the right hand side; solutions are at the crossings. Also shown are the limits of the right hand side of Eq. (1.101) associated to Dirichlet (blue) and Neumann (red) problems. While solutions for larger k tend toward the Neumann problem typical of 'open boundary' systems, solutions for $j = 1$ resemble more to the Dirichlet problem characteristic of total reflection phenomenon. 38

2.1 Top view of the dielectric cavity and its surroundings. The cavity itself is a thin slab of dielectric material of width w along the Oz axis (close-up box) and is restricted to a cylindrical domain of radius $R_{\max}$. This cylinder is placed inside a large coaxial annular cylinder whose radius R_V shall eventually reach infinity. 43

2.2 Dichotomy in the positions of the zeros and poles of the **S** matrix. The scattering description presented in this chapter extracts the system's information from the complex k plane as one moves along the real k axis. 48

2.3 Description of the scattering event (a) in the centered scenario and (b) in the displaced scenario. It is clear that, although both situations hold the same amount of dielectric material, the effective cavities inside the dashed circles are qualitatively different. 52

2.4 (a) Centered homogeneous disc cavity spectrum, (b) displaced homogeneous disc cavity spectrum $d/R_0 = 0.1$ and (c) displaced homogeneous disc cavity spectrum $d/R_0 = 0.5$. Gray lines: centered disc; black lines: displaced disc; gray areas: application of Eq. (2.46) on the unmoved disc eigenvalues. 54

2.5 Schematics of the avoided-crossing of two delay levels for a displaced cavity following Eqs. (2.49)-(2.53) and the ensuing discussion. 57

2.6 Autocorrelation as defined in Eq. (2.55) and far-field for two mode symmetries of the square cavity, see Tab. 2.1. Although the maxima of $C^p(\phi)$ indicate the same symmetry axis (autocorrelation reaches 1 at $\phi = \{0, \pi/4, \pi/2, 3\pi/4\}$), it is observed that the behaviour of the field differs at these specific locations, hence the different symmetries. 59

2.7 Partial spectra of two sets of mode symmetries of the square cavity. See Tab. 2.1 for the description of the symmetries. 60

2.8 (a) Degenerate delay levels of the square cavity and (b) the corresponding levels in the rectangular cavity. The circles indicate the position of the modes presented on Fig. 2.9. 61

2.9 Near-field patterns for resonant degenerate modes of (a)-(b) the square cavity and (c)-(d) corresponding symmetry modes of the rectangular cavity. The degeneracy of mode symmetries 1a and 1b of the square cavity is easily understood from Figs. (a)-(b): only a $\pi/2$ rotation separates these modes, a geometrical change that does not alter the quality factor (capacity of energy containment) of any of the modes having symmetry $1a$ and $1b$. 62

2.10 Conceptual view of the annular decomposition of the cavity. Two adjacent annular domains of thickness 2ϵ are displayed. Incoming and outgoing coefficients with respect to the circular interface located at $r_j + \epsilon = r_{j+1} - \epsilon$ are also shown. Dashed circles indicate the mean radius of the annular domains. 63

2.11 Conceptual view of the assembly process leading to matrix $\mathbf{S}^{j,j+2}$. The boundaries between the annuli are represented by vertical lines. Matrices $\mathbf{S}^{j}$ and $\mathbf{S}^{j+1}$ are first blended into a matrix $\mathbf{S}^{j,j+1}$, which in turn is combined with $\mathbf{S}^{j+2}$to yield $\mathbf{S}^{j,j+2}$. This cumulative matrix shares the same status with respect to the pairs $\{\mathbf{b}^{j}, \mathbf{b}^{j+3}\}$ and $\{\mathbf{a}^{j}, \mathbf{a}^{j+3}\}$ as the matrix $\mathbf{S}^{j}$ has between $\{\mathbf{b}^{j}, \mathbf{b}^{j+1}\}$ and $\{\mathbf{a}^{j}, \mathbf{a}^{j+1}\}$ 64

2.12 Circular innermost domain of radius r_0 and outermost limit of the cavity at $R_{\max} = r_N + \epsilon$. The disc shaped region inside the cavity is considered to be of constant refractive index n_{in}, and the outer domain $r > R_{\max}$, of index n_o. 66

2.13 (Color online) Maximum deviation, expression (2.76), for the homogeneous disc cavity separated in 2 annular regions (inset) of thickness 2ϵ. Computations are carried out with $n_c = 3.2$, $n_o = 1$ and $R_0 = 1$ for six wave numbers, $kR_0 = \{2.5,\ 5,\ 10,\ 20,\ 40,\ 80\}$. The maximum deviation decreases uniformly from a value $k2\epsilon \approx 0.33$ common to all wave numbers until a saturation limit is reached at small ϵ values. 68

2.14 (Color online) Example of matrices involved in termwise product (2.78); log of absolute value of matrix elements. Color scale is logarithmic, spanning from white (low) to dark (high). White dash lines indicate the $|m'| = \lceil n_c k R_{\max} \rceil$ limits. The product of exponentially increasing elements in (a) with saturation terms due to numerical roundoff in (b) yields an ill-behaved scattering matrix. 69

2.15 (Color online) Maximum deviation $e_{\max}$, expression (2.76), for the circular inclusion of the annular cavity (inset) with respect to wavenumber-normalized annuli thickness $k2\epsilon$. Computation is carried out for five truncation sizes, $M = \{8,\ 16,\ 32,\ 64,\ 128\}$. For constant M, the maximum deviation decreases uniformly at first, then settles on a plateau. The plateau levels, $\bar{e}_{\max}(M)$, decrease by approximately an order of magnitude with a doubling of the truncation size, i.e. $\bar{e}_{\max}(M)/\bar{e}_{\max}(2M) \sim 10$. 70

2.16 Mesh for the annular cavity with a hole of radius $r_0 = 0.1R_0$ at $d = 0.15R_0$. Cavity radius is $R_0 = 1$ and the mesh size follows the refractive index of the media. For instance, in this figure the typical mesh element has a length ratio 3.2 to 1 in the hole region where the index is $n_h = 1$ with respect to the cavity domain having $n_c = 3.2$. 75

2.17 Delay spectra of (a) the homogeneous disc (hd) cavity ($n_c = 3.2$, $n_o = 1$, $R_0 = 1$) and of (b) the annular cavity (ac) ($n_c = 3.2$, $n_o = 1$, $R_0 = 1$, $n_h = 1$, $r_0 = 0.1R_0$, $d = 0.25R_0$). The resonant modes are identified by 2 integers, (m, n): m is the azimuthal angular number, and n is the number of radial nodes inside the cavity. This nomenclature is used in both spectra, although one must regard the labels in the annular cavity spectrum as adiabatical remnants of the hd cavity modes through the parametric deformation. 77

2.18 Comparison of two annular cavity resonances field distributions $|\psi(\mathbf{r})|^2$: (a)-(c) for the resonant wavenumber pole description and (b)-(d) for the characteristic modes definition (maximum of delay; see delay spectrum 2.17(b)). Color scale is linear from white/bright (low) to black/dark (high). The external ring refers to the outgoing far-field distribution. The modes investigated are perturbed versions of modes $(14, 5)$, (a)-(b), and $(7, 8)$, (c)-(d). The outgoing coefficients $\mathbf{B}$ collected from resonant pole and characteristic modes descriptions overlap nicely to a value of 0.9999987 for the $(14, 5)$ mode , and 0.985 for the $(7, 8)$ mode. 78

3.1 Schematic decomposition of the complete cavity $\mathbf{S}$ matrix into two contributions, one due to the main disc cavity, $\mathbf{S}^{(0)}$, and the other, $\mathbf{S}^{(1)}$, due to the effect of the extra medium $\tilde{n}(\mathbf{r}; \epsilon)$. A test channel of angular momentum m' is impinging on a cavity, which responds by releasing a number of coefficients affecting many outgoing channels m. 83

3.2 Phase factor between incoming and outgoing waves having an angular momentum m_0, (a) in the homogeneous disc case, and (b) in the perturbed disc scenario. Although the composition on the perturbed wavefield consists in many angular channels, the effect on the phase θ appears mainly in the unperturbed channel m_0 component. 84

3.3 (a) Schematic of a geometrically deformed disc cavity according to Eq. (3.63). (b) Separation of interior (blue areas) and exterior (red areas) contributions to the refractive index. The value of $|\mathbf{r}|$ is always larger than the maximum radius of the cavity $R_0(1 + \epsilon \max_\phi\{f(\phi)\})$. 94

3.4 Representation of the physical interpretation of the five contributions to the complete first-order scattering matrix: disc cavity in gray, deformed area in blue (concave deformation) and red (convex deformation). The outgoing wave (*leaving arrow* relative to the cavity) comes from a path involving only one interaction with the boundary deformation in each case. This is indicative of a first-order correction. 95

3.5 Schematics of the cavity and inclusion system. The natural coordinates for the cavity (r, ϕ) and inclusion (ρ, θ) are shown, along with parameters d and ϵ. The refractive index inside the inclusion is n_h, while the index of the cavity and outside media are respectively n_c and n_o. 100

3.6 (a) Evaluation of $|\Delta_m|^{-2}$, Eq. (3.10), using $kR_0 = 9$, $n_c = 3.2$ and $n_o = 1$ ($Z_o = 9$, $Z_c = 28.8$) (black dots) over a symmetrical range of m. The green continuous line indicates the envelop trends given by Eqs. (3.121) and (3.122) for the corresponding domain of application; origin at $m = 0$ for Eq. (3.121), origin at $m = \pm Z_c$ for Eq. (3.122). (b) Evaluation of $|S^{(1)}_{mm'}|$ along the column $m' = 20$ for the circular inclusion cavity, $n_h = 1$ and $d/R_0 = 0.5$. The diagonal term $|S^{(1)}_{m'm'}|$ is highlighted by a red circle. Notice the ridge region, $|m| < Z_o$, having a larger scattering amplitude than terms located near the diagonal component at $m = 20$. 106

3.7 Mapping of $|\Delta_m|^{-1}|\Delta_{m'}|^{-1}$ (a) from analytical considerations, Eqs. (3.120) and (3.121), and (b) from exact evaluation, Eq. (3.10). The parameters are the same as the ones used on Fig. 3.6. The color gradient in (b) scales with the logarithm of $|\Delta_m|^{-1}|\Delta_{m'}|^{-1}$. Note the *ridges* in regions with $|\nu| < Z_o$ and $|\nu'| > Z_o$ where $\nu = \{m, m'\}$ and $\nu' = \{m', m\}$. . . . 107

3.8 Schematic representation of the removal of degeneracy due to perturbation in the delay spectrum. (a) Splitting of a resonant mode (left spectrum) into even and odd modes relative to an appropriate symmetry axis (right spectrum). The light pink line on the right picture indicates the position of the former unperturbed degenerate resonant peak. (b) Splitting of two resonant modes (left spectrum) into even and odd modes relative to an appropriate common symmetry axis (right spectrum). The close-up view of the accidental crossing between modes with angular momentum m_0 and $m_0{}'$ reveals avoided-crossings between the delay levels of modes of same symmetry. Note that the "pure" m_{0a} (m_{0b}) and m'_{0a} (m'_{0b}) modes follow *diabatic* levels (discontinuous lines) that cross over the gap between *adiabatic* levels (continuous lines): there is a modal character exchange along an adiabatic level going left to right. Consequently, the modes of a given symmetry rearrange themselves in two orthogonal combinations as they go through the avoided-crossing. . 110

3.9 Complete phase factor $\theta_{m_{0a}} = -\theta^{(0)}_{m_{0a}} + \theta^{(1)}_{m_{0a}}(\epsilon)$ (dark red curve) near resonance $(18, 7)$ at $k_{(18,7)}R_0 \simeq 13.8916$ for the disc cavity + inclusion corresponding to the physical setup $n_c = 3.2$, $n_o = 1$, $n_h = 1$, $R_0 = 1$, $d/R_0 = 0.81$ and $\epsilon = 0.01$. The individual terms $-\theta^{(0)}_{m_{0a}}$ (black) and $\theta^{(1)}_{m_{0a}}(\epsilon)$ (blue) add up to move the resulting curve (dark red) toward larger k values. The length and direction of the blue arrows are obtained by the evaluation of $\theta^{(1)}_{m_{0a}}(\epsilon)$. Note the large phase change as the wavenumber goes through the resonance, almost by 2π, with the inflexion position around a phase shift of π [88]. See Fig. 3.10 for the corresponding delay spectrum. 111

3.10 Delay spectrum of the disc cavity even mode $(18, 7)$ found at $k_{(18,7)}R_0 \simeq 13.8916$ for $\epsilon = 0$ (unperturbed reference, black) and the inclusion scenario $\epsilon = 0.01$ (red, $d/R_0 = 0.81$; orange, $d/R_0 = 0.90$). (a) exact computation from the analytical model of Appendix D and (b) perturbation method of this Chapter (perturbation of the **S** matrix *and* eigenvalues obtained from perturbation theory). The lateral motion of the peaks is mostly determined by the $q^{(1)}_{m_{0a}}$ factor while most of the amplitude decay is due to the normalization factor $1 + (\eta\beta_{m_{0a}})^2$ $(\eta = 1)$. 112

3.11 Radial cut of the wavefunction $\left|\psi^{(0)}_{m_0=18}\right|^2$, Eq. (3.6), near the resonance at $k_{(18,7)}R_0 \simeq 13.8916$ and the corresponding effective potential (see Introduction, Chapter 1). Note the decaying portion of the field inside the semi-classical caustic radius $m_0/n_c k \simeq 0.401R_0$. 113

3.12 Coefficients $\left|A^{(1)}_m\right|^2$ $(\epsilon = 1)$ for $d/R_0 = 0.28$ (dark red), $d/R_0 = 0.33$ (dark orange) and $d/R_0 = 0.38$ (orange). Main channel $|m_0| = 18$ is indicated by thicker line and hollow marker. Physical parameters are the same as those used in Fig. 3.9. The evaluation is performed at the resonance maximum delay value of the perturbed $(18, 7)$ even mode. 114

4.1 The parametric perturbations of the disc cavity investigated in this Chapter are of two types: (a) inclusion displacement and (b) inclusion growth. In the second scenario, the inclusion radius r_0 is increased while the distance $d + r_0$ remains constant. This type of deformation is suggested from the results of the first parametric study. 118

4.2 Separation of the matrix $\mathbf{S}^{(1)}$ with regards to the respective contributions of $\Delta_m^{-1}\Delta_{m'}^{-1}$ and $J_m(n_c kd)J_{m'}(n_c kd)$. The colored areas are associated with the definitions found in Fig. 3.7(a), and the hatched areas indicate the domain of applicability of the oscillatory behavior of $J_m(Z_d)$ (single hatched: oscillatory on lines (columns), exponential decay on columns (lines); double hatched: oscillatory over lines and columns). As the inclusion position d is increased from (a) to (b), the underlying ridge region ($|m| < Z_o$) becomes completely covered by the non-decreasing terms. Given a line (or column) $m = m_0$ and $Z_c > |m_0| > Z_o$, not only is the ridge region becoming exponentially stronger with increasing d (see Eq. (A.51)), but also many more channels are being included with significant amplitude. The broadening eventually stops as Z_d reaches Z_o ($d/R_0 = n_o/n_c$): the d independent exponential decrease in m due to $\Delta_{m_0}^{-1}\Delta_m^{-1}$ remains the dominant behaviour in the region $|m| > Z_o$. . . . 121

4.3 Numerical evaluation of the line $S^{(1)}_{m_0 m}$, $m_0 = 11$, for different values of d/R_0: $n_c = 3.2$, $n_o = n_h = 1$, $kR_0 = 4.5$ and $R_0 = 1$. The vertical gray lines bound the oscillatory regime of Δ_m^{-1} (maximum size of the ridge, $\pm Z_o = \pm n_o kR_0$). The ridge domain grows in size with d until $d/R_0 = n_o/n_c$ is reached. Then a monotonic exponential increase of the whole structure follows. 122

4.4 Delay spectrum of (a) the homogeneous disc cavity and of (b) the annular cavity with $d/R_0 = 0.388$ and $r_0/R_0 = 0.2$. The red curves represent the delays for the Ox axis odd symmetry mode and the green curves are associated to even symmetry modes. The resonant position of modes $(5, 3)$, $(11, 1)$ and $(8, 2)$ are shown. Note however that in the annular case, these labels have to be understood as a result of an adiabatic parametric follow-up of the disc resonances: in many instances, the effect of the inclusion may be so disruptive that the near-field looses its WGM aspect. 123

4.5 Displacement of the resonant wavenumber position of mode $(11, 1)$ relative to the corresponding one in a disc cavity with a centered ($d = 0$) inclusion. Five inclusion sizes r_0/R_0 are investigated and show similar behaviours as $d + r_0$ increases. The displacement becomes especially strong as $d + r_0$ approaches the caustic radius (dashed vertical line at $\simeq 0.76$). 124

4.6 Resonant delay value of mode $(11, 1)$ relative to the center-to-center distance d for five inclusion sizes r_0/R_0. The premature drop observed for radii $r_0/R_0 = \{0.1,\ 0.2\}$ is explained by a resonant coupling with a secondary mid-size resonance. This topic is discussed in Section 4.3. . . 125

4.7 Evaluation of Eq. (4.2) for mode $(11, 1)$ at $r = R_0$ (blue curve) and $r \to \infty$ (red curve). The gray parametric region has both near-field WGM aspect ($< 1\%$ deviation) and far-field non-uniformity ($> 50\%$). Insets show the near-field ($r = R_0$, inner ring) and the outgoing far-field ($r = \infty$, outer ring) polar distribution of $|\psi(r, \phi)|^2$ for $d/R_0 = \{0.352,\ 0.602,\ 0.85\}$ (respectively, left to right). 126

4.8 Multiple reflections/scatterings description of the annular cavity field. The incoming and outgoing coefficients representation is used for the sake of simplicity. The total field inside the region $R_0' \leq r \leq R_0$ is decomposed as a series of scattering by the internal effective boundary at $r = R_0'$ and reflections by the external boundary at $r = R_0$. 127

4.9 Amplitude of the terms found on the line $m = 11$ of $\mathbf{S}'$ and $\mathbf{S}$; $n_c = 3.2$, $n_h = n_o = 1$, $R_0 = 1$, $d/R_0 = 0.4$, $r_0/R_0 = 0.2$ and $k = 4.499$. The ridge of the perturbation scattering matrix (see Fig. 4.3 for instance) is also found in both internal and external scattering matrix, but appears more asymmetrical in the former case. 128

4.10 Reflection and transmission matrices, Eqs (4.11)-(4.12), versus the semi-classical momentum $p_m = m/Z_c$. The parameters are those of the cavity under investigation $n_c = 3.2$, $n_o = 1$, $k = 4.5$ and $R_0 = 1$. As a base for comparison, the Fresnel reflection coefficient and the total internal reflection (TIR) limit ($p_{\mathrm{TIR}} = n_o/n_c$) are displayed 130

4.11 Close-up view of escape mechanisms within a single round trip. Plain arrows are associated with portions of the field with angular momentum m_0 that remain inside the annular region $R_0' \leq r \leq R_0$. Dashed arrows represent the field that escapes the specific components $|m| = m_0$ of the field either by coupling to other angular channels through internal scattering, or by transmission to the outside. 131

4.12 Transition probability to other angular momenta (red) and transmission probability to the exterior of the physical cavity (blue) according to Eqs (4.15) and (4.16) respectively. Both escape probabilities reach the same value at $(d + r_0)/R_0 \simeq 0.482$: using a particle picture of the system, at this parametric position it is equally probable for a photon to escape mode $(11, 1)$ by regular potential tunneling than it is by coupling to angular momentum components different from m_0. 132

4.13 (a) Delay value for mode $(11, 1)$ with respect to parameter r_0 ($(d + r_0)/R_0 = 0.55$). (b) Contrast measure in the far-field ($r \to \infty$) and in the near-field ($r = R_0$). According to the contrast measure, the near-field WGM aspect is unaffected by the inclusion while the far-field gets strongly modified. Blue circles mark evaluation positions of the far-field patterns of Fig. 4.14. 135

4.14 Normalized far-field profile for three sets of parameters $(d/R_0,\ r_0/R_0)$. 136

4.15 (a) Representation of the canonical coordinates $(s, p = \sin\chi)$ in configuration space and (b) in phase space. The reflection of rays on the exterior boundary is specular while the internal disc inclusion permits transmission according to Fresnel coefficients [29]. Consecutive impact positions on the exterior boundary are recorded in phase space. For clarity, only trajectories within the NR region are displayed. The trajectories in the regular domain have a constant p momentum and would appear as horizontal sequences of markers in phase space. 137

4.16 (a) Limits of the incoming scattered rays by the inclusion in configuration space (red arrows). The outgoing scattered rays (blue arrows) are obtained through time inversion (reversing the arrows) of the incoming trajectories. (b) Dynamical subdomains of phase space $H_{\rm in}$ (dashed blue limits) and $H_{\rm out}$ (plain red limits). Trajectories outside $H_{\rm in}$ keep their momentum p (orange arrows) until they reach $H_{\rm in}$ and exit through $H_{\rm out}$ with a different p value. 139

4.17 Representation of incoming/outgoing waves relative to the external boundary. 141

4.18 Decomposition of the field in a series of iterates. 143

4.19 (a) Representation in phase space of $\left|\left\langle\ \beta_\kappa(s,p)\ \right|\ \psi^{c+,(1),\rm NR}\ \right\rangle\right|^2$ obtained after inner scattering from the initial state $\left|\ \psi^{c-,(1),\rm NR}\ \right\rangle$; $(d+r_0)/R_0 = 0.55$, $r_0/R_0 = 0.165$ and $kR_0 = 4.5$. The classical $H_{\rm out}$ region is shown as well as the $p_{\rm NR}$ limits (straight horizontal lines). The Husimi distribution resulting from the scattering by the inner virtual boundary falls within the $H_{\rm out}$ limits. This is to be compared with (b) where initial conditions inside $H_{\rm in}$ (red dots) and their first iteration to $H_{\rm out}$ (blue dots) are displayed. 144

4.20 Reflection coefficients using the infinite flat interface model (Fresnel), locally curved interface Eq. (4.29) inspired from Snyder and Love (S-L) [136] (curvature radius $\rho = 1$) and modified Fresnel laws for dielectric cavities of Hentschel and Schomerus (H-S) [61] (cavity radius $R_0 = 1$). This illustrative computation is for an incidence medium of refractive index of value 2, a transmission medium of index 1 and a wavenumber $kR_0 = k\rho = 15$. 145

4.21 Positions in phase space of the escaping rays/field from the non-regular region; (a)-(c) Gaussian-smoothed results from ray optics simulations and (b)-(d), outgoing Husimi distributions obtained from wave simulations for the resonant mode $(11, 1)$. The radius of the inclusion r_0 is set to $0.03R_0$ for the top figures and to $0.165R_0$ for the bottom ones, while parameter $d+r_0$ is kept constant at $0.55R_0$. Although classical and wave results appear to agree well on the distribution peaks for parameter value $r_0 = 0.165R_0$ (c)-(d), the same does not seem to hold at a smaller inclusion size (a)-(b). The inability of the wave to resolve the thin $H_{\text{in}}/H_{\text{out}}$ structures may be the cause. Note however that the 'conveyor belt' motion, Fig. 4.16, is easily identified by the sequence of spots in (b): a small inclusion may not cause the field to be strongly diverted into H_{out}, yet, it follows the conveyor belt within this resolving power. 147

4.22 Far-field patterns from the classical simulations discussed in this Section (gray areas) and from numerical wave simulations (black curves) for two of the three sets of parameters $(d/R_0,\ r_0/R_0)$ used in Fig. 4.14. The classical far-fields are obtained by the distribution of 1.3×10^5 emitted trajectories over $N = 200$ angular bins. 148

4.23 Schematics of two coupled oscillators in their harmonic potential. These resonators possess different resonant frequencies, ω_1 and ω_2, different forcing terms, c_1 and c_2, and different environment induced damping coefficients, Γ_1 and Γ_2. 150

4.24 Eigenvalues of $\mathcal{E}$, Eqs. (4.44), for parameters $\Gamma_1/\omega_1 = 10^{-3}$, $\Gamma_2/\omega_1 = 10^{-1}$ and $\kappa/\omega_1^2 = 10^{-2}$, i.e. $|\kappa|^2 = \omega_1^2\Gamma_1\Gamma_2$ and $|\kappa|/\omega_1^2 = 10^{-2} < (\Gamma_1 + \Gamma_2)/2 \simeq 5 \times 10^{-2}$. Thick pale blue and red curves serve as reference to the uncoupled oscillators energy, Eq. (4.43). Two configurations are presented: (a), non-resonant coupling; (b), resonant coupling. Note the color exchange of the $\mathcal{E}_\pm$ curves in (a): this is due to a local avoided crossing inherited from the adiabatic process of obtaining $\mathcal{E}_\pm$. 154

4.25 Components of the eigenvector associated with the eigenvalue $\mathcal{E}_+$ for the resonance cases presented in Fig. 4.24. In both cases, at the uncoupled resonant frequency $\omega = \omega_1$, the forcing is almost completely on the first oscillator. Note the counterpart effect of the avoided crossing on the eigenvector components in (a). 154

4.26 Delay value at the peak of even mode $(11, 1)$. The semi-log graph reveals a premature fall of the delay at $d/R_0 \simeq 0.3$ and a recovery at $d/R_0 \simeq 0.6$ with respect to the monotonous delay spoiling caused by the exponentially increasing amount of field being diverted from angular momentum $m = 11$ to other channels. The markers indicate the positions at which the spectra of Fig. 4.27 are drawn. Also, the expected delay spoiling curve (dashed line) is presented (see Eq. (4.50)). 156

4.27 Spectra for four values of the parameter d. Odd symmetry modes with respect to the Ox axis of the cavity (Fig. 4.1) appear in green, and even symmetry modes appear in red. The peak labeled $(5, 3)$even moves first across the main resonance $(11, 1)$ and nearly returns to its starting position as the parameter d is varied. 157

4.28 (a) Corrected peak value of resonance $(11, 1)$ relative to the homogeneous disc peak value versus the deformation parameter d and (b) peak value of the energy $\mathcal{E}_+$ relative to the uncoupled scenario versus secondary resonance position ω_2. Markers on (a) point to Figs 4.27(b)-(d). Although we do not have direct control over the $(5, 3)$ mode resonant position, we may still force it to move across the mode $(11, 1)$ using the inclusion position d as a control parameter. The resulting effect is similar to that found in the coupled resonators system. 158

4.29 (a) Disc cavity affected by (b) the boundary roughness function $\Delta r(\phi)$. 159

4.30 Spectrum for the disc cavity affected by boundary roughness. The labels 'even' and 'odd' of the peaks follow the indications from perturbation theory which predicts that 'odd' symmetry modes move to lower wavenumbers and 'even' symmetry modes move to higher wavenumbers with respect to the unperturbed disc cavity. Here, $(11, 1)$ 'odd' is found at $kR_0 \simeq 4.4971$ and $(11, 1)$ 'even', at $kR_0 \simeq 4.5010$ (perfect disc: $kR_0 \simeq 4.4989$), and $(8, 2)$ 'odd' is found at $kR_0 \simeq 4.5897$ and $(8, 2)$ 'even', at $kR_0 \simeq 4.5924$ (perfect disc: $kR_0 \simeq 4.5910$). 161

4.31 Outgoing near-field projections at $r = R_0$ for the two 'symmetries' of resonant modes $(11, 1)$ and $(8, 2)$ (see the spectrum on Fig. 4.30). The two 'symmetries' (*even*, blue curves; *odd*, red curves) are seen to intertwine, expressing their quadrature with respect to some effective axis. 162

4.32 Line $m_0 = 11$ of the scattering matrix for the annular cavity and the disc cavity affected by wall roughnesses. We used the scattering matrices located at the resonance position of odd symmetry modes $(11, 1)$. The parameters used for the annular cavity are those of Fig. 4.9. 162

5.1 Schematic representation of the waveguide-cavity coupling. Right-most inset presents a perspective view of the system composed of thin waveguide and cavity arranged in a common plane. The guided field is assumed to originate from a continuous wave (*i.e.* monochromatic) source and is recorded by a perfect detector. The comparison of the input and output power defines a transmission coefficient that is strongly affected by the amount of field diverted by the cavity. This is especially true around resonances of the cavity. 166

5.2 Coordinate system for the description of the evanescent field emanating from the waveguide. 168

5.3 Schematics of the coupled system (cavity + waveguide). Only the electric field is displayed. The domain occupied by the cavity is identified by D_C. 171

5.4 Representation of the input and output envelopes of the guided waves. The $\mathbf{W} = \exp[\mathbf{G}^0]$ matrix is a mathematical representation of the combined waveguide-cavity system as seen from the ends of the waveguide. 175

5.5 Coordinate system for the integration over the contour C (pink rectangle). The normal vectors $\hat{\nu}$ are those of the contributing surfaces of the waveguide in regards of Eq. (5.72). 178

5.6 Excitation cycle of the cavity: forward propagating '+' waves pictured. 1) An initial evanescent field excites the cavity which responds by producing a characteristic field. 2) This field in turn induces a source field in a section dx of the waveguide. 3) At x', the waveguide field is made up of a superposition of induced fields produced 'upstream'; this results in the creation of an effective amplitude $A(x')$. This waveguide field has an evanescent component that excites anew the cavity. Note that the induction phenomenon in step 2) also produces backward propagating '−' waves. These contribute to the reflection coefficient of the waveguide. 183

5.7 Dealy spectrum for a homogeneous disc with parameters of Tab. 5.1. A few resonances are identified (usual notation (m, n), m: angular momentum; n: number of radial nodes). 187

5.8 Test of assumptions (5.34) and (5.36) as a function of x for 3 values of d; $kR_0 \simeq 20.1964$ is the position of the resonance $(26, 1)$. The blue (red) curves are associated with the overlap of the field caused by the interaction with a waveguide mode propagating towards $+\infty$ $(-\infty)$. The values are normalized to that of P and βP, Eq. (5.38), so that the light gray line at a constant value of 1 is the comparison figure. 189

5.9 Test of assumptions (5.97) and (5.98) as a function of x for 3 values of d; $kR_0 \simeq 20.1964$ is the position of the resonance $(26, 1)$. The blue (red) curves are associated with the overlap of the field caused by the interaction with a waveguide mode propagating towards $+\infty$ $(-\infty)$. The values are normalized to that of $\hat{P}$ and $\beta\hat{P}$, Eq. (5.101), so that the light gray line at a constant value of 1 is the comparison figure. 190

5.10 Integrals involved in the expressions (5.44)-(5.47). One notices that the contributions of the integral over χ tot the corresponding element of the matrix $\mathbf{G}^0$ is of the same order of magnitude as the contributions of the related integral over $\kappa_\pm$. 191

5.11 (a) Transmission spectrum $|T(k)|^2$ along a waveguide coupled to an homogeneous cavity. The results for three values of d/R_0 are displayed (blue lines) and the $1 - \mathrm{Tr}\{\mathbf{Q}\}/\max\{\mathrm{Tr}\{\mathbf{Q}\}\}$ value is pictured as well for reference (gray line). The reflection coefficient maximum value for $d/R_0 = 0.1$ is about 10^{-31}. (b) Evaluation of $1 - |T(k)|^2$ on a semi-log graph showing the secondary contributions of modes $(22, 2)$ and $(23, 2)$ nearby the main resonances (see delay spectrum Fig. 5.7). The graph of $\mathrm{Tr}\{\mathbf{Q}\}/\max\{\mathrm{Tr}\{\mathbf{Q}\}\}$ is also illustrated on top of this transmission spectrum to provide a useful comparison figure. 192

6.1 (a) Bending a waveguide around a nearby cavity yields (b) a composite structure inheriting the convenient properties of both dielectric subcomponents. The purpose of the ring cavity is to confine large amounts of energy in a small volume while the inner cavity acts as a transformation unit converting the regular clockwise (CW) and counterclockwise (CCW) rotating near-field components into directional far-field. 201

6.2 Effect of the introduction of an inner boundary on the resonant modes of a disc cavity represented by the effective potential model (see Chapter 1 and [67]). For the disc cavity, $R_0 = 1$, $n_o = 1$ and $n_A = n_B = n_C = 1.5$, and for the ring cavity, $R_0 = 1$, $R_1 = 0.9R_0$, $n_o = 1$, $n_A = 1.5$ and $n_B = n_C = 1$, see Fig. 6.1(b) for the definitions. Under certain combinations of physical parameters such as the one selected here, it may be possible to diminish the low quality modes of the disc cavity (a)-(b) and to retain only their high delay counterparts (c)-(d). 202

6.3 Spectra from the disc and ring cavities. The resonant modes of the disc cavity are forced to settle at different wavenumbers by the ring inner boundary. Given adequate parametric conditions (here $R_0 = 1$, $R_1 = 0.9R_0$, $n_o = 1$, $n_A = 1.5$ and $n_B = n_C = 1$, see Fig. 6.2), the disc spectrum (a) may be modified to leave only the high delay modes to stand out (b). Notice that the peaks of lower quality resonant modes $(25, 2)$, $(26, 2)$, ... do not actually disappear: they are relocated somewhere out of this selected wavenumber window. 203

6.4 (a) Representation of the phase space of the stadium cavity for a set of initial conditions randomly selected inside thin rectangles $[0.95 < |p| < 1] \times [0 \leq \phi \leq 2\pi]$ (4 000 initial conditions). The linear side walls of the stadium have a length of $2r_s$, $r_s = 0.425$ being the radius of its semi-circular sections. Thus, the full length of the stadium is $4r_s$ and its full width is $2r_s$. The refractive index inside the stadium is 1.5 (glass) and 1.0 outside. These values specify the Fresnel reflection coefficient Eq. (4.14) that progressively decreases the circulating intensity I of the trajectories (dark blue: $I = 1$; white: $I = 0$). The green horizontal lines are the TIR limits, $p_{\text{TIR}} = 2/3$. (b) An overview of the near-field corresponding to the phase space (a) is also presented. Notice that the color of the trajectories scales from dark blue to white with the decreasing intensity (normal irradiance over unit area). (c) The classical far-field of the stadium cavity for a set of 40 000 randomly chosen initial conditions. The far-field is built from the distribution of the escaping intensity of all trajectories into 200 far-field angular bins. 204

6.5 (a) Delay spectrum computed for the stadium cavity of Fig. 6.4 alone and (b) delay spectrum of the combined ring and stadium cavity. The geometrical center of the stadium cavity is fixed at the center of the ring cavity. This setup forces the expression of the $Ox - Oy$ symmetry axes of the stadium into the modes of the ring cavity: light blue is $Ox - Oy$=odd-odd (oo), purple is even-even (ee), red is even-odd (eo) and green is odd-even (oe). 205

6.6 (a) A resonant mode of the stadium cavity is found to be dominant in (b)-(c) the near-field of the ring and stadium hybrid cavity mode $(30, 1) - oo$. Figure (c) is produced by masking all but a rectangular section of the field presented in (b). Notice the similarity in the far-field for the stadium and the hybrid cavities (outer ring of (a) and (b)). 207

6.7 Classical far-fields (grey areas) and wave simulated far-fields $|\psi(\infty,\phi)|^2$ (colored lines) for the resonant modes of Fig. 6.5(b) . The color code for the symmetries is the same as the one employed for the spectra. The initial conditions for the classical simulations are selected from the H_{in} domain of phase space with a decreasing gaussian distribution (Husimi distribution of the circulating WGMs) as in Chapter 4. Among the key features of the classical far-field are the 4-points peaks of Fig. 6.4(c) directly inherited from the stadium sub-structure. 208

A.1 Interprétation géométrique des éléments constitutifs du théorème de déplacement de Graf. Cette représentation ne s'applique que lorsque les arguments des fonctions de Bessel sont réels et positifs. 213

A.2 Évaluation numérique de $J_m(x)$ and $Y_m(x)$ pour $m = 3$ et $m = 13$ (trait noir discontinu) et évaluation des développements approximatifs aux grands ordres correspondants: trait plein bleu, $x < m - m^{-1/3}$; trait plein vert, $m-m^{-1/3} < x < m+m^{-1/3}$; trait plein orangé, $m+m^{-1/3} < x$. Les développements aux grands ordres obtenus sont remarquablement précis, même pour $m = 3$. 220

B.1 Distribution de Husimi pour $\kappa = 1$ en amplitude linéairement croissante de jaune à noir, et trajectoire classique dans l'espace des phases pour l'oscillateur harmonique (trait bleu discontinu); $\Delta\hat{q}_\alpha = 1/\sqrt{2}$, $\hbar = 1$. (a) Niveau d'énergie $n = 1$ de l'oscillateur quantique. (b) Niveau d'énergie $n = 10$ de l'oscillateur quantique. 232

B.2 Distribution de Husimi (B.81) pour le niveau $n = 10$ de l'oscillateur harmonique. (a) Distribution comprimée sur q ($\Delta\hat{q}_\beta = 1/\sqrt{42} \cdot \Delta\hat{q}_\alpha = 1/\sqrt{84} \approx 0.11$, $\Delta\hat{p}_\beta \approx 4.58$). (b) Distribution comprimée sur p ($\Delta\hat{p}_\beta = 1/\sqrt{42} \cdot \Delta\hat{p}_\alpha = 1/\sqrt{84} \approx 0.11$, $\Delta\hat{q}_\beta \approx 4.58$). 232

B.3 Coupe à $p = 0$ de la distribution de Husimi présentée à la figure B.2(a) et fonction d'onde $|\psi_{10}(q)|^2$ de l'oscillateur harmonique. Les courbes sont normalisées à leur valeur maximale respective. Une coupe semblable peut être obtenue pour la distribution en p. 233

C.1 (a) Représentation schématique de la séparation de la surface de la cavité en domaines annulaires. L'indice de réfraction constant à l'intérieur du disque intérieur est n_{in} et à l'extérieur, n_o. Notez que le rayon intérieur r_0 est situé à ϵ (et non 2ϵ) du rayon r_1, tout comme le rayon $R_{\max}$ par rapport à r_N. (b) Coefficients de développement $\mathbf{a}^j$ et $\mathbf{b}^j$ sur des couches successives. 238

D.1 (a) L'objet de cette section est de transformer une fonction d'onde décrite par rapport à une origine en O' et connue à l'extérieur d'un domaine circulaire D', en une nouvelle forme possédant des coordonnées centrées sur l'origine O. On cherchera donc à écrire les coefficients $\mathbf{A}$ et $\mathbf{B}$ des ondes partielles valides à l'extérieur d'un disque D en fonction des coefficients $\mathbf{A}'$ et $\mathbf{B}'$ autour du domaine D'. (b) Construction géométrique de la translation pour $r > d$. 244

D.2 Construction géométrique de la translation pour $r < d$. 246

D.3 (a) Schéma de la cavité annulaire, ses paramètres et coordonnées, et (b) présentation des différents domaines de développement en ondes partielles de la fonction d'onde. Le domaine D_h (disque blanc) d'indice n_h repésente l'inclusion de la cavité annulaire, le domaine D_c (gris sur (a); vert, jaune, bleu et rouge sur (b); indice n_c) est le corps de la cavité et D_o (blanc) est le milieu extérieur (indice n_o). La fonction d'onde peut être développée en ondes partielles sur les coordonnées (ρ, θ) dans les zones jaune et verte et sur (r, ϕ) dans les zones verte, bleue ainsi que sur la totalité de D_o. La zone rouge n'est pas toujours couverte par le développement en ondes partielles entrantes et sortantes autour de l'origine de ces deux systèmes de coordonnées: les paramètres de construction doivent satisfaire (D.37) afin que le développement en ondes partielles recouvre totalement D_c. 251

E.1 Représentation de la section du guide d'onde plan et de l'amplitude du champ. Il s'agit d'une coupe sur le plan $OxOy$ de la plaque diélectrique infinie apparaissant dans le coin supérieur droit de la Fig. 254

E.2 (a) Solution graphique du système d'équations (E.3)-(E.5): en bleu, Eq. (E.3) pour les différents modes du guide et en rouge, l'espression de la conservation du nombre d'onde Eq. (E.5) pour $v = 4$. Les modes TE sont représentés en traits continus et les modes TM, en traits discontinus. Un espace paramétrique continu d'indices de réfraction, de nombres d'onde et d'épaisseurs de guide satisfont cette égalité. Dans ce cas d'espèce, le guide supporte trois modes propagatoires et le mode TM est calculé pour un ratio d'indices $n_o/n_g = 2/3$. (b) Solution du système d'équations (E.3)-(E.5) pour un intervalle de v allant de 0 jusqu'à la fréquence de coupure du mode $j = 1$ pour les deux polarisations (TE: trait continu; TM: trait discontinu, $n_o/n_g = 2/3$). On obtient ainsi les solutions s (rouge) et u (bleu) pour le guide monomode. La ligne verte est le résultat de $\sqrt{u^2 + s^2}$, soit v. 255

E.3 Indice effectif tel que défini par Eq. (E.8) en fonction de l'épaisseur normalisée au nombre d'onde pour le premier mode (TE: trait continu; TM: trait discontinu). Les constantes utilisées sont $n_g = 1.5$ (verre), $n_o = 1.0$ et $k = 1$. L'indice effectif pour une épaisseur nulle est n_o, mais n'atteint qu'asymptotiquement la valeur n_g pour un guide infiniment épais. 256
E.4 Parcours C' de la représentation (E.9) de la fonction de Hankel $H^{(1)}(z)$; $\theta = u + iv$. 257
E.5 Parcours C' modifié en fonction de l'expression (E.10). 258
E.6 Convention de coordonnées pour le développement asymptotique de l'intégrale (E.19). 260
E.7 $\log_{10}(\text{Err})$ en fonction de $\log_{10}(\eta_0)$. Une régression linéaire a été calculée. La pente obtenue est de -2.3 ce qui est plus élevé que prévu par le développement asymptotique (~ -1.5). Nous n'avons pas poussé l'investigation plus loin mais il se peut qu'une symétrie dans l'intégrale du terme d'ordre $-(2+1/2)$ augmente la convergence en η_0. Un résultat semblable a été obtenu pour $m = 3$ (pente ~ -2.5). Il faut probablement voir $\mathcal{O}(|\eta|^{-(1+1/2)})$ comme une borne supérieure. 263
E.8 Convention des coordonnées polaires locales autour des points $z = \{\pm i\}$. 265
E.9 Parcours d'intégration pour $f_+(z)$ et $\tilde{f}_+(z)$. 267
E.10 Parcours d'intégration pour $f_-(z)$ et $\tilde{f}_-(z)$. 268
E.11 Parcours d'intégration C composé des segments droits C_+ et C_- ainsi que des arcs de cercle C_r et C_R d'angle $\theta_0/2$ centrés sur l'origine. On considère C_R dans sa limite à l'infini. 269
E.12 Convergence de I_5 et I_6 en fonction de $\xi = \kappa\tilde{x}$ pour deux valeurs de m. Les traits bleus continus sont associés à I_{50} et I_{60} alors que les traits bleus discontinus correspondent aux termes correctifs ϵ_5 et ϵ_6. La ligne verte verticale indique la position $\xi = m$. 274

F.1 Représentation des positions de la source $\mathbf{r}'$ et du point d'observation $\mathbf{r}$ des six cas de fonction de Green pour le disque homogène (disque gris). Sous échange des positions $\mathbf{r}$ et $\mathbf{r}'$, les situations présentées aux figures (a) et (b), et (c) et (d) sont équivalentes pour les fonctions de Green. La même équivalence peut être établie entre $G_{co}(\mathbf{r}, \mathbf{r}')$, (e), et $G_{oc}(\mathbf{r}, \mathbf{r}')$, (f). 280

List of Tables

1 Notation for coordinates. xxxvii

2 Notation for common operators. xxxvii

3 Matrix and vectors. xxxvii

4 Notation for common special functions. See Appendix A. xxxviii

5 Notation for physical quantities. xxxviii

1.1 Comparison of some of the resonances for the homogeneous disc ($n_c = 1.5$, $n_o = 1.0$, $R_0 = 1$) as determined by the computation of the poles of the **S** matrix, problem (1.64), and from the **Q** matrix, maximization of (1.63). All digits are kept up to the last two disagreeing significant digits. Numerical resolution is 10^{-12} on the wavenumber value for the pole search and peak maximization. 29

1.2 Comparison of exact peak position of selected resonances from the delay matrix and solutions of the semi-classical approximation Eq. (1.101) for the disc cavity of radius $R_0 = 1$ and refractive index $n_c = 1.5$ and $n_o = 1.0$. The decreasing relative difference from $m = 21$ to $m = 31$ for a given j is expected from the semi-classical approximation. 39

2.1 The mode symmetries of the square cavity. Note that the parity of degenerate modes $1a$ and $1b$ is indicative only: because of the degeneracy, any linear combinations of these modes, at a common wavenumber, are acceptable. Most of these linear combinations result however in a field not having the expected symmetry axis of the square cavity. 58

2.2 Comparison of resonant wavenumber positions for the modes displayed in Fig. 2.18; numbers in parentheses belong to the characteristic modes description and the bracketed digits indicate the uncertainty on the last digit (stepsize of k). The label e/o stands for even or odd parity with respect to the Ox axis. The equivalent of the 'imaginary part' of the wavenumber in the case of characteristic modes is calculated using relation $2R_0/c\tau$. The total delay is composed of an entrance delay and of an escape delay; for characteristic modes, because of incoming/outgoing symmetry, these are of the same magnitude, hence the factor 2. See Eq. (2.33) and the associated discussion for further explanations using Simonius' model. 79

5.1 Physical parameters of the coupled cavity-waveguide system. 186
5.2 Waveguide physical constants. 186

6.1 Summary of the computed resonant delays for the hybrid ring+stadium cavity Fig. 6.5(b) *vs* the plain ring cavity 6.3(b). Values in parentheses indicate the results for the corresponding symmetries. The overall variation of the peak delays caused by the stadium cavity is approximately $60 - 70\%$ of the nominal ring cavity resonant delays. Notice that the modes having an even m_0 number separate into $(Ox - Oy)$ even-even and odd-odd symmetries and that the modes having an odd m_0 number separate into even-odd and odd-even symmetries. This is a consequence of the number of times it may be possible for a given m_0 to separate both the nodes and extrema (minima and maxima) of the ring field distribution with respect to the symmetry axes imposed by the inner scatterer. 206

Notation

Character	Description
r, ϕ	Polar coordinates
x, y, z	Cartesian coordinates
t	Time

Tab. 1 Notation for coordinates.

Character	Description
$\cdot$	Scalar product
$\times$	Vector product
$\frac{df(\eta)}{d\eta} = f'(\eta)$	Shorthand notation for the derivative; Depending on the context, the $'$ notation may be used on constants to denote different values attributed to a unique character. For instance, m and m' for two different angular momenta.
$\nabla\cdot$	Divergence operator
$\nabla\times$	Curl operator
∇^2	Laplacian operator

Tab. 2 Notation for common operators.

Character	Description
$\mathbf{v}$	Vector (lower case bold unless stated otherwise)
$\mathbf{M}$	Matrix (upper case bold unless stated otherwise)
v_j	Component j of vector $\mathbf{v}$
$M_{jj'}$	Component on line j column j' of matrix $\mathbf{M}$
$\hat{v}$	Unit length vector for coordinate v; When specified, $\hat{}$ notation may also refer to an abstract operator
$\vert \quad \rangle$	Abstract vector notation for a function; uses same algebra as in quantum mechanics [36]

Tab. 3 Matrix and vectors.

Character	Description
$J_\nu(\eta)$	Bessel function of the first kind of order ν
$Y_\nu(\eta)$	Bessel function of the second kind (Neumann function) of order ν
$H_\nu^{(1)}(\eta)$	Hankel function of the first kind of order ν
$H_\nu^{(2)}(\eta)$	Hankel function of the second kind of order ν

Tab. 4 Notation for common special functions. See Appendix A.

Character	Description
ϵ_0	Vacuum permittivity
μ_0	Vacuum permeability
c	Speed of light in vacuum, $c = 1/\sqrt{\mu_0\epsilon_0}$
$\mathbf{E}$	Electric field (vector)
$\mathbf{H}$	Magnetic field density (vector)
ψ	Wavefunction, E_z or H_z (scalar)
n	Refractive index
k	Wavenumber
ω	Angular frequency
τ	Delay, lifetime
m	Quantized angular momentum
$\mathbf{S}$	Scattering matrix
$\mathbf{Q}$	Delay matrix
$\mathbf{A}$	Vector of incoming coefficients for ψ outside the cavity
$\mathbf{B}$	Vector of outgoing coefficients for ψ outside the cavity

Tab. 5 Notation for physical quantities.

Angular momentum m arrangement of matrix $\mathbf{U}$ with matrix element $U_{mm'}$:

$$\mathbf{U} = \begin{array}{c} \\ m \\ \end{array} \begin{array}{c} \begin{array}{ccccc} \multicolumn{5}{c}{m'} \\ + & & 0 & & - \end{array} \\ \begin{pmatrix} \ddots & & & & & \\ & U_{+2,+2} & U_{+2,+1} & U_{+2,0} & U_{+2,-1} & U_{+2,-2} \\ & U_{+1,+2} & U_{+1,+1} & U_{+1,0} & U_{+1,-1} & U_{+1,-2} \\ & U_{0,+2} & U_{0,+1} & U_{0,0} & U_{0,-1} & U_{0,-2} \\ & U_{-1,+2} & U_{-1,+1} & U_{-1,0} & U_{-1,-1} & U_{-1,-2} \\ & U_{-2,+2} & U_{-2,+1} & U_{-2,0} & U_{-2,-1} & U_{-2,-2} \\ & & & & & \ddots \end{pmatrix} \end{array} \begin{array}{l} + \\ 0 \\ - \end{array}$$

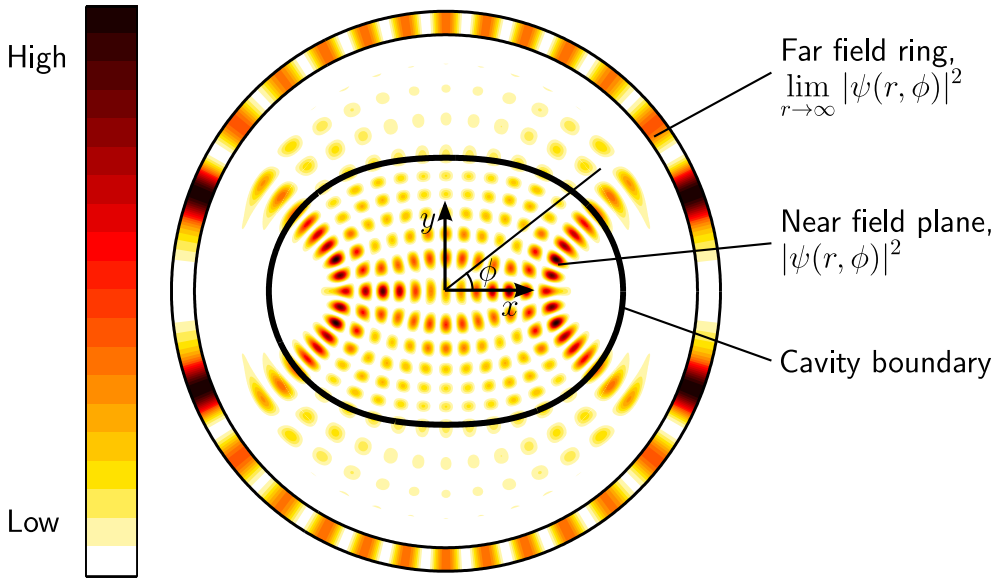


Fig. 1 Description of the field display. The far-field is depicted as a ring surrounding the near field of the cavity. The amplitude increases with the color scale from light yellow to dark brown.

After long months of ceaseless anxiety and strain, after times when hope beat high and times when the outlook was black indeed, the end of the Endurance has come. But though we have been compelled to abandon the ship, which is crushed beyond all hope of ever being righted, we are alive and well, and we have stores and equipment for the task that lies before us. The task is to reach land with all the members of the Expedition.

Sir Ernest Shackleton,

Alors que le sort de l'*Endurance* est scellé par la poussée de la banquise de la mer de Weddell et qu'une longue marche à travers le désert de glaces s'annonce. Extrait tiré de *South: The Last Antarctic Expedition of Shackleton and the Endurance*, Lyons Press, 1998

Chapter 1

Introduction

This Chapter introduces the scope of this thesis within the framework of the study of optical dielectric microcavities. The derivation of the main partial differential equation - the scalar Helmholtz wave equation - is obtained through a series of hypotheses on the electromagnetic field and on the media in which it stands. The solution for the homogeneous disc cavity is presented and interpreted through an effective potential model and semi-classical physics.

The technological capacity to produce nano and micrometer-sized glass or silicon structures offers great promises as to the implantation of *microcavities* in modern visible and near infrared optical devices. The distinguishing property of these resonators to accumulate extremely large amounts of field within a small volume makes them candidates of choice in technological applications such as low threshold lasers [64, 137, 162] and high quality sensors [7, 6, 43, 110, 114, 151, 152, 156, 170, 169]. Moreover, it appears feasible to arrange many of these microstructures in 'macro' devices that allow for multiplexing through evanescent coupling with a multitude of thin on-chip waveguides. This in turn may yield simultaneous multi-diagnostic bio-sensor [80, 153, 157] or possible multidirectional gyroscope devices [138, 141, 142] that possess a small footprint, have a low energy consumption, and allow for redundancy and environmental monitoring (for instance, measurements of various parameters such as temperature changes [78]). These combined advantages improve the overall reliability of the device. Keeping these technological advances in sight, the thematic of electromagnetic (quasi-) two-dimensional cavities will constitute the subject of the present work.

One topic that seems especially elusive concerning two-dimensional cavities is the far-field directionality *versus* high quality (HQ) mode duality. On the one hand, highly

directional modes in the far-field usually have poor quality factor (the stadium cavity for instance [47, 46]), and on the other hand, high quality modes often have uniform far fields (the disc cavity for instance, see section 1.3 on this topic). Early attempts to mix these properties together involved the geometrical deformation of disc cavities. The quadrupolar deformation is emblematic of these Asymmetric Resonant Cavities (ARCs) [89]. While recent publications indicate great success in achieving high directional/high quality modes [155], at the time I started working on the subject even the present gold-standard numerical method for solving the homogeneous 'open cavity problem' had just been published [158]. With this goal in mind, it was proposed to control the output far-field of a disc cavity through the continuous deformation of its bulk refractive index instead of its boundary shape. A ray optics model of the *inhomogeneous* refractive index cavity had already been developed and it would serve as a guide for the investigation [122].

This physical system raised the issue of solving the wave equation - the 'open' Helmholtz equation - over a volume of refractive index that is not necessarily defined in piecewise sections of constant value. Furthermore, the usual description of the *resonant behaviour* of an object teaches us to look for *emission modes* [88]. These modes are divergent solutions of the wave equation with a discrete resonant wavenumber k located in the complex k-plane: the real part is associated with the oscillating, propagating component, and the imaginary part is proportional to the *inverse* of a resonant mode's lifetime. The emission modes description of the cavity provides an intuitive representation of open systems such as lasers in regards to their contain-and-release behaviour.

However, the mainstream technique of boundary integral equations implemented through the Boundary Element Method (BEM) [159] relies on a piece-wise free-space Green function to solve the Helmholtz equation. Therefore, it cannot be adapted in a straightforward manner to our scenario of inhomogeneous refractive index: the preliminary computation of a non-free Green function adapted to the continuous refractive index variation of our matter appeared to defeat the usefulness of the BEM approach. It then came to our attention that a numerical method exactly suited to solve Helmholtz equation over an inhomogeneous refractive index surface existed [112, 113], but only for real wavenumber values[1]. Although the method gives a numerical approximation of the *scattering matrix* $\mathbf{S}(k)$, it does not permit the exploration of the complex wavenumber k-plane in order to obtain its poles, *i.e* the singular solutions to the wave equation needed for the emission modes description of the cavity.

[1]The numerical method demands that the field over a thin annulus covering part of the cavity be expanded over a complete orthogonal basis of functions. The condition on reality of the wavenumber ensures that such a basis exists. An adaptation of the method is presented in Chapter 2, with further details in Appendix C.

To get around this issue, the authors of [112, 113] make use of the trace of *Smith's delay matrix* $\mathbf{Q}$ [135]. Most of their original study was concerned with the perturbation of the strong resonances of a disc cavity: a look at the trace of the delay matrix near clearly visible peaks (*i.e.* resonant modes with a small imaginary wavenumber close to the real k-line) gives an idea of how the underlying high quality modes of the disc respond to perturbations of the cavity geometry. It remains unclear, however, how to investigate the many other lower quality modes of the disc, if the method is to be adapted to strongly deformed disc cavities, and how exactly to obtain 'something more specific' than a simple average delay line expressing the global behaviour of a cavity. As it turned out, the numerical method designed to solve the problem of inhomogeneous refractive index cavities raised an issue of its own in the form of a somewhat more physical topic concerning the expression on the real-k line of the poles of the scattering matrix.

1.1 Summary of content

The initial motivation of studying inhomogeneous cavities and the apparent incapacity to solve the corresponding wave equation in the complex plane, as usually done for emission modes, led me to seek other ways to express the modes of a cavity on the real-k line. The article by Rahachou and Zozoulenko [113] showed that one promising avenue of investigation would be related to Smith's delay matrix[2].

In Chapter 2, I present a 'bottom-up' development of an electromagnetic energy formalism for the modes of a dielectric cavity. This derivation properly justifies the use of the delay matrix as a central feature of a cavity on the real-k line, and defines a basis of modes that are related to the poles of the scattering matrix. In view of this, this basis of modes is understood to be characteristic of the cavity under study just as are the singular diverging solutions of the wave equation in the complex plane. The numerical method used to solve the problem is also presented with some early results.

Since many results of Chapter 2 were not readily found in the literature, it appeared important to show certain cases where analytical results could be derived in order to confirm the ideas presented. Unfortunately, solvable cases of open cavities are scarce, and, when they exist, they are usually difficult to follow analytically (see Appendix D for instance). This led me to develop a perturbation formalism for the delay matrix of the disc cavity. This subject is addressed in Chapter 3. Along with the general

[2]Notice that the expression of the trace of Smith's delay matrix is also known as Krein's trace formula for the density of states [21, 70].

development of the formalism, two applications are investigated: boundary deformation and dielectric particle inclusion.

As may be understood from Chapter 3, an important feature of the perturbed disc cavity is the contamination of high quality modes of the disc cavity by many lower quality modes. The energy contained in a high quality mode is not only shared with these low quality modes, but also more easily lost through them. This results in a decrease in quality of the high quality modes of the disc cavity to the benefit of many low quality modes. These, in turn, tend to be more directional in the far-field, hence providing the high quality modes some directional features. Among the results of Chapter 3, many are about the disc cavity with a small circular inclusion. This cavity, a perturbed limit of the *annular cavity*, seems appropriate to extend the perturbation results to full numerical computations[3]. The competition between two field emission mechanisms that appear to structure the transition from high quality/low directional modes to high quality/high directional modes lies at the heart of Chapter 4. The Chapter is also complemented with results on the coupling of resonances and boundary roughness.

Throughout this investigation, I remained attached to the experimental realisation of the concepts that were elaborated in the theory. This is the reason why a simple model of the coupling of a cavity with a waveguide was developed. This configuration is often found as a means of simultaneously routing electromagnetic power to a cavity through the input port of the waveguide and measuring events affecting the cavity by the output port of the waveguide. A short discussion on the exact context of application and the model itself are presented in Chapter 5.

The Conclusion 6 of this work presents a necessary summary of the main results obtained throughout the preceding Chapters. The Section 6.1 could prove useful as a reading guide, for the reader as it traces back results and observations to the appropriate figure, equation or text section in the form of a list separated by chapters. The Conclusion also presents some perspectives about the main goal of this work - highly directional high quality cavities - an attempt to tie together some of the results obtained into a single cavity design.

[3]The annular cavity is a kind of inhomogeneous index cavity. The continuously varying refractive index of a disc cavity that was foreseen at the very beginning of my graduate studies appeared in the end to be complicated to realize experimentally. The intended idea was to 'coat' a solid-state 2D cavity with nematic molecules to form a liquid crystal layer that could be manipulated externally to induce specific directional light outputs. This concept was essentially abandoned. From then on, the annular cavity appeared more easily interpretable (the geometrical rays in a continuous inhomogeneous medium are curves which complicates the analysis) and provided many semi-analytical results. The smooth inhomogeneous cavity concept was implemented recently to control the resonance position of a ring resonator [109].

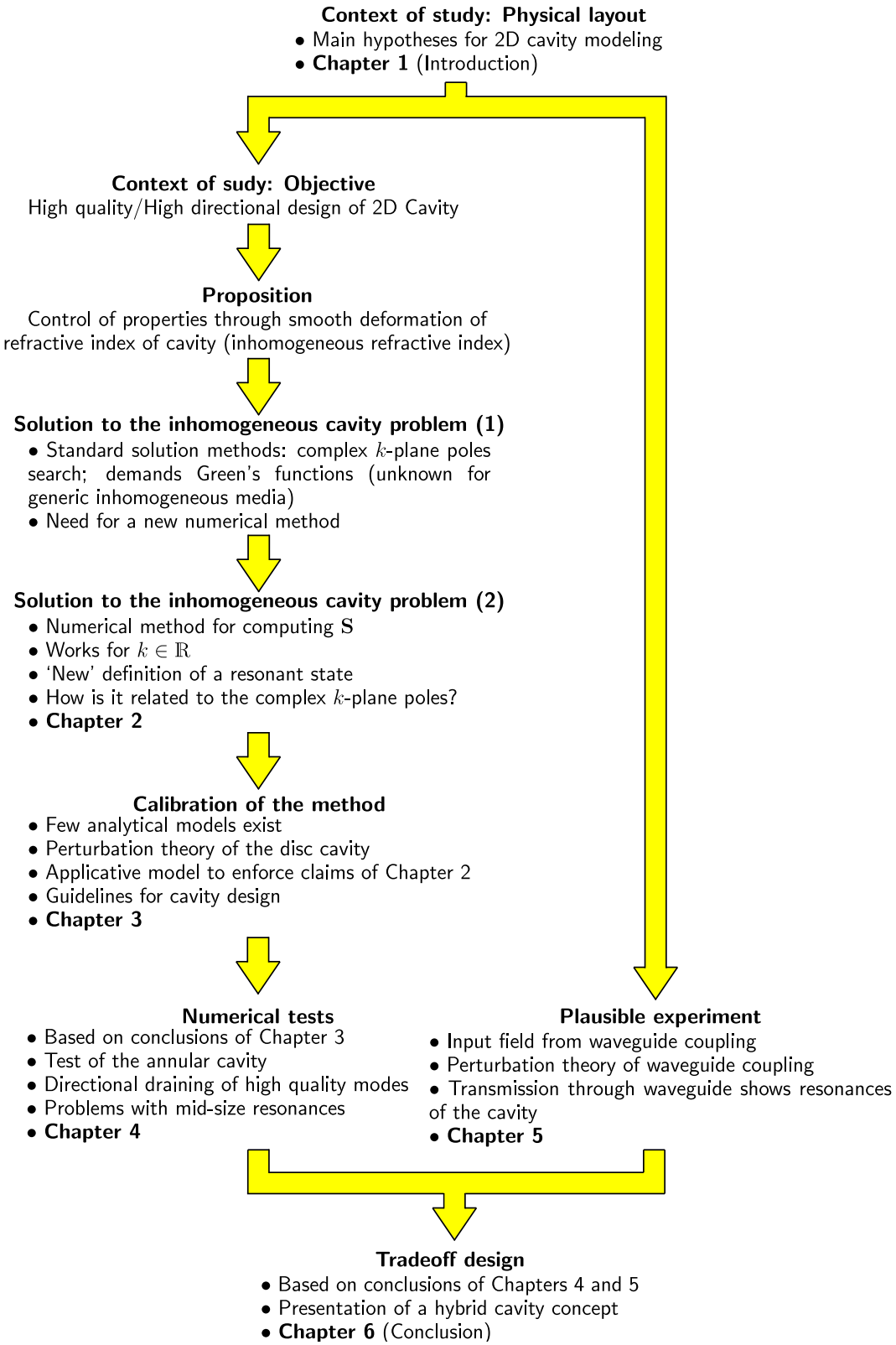


Fig. 1.1 Flow chart of the thesis.

It appears appropriate to define exactly the problem at hand to avoid any ambiguities regarding the results of the coming Chapters. After a short discussion of cavities, the following Section presents a series of hypotheses about the electromagnetic field and the material substrate in which it stands in the context of the study of dielectric microcavities. These hypotheses lead to a wave equation and to characteristic continuity relations for the field. In line with this development, the homogeneous cavity case is discussed as an illustrative application, both in the full wave perspective and in the semi-classical limit. Although of great simplicity, the results derived for the homogeneous disc cavity will often be recalled throughout this work.

The flow chart of the thesis is presented in Fig. 1.1.

Although the peer-reviewed publication output of my work is small, I stress that many ideas and results presented in this thesis are novel and original. This is to be understood from the literature review standpoint of early 2011, at which point my scientific involvement declined sharply due to higher priority external obligations. Some topics presented in this thesis were reviewed as part of conference proceedings: the description of the cavity through a scattering formalism with emphasis on the delay matrix as a central object of interest [95] (Chapter 2 of this thesis), the competition of escape mechanisms from an annular cavity [101] and the use of specific areas of phase space to predict far-field emission of an annular cavity [106] (Chapter 4 of this thesis). These and other unpublished results were presented as part of original contributions to scientific conferences: ICTON 2013 [96], WOMA 2011 [94], ICTON 2010 [100, 105], SIAM Conference on dynamical systems 2009 [99, 98], CAP Conference 2008 [102, 97] and SIAM Conference on dynamical systems 2007 [123, 103]. This thesis is built around the manuscripts of four articles -one for Chapter 2, one for Chapter 3, and two for Chapter 4- that were intended for publication as contributions in peer-reviewed journals. These never entered an internal reviewing process within the research group and I abandoned the idea of having them published within a reasonable time window for the benefit of higher priority issues.

1.2 Preliminary considerations

This Section introduces the two-dimensional cavity model for electromagnetic waves. A short discussion of the different aspects of 2D cavities is followed by the derivation of the main mathematical equations modeling the electromagnetic field interaction with dielectric cavities. The relevant expressions are then applied to the homogeneous disc cavity.

1.2.1 A short discussion of cavities

The last quarter of century has seen the rise of integrated micro-optics as a new technological paradigm [8, 87]. Amongst the key components that are especially coveted are *micro-resonators* (or *micro-cavities*) [163], small structures that can efficiently concentrate light in a finite volume at specific wavelengths. Although all physical resonators are three-dimensional, certain combinations of cavity material distribution and wavelength bandwidth reduce the effective number of degrees of freedom of the trapped light field. In turn, the dimensionality or geometry of the physical cavity is reduced as well. Linear resonators formed by stacks of different materials ('Bragg reflectors') may be considered one-dimensional (e.g. the Vertical Cavity Surface-Emitting Laser (VCSEL) [71]; Fig. 1.2(a)), thin planar slabs of material form 2D resonators Fig. 1.2(b), and highly symmetrical 3D structures, including the extremely high quality microspheres [150], may confine the light field into an equatorial plane [30, 137], Fig. 1.2(c). Resonators made out of plain dielectric material like the discs of Fig. 1.2(b) or the spheres of Fig. 1.2(c) rely on partial reflections of the circulating field at the media discontinuity (e.g. air-silica boundary) to retain the electromagnetic energy, see inset of Fig. 1.2(b).

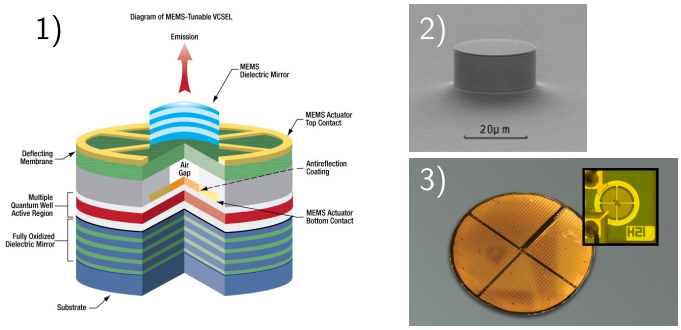
Two-dimensional cavities hold a special place in this classification since they represent *open* versions of well studied *quantum billiards*. It is observed that the level-spacing statistics of quantum billiards, or *closed cavities*, share common features with equivalent measurements done on certain nuclear and atomic reactions (see [117] for instance). In turn, the particular level-spacing statistics of closed cavities would appear to be related to the dynamics of their *classical billiard* counterpart, especially regarding their chaotic dynamical features [48, 79, 84, 108, 166, 167]. Because of similar statistical behaviours, quantum billiards provide a model for more complex physical systems in regards to wave-particle dualism in the less intuitive entrenchment of classical mechanics [59, 52, 139, 51, 20].

The quantum billiards themselves are finite ideal 2D domains where the Helmholtz wave equation is solved as a Dirichlet problem for the field distribution $\psi(\mathbf{r})$ [4] (see [83, 154, 65] for some published results),

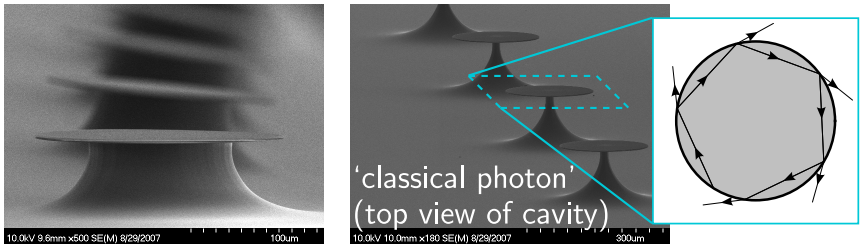
$$\nabla^2\psi(\mathbf{r};k) + k^2\psi(\mathbf{r};k) = 0 \ , \ \psi(\mathbf{r}=\mathbf{r}_{\mathrm{bnd}}) = 0 \quad . \tag{1.1}$$

This system is an eigenvalue problem whose solutions $\{\psi_j(\mathbf{r};k)\}$ form a discrete spectrum of real wavenumber values $k = \{k_j\}$, Fig. 1.3.

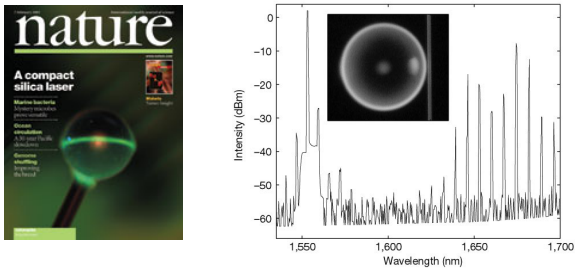
[4] The Helmholtz equation is found in many areas of physics. It is the monochromatic scalar wave equation commonly found in quantum mechanics [36], electromagnetics [29] and acoustics [72] for instance.



(a) 1D cavity



(b) 2D cavity



(c) 3D cavity

Fig. 1.2 (a) Left: Principle of action of a tunable VCSEL (Thor Labs www.thorlabs.com); Upper right: Scanning Electron Microscope (SEM) rendition of a VCSEL (Ferdinand-Braun Institut www.fbh-berlin.com); Lower right: Array of VCSELs on a single wafer (Thor Labs). (b) SEM rendition of silica micro-discs on their support pilar, S. Saïdi and Y.-A. Peter, École Polytechnique de Montréal 2009. Right inset: The trapped light field is reflected at the media discontinuity. (c) Left: A laser microsphere makes the front cover of the Nature issue of February 2002, S. M. Spillane *et al.* [137]. Right: The laser microsphere spectrum.

The classical counterpart of quantum billiards, simply *billiards*, are enclosures where the free-moving, yet trapped, point particles obey specular reflection at the boundaries [14]. The correspondence between quantum and classical billiards from a mathematical equations perspective is revealed by letting the wavelength λ appearing in Helmholtz's equation (1.1) through the wavenumber $k = 2\pi/\lambda$ become very small with respect to the characteristic length scale l of the cavity $\lambda \ll l$. An acceptable characteristic length might be the average radius of the cavity. The small wavelength limit paves the way toward the geometrical 'ray' optics. The underlying dynamical system of bouncing light

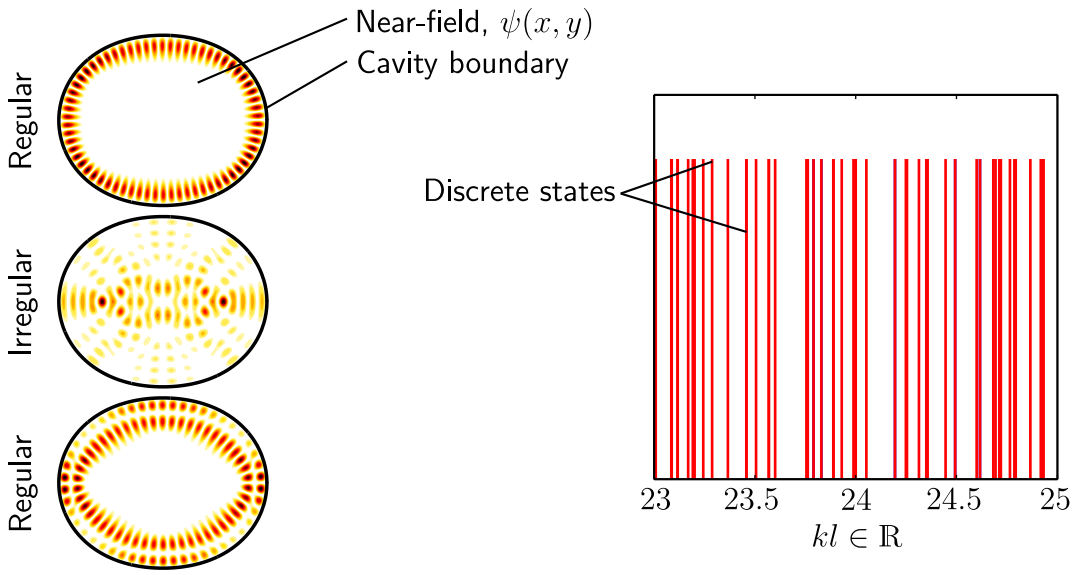


Fig. 1.3 Left: Some eigenfunctions $\psi_j(\mathbf{r})$ that solve problem (1.1) for a quadripolar deformation of the disc. The boundary of this specific cavity is defined by the radial function $r_{\rm bnd}(\phi) = R_0(1 + \epsilon\cos 2\phi)$ with respect to polar angle ϕ and numerical values $R_0 = 1$ and $\epsilon = 0.1$. The labels 'regular' and 'irregular' attributed to each modes refer to trajectories found in the classical billiard picture, Fig. 1.4. The eigenfunctions shown here have eigen-wavenumber values pertaining to the discrete spectrum $k = \{k_j\}$ presented to the right. The non-dimensional abscissa of the spectrum is in kl units where l is the mean radius of the cavity ($l = R_0 = 1$).

particles falls within the hamiltonian formalism [89], and the motion of the captive rays for a certain billiard geometry defines the overall dynamical category that this geometry pertains to. A useful representation of the dynamics of billiards is provided by the *phase space*. Technically, the phase space of billiards - or more precisely, the Poincaré section of phase space - is built from the record of impact positions and incident angles on the cavity boundary for many different trajectories [14], Fig. 1.4.

While some billiard geometries are fully integrable[5] almost all of them show a certain amount of random-looking trajectories resulting from the presence of hamiltonian chaos [93]. Extreme cases such as the stadium cavity [33] are completely chaotic, and intermediate scenarios like the quadripolar deformed disc [14, 89, 126] present both chaotic and regular trajectories, Fig. 1.4. These billiards, mixed-dynamics billiards, show a phase space with both regular dynamics domains (regular 'islands') and a chaotic sea.

[5]In an integrable hamiltonian system, there are as many constants of motion as there are degrees of freedom [93]. For billiards, besides the circular cavity, the prominent member of this dynamical class is the elliptic cavity. Apart from energy conservation, this cavity supports trajectories that keep constant their angular momentum with respect to the foci of the ellipse [89].

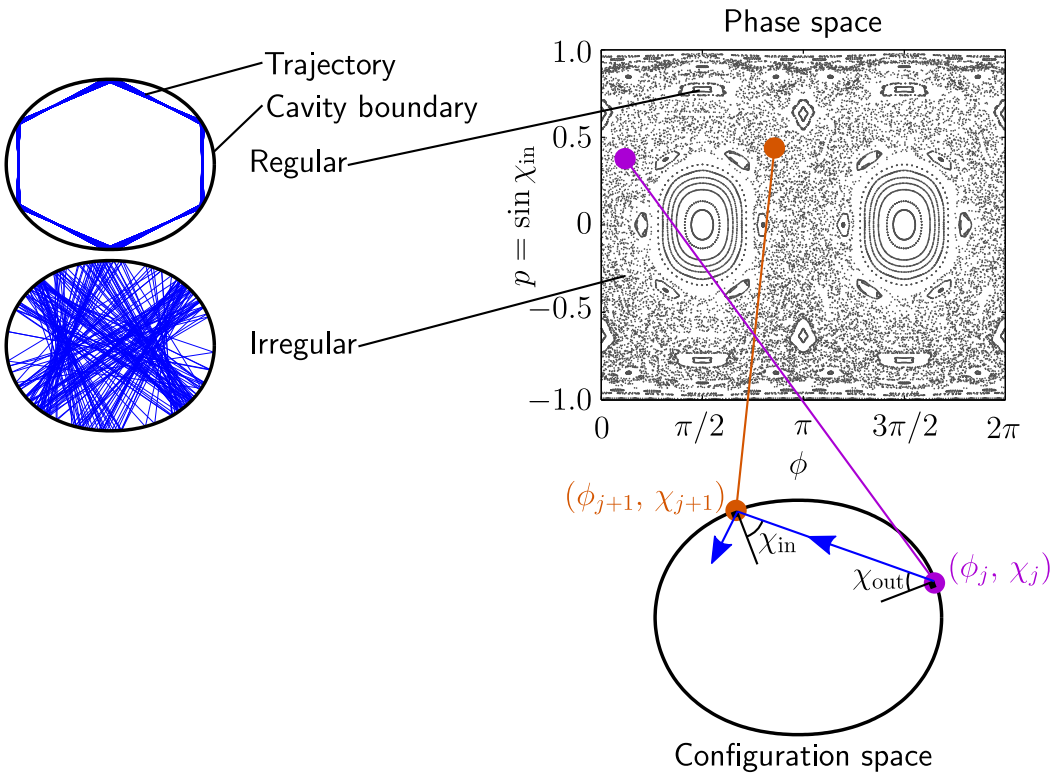


Fig. 1.4 Classical trajectories of the quadripole billiard. The cavity geometry is the same as the one of Fig. 1.3. Typical regular and irregular 'chaotic' trajectories are shown in configuration space on the left and in phase space on the right. The correspondence between configuration space and phase space is schematically represented on the right. The phase space itself summarizes the overall dynamical properties of a given billiard geometry: regular trajectories appear as 'stable islands', and irregular trajectories quickly fill (part of) the 'chaotic sea'.

The correspondence between wave modes Fig. 1.3 and classical trajectories Fig. 1.4 lies at the heart of the historical motivation of the study of 2D cavities.

Returning to the wave problem (1.1), we may decide to give the cavity a certain physical density. This property is characterized in an optical context by the *refractive index* $n(\mathbf{r})$. Doing this affects the effective size of the wavenumber, which is then replaced by $k^2 \to n^2 k^2$ in problem (1.1) [6].

Furthermore, we may 'open' the cavity by defining its boundary through a media discontinuity from a finite 'optically dense' domain of refractive index n_c, the cavity, to an infinite 'thinner' surrounding of index $n_o < n_c$. Opening the cavity by granting the field ψ access to any area of the xy-plane has a definitive impact on the modes of the formerly closed cavity: The well-defined quantized spectrum of modes with real

[6] For the sake of comparison with Fig. (1.5), the solutions presented in Fig. (1.3) are computed with a cavity refractive index $n = n_c = 1.5$.

wavenumber eigenvalues $\{k^j\}$ ceases to exist and is replaced by a continuum of acceptable real wavenumbers k.

Since the exterior field, located far enough from the cavity, is separable into incoming and outgoing components with respect to the cavity position, the open cavity configuration may now be defined through *scattering theory* [88]. The absence of restriction on the wavenumber k means that we may now choose freely both the wavenumber and incoming waveform incident at the cavity[7]. Solving the Helmholtz equation with a refractive index distribution $n^2(\mathbf{r})$ of the cavity *and* its surroundings,

$$\nabla^2\psi(\mathbf{r};k) + n^2(\mathbf{r})k^2\psi(\mathbf{r};k) = 0 \tag{1.2}$$

for a given incoming field pattern, determines the appropriate outgoing waveform corresponding to the interaction of the incoming wave with the cavity, see Fig. 1.5(a).

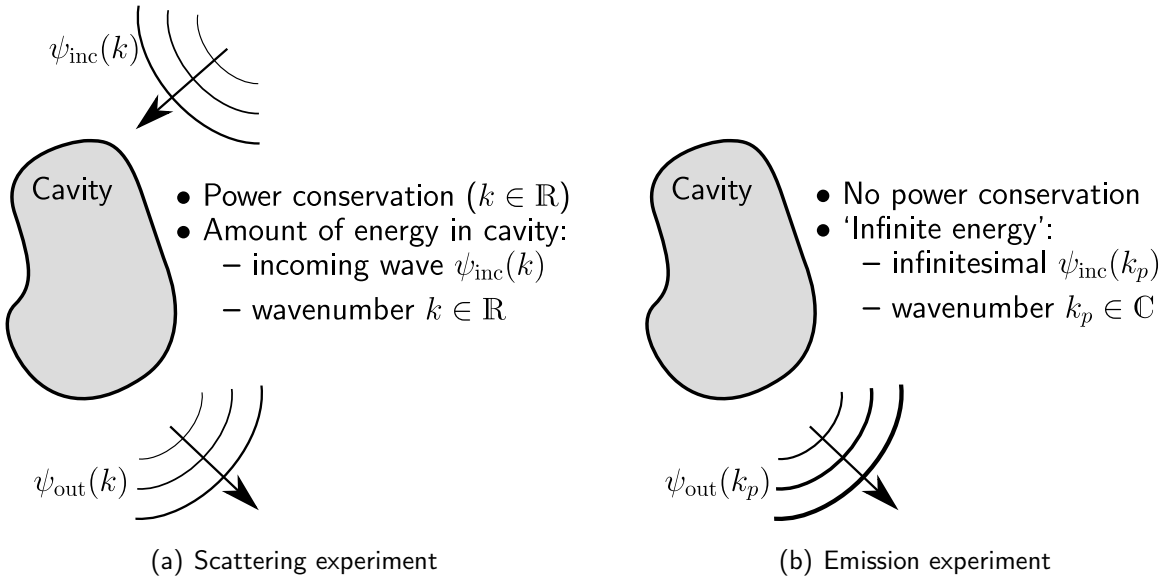


Fig. 1.5 Differences between (a) the scattering experiment and (b) the emission experiment. While the scattering experiment may be solved for all real wavenumbers and all incoming fields ψ_{inc} solving Eq. (1.2), the emission experiment seeks to obtain singular solutions of Eq. (1.2) that result solely in an outgoing wave ψ_{out}. These singular solutions lie in the complex k-plane in the form of poles of the scattering matrix $\mathbf{S}(k)$.

At this point, one may wonder about the contrast between the well-defined eigenproblem of the closed cavity problem (1.1) and the '(almost) everything works problem' of the open cavity problem (1.2). This issue actually calls for modes of intrinsically open systems [8]. As it turns out, all the combinations of incoming fields and wavenumbers do not have the same outcome: certain incident field patterns over specific real wavelength

[7] Provided of course that the incoming waveform be expandable in solutions of Helmholtz equation.
[8] See the discussion found in the related field of quantum optics [42].

range may cause the electromagnetic field to accumulate in large density inside the cavity. The origin of this *resonant* behaviour does not lie on the real-k line, but belongs to the *complex* k-plane. The cavity possesses quasi-normal modes (*i.e.* modes of Eq. (1.2) that have a complex wavenumber eigenvalue [27]) that appear as discrete singular divergent solutions of (1.2) in the fourth quadrant of the complex k-plane, see Fig. (1.6).

Assuming that a scattering experiment is, abstractly, carried out at such a discrete complex wavenumber position, an incoming plane wave will cause an 'infinitely' large response of the cavity, and the exterior field will be 'infinitely dominated' by the outgoing wave component: the quasi-normal mode. The complex wavenumber positions corresponding to singular solutions (1.2) are poles of the *scattering matrix* $\mathbf{S}(k)$, an object that transforms the incoming wave into an outgoing wave [88]. The imaginary part of the wavenumber of a given resonance k_p in the complex plane is inversely proportional to the lifetime of the resonance: a small imaginary part close to the real k line indicates a long lifetime of the associated mode, while a large imaginary part denotes a rapid decay rate. This result stems from the prior hypothesis of a mono-chromatic field with an $\mathrm{e}^{-i\omega t}$ time dependency [9]: replacing back the complex resonant wavenumber value $\omega_p = ck_p$ in this expression results in a time-decreasing field with a decay constant $c|\mathrm{Im}\{k_p\}|$.

Cavities are often characterized by their *quality factor* [77, 104],

$$Q_p = \frac{\mathrm{Re}\{k_p\}}{2|\mathrm{Im}\{k_p\}|} \quad . \tag{1.3}$$

This simple expression gives a non-dimensional number which denotes the amount of field oscillations over the time it takes for a decrease in amplitude of $1/\mathrm{e} \simeq 37\%$ (or $1/\mathrm{e}^2 \simeq 14\%$ intensity). Notice however that unlike a one-dimensional resonator, a two-dimensional cavity may possess both low quality and *high quality modes* over a small wavenumber range, therefore blurring the prescription *high quality cavity*.

Not unlike the closed quantum billiard system, it was observed that open cavity resonant modes may show a field distribution that resembles the classical trajectories observed in the billiard system (see for instance [40, 77, 128, 147]). Therefore, the investigation of the dynamical features of the classical billiard may help to understand the properties of the open cavity.

[9] $\omega = ck$, c being the speed of light in the vacuum.

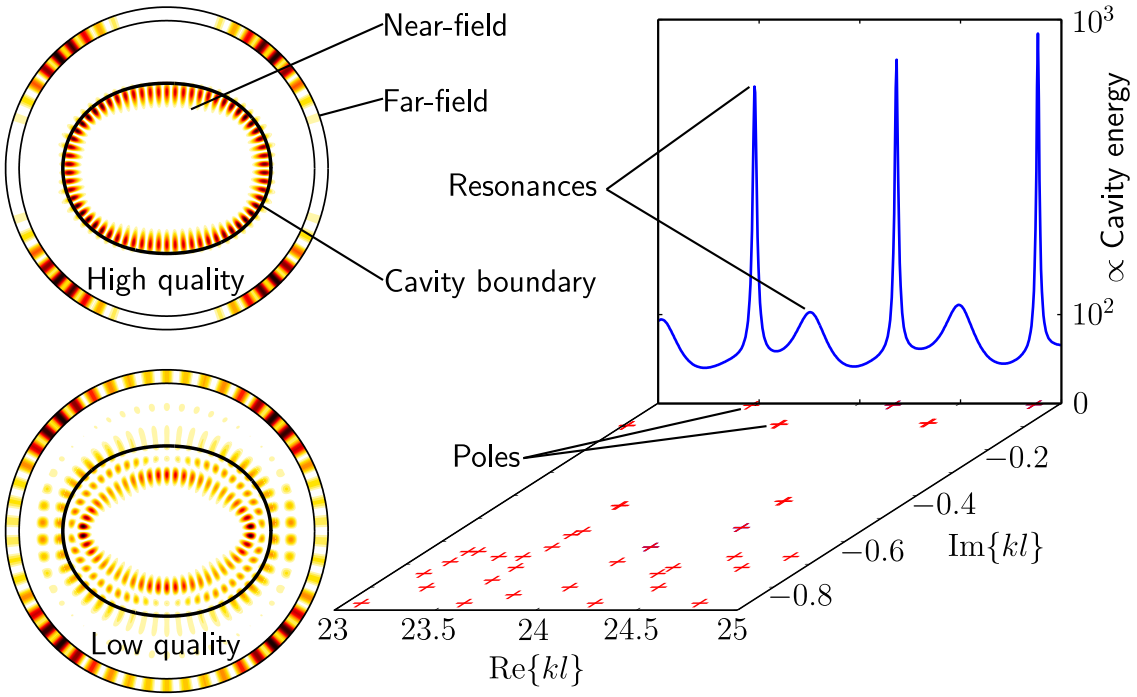


Fig. 1.6 Left: Some modes of the open quadripole cavity solving Eq. (1.2). The cavity geometry is the same as the one of Fig. 1.3, supplemented with a cavity refractive index $n_c = 1.5$ and an outside medium refractive index $n_o = 1$. Notice the far-field intensity distribution (*i.e.* $|\psi(\mathbf{r})|^2$ as $|\mathbf{r}| \to \infty$) represented by a color-scaled ring encircling the cavity. Right: 'Energy' spectrum of the quadripole cavity and some of its poles located in the complex k-plane.

1.2.2 Definition of the physical content

One of the pioneers of asymptotic physics, Joseph B. Keller, clearly defines in [69] a common problem involving partial differential equations. In essence, provided that the governing equations of motion of some phenomenon are found, and that these equations are governed by *partial differential equations* (PDE), as they often are in nature, we are faced with an infinite number of acceptable solutions. We cannot eliminate any of these because we are not being specific enough on the object that is investigated. For instance, Maxwell's equations solve all scenarios involving classical electromagnetic fields. What is needed are *auxiliary conditions*: these are initial conditions, boundary conditions, or even general properties of the object at hand that reduce the number of acceptable solutions. Although there may still be an infinite number of solutions left, these solutions are now specific to their context. The combination of partial differential equations and of auxiliary conditions defines a *PDE problem*.

The system of interest here consists in a classical electromagnetic field that interacts with a volume of material. Therefore, the governing equations of motion for this setup

are Maxwell's equations [66],

$$\nabla \times \tilde{\mathbf{E}} = -\frac{\partial}{\partial t}\tilde{\mathbf{B}} \tag{1.4}$$

$$\nabla \times \tilde{\mathbf{H}} = \tilde{\mathbf{J}} + \frac{\partial}{\partial t}\tilde{\mathbf{D}} \tag{1.5}$$

$$\nabla \cdot \tilde{\mathbf{D}} = \tilde{\rho} \tag{1.6}$$

$$\nabla \cdot \tilde{\mathbf{B}} = 0 \tag{1.7}$$

where

$\tilde{\mathbf{E}} = \tilde{\mathbf{E}}(\mathbf{r}, t)$	is the electric field
$\tilde{\mathbf{H}} = \tilde{\mathbf{H}}(\mathbf{r}, t)$	is the magnetic field
$\tilde{\mathbf{D}} = \tilde{\mathbf{D}}(\mathbf{r}, t)$	is the electric displacement field
$\tilde{\mathbf{B}} = \tilde{\mathbf{B}}(\mathbf{r}, t)$	is the magnetic flux density
$\tilde{\rho} = \tilde{\rho}(\mathbf{r}, t)$	is the density of free charges
$\tilde{\mathbf{J}} = \tilde{\mathbf{J}}(\mathbf{r}, t)$	is the free current density.

These coupled partial differential equations describe any classical electromagnetic field. They are known to be notoriously hard to solve in their full vectorial form and it is common usage to assume certain conditions to simplify their form. With regards to the definition of a PDE problem, the first set of auxiliary conditions consists in general assumptions about the medium where the field is assumed to propagate.

We will assume that the medium does not hold any free currents or charges ($\tilde{\mathbf{J}} = 0$ and $\tilde{\rho} = 0$ in Eqs (1.5) and (1.6)). With regards to the polarization of the medium, we will assume that the medium is lossless (or gainless), isotropic and linear. This makes it possible to write $\mathbf{D} = \epsilon\mathbf{E}$ where ϵ is the scalar permittivity of the medium. Also, we will assume that the medium has a constant response over the frequency bandwidth of interest (*i.e.* the permittivity is time independent, $\epsilon = \epsilon(\mathbf{r})$). Finally, we will assume that the medium is non-magnetic, so that $\mathbf{B} = \mu\mathbf{H} = \mu_0\mathbf{H}$ where μ_0 is the magnetic permeability of vacuum.

In the following, the permittivity will be replaced with the *refractive index*. The permittivity and refractive index are related to each other by $\epsilon(\mathbf{r}) = n^2(\mathbf{r})\epsilon_0$ where ϵ_0 is the permittivity of vacuum. Notice that the *speed of light in vacuum* c is computed from $c = 1/\sqrt{\epsilon_0\mu_0}$.

Since we aim to investigate propagating waves, it is convenient to decompose the elec-

tromagnetic field into time harmonics[10] to expose its oscillating properties,

$$\tilde{\mathbf{E}}(\mathbf{r},t) = \frac{1}{2\pi}\int_{-\infty}^{+\infty} d\omega\, \mathrm{e}^{-i\omega t}\mathbf{E}(\mathbf{r},\omega) \tag{1.8}$$

$$\tilde{\mathbf{H}}(\mathbf{r},t) = \frac{1}{2\pi}\int_{-\infty}^{+\infty} d\omega\, \mathrm{e}^{-i\omega t}\mathbf{H}(\mathbf{r},\omega) \quad . \tag{1.9}$$

These hypotheses about the medium greatly simplify Maxwell's equations (1.4)-(1.7),

$$\nabla \times \mathbf{E} = +i\omega\mu_0\mathbf{B} \tag{1.10}$$

$$\nabla \times \mathbf{H} = -i\omega\epsilon_0 n^2(\mathbf{r})\mathbf{E} \tag{1.11}$$

$$\nabla \cdot n^2(\mathbf{r})\mathbf{E} = 0 \tag{1.12}$$

$$\nabla \cdot \mathbf{H} = 0 \quad . \tag{1.13}$$

Taking the curl operator of Eqs (1.10) and (1.11) so that a wave equation may be retrieved, we obtain

$$\nabla \times \nabla \times \mathbf{E} = +n^2(\mathbf{r})k^2\mathbf{E} \tag{1.14}$$

$$\nabla \times \nabla \times \mathbf{H} = -i\omega\epsilon_0 \nabla \times n^2(\mathbf{r})\mathbf{E} \tag{1.15}$$

where we have used the relation $k = \omega/c$ for wavenumber $k = 2\pi/\lambda$ with λ, the vacuum wavelength of the field.

At this point, we introduce the main hypothesis upon which this work stands. This assumption is that the cavity is a *finite cross-section* cylindrical symmetry structure that is *optically thin* with respect to its planar cross-section. The finite cross-section ensures that we are not dealing with guiding structures, and the thinness hypothesis is to be understood in the sense that only the fundamental mode exists in the transverse direction for both the electric and magnetic field (see Appendix E). This relaxes the modeling effort to the plane cross section of the cavity, Fig. 1.7. The optical thinness hypothesis actually aims at 'trivializing' any z-dependent component of the field in much the same way the treatment of the infinite length cylinder would prescribe. This hypothesis comes together with the *effective refractive index hypothesis* - a compensation on the value of the refractive index for the finite extent of the cavity along the Oz axis, Appendix E - that was verified experimentally in [19, 17, 18] [11].

This planar configuration also offers a way to separate the two polarization states of the field with respect to the plane of the cavity, Fig. 1.7. We define a Transverse Magnetic

[10] $i \equiv \sqrt{-1}$ is used throughout this work.

[11] Notice that one of the conclusions of [19] is that the experimental resonance spectrum is a frequency-shifted version of the theoretical one. Even if the agreement is not exact in a quantitative way for predicting the resonances positions, predictions regarding the overall behaviour of the field in a thin cavity appears to be well modeled. Experimental realizations of thin cavities show that the emitted field is well predicted by this model, see for instance [164].

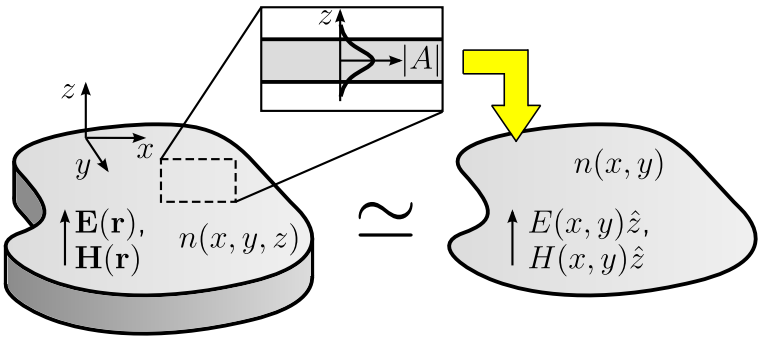


Fig. 1.7 The optical thinness hypothesis for the dielectric cavity. This hypothesis asserts that the amplitude $|A|$ of the electromagnetic field along the z axis resembles that the fundamental mode of a planar waveguide (see Appendix E). It is assumed that any z dependency may be factored out of the electromagnetic field.

(TM) polarization for the case where the electric field vector is along the Oz axis (and the magnetic field vector is within the xy plane), and conversely, a Transverse Electric (TE) polarization for the case where the magnetic field vector is along the Oz axis (and the electric field vector is within the xy plane). This additional prescription leads to considerable simplifications in Eqs (1.14) and (1.15).

For the TM polarization $\mathbf{E} = E(x, y)\hat{z}$, using identity $\nabla \times \nabla \times = \nabla\nabla \cdot -\nabla^2$, we find

$$\text{(TM)} \qquad \nabla(\nabla \cdot \mathbf{E}) - \nabla^2\mathbf{E} = n^2k^2\mathbf{E} \quad . \tag{1.16}$$

Assuming that $n(\mathbf{r}) = n(x, y)$, and using Eq. (1.12) we find that

$$\text{(TM)} \qquad n\nabla \cdot \mathbf{E} = 0 \tag{1.17}$$

which in turn simplifies Eq. (1.16),

$$\text{(TM)} \qquad \nabla^2 E + n^2k^2E = 0 \quad . \tag{1.18}$$

Equation (1.18) is the Helmholtz equation (1.2).

The treatment of the TE polarization $\mathbf{H} = H\hat{z}$ is somewhat more involved. Redefining $\mathbf{H} = n(\mathbf{r})\mathbf{h} = n(x, y)h(x, y)\hat{z}$ [39], we expand the left hand side of (1.15) [12],

$$\text{(TE)} \qquad \nabla \times \nabla \times \mathbf{H} = -n\nabla^2\mathbf{h} - \mathbf{h}\nabla^2 n - 2\hat{z}\nabla n \cdot \nabla h \tag{1.22}$$

[12] Some useful vectorial calculus identities [50]:

$$\nabla \times f\mathbf{A} = f\nabla \times \mathbf{A} - \mathbf{A} \times \nabla f \tag{1.19}$$

$$\nabla \times (\mathbf{A} \times \mathbf{B}) = \mathbf{A}\nabla \cdot \mathbf{B} - \mathbf{B}\nabla \cdot \mathbf{A} + (\mathbf{B} \cdot \nabla)\mathbf{A} - (\mathbf{A} \cdot \nabla)\mathbf{B} \tag{1.20}$$

$$\mathbf{A} \times (\mathbf{B} \times \mathbf{C}) = (\mathbf{A} \cdot \mathbf{C})\mathbf{B} - (\mathbf{A} \cdot \mathbf{B})\mathbf{C} \quad . \tag{1.21}$$

Using Eqs (1.10) and (1.11), we expand the right hand side of Eq. (1.15),

$$\text{(TE)} \qquad -i\omega\epsilon_0\nabla\times n^2(\mathbf{r})\mathbf{E} = -i\omega\epsilon_0\left[n^2(+i\omega\mu_0 n\mathbf{h}) - i\frac{1}{\omega\epsilon_0}\frac{1}{n^2}(\nabla\times n\mathbf{h})\times\nabla n^2\right]$$
$$= n^3k^2\mathbf{h} - 2(\nabla n)\cdot(\nabla h)\hat{z} - 2\frac{(\nabla n)^2}{n^2}\mathbf{h} \quad . \tag{1.23}$$

Canceling out common terms of Eqs. (1.22) and (1.23), we find a wave equation similar to the Helmholtz equation (1.18),

$$\text{(TE)} \qquad \nabla^2 h + \left[n^2k^2 + \frac{\nabla^2 n}{n} - 2\frac{(\nabla n)^2}{n^2}\right]h = 0 \tag{1.24}$$

the only difference being the supplementary k-independent contribution from the smooth variation of the refractive index. For a medium constituted of piecewise constant valued domains of refractive index, the Helmholtz equation is retrieved in its exact form.

The refractive index derivatives of Eq. (1.24) belong to parts of the cavity that do not change discontinuously: discontinuous steps of the refractive index are dealt with specific boundary conditions. The general forms of the boundary conditions for source-less media are [29]

$$\hat{\nu}\times\left[\mathbf{E}\big|_{\partial D_1} - \mathbf{E}\big|_{\partial D_2}\right] = 0 \tag{1.25}$$
$$\hat{\nu}\cdot\left[\mathbf{D}\big|_{\partial D_1} - \mathbf{D}\big|_{\partial D_2}\right] = 0 \tag{1.26}$$
$$\hat{\nu}\times\left[\mathbf{H}\big|_{\partial D_1} - \mathbf{H}\big|_{\partial D_2}\right] = 0 \tag{1.27}$$
$$\hat{\nu}\cdot\left[\mathbf{B}\big|_{\partial D_1} - \mathbf{B}\big|_{\partial D_2}\right] = 0 \tag{1.28}$$

where $\hat{\nu} = \nabla f(\mathbf{r})/|\nabla f(\mathbf{r})|$ is the unit normal vector to a boundary line ∂D defined by a certain parametric curve $f(\mathbf{r})$. The indices 1 and 2 identify the medium on both sides of the separation, see Fig. 1.8.

For the TM boundary condition, using Eqs (1.25) and (1.27) together with Eq. (1.10), we find

$$\text{(TM)} \qquad E\big|_{\partial D_1} = E\big|_{\partial D_2} \tag{1.29}$$
$$\text{(TM)} \qquad \frac{\partial}{\partial\nu}E\bigg|_{\partial D_1} = \frac{\partial}{\partial\nu}E\bigg|_{\partial D_2} \tag{1.30}$$

where $\frac{\partial}{\partial\nu}$ is the normal derivative to the boundary.

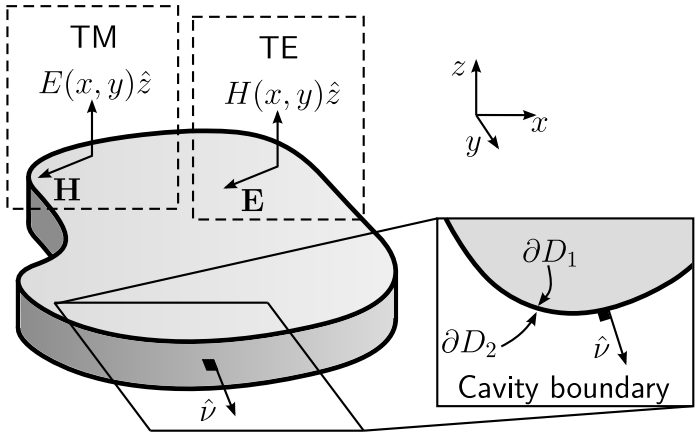


Fig. 1.8 Two-dimensional cavity and assumed TM and TE polarization states with details on the boundary including the unit normal vector $\hat{\nu}$.

For the TE boundary condition, using Eqs (1.25) and (1.27) together with Eq. (1.11), we find

$$\text{(TE)} \qquad H\big|_{\partial D_1} = H\big|_{\partial D_2} \tag{1.31}$$

$$\text{(TE)} \qquad \frac{1}{n_1}\frac{\partial}{\partial \nu}H\bigg|_{\partial D_1} = \frac{1}{n_2}\frac{\partial}{\partial \nu}H\bigg|_{\partial D_2} \quad . \tag{1.32}$$

Equations (1.29) through (1.32) identify that the electric field and its normal derivative are continuous for the TM polarization, and that the magnetic field and its *weighted* normal derivative are continuous for the TE polarization. These equations form another set of auxiliary equations specific to the behaviour of the field for discontinuous media.

Although the boundary conditions of the TM and TE polarizations lead to different wave behaviours, in this work we shall focus solely on the TM polarization. This choice is done for the sake of simplicity.

At this point, we still need to identify the asymptotic boundary conditions to clearly define the problem. Since we assume that the cavity is of finite size and embedded into a medium of constant refractive index n_o, and that nowhere in the infinite plane exists a physical boundary performing anything else than smoothness of the fields, Eqs (1.29)-(1.32), we are immediately led to *Sommerfeld's radiation condition* [88],

$$\psi_{\pm}(|\mathbf{r}| \to \infty) \sim \frac{\mathrm{e}^{\pm i n_o k|\mathbf{r}|}}{\sqrt{|\mathbf{r}|}} \tag{1.33}$$

where ψ holds for the TM electric or the TE magnetic fields alike. This condition asserts that far enough from the scatterer whose position is about the origin $\mathbf{r} \simeq 0$, the field ψ is a radial wave with a geometrically decreasing amplitude with respect to the distance. Two types of radiating waves exist: with regards to an implicit $\mathrm{e}^{-i\omega t}$ time dependence

of the field, ψ_+ is moving away from the origin while ψ_- is coming toward the origin. For a *source* of field located near the origin, the appropriate type of radiation is ψ_+, and for a *sink* of field located near the origin, the appropriate type of radiation is ψ_-.

Outside a circular domain of radius $R_{\max}$ completely enclosing the cavity, see Fig. 1.9, the refractive index has a constant value n_o. In this exterior domain, Eqs (1.18) and (1.24) have the exact same form,

$$\nabla^2\psi + n_o^2 k^2 \psi = 0 \quad r \geq R_{\max} \quad . \tag{1.34}$$

Using cylindrical coordinates and neglecting any z axial contributions (optical thinness), we separate the field $\psi(\mathrm{r})$ into a product of radial and angular functions, $\psi(\mathrm{r}) = \mathcal{R}(r)\Phi(\phi)$. This Ansatz is motivated by the absence of any features in the exterior domain that would introduce intricate coupling between angular and radial coordinates. Inserting this solution into Eq. (1.34) immediately leads to two *ordinary* differential equations for the radial function and the angular function,

$$r^2\frac{d^2\mathcal{R}}{dr^2} + r\frac{d\mathcal{R}}{dr} + \left(n_o^2k^2r^2 - m^2\right)\mathcal{R} = 0 \tag{1.35}$$

$$\frac{d^2\Phi}{d\phi^2} + m^2\Phi = 0 \tag{1.36}$$

where m^2 is a constant[13]. Equation (1.36) is an eigenvalue problem taking the form of the harmonic oscillator differential equation. The solutions take the form $\mathrm{e}^{\pm im\phi}$ and must satisfy *periodicity around the origin* (the field must be continuous on a closed path encircling the disc of radius $R_{\max}$). This fixes the unknown constant m to integer values,

$$m = \{0,\, \pm 1 \,\pm 2,\, \pm 3 \ldots\} \tag{1.37}$$

Equation (1.35) is the Bessel differential equation whose general solutions are the well known Bessel functions of the first and second kind, $J_m(n_okr)$ and $Y_m(n_okr)$ respectively ($Y_m(n_okr)$ are also known as Neumann function), or linear combinations of these: Hankel functions $H_m^{(1)}(n_okr) = J_m(n_okr) + iY_m(n_okr)$ and $H_m^{(2)}(n_okr) = J_m(n_okr) - iY_m(n_okr)$. The properties of these functions are thoroughly discussed in Appendix A.

The solutions to Eq. (1.35) we are looking for must satisfy the Sommerfeld radiation condition (1.33). This condition is immediately satisfied by the two Hankel functions (see Eqs. (A.30) and (A.31))

$$\psi_+ \;:\; \lim_{r\gg R_{\max}} H_m^{(1)}(n_okr) \sim \sqrt{\frac{2}{\pi n_okr}}\mathrm{e}^{+in_okr}\mathrm{e}^{-im\frac{\pi}{2}-i\frac{\pi}{4}} \tag{1.38}$$

$$\psi_- \;:\; \lim_{r\gg R_{\max}} H_m^{(2)}(n_okr) \sim \sqrt{\frac{2}{\pi n_okr}}\mathrm{e}^{-in_okr}\mathrm{e}^{+im\frac{\pi}{2}+i\frac{\pi}{4}} \quad . \tag{1.39}$$

[13]This constant common to both equations is an immediate consequence of the separation Ansatz.

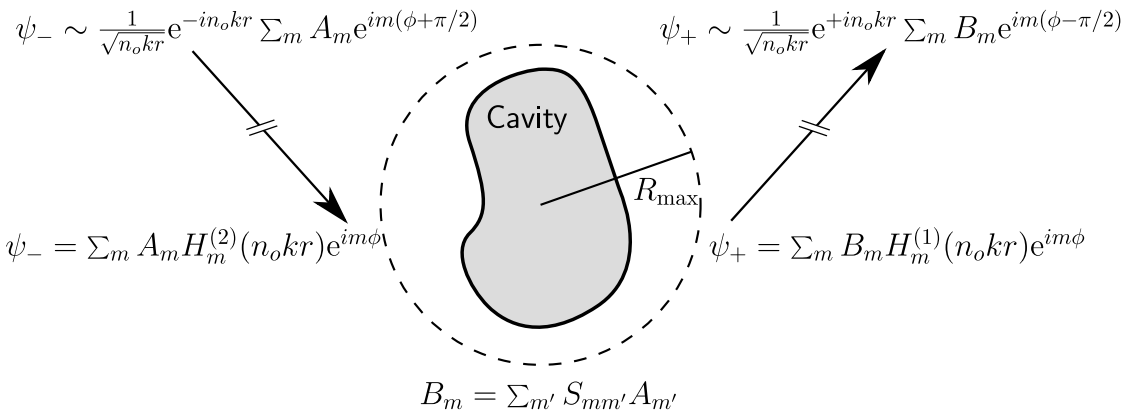


Fig. 1.9 A continuous wave scattering event with a finite-sized dielectric cavity with proper radiation condition at infinity. With regards to incoming and outgoing waves, the presence of the cavity inside the circular domain of radius $R_{\max}$ is expressed by the scattering matrix $\mathbf{S}$.

The first Hankel function, $H_m^{(1)}$, is associated with an outgoing wave while the second Hankel function, $H_m^{(2)}$, is associated with an incoming wave. A general solution to Eq. (1.34) complemented by the radiation condition is therefore

$$\psi(\mathbf{r}) = \sum_{m=-\infty}^{+\infty} \left[A_m H_m^{(2)}(n_o kr) + B_m H_m^{(1)}(n_o kr)\right] e^{im\phi} \quad r \geq R_{\max} \quad . \tag{1.40}$$

Since the Hankel functions are associated with incoming and outgoing waves relative to the origin and that this origin is also precisely at the geometrical center of the domain of radius $R_{\max}$ embedding the cavity, the coefficients $\mathbf{A} = \{A_m\}$ and $\mathbf{B} = \{B_m\}$ of Eq. (1.40) must be related to one another by the interaction of the incoming field with the physical content of the domain $|\mathbf{r}| < R_{\max}$. Since we assume that the field is linear, the relation between $\mathbf{A}$ and $\mathbf{B}$ is linear as well,

$$\mathbf{B} = \mathbf{S}\mathbf{A} \tag{1.41}$$

where $\mathbf{S}$ is the *scattering matrix* whose purpose is to transform the incoming angular coefficients $\mathbf{A}$ into outgoing coefficients $\mathbf{B}$ with respect to the 'mixing' and 'phase-offsetting' properties of the cavity. The complete picture of the continuous wave scattering experiment is schematically presented in Fig. 1.9.

Since the coefficients $\mathbf{A}$ and $\mathbf{B}$ must satisfy power conservation for real refractive index and wavenumber, the matrix $\mathbf{S}$ is unitary,

$$\mathbf{S}^\dagger \mathbf{S} = \mathbf{S}\mathbf{S}^\dagger = \mathbb{1} \quad n \in \mathbb{R},\, k \in \mathbb{R} \tag{1.42}$$

Obviously, $\mathbf{S}$ does not only depend upon the refractive index distribution of the cavity, it also changes with respect to the wavenumber k. For a given constant incoming

coefficient vector $\mathbf{A}$, the output vector $\mathbf{B}$ may vary much with k. Even more striking is the aspect of the near-field which may rapidly increase (and decrease) in amplitude as the wavenumber is linearly changed. The cavity is *resonant*: peaks of stored energy (or increasing cross-section) are related to the presence of *poles* of the scattering matrix in the complex k-plane [88]. The poles of the scattering matrix are found by solving

$$\det\{\mathbf{S}(k)\}^{-1} = 0 \quad k \in \mathbb{C} \tag{1.43}$$

for the wavenumber k. At these complex k-plane positions, an incoming wave with an infinitesimal amplitude produces an 'infinite' outgoing response from the cavity.

The roots of Eq. (1.43) have a *negative imaginary part*. Equation (1.38) must be increasing in amplitude with r because of causality: the field located far from the cavity recorded at time t_f was released from the cavity at an earlier time $t_i \ll t_f$ when the amount of field inside the cavity was larger than it is at t_f. The complex root condition (1.43) defines the emission problem.

For k on the real line however, any incoming vector $\mathbf{A}$ produces an acceptable solution to the scattering relation (1.41). This poses the issue of the 'definiteness' of the scattering problem. Yet, it appears that some choices of incoming vectors $\mathbf{A}$ would be more appropriate to select resonant modes on the real-k line. After all, the poles of the scattering matrix have an imprint on the real-k line through the observation of resonances: it is reasonable to suppose that carefully selected incoming vectors $\{\mathbf{A}\}$ at a given k may identify the signature of single specific poles on the real-k line. Therefore, we need to define an observable that is characteristic of the resonance phenomenon at hand.

In this work, we argue that Smith's delay matrix [135] provides a characteristic expansion basis for the representation of the resonances of the real-k line. In Chapter 2, we determine that the overall extra electromagnetic energy that accounts for the presence of the cavity with respect to an otherwise empty universe is proportional to the delay matrix

$$\mathbf{Q} = -i\mathbf{S}^\dagger \frac{\partial \mathbf{S}}{\partial k} \quad k \in \mathbb{R} \quad . \tag{1.44}$$

The *characteristic modes* of the cavity are defined through the eigen-quantities of this matrix: locally non-interacting modes are defined by the incoming vectors $\{\mathbf{A}^p\}$ through the eigenvectors of $\mathbf{Q}$ while the eigenvalues are immediately related to the average time a given mode will be delayed by the cavity with respect to free propagation. Since the delay matrix is hermitian symmetric, its eigenvalues are real and its eigenvectors form an orthonormal basis. Also, the so-defined characteristic modes of the cavity are time-reversible: the complete outgoing wavefield is a phase-offset complex conjugate version of the incoming wavefield. In other words, the characteristic modes are self-

replicating fields through the interaction with the cavity. This motivated us to interpret the characteristic modes as a special set of modes sitting on the real k-line half-way between the poles of the scattering matrix Eq. (1.43) (pure emission) and *zeros* of the scattering matrix (pure absorption). A formal comparison of the emission poles description of the cavity and of the characteristic modes description is provided in Section 2.1.3.

With regards to the definition of a PDE problem provided at the beginning of this section, the description of the physical problem of investigating two-dimensional dielectric cavities is summarized in Fig. 1.10. I also pushed this description beyond the point of defining the PDE problem to indicate that we may still have a choice to do regarding the point of view we want to exploit regarding the PDE problem at hand. The 'proper' choice is one of the main objects of this thesis.

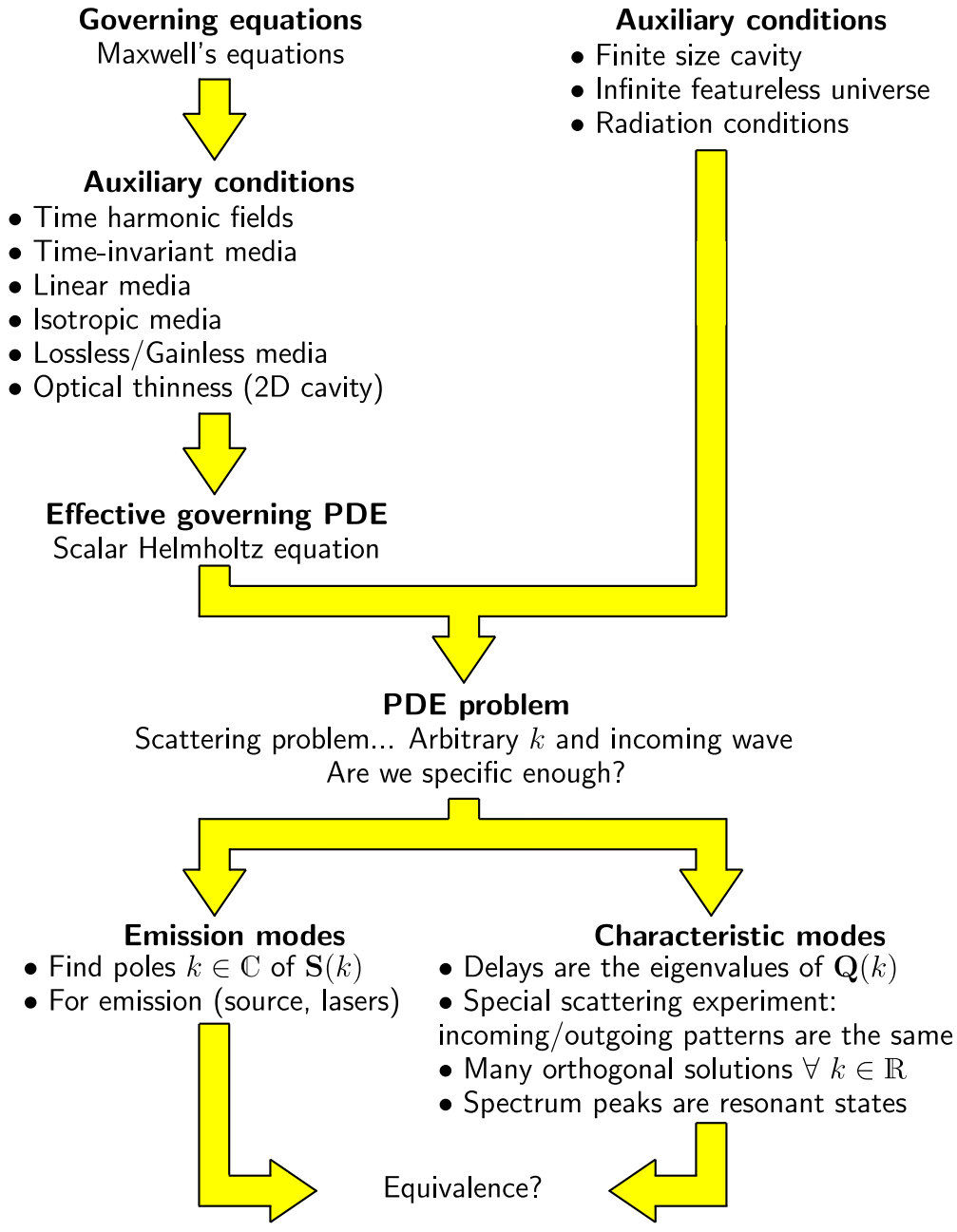


Fig. 1.10 Definition of the PDE problem for the two-dimensional dielectric cavity.

1.3 A solvable case: The homogeneous cavity

Although it does not display the complex features of other cavities, the open homogeneous disc cavity remains the only cavity having a simple, analytically trackable solution. This is important for developing physical intuition and to gather basic formulae to describe the behaviour of the electromagnetic field. Moreover, since most of this thesis is concerned with the deformation of the disc cavity, knowledge of its modes provides the known eigenbasis for comparison and for setting a perturbation calculation.

The refractive index of the homogeneous disc cavity of radius $r = R_0$ is defined by

$$n^2(\mathbf{r}, \phi) = n_c^2 + \left[n_o^2 - n_c^2\right] U(r - R_0) \tag{1.45}$$

where n_c is the bulk material refractive index of the disc, $n_o < n_c$ is the refractive index of the environment exterior to the cavity, and $U(x)$ is the Heaviside step function: $U(x) = 0$ for $x < 0$, and $= 1$ for $x > 0$. The partial differential equation to consider is (1.18),

$$\nabla^2\psi(\mathbf{r}) + n^2(\mathbf{r})k^2\psi(\mathbf{r}) = 0 \tag{1.46}$$

with continuity boundary conditions (1.29)-(1.30)

$$\psi\big|_{r=R_0} = \psi\big|_{r=R_0} \tag{1.47}$$

$$\frac{\partial}{\partial\nu}\psi\big|_{r=R_0} = \frac{\partial}{\partial\nu}\psi\big|_{r=R_0} \tag{1.48}$$

and radiation condition (1.33)

$$\psi_\pm(|\mathbf{r}| \to \infty) \sim \frac{\mathrm{e}^{\pm i n_o k|\mathbf{r}|}}{\sqrt{|\mathbf{r}|}} \quad . \tag{1.49}$$

This problem has already been solved for the exterior domain: the general solution consists in a linear superposition of Hankel functions (1.40)

$$\psi(\mathbf{r}) = \sum_{m=-\infty}^{+\infty} \left[A_m H_m^{(2)}(n_o k r) + B_m H_m^{(1)}(n_o k r)\right] \mathrm{e}^{im\phi} \quad r \geq R_0 \quad . \tag{1.50}$$

The same coordinate separation procedure can readily be done again for the interior domain, resulting in the differential equations (1.35) and (1.36) only now with $n_o \to n_c$. For the interior domain $r < R_0$, a solution of the kind of Eq. (1.50) will be divergent at the origin unless $A_m = B_m$ (see the small argument expansions of Bessel and Hankel functions presented in Appendix A). Setting $A_m = B_m = 1/2\, a_m$ in (1.50) yields Bessel functions of the first kind,

$$\psi(\mathbf{r}) = \sum_{m=-\infty}^{+\infty} a_m J_m(n_c k r)\mathrm{e}^{im\phi} \quad r \leq R_0 \quad . \tag{1.51}$$

The task now is to determine the different unknown coefficients $\{A_m\}$, $\{B_m\}$ and $\{a_m\}$. These are obtained through the boundary conditions (1.47) and (1.48). Since there is one more set of unknown coefficients than there are boundary conditions, the two other sets of unknown coefficients will be defined through the first one. We choose the $\{A_m\}$ coefficients as the independent ones. This choice is convenient in regard of the scattering experiment where a wave incident to the cavity is defined through the $\{A_m\}$ coefficients. The application of the boundary conditions yields

$$\sum_{m'} \left[A_{m'} H^{(2)}_{m'}(Z_o) + B_{m'} H^{(1)}_{m'}(Z_o) \right] \mathrm{e}^{im'\phi} = \sum_{m'} a_{m'} J_{m'}(Z_c) \mathrm{e}^{im'\phi} \tag{1.52}$$

$$n_o \sum_{m'} \left[A_{m'} H^{(2)'}_{m'}(Z_o) + B_{m'} H^{(1)'}_{m'}(Z_o) \right] \mathrm{e}^{im'\phi} = n_c \sum_{m'} a_{m'} J'_{m'}(Z_c) \mathrm{e}^{im'\phi} \tag{1.53}$$

where $Z_o = n_o k R_0$ and $Z_c = n_c k R_0$, and $'$ denotes the argument derivative for the Bessel and Hankel functions.

Assuming that an incident wave has *angular momentum*[14] m (*i.e.* a single incoming coefficient $A_m = \delta_{mm'} A_{m'}$ is chosen), we would be interested in obtaining knowledge of the distribution of the coefficients $\{B_{m'}\} = \{S_{m'm} A_m\}$ and $\{a_{m'}\} = \{T_{m'm} A_m\}$. This is done by projecting on the appropriate angular basis function, $\left\langle \phi \,\middle|\, \Phi_m \right\rangle = \mathrm{e}^{im\phi}$, equations (1.52) and (1.53),

$$A_m H^{(2)}_m(Z_o) + B_m H^{(1)}_m(Z_o) = a_m J_m(Z_c) \tag{1.54}$$

$$n_o \left[A_m H^{(2)'}_m(Z_o) + B_m H^{(1)'}_m(Z_o) \right] = n_c a_m J'_m(Z_c) \quad . \tag{1.55}$$

We readily solve this linear system of algebraic equations for B_m and a_m,

$$B_m = -\frac{\bar{\Delta}_m}{\Delta_m} A_m \tag{1.56}$$

$$a_m = -\frac{4i}{\pi k R_0} \frac{1}{\Delta_m} A_m \tag{1.57}$$

with

$$\bar{\Delta}_m = n_c H^{(2)}_m(Z_o) J'_m(Z_c) - n_o H^{(2)'}_m(Z_o) J_m(Z_c) \tag{1.58}$$

$$\Delta_m = n_c H^{(1)}_m(Z_o) J'_m(Z_c) - n_o H^{(1)'}_m(Z_o) J_m(Z_c) \quad . \tag{1.59}$$

In regards to the description of the scattering matrix $\mathbf{S}$ and transfer matrix $\mathbf{T}$ as the linear transformation relating an incoming wave to the outgoing wave, $\{B_{m'}\} = \{S_{m'm} A_m\}$, and to the field inside the cavity, $\{a_{m'}\} = \{T_{m'm} A_m\}$, we associate

$$S^{(0)}_{mm'} = -\frac{\bar{\Delta}_m}{\Delta_m} \delta_{mm'} \tag{1.60}$$

$$T^{(0)}_{mm'} = -\frac{4i}{\pi k R_0} \frac{1}{\Delta_m} \delta_{mm'} \quad . \tag{1.61}$$

[14] The use of this nomenclature for the index m will appear evident from a semi-classical result obtained in this Section.

The scattering matrix (and transfer matrix) for the homogeneous disc cavity is diagonal. This form of the $\mathbf{S}$ matrix could already have been predicted from the separation of coordinates Eqs (1.35) and (1.36) that applies for the whole configuration plane: the orthogonal expansion basis indexed through the angular momenta $\{m\}$ is the eigenbasis for the homogeneous cavity scattering matrix. One such function is depicted in Fig. 1.11.

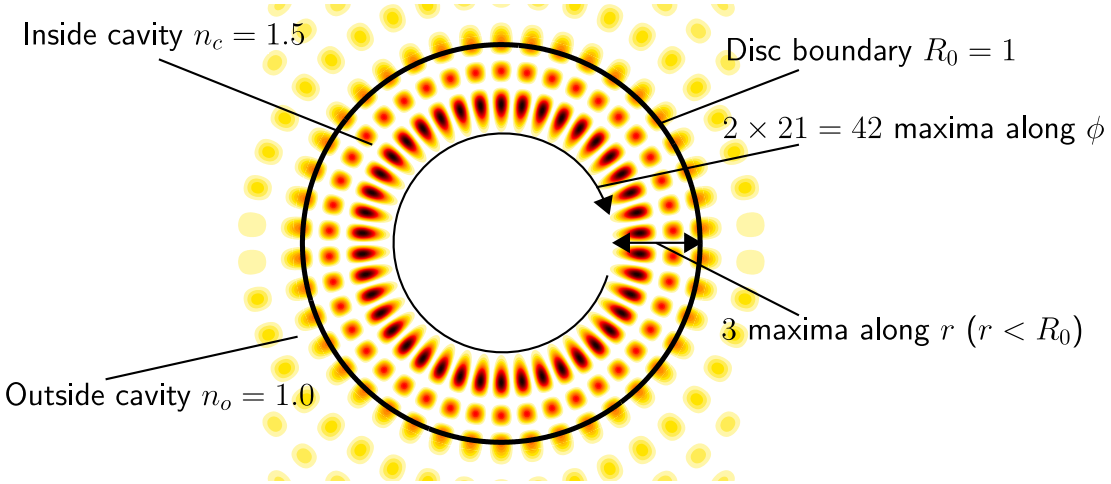


Fig. 1.11 Representation of $|\psi(\mathbf{r})|^2$ for one of the modes of the disc cavity $n_c = 1.5$, $n_o = 1.0$ and $R_0 = 1$; dark = high amplitude, white = low amplitude. This (resonant) mode is labeled $(21, 3)$ because it possesses angular momentum $|m| = 21$ and presents 3 maxima along its radial line inside the cavity. We arbitrarily choose to set the incoming coefficients $A_{+21} = A_{-21} = 1/\sqrt{2}$ to select the odd symmetry mode with respect to the horizontal axis of this picture. Accordingly, this mode has a degenerate (orthogonal) companion with even symmetry obtained by setting $A_{+21} = +1/\sqrt{2}$ and $A_{-21} = -1/\sqrt{2}$.

For $k \in \mathbb{R}$, $\Delta_m^* = \bar{\Delta}_m$ (see Appendix A) and the $\mathbf{S}$ matrix is unitary,

$$\mathbf{S}^\dagger \mathbf{S} = \mathbf{S}\mathbf{S}^\dagger = \mathbb{1} \quad . \tag{1.62}$$

The diagonal elements of the scattering matrix lie on the complex unit circle, $S_{mm'} = \mathrm{e}^{i\theta_m}\delta_{mm'}$, and the rate of change of the eigenphases $\{\theta_m(k)\}$ with respect to the wavenumber corresponds to the eigenvalues of the delay matrix (1.44), also diagonal in the homogeneous disc case,

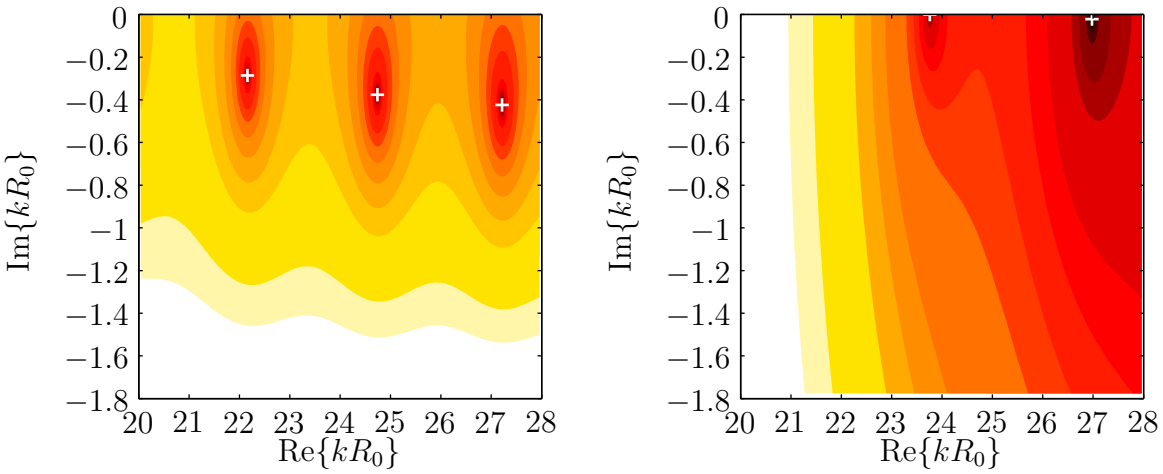
$$\frac{\partial \theta_m}{\partial k} = Q_{mm} = \frac{c\tau}{R_0} = -iS_{mm}^* \frac{\partial S_{mm}}{\partial k} = -i\left(\frac{1}{\bar{\Delta}_m}\frac{\partial \bar{\Delta}_m}{\partial k} - \frac{1}{\Delta_m}\frac{\partial \Delta_m}{\partial k}\right) \quad . \tag{1.63}$$

Large variations of the eigenphases with respect to the wavenumber are associated with resonances of the cavity. Because $S_{+m+m} = S_{-m-m}$ or $Q_{+m+m} = Q_{-m-m}$, the modes of a given angular momentum $|m|$ are degenerate: the rotational symmetry of the system implies that all quantities found for mode $+m$ equally apply for mode $-m$. The loss of this rotational degeneracy is considered in Chapter 3.

The poles of the scattering matrix (1.60) are found by solving

$$\Delta_m(k) \stackrel{!}{=} 0 \tag{1.64}$$

for wavenumber k. Since the different Bessel and Hankel functions have an oscillating behaviour for an argument $Z > m$, $Z = \{Z_o, Z_c\}$, we expect that many solutions to problem (1.64) exist. Approximate expansions for $\Delta_m(k)$ showing this oscillatory feature may be found in Chapter 3 Eqs (3.118)-(3.120). The complex k-plane amplitude of the $\Delta_m(k)$ function is depicted in Fig. 1.12 for two values of m; some solutions to problem (1.64) are marked by white crosses. These positions correspond to singular values of the scattering matrix, or emission modes. They are almost evenly spaced with respect to their real wavenumber component, a consequence of the monotonic phase evolution of the oscillating Bessel and Hankel functions.

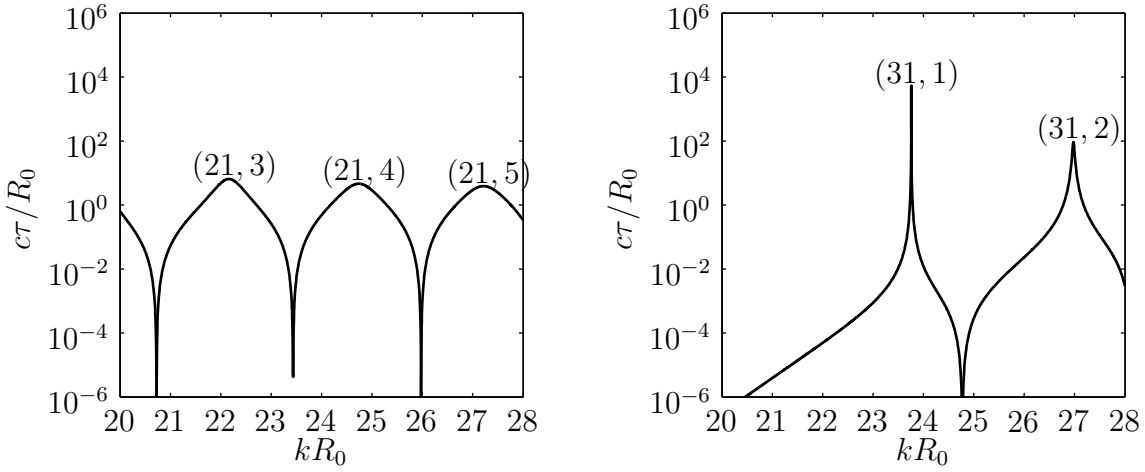


(a) $m = 21$ (b) $m = 31$

Fig. 1.12 Complex k-plane amplitude of $\Delta_m(k)$ Eq. (1.59) for a homogeneous disc cavity of radius $R_0 = 1$ and refractive index $n_c = 1.5$ immersed in an environment $n_o = 1.0$. The (logarithmic) color scale ranges from dark near zero values (largely negative on a logarithmic scale) to bright for high $|\Delta_m(k)|$ values. The poles of the $\mathbf{S}$ matrix (1.60) for the two angular momenta presented are indicated by white crosses.

The existence of multiple resonances for a given angular momentum m has an impact on the delays of the delay matrix (1.63), presenting a series of resonant delay peaks as shown in Fig. 1.13.

Table 1.1 presents a comparison of the different numerical values computed for the position and size of the resonances presented in Figs 1.12 and 1.13. The equivalent delay



(a) $m = 21$ (b) $m = 31$

Fig. 1.13 Non-dimensional delay $c\tau/R_0$ (c is the speed of light in vacuum) as computed by Eq. (1.63) for the homogeneous disc cavity defined by the same parameters as those used for Fig. 1.12, and the same two angular momenta. The labeling (m, j) of the different resonant peaks refers to the angular momenta m, and the number j of in-cavity radial extrema of the field. For instance, $(31, 1)$ is the first - and largest lifetime - resonance of the $|m| = 31$ series; no other $|m| = 31$ resonances exist at smaller wavenumber values.

value for the pole positions is computed using $2/|\mathrm{Im}\{kR_0\}|$ [15], and the identification of the modes is done using the usual convention (m, j), m being the angular momentum and j, the number of radial maxima inside the disc domain $r < R_0$. Modes $(21, 1)$ and $(21, 2)$ are added for the sake of comparison with modes $(31, 1)$ and $(31, 2)$. The differences between the pole and the delay matrix descriptions regarding the resonant modes' position increase with the number of radial maxima within a given angular momentum (modes $(21, 1)$ through $(21, 5)$), and decrease with angular momenta (modes $(21, 1 - 2)$ and $(31, 1 - 2)$). This is explained by the greater proximity of the poles to the real-k line for larger momenta m at constant j, and lower indices j at constant m. The pole description demands that a certain fraction of the complete wavenumber - the imaginary part - be dedicated to an evanescent-like behaviour while the delay description relies solely on a 'propagating' real wavenumber to model the wave. In this latter description, any evanescent features are relegated to the waveform of the field.

The interpretation of the many solutions to problem (1.64) or of the many peaks of (1.63) is facilitated by an intuitive model of the disc cavity.

[15] The factor 2 in this expression is needed to double the emission time: because of time reversibility of the scattering experiment, the complete time delay as measured by the delay matrix is (approximately) twice the emission time.

Mode	Poles of $\mathbf{S}$		Resonant delays of $\mathbf{Q}$	
(m,j)	$\mathrm{Re}\{kR_0\}$	$2/\lvert\mathrm{Im}\{kR_0\}\rvert$	kR_0	$c\tau/R_0$
$(21,1)$	16.5962405654	2.41794×10^2	16.5962405645	2.41779×10^2
$(21,2)$	19.48301	1.652×10^1	19.48299	1.631×10^1
$(21,3)$	22.16182	7.0	22.16152	6.5
$(21,4)$	24.73855	5.3	24.73813	4.6
$(21,5)$	27.21555	4.7	27.21516	3.9
$(31,1)$	23.75862762963	5.2572886×10^3	23.75862762948	5.2572879×10^3
$(31,2)$	26.97732192	9.3098×10^1	26.97732188	9.3060×10^1

Tab. 1.1 Comparison of some of the resonances for the homogeneous disc ($n_c = 1.5$, $n_o = 1.0$, $R_0 = 1$) as determined by the computation of the poles of the $\mathbf{S}$ matrix, problem (1.64), and from the $\mathbf{Q}$ matrix, maximization of (1.63). All digits are kept up to the last two disagreeing significant digits. Numerical resolution is 10^{-12} on the wavenumber value for the pole search and peak maximization.

1.3.1 The effective potential description

The generalization for all values of r of the differential equation for the radial function Eq. (1.35) for the disc cavity takes the form

$$r^2 \frac{d^2\mathcal{R}}{dr^2} + r\frac{d\mathcal{R}}{dr} + \left[n^2(r)k^2r^2 - m^2\right]\mathcal{R} = 0 \tag{1.65}$$

with $n^2(r)$ the refractive index of the disc as defined by Eq. (1.45) and m is an integer constant. This differential equation is quite similar to the 1D time independent Schrödinger equation. This is even more obvious if the first derivative is removed [67, 89] by defining a scaled version of the radial function $\mathcal{R}(r)$,

$$\mathcal{R}(r) = \frac{f(r)}{\sqrt{r}} \quad . \tag{1.66}$$

This leads to a new second order differential equation

$$\frac{d^2f(r)}{dr^2} - \left[-n^2(r)k^2 + \frac{m^2 - 1/4}{r^2}\right] f(r) = 0 \quad . \tag{1.67}$$

Using a convenient reference 'energy level' $n_o^2k^2$, we readily obtain a Schrödinger-like equation

$$-\frac{d^2f(r)}{dr^2} + V_{\text{eff}}(r)f(r) = n_o^2k^2f(r) \quad . \tag{1.68}$$

with the k-dependant effective potential

$$V_{\text{eff}}(r) = \left[[n_o^2 - n^2(r)]k^2 + \frac{m^2 - 1/4}{r^2}\right] \quad . \tag{1.69}$$

This potential is everywhere decreasing except at the cavity boundary $r = R_0$ where $n(r)$ steps from n_c to $n_o < n_c$. This produces a 'dent' in the potential, allowing for

resonant states to exist behind the so-formed barrier Fig. 1.14. Resonant states are not bound states: they are not localized solely within the cavity boundary. Given an angular momentum m, the height of the potential barrier remains the same at a value of $(m^2 - 1/4)/R_0^2$ but its depth increases with wavenumber k.

This simple potential model for the disc cavity provides a way to show that three domains of wavenumber exist for a given m, each exhibiting a typical behaviour[16]:

- **Below barrier regime** $kR_0 < \frac{\sqrt{m^2-1/4}}{n_c}$**:** The high angular momentum of the field with respect to the wavenumber 'energy level' prevents the field to reach the cavity, Fig. 1.14(a);

- **In-barrier regime** $\frac{\sqrt{m^2-1/4}}{n_c} < kR_0 < \frac{\sqrt{m^2-1/4}}{n_o}$**:** The angular momentum and the wavenumber balance each other and enable the resonant behaviour where the field gets captured behind the potential barrier, Figs 1.14(b) and 1.14(c);

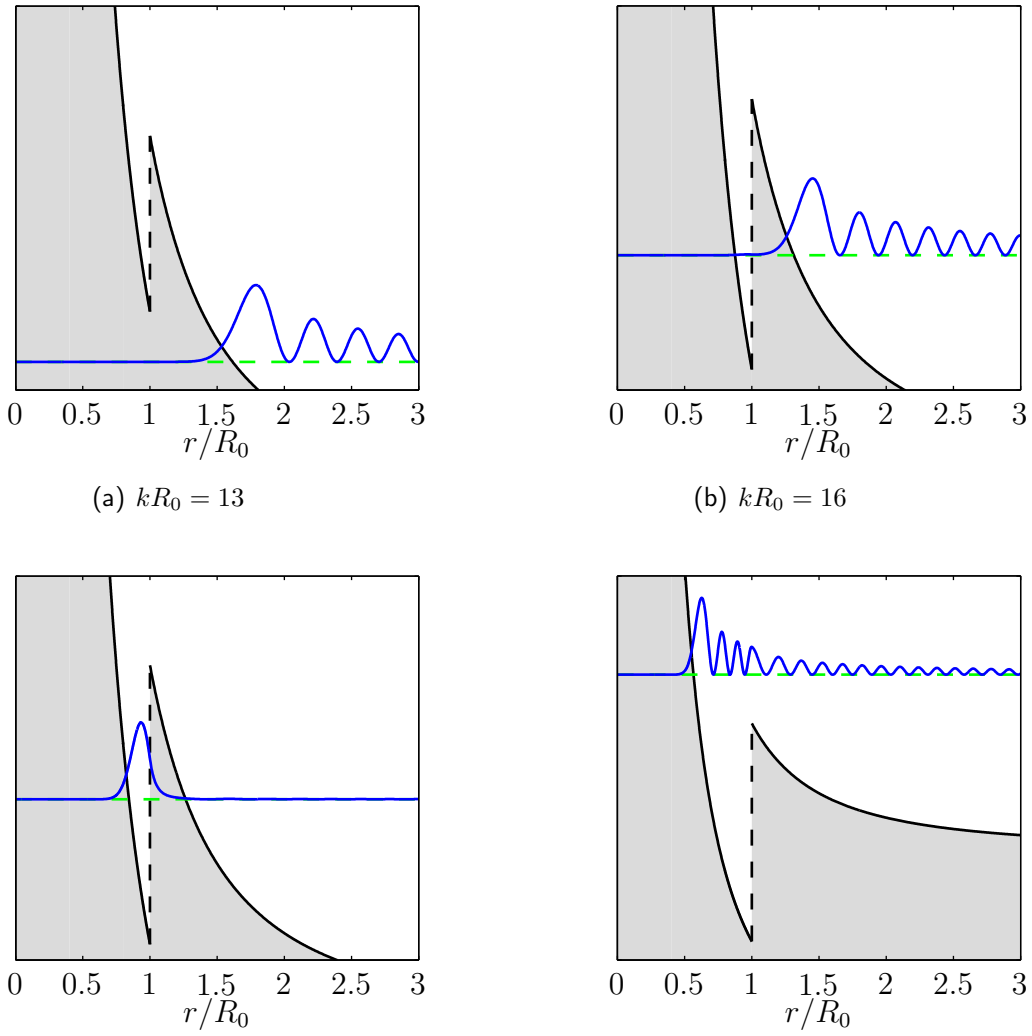
- **Above barrier regime** $\frac{\sqrt{m^2-1/4}}{n_o} < kR_0$**:** The angular momentum is too small for the wavenumber 'energy level' $n_o^2 k^2$, and the field easily has access to the cavity, sometimes with larger amplitudes giving rise to a series of low-lying resonances, filling the baseline of the delay spectrum, Fig. 1.14(d).

Given an angular momentum m, increasing the real wavenumber k from 0 to the barrier limit shows a monotonous increase in the amount of field found in the cavity. Then, a finite number of large resonances appear as the wavenumber gets in the in-barrier regime (for $m = 21$, resonances $(21, 1)$ and $(21, 2)$ are in this regime). The barrier gets thinner as the wavenumber 'energy level' grows, leading to smaller resonant lifetimes. Finally, the above barrier regime shows an infinite series of low-lying resonances. Reference to these domains will appear throughout the thesis.

1.3.2 The semi-classical limit

Another useful interpretation of the homogeneous disc cavity modes comes from semi-classical physics. A complete discussion on the subject is largely beyond the scope of this work, but we will outline the main ideas and results that we will often refer to (see [147] for a general discussion on the semi-classical physics of the disc cavity).

[16] The off-resonance results belong to the scattering description of the field, the wavenumber is real.



(a) $kR_0 = 13$ (b) $kR_0 = 16$

(c) $kR_0 = 16.5962405645$ (d) $kR_0 = 24.73813$

Fig. 1.14 Effective potential representation of the homogeneous disc cavity with $n_c = 1.5$, $n_o = 1.0$ and $R_0 = 1$ for $|m| = 21$. The 'classically forbidden' regions of the potential are colored in gray, and the energy level $(n_o k)^2$ is represented by the dashed green line with the wavefunction $|\psi(r,\phi)|^2 = |\mathcal{R}(r)|^2$ in plain blue trace standing upon it. (a) Below barrier regime (off-resonance); (b) In-barrier regime, off-resonance; (c) In-barrier regime, on-resonance $(21, 1)$; (d) Above barrier regime, on-resonance $(21, 4)$.

The semi-classical *Ansatz* for the scalar wave equation writes [9]

$$\psi(\mathbf{r}) \sim \mathrm{e}^{ikS(\mathbf{r})} \sum_{j=0}^{\infty} \frac{1}{(ik)^j} a_j(\mathbf{r}) \tag{1.70}$$

where $S(\mathbf{r}) \in \mathbb{R}$ is a real phase factor called the *eikonal* and $a_j(\mathbf{r}) \in \mathbb{R}$ are the amplitude factors of an *asymptotic expansion* in wavenumber k (*i.e.* the wavenumber is considered large with respect to the characteristic size of the object under study). The

amplitude factors a_j are supposed to be monotonous with respect to spatial coordinates in distinction to the fast changing kS term. Inserting this expression into the Helmholtz equation (1.18), we get the auxiliary expression arranged in leading powers of k

$$\begin{aligned} 0 \;=\;& k^2\left[-\left(\nabla S\right)^2+n^2(\mathbf{r})\right]\sum_{j=0}^{\infty}\frac{1}{(ik)^j}a_j \\ &+k^1\left[i\left(2\sum_{j=0}^{\infty}\frac{1}{(ik)^j}\nabla S\cdot\nabla a_j+\nabla^2 S\sum_{j=0}^{\infty}\frac{1}{(ik)^j}a_j\right)\right] \\ &+k^0\left[\sum_{j=0}^{\infty}\frac{1}{(ik)^j}\nabla^2 a_j\right] \quad . \end{aligned} \tag{1.71}$$

Keeping only the leading powers of k for the real and imaginary parts, we find a set of partial differential equations

$$\left(\nabla S\right)^2 = n^2 \tag{1.72}$$

$$2\nabla S\cdot\nabla a_0+a_0\nabla^2 S = 0 \quad . \tag{1.73}$$

The first one is the *eikonal* equation and the second one is called the *transport* equation. These are the general expressions that form the very framework of geometrical optics: for given 'initial' amplitude and a phase profile, the eikonal equation traces a series of trajectories or *geometrical rays* perpendicular to constant phase fronts $S(\mathbf{r}) = \text{const.}$, and the transport equation distributes the field amplitude accordingly. The geometrical rays reflect the variations of the refractive index $n(\mathbf{r})$. In the following we shall be especially interested in the complete phase of Eq. (1.70),

$$\theta = kS \quad . \tag{1.74}$$

We rewrite Eq. (1.72) in hamiltonian form

$$\frac{1}{2}\mathbf{p}^2+V(\mathbf{r})=E \tag{1.75}$$

with

$$\text{linear momentum:} \qquad \mathbf{p} = \nabla\theta \tag{1.76}$$

$$\text{potential:} \qquad V(\mathbf{r}) = \frac{1}{2}\left[(n_o k)^2-(n(\mathbf{r})k)^2\right] \tag{1.77}$$

$$\text{constant energy:} \qquad E = \frac{1}{2}(n_o k)^2 \quad . \tag{1.78}$$

For a refractive index defined in a piecewise manner such as the disc cavity, the linear momentum $\mathbf{p}$ is locally constant due to Eq. (1.72) and the classical trajectories associated to (1.75) are straight lines. The position along a trajectory may be cast in a

parametrical form $\mathbf{q}(\tau) = \mathbf{p}\tau + \mathbf{q}(0)$ where τ is a scalar parameter running along one trajectory. For smoothly varying refractive indices, trajectories are bent [122].

At this point, the equations for the motion of individual light particles in dielectric cavities are known, regardless of our ability to solve exactly Eqs (1.72) and (1.73). However the disc cavity is a special case that allows for an exact solution of *all* the trajectories at once, that is, the solution for θ through the eikonal equation (1.72).

Taking into account the natural symmetry of the problem in polar coordinates - $V(\mathbf{r}) = V(r) = V_0$ for $r < R_0$ - we first assume separability of the phase θ into radial and angular parts,

$$\theta(r, \phi) = \theta_r(r) + \theta_\phi(\phi) \quad . \tag{1.79}$$

Inserting into Eq. (1.75) leads to

$$\left(\frac{d\theta_r}{dr}\right)^2 + \frac{1}{r^2}\left(\frac{d\theta_\phi}{d\phi}\right)^2 + V_0 = E \tag{1.80}$$

Since no quantity in this expression explicitly depends on the angular position ϕ other that $\theta_\phi(\phi)$, we must have

$$\frac{d\theta_\phi}{d\phi} = K_0 = \text{const.} \quad . \tag{1.81}$$

Taking the positive root of the differential component of Eq. (1.81), the formal solution to (1.81) is

$$\theta_r = \int dr \sqrt{(E - V_0) - K_0^2/r^2} + K_1 \tag{1.82}$$

where K_1 is an arbitrary constant. Following the change of variable

$$\eta = \frac{K_0}{\sqrt{E - V_0}}\frac{1}{r} \tag{1.83}$$

the integral (1.82) becomes

$$\theta_r = K_0 \int d\eta \, \frac{1}{\eta^2}\sqrt{1 - \eta^2} + K_1 \tag{1.84}$$

which is easily solved by integration by parts[17]. For $r > K_0/\sqrt{E - V_0}$, the solution to (1.84) is

$$\theta_r = -\sqrt{(E - V_0)r^2 - K_0^2} + K_0 \arccos \frac{K_0}{\sqrt{(E - V_0)}r} + K_1 \quad . \tag{1.85}$$

Recalling that this is the solution for the positive root of the differential component of Eq. (1.81), we write the two solutions for θ_r

$$\theta_r^{\pm}(r) = \pm \left[+\sqrt{(E - V_0)r^2 - K_0^2} - K_0 \arccos \frac{K_0}{\sqrt{(E - V_0)}r}\right] + K_1^{\pm} \quad , \; r > K_0/\sqrt{E - V_0} \quad . \tag{1.86}$$

[17] $\int udv = \int d(uv) - \int vdu$ and $u = \sqrt{1 - \eta^2}$ and $v = -1/\eta$

The complete solution for Eq. (1.72) in cylindric coordinates for a constant refractive index n, and $r > K_0/nk$ is therefore

$$\theta^{\pm}(r,\phi) = \pm\left[+\sqrt{n^2k^2r^2 - K_0^2} - K_0 \arccos\frac{K_0}{nkr}\right] + K_1^{\pm} + K_0\phi \quad , \; r > \frac{K_0}{nk} \quad . \tag{1.87}$$

Taking the gradient of this function in order to compute the trajectories' momentum $\mathbf{p}$ Eq. (1.76), we find

$$\mathbf{p}^{\pm} = \nabla\theta^{\pm} = \pm\frac{\sqrt{(nkr)^2 - K_0^2}}{r}\hat{r} + \frac{K_0}{r}\hat{\phi} \quad . \tag{1.88}$$

This result shows that free-propagating trajectories forming straight lines are actually each composed of two line segments coalescing into a circle of radius $r = K_0/nk$: for a given trajectory, $\mathbf{p}^-$ is incident on this circle (the $\hat{r}$ component is negative), and $\mathbf{p}^+$ is leaving the circle, Fig. 1.15. This accumulation line of all trajectories is referred to as a *caustic curve* [9]. The scattering process onto a caustic curve results for an outgoing trajectory in a $-\pi/2$ phase offset with respect to the incoming one [9, 28]. This motivates us to set $K_1^{\pm} = \mp\pi/4$ in Eq. (1.87) so that scattering by the caustic is naturally taken into account in a symmetrical way by θ^+ and θ^-,

$$\theta^{\pm}(r,\phi) = \pm\left[+\sqrt{n^2k^2r^2 - K_0^2} - K_0 \arccos\frac{K_0}{nkr} - \frac{\pi}{4}\right] + K_0\phi \quad , \; r > \frac{K_0}{nk} \quad . \tag{1.89}$$

For waves below the caustic radius $r < K_0/nk$, the analysis of *complex* rays [68, 28] shows that the Eikonal takes the form

$$\Lambda^{\pm}(r,\phi) = \mp i\left[+\sqrt{K_0^2 - n^2k^2r^2} - K_0 \operatorname{arccosh}\frac{K_0}{nkr}\right] + K_0\phi \quad , \; r < \frac{K_0}{nk} \quad . \tag{1.90}$$

Recalling that one idea behind the semi-classical *Ansatz* (1.70) involves the separation of a slow moving amplitude term and a fast evolving phase term, this *complexified* eikonal suppresses the amplitude terms a_j on a shorter length scale than they would do on their own. Notice that these formulations for the phase are the same as the ones for the large m expansion for the different Bessel and Hankel functions Eq. (A.32).

For K_0 not an integer, the wave function as defined by Eq. (1.70) is not continuous over a round trip about the origin. Because of this, K_0 will be set to an integer value m.

Computing $\mathbf{L} = \mathbf{r} \times \mathbf{p}$ confirms that m is the modulus of the classical angular momentum, and the same for both function θ^+ and θ^- Eq. (1.89). This enforces our nomenclature for m being the angular momentum in the full wave description of the field.

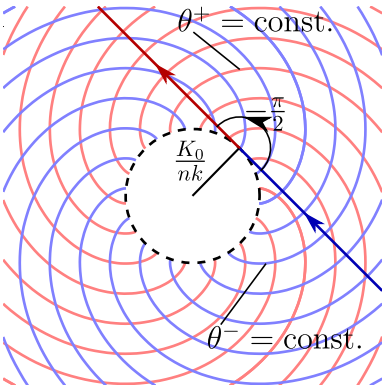


Fig. 1.15 Phases $\theta^-(r,\phi)$ (blue) and $\theta^+(r,\phi)$ (red) according to Eq. (1.89) evaluated at evenly spaced constant values. A geometrical trajectory 'optical ray' perpendicular to the constant phase levels Eq. (1.88) is also shown with emphasis on the changeover at the caustic from the incoming wave in blue to the outgoing wave in red. The scattering by the caustic curve causes a phase offset of $-\pi/2$ between the two wave types.

So far, we have only managed to solve the eikonal equation in polar coordinates irrespective of the actual cavity shape. The benefits of this procedure appear as we apply the boundary conditions of a disc cavity to Eq. (1.89).

The solution of the disc cavity problem with refractive index (1.45) demands that the boundary conditions (1.29)-(1.30) be satisfied. This can be done with a superposition of first order waves $a_0 e^{i\theta}$ or $a_0 e^{i\Lambda}$ known to solve the Eikonal and transport equations (1.72)-(1.73) for a given geometry,

$$\psi_0(\mathbf{r}) = \sum_l a_0^l e^{i\theta^l} + \sum_l \alpha_0^l e^{i\Lambda^l} \quad . \tag{1.91}$$

For the cylindrical coordinates, we have found in Eq. (1.89) that two real wave types exist above the caustic: one directed toward the caustic and the other, leaving it. The presence of a physical circular boundary at $r = R_0$ concentric to the caustic $r = m/n_c k$ implies that the incoming and outgoing waves to the caustic must be connected to each other again at the exterior interface $R_0 > m/n_c k$, Fig. 1.17. For the sake of simplicity, we will assume that the cavity does not leak: the reflection at the physical boundary at $r = R_0$ leaves the amplitudes a_0^l untouched except, perhaps, for a *phase offset that is to be transferred to the phase term* θ^l *in any case.*

How many waves need to be superimposed in Eq. (1.91) to solve the disc problem? Since we are concerned with waves keeping their total energy (the media are lossless everywhere including the boundaries), and that the linear momentum at the circular boundary from an incoming trajectory $|\mathbf{p}^+ \cdot \hat{r}|$ to a reflected one $|\mathbf{p}^- \cdot \hat{r}|$ is constant for a given m, we may assume that a single pair of $\theta^+ = \theta_m^+$ and $\theta^- = \theta_m^-$ is sufficient to solve the problem of elastic reflection at the interface for $r < R_0$. We may of course superpose

waves of different values of angular momentum, but these will not interact with each other: wavefunctions labeled with integer angular momenta form an orthogonal set of functions.

For $r > R_0$, we shall rely on the decaying types of waves involving $\Lambda^{\pm} = \Lambda_m^{\pm}$ phase factors (1.90). This prescription is indicated since we want the 'real' waves to remain within the cavity. This description is closely related to the one used for the total internal reflection phenomenon [58]. Notice that in this case, the cavity is enclosed in a second caustic boundary located at $r = m/n_o k > R_0$.

Under these conditions, the complete semi-classical field is modeled as

$$\psi_0(\mathbf{r}) = \begin{cases} a^+ e^{i\theta_m^+} + a^- e^{i\theta_m^-} & r \leq R_0 \\ \alpha^- e^{i\Lambda_m^-} & r \geq R_0 \end{cases} \tag{1.92}$$

with the explicit phase functions

$$\theta_m^{\pm}(r,\phi) = \pm\left[+\sqrt{n_c^2 k^2 r^2 - m^2} - m\arccos\frac{m}{n_c k r} - \frac{\pi}{4}\right] + m\phi \tag{1.93}$$

$$\Lambda_m^{-}(r,\phi) = +i\left[+\sqrt{m^2 - n_o^2 k^2 r^2} - m\,\mathrm{arccosh}\frac{m}{n_o k r}\right] + m\phi \quad . \tag{1.94}$$

The application of the TM boundary conditions (1.29)-(1.30) on (1.92) should indicate any phase offset conditions on the boundary reflected cavity waves, and no changes in internally reflected waves should be observed.

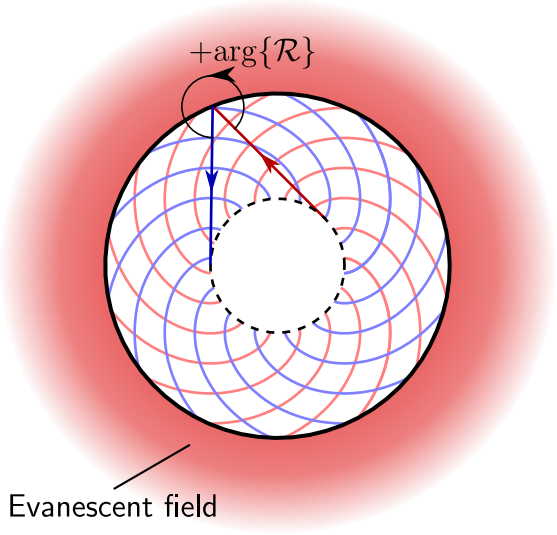


Fig. 1.16 Application of Eq. (1.89) to the disc cavity of radius R_0 in a no loss scenario. A trajectory perpendicular to constant phase levels is reflected at the boundary of the cavity and undergoes a phase shift as it moves from an outgoing wave to an incoming wave.

Using the TM boundary conditions (1.29)-(1.30), we are led to

$$\left[a_0^+ \mathrm{e}^{i\theta_m^+} + a_0^- \mathrm{e}^{i\theta_m^-}\right]_{r=R_0} = \left[\alpha_0^- \mathrm{e}^{i\Lambda_m^-}\right]_{r=R_0} \tag{1.95}$$

$$\frac{\partial}{\partial r}\left[a_0^+ \mathrm{e}^{i\theta_m^+} + a_0^- \mathrm{e}^{i\theta_m^-}\right]_{r=R_0} = \frac{\partial}{\partial r}\left[\alpha_0^- \mathrm{e}^{i\Lambda_m^-}\right]_{r=R_0} \quad . \tag{1.96}$$

These conditions are valid for all angles ϕ.

Recalling that our semi-classical model implies that the phase factors are rapidly changing in comparison to the amplitude factors, condition (1.96) may be simplified by keeping only the leading terms involving phase derivatives,

$$\left[a_0^+ \mathrm{e}^{i\theta_m^+} \frac{\partial \theta_m^+}{\partial r} + a_0^- \mathrm{e}^{i\theta_m^-} \frac{\partial \theta_m^-}{\partial r}\right]_{r=R_0} \simeq \left[\alpha_0^- \mathrm{e}^{i\Lambda_m^-} \frac{\partial \Lambda_m^-}{\partial r}\right]_{r=R_0} \quad . \tag{1.97}$$

Using condition (1.95) to form a ratio with (1.97), the α_0^- coefficient is canceled out, leaving

$$\frac{a_0^+ \mathrm{e}^{i\theta_m^+} \frac{\partial \theta_m^+}{\partial r} + a_0^- \mathrm{e}^{i\theta_m^-} \frac{\partial \theta_m^-}{\partial r}}{a_0^+ \mathrm{e}^{i\theta_m^+} + a_0^- \mathrm{e}^{i\theta_m^-}} = \left.\frac{\partial \Lambda_m^-}{\partial r}\right|_{r=R_0} \quad . \tag{1.98}$$

Using Eqs (1.93) and (1.94), the radial derivatives are evaluated and we readily obtain the relation between the incoming and reflected waves,

$$\left. a_0^- \mathrm{e}^{i\theta_m^-}\right|_{r=R_0} = \left. a_0^+ \mathrm{e}^{i\theta_m^+ + i\arg\{\mathcal{R}\}}\right|_{r=R_0} \tag{1.99}$$

with the argument of the reflection coefficient

$$\arg\{\mathcal{R}\} = -2\arctan\left(\frac{\sqrt{m^2 - (n_o k R_0)^2}}{\sqrt{(n_c k R_0)^2 - m^2}}\right) \quad . \tag{1.100}$$

The relation (1.99) implies that the phases must be equal, leading to the condition on the only undetermined parameter k

$$\sqrt{n_c^2 k^2 R_0^2 - m^2} - m \arccos\frac{m}{n_c k R_0} - \frac{\pi}{4} = \arctan\left(\frac{\sqrt{m^2 - (n_o k R_0)^2}}{\sqrt{(n_c k R_0)^2 - m^2}}\right) + (j-1)\pi \ , \ j \in \mathbb{Z} \quad . \tag{1.101}$$

Since the left hand side of Eq. (1.101) is monotonically *increasing* with k from a minimum value of $-\pi/4$ at $k = m/n_c R_0$, and that the right hand side is monotonically *decreasing* from $j\pi - \pi/2$ at $k = m/n_c R_0$ to $j\pi - \pi$ at $k = m/n_o R_0$, we expect that some values of $j \geq 1$ might lead to solutions of Eq. (1.101). This result is in accord with the onset, at a certain wavenumber value, of series of resonant solutions of a given m, as observed in Figs 1.13 and 1.12.

The limiting values of the right hand side of Eq. (1.101) are known to correspond to Dirichlet (the total wavefunction is zero) and Neumann boundary conditions (the

wavefunction *derivative* is zero) [68]. This description fits well with the in-barrier case of the 1D potential model found in Section 1.3.1, the 'most reflected' waves being localised at the bottom of the potential 'dent' (Dirichlet) and 'free boundary' modes appearing near the top of the barrier (Neumann).

An example of graphical solution to Eq. (1.101) is presented in Fig. 1.17, and comparison of wavenumber values from peaks of the delay matrix and semi-classical approximation is provided in Tab. 1.2.

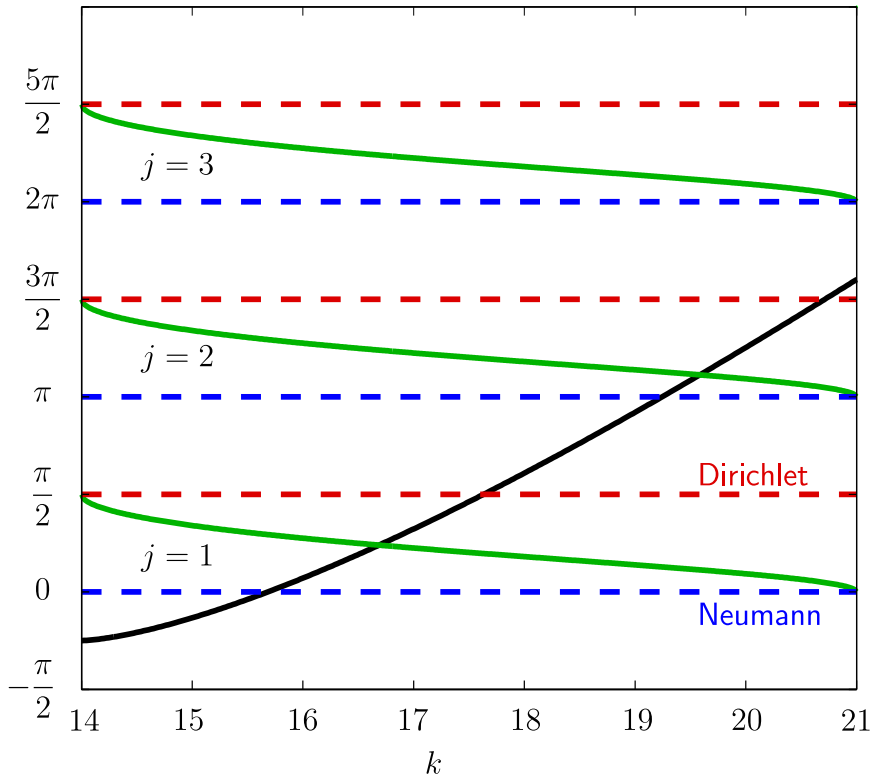


Fig. 1.17 Graphical solution to problem (1.101) for $m = 21$ and $n_c = 1.5$, $n_o = 1.0$ and $R_0 = 1$. The black line is the left hand side of (1.101) and green curves correspond to the right hand side; solutions are at the crossings. Also shown are the limits of the right hand side of Eq. (1.101) associated to Dirichlet (blue) and Neumann (red) problems. While solutions for larger k tend toward the Neumann problem typical of 'open boundary' systems, solutions for $j = 1$ resemble more to the Dirichlet problem characteristic of total reflection phenomenon.

As noted in [68], the semi-classical approximation yields surprisingly accurate results even for small values of the wavenumber. The use of the semi-classical result (1.101) provides a good approximation of the disc's high quality resonant peak positions while being easy to evaluate in comparison to peak delay detection or identification of poles of $\mathbf{S}$ near the real axis as indicated by Eqs (1.63) and (1.64) respectively. Also, the normalized component of the linear momentum (1.88) that is tangential to the disc

Mode (m, j)	kR_0 from peaks of $\mathbf{Q}$	kR_0 from Eq. (1.101)	% difference
$(21, 1)$	16.60	16.69	0.5%
$(21, 2)$	19.48	19.58	0.5%
$(31, 1)$	23.76	23.81	0.2%
$(31, 2)$	26.98	27.06	0.3%
$(31, 3)$	29.99	29.62	1.2%

Tab. 1.2 Comparison of exact peak position of selected resonances from the delay matrix and solutions of the semi-classical approximation Eq. (1.101) for the disc cavity of radius $R_0 = 1$ and refractive index $n_c = 1.5$ and $n_o = 1.0$. The decreasing relative difference from $m = 21$ to $m = 31$ for a given j is expected from the semi-classical approximation.

boundary is readily linked to the incidence angle χ

$$p = \frac{m}{n_c k R_0} = \sin\chi \quad . \tag{1.102}$$

This last relation will often be recalled throughout the thesis as it provides a direct relation from the wave picture to the classical billiard model.

Although extremely appealing at first, the semi-classical approximation of the field fails rapidly for geometries departing from the disc. The reason is that the sum (1.91) needs a finite number of terms to converge. This predicament is discussed in [140] where the case for chaotic cavities - or cavities showing some degree of chaos - is explained to be especially pathological with regards to the semi-classical model. For these often encountered cavities, an infinite number of contributions to (1.91) is expected.

Nevertheless, we shall use the classical picture of propagating rays provided by (1.76) to gather dynamical properties of large sets of trajectories. The idea behind this convenient theoretical shortcut is that a wave is expected to have a certain resolving power at a given finite wavelength. It may not be enough to identify minute trajectories, but large ensembles of trajectories might be within the modeling scope. Chapter 4 explores an application of the concept.

Chapter 2

Formalism I: Theoretical and numerical approach

We develop in this Chapter a *scattering description* of the resonant modes of 2D dielectric cavities. The first Section is concerned with the formal development of the method together with its fundamental properties and idiosyncrasies. The scattering matrix **S** and the Wigner-Smith delay matrix **Q** are introduced and special attention to their numerical implementations are discussed in Section 2.2 and 2.4 respectively. Section 2.3 is devoted to the reconstruction of the wavefunction over all space and we propose a hybrid method composed of our scattering approach and a Finite Element Method for completing this task. The *homogeneous disc* and the *annular cavity* (both of which have a closed-form **S** matrix) are used extensively for numerical calibrations of our computations. The benchmark calculations serve to insure the reliability of the numerical results to be presented in the subsequent Chapters. Two Appendices (C and D) complete the theoretical and numerical descriptions.

The dielectric cavities investigated in this Chapter are assumed to be of finite volume with a small thickness along the Oz axis. The field dynamics is then essentially confined to the $OxOy$ plane, and a convenient separation of the two polarization states relative to that plane is possible. Despite recent concerns about the *quantitative* predictions of this model [17, 18, 19], we argue that a qualitative (in all cases) or semi-quantitative (in most cases) agreement with experiment can readily be achieved as validated by a number of experimental realisations of quasi-2D cavities (see [56] for a recent review and references therein). For the sake of simplicity, we concentrate on TM polarization only (electric field along Oz axis).

The electromagnetic resonant modes of a cavity are usually defined through the complex wavenumber poles of the scattering matrix, the *emission viewpoint*. Poles located in the lower half of the complex wavenumber plane are associated with emission modes of the cavity (the field exponentially *increasing* in the far-field) while *zeros* in the upper half of the complex plane describe completely absorbing resonances (the field exponentially *decreasing* in the far-field). In this Chapter however, we will focus on a *scattering viewpoint* and will present an alternative way of defining the modes of a cavity. At times, we will oppose and compare the results obtained from the *emission* and the *scattering* point of view.

The original content of this Chapter revolves around the use of the characteristic modes of a dielectric cavity obtained through the diagonalisation of the delay matrix to describe the behaviour of the electromagnetic field resulting from the interaction with the said cavity. The derivation of the energy matrix/delay matrix Eq. (2.14), based on the one of Smith [135], and the related consequences to its use, Sections 2.1.2 and 2.1.3, and the comparison between characteristic modes and emission modes of Sections 2.1.3 and 2.4, are understood to be original [95, 96, 94]. Also, an important simplification leading to Eq. (2.71) in the numerical algorithm used to compute the scattering matrix [113, 112] may be considered original as well [103, 96, 94].

2.1 An energy description of the modes

2.1.1 Main derivation

The *time-averaged electromagnetic energy* inside a volume V occupied by a monochromatic real electric field $\tilde{\mathbf{E}}(\mathbf{r},t) = \frac{1}{2}\left[\mathbf{E}(\mathbf{r})\mathrm{e}^{-i\omega t} + \mathbf{E}^*(\mathbf{r})\mathrm{e}^{+i\omega t}\right]$, $\omega \in \mathbb{R}$, and its associated magnetic field, $\tilde{\mathbf{H}}(\mathbf{r},t) = \frac{1}{2}\left[\mathbf{H}(\mathbf{r})\mathrm{e}^{-i\omega t} + \mathbf{H}^*(\mathbf{r})\mathrm{e}^{+i\omega t}\right]$ is

$$\mathcal{E}^V = \int_V d^3\mathbf{r} \ \left[\frac{1}{4}\varepsilon\mathbf{E}^*\cdot\mathbf{E} + \frac{1}{4}\mu\mathbf{H}^*\cdot\mathbf{H}\right] \tag{2.1}$$

where $\varepsilon = \varepsilon_0 n^2(\mathbf{r}) \in \mathbb{R}$ is a time/frequency independent permitivity and $\mu = \mu_0$ is the magnetic permeability of vacuum. The speed of light in vacuum, $c = 1/\sqrt{\epsilon_0\mu_0}$, relates the angular frequency ω to the wavenumber k via the dispersion relation $\omega = ck$. For Eq. (2.1) to be useful, one must specify the electromagnetic field that satisfies propagation properties in a medium of refractive index $n(\mathbf{r})$ with appropriate boundary conditions.

The cavity may always be enclosed in a cylindrical volume V_c of radius $R_{\max}$ and 'small' width w, itself contiguous to a larger annular cylindrical volume $V - V_c$ of exterior radius

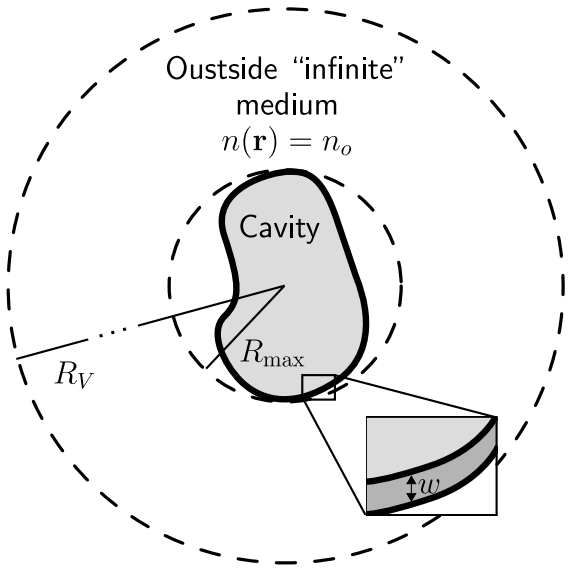


Fig. 2.1 Top view of the dielectric cavity and its surroundings. The cavity itself is a thin slab of dielectric material of width w along the Oz axis (close-up box) and is restricted to a cylindrical domain of radius $R_{\max}$. This cylinder is placed inside a large coaxial annular cylinder whose radius R_V shall eventually reach infinity.

R_V (see Fig. 2.1). Inside the latter domain of dielectric constant n_o, a component of the electric field $\mathbf{E}(\mathbf{r}) = \psi(\mathbf{r})\hat{z}$ solving Helmholtz' equation

$$\left[\nabla^2 + n_o^2 k^2\right] \psi_m(\mathbf{r}) = \left[\frac{\partial^2}{\partial r^2} + \frac{1}{r}\frac{\partial}{\partial r} + \frac{1}{r^2}\frac{\partial^2}{\partial \phi^2} + n_o^2 k^2\right] \psi_m(r,\phi) = 0 \tag{2.2}$$

may be written as

$$\psi_m(\mathbf{r}) = H_m^{(2)}(n_o k r)\mathrm{e}^{im\phi} + \sum_{m'=-\infty}^{+\infty} S_{m'm}(k) H_{m'}^{(1)}(n_o k r)\mathrm{e}^{im'\phi} \tag{2.3}$$

where $H_\nu^{(1,2)}(\xi)$ are Hankel functions and $\{S_{m'm}\}$ are the cavity scattering matrix elements in an angular momentum basis. The infinite summation will be practically truncated to a finite symmetric range from $-M$ to $+M$ for numerical implementation. For real k, the scattering matrix $\mathbf{S}$ is unitary ($\mathbf{S}^{-1} = \mathbf{S}^\dagger$) due to flux conservation, and satisfies 'time reversal symmetry' through the complex transpose operation † on the wavefunction. This property enables one to deduce a special characteristic of the $\mathbf{S}$ matrix that will be useful in the numerical implementation of Section 2.2.

Consider the outgoing wave components labeled $\{m'\}$ resulting from incoming wave component m. Outgoing/Incoming wave convention refers to the asymptotic expansions of Hankel functions found in [1] (or see Appendix A) relative to an implicit time dependence $\mathrm{e}^{-i\omega t}$. The following succession of operations lead to a particularly useful

property of the **S** matrix elements:

$$\begin{aligned} H_m^{(2)}(z)\mathrm{e}^{+im\phi} &\rightarrow \sum_{m'} S_{m'm} H_{m'}^{(1)}(z)\mathrm{e}^{+im'\phi} && \text{initial reaction} \\ \sum_m S^*_{m'm} H_m^{(2)}(z)\mathrm{e}^{+im\phi} &\rightarrow H_{m'}^{(1)}(z)\mathrm{e}^{+im'\phi} && \text{unitarity of } \mathbf{S} \\ \sum_m S_{m'm} H_m^{(1)}(z)\mathrm{e}^{-im\phi} &\leftarrow H_{m'}^{(2)}(z)\mathrm{e}^{-im'\phi} && \text{time-reversed reaction } (*) \end{aligned}$$

Finally, using the property $H_{-m}^{(1,2)}(z) = (-1)^m H_m^{(1,2)}(z)$ [1] and comparing the time-reversed reaction with the initial one, we conclude that (see Notation for angular momentum ordering of **S**)

$$S_{m'm} = (-1)^{m'} S_{-m-m'} (-1)^m \tag{2.4}$$

or, in matrix notation,

$$\mathbf{S} = \mathbf{P}\,\mathbf{S}^T\,\mathbf{P}\ , \tag{2.5}$$

where $\{\mathbf{P}\}_{mm'} = (-1)^m \delta_{-mm'}$ and superscript T denotes the (non-complex) transpose operation. Matrix **P** is simultaneously its own inverse ($\mathbf{P}^2 = \mathbb{1}$) and transpose.

Although the field inside V_c is not simply expressible as in Eq. (2.3), we will retain the label m to identify the field $\psi(\mathbf{r})$ inside $r < R_{\max}$ as well. Recalling expression (2.1), we define a (complex) *energy matrix* inside volume V, whose elements are

$$\mathcal{E}^V_{mm'} = \int_V d^3\mathbf{r} \left[\frac{1}{4}\varepsilon \mathbf{E}^*_m \cdot \mathbf{E}_{m'} + \frac{1}{4}\mu \mathbf{H}^*_m \cdot \mathbf{H}_{m'}\right] \quad . \tag{2.6}$$

Using Maxwell's equations for a monochromatic electric field along the Oz axis, we obtain

$$\mathcal{E}^V_{mm'} = \frac{\varepsilon_0}{2}\int_V d^3\mathbf{r} \left[\psi^*_m \psi_{m'} + \frac{1}{2k^2}\nabla\cdot(\psi_{m'}\hat{z} \times \nabla \times \psi^*_m \hat{z})\right]. \tag{2.7}$$

From the parametric derivative of Helmholtz' equation, we can show that [135]

$$n^2(\mathbf{r})\psi^*_m\psi_{m'} = \frac{1}{2k}\nabla\cdot\left[\frac{\partial\psi_{m'}}{\partial k}\nabla\psi^*_m - \psi^*_m\nabla\frac{\partial\psi_{m'}}{\partial k}\right] \tag{2.8}$$

transforming (2.7) to

$$\begin{aligned} \mathcal{E}^V_{mm'} \;=\; & \frac{\varepsilon_0}{4k}\int_V d^3\mathbf{r}\ \nabla\cdot\left(\frac{\partial\psi_{m'}}{\partial k}\nabla\psi^*_m - \psi^*_m\nabla\frac{\partial\psi_{m'}}{\partial k}\right) \\ & + \frac{\varepsilon_0}{4k^2}\int_V d^3\mathbf{r}\ \nabla\cdot(\psi_{m'}\hat{z}\times\nabla\times\psi^*_m\hat{z})\,. \end{aligned} \tag{2.9}$$

Equation (2.9) is then integrated over the thin cylindrical volume V using the divergence theorem, resulting in

$$\begin{aligned} \mathcal{E}^V_{mm'} \;=\; & \frac{\varepsilon_0 w R_V}{4k}\int_0^{2\pi} d\phi\ \left(\frac{\partial\psi^*_m}{\partial r}\frac{\partial\psi_{m'}}{\partial k} - \psi^*_m\frac{\partial^2\psi_{m'}}{\partial k\partial r}\right) \\ & + \frac{\varepsilon_0 w R_V}{4k^2}\int_0^{2\pi} d\phi\ \frac{\partial\psi^*_m}{\partial r}\psi_{m'}. \end{aligned} \tag{2.10}$$

Inserting (2.3) in the preceding expression solves the integration over angle ϕ. Taking the limit $R_V \to \infty$ permits the use of asymptotic expressions for the different Hankel functions (Appendix A) and the complex energy matrix element now takes the form

$$\begin{aligned} \mathcal{E}^{\infty}_{mm'} &= \lim_{R_V\to\infty} \mathcal{E}^{V}_{mm'} && (2.11)\\ &= \lim_{R_V\to\infty} \left[\frac{4\varepsilon_0 n_o R_V w}{k} + \mathcal{O}(R_V^{-1})\right]\delta_{mm'} + \frac{2\varepsilon_0 w}{k}\left(-i\sum_j S^*_{jm}\frac{\partial S_{jm'}}{\partial k}\right) && (2.12)\\ &\equiv \mathcal{E}^{0}_{mm'}\delta_{mm'} + \mathcal{E}_{mm'}. && (2.13) \end{aligned}$$

The first term $\mathcal{E}^0_{mm'}$ is associated with the linearly increasing energy inside a large cylinder of refractive index n_o. This diverging 'free-space' energy is denoted by $\mathcal{E}^0$. The second term $\mathcal{E}_{mm'}$ however is independent of R_V and represents the *excess energy* inside the volume V and attributed to the presence of the cavity. We then write the *excess energy matrix*

$$\mathcal{E} = \frac{2\varepsilon_0 w}{k}\left(-i\mathbf{S}^\dagger\frac{\partial \mathbf{S}}{\partial k}\right). \tag{2.14}$$

Since $\mathbf{S}$ is unitary for real wavenumbers, $\mathcal{E}$ is hermitian symmetric.

Of course, any electromagnetic field substituted into (2.1) should yield a real energy. One then looks for a fundamental set of fields $\{\mathbf{E}^p\} = \{\psi^p\hat{z}\}$ such that

$$\mathcal{E}^{\infty}_{pp'} = \int_V d^3\mathbf{r}\ \left[\frac{1}{4}\varepsilon\mathbf{E}^{p*}\cdot\mathbf{E}^{p'} + \frac{1}{4}\mu\mathbf{H}^{p*}\cdot\mathbf{H}^{p'}\right] \equiv e^{\infty}_p\delta_{pp'}. \tag{2.15}$$

This expression states our intention of finding a set of non-interacting *characteristic modes*. These modes in turn may always be represented outside $R_{\max}$ in the angular momentum basis by an expression of the form

$$\psi^p(\mathbf{r}) = \sum_m \left[A^p_m H^{(2)}_m(n_o kr) + B^p_m H^{(1)}_m(n_o kr)\right]\mathrm{e}^{im\phi} \tag{2.16}$$

where $B^p_m = \sum_{m'} S_{mm'}A^p_{m'}$. Equation (2.15) is simply the expression of the eigen-decomposition of total energy equation (2.12). Because $\mathcal{E}^0$ is *independent of the angular momentum basis*, however divergent it might be, any field satisfying $\mathbf{A}^{p\dagger}\cdot\mathbf{A}^{p'} \propto \delta_{pp'}$ in expression (2.15) automatically yields a real free-space energy component. And since the only relevant physical quantity is the excess energy matrix (2.14), it will easily be diagonalized in an orthogonal basis conveniently chosen to satisfy the reality of the free-space energy $\mathcal{E}^0$.

2.1.2 Energy modes as stationary scattering states

The scattering matrix found in the expression of excess energy (2.14) satisfies the time reversibility condition (2.5). Using this relation and letting $\mathbf{A}^p$ be an eigenvector of

matrix $\mathcal{E}$ with eigenvalue e_p, it is found that vector $\mathbf{S}^\dagger\mathbf{P}\mathbf{A}^{p*}$ is also an eigenvector of $\mathcal{E}$ with the same eigenvalue e_p, i.e.

$$\mathcal{E}\mathbf{A}^p = e_p\mathbf{A}^p \quad \xrightarrow{(2.5)} \quad \mathcal{E}\left(\mathbf{S}^\dagger\mathbf{P}\mathbf{A}^{p*}\right) = e_p\left(\mathbf{S}^\dagger\mathbf{P}\mathbf{A}^{p*}\right) \ . \tag{2.17}$$

For normalized $\mathbf{A}^p$, the vectors $\mathbf{S}^\dagger\mathbf{P}\mathbf{A}^{p*}$ are also normalised ($\mathbf{P} = \mathbf{P}^{-1} = \mathbf{P}^\dagger$ and $\mathbf{S}$ is unitary), and they can only be related to each other by a phase factor, i.e.

$$\mathbf{A}^p = \mathrm{e}^{-i\theta_p}\mathbf{S}^\dagger\mathbf{P}\mathbf{A}^{p*} \quad . \tag{2.18}$$

As it stands, this relation is also retrieved considering that the channel wavefunction $\psi_p(\mathbf{r})$, for $r \geq R_{\max}$, is made up of an incoming $\psi^p_{\text{in}}(\mathbf{r})$ and an outgoing $\psi^p_{\text{out}}(\mathbf{r})$ part

$$\begin{aligned} \psi^p(\mathbf{r}) &= \psi^p_{\text{in}}(\mathbf{r}) + \psi^p_{\text{out}}(\mathbf{r}) \\ &= \left(\sum_m A^p_m H^{(2)}_m(n_o kr)\mathrm{e}^{im\phi}\right) + \left(\sum_m B^p_m H^{(1)}_m(n_o kr)\mathrm{e}^{im\phi}\right) \end{aligned} \tag{2.19}$$

leading to

$$[\psi^p_{\text{in}}(\mathbf{r})]^* = \mathrm{e}^{-i\theta_p}\psi^p_{\text{out}}(\mathbf{r}). \tag{2.20}$$

The eigenvectors of the excess energy matrix are then understood as *self-replicating waves* through the interaction with the cavity. Relation (2.18) itself represents the action of an anti-unitary operator on vector $\mathbf{A}^p$, a property revealing the reversibility of the associated wavefunction [52]. Vectors $\{\mathbf{A}^p\}$ define a fundamental set of electromagnetic modes that are captured by the cavity in the exact same fashion as they are released, hence the name *characteristic modes of the cavity*. The phase factor $\mathrm{e}^{-i\theta_p}$, due to the cavity, embodies the lag between incoming and outgoing parts of a given reference angular momentum channel. It may always be eliminated by a suitable choice of phase for $\mathbf{A}^p$. This implies that the complete wave function $\psi^p_{\text{in}} + \psi^p_{\text{out}}$ may always be taken real. One observes further that the reversibility property of characteristic modes are closely related to the duality of absorption zeros/emission poles in the complex k plane (see Fig. 2.2 for instance). This specific topic is discussed in the next subsection.

The delay associated with the presence of the cavity with respect to free-space propagation may be understood as the ratio of the excess energy to the incoming/outgoing total power. This calculation is needed to properly normalize the overall excess energy (*i.e.* the delay must be independent of the amplitude of the field). The incoming power is computed over the external boundary of the large cylinder (see Fig. 2.1). The modulus of the incoming/outgoing electromagnetic power for a characteristic mode may be shown to be $(\mathbf{A}^{p\dagger}\mathbf{A}^p)2w/ck\mu_0$. Assuming normalization of the $\mathbf{A}^p$ coefficients, the *channel delay* $c\tau_p$ (in length units) of a characteristic mode of the cavity is then

$$c\tau_p = \mathbf{A}^{p\dagger}\left(-i\mathbf{S}^\dagger\frac{\partial\mathbf{S}}{\partial k}\right)\mathbf{A}^p \equiv \mathbf{A}^{p\dagger}\,\mathbf{Q}\,\mathbf{A}^p \quad . \tag{2.21}$$

One recognizes the matrix $\mathbf{Q}$ as the celebrated *lifetime matrix* of Felix Smith [135] introduced in the context of quantum mechanical multichannel scattering. It is also referred to as the *Wigner-Smith time-delay matrix* by some authors [26, 131]. We will adopt the denomination *delay matrix* or sometimes *time-delay matrix*. The characteristic modes [1] are therefore simply the eigenvectors of $\mathbf{Q}$.

Assuming $\theta = \theta_p$ being fixed relative to a given angular momentum channel, expression (2.20) may also be used as a starting point leading to the usual definition of *group delay*. Suppose that one knows an incoming wave $\psi_{\text{in}}(\mathbf{r})$ as defined above satisfying relation (2.20). From this expression, we obtain the identity

$$\left[\psi^*_{\text{out}}\frac{\partial\psi_{\text{out}}}{\partial k} - \psi_{\text{out}}\frac{\partial\psi^*_{\text{out}}}{\partial k}\right] + \left[\psi^*_{\text{in}}\frac{\partial\psi_{\text{in}}}{\partial k} - \psi_{\text{in}}\frac{\partial\psi^*_{\text{in}}}{\partial k}\right] = 2i\psi^*_{\text{in}}\psi_{\text{in}}\frac{\partial\theta}{\partial k}. \tag{2.22}$$

This equation is then integrated over ϕ and the large argument expansions of the Hankel functions are used (see Appendix A). Once the limit $r \to \infty$ is taken, we find to leading order an equivalence between the definition of the group delay and Smith's lifetime matrix,

$$\frac{\partial\theta}{\partial k} = \mathbf{A}^\dagger\left(-i\mathbf{S}^\dagger\frac{\partial\mathbf{S}}{\partial k}\right)\mathbf{A}. \tag{2.23}$$

This expression does not specify however the exact nature of the vector $\mathbf{A}$: it only establishes that the group delay between two waves, defined as the derivative of the phase offset relative to k, is measured by the delay matrix.

Finally, note that *not* every linear superpositions of vectors in the set $\{\mathbf{A}^p\}$ satisfy the reversibility property (2.20). An intuitive example is the scattering of an incident plane wave: although the incoming wave may be projected into the characteristic modes, the outgoing wave is unlikely to satisfy the self-replication condition (2.20).

2.1.3 Some properties of the Q matrix

• The fundamentals

Since the $\mathbf{S}$ and the $\mathbf{Q}$ matrices occupy central stage in our discussion, it is perhaps interesting to present some of their basic properties. We will focus on a formulation that sheds some light on their physical interpretation. Let the matrix

$$\mathbf{S}_j(k) = \mathbb{1} - \frac{i\Gamma_j}{k - k_j}\mathbf{P}_j \tag{2.24}$$

[1] Shimamura [131] has recently coined the term *Q-eigenchannels* to refer to the eigenvectors $\mathbf{A}^p$.

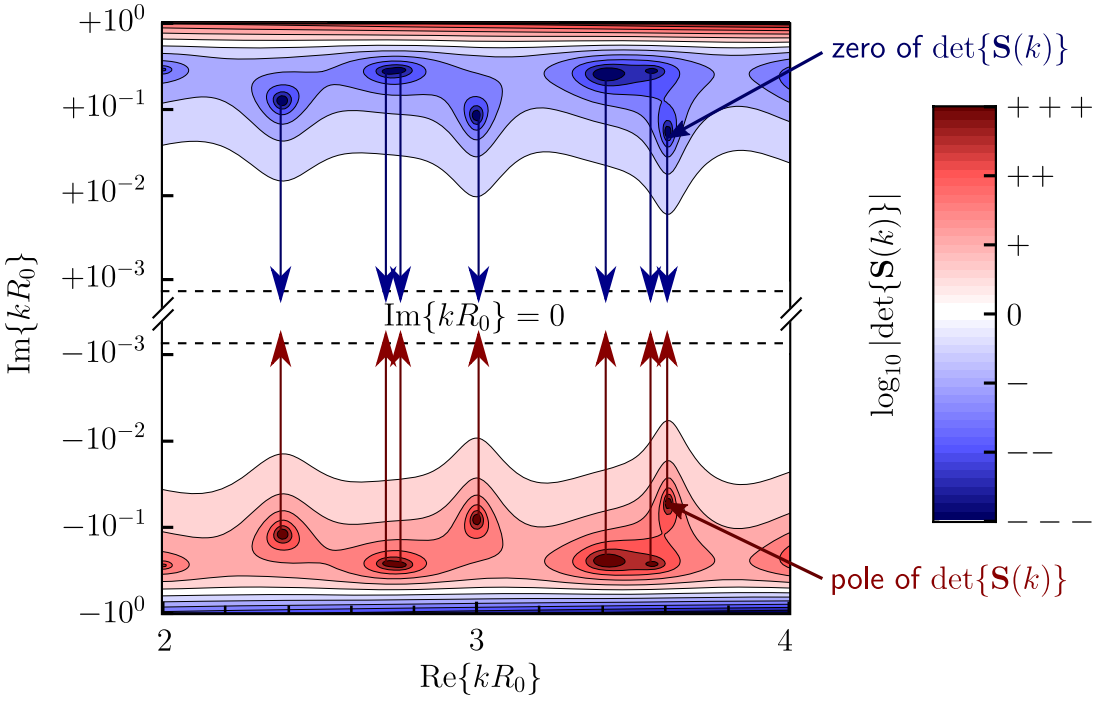


Fig. 2.2 Dichotomy in the positions of the zeros and poles of the **S** matrix. The scattering description presented in this chapter extracts the system's information from the complex k plane as one moves along the real k axis.

where $\mathbf{P}_j = \left|\, p_j \,\right\rangle\!\left\langle\, p_j \,\right|$ is a projector (rank 1 matrix) independent of k, and

$$k_j = \mathrm{Re}\{k_j\} - i\Gamma_j/2 \tag{2.25}$$

are the *complex resonance positions*. The set of *resonance channels* $\{\left|\, p_j \,\right\rangle\}$ are eigenvectors of the *channel* matrix $\mathbf{S}_j$ such that

$$\mathbf{S}_j(k)\left|\, p_j \,\right\rangle = \frac{k - k_j^*}{k - k_j}\left|\, p_j \,\right\rangle. \tag{2.26}$$

The usefulness of these channel matrices resides in the observation made by Simonius [134] that the full scattering matrix takes a product form

$$\mathbf{S}(k) = \prod_{j=1}^{\infty} \mathbf{S}_j(k) \quad , \tag{2.27}$$

that will make explicit the contributions of the individual resonances k_j. Clearly, this partition of the **S** matrix assumes that the scattering matrix possesses only simple poles located at positions $\{k_j\}$. Since $\mathbf{P}_j$ is a rank 1 projector with one eigenvalue equal to 1, the others being zero, taking the determinant of this expression yields

$$\det\{\mathbf{S}(k)\} = \prod_{j=1}^{\infty} \left(\frac{k - k_j^*}{k - k_j}\right) \quad . \tag{2.28}$$

The formulation (2.27) has the interesting property that the scattering matrix displays explicitly its simple poles and their corresponding complex conjugate zeros.

For complex k, the product $\mathbf{S}_j^\dagger \mathbf{S}_j$ loses its unitarity according to

$$\mathbf{S}_j^\dagger \mathbf{S}_j = \mathbb{1} - 2\mathrm{Im}\{k\} \frac{\Gamma_j}{|k-k_j|^2} \mathbf{P}_j \quad . \tag{2.29}$$

The unitarity deficit of the complete scattering matrix reads

$$\mathbf{S}^\dagger \mathbf{S} - \mathbb{1} = -2\mathrm{Im}\{k\} \sum_{j=1}^{\infty} \frac{\Gamma_j}{(k-k_j)\left(k^*-k_j^*\right)} \left(\mathbf{S}^\dagger \mathbf{\Lambda}_j^{\dagger -1} \big|\, p_j \,\right\rangle \left)\left(\mathbf{S}^\dagger \mathbf{\Lambda}_j^{\dagger -1} \big|\, p_j \,\right\rangle\right)^\dagger \tag{2.30}$$

where

$$\mathbf{\Lambda}_j(k) = \prod_{j'=1}^{j} \mathbf{S}_{j'}(k) \quad . \tag{2.31}$$

Loss of unitarity indicates overall loss of flux conservation directly proportional to the imaginary part of the wavenumber. Singularities appear again at the positions of the poles of the scattering matrix.

In general, the projection matrices $\{\mathbf{P}_j\}$ do not commute. When they do however, this is a manifestation of underlying symmetries. Expansion (2.27) may then be broken down into symmetry groups, each behaving independently from the others.

With this description of the $\mathbf{S}$ matrix, the delay matrix ($k \in \mathbb{R}$) takes the form

$$\mathbf{Q} = \sum_{j=1}^{\infty} \frac{\Gamma_j}{(k-k_j)\left(k-k_j^*\right)} \left(\mathbf{S}^\dagger \mathbf{\Lambda}_j \big|\, p_j \,\right\rangle \left)\left(\mathbf{S}^\dagger \mathbf{\Lambda}_j \big|\, p_j \,\right\rangle\right)^\dagger \quad . \tag{2.32}$$

It can be seen as a continuation onto the real k line of the *defect matrix* [2] (2.30) (omitting the obvious $2\mathrm{Im}\{k\}$ prefactor), emphasising the relation between losses in the complex k-plane and modes obtained from the delay matrix on the real k line, as illustrated in Fig. 2.2.

Letting $\big|\, v_j \,\right\rangle = \mathbf{S}^\dagger \mathbf{\Lambda}_j \big|\, p_j \,\right\rangle = \sum_p c_p^j \big|\, q_p \,\right\rangle$ where the vectors $\{\big|\, q_p \,\right\rangle\}$ are eigenvectors of the hermitian delay matrix, the eigenvalues of the delay matrix are

$$q_p = \sum_j \frac{\Gamma_j}{(k-k_j)\left(k-k_j^*\right)} |c_p^j|^2 \quad , \tag{2.33}$$

where the expansion coefficients are such that $\sum_p |c_p^j|^2 = 1$ since $\mathbf{S}^\dagger \mathbf{\Lambda}_j$ is unitary. The channel delays are then understood as a superposition of many Lorentzian curves,

[2] On the real k line, $\mathbf{\Lambda_j}^{\dagger\,-1}(k) = \mathbf{\Lambda_j}(k)$.

a property inherited from the scattering matrix, each of which weighted by a factor $|c_p^j|^2 \leq 1$. This is in conformity with the theory of the $\mathbf{S}$ matrix stating that the phase shift is the cumulative effect of many individual resonances (poles) [57]. On the real k axis, the eigenvalues $\{q_p\}$ are composed of symmetric contributions from the resonant poles and zeros of the scattering matrix,

$$q_p = \sum_j \left[\frac{i}{k - k_j} - \frac{i}{k - k_j^*} \right] |c_p^j|^2 \quad . \tag{2.34}$$

Our result concerning the reversible character of the energy modes is then rooted in the complex plane singularities, $\{k_j\}$, and zeros, $\{k_j^*\}$, of the $\mathbf{S}$ matrix contributing equally on the real k line to the modes of the delay matrix.

• Equivalent forms of the Q matrix

There exist in the literature 2 different expressions for the $\mathbf{Q}$ matrix: the one that we are using (see also [118])

$$\mathbf{Q} = -i\mathbf{S}^\dagger \frac{\partial \mathbf{S}}{\partial k} = i \frac{\partial \mathbf{S}^\dagger}{\partial k} \mathbf{S} \tag{2.35}$$

and the expression originally derived in [135] (see also [131])

$$\overline{\mathbf{Q}} = i\mathbf{S} \frac{\partial \mathbf{S}^\dagger}{\partial k} = -i \frac{\partial \mathbf{S}}{\partial k} \mathbf{S}^\dagger \ . \tag{2.36}$$

Clearly both matrices are hermitian with real eigenvalues. They are also related to each other by a similarity transformation

$$\mathbf{Q} = \mathbf{S}^\dagger \, \overline{\mathbf{Q}} \, \mathbf{S} \tag{2.37}$$

meaning that their eigenspectrum is identical. Furthermore, if $\{\mathbf{A}^p\}$ denote the eigenvectors of $\mathbf{Q}$ with eigenvalues q_p,

$$\mathbf{Q}\mathbf{A}^p = q_p \mathbf{A}^p \tag{2.38}$$

then the eigenvectors of $\overline{\mathbf{Q}}$ are simply related to those of $\mathbf{Q}$ by

$$\overline{\mathbf{Q}}(\mathbf{S}\mathbf{A}^p) = q_p(\mathbf{S}\mathbf{A}^p) = q_p \mathbf{B}^p \ . \tag{2.39}$$

In other words, $\overline{\mathbf{Q}}$ is to the *outgoing* eigenvectors $\{\mathbf{B}^p\}$ what $\mathbf{Q}$ is to the *incoming* eigenvectors $\{\mathbf{A}^p\}$. Both objects are completely equivalent.

An interesting relation was previously presented in Eq. (2.17) stating that $\mathbf{A}^p$ and $\mathbf{S}^\dagger \mathbf{P} \mathbf{A}^{p*}$ are simultaneous eigenvectors of $\mathbf{Q}$. We now derive this property as a commutation relation between $\mathbf{Q}$ and a matrix (operator) $\mathbf{\Omega} = \mathbf{S}^\dagger \mathbf{P} \mathbf{K}$ where $\mathbf{K}$ is the

anti-unitary matrix (operator) of complex conjugation ($\mathbf{K}^2 = \mathbb{1}$, $\mathbf{KO} = \mathbf{O}^*\mathbf{K}$):

$$\begin{aligned}[\mathbf{Q}, \mathbf{\Omega}] &= \mathbf{Q}\mathbf{S}^\dagger\mathbf{P}\mathbf{K} - \mathbf{S}^\dagger\mathbf{P}\mathbf{K}\mathbf{Q} \\ &= \mathbf{Q}\mathbf{S}^\dagger\mathbf{P}\mathbf{K} - \mathbf{S}^\dagger\mathbf{P}\mathbf{Q}^*\mathbf{K} \\ &= \mathbf{Q}\mathbf{S}^\dagger\mathbf{P}\mathbf{K} - \mathbf{S}^\dagger\mathbf{P}\left(i\mathbf{S}^T\frac{\partial\mathbf{S}^*}{\partial k}\right)\mathbf{K} \end{aligned} \tag{2.40}$$

Then, using reversibility property Eq. (2.5) and $\mathbf{P}^2 = \mathbb{1}$,

$$\begin{aligned}[\mathbf{Q}, \mathbf{\Omega}] &= \mathbf{Q}\mathbf{S}^\dagger\mathbf{P}\mathbf{K} - \mathbf{S}^\dagger\mathbf{P}\left(i\mathbf{P}\mathbf{S}\mathbf{P}\frac{\partial\mathbf{P}\mathbf{S}^\dagger\mathbf{P}}{\partial k}\right)\mathbf{K} \\ &= \mathbf{Q}\mathbf{S}^\dagger\mathbf{P}\mathbf{K} - \left(i\frac{\partial\mathbf{S}^\dagger}{\partial k}\right)\mathbf{P}\mathbf{K} \end{aligned} \tag{2.41}$$

Finally, since for real k, $\mathbf{S}^\dagger = \mathbf{S}^{-1}$, and that for the derivative of an inverse matrix, we find $d\mathbf{O}^{-1}/dk = -\mathbf{O}^{-1}\, d\mathbf{O}/dk\, \mathbf{O}^{-1}$,

$$\begin{aligned}[\mathbf{Q}, \mathbf{\Omega}] &= \mathbf{Q}\mathbf{S}^\dagger\mathbf{P}\mathbf{K} - \left(-i\mathbf{S}^\dagger\frac{\partial\mathbf{S}}{\partial k}\right)\mathbf{S}^\dagger\mathbf{P}\mathbf{K} \\ &= \mathbf{Q}\mathbf{S}^\dagger\mathbf{P}\mathbf{K} - \mathbf{Q}\mathbf{S}^\dagger\mathbf{P}\mathbf{K} \\ &= \mathbf{0}\ . \end{aligned} \tag{2.42}$$

This immediately implies that if $\mathbf{A}^p$ is eigenvector of $\mathbf{Q}$, $\mathbf{\Omega}\mathbf{A}^p$ is also eigenvector with the same eigenvalue. This is precisely the result presented in Eq. (2.18). Similarly, one can show that $[\overline{\mathbf{Q}}, \overline{\mathbf{\Omega}}] = 0$ where $\overline{\mathbf{\Omega}} = \mathbf{SPK}$. And again if $\mathbf{B}^p$ is eigenvector of $\overline{\mathbf{Q}}$, $\overline{\mathbf{\Omega}}\mathbf{B}^p$ is also eigenvector with the same eigenvalue.

There seems to have been renewed interest of late on the properties of the $\mathbf{Q}$ matrix in different contexts, and we refer the reader to some recent publications for further details [31, 118, 127, 131].

• Effect of the reference frame on the delay spectrum

Suppose now that we have obtained the scattering matrix $\mathbf{S}'$ of a cavity in a given reference frame having origin O, and that we want to obtain the scattering matrix $\mathbf{S}$ for the same cavity, but displaced a distance d from O. It is shown in Appendix D that the matrix $\mathbf{S}$ is simply related by a similarity transform to the original scattering matrix, namely

$$\mathbf{S} = \mathbf{T}(n_o kd)\ \mathbf{S}'\ \mathbf{T}^\dagger(n_o kd) \tag{2.43}$$

where n_o is the refractive index of the medium in which the cavity has been displaced and $\mathbf{T}(n_o kd)$ is a unitary matrix composed of Bessel functions. That $\mathbf{S}$ and $\mathbf{S}'$ are related by a similarity transformation is of course the expression of *translation invariance* of

the system under study. For the sake of simplicity, we assume that the cavity is only displaced and not rotated about O (hence $\phi_0 = 0$ in Eq. (D.8)). It is then easy to show (see Appendix D) that the displaced delay matrix $\mathbf{Q}$ takes the form

$$\mathbf{Q} = \mathbf{T}\left[\mathbf{Q}' + \mathbf{D}\right]\mathbf{T}^\dagger \tag{2.44}$$

with $\mathbf{Q}' = -i\mathbf{S}'^\dagger \partial \mathbf{S}'/\partial k$ is the delay matrix for the unmoved cavity (original system), and $\mathbf{D}$ is a displacement matrix proportional to $n_o d$. In contrast to the scattering matrix, the effect of the displacement in this case is not simply a similarity transform: there is an additional term $\mathbf{D}$, a displacement term, that must be added to $\mathbf{Q}'$. However, since the eigenvalues of a matrix are invariant under a similarity transform, $\mathbf{Q}$ and $\mathbf{Q}' + \mathbf{D}$ have an identical spectrum and we will focus on the properties of the main term $\mathbf{Q}' + \mathbf{D}$.

In Appendix D, we have shown that the matrix $\mathbf{D}$ has zero trace. This result stems from the observation that $\mathbf{D}$ is composed of a sum of matrices having eigenvalues coming in pairs of opposite signs, and one eigenvalue equals to zero. This in turn is indication that we did not change anything to the physical system: the cavity retains its mean properties independent of the reference frame, as it should.

Although the matrix $\mathbf{D}$ has trace zero, hence preserving the overall physics of the system, it may still affect individual eigenvalues of the initial $\mathbf{Q}'$ matrix. Moving the cavity while maintaining the reference frame for the wavefield modifies the $\mathbf{S}'$ matrix into a physically new $\mathbf{S}$ matrix having a different behaviour, see Fig. 2.3.

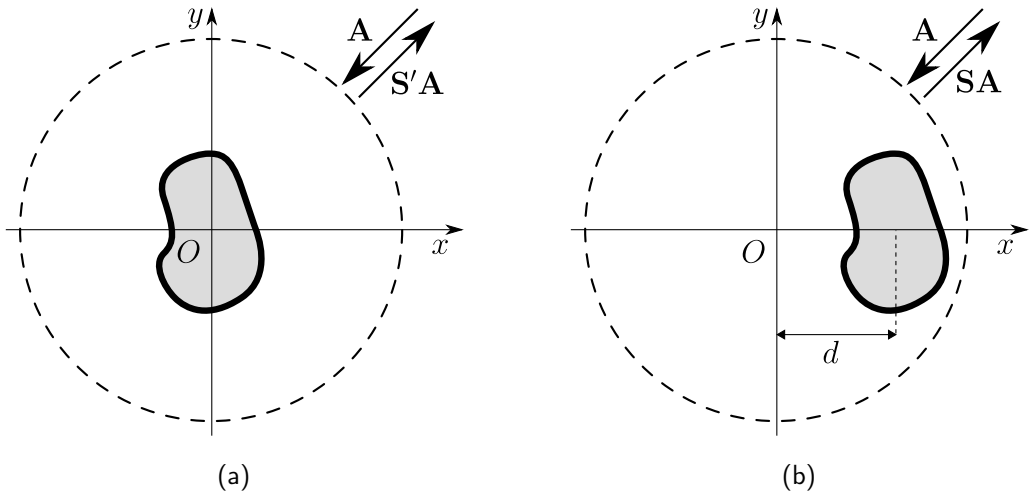


Fig. 2.3 Description of the scattering event (a) in the centered scenario and (b) in the displaced scenario. It is clear that, although both situations hold the same amount of dielectric material, the effective cavities inside the dashed circles are qualitatively different.

The effect of the displacement is analytically tractable, meaning that the sole knowledge

of $\mathbf{S}'$ and its wavenumber derivative is sufficient to compute the delay matrix $\mathbf{Q}$ of the displaced cavity. In view of this, the displaced cavity is an excellent test bed for validating both the theoretical development and the numerical computation methods.

Note that the spectral radius of $\mathbf{Q}$, $\rho(\mathbf{Q})$, is smaller or equal to the individual spectral radius of $\mathbf{Q}'$ and $\mathbf{D}$,

$$\rho(\mathbf{Q}) \leq \rho(\mathbf{Q}') + \rho(\mathbf{D}) \quad . \tag{2.45}$$

We can even go further by the use of Weyl's inequality [15]. Letting the decreasing ordered eigenvalues of $\mathbf{Q}' + \mathbf{D}$ and $\mathbf{Q}'$ be $\{q_j\}$, and $\{q'_j\}$ respectively, Weyl's inequality applied to our system asserts that

$$q'_j - \rho(\mathbf{D}) \leq q_j \leq q'_j + \rho(\mathbf{D}) \tag{2.46}$$

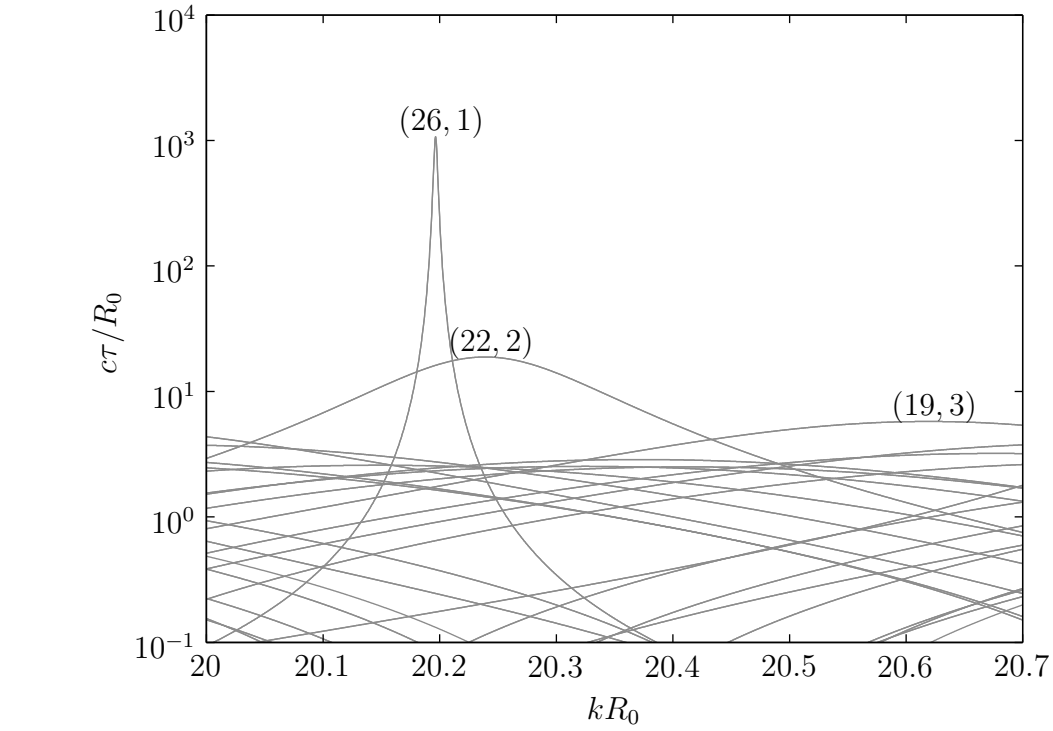
where $\rho(\mathbf{D})$ is the spectral radius of $\mathbf{D}$. Since $\rho(\mathbf{D}) \sim \mathcal{O}(n_o d)$, roughly the extra optical length, we expect that most of the effect of the displacement is captured by low lying modes having an initial undisplaced delay value of comparable magnitude.

An illustration of these results is presented in Fig. 2.4 for two displacements of an homogeneous disc cavity having refractive index $n_c = 1.5$ and radius $R_0 = 1$ immersed in a medium of index $n_o = 1$. The eigenvalues of $\mathbf{Q}'$ (geometrically centered disc) are represented by gray lines and the eigenvalues of $\mathbf{Q}$ (displaced disc) are represented by black lines. The gray portions of the spectrum corresponds to the application of Weyl's inequality Eq. (2.46) on the unmoved homogeneous disc cavity spectrum. Although this rule seems to provide a somewhat conservative uncertainty envelope around the unmoved eigenvalues, it captures the overall extent of the perturbation on the delay spectrum by showing the gradual flooding of its base. For 'large' delay resonant modes however, modifications of the delay are insignificant; see, for instance, the three identified peaks on Figs. 2.4(c). The delay value of the resonant modes are only weakly affected by the choice of reference frame, or to any 'reasonably misplaced' system's origin.

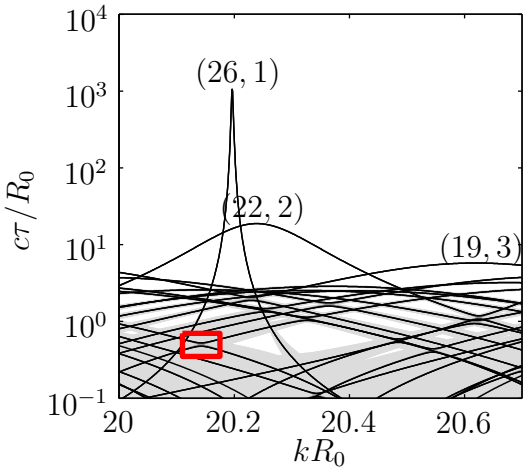
The discussion presented here may seem like a technical curiosity of the method supported in this work. Although the setup of the system reference frame seems straightforward for highly symmetrical geometries [3] [4], it may become difficult to define even for simple geometries such as the scalene triangle, not to mention 'potatoid' shape cavities like the one in the schematics of Fig. 2.3. We would like to point out that this problem is not solely an artifact of the characteristic modes description of the field presented

[3] *e.g* discs, squares, rectangles, ellipses, quadrupoles, stadia, or other single-disc-based geometries like the annular cavity

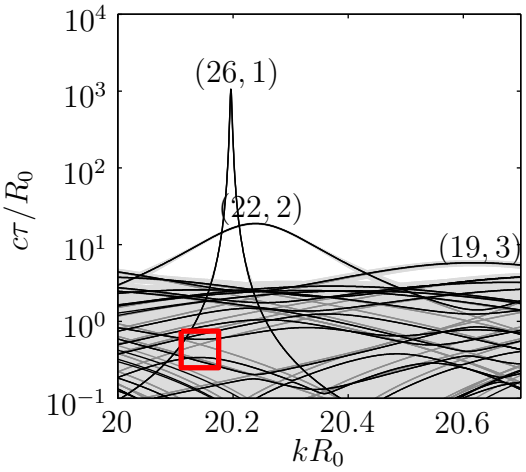
[4] Notable reference frame determination methods: searching the circle of minimal radius completely enclosing the cavity, or maximization of the number of symmetries.



(a) $d/R_0 = 0$



(b) $d/R_0 = 0.1$



(c) $d/R_0 = 0.5$

Fig. 2.4 (a) Centered homogeneous disc cavity spectrum, (b) displaced homogeneous disc cavity spectrum $d/R_0 = 0.1$ and (c) displaced homogeneous disc cavity spectrum $d/R_0 = 0.5$. Gray lines: centered disc; black lines: displaced disc; gray areas: application of Eq. (2.46) on the unmoved disc eigenvalues.

here, but also exists in the usual complex wavenumber pole emission representation of the field. Although in this latter scenario, the pole positions are not affected by the choice of reference frame, the field profile, especially the far-field, will be affected.

This apparent problem appears to be the result of an *absolute* definition of the system: in both descriptions, the only inputs defining the system are the distribution of the refractive material and the wavenumber. Placing the system in context, for instance, *relative* to a well defined field, fixes the coordinate reference frame and eliminates the ambiguous nature of the system's origin. In this case of figure, one may then proceed to interpret the response of the cavity through the use of the 'absolute' characteristic modes or their related emission modes.

This being said, in any given calculation, there is a natural choice that should prevail. e.g. we have adopted the position of the centroid of the cavity (or more generally a combination of cavities) as the origin for our coordinate system. The centroid coordinates (C_x, C_y) of an object of any shape or form can be calculated from the expressions

$$C_x = \frac{1}{A}\int_{\mathcal{R}} xS_y(x)\,dx \qquad , \qquad C_y = \frac{1}{A}\int_{\mathcal{R}} yS_x(y)\,dy \tag{2.47}$$

where A is the area of the region $\mathcal{R}$ and $S_y(x)$ ($S_x(y)$) is the vertical (horizontal) distance to the boundary of $\mathcal{R}$ measured from the point $(x, y) \in \mathcal{R}$. This prescription is easily applicable, coincides with the geometric center for symmetric cavities and removes the arbitrariness just discussed.

• Delay levels anti-crossings

Notable features becoming prominent as the distance d grows larger are the *avoided crossings* that can be seen in Figs. 2.4(b)-(c). In this case, the avoided crossings are between accidentally degenerate levels of the undisplaced cavity. One avoided crossing (highlighted with a red square) is clearly seen in the neighborhood of position (20.14, 0.48). As it turns out, avoided crossing events are not restricted to reference frame change, but appear generically for any deformation of the disc. More on this matter in Section 2.4.

As an illustration, we focus on the displaced cavity system previously discussed. Suppose that the delays of two different modes of the centered disc cavity ($d = 0$) having angular momenta m_1 and m_2 cross at position $(k_0R_0,\, c\tau_0/R_0)$. As the cavity is displaced a small distance d from its initial origin, we may assume that the local slopes μ_{m_1} and μ_{m_2} of the two modes delay level remain essentially constant with respect to d. However, small interaction terms scaling with d will appear and affect the delays computed through the diagonalization of $\mathbf{Q}$. Considering these conditions, we define a *local delay hermitian matrix*

$$\mathbf{Q}_{\text{loc}} = \begin{pmatrix} Q_{m_1m_1} & Q_{m_1m_2} \\ Q_{m_2m_1} & Q_{m_2m_2} \end{pmatrix} = \begin{pmatrix} \mu_{m_1}(k-k_0)R_0 + c\tau_0/R_0 & d\kappa_{m_1m_2} \\ d\kappa_{m_2m_1} & \mu_{m_2}(k-k_0)R_0 + c\tau_0/R_0 \end{pmatrix} \tag{2.48}$$

whose eigenvalues are

$$c\tau_\pm/R_0 = \left[\frac{\mu_{m_1}+\mu_{m_2}}{2}(k-k_0)R_0 + c\tau_0/R_0\right] \pm \sqrt{\left(\frac{\mu_{m_1}-\mu_{m_2}}{2}(k-k_0)R_0\right)^2 + d^2|\kappa_{m_1m_2}|^2} \tag{2.49}$$

Exactly at the crossing, $k = k_0$, we get

$$c\tau_+/R_0 = c\tau_0/R_0 + d|\kappa_{m_1m_2}| \tag{2.50}$$

$$c\tau_-/R_0 = c\tau_0/R_0 - d|\kappa_{m_1m_2}| \quad . \tag{2.51}$$

while far from it, the eigenvalues return to their $d = 0$ values,

$$c\tau_+/R_0 \sim \begin{cases} \mu_{m_1}(k-k_0)R_0 + c\tau_0/R_0 & , \ k < k_0 \\ \mu_{m_2}(k-k_0)R_0 + c\tau_0/R_0 & , \ k > k_0 \end{cases} \tag{2.52}$$

$$c\tau_-/R_0 \sim \begin{cases} \mu_{m_2}(k-k_0)R_0 + c\tau_0/R_0 & , \ k < k_0 \\ \mu_{m_1}(k-k_0)R_0 + c\tau_0/R_0 & , \ k > k_0 \end{cases} \quad . \tag{2.53}$$

This shows that the accidental degeneracy is lifted by the cavity displacement. The size of the level splitting at $k = k_0$ is about the same magnitude as that of the coupling term. Also, the eigenvectors of Eq. (2.48) show that the states labeled m_1 and m_2 mix in a 1/1 ratio at the crossing. This idealization of the delay matrix behaviour is closely related to the Landau-Zener model of the time dependent quantum mechanical interaction between two states [168]. The difference here is that the time variable is replaced with the wavenumber k. This model is an example of application of the *adiabatic theorem*, from which we shall keep the terminology:

Diabatic levels are associated with 'rapid' (instant) evolution of a time dependent Hamiltonian where the system goes through the anti-crossing as if there weren't any;

Adiabatic levels are associated with 'slow' (zero velocity) evolution of a time dependent Hamiltonian where the system is allowed to adjust completely after each change in time.

In our system however, since every diagonalization of $\mathbf{Q}$ at a position k is independent of those at neighbouring values of k, we invariably find the adiabatic levels of delay. The overall picture of this simple model for the displaced cavity is illustrated on Fig. 2.5.

The picture becomes more complicated as the external parameter d is increased beyond the perturbation regime. In this case, the local slopes μ_{m_1} and μ_{m_2} may become dependent on d, consequently displacing the crossing position $(k_0R_0,\ c\tau_0/R_0)$. Moreover

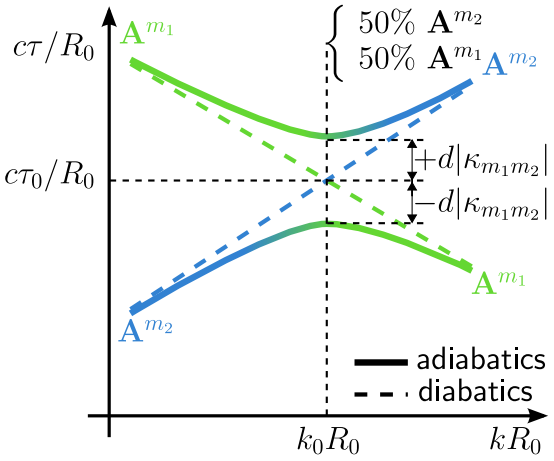


Fig. 2.5 Schematics of the avoided-crossing of two delay levels for a displaced cavity following Eqs. (2.49)-(2.53) and the ensuing discussion.

many avoided crossings tend to overlap each other. With respect to Eq. (2.48), the local delay model becomes larger than a 2×2 matrix, and a complicated pattern of avoided-crossings forms. Depending on the wavenumber density of avoided-crossings, it may even become impossible to identify 'true modes' away from the crossover region (see Eqs. (2.52)-(2.53)). An illustration of this developing non-perturbative regime is pictured on Fig. 2.4(c): most low-lying delay modes have already changed considerably from the $d = 0$ level (gray lines), and some regions, having closely packed $d = 0$ crossings, are turning to a 'forbidden' band emptied of levels in the $d/R_0 = 0.5$ regime.

The appearance of avoided-crossings is not restricted to the displacement of the cavity: it is actually generic to cavity shapes having a finite number of symmetries, or even no symmetry at all. We will show in Chapter 3 that a perturbative geometrical deformation leads to a removal of the degeneracy of the modes of the disc cavity. The perturbed modes then orient themselves on the cavity symmetry axis. The investigation of the perturbation of accidental degeneracies of the disc cavity shows that modes sharing the same symmetry undergo a local avoided-crossing, but do not interact in any other way with other symmetry modes.

We illustrate these assertions with the square cavity as an example. The square cavity possesses a total of 4 symmetry axes, $\phi = \{0, \pi/4, \pi/2, 3\pi/4\}$, each having 3 possible parity states: even, odd or none. The parity state identifies whether the field has a zero on a given symmetry axis (odd parity), a local extremum (even parity), or none. Cavities having an undefined symmetry state along a given symmetry axis usually exhibit delay levels degeneracy. In the square cavity, 4 mode symmetries are well defined, and 2 remain degenerate (see Tab. 2.1). For comparison, we also display the

Mode	0	$\pi/4$	$\pi/2$	$3\pi/4$
$1a$	even	none	odd	none
$1b$	odd	none	even	none
2	even	odd	even	odd
3	odd	even	odd	even
4	odd	odd	odd	odd
5	even	even	even	even

Tab. 2.1 The mode symmetries of the square cavity. Note that the parity of degenerate modes $1a$ and $1b$ is indicative only: because of the degeneracy, any linear combinations of these modes, at a common wavenumber, are acceptable. Most of these linear combinations result however in a field not having the expected symmetry axis of the square cavity.

far-field distribution defined by

$$|\psi_{FF}|^2 = \lim_{r\to\infty} |\psi^p_{\text{out}}(r,\phi)|^2 \propto \left|\sum_m B^p_m \mathrm{e}^{im(\phi-\pi/2)}\right|^2 \quad . \tag{2.54}$$

For a given field defined by the incoming vector $\mathbf{A}^p$, obtained by the diagonalization of the delay matrix, we identify the symmetry axis by looking at the position where the norm of the far-field autocorrelation function is 1 (numerically, a maximum close to 1),

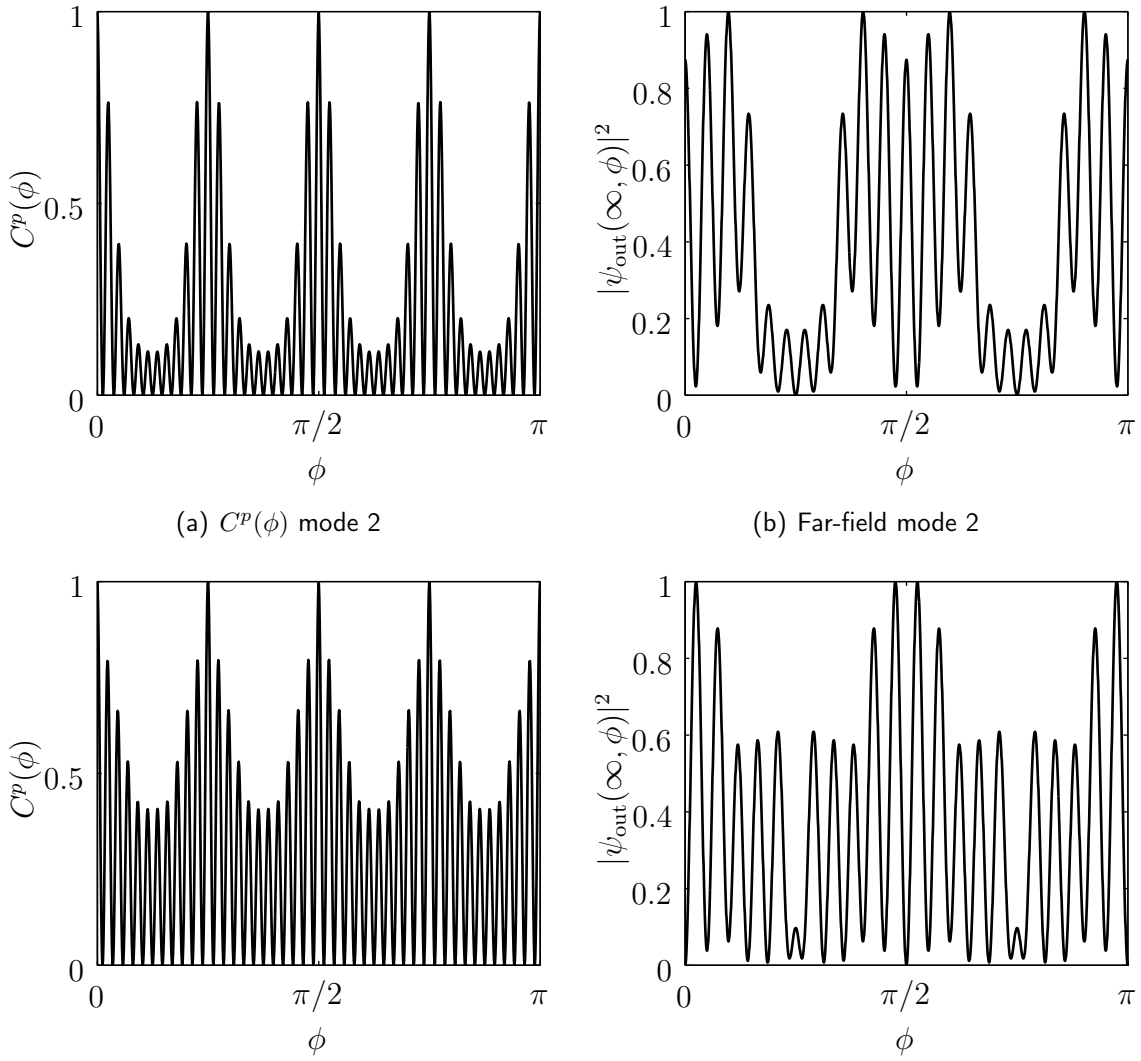
$$\left|\frac{1}{2\pi}\int_0^{2\pi} d\chi \lim_{r\to\infty} \psi^{p*}(r,\,\phi-\chi)\psi^p(r,\,\phi+\chi)\right|^2 \sim \left|\sum_m A^{p*}_m A^p_{-m}\mathrm{e}^{im(\pi-2\phi)}\right|^2 = C^p(\phi) \quad . \tag{2.55}$$

Once the symmetry axes are defined, we readily verify whether the field has a zero (odd parity) or an extremum (even parity) about each one. Examples are provided in Fig. 2.6.

Putting the same mode symmetries in a common set enables us to draw partial delay spectra. The partial spectra for mode symmetries 2 and 3 are pictured in Fig. 2.7 for a square cavity having $n_c = 1.5$ and side wall size $2\times\sqrt{2}R_0/2$ [5], $R_0 = 1$, immersed in a medium $n_o = 1$. As expected, delay levels of modes of a specific symmetry do not overlap, but may still cross over delay levels of other symmetries.

A word of caution here: a numerical artifact may occur for avoided-crossings having a size smaller than the finite wavenumber step size used to carry out the computation of the spectrum, causing an apparent crossing. Crossings of this type are easily handled by using a smaller step size. With regards to the diabatic/adiabatic dichotomy, this

[5] The length of half the diagonal of the cavity is then equal to 1: the square may be embedded in a circle of radius 1.



(a) $C^p(\phi)$ mode 2

(b) Far-field mode 2

(c) $C^p(\phi)$ mode 3

(d) Far-field mode 3

Fig. 2.6 Autocorrelation as defined in Eq. (2.55) and far-field for two mode symmetries of the square cavity, see Tab. 2.1. Although the maxima of $C^p(\phi)$ indicate the same symmetry axis (autocorrelation reaches 1 at $\phi = \{0, \pi/4, \pi/2, 3\pi/4\}$), it is observed that the behaviour of the field differs at these specific locations, hence the different symmetries.

may be viewed as a rapid process showing the local diabatic levels only. Also, the size of the avoided-crossings vary considerably along a single delay level. This is due to the state exchange undergone at the avoided-crossing (see Fig. 2.5), which alters the state supported along the adiabatic level, itself having a varying interaction strength with other states. Note that the complete spectrum superimposes three other different partial spectra (two symmetries are degenerate), which then appears as a very complicated structure of interlaced levels. Separating the symmetries simplifies the overall appearance of the level structure without loss of information.

We take the time here to also illustrate the effect on degenerate states of the symmetry

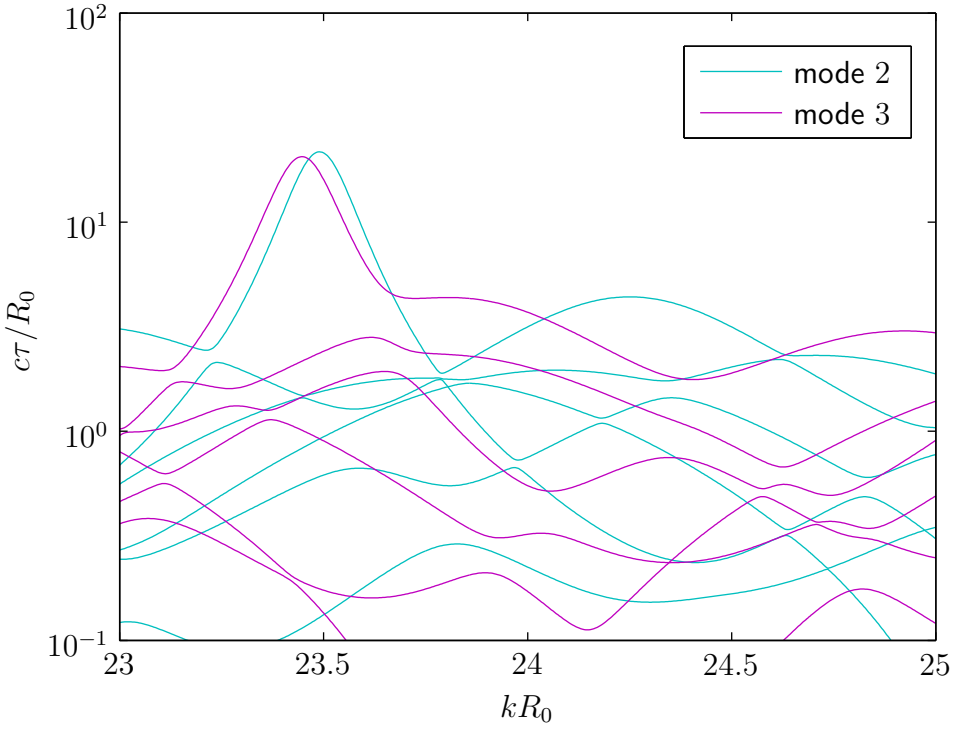
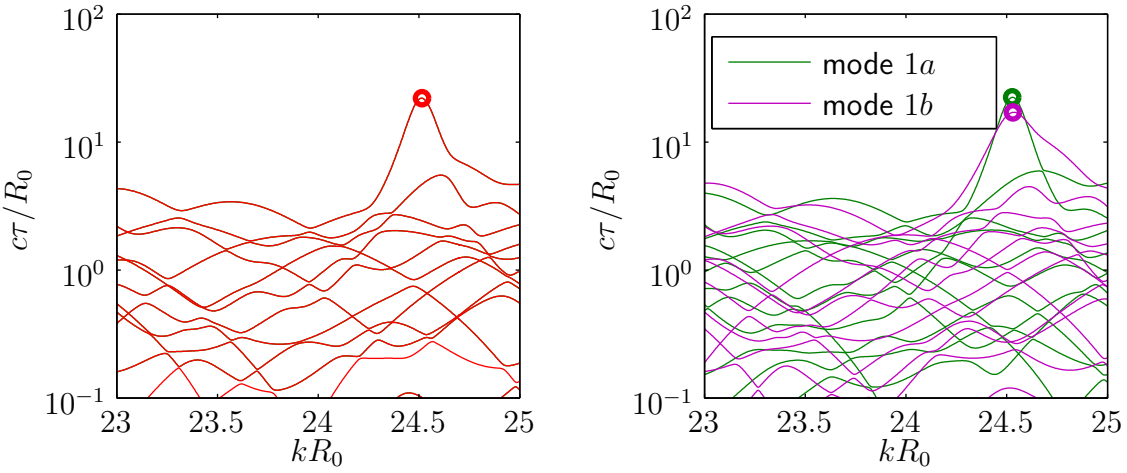


Fig. 2.7 Partial spectra of two sets of mode symmetries of the square cavity. See Tab. 2.1 for the description of the symmetries.

breaking by a 10% squeeze (in the x-direction) of the square cavity. Two sets of near-fields are displayed on Fig. 2.9 for the resonant modes identified by the circle marks on Fig. 2.8. We estimate, by computing the inner product of the vector $\mathbf{A}$ for the square and the rectangular cavity of one symmetry, that the modes pictured in Figs. 2.9(a)-(c) are 88% alike, while the modes in Figs 2.9(b)-(d) overlap at only about 56%. This discrepancy in the projection values is due to a local interaction with another resonance near $kR_0 = 24.5$ for mode symmetry $1b$. This secondary resonance appears as a bump on the right side of the purple resonant peak in Fig. 2.8(b). The whole peak structure is in fact composed of two resonances undergoing an avoided crossing in close proximity. The resonance having the highest quality then loses part of its field containment capacity, as seen in Fig. 2.8(b) with reference to the $1a$ symmetry peak. This aspect of the resonance behaviour is important for engineering robustness concerns: one does not want to inadvertently couple together two resonances resulting in the loss of some important properties. Remember that the difference between the square and the rectangle here is only 10% in sidewall length. This specific issue of resonance coupling will be addressed in Chapter 4.



(a) Square (b) Rectangle

Fig. 2.8 (a) Degenerate delay levels of the square cavity and (b) the corresponding levels in the rectangular cavity. The circles indicate the position of the modes presented on Fig. 2.9.

2.2 Numerical calculation of the S matrix

2.2.1 A transfer matrix algorithm

We have seen in the last Section that the relevant object for the modal characterization of the cavity is the scattering matrix. Unfortunately, there exist only a few cavity geometries allowing closed form calculation of **S**. Computation is therefore usually carried through by intensive numerical methods. We review, extend and upgrade a method [111, 113] recently introduced that has the potential to treat a wide variety of geometrical and refractive index deformations.

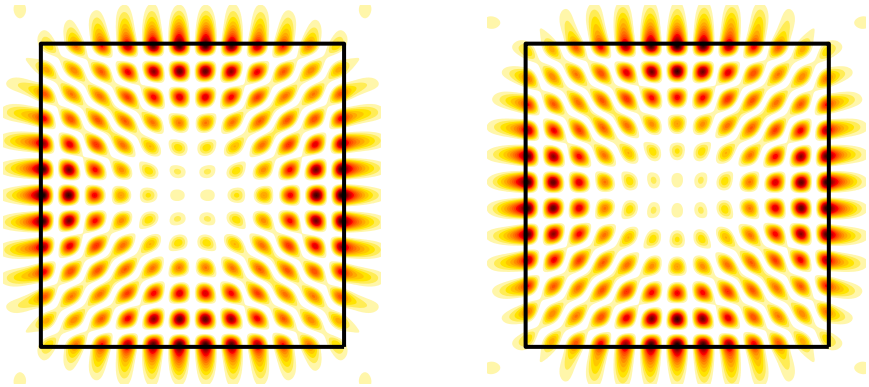
As mentioned above, the field $\psi(\mathbf{r})$ must satisfy Helmholtz' equation,

$$\left[\nabla^2 + n^2(\mathbf{r})k^2\right]\psi(\mathbf{r}) = 0 \tag{2.56}$$

which, in polar coordinates, takes the form

$$\left[r^2\frac{\partial^2}{\partial r^2} + r\frac{\partial}{\partial r} + \frac{\partial^2}{\partial \phi^2} + n^2(r,\phi)k^2r^2\right]\psi(r,\phi) = 0. \tag{2.57}$$

Although there exist general conditions under which the Helmholtz equation is separable [5], exact solutions are scarce and far between. For demonstration and calibration purposes, we will concentrate essentially on the *homogeneous disc* (hd) and the *annular cavity* (ac), two special cases for which closed form expressions are available. Needless



(a) Square $1a$ (b) Square $1b$

(c) Rectangle $1a$ (d) Rectangle $1b$

Fig. 2.9 Near-field patterns for resonant degenerate modes of (a)-(b) the square cavity and (c)-(d) corresponding symmetry modes of the rectangular cavity. The degeneracy of mode symmetries 1a and 1b of the square cavity is easily understood from Figs. (a)-(b): only a $\pi/2$ rotation separates these modes, a geometrical change that does not alter the quality factor (capacity of energy containment) of any of the modes having symmetry $1a$ and $1b$.

to say that the methodology developed is much more general and readily applicable to homogeneous or inhomogeneous media within regular or irregular geometries.

To set up the procedure, let us focus our attention on a thin annular region of width 2ϵ and central radius r_j, $j = 1, 2...N$, covering part of a generic cavity (see Fig. 2.10). Over this region, we assume the refractive index to be dependent upon ϕ only. Expression $n^2(r, \phi)r^2$ is then evaluated at r_j for all ϕ. Turning to (2.57), we obtain an approximate local expansion of the differential equation over $|r - r_j| \leq \epsilon$,

$$\left[r^2\frac{\partial^2}{\partial r^2} + r\frac{\partial}{\partial r} + \frac{\partial^2}{\partial \phi^2} + n^2(r_j, \phi)k^2 r_j^2\right]\psi^j(r, \phi) = 0. \tag{2.58}$$

This differential equation is separable for the local wavefunction $\psi^j(r, \phi)$. Under the

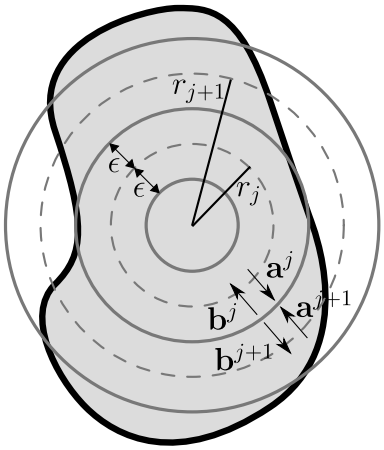


Fig. 2.10 Conceptual view of the annular decomposition of the cavity. Two adjacent annular domains of thickness 2ϵ are displayed. Incoming and outgoing coefficients with respect to the circular interface located at $r_j + \epsilon = r_{j+1} - \epsilon$ are also shown. Dashed circles indicate the mean radius of the annular domains.

Ansatz $\psi^j(r,\phi) = \mathcal{R}^j(r)\Phi^j(\phi)$, we obtain two exact differential equations

$$\left[\rho_j^2 \frac{d^2}{d\rho_j^2} + \rho_j \frac{d}{d\rho_j} - \xi^j\right] \mathcal{R}^j(\rho_j) = 0 \tag{2.59}$$

$$\left[\frac{d^2}{d\phi^2} + \left(n^2(r_j,\phi)k^2 r_j^2 + \xi^j\right)\right] \Phi^j(\phi) = 0 \tag{2.60}$$

where $\rho_j = r/r_j$ and ξ^j is a separation constant. Imposing periodic boundary conditions on Eq. (2.60) and expanding $\Phi^j(\phi)$ and $n^2(r_j,\phi)$ in a Fourier series, we end up with an eigenvalue problem of an hermitian symmetric matrix. Its eigenvalues specify the set of constants $\{\xi_\mu^j\}$, and the associated eigenvectors define a basis of normalized eigenfunctions $\{\Phi_\mu^j(\phi)\}$. We may then solve the Cauchy-Euler differential equation (2.59) exactly,

$$\mathcal{R}_\mu^j(\rho_j) = a_\mu^j \rho_j^{+\sqrt{\xi_\mu^j}} + b_\mu^j \rho_j^{-\sqrt{\xi_\mu^j}} \tag{2.61}$$

where a_μ^j and b_μ^j are constants to be obtained from the boundary conditions. The sign of ξ_μ^j renders $\mathcal{R}_\mu^j(\rho_j)$ evanescent (+ sign) or propagating (- sign).

This procedure is propagated to an adjacent thin annular domain of thickness 2ϵ centered on $r_{j+1} = r_j + 2\epsilon$. Boundary conditions for TM polarization assume continuity of ψ^j and ψ^{j+1} and their normal (radial) derivative at their common boundary

$\rho_{j+} = 1 + \epsilon/r_j$ and $\rho_{j+1-} = 1 - \epsilon/r_{j+1}$. Once applied, these lead to the set of equations

$$\left[a^j_{\mu'}\rho_{j+}^{\sqrt{\xi^j_{\mu'}}} + b^j_{\mu'}\rho_{j+}^{-\sqrt{\xi^j_{\mu'}}}\right]\delta_{\mu\mu'} = \sum_{\mu'}\left[b^{j+1}_{\mu'}\rho_{j+1-}^{\sqrt{\xi^{j+1}_{\mu'}}} + a^{j+1}_{\mu'}\rho_{j+1-}^{-\sqrt{\xi^{j+1}_{\mu'}}}\right]U^j_{\mu\mu'}$$

$$\left[a^j_{\mu'}\rho_{j+}^{\sqrt{\xi^j_{\mu'}}} - b^j_{\mu'}\rho_{j+}^{-\sqrt{\xi^j_{\mu'}}}\right]\delta_{\mu\mu'} = \sum_{\mu'}\frac{\sqrt{\xi^{j+1}_{\mu'}}}{\sqrt{\xi^j_{\mu}}}\left[b^{j+1}_{\mu'}\rho_{j+1-}^{\sqrt{\xi^{j+1}_{\mu'}}} - a^{j+1}_{\mu'}\rho_{j+1-}^{-\sqrt{\xi^{j+1}_{\mu'}}}\right]U^j_{\mu\mu'}$$

where $U^j_{\mu\mu'} = \int_0^{2\pi} d\phi\ \Phi^{j*}_{\mu}(\phi)\Phi^{j+1}_{\mu'}(\phi)$. We use the convention that the coefficients $\{\mathbf{a}^j\}$ define waves incident / evanescent on the interface and the coefficients $\{\mathbf{b}^j\}$ define waves leaving / evanescent from the interface.

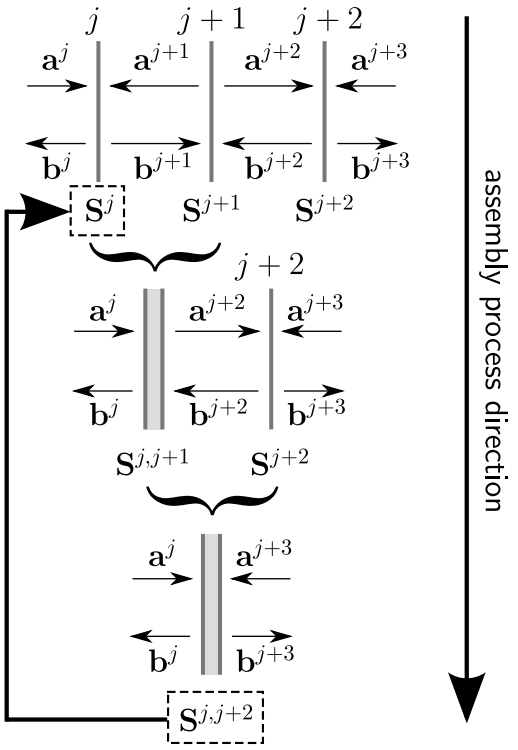


Fig. 2.11 Conceptual view of the assembly process leading to matrix $\mathbf{S}^{j,j+2}$. The boundaries between the annuli are represented by vertical lines. Matrices $\mathbf{S}^j$ and $\mathbf{S}^{j+1}$ are first blended into a matrix $\mathbf{S}^{j,j+1}$, which in turn is combined with $\mathbf{S}^{j+2}$to yield $\mathbf{S}^{j,j+2}$. This cumulative matrix shares the same status with respect to the pairs $\{\mathbf{b}^j, \mathbf{b}^{j+3}\}$ and $\{\mathbf{a}^j, \mathbf{a}^{j+3}\}$ as the matrix $\mathbf{S}^j$ has between $\{\mathbf{b}^j, \mathbf{b}^{j+1}\}$ and $\{\mathbf{a}^j, \mathbf{a}^{j+1}\}$

The outgoing coefficients $\mathbf{b}^j$ and $\mathbf{b}^{j+1}$ are written as a linear combination of incoming coefficients $\mathbf{a}^j$ and $\mathbf{a}^{j+1}$ using the *general scattering block matrix* $\mathbf{S}^j$ on annular boundary j,

$$\begin{pmatrix} \mathbf{b}^j \\ \mathbf{b}^{j+1} \end{pmatrix} = \mathbf{S}^j \begin{pmatrix} \mathbf{a}^j \\ \mathbf{a}^{j+1} \end{pmatrix} = \begin{pmatrix} \mathbf{S}^j_{11} & \mathbf{S}^j_{12} \\ \mathbf{S}^j_{21} & \mathbf{S}^j_{22} \end{pmatrix} \begin{pmatrix} \mathbf{a}^j \\ \mathbf{a}^{j+1} \end{pmatrix} \tag{2.62}$$

Individual submatrices of $\mathbf{S}^j$ are computed using a well-known formula for the inverse of a block-matrix that uses Schur's complement [85]. Careful algebraic manipulations enables ones to 'skip' one annular region, keeping only the expansion coefficients of rings j and $j+2$ (see Fig. 2.11 for a visual description)

$$\begin{pmatrix} \mathbf{b}^j \\ \mathbf{a}^{j+2} \end{pmatrix} = \mathbf{S}^{j,j+1} \begin{pmatrix} \mathbf{a}^j \\ \mathbf{b}^{j+2} \end{pmatrix} = \begin{pmatrix} \mathbf{S}_{11}^{j,j+1} & \mathbf{S}_{12}^{j,j+1} \\ \mathbf{S}_{21}^{j,j+1} & \mathbf{S}_{22}^{j,j+1} \end{pmatrix} \begin{pmatrix} \mathbf{a}^j \\ \mathbf{b}^{j+2} \end{pmatrix} \tag{2.63}$$

where the different submatrices are obtained from $\mathbf{S}^j$ and $\mathbf{S}^{j+1}$,

$$\mathbf{S}_{11}^{j,j+1} = \mathbf{S}_{11}^j + \mathbf{S}_{12}^j \left(\mathbb{1} - \mathbf{S}_{11}^{j+1}\mathbf{S}_{22}^j\right)^{-1} \mathbf{S}_{11}^{j+1}\mathbf{S}_{21}^j \tag{2.64}$$

$$\mathbf{S}_{12}^{j,j+1} = \mathbf{S}_{12}^j \left(\mathbb{1} - \mathbf{S}_{11}^{j+1}\mathbf{S}_{22}^j\right)^{-1} \mathbf{S}_{12}^{j+1} \tag{2.65}$$

$$\mathbf{S}_{21}^{j,j+1} = \mathbf{S}_{21}^{j+1} \left(\mathbb{1} - \mathbf{S}_{22}^j\mathbf{S}_{11}^{j+1}\right)^{-1} \mathbf{S}_{21}^j \tag{2.66}$$

$$\mathbf{S}_{22}^{j,j+1} = \mathbf{S}_{22}^{j+1} + \mathbf{S}_{21}^{j+1} \left(\mathbb{1} - \mathbf{S}_{22}^j\mathbf{S}_{11}^{j+1}\right)^{-1} \mathbf{S}_{22}^j\mathbf{S}_{12}^{j+1}. \tag{2.67}$$

Following the procedure again on the next interface, but using the 'one-layer-equivalent' $\mathbf{S}^{j,j+1}$ as the starting matrix instead leads to a '2-layers-equivalent' coupling block-matrix $\mathbf{S}^{j,j+2}$,

$$\begin{pmatrix} \mathbf{b}^j \\ \mathbf{b}^{j+3} \end{pmatrix} = \mathbf{S}^{j,j+2} \begin{pmatrix} \mathbf{a}^j \\ \mathbf{a}^{j+3} \end{pmatrix} \quad . \tag{2.68}$$

Note that $\mathbf{S}^{j,j+2}$ correctly satisfies the incoming and outgoing waves convention regarding the $\mathbf{a}$ and $\mathbf{b}$ coefficients (Fig. 2.11). This proves to be a useful result since we can reuse the procedure leading from (2.62) to (2.68), only now with proper replacement of $\mathbf{S}^{j,j+2}$ in place of $\mathbf{S}^j$ in expression (2.62). One keeps on going until all the surface of interest is covered by N annular layers. Obtaining the final scattering matrix still remains a daunting computational task and the following additional remarks are meant to alleviate the necessary labour.

The region under study is divided in an innermost disc of a homogeneous medium of refrative index n_{in} and radius r_0 and N circular domains of width 2ϵ extending to a maximum radius $R_{\max} = r_N + \epsilon$. There are therefore $(N+1)$ interfaces $(j = 0, 1, \ldots, N)$ located a distance $R_j = r_0 + 2j\epsilon$ from the chosen origin (Fig. 2.12).

The field inside this inner region is composed of Bessel functions of the first kind,

$$\psi^0(r,\phi) = \sum_m a_m^0 J_m(n_{\text{in}}kr)\mathrm{e}^{im\phi},\ r \le r_0 \quad . \tag{2.69}$$

Application of boundary conditions at interface $r = r_0$ between the disc region and the first annular region, itself connected to the second annular region, yields the $\mathbf{S}^{0,1}$ matrix, as defined by expressions (2.64)-(2.67). However, two submatrices of $\mathbf{S}^0$ have special

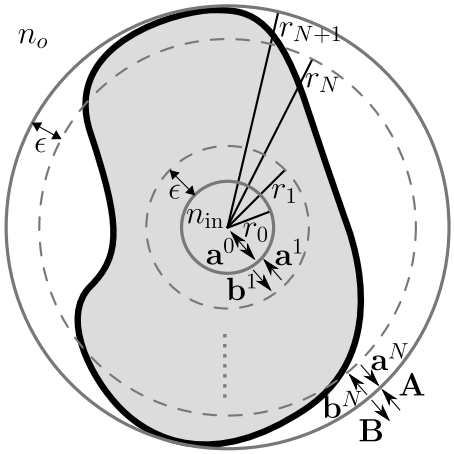


Fig. 2.12 Circular innermost domain of radius r_0 and outermost limit of the cavity at $R_{\max} = r_N + \epsilon$. The disc shaped region inside the cavity is considered to be of constant refractive index $n_{\rm in}$, and the outer domain $r > R_{\max}$, of index n_o.

forms: $\mathbf{S}_{11}^0 = -\mathbb{1}$, and $\mathbf{S}_{21}^0 = \mathbf{0}$. With respect to the iterative procedure described above, this implies that all other coupling matrices $\mathbf{S}^{0,j}$, $j > 0$, possess the same submatrices up to the last interface,

$$\mathbf{S}_{11}^{0,j} = -\mathbb{1} \quad , \quad \mathbf{S}_{21}^{0,j} = \mathbf{0} \; . \tag{2.70}$$

Furthermore, the $\mathbf{S}_{22}^{0,j}$ matrices are 'self-contained',

$$\mathbf{S}_{22}^{0,j} = \mathbf{S}_{21}^{j} \left(\mathbb{1} - \mathbf{S}_{22}^{0,j-1} \mathbf{S}_{11}^{j} \right)^{-1} \mathbf{S}_{22}^{0,j-1} \mathbf{S}_{12}^{j} + \mathbf{S}_{22}^{j} \tag{2.71}$$

that is, only submatrix $\mathbf{S}_{22}^{0,j-1}$ from the preceding interfaces is required for the computation of $\mathbf{S}_{22}^{0,j}$.

The solution outside the cavity ($r \geq R_{\max}$) is a superposition of Hankel functions,

$$\psi(r,\phi) = \sum_m \left[A_m H_m^{(2)}(n_o k r) + B_m H_m^{(1)}(n_o k r) \right] \mathrm{e}^{im\phi}. \tag{2.72}$$

Given that the interfaces are labeled from 0 to N, the scattering matrix $\mathbf{S}^{0,N+1}$ is finally obtained as

$$\begin{pmatrix} \mathbf{a}^0 \\ \mathbf{B} \end{pmatrix} = \mathbf{S}^{0,N+1} \begin{pmatrix} \mathbf{a}^0 \\ \mathbf{A} \end{pmatrix}. \tag{2.73}$$

Since we are only interested in the linear relation between the $\mathbf{A}$ and $\mathbf{B}$ coefficients, and from the preceeding considerations on the submatrices of cumulative matrix $\mathbf{S}^{0,j}$, it then appears that the only submatrix of interest is $\mathbf{S}_{22}^{0,N+1}$.

Further details of the precise numerical implementation of the procedure are described in Appendix C together with further remarks in the following examples.

2.2.2 Testing the main approximation

The *homogeneous disc* (hd) cavity is a straightforward test for the segmentation approximation of (2.58). Since the refractive index n_c is everywhere constant inside the disc cavity of radius R_0, truncation related issues for the different matrices are irrelevant as the annular domains share the same geometrical center as that of the cavity. We may then focus strictly on the effect of decomposition into finite size annular regions. The numerical scattering matrix $\bar{\mathbf{S}}$ may then be compared with the exact expression $\mathbf{S}_{hd}$

$$\{\mathbf{S}_{hd}\}_{mm'} = -\frac{\Delta_m^{(2)}}{\Delta_m^{(1)}}\delta_{mm'} \tag{2.74}$$

where

$$\Delta_m^{(i)} = n_c H_m^{(i)}(Z_o) J_m'(Z_c) - n_o H_m^{(i)'}(Z_o) J_m(Z_c) \tag{2.75}$$

and $Z_c = n_c k R_0$, $Z_o = n_o k R_0$, and $'$ denotes the derivative with respect to the argument. The measure adopted is the maximal termwise deviation between the numerical approximation of the scattering matrix, $\bar{\mathbf{S}}$, following the procedure described above, and the exact solution, $\mathbf{S}_{hd}$, from expression (2.74)

$$e_{\max} = \max\left\{\sqrt{\left|\bar{\mathbf{S}} - \mathbf{S}_{hd}\right|^2}\right\}. \tag{2.76}$$

We study the approximate discretisation of space with a small number of $N = 2$ annular layers (3 interfaces) sufficient to complete the assembly process of Fig. 2.11, as a function of the annular width 2ϵ, and look at the deviation from the analytic result as ϵ is decreased. The annular domains cover the radii from $r_0 = R_0 - 4\epsilon$ to $R_0 = R_{\max} = 1$. Also, because the underlying resolution changes with wavelength, we use a normalised wavenumber $2\epsilon k$ to compare the different sets of calculations performed at different wavelengths. Finally, the truncation of the angular decomposition is also wavenumber adjusted to $M = [n_c k R_{\max}]$, where $[x]$ denotes the integer part of x plus 1.

Results presented on Fig. 2.13 show that modelization needs are met at a value $k2\epsilon \approx 0.33$ for all investigated wavenumbers. From then on, any decrease in annuli thickness is associated with a monotonic descent of the maximum deviation $e_{\max}$. One finds a power law dependence of the form $e_{\max} \propto (2\epsilon k)^\alpha$ where α is estimated at ~ 3.2. A saturation level is eventually reached at very low annuli thickness values.

2.2.3 Testing a non-diagonal case

The previous benchmark has ascertained the convergence of the method with respect to spatial discretisation for a *diagonal* case for which an analytic expression is available.

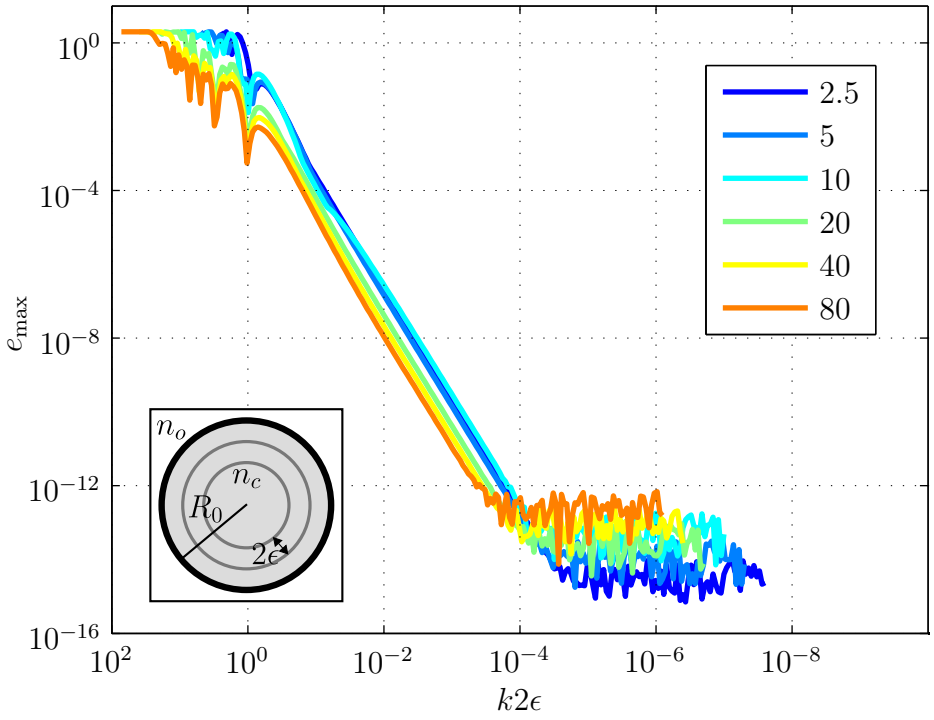


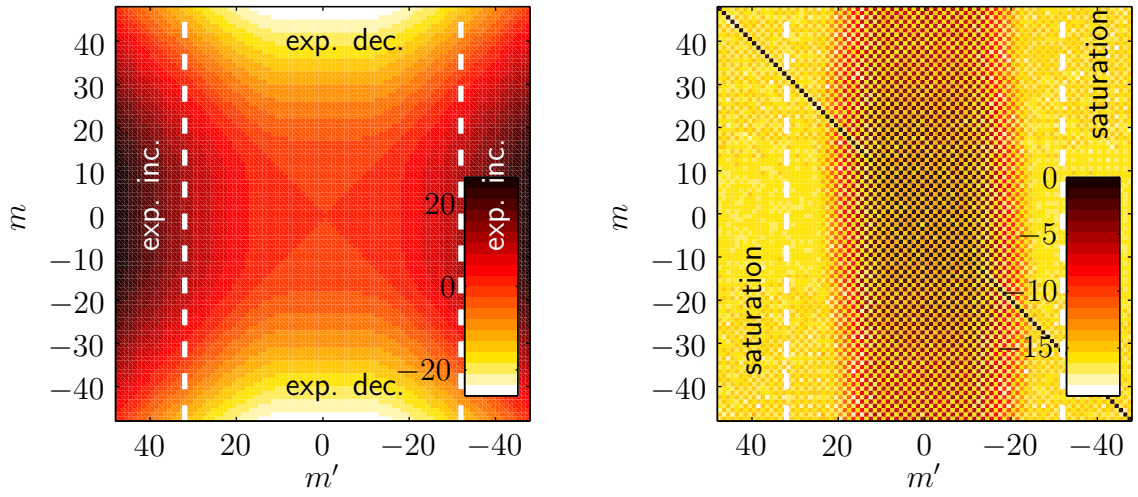
Fig. 2.13 (Color online) Maximum deviation, expression (2.76), for the homogeneous disc cavity separated in 2 annular regions (inset) of thickness 2ϵ. Computations are carried out with $n_c = 3.2$, $n_o = 1$ and $R_0 = 1$ for six wave numbers, $kR_0 = \{2.5,\ 5,\ 10,\ 20,\ 40,\ 80\}$. The maximum deviation decreases uniformly from a value $k2\epsilon \approx 0.33$ common to all wave numbers until a saturation limit is reached at small ϵ values.

The *annular cavity* (ac) with an *off-centre* inclusion of refractive index n_h offers an example of interest since its **S** matrix is highly non-trivial, *non-diagonal*[6], but still with a closed-form solution ideal for testing of our numerical approach. The derivation of the annular cavity scattering matrix, $\mathbf{S}_{ac}$, is reviewed in Appendix D. This is but one example of non-diagonal **S** matrix where different angular momentum channels interact, and in generic cases matrix truncation (the value of M) will become a concern. This question is pursued in the following calculations.

For comparison purposes, we will consider the scattering matrix of the displaced inclusion $\mathbf{S}^c$ expression (D.40). Attention is then put on a circular inclusion of radius R_0 and index n_c embedded in a dielectric medium n_o at a distance d from the origin.

Our first observation is directed to an inherent difficulty/instability common to *all* methods involved in the present type of calculations. Numerically, obtaining $\bar{\mathbf{S}} = \mathbf{S}_{22}^{0,N+1}$

[6]Clearly, if the inclusion is moved to the centre of the enclosing circular cavity, the resulting **S** is again *diagonal*.



(a) $\mathcal{H}$ (b) $\mathcal{S}_{22}^{0,N+1}$

Fig. 2.14 (Color online) Example of matrices involved in termwise product (2.78); log of absolute value of matrix elements. Color scale is logarithmic, spanning from white (low) to dark (high). White dash lines indicate the $|m'| = \lceil n_c k R_{\max} \rceil$ limits. The product of exponentially increasing elements in (a) with saturation terms due to numerical roundoff in (b) yields an ill-behaved scattering matrix.

from (2.73) involves the product

$$\mathbf{S}_{22}^{0,N+1} = \left\{\mathbf{H}^1\right\}^{-1} \mathcal{S}_{22}^{0,N+1} \mathbf{H}^2 \tag{2.77}$$

where $\{\mathbf{H}^{1,2}\}_{mm'} = H_m^{(1,2)}(n_c k R_{\max})\delta_{mm'}$, $R_{\max} = d + r_0$, and where the complete transfer matrix $\mathcal{S}_{22}^{0,N+1}$ is defined in Appendix C. This expression may be written otherwise as a Hadamard product (*i.e.* termwise product)

$$\mathbf{S}_{22}^{0,N+1} = \mathcal{H} \circ \mathcal{S}_{22}^{0,N+1} \tag{2.78}$$

with $\{\mathcal{H}\}_{mm'} = H_{m'}^{(2)}(n_c k R_{\max})/H_m^{(1)}(n_c k R_{\max})$. Terms in the matrix $\mathcal{H}$ are exponentially increasing for $|m'| > |m| \geq n_c k R_{\max}$ and exponentially decreasing for $|m| > |m'| \geq n_c k R_{\max}$ (see example Fig. 2.14(a) and reference [1]). However, because of numerical roundoff in the computation of $\mathcal{S}_{22}^{0,N+1}$, some elements of $\mathbf{S}_{22}^{0,N+1}$ that should be the product of rapidly decreasing $\{\mathcal{S}_{22}^{0,N+1}\}_{mm'}$ terms and increasing $\{\mathcal{H}\}_{mm'}$ terms are computed from the product of saturated $\{\mathcal{S}_{22}^{0,N+1}\}_{mm'}$ terms and increasing $\{\mathcal{H}\}_{mm'}$ terms. The term *saturation* denotes the fact that decreasing terms have reached the *numerical* zero ($\sim 10^{-15} - 10^{-16}$in double precision artihmetic). This inevitably leads to incorrect terms in $\mathbf{S}_{22}^{0,N+1}$. However, since saturation terms in $\mathcal{S}_{22}^{0,N+1}$ are located in vertical bands of angular momentum $|m'| > n_c k R_{\max}$ (see Fig. 2.14(b)), relation (2.4) may then be used to replace elements in pathological regions with terms unaffected by

numerical roundoff. This solution has shown to be quite effective in stabilising the final results.

We proceed as previously with evaluation of the maximum deviation $e_{\max}$ (2.76), only this time with $\mathbf{S}_{hd}$ being the displaced matrix $\mathbf{S}_c$ found in Appendix D. Computations are carried with physical parameters $n_c = 3.2$, $n_h = 1$, $R_0 = 1$, $d = 0.15R_0$, $r_0 = 0.1R_0$ and $kR_0 = 10$. The number N of thin annular regions covering the large annular domain ranging from $r = d - R_0$ to $r = d + R_0$ (see inset of Fig. 2.15) is used as a variable to adjust the annuli thickness 2ϵ. The computed scattering matrix is defined over a set of angular momenta ranging from $-M$ to $+M$. The total number of angular channels $2M + 1$ is then a control parameter. Although $e_{\max}$ is obtained for five truncation numbers, we shall consider only the square subset of angular momenta $[-8,\ 8]$ so that $e_{\max}$ is effectively computed from comparable elements of the scattering matrix in every cases.

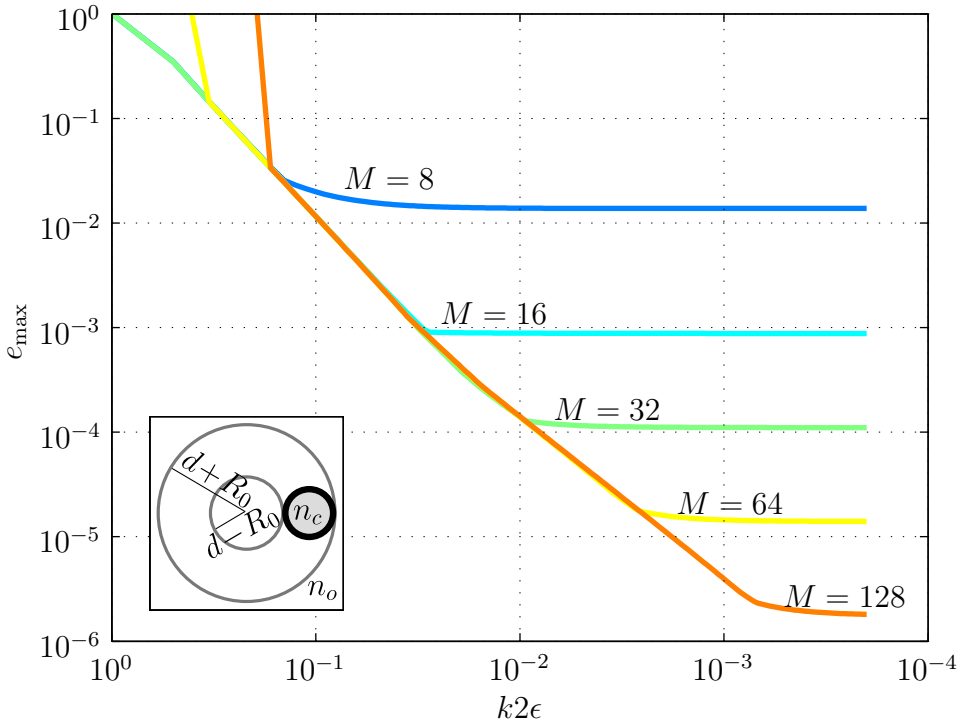


Fig. 2.15 (Color online) Maximum deviation $e_{\max}$, expression (2.76), for the circular inclusion of the annular cavity (inset) with respect to wavenumber-normalized annuli thickness $k2\epsilon$. Computation is carried out for five truncation sizes, $M = \{8,\ 16,\ 32,\ 64,\ 128\}$. For constant M, the maximum deviation decreases uniformly at first, then settles on a plateau. The plateau levels, $\bar{e}_{\max}(M)$, decrease by approximately an order of magnitude with a doubling of the truncation size, i.e. $\bar{e}_{\max}(M)/\bar{e}_{\max}(2M) \sim 10$.

The results of Fig. 2.15 show that truncation size affects the overall convergence in thickness 2ϵ: a mimimum achievable deviation $e_{\max}$ is reached for every M, the larger M the smaller the value of the deviation. By verifying the unitarity of $\bar{\mathbf{S}}$ for all trun-

cation sizes ($\max\{|\bar{\mathbf{S}}^\dagger\bar{\mathbf{S}} - \mathbb{1}|\} \sim 10^{-10}$), we conclude that flux is conserved, as it should, and it is not the source of this leveling behaviour. Satisfying unitarity with a matrix too small for an adequate modeling means that some channels will be contaminated (overestimated) and diminishing the annulus sizes is not going to solve this issue. On the other hand, the increase of the truncation size releases the erroneous contributions to higher channels and allows for further improvement in precision until another plateau is reached. Doubling the truncation size results in a decrease of $\bar{e}_{\max}(M)$ by about one order of magnitude, but then, computations become 4 times more costly.

These sets of computations (for the diagonal and non-diagonal cases) are two representative samples of a battery of tests that have been performed to assert the reliability and accuracy of our approach. In every calculations to appear in this thesis, care has been taken to insure convergence in angular space decomposition (large enough M) and spatial discretisation (small enough $2\epsilon k$).

2.3 Wavefunction reconstruction

The implementation of our propagation method is specifically geared for an efficient calculation of the scattering information coded in the $\mathbf{S}$ matrix and the associated $\mathbf{A}$ and $\mathbf{B}$ coefficients. In most instances, this is all one needs since this gives direct access to the far-field ($R \gg R_{\max}$) for microlaser applications and the near-field ($R = R_{\max}$) for microsensing applications. However, the coefficients $\{\mathbf{a}^j\}$ and $\{\mathbf{b}^j\}$ are not kept during the computation as one moves from the inner circle to the outermost shell, i.e. the information necessary to reconstruct the local wavefunction within the cavity ($R \leq R_{\max}$) is not directly available.

Since it may be useful to look at the complete wavefunction, if only for comparison purposes, we have looked at different approaches to extract the missing information. Most approaches have failed because of inherent numerical instabilities - we mention briefly some of these attempts in the next sub-section - and we have finally settled for a hybrid method to be described shortly.

2.3.1 Early and failed attempts

- **Direct reconstruction (Take 1)**

  The first attempt was native to the propagation method in that we have recuper-

ated the coefficients $\{\mathbf{a}^j\}$ et $\{\mathbf{b}^j\}$ of the different shells for a local construction of the field. This demands a backward propagation of the connecting matrices and turned out to be only feasible for $\mathbf{S}$ matrices of small dimension due to numerical instabilities. This limits the applicability to dimensions of the order of $M_{\min} = n_{\max} k R_{\mathbf{max}}$.

One first recalls that the number of angular harmonics $2M+1$ necessary to adequately construct the $\mathbf{S}$ matrix is greater than $2M_{\min}+1$. Second, since the radial differential equation is in polar coordinates, 2 solutions are possible: a regular and physical solution behaving as $\sim (nkr)^m$ for each angular momentum m and an irregular solution behaving as $\sim (nkr)^{-m}$. In moving backwards, the numerical approximations feed a small part of the irregular solution into the physical solution and if one is not careful this unphysical piece completely overwhelms the regular solution[7]. This behaviour towards the origin is then such that increasing $M_{\min}$ (for example by increasing k) decreases the radius of convergence of the method.

To alleviate this divergence, we have then tried a 'shooting'-like method, starting a regular solution at the origin towards an intermediate value of r and matching at that value with a solution propagating from the boundary towards the centre. The gain in stability varied from one geometry to the other, but reliable results were not obtained above $M_{\min} \sim 25$.

- **Direct reconstruction (Take 2)**

  We have then looked at a complete numerical integration of the radial partial differential equations transformed into $2M+1$ coupled ordinary differential equations by separation in angular harmonics where the coupling is provided by the index of refraction. An adaptive Runge-Kutta of order 4-5 was used for this task.

  Unfortunaltely, the approach shares the instabilities of the previous method. It is very difficult to try to control each m channel, because the large m diverge faster (earlier) than the small ones. Since one imposes the behaviour at the origin, the numerical parameters are very much dependent on the initial conditions (values and slopes) and this sensitivity makes the approach unreliable. Several tests of the simplest case (an homogeneous disc) reveal that the parameters turn out to be quite different from those expected on theoretical grounds (Frobenius expansion at the origin for instance). In this case, although the solutions appeared similar to the analytical Bessel functions J_m, their behaviour at the origin was quite different.

[7] Since our method used a normalised radial coordinate whitin each shell, the divergence appears only in the coefficients $\{\mathbf{a}^j\}$ et $\{\mathbf{b}^j\}$, but not in the connecting matrices.

- **Basis set reconstruction: Spectral and pseudo-spectral methods**

  The next thought was to select a basis set and develop the solution over the entire domain, a solution which is after all a smooth function. *Spectral* or pseudo-spectral methods [24], as they may be called, build 'matrices of matrices' no matter what the chosen basis set. The wavefunction is then obtained through the solution of a large linear system of equations.

  The *spectral method* involves the calculations of double integrals for each element of the projection matrix. Since the number of basis functions increase with k, this method becomes prohibitively time consuming making it less attractive than the 'dangerous' methods previously discussed under the *caveat* already discussed. No in depth attempts have been made to make this approach viable.

  The *pseudo-spectral method* on the other hand replaces the explicit integration by an evaluation of the basis functions on a discrete mesh. By an appropriate choice of the mesh, one obtains an *equivalent quadrature* instead of a direct integration as in the spectral method. For a unique solution, the number of collocation points of the mesh must be equal to the number of basis functions. One may also force overdetermination (more collocation points that basis functions), in which case the solution is obtained with a pseudo-inverse of the collocation matrix. This demands in turn that small singular values be eliminated beforehand. The few tests performed have indicated that the final results are quite dependent on which singular values are indeed removed.

  In fact, both methods suffer from the same predicament, namely that the associated matrices (projection or collocation) are ill-conditioned, mainly caused by the second derivatives of the Laplacian being applied to polynomials of high orders. Moreover the dimension of these matrices grows rapidly (e.g. for the pseudo-spectral method: (Nb points $y \times$ Nb points x) $\times$ (Nb bases $y \times$ Nb bases x)) making computer memory management a further task to be addressed.

2.3.2 The adopted procedure: A hybrid finite element approach

Faced with the difficulties just described, we have searched for a new strategy. In this thesis - except otherwise stated - whenever a wave function is represented (for example at the end of sub-section 2.1.3) in the entire domain of interest, we have adopted a hybrid method combining the scattering information obtained from our approach together with a *Finite Element Method* (FEM) algorithm provided by the commercial software COMSOL Multiphysics [37]. This procedure has proven to be accurate, fast, flexible, and reliable.

Specifically, the procedure goes like this. The field at a given wavenumber k with incoming $\mathbf{A}$ and outgoing $\mathbf{B}$ coefficients at the last interface is used as boundary condition on a circular region of radius $R \geq R_{\mathbf{max}}$ for the FEM algorithm. The FEM solver is then applied to build the wavefunction on a discrete mesh over the entire region. We do not impose continuity of the normal derivative, since it would lead to an overdetermined differential equation, but instead we use the discrepancy with the expected derivative as a measure of the accuracy of the FEM reconstruction. The normal derivative at a circular region ∂D of radius R can be written as

$$\frac{\partial}{\partial r}\bar{\psi}\big|_{\partial D} = n_o k \sum_m \left[A_m H_m^{(2)\prime}(n_o k R) + B_m H_m^{(1)\prime}(n_o k R) \right] \mathrm{e}^{im\phi} \; . \tag{2.79}$$

Our measure of the difference between the propagation result $\bar{\psi}$ and the FEM reconstruction ψ_{FEM} is chosen as

$$C_1 = \frac{\frac{1}{2\pi}\int_0^{2\pi} d\phi \;\; \left[\frac{\partial}{\partial r}\left(\bar{\psi} - \psi_{\mathrm{FEM}}\right)^* \cdot \frac{\partial}{\partial r}\left(\bar{\psi} - \psi_{\mathrm{FEM}}\right) \right]\big|_{\partial D}}{\frac{1}{2\pi}\int_0^{2\pi} d\phi \;\; \left[\frac{\partial}{\partial r}\bar{\psi}^* \cdot \frac{\partial}{\partial r}\bar{\psi} \right]\big|_{\partial D}} \quad . \tag{2.80}$$

The integrals are calculated with a *Fast Fourier Transform* (FFT) and the result is then compared to that of C_0, which reveals to what extent the boundary condition is satisfied:

$$C_0 = \frac{\frac{1}{2\pi}\int_0^{2\pi} d\phi \;\; \left[\left(\bar{\psi} - \psi_{\mathrm{FEM}}\right)^* \cdot \left(\bar{\psi} - \psi_{\mathrm{FEM}}\right) \right]\big|_{\partial D}}{\frac{1}{2\pi}\int_0^{2\pi} d\phi \;\; \left[\bar{\psi}^* \cdot \bar{\psi} \right]\big|_{\partial D}} \quad . \tag{2.81}$$

The maximum size of the longest side of the finite elements (triangular or quadratic) is limited to $\lambda/10$, where λ is the wavelength in the corresponding medium. The FEM algorithm has proven quite robust and the automatic mesh construction has made it possible to obtain very accurate (imposed) continuity in the function (the C_0 measure) and its (not-imposed) normal derivative (the C_1 measure).

A sample mesh is shown in Fig. 2.16. The figure of merit for the quality of the mesh is calculated according to the following expression [37]

$$q = \frac{4\sqrt{3}A}{h_1^2 + h_2^2 + h_3^2} \tag{2.82}$$

where A is the area of the triangle and $\{h_i\}$ are the lengths of the the sides of the triangle. Recalling Heron's formula for the area of a triangle in terms of $\{h_i\}$

$$A = \sqrt{\frac{1}{16}(h_1^2 + h_2^2 + h_3^2)^2 - \frac{1}{8}(h_1^4 + h_2^4 + h_3^4)}, \tag{2.83}$$

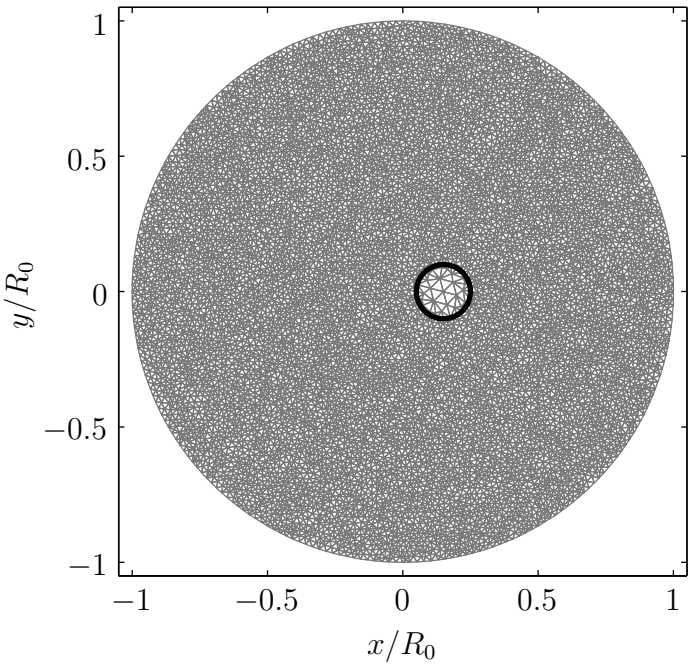


Fig. 2.16 Mesh for the annular cavity with a hole of radius $r_0 = 0.1R_0$ at $d = 0.15R_0$. Cavity radius is $R_0 = 1$ and the mesh size follows the refractive index of the media. For instance, in this figure the typical mesh element has a length ratio 3.2 to 1 in the hole region where the index is $n_h = 1$ with respect to the cavity domain having $n_c = 3.2$.

we find that $q = 1$ for an equilateral triangle. For the system whose mesh is presented in Fig. 2.16, the elements of least quality (most asymmetric) are found along the junction of the 2 domains (at the centre and the right-hand side of the figure).

Various tests - not presented here - have been performed to assert the effectiveness and reliability of the procedure and have confirmed the usefulness and generality of the approach. As mentioned earlier, whenever a wavefunction will be presented in the next Chapters, one should assume that it has been constructed with the present hybrid method.

2.4 Numerical calculation of the Q matrix

This Section deals with the evaluation of the delay matrix

$$\mathbf{Q} = -i\mathbf{S}^{\dagger}\partial\mathbf{S}/\partial k$$

and the comparison with results from the usual resonant pole description of the cavity modes. Again we will use the annular cavity as a benchmark for our calculations (see Appendix D). Some of the discussion here is an extension of the remarks made towards the end of the sub-section 2.1.3.

The evaluation of the derivative of $\mathbf{S}$ with respect to wavenumber k is carried out numerically following Ridder's method [107]. Convergence of the differentiation is set by the comparison of the trace of the direct centered difference scheme,

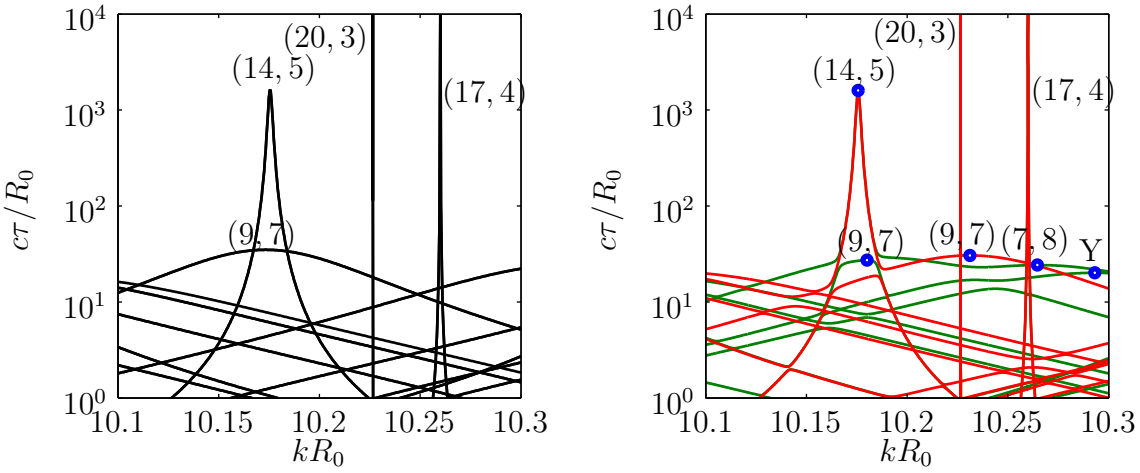
$$\frac{\partial \mathbf{S}}{\partial k} \approx \frac{\mathbf{S}(k+\delta k) - \mathbf{S}(k-\delta k)}{2\delta k} \tag{2.84}$$

with an extrapolated value for $\delta k \to 0$ obtained from data gathered beforehand with $\delta k' > \delta k$. The numerical differentiation scheme is terminated as soon as the difference between $\mathbf{S}(k+\delta k)$ and $\mathbf{S}(k-\delta k)$ becomes comparable in magnitude with the error on the unitarity of $\mathbf{S}$.

The eigenvalue decomposition of the delay matrix yields a basis of orthogonal vectors $\{\mathbf{A}^p\}$ for every real wavenumber k. In generic cases, for two sets of orthogonal vectors $\{\mathbf{A}^p(k)\}$ and $\{\mathbf{A}^p(k+\Delta k)\}$ separated by a small wavenumber distance Δk, we are able to follow individual characteristic modes since the basis at $k + \Delta k$ is only a minute rotation away from the basis at k. This may be understood as an adiabatic process on the characteristic modes where the wavenumber k acts as the external parameter.

Since the annular cavity is a deformation of the homogeneous disc cavity, a few preliminary comments on the latter are appropriate at this point. First, like the $\mathbf{S}$ matrix, the delay matrix of the disc cavity is diagonal in the angular momentum representation. Moreover, because of rotational symmetry, all characteristic delays are degenerate at least two times. Accidental degeneracies between levels of different angular momenta are also common. A typical disc cavity delay spectrum is presented in Fig. 2.17(a).

The insertion of a circular scatterer inside a disc cavity has dramatic consequences for the delay spectrum. Breaking the rotation symmetry by restricting modes to be either even or odd relative to the annular cavity's symmetry axis lifts the twofold degeneracy of same angular momentum modes. However, it is near the accidental degeneracies found in the disc cavity delay spectrum that the effect of the inclusion is most important (compare spectra 2.17(a) and (b)). In the neighbourhood of these accidental degeneracies, the adiabatic delay level switches from a crossing pattern to an anti-crossing pattern between modes of the same symmetry. In the figure, these are traced in red for the odd-symmetry and green for the even-symmetry with respect to the Ox axis. The extent of the anti-crossing depends on the interaction strength between the involved modes as already discussed in sub-section 2.1.3.



(a) Homogeneous cavity (b) Annular cavity

Fig. 2.17 Delay spectra of (a) the homogeneous disc (hd) cavity ($n_c = 3.2$, $n_o = 1$, $R_0 = 1$) and of (b) the annular cavity (ac) ($n_c = 3.2$, $n_o = 1$, $R_0 = 1$, $n_h = 1$, $r_0 = 0.1R_0$, $d = 0.25R_0$). The resonant modes are identified by 2 integers, (m, n): m is the azimuthal angular number, and n is the number of radial nodes inside the cavity. This nomenclature is used in both spectra, although one must regard the labels in the annular cavity spectrum as adiabatical remnants of the hd cavity modes through the parametric deformation.

Computation of the annular cavity spectrum is carried out with the algorithm of Section 2.2 (500 layers over the inclusion region, 70 *positive* angular channels (141 total)).

The annular cavity model discussed in Appendix D may also be used to find resonant poles of the scattering matrix in the complex wavenumber plane. Setting $\mathbf{A} = 0$ in (D.10) defines a complex wavenumber root search for emission modes ($\mathrm{Im}\{k\} < 0$) . Since $\mathbf{B} = \mathbf{SA}$, or equivalently $\mathbf{S}^{-1}\mathbf{B} = \mathbf{A}$, setting $\mathbf{A} = 0$ implies that $\det \mathbf{S}^{-1}$ must be equal to zero for a non-trivial $\mathbf{B}$ solution. And the zeros of the $\det \mathbf{S}^{-1}$ are the poles of $\det \mathbf{S}$ as illustrated in Fig. 2.2.

Some singular modes lying in the complex plane are displayed in Fig. 2.18 along with comparable modes retrieved from the characteristic modes description. The resemblance between the near-field and (outgoing) far-field representations from the two descriptions is notable. Numerical values of wavenumber resonant pole positions and delay values at resonance (maximum delay) agree as well (see Table 2.2). Discrepancy in the field distribution and the resonance positions between the two descriptions are attributed to the many avoided-crossings in the neighbourhood of a given maximum delay wavenumber position.

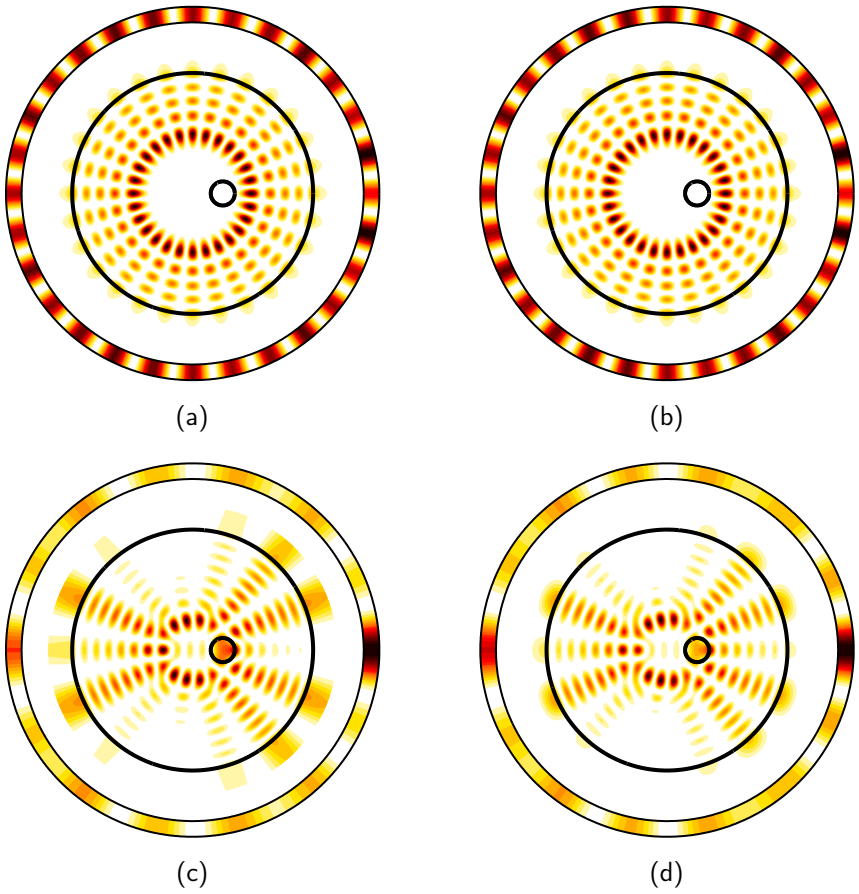


Fig. 2.18 Comparison of two annular cavity resonances field distributions $|\psi(\mathbf{r})|^2$: (a)-(c) for the resonant wavenumber pole description and (b)-(d) for the characteristic modes definition (maximum of delay; see delay spectrum 2.17(b)). Color scale is linear from white/bright (low) to black/dark (high). The external ring refers to the outgoing far-field distribution. The modes investigated are perturbed versions of modes $(14, 5)$, (a)-(b), and $(7, 8)$, (c)-(d). The outgoing coefficients $\mathbf{B}$ collected from resonant pole and characteristic modes descriptions overlap nicely to a value of 0.9999987 for the $(14, 5)$ mode , and 0.985 for the $(7, 8)$ mode.

Mode	$\mathrm{Re}\{kR_0\}$		$\lvert\mathrm{Im}\{kR_0\}\rvert$	
$(20,3)$ e	10.226504923	(10.226504925[6])	5.7×10^{-9}	(6.2×10^{-9})
$(20,3)$ o	10.226504923	(10.226504925[6])	5.7×10^{-9}	(6.2×10^{-9})
$(17,4)$ e	10.2599778	(10.259978[2])	6.39×10^{-6}	(6.40×10^{-6})
$(17,4)$ o	10.2599778	(10.259978[2])	6.40×10^{-6}	(6.42×10^{-6})
$(14,5)$ e	10.1757	(10.1757[2])	1.255×10^{-3}	(1.256×10^{-3})
$(14,5)$ o	10.1757	(10.1757[2])	1.2491×10^{-3}	(1.2492×10^{-3})
$(9,7)$ e	10.1888	(10.1801[2])	6.9×10^{-2}	(7.3×10^{-2})
$(9,7)$ o	10.2311	(10.2311[2])	6.4×10^{-2}	(6.5×10^{-2})
$(7,8)$ e	10.2676	(10.2647[2])	8.1×10^{-2}	(8.3×10^{-2})
"Y" e	10.2959	(10.2932[2])	9.4×10^{-2}	(9.9×10^{-2})

Tab. 2.2 Comparison of resonant wavenumber positions for the modes displayed in Fig. 2.18; numbers in parentheses belong to the characteristic modes description and the bracketed digits indicate the uncertainty on the last digit (stepsize of k). The label e/o stands for even or odd parity with respect to the Ox axis. The equivalent of the 'imaginary part' of the wavenumber in the case of characteristic modes is calculated using relation $2R_0/c\tau$. The total delay is composed of an entrance delay and of an escape delay; for characteristic modes, because of incoming/outgoing symmetry, these are of the same magnitude, hence the factor 2. See Eq. (2.33) and the associated discussion for further explanations using Simonius' model.

Chapter 3

Formalism II: Perturbation series

In this Chapter, we present a perturbation approach for the description of the wavefield produced by the modification of the refractive index of an homogeneous disc cavity. We do so in the perspective of the results of Chapter 2. We first use the Born approximation in the near field of the disc cavity to obtain a first order correction to its scattering matrix. Then, we use matrix perturbation theory to obtain the perturbed first order eigenvalues and eigenvectors of the delay matrix presented in the previous Chapter. Finally, we illustrate the method for two perturbation scenarios: boundary deformations and inclusions. The inclusion arrangement is discussed in great details and will lead to further investigations in the following Chapter.

Before moving on to a complete application of the numerical method presented in the previous Chapter, we will take some time to explore the possibilities of analytical solutions to the perturbed homogeneous disc cavity. To the author's knowledge, outside of the disc geometry, only the elliptic cavity permits an exact solution to Helmholtz equation in terms of Mathieu functions [154]. This is the reason that a perturbation solution for a small refractive index deformation of the disc cavity is investigated. The idea is to guide, through analytically tractable means, the investigation towards high quality cavities with high directional emission properties. Also, as a side product of the analysis, the results will show just how the theory developed in Chapter 2 is accurate on a perturbation level.

The method developed next is inspired by the work of Dubertrand *et al.* [41]. However, unlike the usual complex wavenumber poles description followed by these authors and others [144, 145, 38, 39], we will rely on our delay matrix to obtain significant and reliable results about the modes of the cavity system.

This Chapter is organized in a two-step scheme, development of the theory followed by its applications to specific problems. First, we define the refractive index perturbation on an abstract level and derive the associated first order correction to the scattering matrix. In line with the theory of Chapter 2, we then seek a matrix perturbation solution to the delay matrix eigen-decomposition. Finally, using our general expressions, we obtain the perturbation solution to two important classes of deformations: boundary deformations and inclusions. The latter case will be studied in depth and will provide useful information for further study in the coming Chapter.

The original contributions of this Chapter are in line with the theoretical developments presented in Chapter 2. The use of a first perturbation series applied on the scattering matrix of the disc cavity, eventually leading to Eq. (3.15), and the computation of a perturbed delay matrix Eq. (3.25) may be considered original to the field. The manner the characteristic delays of the delay matrix are extracted, eventually leading to Eq. (3.62), is also perceived as original, as well as the illustrative examples provided in Sections 3.2 and 3.3. Particularly, the analytical comparison of one case of inhomogeneous cavity with the boundary deformed cavity presented in Section 3.3.3 is a new result.

3.1 Small deformations of the disc cavity

In this Section we obtain a first order approximation of the scattering matrix for a slightly modified homogeneous disc cavity, and present a perturbative treatment of its characteristic modes. The full procedure consists of *two* consecutive perturbative treatments of a different nature:

- the first one, for the scattering matrix, uses the standard *Born approximation*, while
- the second one, for the eigenmodes of the perturbed delay matrix, applies the usual *matrix perturbation theory*.

What is meant here by *perturbation* involves the slight modification of the wavefield in the near-field region of space, *i.e.* close to the cavity. The reason for this stems from our intention to deform the disc, affecting in the first place the near-field. This description is especially suited for large delay modes (high quality modes) having a dominant angular momentum component m_0. However, because of the dichotomy between the near-field and the far-field of the characteristic modes of the cavity, we will see that the overall

aspect of the latter may be even more affected by low magnitude deformations than the former.

The alteration of the disc cavity is embodied in a perturbative index, $\tilde{n}(\mathbf{r};\epsilon)$, where the dimensionless parameter ϵ governs the size of the perturbation. The smallness of $\tilde{n}(\mathbf{r};\epsilon)$ prescribes the decomposition of the wavefield into two contributions. This results in a $\mathbf{S}$ matrix having a zeroth order part from the disc cavity, $\mathbf{S}^{(0)}$, and a first-order correction part, $\mathbf{S}^{(1)}$, arising from the additional refractive index (see Fig. 3.1).

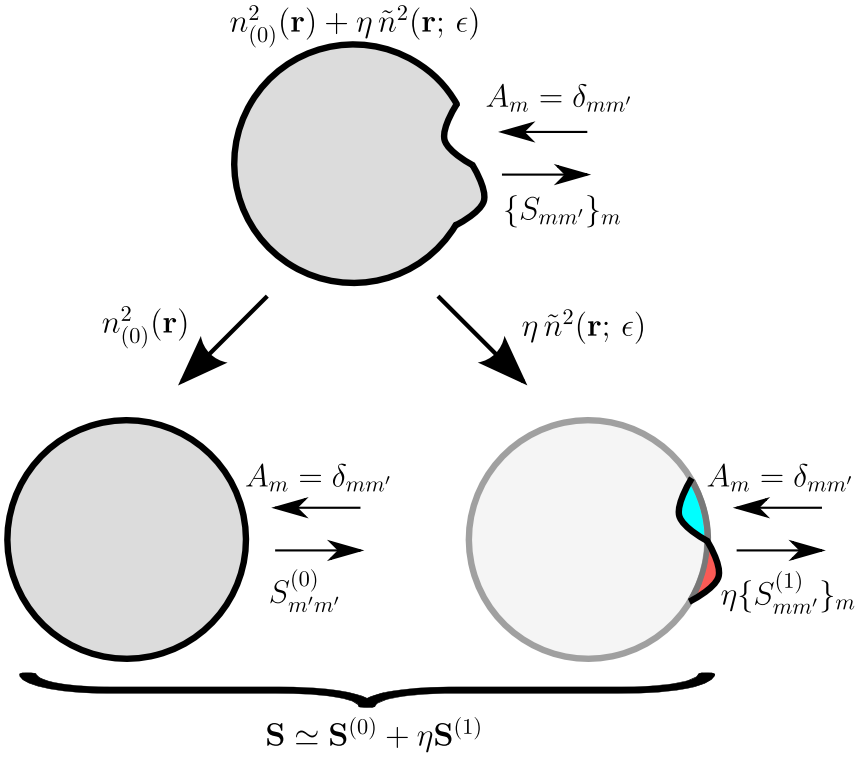


Fig. 3.1 Schematic decomposition of the complete cavity $\mathbf{S}$ matrix into two contributions, one due to the main disc cavity, $\mathbf{S}^{(0)}$, and the other, $\mathbf{S}^{(1)}$, due to the effect of the extra medium $\tilde{n}(\mathbf{r};\epsilon)$. A test channel of angular momentum m' is impinging on a cavity, which responds by releasing a number of coefficients affecting many outgoing channels m.

Once the approximate scattering matrix is known, we may readily compute a perturbed delay matrix. We shall rely on the reciprocal property between incoming and outgoing modes of the delay matrix $\mathbf{Q}$, see Chapter 2,

$$\psi^{\text{in}*} = \mathrm{e}^{-i\theta}\psi^{\text{out}}$$

to obtain a supplementary phase factor, $\theta^{(1)}_{m_0}$, to the already known disc cavity phase $\theta^{(0)}_{m_0}$ (see Fig. 3.2). The perturbed delay is computed by the wavenumber differentiation of the full phase factor $-\theta_{m_0} \simeq -\theta^{(0)}_{m_0} + \theta^{(1)}_{m_0}(\epsilon)$.

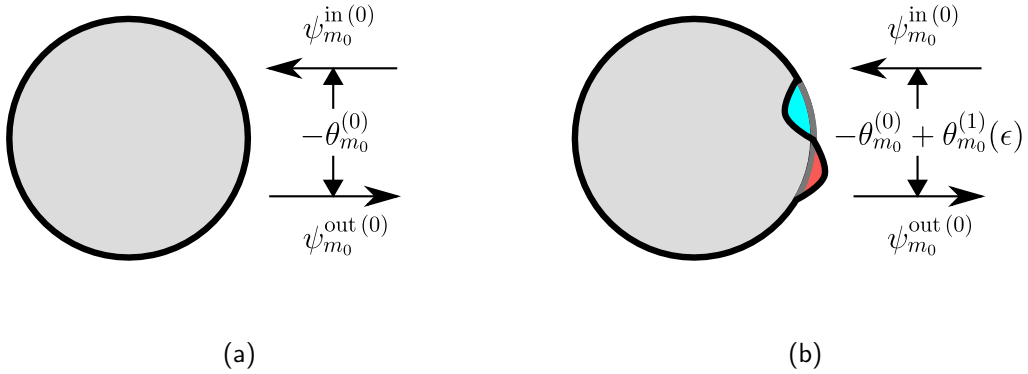


Fig. 3.2 Phase factor between incoming and outgoing waves having an angular momentum m_0, (a) in the homogeneous disc case, and (b) in the perturbed disc scenario. Although the composition on the perturbed wavefield consists in many angular channels, the effect on the phase θ appears mainly in the unperturbed channel m_0 component.

A series of assumptions will be made all along the perturbative developments. They will be summarized at the end of the Section and fully justified in the illustrative examples of the following Section. The perturbation approach presented provides a series of non-trivial analytical results for the theory of Chapter 2, and will spur further investigations in Chapter 4.

3.1.1 Perturbation correction of the S matrix

The refractive index of the cavity may be separated into two contributions

$$n^2(\mathbf{r}) = n_{(0)}^2(\mathbf{r}) + \eta\, \tilde{n}^2(\mathbf{r};\epsilon) \tag{3.1}$$

and

$$n_{(0)}^2(\mathbf{r}) = n_c^2 + \left[n_o^2 - n_c^2\right] U(r - R_0) \tag{3.2}$$

is the refractive index of a disc cavity of radius R_0, and $U(x)$ is the Heaviside step function: $U(x) = 0$ for $x < 0$, and $= 1$ for $x > 0$. The *compensation refractive index* $\tilde{n}^2(\mathbf{r};\epsilon)$ adds and/or subtracts dielectric material from the main disc cavity. Notice that η will serve to order the perturbation series whereas ϵ will act as a (small) parameter to control the size of the perturbation.

We rewrite Helmholtz' equation as

$$\left[\nabla_{\mathbf{r}}^2 + n_{(0)}^2(\mathbf{r})k^2\right] \psi(\mathbf{r}) = -\eta\, \tilde{n}^2(\mathbf{r};\epsilon) k^2 \psi(\mathbf{r}) \tag{3.3}$$

whose formal solution is

$$\psi(\mathbf{r}) = \psi^{(0)}(\mathbf{r}) - \eta \int d^2\mathbf{r}'\, G^{(0)}(\mathbf{r},\mathbf{r}') \tilde{n}^2(\mathbf{r}';\epsilon) k^2 \psi(\mathbf{r}') \tag{3.4}$$

where $G^{(0)}(\mathbf{r},\mathbf{r}')$ is the Green function of the disc cavity satisfying

$$\left[\nabla^2_{\mathbf{r}} + n^2_{(0)}(\mathbf{r})k^2\right] G^{(0)}(\mathbf{r},\mathbf{r}') = \delta(\mathbf{r}-\mathbf{r}') \quad . \tag{3.5}$$

The homogeneous wavefunction $\psi^{(0)}(\mathbf{r})$ for the disc cavity is written as usual

$$\begin{cases} \sum_m \left[A_m H^{(2)}_m(n_o kr) + B_m H^{(1)}_m(n_o kr)\right] \mathrm{e}^{im\phi} & r \geq R_0 \\ \sum_m a_m J_m(n_c kr)\mathrm{e}^{im\phi} & r \leq R_0 \end{cases} \quad . \tag{3.6}$$

The coefficients $\mathbf{A}$ and $\mathbf{B}$ are related to one another by $\mathbf{B} = \mathbf{S}^{(0)}\mathbf{A}$, where the scattering matrix elements are given by

$$S^{(0)}_{mm'} = -\frac{\bar{\Delta}_m}{\Delta_m}\,\delta_{mm'} \ . \tag{3.7}$$

The coefficients $\mathbf{a}$ are related to the coefficients $\mathbf{A}$ by $\mathbf{a} = \mathbf{T}^{(0)}\mathbf{A}$, with

$$T^{(0)}_{mm'} = -\frac{4i}{\pi k R_0}\frac{1}{\Delta_m}\,\delta_{mm'} \quad . \tag{3.8}$$

We recall from Chapter 2 that

$$\bar{\Delta}_m = n_c H^{(2)}_m(Z_o) J'_m(Z_c) - n_o H^{(2)'}_m(Z_o) J_m(Z_c) \tag{3.9}$$

$$\Delta_m = n_c H^{(1)}_m(Z_o) J'_m(Z_c) - n_o H^{(1)'}_m(Z_o) J_m(Z_c) \tag{3.10}$$

where the arguments of the cylindrical functions are $Z_c = n_c k R_0$ and $Z_o = n_o k R_0$. Clearly, for real k, $\bar{\Delta}^*_m = \Delta_m$.

Now the stage is set for a Born-like approximation [36]. We expand the wave field in powers of η

$$\psi(\mathbf{r}) = \sum_j \eta^j \psi^{(j)}(\mathbf{r}) \simeq \psi^{(0)}(\mathbf{r}) + \eta\psi^{(1)}(\mathbf{r};\epsilon) + \mathcal{O}(\eta^2) \tag{3.11}$$

insert it in the formal solution (3.4) and collecting terms of equal orders in η, we identify the first order correction of the unperturbed wavefunction as

$$\psi^{(1)}(\mathbf{r};\epsilon) = -\int d^2\mathbf{r}'\, G^{(0)}(\mathbf{r},\mathbf{r}')\tilde{n}^2(\mathbf{r}';\epsilon)k^2\psi^{(0)}(\mathbf{r}') \ . \tag{3.12}$$

Before moving on to a more detailed calculation of the wavefunction, we first have to address the exact nature of the Green function found in Eq. (3.12).

Replacing back Eq. (3.12) into Helmholtz' equation, we find that $\psi^{(1)}(\mathbf{r};\epsilon)$ may be interpreted as the field resulting from the action of the source $-\tilde{n}^2(\mathbf{r};\epsilon)k^2\psi^{(0)}(\mathbf{r})$ on the disc cavity,

$$\left[\nabla^2_{\mathbf{r}} + n^2_{(0)}(\mathbf{r})k^2\right] \psi^{(1)}(\mathbf{r};\epsilon) = -\tilde{n}^2(\mathbf{r};\epsilon)k^2\psi^{(0)}(\mathbf{r}). \tag{3.13}$$

Since the field source is in the neighborhood of the cavity, the far-field behaviour of the wavefunction $\tilde{\psi}$ should be related to an outgoing wave as $|\mathbf{r}| \to \infty$. The Green function solving (3.5) will then be chosen with an asymptotically outgoing behaviour. Depending upon the relative position of the source $\mathbf{r}'$ to both the observation point $\mathbf{r}$ and the disc boundary at $r = R_0$, six possible solutions of Green functions are found: they are derived in Appendix F and displayed in Fig. F.1.

Our interest lies in the scattering matrix. This translates in the selection of the Green functions with the observation position $\mathbf{r}$ *outside* the cavity. Only two possible forms of the Green functions are then of importance in the following development, denoted $G_{oo}(\mathbf{r}, \mathbf{r}')$ and $G_{co}(\mathbf{r}, \mathbf{r}')$ in Appendix F.

Our concern is to obtain a correction term to the disc cavity scattering matrix. For this purpose, we use an incoming wave having a specific angular momentum channel as our zeroth order wavefunction $\psi^{(0)} = \psi^{(0)}_{m'}$. We set $A_m = A^{(0)}_m = \delta_{mm'}$ in Eq. (3.6) as a test incoming channel, and focus on the scattered field that embodies both the outgoing homogeneous field and the partial wave components generated by the perturbation, $\{\psi^{(1)}_{mm'}\}$ (see Fig. 3.1 for an illustration).

So far, our approximation of the wavefunction has lead us to compute the first correction provided by the action of a single angular momentum channel on the cavity,

$$\psi_{m'}(\mathbf{r}) \simeq \psi^{(0)}_{m'}(\mathbf{r}) + \eta \sum_m \psi^{(1)}_{mm'}(\mathbf{r}) \quad . \tag{3.14}$$

Because the components $\{\psi^{(1)}_{mm'}\}$ are by construction made of outgoing waves resulting from a single incoming channel m', we are able to assemble a matrix relating incoming to outgoing amplitude by direct inspection of Eq. (3.14). Doing so, we extract the corrected scattering matrix

$$\mathbf{S} = \mathbf{S}^{(0)} + \eta \mathbf{S}^{(1)} + \mathcal{O}(\eta^2) \quad . \tag{3.15}$$

For real wavenumber k, the exact scattering matrix is unitary, $\mathbf{S}^\dagger \mathbf{S} = \mathbb{1}$. With respect to the series in Eq. (3.15), we compute the unitarity condition

$$\mathbf{S}^\dagger \mathbf{S} = \mathbb{1} + \eta \left[\mathbf{S}^{(0)\dagger} \mathbf{S}^{(1)} + \mathbf{S}^{(1)\dagger} \mathbf{S}^{(0)} \right] + \mathcal{O}(\eta^2) \; . \tag{3.16}$$

As we will see shortly, we inherit from the Born approximation the property that, if the wavefunction is correct to first-order, the loss of unitarity of the approximate $\mathbf{S}$ matrix is to second-order, in other words $\mathbf{S}^\dagger \mathbf{S} = \mathbb{1} + \mathcal{O}(\eta^2)$, implying directly that

$$\mathbf{S}^{(0)\dagger} \mathbf{S}^{(1)} = -\mathbf{S}^{(1)\dagger} \mathbf{S}^{(0)} \quad . \tag{3.17}$$

This result will be confirmed explicitly in the next Section. Another useful property of

the exact $\mathbf{S}$ matrix, namely

$$S_{m'm} = (-1)^{m'} S_{-m-m'} (-1)^{m} \tag{3.18}$$

derived in Chapter 2, is also shared by the first two orders of approximations $\mathbf{S}^{(0)}$ and $\mathbf{S}^{(1)}$ appearing in Eq. (3.15),

$$S^{(0,1)}_{m'm} = (-1)^{m'} S^{(0,1)}_{-m-m'} (-1)^{m} \ . \tag{3.19}$$

3.1.2 Perturbation treatment of the corrected delay matrix modes

Having obtained the first correction to the scattering matrix, we may now turn to the investigation of the effect of the index perturbation on the resonances. In line with the preceding Chapter, we seek the *excess energy* associated with the presence of the cavity in a featureless 'universe'. Comparing this extra energy to the incoming flux, we compute the time delay due to the presence of the cavity. The resonances appear as prominent peaks of this time delay as a function of wavenumber k.

As is shown in Chapter 2, the time-average excess energy matrix in the angular momentum basis is

$$\mathcal{E} = \frac{2w\varepsilon_0}{k} \left(-i\mathbf{S}^{\dagger} \frac{d\mathbf{S}}{dk} \right) \tag{3.20}$$

where w is the height of the cavity along Oz, and ε_0 is the permittivity of vacuum. The characteristic energy modes of the cavity are defined through incoming wavefield coefficients $\mathbf{A}^p = \{A^p_m\}$ that diagonalize the hermitian matrix, $\mathcal{E}$. The mean energy associated with a specific characteristic mode labeled p is then

$$e_p = \mathbf{A}^{p\dagger} \mathcal{E} \mathbf{A}^p \quad . \tag{3.21}$$

For mode p, the time-average incoming power is

$$P_p = \frac{2w}{ck\mu_0} \mathbf{A}^{p\dagger} \mathbf{A}^p \tag{3.22}$$

with μ_0 the permeability of vacuum and c, the speed of light in vacuum. The computed time delay τ_p associated with the mode p is then

$$c\tau_p = c\frac{e_p}{P_p} = \frac{1}{\mathbf{A}^{p\dagger}\mathbf{A}^p} \mathbf{A}^{p\dagger} \left(-i\mathbf{S}^{\dagger} \frac{d\mathbf{S}}{dk} \right) \mathbf{A}^p = \frac{1}{\mathbf{A}^{p\dagger}\mathbf{A}^p} \mathbf{A}^{p\dagger}\, \mathbf{Q}\, \mathbf{A}^p \quad . \tag{3.23}$$

This expression gives directly the eigenvalues of the delay matrix $\mathbf{Q}$ [135]. Resonances are identified as peaks of $c\tau_p$ versus real k following excitation by a normalized incoming flux. Note that resonances are understood as *special* cases of a general scattering

experiment: the time delay can be computed off resonance and still retains its physical significance.

Also of interest is the reciprocal relation between incoming and outgoing characteristic mode coefficients,

$$\mathbf{B}^p = \mathrm{e}^{-i\theta_p}\mathbf{P}\mathbf{A}^{p*} \quad . \tag{3.24}$$

This relation will be of central importance in the coming development.

Returning to the perturbation method, we compute the corrected delay matrix as

$$\mathbf{Q} \simeq \mathbf{Q}^{(0)} + \eta\mathbf{Q}^{(1)} \tag{3.25}$$

where $\mathbf{Q}^{(0)}$ is the unperturbed delay matrix for the disc cavity and

$$\mathbf{Q}^{(1)} = \left(-i\mathbf{S}^{(0)\dagger}\frac{d\mathbf{S}^{(1)}}{dk} - i\mathbf{S}^{(1)\dagger}\frac{d\mathbf{S}^{(0)}}{dk}\right) \tag{3.26}$$

is the first-order correction to the perturbed delay matrix. It follows from (3.17) that $\mathbf{Q}^{(1)}$ is hermitian,

$$\mathbf{Q}^{(1)\dagger} = \mathbf{Q}^{(1)} \quad . \tag{3.27}$$

Turning to the calculation of Eq. (3.23) with Eq. (3.25), the approximate expressions of the eigenvalues and eigenvectors of the delay matrix can be obtained. The procedure leads to the computation of the zeroth- and first-order eigenvalues $q_p^{(0)}$ and $q_p^{(1)}$, and their corresponding eigenvectors $\mathbf{A}^{p(0)}$ and $\mathbf{A}^{p(1)}$. Since we wish to evaluate the delay $c\tau_p$ as defined in Eq. (3.23), the evaluation of the normalization factor may become problematic,

$$c\tau_p \simeq \frac{q_p^{(0)} + \eta q_p^{(1)}}{1 + \mathcal{O}(\eta^2)} \quad . \tag{3.28}$$

This occurs because the delay $c\tau_p$ is defined through the eigenvalues and eigenvectors of the delay matrix, both being approximations here. Direct numerical computation of $c\tau_p$ by diagonalization of $\mathbf{Q}$ does not suffer from this problem as the eigenvectors are (to numerical precision) exactly normalized. In the following Section, we propose to use Eq. (3.24) to obtain the phase change $\theta^{(1)}(\epsilon)$ due to the perturbation of a mode main angular momentum channel. The time delay is then deduced from the rate of change of the full phase $-\theta(k;\,\epsilon) = -\theta^{(0)}(k) + \theta^{(1)}(k;\,\epsilon)$ with respect to k, $\theta^{(0)}$ being the homogeneous disc phase.

3.1.3 Phase perturbation and time delay

The eigenvalues and eigenvectors of the approximate delay matrix Eq. (3.25) are obtained from standard perturbation theory [36, 82]. For the matrix

$$\mathbf{Q} = \mathbf{Q}^{(0)} + \eta\mathbf{Q}^{(1)}$$

we expand, for a specific mode p, the eigenvalues and eigenvectors associated with an unperturbed angular momentum channel $m = m_0$ in a power series of η,

$$q_{m_0} = q_{m_0}^{(0)} + \eta q_{m_0}^{(1)} + \mathcal{O}(\eta^2) \tag{3.29}$$

$$\mathbf{A}^{m_0} = \mathbf{A}^{m_0(0)} + \eta \mathbf{A}^{m_0(1)} + \mathcal{O}(\eta^2) \quad . \tag{3.30}$$

Strictly speaking we should consider objects denoted like $\mathbf{A}^{p,m}$ for instance. To lighten the notation, we have removed the p index and will assume that we are concentrating our attention on a given characteristic mode p. Normalization of $\mathbf{A}^{m_0}$ reads

$$\mathbf{A}^{m_0\dagger}\mathbf{A}^{m_0} \equiv \mathbb{1} = \mathbb{1} + \eta \left(\mathbf{A}^{m_0(0)\dagger}\mathbf{A}^{m_0(1)} + \mathbf{A}^{m_0(1)\dagger}\mathbf{A}^{m_0(0)} \right) + \mathcal{O}(\eta^2) \; . \tag{3.31}$$

As for the unitarity of $\mathbf{S}$, we will verify later that the normalization is conserved up to second order. This means that $\mathbf{A}^{m_0(0)\dagger}\mathbf{A}^{m_0(1)}$ must be pure imaginary, or zero. Using Eqs (3.15) and (3.16), the same condition on normalization may be computed for the outgoing coefficients $\mathbf{B}^{m_0} = \mathbf{S}\mathbf{A}^{m_0}$.

Since the diagonal matrix $\mathbf{Q}^{(0)}$ states are at least twofold degenerate[1] in the angular momentum basis (*i.e.* $q_{+m_0}^{(0)} = q_{-m_0}^{(0)}$), we first have to find the appropriate combination of individual unperturbed angular channels so that two corrections $q_{m_{0a}}^{(1)}$ and $q_{m_{0b}}^{(1)}$ may be computed. This is done by solving the eigenproblem

$$\begin{pmatrix} Q_{+m_0,+m_0}^{(1)} & Q_{+m_0,-m_0}^{(1)} \\ Q_{+m_0,-m_0}^{(1)} & Q_{-m_0,-m_0}^{(1)} \end{pmatrix} \begin{pmatrix} c_+^{m_{0a,b}} \\ c_-^{m_{0a,b}} \end{pmatrix} = q_{m_{0a,b}}^{(1)} \begin{pmatrix} c_+^{m_{0a,b}} \\ c_-^{m_{0a,b}} \end{pmatrix} \quad . \tag{3.32}$$

Following Eq. (3.19), one verifies that $Q_{+m_0+m_0}^{(1)} = Q_{-m_0-m_0}^{(1)}$, and we can write

$$q_{m_{0a}}^{(1)} = Q_{m_0,m_0}^{(1)} + |Q_{+m_0,-m_0}^{(1)}| \tag{3.33}$$

$$q_{m_{0b}}^{(1)} = Q_{m_0,m_0}^{(1)} - |Q_{+m_0,-m_0}^{(1)}| \tag{3.34}$$

and the eigenvectors

$$\mathbf{c}^{m_{0a}} = \frac{1}{\sqrt{2}} \begin{pmatrix} +\mathrm{e}^{+i\chi_{m_0}} \\ +\mathrm{e}^{-i\chi_{m_0}} \end{pmatrix} \; , \quad \mathbf{c}^{m_{0b}} = \frac{1}{\sqrt{2}} \begin{pmatrix} +\mathrm{e}^{+i\chi_{m_0}} \\ -\mathrm{e}^{-i\chi_{m_0}} \end{pmatrix} \tag{3.35}$$

where $\mathrm{e}^{i2\chi_{m_0}} = Q_{+m_0,-m_0}^{(1)}/|Q_{+m_0,-m_0}^{(1)}|$. Therefore, the zeroth order incoming coefficients are

$$A_m^{m_{0a}(0)} = \frac{1}{\sqrt{2}}\mathrm{e}^{+i\chi_{m_0}}\,\delta_{+m_0,m} + \frac{1}{\sqrt{2}}\mathrm{e}^{-i\chi_{m_0}}\,\delta_{-m_0,m} \tag{3.36}$$

$$A_m^{m_{0b}(0)} = \frac{1}{\sqrt{2}}\mathrm{e}^{+i\chi_{m_0}}\,\delta_{+m_0,m} - \frac{1}{\sqrt{2}}\mathrm{e}^{-i\chi_{m_0}}\,\delta_{-m_0,m} \quad . \tag{3.37}$$

[1]There are also many accidental degeneracies in the unperturbed disc spectrum leading to multiples of 2 locally degenerate states. A interesting case of analytically trackable 4-fold degeneracy is found in the annular cavity where two different sets of angular momenta, say m_0 and $m_0{}'$, lift their twofold degeneracy into even and odd modes, and simultaneously their even-m_0 - even-$m_0{}'$ degeneracy. Details of this special case are given in Section 3.3.2.

The phase χ_{m_0} appears because the perturbation produces a symmetry breaking in the disc cavity. Therefore, it should only depend on geometric parameters, not on the wavenumber k,

$$\frac{\partial \chi_{m_0}}{\partial k} = 0 \quad . \tag{3.38}$$

Also of interest are the first order correction to the coefficient vectors,

$$A_m^{m_{0a}(1)} = \begin{cases} i\beta_{m_{0aa}} A_m^{m_{0a}(0)} + i\beta_{m_{0ab}} A_m^{m_{0b}(0)} & , \quad |m| = m_0 \\ \frac{1}{\sqrt{2}} \frac{Q^{(1)}_{m,+m_0} \mathrm{e}^{+i\chi_{m_0}} + Q^{(1)}_{m,-m_0} \mathrm{e}^{-i\chi_{m_0}}}{q^{(0)}_{m_0} - q^{(0)}_m} & , \quad |m| \neq m_0 \end{cases} \tag{3.39}$$

$$A_m^{m_{0b}(1)} = \begin{cases} i\beta_{m_{0ba}} A_m^{m_{0a}(0)} + i\beta_{m_{0bb}} A_m^{m_{0b}(0)} & , \quad |m| = m_0 \\ \frac{1}{\sqrt{2}} \frac{Q^{(1)}_{m,+m_0} \mathrm{e}^{+i\chi_{m_0}} - Q^{(1)}_{m,-m_0} \mathrm{e}^{-i\chi_{m_0}}}{q^{(0)}_{m_0} - q^{(0)}_m} & , \quad |m| \neq m_0 \end{cases} \quad . \tag{3.40}$$

These expressions may be summarized as a sum of coefficient vectors

$$\mathbf{A}^{m_{0a}(1)} = \bar{\mathbf{A}}^{m_{0a}(1)} + i\beta_{m_{0aa}} \mathbf{A}^{m_{0a}(0)} + i\beta_{m_{0ab}} \mathbf{A}^{m_{0b}(0)} \tag{3.41}$$

$$\mathbf{A}^{m_{0b}(1)} = \bar{\mathbf{A}}^{m_{0b}(1)} + i\beta_{m_{0ba}} \mathbf{A}^{m_{0a}(0)} + i\beta_{m_{0bb}} \mathbf{A}^{m_{0b}(0)} \tag{3.42}$$

where $\bar{\mathbf{A}}^{m_{0a,b}(1)}$ is a vector with no $|m| = m_0$ components (*i.e.* only the bottom lines in (3.39) and (3.40)). An immediate consequence of this is the orthogonality relation

$$\mathbf{A}^{m_{0a,b}(0)\dagger} \bar{\mathbf{A}}^{m_{0a,b}(1)} = 0 \quad . \tag{3.43}$$

With regards to Eq. (3.31), this expression demands that the factors β_{aa} and β_{bb} be real, or zero. This is where our development departs slightly from the usual *choice* of convention that $\mathbf{A}^{m_{0a,b}(0)\dagger} \mathbf{A}^{m_{0a,b}} \in \mathbb{R}$, hence forcing $\beta_{aa,bb}$ to be zero [36]. In our case, the incoming/outgoing coefficients need to satisfy Eq. (3.24). We seek a supplementary term $\theta^{(1)}$ in the complete phase factor θ that appears because of the perturbation. Using Eq. (3.15) and $\mathbf{A} = \mathbf{S}^\dagger \mathbf{B}$, we find

$$\begin{aligned} \mathbf{A}^{m_{0a,b}(0)} + \eta \mathbf{A}^{m_{0a,b}(1)} = \; & \eta^0 \left(\mathrm{e}^{-i\theta_{m_{0a,b}}} \mathbf{S}^{(0)\dagger} \mathbf{P} \mathbf{A}^{m_{0a,b}(0)*} \right) \\ & + \eta^1 \left(\mathrm{e}^{-i\theta_{m_{0a,b}}} \mathbf{S}^{(0)\dagger} \mathbf{P} \mathbf{A}^{m_{0a,b}(1)*} + \mathrm{e}^{-i\theta_{m_{0a,b}}} \mathbf{S}^{(1)\dagger} \mathbf{P} \mathbf{A}^{m_{0a,b}(0)*} \right) \\ & + \mathcal{O}(\eta^2) \; . \end{aligned} \tag{3.44}$$

Upon equating the coefficients of equal powers of η, we obtain

$$\eta^0 : \quad \mathbf{A}^{m_{0a,b}(0)} = \mathrm{e}^{-i\theta_{m_{0a,b}}} \mathbf{S}^{(0)\dagger} \mathbf{P} \mathbf{A}^{m_{0a,b}(0)*} \tag{3.45}$$

$$\eta^1 : \quad \mathbf{A}^{m_{0a,b}(1)} = \mathrm{e}^{-i\theta_{m_{0a,b}}} \mathbf{S}^{(0)\dagger} \mathbf{P} \mathbf{A}^{m_{0a,b}(1)*} + \mathrm{e}^{-i\theta_{m_{0a,b}}} \mathbf{S}^{(1)\dagger} \mathbf{P} \mathbf{A}^{m_{0a,b}(0)*} \quad . \tag{3.46}$$

The projection of $\mathbf{A}^{m_{0a,b}(0)\dagger}$ on these expressions yields the phase factor

$$\mathrm{e}^{-i\theta_{m_{0a,b}}} = \frac{1}{\mathbf{A}^{m_{0a,b}(0)\dagger} \mathbf{S}^{(0)\dagger} \mathbf{P} \mathbf{A}^{m_{0a,b}(0)*}} \tag{3.47}$$

and the $\beta_{m_{0aa,bb}}$ and $\beta_{m_{0ab,ba}}$ coefficients,

$$\beta_{m_{0aa,bb}} = -i\frac{1}{2}\mathrm{e}^{-i\theta_{m_{0a,b}}}\mathbf{A}^{m_{0a,b}(0)\dagger}\mathbf{S}^{(1)\dagger}\mathbf{P}\mathbf{A}^{m_{0a,b}(0)*} \tag{3.48}$$

$$\beta_{m_{0ab,ba}} = -i\frac{1}{2}\mathrm{e}^{-i\theta_{m_{0a,b}}}\mathbf{A}^{m_{0b,a}(0)\dagger}\mathbf{S}^{(1)\dagger}\mathbf{P}\mathbf{A}^{m_{0a,b}(0)*} \quad . \tag{3.49}$$

Note that the phase $\theta_{m_{0a,b}} \equiv \theta^{(0)}_{m_{0a,b}}$ is completely defined through the zeroth-order terms: it is therefore independent of η. Any *change of phase* $\theta^{(1)}_{m_{0a,b}}(k;\,\epsilon)$ due to the perturbation has to be found in the eigenvectors. But what is this change of phase? How can it be recognized amongst the many components of the eigenvectors?

We answer these questions by observing that the only tangible information that we have in this description of the interaction resides in the zeroth-order wave. It is then suitable to attribute $\theta^{(1)}_{m_{0a,b}}(k;\,\epsilon)$ to a phase change explicitly affecting the corresponding unperturbed state vector. Using the various perturbation developments for the $\mathbf{S}$ matrix and $\mathbf{A}^{m_{0a,b}}$ vectors, we collect all terms affecting the vector $\mathbf{B}^{m_{0a,b}(0)}$ on the left-hand side (LHS) of Eq. (3.24) and the vector $\mathbf{A}^{m_{0a,b}(0)}$ on its right-hand side (RHS),

$$\begin{aligned}(1+i\beta_{m_{0aa,bb}}\eta)\mathbf{B}^{m_{0a,b}(0)} + \eta\left(\mathbf{S}^{(0)}\bar{\mathbf{A}}^{m_{0a,b}(1)} + i\beta_{m_{0ab,ba}}\mathbf{B}^{m_{0b,a}(0)} + \mathbf{S}^{(1)}\mathbf{A}^{m_{0a,b}(0)}\right) + \ldots \\ = \mathrm{e}^{-i\theta^{(0)}_{m_{0a,b}}}(1-i\beta_{m_{0aa,bb}}\eta)\mathbf{P}\mathbf{A}^{m_{0a,b}(0)*} + \eta\mathrm{e}^{-i\theta^{(0)}_{m_{0a,b}}}\mathbf{P}\left(\bar{\mathbf{A}}^{m_{0a,b}(1)*} - i\beta_{m_{0ab,ba}}\mathbf{A}^{m_{0b,a}(0)*}\right) + \ldots\end{aligned} \tag{3.50}$$

We then extract and equate the main terms affecting *only* the zeroth-order mode of interest,

$$\mathbf{B}^{m_{0a,b}(0)} = \mathrm{e}^{-i\theta^{(0)}_{m_{0a,b}}}\left(\frac{1-i\eta\beta_{m_{0aa,bb}}}{1+i\eta\beta_{m_{0aa,bb}}}\right)\mathbf{P}\mathbf{A}^{m_{0a,b}(0)*} \quad . \tag{3.51}$$

We may write the phase change $\theta^{(1)}_{m_{0a,b}}$ as

$$\theta^{(1)}_{m_{0a,b}}(k;\,\epsilon) = -2\arctan\left(\eta\beta_{m_{0aa,bb}}\right) \tag{3.52}$$

so that the complete phase of the main zeroth-order channel is $-\theta^{(0)}_{m_{0a,b}} + \theta^{(1)}_{m_{0a,b}}$.

The time delay corresponding to this phase shift is the wavenumber derivative of the phase,

$$\frac{d}{dk}\left(-\theta^{(0)}_{m_{0a,b}} + \theta^{(1)}_{m_{0a,b}}\right) = -\frac{d\theta^{(0)}_{m_0}}{dk} - 2\left(\frac{\eta}{1+\left(\eta\beta_{m_{0aa,bb}}\right)^2}\right)\frac{d\beta_{m_{0aa,bb}}}{dk} \quad . \tag{3.53}$$

A few intermediate results are gathered in order to simplify Eqs (3.47)-(3.49) and Eq. (3.53):

$$\mathbf{S}^{(0)}\mathbf{A}^{m_{0a,b}(0)} = S^{(0)}_{m_0m_0}\mathbf{A}^{m_{0a,b}(0)} \tag{3.54}$$

$$\mathbf{P}\mathbf{A}^{m_{0a}(0)*} = +(-1)^{m_0}\mathbf{A}^{m_{0a}(0)} \tag{3.55}$$

$$\mathbf{P}\mathbf{A}^{m_{0b}(0)*} = -(-1)^{m_0}\mathbf{A}^{m_{0b}(0)} \tag{3.56}$$

The zeroth-order phase between incoming and outgoing waves become simply

$$\mathrm{e}^{-i\theta^{(0)}_{m_{0a}}} = +(-1)^{m_0} S^{(0)}_{m_0 m_0} \tag{3.57}$$

$$\mathrm{e}^{-i\theta^{(0)}_{m_{0b}}} = -(-1)^{m_0} S^{(0)}_{m_0 m_0} \quad . \tag{3.58}$$

These relations present the expected dependence on $\mathbf{S}^{(0)}$. Only a constant phase factor of π exists to differentiate the two modes. We easily find that the wavenumber differentiation of the phases $-\theta^{(0)}_{m_{0a,b}}$ yields the correct zeroth order time delay,

$$-\frac{d\theta^{(0)}_{m_{0a}}}{dk} = -\frac{d\theta^{(0)}_{m_{0b}}}{dk} = q^{(0)}_{m_0} = -i\left(\frac{1}{\bar{\Delta}_{m_0}}\frac{\partial\bar{\Delta}_{m_0}}{\partial k} - \frac{1}{\Delta_{m_0}}\frac{\partial\Delta_{m_0}}{\partial k}\right) \quad . \tag{3.59}$$

The coefficients $\beta_{m_{0aa,bb}}$ satisfying the incoming/outgoing symmetry relation to second order become

$$\beta_{m_{0aa,bb}} = -i\frac{1}{2} S^{(0)}_{m_0 m_0} \mathbf{A}^{m_{0a,b}(0)^\dagger} \mathbf{S}^{(1)\dagger} \mathbf{A}^{m_{0a,b}(0)} \quad . \tag{3.60}$$

Using Eqs. (3.26) and (3.38), and the definition of the eigenvalue $q^{(1)}_{m_{0a,b}}$ in the eigenproblem (3.32), we can show that the wavenumber derivative of Eq. (3.60) yields

$$\frac{d\beta_{m_{0aa,bb}}}{dk} = -\frac{1}{2}\mathbf{A}^{m_{0a,b}(0)\dagger}\mathbf{Q}^{(1)}\mathbf{A}^{m_{0a,b}(0)} = -\frac{1}{2}q^{(1)}_{m_{0a,b}} \quad . \tag{3.61}$$

Using this expression in (3.53), we obtain our final result

$$c\tau_{m_{0a,b}} \simeq \frac{d}{dk}\left(-\theta^{(0)}_{m_{0a,b}} + \theta^{(1)}_{m_{0a,b}}\right) = q^{(0)}_{m_0} + \frac{\eta q^{(1)}_{m_{0a,b}}}{1 + \left(\eta\beta_{m_{0aa,bb}}\right)^2} = \frac{q^{(0)}_{m_0} + \eta q^{(1)}_{m_{0a,b}} + \mathcal{O}(\eta^2)}{1 + \left(\eta\beta_{m_{0aa,bb}}\right)^2} \tag{3.62}$$

This equation should be compared with Eq. (3.28): the normalization factor is now known precisely and properly justified. Although the overall power is normalized up to order η^2, it is understood that the zeroth-order channel $\mathbf{A}^{m_{0a,b}(0)}$ will be increased in amplitude to compensate the losses to other angular momentum channels. This results in a forced normalization of the delay $c\tau_{m_{0a,b}}$ with respect to the zeroth- *and* first-order components of the incoming zeroth-order channel.

Before moving on to some illustrative examples, it is worthwhile to summarize a number of properties that have been taken for granted or assumed during the previous development. The precise verification of the following requirements - necessary for the formalism to stand on firm ground - will be the focus of the next two Sections:

1. Matrix $\mathbf{S}^{(1)}$ verifies unitarity of the $\mathbf{S}$ matrix, Eq. (3.16): $\mathbf{S}^{(0)\dagger}\mathbf{S}^{(1)} + \mathbf{S}^{(1)\dagger}\mathbf{S}^{(0)} = \mathbf{0}$; matrix $\mathbf{Q}^{(1)}$ is hermitian, Eq. (3.26),
2. Matrix $\mathbf{S}^{(1)}$ satisfies $S^{(1)}_{-m,-m'} = (-1)^{m'} S^{(1)}_{m',m}(-1)^m$, Eq. (3.19) and $Q^{(1)}_{+m_0,+m_0} = Q^{(1)}_{-m_0,-m_0}$,

3. Phase χ_{m_0} depends solely on the geometry of the cavity, Eq. (3.38),

4. Coefficients $\bar{\mathbf{A}}^{m_{0a,b}(1)}$ satisfy Eq. (3.46),

5. Coefficients $\beta_{m_{0aa,bb}}$, Eq. (3.60), are real.

These properties will be referred to as properties 1 through 5 in the remainder of this Chapter.

3.2 Two illustrative examples: Presentation

In order to provide some illustration and verification of the above-mentioned properties, we will consider examples where the perturbative approach should apply. The first one deals with a *direct deformation of the disc boundary*, while the second is the simplest case of an inhomogeneous cavity: an *homogeneous disc with a small circular inclusion*. We will show that the first correction to the scattering matrix, $\mathbf{S}^{(1)}$, has the exact same form in both cases. Since the knowledge of the scattering matrix is sufficient to deduce all other significant quantities, the properties found in the boundary deformation case apply immediately to the inclusion case.

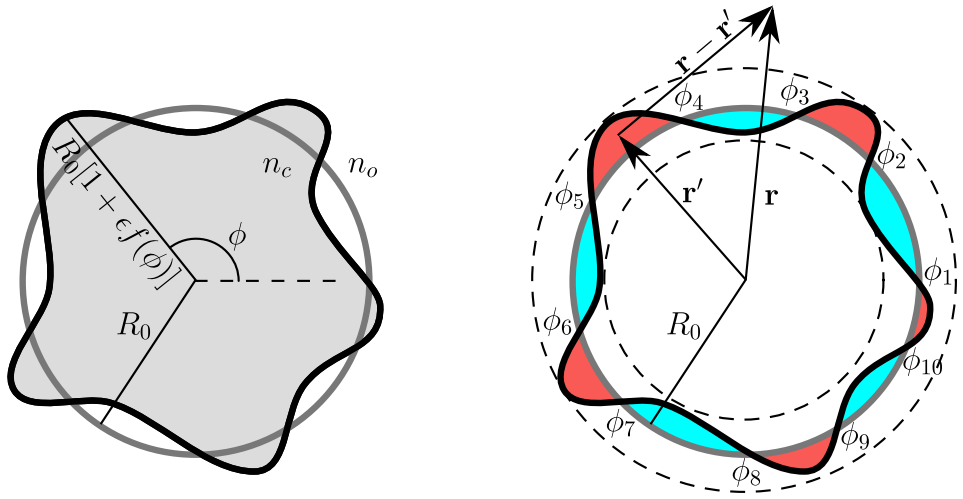
This Section serves to obtain the $\mathbf{S}^{(1)}$ matrix and to verify the properties 1 through 5 for the validity of the perturbation expansion on $\mathbf{S}$ and on the eigenmodes of the delay matrix. The physical interpretation of our results is delayed until the next Section.

3.2.1 Small amplitude boundary deformation

Consider the refractive index of a boundary-deformed homogeneous disc cavity, $n^2(\mathbf{r};\,\epsilon) = n^2_{(0)}(\mathbf{r}) + \eta\,\tilde{n}^2(\mathbf{r};\epsilon)$, where $n^2_{(0)}(\mathbf{r})$ is the disc cavity index distribution and

$$\tilde{n}^2(\mathbf{r};\epsilon) = (n_o^2 - n_c^2)\left[U\left(r - R_0[1+\epsilon f(\phi)]\right) - U\left(r - R_0\right)\right] \tag{3.63}$$

is the compensation index with $f(\phi)$, a periodic function, $f(\phi) = f(\phi + 2\pi)$, schematically pictured in Fig. 3.3(a). Separating the integral Eq. (3.12) into N interior and



(a) (b)

Fig. 3.3 (a) Schematic of a geometrically deformed disc cavity according to Eq. (3.63). (b) Separation of interior (blue areas) and exterior (red areas) contributions to the refractive index. The value of $|\mathbf{r}|$ is always larger than the maximum radius of the cavity $R_0(1+\epsilon\max_\phi\{f(\phi)\})$.

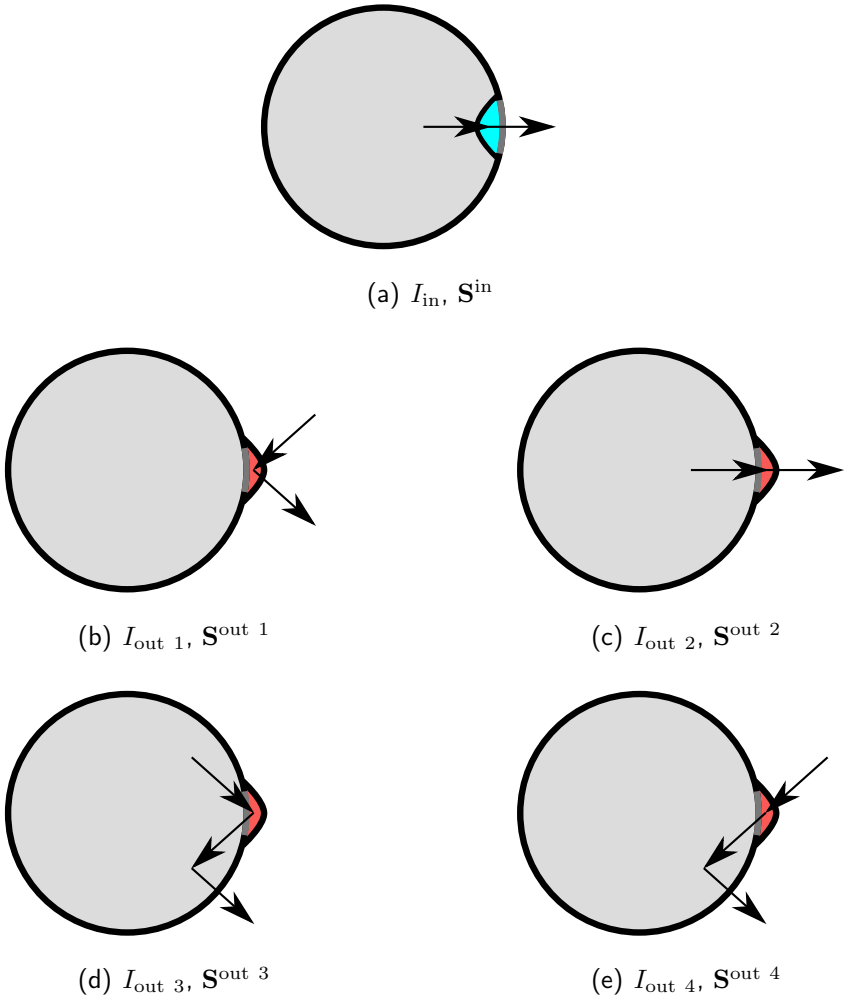
exterior contributions (see Fig. 3.3(b)), we obtain

$$\psi^{(1)}(\mathbf{r};\epsilon) = -k^2\left(n_o^2-n_c^2\right)\left[+\sum_{j=1,3,5,\ldots}^{N-1}\int_{\phi_j}^{\phi_{j+1}}d\phi'\int_{R_0+\epsilon R_0 f(\phi')}^{R_0}dr'\,G_{co}(\mathbf{r},\mathbf{r}')r'\psi^{(0)}(\mathbf{r}')\right.$$
$$\left.-\sum_{j=2,4,6,\ldots}^{N}\int_{\phi_j}^{\phi_{j+1}}d\phi'\int_{R_0}^{R_0+\epsilon R_0 f(\phi')}dr'\,G_{oo}(\mathbf{r},\mathbf{r}')r'\psi^{(0)}(\mathbf{r}')\right] \tag{3.64}$$

with $G_{co}(\mathbf{r},\mathbf{r}')$, the homogeneous disc Green function for a point source located *inside* the cavity at $\mathbf{r}'$ and the field being measured at $\mathbf{r}$ *outside* the cavity, and $G_{oo}(\mathbf{r},\mathbf{r}')$, the homogeneous disc Green function for a point source located *outside* the cavity at $\mathbf{r}'$ and the field being measured at $\mathbf{r}$ *outside* the cavity (see Appendix F). We demand periodicity of $f(\phi)$, $\phi_{N+1}=\phi_1$, and define ϕ_1 as the first angular position where $f(\phi)$ crosses $r=R_0$ with a negative slope (*i.e.* ϕ_1 marks the beginning of the first depression encountered from $\phi=0$).

Following the procedure developed in the preceding Section, we set $A_m=\delta_{mm'}$ in Eq. (3.6). Five distinct contributions to $\psi_m^{(1)}(\mathbf{r};\epsilon)$ are obtained, all of which involving radial integration of Bessel functions,

$$\psi_m^{(1)}(\mathbf{r};\epsilon) = k^2\left(n_o^2-n_c^2\right)\left[-\sum_{j=1,3,5,\ldots}^{N-1}I^j_{m\,\mathrm{in}}+\sum_{j=2,4,6,\ldots}^{N}\left(I^j_{m\,\mathrm{out}\,1}+I^j_{m\,\mathrm{out}\,2}+I^j_{m\,\mathrm{out}\,3}+I^j_{m\,\mathrm{out}\,4}\right)\right] \tag{3.65}$$



(a) $I_{\rm in}$, $\mathbf{S}^{\rm in}$

(b) $I_{\rm out\ 1}$, $\mathbf{S}^{\rm out\ 1}$

(c) $I_{\rm out\ 2}$, $\mathbf{S}^{\rm out\ 2}$

(d) $I_{\rm out\ 3}$, $\mathbf{S}^{\rm out\ 3}$

(e) $I_{\rm out\ 4}$, $\mathbf{S}^{\rm out\ 4}$

Fig. 3.4 Representation of the physical interpretation of the five contributions to the complete first-order scattering matrix: disc cavity in gray, deformed area in blue (concave deformation) and red (convex deformation). The outgoing wave (*leaving arrow* relative to the cavity) comes from a path involving only one interaction with the boundary deformation in each case. This is indicative of a first-order correction.

where

$$I^j_{m\,\rm in} = T^{(0)}_{mm}\sum_{m'} b_{cm'}H^{(1)}_{m'}(z_o)\mathrm{e}^{im'\phi}\int_{\phi_j}^{\phi_{j+1}}d\phi'\int_{R_0[1+\epsilon f(\phi')]}^{R_0} dr'\,r'J_{m'}(z'_c)J_m(z'_c)\mathrm{e}^{i(m-m')\phi'} \tag{3.66}$$

$$I^j_{m\,\rm out1} = \frac{1}{4i}\sum_{m'} H^{(1)}_{m'}(z_o)\mathrm{e}^{im'\phi}\int_{\phi_j}^{\phi_{j+1}}d\phi'\int_{R_0}^{R_0[1+\epsilon f(\phi')]} dr'\,r'J_{m'}(z'_o)H^{(2)}_m(z'_o)\mathrm{e}^{i(m-m')\phi'} \tag{3.67}$$

$$I^j_{m\,\rm out2} = \frac{1}{4i}S^{(0)}_{mm}\sum_{m'} H^{(1)}_{m'}(z_o)\mathrm{e}^{im'\phi}\int_{\phi_j}^{\phi_{j+1}}d\phi'\int_{R_0}^{R_0[1+\epsilon f(\phi')]} dr'\,r'J_{m'}(z'_o)H^{(1)}_m(z'_o)\mathrm{e}^{i(m-m')\phi'} \tag{3.68}$$

$$I^j_{m\,\rm out3} = S^{(0)}_{mm}\sum_{m'} b_{om'}H^{(1)}_{m'}(z_o)\mathrm{e}^{im'\phi}\int_{\phi_j}^{\phi_{j+1}}d\phi'\int_{R_0}^{R_0[1+\epsilon f(\phi')]} dr'\,r'H^{(1)}_{m'}(z'_o)H^{(1)}_m(z'_o)\mathrm{e}^{i(m-m')\phi'} \tag{3.69}$$

$$I^j_{m\,\rm out4} = \sum_{m'} b_{om'}H^{(1)}_{m'}(z_o)\mathrm{e}^{im'\phi}\int_{\phi_j}^{\phi_{j+1}}d\phi'\int_{R_0}^{R_0[1+\epsilon f(\phi')]} dr'\,r'H^{(1)}_{m'}(z'_o)H^{(2)}_m(z'_o)\mathrm{e}^{i(m-m')\phi'} \tag{3.70}$$

and $z_c' = n_c k r'$, $z_o = n_c k r$, and $z_o' = n_o k r'$. An interpretation of these contributions is shown on Fig. 3.4.

For $\epsilon \ll 1$, we expand the integrands of Eqs. (3.67)-(3.70) in power series around $r' = R_0$ and proceed with the integration of each term of the five contributions. All the integrals are expressible as

$$\int_{R_0}^{R_0[1+\epsilon f(\phi')]} dr'\ r' C_m(\lambda r') D_{m'}(\mu r') \ \simeq\ +\epsilon f(\phi') R_0^2 \left[C_m(\lambda R_0) D_{m'}(\mu R_0)\right] \tag{3.71}$$

$$\int_{R_0[1+\epsilon f(\phi')]}^{R_0} dr'\ r' C_m(\lambda r') D_{m'}(\mu r') \ \simeq\ -\epsilon f(\phi') R_0^2 \left[C_m(\lambda R_0) D_{m'}(\mu R_0)\right] \tag{3.72}$$

with $C_m(\cdot)$ and $D_m(\cdot)$ either $J_m(\cdot)$ or $H_m^{(1,2)}(\cdot)$ Bessel/Hankel functions. The individual angular contributions m due to input signal m' is highlighted, yielding the partial scattering matrices (the indices of Eqs. (3.66)-(3.70) are kept)

$$S_{mm'}^{\text{in}} = \epsilon \frac{4i}{\pi} \left(n_o^2 - n_c^2\right) \frac{J_m(Z_c)}{\Delta_m} \Phi_{mm'}^{\text{in}} \frac{J_{m'}(Z_c)}{\Delta_{m'}} \tag{3.73}$$

$$S_{mm'}^{\text{out}\,1} = \epsilon 2\pi \left(n_o^2 - n_c^2\right) k^2 R_0^2 \frac{1}{4i} H_m^{(2)}(Z_o) \Phi_{mm'}^{\text{out}} J_{m'}(Z_o) \tag{3.74}$$

$$S_{mm'}^{\text{out}\,2} = \epsilon 2\pi \left(n_o^2 - n_c^2\right) k^2 R_0^2 S_{mm}^{(0)} \frac{1}{4i} \Phi_{mm'}^{\text{out}} H_m^{(1)}(Z_o) J_{m'}(Z_o) \tag{3.75}$$

$$S_{mm'}^{\text{out}\,3} = \epsilon 2\pi \left(n_o^2 - n_c^2\right) k^2 R_0^2 S_{mm}^{(0)} H_m^{(1)}(Z_o) \Phi_{mm'}^{\text{out}} b_{om'} H_{m'}^{(1)}(Z_o) \tag{3.76}$$

$$S_{mm'}^{\text{out}\,4} = \epsilon 2\pi \left(n_o^2 - n_c^2\right) k^2 R_0^2 H_m^{(2)}(Z_o) \Phi_{mm'}^{\text{out}} b_{om'} H_{m'}^{(1)}(Z_o) \tag{3.77}$$

and

$$\Phi_{mm'}^{\text{in}} = \sum_{j=1,3,5,\ldots}^{N-1} \frac{1}{2\pi} \int_{\phi_j}^{\phi_{j+1}} d\phi'\ f(\phi') \mathrm{e}^{i(m-m')\phi'} \tag{3.78}$$

$$\Phi_{mm'}^{\text{out}} = \sum_{j=2,4,6,\ldots}^{N} \frac{1}{2\pi} \int_{\phi_j}^{\phi_{j+1}} d\phi'\ f(\phi') \mathrm{e}^{i(m-m')\phi'} \quad . \tag{3.79}$$

Substituting b_{cm}, b_{om}, $T_{mm}^{(0)}$ and $S_{mm}^{(0)}$ with their expression in terms of the different Bessel functions (see Appendix F), we find that the exterior components (3.74)-(3.77) complement the interior component (3.73) such that the complete first order correction to the scattering matrix $\mathbf{S}$ simply writes

$$S_{mm'}^{(1)} = \epsilon \frac{4i}{\pi} (n_o^2 - n_c^2) \frac{J_m(Z_c)}{\Delta_m} \Phi_{mm'} \frac{J_{m'}(Z_c)}{\Delta_{m'}} \tag{3.80}$$

with $\Phi_{mm'} = \Phi_{mm'}^{\text{in}} + \Phi_{mm'}^{\text{out}}$, a term in the Fourier series of $f(\phi)$,

$$\Phi_{mm'} = \frac{1}{2\pi} \int_0^{2\pi} d\phi'\ f(\phi') \mathrm{e}^{i(m-m')\phi'} \quad . \tag{3.81}$$

Since $f(\phi)$ is a real function, $\mathbf{\Phi}$ is hermitian ($\Phi_{mm'} = \Phi^*_{m'm}$). Also, we easily derive the symmetry relation $\Phi_{m,m'} = \Phi_{-m',-m}$. In view of Eq. (3.8), Eq. (3.80) is the expression of the product of two properly weighted fields having angular momentum m and m', evaluated at the boundary of the cavity, and coupled to each other through the deformation term $\Phi_{mm'}$.

Property 1. The property of the unitarity of $\mathbf{S}$ (up to second order) is verified by explicit calculation of $S^{(0)*}_{mm}S^{(1)}_{mm'}$ and $S^{(1)*}_{m'm}S^{(0)}_{m'm'}$ and by use of the hermiticity of $\mathbf{\Phi}$. This simultaneously checks the hermiticity of $\mathbf{Q}^{(1)}$. This property may also be verified by inspection of the elements of $\mathbf{Q}^{(1)}$,

$$\begin{aligned} Q^{(1)}_{mm'} &= \epsilon\frac{4}{\pi}(n_o^2-n_c^2)\frac{J_m(Z_c)}{\bar{\Delta}_m}\Phi_{mm'}\frac{J_{m'}(Z_c)}{\Delta_{m'}}\left[-n_cR_0\frac{J'_{m'}(Z_c)}{J_{m'}(Z_c)}+\frac{1}{\bar{\Delta}_{m'}}\frac{\partial\bar{\Delta}_{m'}}{\partial k}\right] \\ &\quad +\epsilon\frac{4}{\pi}(n_o^2-n_c^2)\left[-n_cR_0\frac{J'_m(Z_c)}{J_m(Z_c)}+\frac{1}{\Delta_m}\frac{\partial\Delta_m}{\partial k}\right]\frac{J_m(Z_c)}{\bar{\Delta}_m}\Phi_{mm'}\frac{J_{m'}(Z_c)}{\Delta_{m'}} \end{aligned} \quad (3.82)$$

Property 2. Using $J_{-m}(\cdot) = (-1)^m J_m(\cdot)$ and $\Phi_{m,m'} = \Phi_{-m',-m}$, we readily verify that $S^{(1)}_{-m,-m'} = (-1)^{m'}S^{(1)}_{m'm}(-1)^m$. Also the main diagonal of the scattering and delay matrices are seen to be symmetric with respect to the $S^{(1)}_{00}$ term: $S^{(1)}_{+m,+m} = S^{(1)}_{-m,-m}$, $Q^{(1)}_{+m,+m} = Q^{(1)}_{-m,-m}$.

Property 3. The perturbation treatment often demands the use of the 'corner' element $Q^{(1)}_{m_0,-m_0}$. In the case of the boundary deformation, we define

$$\mathcal{Q}^{(1)}_{m_0} = \epsilon\frac{4}{\pi}(n_o^2-n_c^2)\left|\frac{J_{m_0}(Z_c)}{\Delta_{m_0}}\right|^2\left[-2n_cR_0\frac{J'_{m_0}(Z_c)}{J_{m_0}(Z_c)}+\frac{1}{\Delta_{m_0}}\frac{\partial\Delta_{m_0}}{\partial k}+\frac{1}{\bar{\Delta}_{m_0}}\frac{\partial\bar{\Delta}_{m_0}}{\partial k}\right] \quad (3.83)$$

so that we may rewrite

$$Q^{(1)}_{m_0,-m_0} = (-1)^{m_0}\mathcal{Q}^{(1)}_{m_0}\Phi_{m_0,-m_0} \quad , \quad (3.84)$$

and further $Q^{(1)}_{m_0m_0} = \mathcal{Q}^{(1)}_{m_0}\Phi_{m_0,+m_0}$, so that the eigenproblem (3.32) simplifies to

$$\mathcal{Q}^{(1)}_{m_0}\begin{pmatrix}\Phi_{m_0,m_0} & (-1)^{m_0}\Phi_{m_0,-m_0}\\ (-1)^{m_0}\Phi^*_{m_0,-m_0} & \Phi_{m_0,m_0}\end{pmatrix}\begin{pmatrix}c_+^{m_{0a,b}}\\ c_-^{m_{0a,b}}\end{pmatrix} = q^{(1)}_{m_{0a,b}}\begin{pmatrix}c_+^{m_{0a,b}}\\ c_-^{m_{0a,b}}\end{pmatrix} \quad . \quad (3.85)$$

The eigenvalues are found to follow Eqs. (3.33)-(3.34),

$$\begin{aligned} q^{(1)}_{m_{0a}} &= \mathcal{Q}^{(1)}_{m_0}\left(\Phi_{m_0,m_0}+|\Phi_{m_0,-m_0}|\right) & (3.86)\\ q^{(1)}_{m_{0b}} &= \mathcal{Q}^{(1)}_{m_0}\left(\Phi_{m_0,m_0}-|\Phi_{m_0,-m_0}|\right) & (3.87)\end{aligned}$$

and the eigenvector phase $\exp(i2\chi_{m_0})$ reads

$$\mathrm{e}^{i2\chi_{m_0}} = \mathrm{e}^{im_0\pi}\frac{\Phi_{m_0,-m_0}}{|\Phi_{m_0,-m_0}|} \quad . \quad (3.88)$$

As expected, the phase χ_{m_0} is found to solely depend on the geometrical factors embodied by the boundary Fourier series term $\Phi_{m_0,-m_0}$.

Property 4. The verification of this property is somewhat more involved. Since the $\beta_{m_{0aa,bb}}$ coefficients are computed from Eq. (3.46), they automatically satisfy the reciprocity property. Then, the expression that needs to be verified is

$$\bar{\mathbf{A}}^{m_{0a,b}} \stackrel{!}{=} \mathrm{e}^{-i\theta_{m_{0a,b}}} \left[\mathbf{S}^{(0)\dagger}\mathbf{P}\bar{\mathbf{A}}^{m_{0a,b}*} + \mathbf{S}^{(1)\dagger}\mathbf{P}\mathbf{A}^{m_{0a,b}(0)*}\right] \quad . \tag{3.89}$$

For the sake of simplicity, only the calculational details of mode a are shown, mode b follows exactly the same procedure.

In the previous Section, it was shown that

$$\bar{A}_m^{m_{0a}(1)} = \frac{1}{\sqrt{2}} \frac{Q^{(1)}_{m,+m_0}\mathrm{e}^{+i\chi_{m_0}} + Q^{(1)}_{m,-m_0}\mathrm{e}^{-i\chi_{m_0}}}{q^{(0)}_{m_0} - q^{(0)}_m} \; , |m| \neq m_0 \tag{3.90}$$

$$A_m^{m_{0a}(0)} = \frac{1}{\sqrt{2}}\mathrm{e}^{+i\chi_{m_0}}\,\delta_{m,+m_0} + \frac{1}{\sqrt{2}}\mathrm{e}^{-i\chi_{m_0}}\,\delta_{m,-m_0} \tag{3.91}$$

where $Q^{(1)}_{m,\pm m_0}$is defined by Eq. (3.82), and

$$q^{(0)}_m = -i\left(\frac{1}{\bar{\Delta}_m}\frac{\partial\bar{\Delta}_m}{\partial k} - \frac{1}{\Delta_m}\frac{\partial\Delta_m}{\partial k}\right) \quad . \tag{3.92}$$

The vector element m from the RHS of (3.89) has the following contributions

$$\left\{\mathbf{S}^{(0)\dagger}\mathbf{P}\bar{\mathbf{A}}^{m_{0a}(1)*}\right\}_m = (-1)^m S^{(0)*}_{mm}\bar{A}^{m_{0a}(1)*}_{-m} \tag{3.93}$$

$$\left\{\mathbf{S}^{(1)\dagger}\mathbf{P}\bar{\mathbf{A}}^{m_{0a}(0)*}\right\}_m = \frac{(-1)^{m_0}}{\sqrt{2}}\left[S^{(1)*}_{-m_0m}\mathrm{e}^{-i\chi_{m_0}} + S^{(1)*}_{+m_0m}\mathrm{e}^{+i\chi_{m_0}}\right] \quad . \tag{3.94}$$

so that complete expression becomes

$$\begin{aligned}\{\text{RHS (3.89)}\}_m = \; & \mathrm{e}^{-i\theta_{m_{0a}}}\frac{1}{\sqrt{2}}\frac{1}{q^{(0)}_{m_0} - q^{(0)}_m} \times \\ & \Big[\;\left((-1)^m S^{(0)*}_{mm}Q^{(1)*}_{-m,+m_0} + (-1)^{m_0}(q^{(0)}_{m_0} - q^{(0)}_m)S^{(1)*}_{-m_0,m}\right)\mathrm{e}^{-i\chi_{m_0}} \\ & + \left((-1)^m S^{(0)*}_{mm}Q^{(1)*}_{-m,-m_0} + (-1)^{m_0}(q^{(0)}_{m_0} - q^{(0)}_m)S^{(1)*}_{+m_0,m}\right)\mathrm{e}^{+i\chi_{m_0}}\Big] \; .\end{aligned} \tag{3.95}$$

Since the second member of the bracket is obtained through the change of sign $-m_0 \leftrightarrow +m_0$ ($q^{(0)}_+ = q^{(0)}_-$ and $S^{(0)}_{+m,+m} = S^{(0)}_{-m,-m}$), only the calculation for the first member is carried out. Beginning with the first term, $(-1)^m S^{(0)*}_{mm}Q^{(1)*}_{-m,+m_0}$, we easily determine, by use of symmetry relations of $\Phi_{mm'}$ and the negative order relations for Bessel functions

(Appendix A), that

$$
\begin{aligned}
(-1)^m S^{(0)*}_{mm} Q^{(1)*}_{-m,+m_0} &= \left(S^{(0)*}_{m_0m_0} S^{(0)}_{m_0m_0}\right)(-1)^m S^{(0)*}_{mm} Q^{(1)*}_{-m,+m_0} \\
&= +\epsilon(-1)^{m_0} S^{(0)*}_{m_0m_0} \frac{4}{\pi}(n_o^2 - n_c^2) \times \\
&\quad \left[\frac{J_m(Z_c)}{\bar{\Delta}_m} \Phi_{m,-m_0} \frac{J_{-m_0}(Z_c)}{\Delta_{m_0}} \left(-n_c R_0 \frac{J'_{m_0}(Z_c)}{J_{m_0}(Z_c)} + \frac{1}{\Delta_{m_0}} \frac{\partial \Delta_{m_0}}{\partial k} \right) \right. \\
&\quad \left. + \left(-n_c R_0 \frac{J'_m(Z_c)}{J_m(Z_c)} + \frac{1}{\bar{\Delta}_m} \frac{\partial \bar{\Delta}_m}{\partial k} \right) \frac{J_m(Z_c)}{\bar{\Delta}_m} \Phi_{m,-m_0} \frac{J_{-m_0}(Z_c)}{\Delta_{m_0}} \right] .
\end{aligned}
\tag{3.96}
$$

The second term, $(-1)^m(q^{(0)}_{m_0} - q^{(0)}_m)S^{(1)*}_{-m_0,m}$, is treated in a similar fashion,

$$
\begin{aligned}
(-1)^m(q^{(0)}_{m_0} - q^{(0)}_m)S^{(1)*}_{-m_0,m} &= \left(S^{(0)*}_{m_0m_0} S^{(0)}_{m_0m_0}\right)(-1)^m(q^{(0)}_{m_0} - q^{(0)}_m)S^{(1)*}_{-m_0,m} \\
&= \epsilon(-1)^{m_0} S^{(0)*}_{m_0m_0} \frac{4}{\pi}(n_o^2 - n_c^2) \times \\
&\quad \left[\frac{J_m(Z_c)}{\bar{\Delta}_m} \Phi_{m,-m_0} \frac{J_{-m_0}(Z_c)}{\Delta_{m_0}} \left(\frac{1}{\bar{\Delta}_{m_0}} \frac{\partial \bar{\Delta}_{m_0}}{\partial k} - \frac{1}{\Delta_{m_0}} \frac{\partial \Delta_{m_0}}{\partial k} \right) \right. \\
&\quad \left. - \left(\frac{1}{\bar{\Delta}_m} \frac{\partial \bar{\Delta}_m}{\partial k} - \frac{1}{\Delta_m} \frac{\partial \Delta_m}{\partial k} \right) \frac{J_m(Z_c)}{\bar{\Delta}_m} \Phi_{m,-m_0} \frac{J_{-m_0}(Z_c)}{\Delta_{m_0}} \right] .
\end{aligned}
\tag{3.97}
$$

Combining Eqs. (3.96)-(3.97), we see that the terms $\Delta^{-1}_{m_0}\,\partial\Delta_{m_0}/\partial k$ and $\bar{\Delta}^{-1}_m\,\partial\bar{\Delta}_m/\partial k$ cancel in pairs. Then, the first member of the RHS of Eq. (3.89) becomes

$$
(-1)^m S^{(0)*}_{mm} Q^{(1)*}_{-m,+m_0} + (-1)^{m_0}(q^{(0)}_{m_0} - q^{(0)}_m)S^{(1)*}_{-m_0,m} = (-1)^{m_0} S^{(0)*}_{m_0m_0} Q^{(1)}_{m,-m_0} \quad . \tag{3.98}
$$

As for the second member of Eq. (3.89), we find similarly

$$
(-1)^m S^{(0)*}_{mm} Q^{(1)*}_{-m,-m_0} + (-1)^{m_0}(q^{(0)}_{m_0} - q^{(0)}_m)S^{(1)*}_{+m_0,m} = (-1)^{m_0} S^{(0)*}_{m_0m_0} Q^{(1)}_{m,+m_0} \quad . \tag{3.99}
$$

Using the expression of $\mathrm{e}^{-i\theta_{m_0a}}$ found at Eq. (3.57) and replacing back expressions (3.98) and (3.99) into Eq. (3.89), we finally obtain

$$
\{\text{RHS (3.89)}\}_m = \frac{1}{\sqrt{2}} \frac{Q^{(1)}_{m,+m_0}\mathrm{e}^{+i\chi_{m_0}} + Q^{(1)}_{m,-m_0}\mathrm{e}^{-i\chi_{m_0}}}{q^{(0)}_{m_0} - q^{(0)}_m} = \bar{A}^{m_{0a}(1)}_m \quad . \tag{3.100}
$$

This verifies property 4 for mode a and by the same procedure for mode b.

Property 5. The coefficients $\beta_{m_{0aa,bb}}$, Eq. (3.60), are computed directly with the expressions of $S^{(1)}_{mm'}$, Eq. (3.80), the vectors $\mathbf{A}^{m_{0a,b}(0)}$, Eqs. (3.36)-(3.37), and Eq. (3.87),

$$
\beta_{m_{0aa}} = \epsilon\frac{2}{\pi}(n_o^2 - n_c^2)\left|\frac{J_{m_0}(Z_c)}{\Delta_{m_0}}\right|^2 (\Phi_{m_0m_0} + |\Phi_{m_0,-m_0}|) \tag{3.101}
$$

$$
\beta_{m_{0bb}} = \epsilon\frac{2}{\pi}(n_o^2 - n_c^2)\left|\frac{J_{m_0}(Z_c)}{\Delta_{m_0}}\right|^2 (\Phi_{m_0m_0} - |\Phi_{m_0,-m_0}|) \quad . \tag{3.102}
$$

Because $\Phi_{m_0 m_0}$ is a real number, we conclude that $\beta_{m_{0aa,bb}}$ are also real, hence fulfilling property 5.

3.2.2 Small circular inclusion

A second interesting application of the perturbation method is the addition of a (minute) circular inclusion inside the cavity. This is our well-known *annular cavity* (Chapter 2 and Appendix D), except that here the radius of the inclusion is perturbatively small. The system consists in a homogeneous disc cavity having a circular inclusion of radius ϵR_0 and index n_h located at a distance d along the Ox axis from the geometrical center of the cavity. In the inclusion's own coordinates (ρ, θ), the compensation index Eq. (3.1) takes the form

$$\tilde{n}^2(\rho, \theta; \epsilon) = \left(n_h^2 - n_c^2\right) U(\epsilon R_0 - \rho) \quad . \tag{3.103}$$

The complete system is represented schematically in Fig. (3.5).

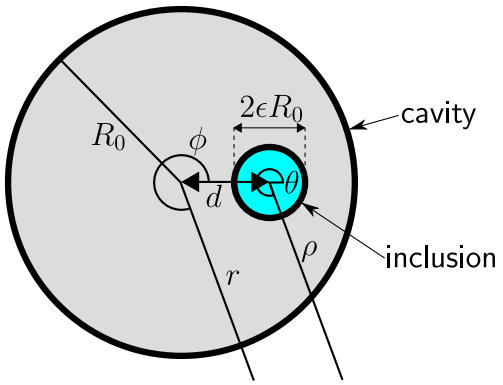


Fig. 3.5 Schematics of the cavity and inclusion system. The natural coordinates for the cavity (r, ϕ) and inclusion (ρ, θ) are shown, along with parameters d and ϵ. The refractive index inside the inclusion is n_h, while the index of the cavity and outside media are respectively n_c and n_o.

In view of Eq. (3.12), the proper Green function to use here is $G_{co}(\mathbf{r}, \mathbf{r}')$,

$$G_{co}(\mathbf{r}, \mathbf{r}') = \sum_{m'} b_{cm'} J_{m'}(z_c') \mathrm{e}^{-im'\phi'} H_{m'}^{(1)}(z_o) \mathrm{e}^{im'\phi} \quad , \tag{3.104}$$

and the unperturbed wavefunction $\psi^{(0)}(\mathbf{r}')$ has the form

$$\psi_m^{(0)}(\mathbf{r}') = T_{mm}^{(0)} J_m(z_c') \mathrm{e}^{im\phi'} \quad . \tag{3.105}$$

Using Graf's displacement theorem (see Appendix A), the reference frame is relocated on the inclusion coordinates (ρ, θ) so that we may write Eq. (3.12) as

$$\psi_m^{(1)}(\mathbf{r}; \epsilon) = k^2 \left(n_c^2 - n_h^2\right) \int_0^{\epsilon R_0} d\rho\, \rho \int_0^{2\pi} d\theta\, G_{co}(\mathbf{r}, \mathbf{r}'(\rho, \theta)) \psi_m^{(0)}(\mathbf{r}'(\rho, \theta)) \tag{3.106}$$

with

$$G_{co}(\mathbf{r},\mathbf{r}')\psi_m^{(0)}(\mathbf{r}') = T_{mm}^{(0)}\sum_{m',j,j'} b_{cm'}(-1)^{m'}\left[J_{m+j}(n_c kd)J_{-m'-j'}(n_c kd)\right] \times\left[J_{-j}(\zeta_c)J_{j'}(\zeta_c)\mathrm{e}^{i(j'-j)\theta}\right]H_{m'}^{(1)}(z_o)\mathrm{e}^{im'\phi} \quad (3.107)$$

and $\zeta_{o,c} = n_{o,c}k\rho$. Integration over θ in Eq. (3.106) simplifies the expression for $\psi_m^{(1)}(\mathbf{r};\epsilon)$,

$$\psi_m^{(1)}(\mathbf{r};\epsilon) = 2\pi\left(n_c^2-n_h^2\right)T_{mm}^{(0)}\sum_{m',j} b_{cm'}H_{m'}^{(1)}(z_o)\mathrm{e}^{im'\phi}\left[J_{m+j}(n_c kd)J_{m'+j'}(n_c kd)\right] \times\int_0^{\epsilon R_0} d\rho\,\rho\left[J_j(\zeta_c)\right]^2 \quad . \quad (3.108)$$

The integration range over the ρ coordinate scales with $\epsilon \ll 1$. It is then justified to expand the integrand near the origin (see Appendix A),

$$\left[J_j(\zeta_c)\right]^2 = \left[J_{|j|}(\zeta_c)\right]^2 = \frac{\left(\frac{1}{2}\zeta_c\right)^{2|j|}}{(|j|!)^2}\left[1-2\frac{\left(\frac{1}{2}\zeta_c\right)^2}{(|j|+1)}+\mathcal{O}\left(\zeta_c^4\right)\right] \quad . \quad (3.109)$$

Using this expansion, the integral in Eq. (3.108) is evaluated term by term,

$$\int_0^{\epsilon R_0} d\rho\;\rho\left[J_j(\zeta_c)\right]^2 = \epsilon^{2|j|+2}\left(\frac{1}{2}\right)^{2|j|}\frac{R_0^2 Z_c^{2|j|}}{2(|j|+1)(|j|!)^2}\left[1-\epsilon^2\frac{2}{|j|+2}\left(\frac{1}{2}Z_c\right)^2+\mathcal{O}(\epsilon^4)\right] . \quad (3.110)$$

For $\epsilon^2\left(\frac{1}{2}Z_c\right)^2 \ll 1$, only the first term of the preceding series is relevant. Also, integrals with orders $|j| > 0$ rapidly become negligible with respect to the zeroth order term [2]. Setting $j = 0$ in Eq. (3.108), the approximate first correction to the wavefunction outside the cavity, Eq (3.12), is

$$\psi_m^{(1)}(\mathbf{r};\epsilon) = \epsilon^2\pi k^2 R_0^2\left(n_c^2-n_h^2\right)\sum_{m'}\left\{T_{mm}^{(0)}J_m(n_c kd)J_{m'}(n_c kd)b_{cm'}\right\}H_{m'}^{(1)}(n_o kr)\mathrm{e}^{im'\phi} \quad (3.112)$$

or with proper substitution of the expressions for $T_{mm}^{(0)}$ and $b_{cm'}$,

$$\psi_m^{(1)}(\mathbf{r};\,\epsilon) = \epsilon^2\sum_{m'} S_{mm'}^{(1)}H_{m'}^{(1)}(n_o kr)\mathrm{e}^{im'\phi} \quad (3.113)$$

where the first correction term to the scattering matrix is

$$S_{mm'}^{(1)} = \epsilon^2\frac{i2}{\pi}\left(n_c^2-n_h^2\right)\frac{J_m(n_c kd)}{\Delta_m}\frac{J_{m'}(n_c kd)}{\Delta_{m'}} \quad . \quad (3.114)$$

[2] The J_0 Bessel function is the only one being non-zero at the origin. For $j = 0$, we have

$$\int_0^{\epsilon R_0} d\rho\,\rho\left[J_0(\zeta_c)\right]^2 \simeq \epsilon^2\frac{1}{2}R_0^2 \quad . \quad (3.111)$$

This last expression is closely related to its small boundary deformation counterpart, Eq. (3.80), the differences being a constant factor and $\Phi_{mm'} = 1$. We conclude that the circular inclusion cavity inherits all the properties derived for the boundary deformation case. We state here only the first order delay matrix $\mathbf{Q}^{(1)}$,

$$\begin{aligned} Q^{(1)}_{mm'} &= \epsilon^2 \frac{2}{\pi}(n_c^2 - n_h^2) \frac{J_m(n_c kd)}{\bar{\Delta}_m} \frac{J_{m'}(n_c kd)}{\Delta_{m'}} \left[-n_c d \frac{J'_{m'}(n_c kd)}{J_{m'}(n_c kd)} + \frac{1}{\bar{\Delta}_{m'}} \frac{\partial \bar{\Delta}_{m'}}{\partial k} \right] \\ &\quad + \epsilon^2 \frac{2}{\pi}(n_c^2 - n_h^2) \left[-n_c d \frac{J'_m(n_c kd)}{J_m(n_c kd)} + \frac{1}{\Delta_m} \frac{\partial \Delta_m}{\partial k} \right] \frac{J_m(n_c kd)}{\bar{\Delta}_m} \frac{J_{m'}(n_c kd)}{\Delta_{m'}} \end{aligned} \tag{3.115}$$

and $\beta_{m_0 aa,bb}$ coefficients

$$\beta_{m_0 aa} = \epsilon^2 \frac{2}{\pi} \left(n_c^2 - n_h^2\right) \left| \frac{J_{m_0}(n_c kd)}{\Delta_{m_0}} \right|^2 \tag{3.116}$$

$$\beta_{m_0 bb} = 0 \quad . \tag{3.117}$$

3.2.3 Perspectives for other systems

A similar procedure may be undertaken for a circular *exclusion*: a small circular object located outside the cavity. In this case however, the Green function to consider is $G_{oo}(\mathbf{r}, \mathbf{r}')$, and the zeroth-order wavefunction is composed of both incoming and outgoing components, which results in four different contributions to the complete first order scattering matrix $\mathbf{S}^{(1)}$. This is closely related to the description of the perturbed boundary cavity, see Figs. 3.4(b) through 3.4(e), only with the perturbation being located away from the disc boundary. The result however does not simplify as nicely as the cases studied so far. This scenario is especially suited for the analytical study of the detection of small biological entities [2, 125, 133].

One can also consider a small non-circular inclusion/exclusion which would add a form factor depending on the mean radius of the dielectric perturbation. The *a priori* knowledge of the end result for the disc inclusion/exclusion would allow to immediately set $j = j' = 0$ in Eq. (3.107), and to carry out a 2D integration in Eq. (3.106) with the small argument approximation on $J_0(\zeta_c)$.

This method is not bound to single inclusion/exclusion: we could consider the effect of multiple non-interacting obstacles on the scattering matrix. Finally, note that the refractive index of the inclusion/exclusion can be set to a complex number to model absorption or emission phenomena.

3.3 Two illustrative examples: Further analysis and numerical results

In this final Section, we present some further general analytical properties of the scattering and delay matrices derived in the previous Sections. We first extract a qualitative picture of the $\mathbf{S}^{(1)}$ matrix by exploiting the asymptotic forms for the Bessel functions. Among other things, we identify a transition probability *ridge* connecting high angular momentum components to the innermost angular momenta region. Outside this region, the off-diagonal terms of the scattering and delay matrices decrease exponentially. This observation enforces the use of an amplitude cut-off for pathological terms in the numerical evaluation of the $\mathbf{S}$ matrix (Chapter 2).

We also analyze in more detail the characteristic modes obtained from perturbation theory with emphasis on the near resonance behaviour. The results indicate that the ridge found in the scattering matrix has a dramatic effect on the far-field properties of the wavefunction. These properties provide useful insights for the study to be undertaken in Chapter 4.

Finally, we propose an answer to a theoretical question: is it possible to recreate, through a boundary deformation of the disc cavity, the effect of an index deformation of the homogeneous disc?

3.3.1 Global behaviour of the scattering matrix

The first order correction to the scattering matrix found in the two illustrative examples possess the same dependence upon the product of factors $\Delta_m \Delta_{m'}$. This term proves to determine the behaviour of the off-diagonal elements of the scattering matrix. The analysis provides further evidence for the optimal truncation size of the relevant matrices and justifies the use of a small amplitude cutoff to avoid numerical errors (see Chapter 2).

The critical term to analyze is the Δ_m function, Eq. (3.10). Because it is defined through Bessel and Hankel functions, Δ_m will inherit their evanescent and/or oscillating features. The relative size of the argument versus order of the cylindrical functions determine their behaviours (see Appendix A). Three particular regimes can be identified

[3]:

- $0 < m < Z_c$ and $0 < m < Z_o$

$$\Delta_m \simeq -\frac{2}{\pi}\frac{1}{\sqrt{Z_c Z_o}}\mathrm{e}^{i\Theta_m^o}\left[n_c\left(\frac{1-(m/Z_c)^2}{1-(m/Z_o)^2}\right)^{1/4}\sin\Theta_m^c + in_o\left(\frac{1-(m/Z_o)^2}{1-(m/Z_c)^2}\right)^{1/4}\cos\Theta_m^c\right] \tag{3.118}$$

- $0 < m < Z_c$ and $\quad m > Z_o$

$$\begin{aligned}\Delta_m \;\simeq\; -\frac{1}{\pi}\sqrt{\frac{2}{Z_c}}\Bigg[\;&\frac{n_c}{\sqrt{m}}\left(\frac{1}{\sqrt{2}}\mathrm{e}^{-\Lambda_m^o} - i\sqrt{2}\mathrm{e}^{+\Lambda_m^o}\right)\left(\frac{1-(m/Z_c)^2}{1-(Z_o/m)^2}\right)^{1/4}\sin\Theta_m^c \\ &+\frac{n_o\sqrt{m}}{Z_o}\left(\frac{1}{\sqrt{2}}\mathrm{e}^{-\Lambda_m^o} + i\sqrt{2}\mathrm{e}^{+\Lambda_m^o}\right)\left(\frac{1-(Z_o/m)^2}{1-(m/Z_c)^2}\right)^{1/4}\cos\Theta_m^c\Bigg]\end{aligned} \tag{3.119}$$

- $\quad m > Z_c$ and $\quad m > Z_o$

$$\begin{aligned}\Delta_m \;\simeq\; \frac{1}{\sqrt{2}\pi}\mathrm{e}^{-\Lambda_m^c}\Bigg[\;&\frac{n_c}{Z_c}\left(\frac{1}{\sqrt{2}}\mathrm{e}^{-\Lambda_m^o} - i\sqrt{2}\mathrm{e}^{+\Lambda_m^o}\right)\left(\frac{1-(Z_c/m)^2}{1-(Z_o/m)^2}\right)^{1/4} \\ &-\frac{n_o}{Z_o}\left(\frac{1}{\sqrt{2}}\mathrm{e}^{-\Lambda_m^o} + i\sqrt{2}\mathrm{e}^{+\Lambda_m^o}\right)\left(\frac{1-(Z_o/m)^2}{1-(Z_c/m)^2}\right)^{1/4}\Bigg]\end{aligned} \tag{3.120}$$

In these expressions, $Z_c = n_c kR_0 > Z_o = n_o kR_0$, and $\Lambda_m^{o,c} = \Lambda_m(Z_{o,c})$ and $\Theta_m^{o,c} = \Theta_m(Z_{o,c})$ (see Appendix A for the exact expressions). The transient regime between oscillatory and evanescent behaviour is not considered here because it would add cumbersome expressions for a range of angular momenta that remains narrow for any reasonable value of kR_0. Therefore, the regimes having $Z_{o,c} - Z_{o,c}^{-1/3} < m < Z_{o,c} + Z_{o,c}^{-1/3}$ are ignored, and the transition between oscillatory and evanescent behaviours are assumed to happen sharply at $m = Z_c$ and $m = Z_o$.

- *First regime*: because of the trigonometric oscillating terms in Eq. (3.118), we may find combinations of m and k (through Z_o and Z_c) minimizing the overall value of Δ_m. The effect with regards to the delay matrices Eqs. (3.82) and

[3] We consider here that $m > 0$. However, using Eqs. (A.4)-(A.7) we show that $\Delta_{-m} = \Delta_m$, so that Eqs. (3.118)-(3.120) also apply to negative orders. For any realistic value of kR_0, the case $m = 0$ is such that the different cylindrical functions behave in the far-field as oscillating functions. This restricts Δ_0 to the first regime.

(3.115) is an increase in the magnitude of the corresponding element, indicating a neighboring resonance. The overall m dependence in this regime reads

$$|\Delta_m| \propto \frac{1}{(Z_o^2 - m^2)^{1/4}(Z_c^2 - m^2)^{1/4}} \quad . \tag{3.121}$$

- *Second regime*: the expression for the intermediate angular momentum domain, Eq. (3.119), is similar to the preceding one, Eq. (3.118). However, the overall envelope in this intermediate regime for Δ_m is an increasing exponential,

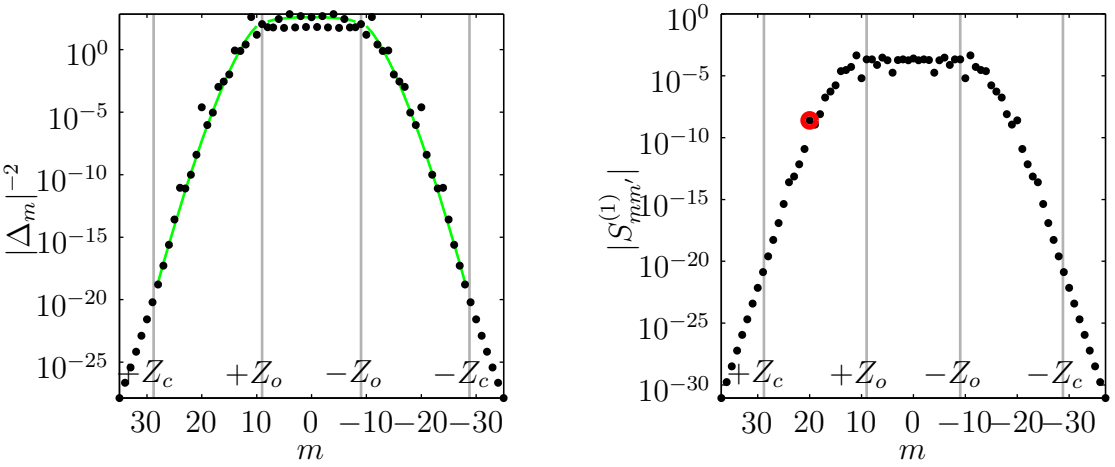
$$|\Delta_m| \propto \mathrm{e}^{+\Lambda_m^o} \quad . \tag{3.122}$$

- *Third regime*: according to the fact that $\Lambda_m^c < \Lambda_m^o$ (Appendix A), the dominant factor in the third region, $|m| > Z_c$, shows Δ_m as an exponentially, but monotonically, increasing function of m. There are then no resonances in this semi-infinite range.

An example of evaluation of Δ_m is illustrated in Fig. 3.6. We also display in Fig. 3.7(a) the predicted overall appearance of $\Delta_m^{-1}\Delta_{m'}^{-1}$ according to Eqs. (3.120) and (3.121), and the corresponding exact evaluation on Fig. 3.7(b). Note the *ridge* structures where the evaluation of $\Delta_m^{-1}\Delta_{m'}^{-1}$ rises, then drops exponentially along a single line or column (see Fig. 3.6(b)). These structures have direct consequences on the scattering features for modes having a dominant angular momentum component $|m| = m_0 > Z_o$: these modes are more likely to escape through low angular momentum components than neighboring high angular momentum ones.

These results may be interpreted through the semi-classical picture of the cavity system, where Z_o and Z_c hold respectively for the total internal reflection (TIR) limit and the 'real rays' limit (see Chapter 1). This is readily seen from the expression of the semiclassical momentum for the disc cavity, $p = m/Z_c$, and letting $m = Z_o$ (TIR limit), or $m = Z_c$ (real rays limit). Above the real rays limit exist evanescent fields ('imaginary' rays). In view of this interpretation, resonant modes with angular momentum $|m| < Z_o$ are then less confined inside the cavity than those with $Z_o < |m| < Z_c$.

The $J_m(Z)\Phi_{mm'}J_{m'}(Z)$ terms appearing in the scattering and delay matrices embody completely the differences between cavities of different kinds. They discriminate, so to speak, one type of perturbation from the other, e.g. the boundary modification versus the inclusion.



(a) $|\Delta_m|^{-2}$ (b) $\left|S^{(1)}_{m,+20}\right|$

Fig. 3.6 (a) Evaluation of $|\Delta_m|^{-2}$, Eq. (3.10), using $kR_0 = 9$, $n_c = 3.2$ and $n_o = 1$ ($Z_o = 9$, $Z_c = 28.8$) (black dots) over a symmetrical range of m. The green continuous line indicates the envelop trends given by Eqs. (3.121) and (3.122) for the corresponding domain of application; origin at $m = 0$ for Eq. (3.121), origin at $m = \pm Z_c$ for Eq. (3.122). (b) Evaluation of $|S^{(1)}_{mm'}|$ along the column $m' = 20$ for the circular inclusion cavity, $n_h = 1$ and $d/R_0 = 0.5$. The diagonal term $|S^{(1)}_{m'm'}|$ is highlighted by a red circle. Notice the ridge region, $|m| < Z_o$, having a larger scattering amplitude than terms located near the diagonal component at $m = 20$.

3.3.2 Results from perturbation theory

For the *boundary perturbation example*, we have shown in Eqs. (3.86) and (3.87) that the first corrections to the eigenvalues of the approximate delay matrix $\mathbf{Q}^{(0)} + \eta\mathbf{Q}^{(1)}$ are

$$q^{(1)}_{m_{0a}} = \mathcal{Q}^{(1)}_{m_0}\left(\Phi_{m_0,m_0} + |\Phi_{m_0,-m_0}|\right) \tag{3.123}$$

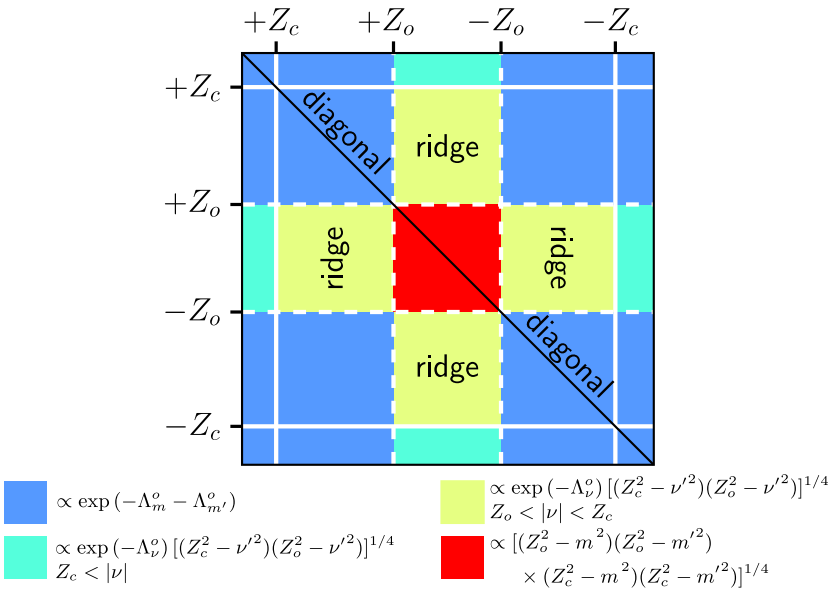
$$q^{(1)}_{m_{0b}} = \mathcal{Q}^{(1)}_{m_0}\left(\Phi_{m_0,m_0} - |\Phi_{m_0,-m_0}|\right) \tag{3.124}$$

with $\mathcal{Q}^{(1)}_{m_0}$ defined in Eq. (3.83). The first order corrections change with the cavity mean radius Φ_{m_0,m_0}. This agrees with the observation that the delay spectra for two discs having radii R_0 and R'_0 are only shifted along the wavenumber axis with respect to another. The level degeneracy is lifted only if $\Phi_{m_0,-m_0} \neq 0$.

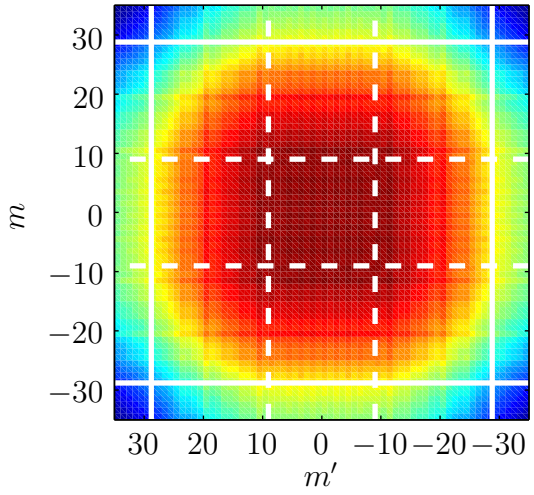
For a boundary deformation defined through a *finite* Fourier series, only a finite number of levels will have their degeneracy lifted in the first order. An illustration of this point is found in a *quadrupolar deformation*

$$R(\phi) = R_0(1 + \epsilon\cos 2\phi) \tag{3.125}$$

for which the matrix $\mathbf{\Phi}$ has only two satellite diagonals along the main diagonal. In



(a)



(b)

Fig. 3.7 Mapping of $|\Delta_m|^{-1}|\Delta_{m'}|^{-1}$ (a) from analytical considerations, Eqs. (3.120) and (3.121), and (b) from exact evaluation, Eq. (3.10). The parameters are the same as the ones used on Fig. 3.6. The color gradient in (b) scales with the logarithm of $|\Delta_m|^{-1}|\Delta_{m'}|^{-1}$. Note the *ridges* in regions with $|\nu| < Z_o$ and $|\nu'| > Z_o$ where $\nu = \{m, m'\}$ and $\nu' = \{m', m\}$.

this special case, only the mode $m_0 = 2$ is able to lift its degeneracy through first order perturbation.

Using Eqs (3.88) and (3.6), we readily verify that

$$\psi^{(0)}_{m_{0a}} \propto \cos\left(m_0\phi + \frac{1}{2}\arg\{\Phi_{m_0,-m_0}\}\right) \tag{3.126}$$

$$\psi^{(0)}_{m_{0b}} \propto \sin\left(m_0\phi + \frac{1}{2}\arg\{\Phi_{m_0,-m_0}\}\right) \quad . \tag{3.127}$$

The modes labeled a and b are then respectively of even and odd symmetry with respect to the angular position $\frac{1}{2}\arg\{\Phi_{m_0,-m_0}\}$, a reference *symmetry axis* of the cavity recognized by the mode m_0. The number of different symmetries in a deformed cavity is then related to the amount of different phases found in the Fourier series of the boundary deformation.

We now discuss a few more properties of the delay spectrum with respect to the mode symmetry. In terms of delay levels, different m_0 odd and even modes, relative to a uniquely defined symmetry axis, may cross each other. However, the picture is more involved for same symmetry modes: accidental degeneracy found in the homogeneous disc spectra become (at least) twofold anti-crossings[4] (see Fig. 3.8 for a descriptive representation). For a given symmetry, the overall delay spectrum becomes a series of avoided crossings between levels, the sizes of which are related to interaction strength. Complete spectral mayhem appears for cavities having no clearly defined symmetry axis (*e.g.* random boundary roughness or spiral cavity). In these cases, as it is always possible to find a projection of a given symmetry mode into the others, every level will

[4] A very special exactly solvable case of level avoidance is the *circular inclusion cavity*. We can show that the 4×4 generalization of the eigenproblem Eq. (3.32) reads

$$\begin{pmatrix} Q^{(1)}_{m_0m_0} & (-1)^{m_0}Q^{(1)}_{m_0m_0} & 1Q^{(1)}_{m_0m_0'} & (-1)^{m_0'}Q^{(1)}_{m_0m_0'} \\ (-1)^{m_0}Q^{(1)}_{m_0m_0} & Q^{(1)}_{m_0m_0} & (-1)^{m_0}Q^{(1)}_{m_0m_0'} & (-1)^{m_0+m_0'}Q^{(1)}_{m_0m_0'} \\ Q^{(1)*}_{m_0m_0'} & (-1)^{m_0}Q^{(1)*}_{m_0m_0'} & 1Q^{(1)}_{m_0'm_0'} & (-1)^{m_0'}Q^{(1)}_{m_0'm_0'} \\ (-1)^{m_0'}Q^{(1)*}_{m_0m_0'} & (-1)^{m_0+m_0'}Q^{(1)*}_{m_0m_0'} & (-1)^{m_0'}Q^{(1)}_{m_0'm_0'} & Q^{(1)}_{m_0'm_0'} \end{pmatrix} \begin{pmatrix} c_+^{m_0} \\ c_-^{m_0} \\ c_+^{m_0'} \\ c_-^{m_0'} \end{pmatrix} = q^{(1)} \begin{pmatrix} c_+^{m_0} \\ c_-^{m_0} \\ c_+^{m_0'} \\ c_-^{m_0'} \end{pmatrix} \tag{3.128}$$

which has the following characteristic polynomial

$$q^{(1)^2}\left[q^{(1)^2} + \left(-2Q^{(1)}_{m_0m_0} - 2Q^{(1)}_{m_0'm_0'}\right)q^{(1)} + \left(4Q^{(1)}_{m_0m_0}Q^{(1)}_{m_0'm_0'} - 4|Q^{(1)}_{m_0m_0'}|^2\right)\right] = 0 \tag{3.129}$$

whose roots, perhaps surprisingly, can be written down analytically: $q^{(1)} = 0$ (twice degenerate) and $q^{(1)} = \left(Q^{(1)}_{m_0m_0} + Q^{(1)}_{m_0'm_0'}\right) \pm \sqrt{\left(Q^{(1)}_{m_0m_0} - Q^{(1)}_{m_0'm_0'}\right)^2 + 4|Q^{(1)}_{m_0m_0'}|^2}$. Away from the accidental crossing, the $Q^{(1)}_{m_0m_0'}(k)$ is small and we find eigenvalues having proper values (see forthcoming paragraphs). Since the coupling term $Q^{(1)}_{m_0m_0'}(k)$ increases with k near accidental crossings of the unperturbed cavity, the overall effect is the splitting of 2 levels. As we will see in the development of the inclusion cavity, odd modes delays of this specific cavity are not affected by first order perturbation. This result is in agreement with the four levels interaction where two eigenvalues remain degenerate and equal to zero. Further analysis show that the zeroth-order eigenvector coefficients are a linear superposition of two even modes belonging to angular momenta m_0 and m_0'.

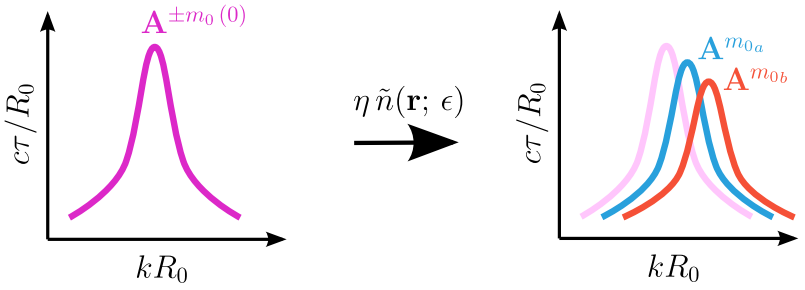
interact with each other in anti-crossing events.

The *cavity inclusion* example is particularly attractive since it demands only a few minor alterations to the results of those of the boundary modification. The most important difference resides in the fact that in this case $\Phi_{mm'} = 1$ for all angular momentum pairs. Following the preceding discussion on symmetry issues, we immediately find that having $\Phi_{mm'} = 1$ implies that the odd modes relative to the Ox axis have $q^{(1)}_{m_{0b}} = 0.$, i.e. odd modes remain unaffected to first order. The reason is that the odd disc modes have zero amplitude on the Ox axis. Furthermore, the sign on $\beta_{m_{0aa}}$, Eq. (3.116), only depends on the difference $n_c^2 - n_h^2$. From the definition Eq. (3.52), this implies that $\theta^{(1)}_{m_{0a}}(k;\epsilon) < 0$ for $n_c^2 > n_h^2$ and $\theta^{(1)}_{m_{0a}}(k;\epsilon) > 0$ for $n_c^2 < n_h^2$. Since the slope of $-\theta^{(0)}(k)$ is positive with respect to k (because of its relation with the positive delay, Eq. (3.59)), the complete phase $\theta_{m_{0a}}(k) = -\theta^{(0)}_{m_{0a}}(k) + \theta^{(1)}_{m_{0a}}(k;\epsilon)$ moves towards larger k values for $n_c^2 > n_h^2$, and the other way around for $n_c^2 < n_h^2$. A numerical example of this observation is shown in Fig. 3.9.

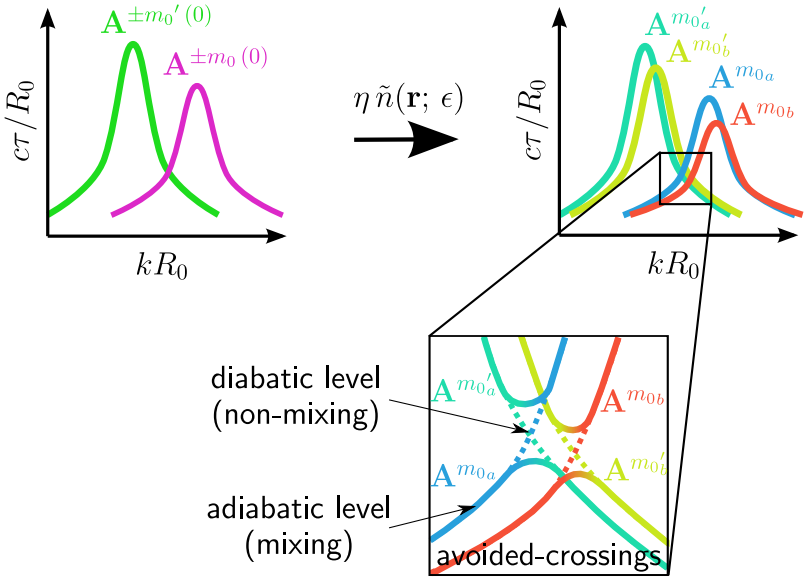
An illustration of the perturbation method of this Chapter is presented in Fig. 3.10 for the inclusion system and a near resonance scenario (mode $(18, 7)$ for instance). In this example, the condition $(\epsilon Z_c/2)^2 \ll 1$ is well respected (Eqs 3.110 and 3.111), $(\epsilon Z_c/2)^2 \simeq 0.05$ for the parameters used in Fig. 3.10. Although the overall agreement between the two sets of evaluations is much better at $d/R_0 = 0.81$ than it is at $d/R_0 = 0.90$. This is attributed to the oscillating amplitude of the $J_{18}(n_c k d)$ Bessel function affecting the range of validity of both perturbation treatments with respect to the total amount of $\psi^{(0)}_{m_0=18}$ field being diverted by the inclusion (see Fig. 3.11). The orange peak of Fig. 3.10(b) is even turning asymmetric, a symptom that the correction term $q^{(1)}_{m_{0a}}$ is becoming non-perturbatively large. The numerical evaluation loses some of its validity near the maximum of $|\psi^{(0)}|^2$ at $r/R_0 \simeq 4.5$.

Although the numerical evaluation of the perturbation series may be worrisome due to its poorly defined range of validity, we would like to emphasize that we could, in principle, always find an ϵ deformation parameter suitable for a 'converged' first-order perturbation treatment.

The expression for $\beta_{m_{0aa}}$, Eq. (3.116), is also useful in the evanescent regime inside the caustic radius $m_0/n_c k$ (see Chapter 1). This is interesting because, in this region, the zeroth-order field changes exponentially with the radius (see Appendix A for large order Bessel $J_m(x)$ functions), in contrast with the continuous oscillations affecting the region above the semi-classical caustic. This behaviour could prove useful as we attempt to control the amount of field being diverted to other momentum field components $|m| \neq m_0$. Figure 3.12 presents the first order incident coefficients Eq. (3.39) for three



(a) Effect of perturbation on single degenerate peak



(b) Effect of perturbation on two degenerate peaks. The avoided-crossing behaviour between same symmetry modes is highlighted

Fig. 3.8 Schematic representation of the removal of degeneracy due to perturbation in the delay spectrum. (a) Splitting of a resonant mode (left spectrum) into even and odd modes relative to an appropriate symmetry axis (right spectrum). The light pink line on the right picture indicates the position of the former unperturbed degenerate resonant peak. (b) Splitting of two resonant modes (left spectrum) into even and odd modes relative to an appropriate common symmetry axis (right spectrum). The close-up view of the accidental crossing between modes with angular momentum m_0 and $m_0{}'$ reveals avoided-crossings between the delay levels of modes of same symmetry. Note that the "pure" m_{0a} (m_{0b}) and m_{0a}' (m_{0b}') modes follow *diabatic* levels (discontinuous lines) that cross over the gap between *adiabatic* levels (continuous lines): there is a modal character exchange along an adiabatic level going left to right. Consequently, the modes of a given symmetry rearrange themselves in two orthogonal combinations as they go through the avoided-crossing.

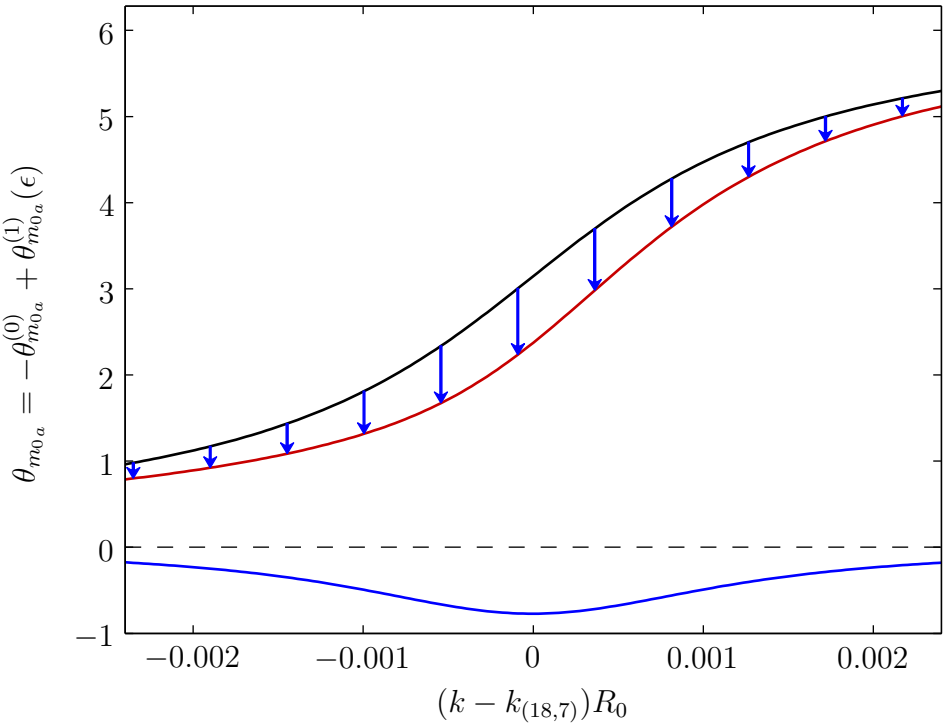


Fig. 3.9 Complete phase factor $\theta_{m_{0a}} = -\theta^{(0)}_{m_{0a}} + \theta^{(1)}_{m_{0a}}(\epsilon)$ (dark red curve) near resonance $(18, 7)$ at $k_{(18,7)}R_0 \simeq 13.8916$ for the disc cavity + inclusion corresponding to the physical setup $n_c = 3.2$, $n_o = 1$, $n_h = 1$, $R_0 = 1$, $d/R_0 = 0.81$ and $\epsilon = 0.01$. The individual terms $-\theta^{(0)}_{m_{0a}}$ (black) and $\theta^{(1)}_{m_{0a}}(\epsilon)$ (blue) add up to move the resulting curve (dark red) toward larger k values. The length and direction of the blue arrows are obtained by the evaluation of $\theta^{(1)}_{m_{0a}}(\epsilon)$. Note the large phase change as the wavenumber goes through the resonance, almost by 2π, with the inflexion position around a phase shift of π [88]. See Fig. 3.10 for the corresponding delay spectrum.

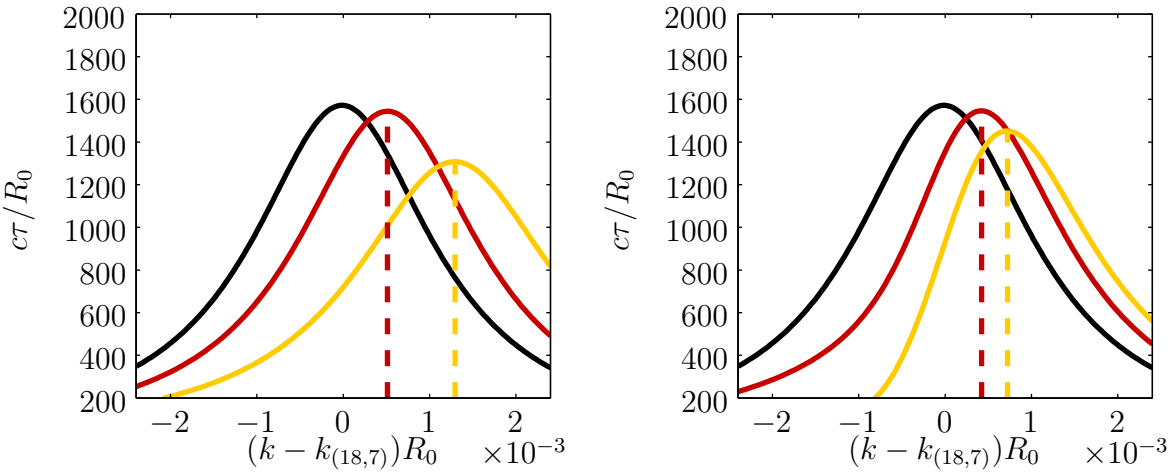
values of d/R_0. Results show that the coefficients outside the ridge, $|m| < Z_o$, differ only by a common scaling factor for different d/R_0.

Not only do the terms inside the ridge become larger in amplitude, they also seem to change quite a lot over the relatively small parametric interval sampled here. Since the outgoing far-field for characteristic delays reads

$$\psi_{\text{out}}(\mathbf{r}) = \mathrm{e}^{-i\theta}\psi^*_{\text{inc}}(\mathbf{r}) \sim \sum_m A^*_m \mathrm{e}^{-im\phi - m\pi/2} \ , \tag{3.130}$$

the far-field is prone to vary strongly as the inclusion is displaced inside the evanescent field region. Hence, the emission properties of a high quality mode seem to be dictated by the low angular momentum components. This observation will be the subject of a detailed investigation in the next Chapter.

The appearance of the ridge in the evaluation of the first order coefficients $A^{(1)}_m$, Eqs (3.39)-(3.40), stems from the presence of $Q^{(1)}_{m,\pm m_0}$ producing the features shown on Figs.



(a) Exact (b) Perturbation

Fig. 3.10 Delay spectrum of the disc cavity even mode $(18, 7)$ found at $k_{(18,7)}R_0 \simeq 13.8916$ for $\epsilon = 0$ (unperturbed reference, black) and the inclusion scenario $\epsilon = 0.01$ (red, $d/R_0 = 0.81$; orange, $d/R_0 = 0.90$). (a) exact computation from the analytical model of Appendix D and (b) perturbation method of this Chapter (perturbation of the **S** matrix *and* eigenvalues obtained from perturbation theory). The lateral motion of the peaks is mostly determined by the $q^{(1)}_{m_{0_a}}$ factor while most of the amplitude decay is due to the normalization factor $1 + (\eta\beta_{m_{0_a}})^2$ $(\eta = 1)$.

3.6 and 3.7. Physically, the existence of the ridge can be understood by the position of the caustic radius of low-lying delay modes. These modes are strongly affected by a perturbation well inside the evanescent region of a high quality mode, and therefore more likely to connect to other angular momentum modes, including the resonant ones. Because the amplitude deflected by the inclusion is largely modified by the behaviour of the $J_m(x)$ Bessel function, a characteristic of these low quality modes, the net effect is a continuously changing amplitude $|A^{(1)}_m|^2$ inside the ridge. For instance, the mode $(18, 7)$, shown in Fig. 3.11, is itself a low-lying component of another high quality mode having its evanescent region well inside the oscillating part of $(18, 7)$.

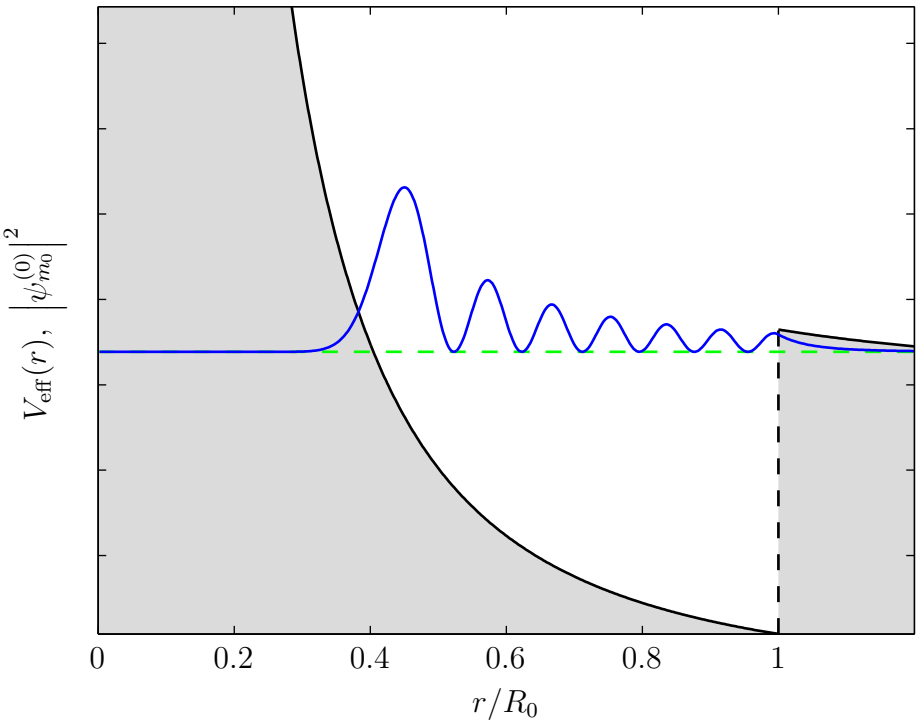


Fig. 3.11 Radial cut of the wavefunction $\left|\psi^{(0)}_{m_0=18}\right|^2$, Eq. (3.6), near the resonance at $k_{(18,7)}R_0 \simeq 13.8916$ and the corresponding effective potential (see Introduction, Chapter 1). Note the decaying portion of the field inside the semi-classical caustic radius $m_0/n_c k \simeq 0.401 R_0$.

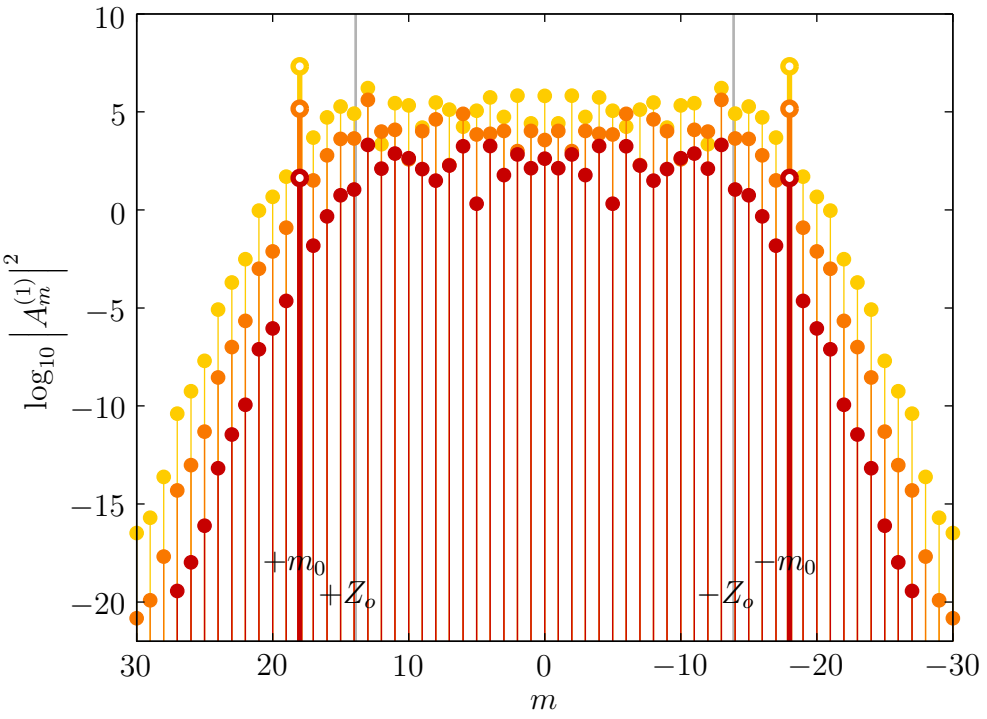


Fig. 3.12 Coefficients $\left|A_m^{(1)}\right|^2$ ($\epsilon = 1$) for $d/R_0 = 0.28$ (dark red), $d/R_0 = 0.33$ (dark orange) and $d/R_0 = 0.38$ (orange). Main channel $|m_0| = 18$ is indicated by thicker line and hollow marker. Physical parameters are the same as those used in Fig. 3.9. The evaluation is performed at the resonance maximum delay value of the perturbed $(18, 7)$ even mode.

3.3.3 Inhomogeneous versus Deformed disc cavity

One question that may be asked regarding the much studied annular cavity is how original (in the sense of producing novel results) is this design compared to other geometrically deformed cavities. In other words, and more generally, can one always devise a purely geometrical deformation of the homogeneous disc cavity such that its measured delay spectrum (or pole positions) is identical to that of a disc cavity with an inhomogeneous refractive index? The preceding results, regarding first-order correction to the disc scattering matrix, provide some answers.

Since the $\mathbf{S}$ matrix is central to both the emission/absorption description of complex poles and the real k time delay characterization, we will concentrate on this specific quantity to address the question stated above. Let the effect of a small circular inclusion on the disc cavity result in a $\mathbf{S}$ matrix series of the form of Eq. (3.15). It would seem reasonable to investigate small geometrical deformations of the circle such that the zeroth-order term $\mathbf{S}^{(0)}$ remains unchanged.

Turning our attention to the $\mathbf{S}^{(1)}$ contributions of our two illustrative examples, Eqs (3.80) and (3.114), we first discard the case $d = R_0$ in $\mathbf{S}^{(1)}$ because it would mean that the small, albeit finite size inclusion, would be *on* the boundary. This in turn would imply that we have to set $\Phi_{mm'} = \text{const.}$ for all m and m' in Eq. (3.114). For that to happen, $f(\phi) \propto \sum_j \mathrm{e}^{ij\phi}$, a notoriously ill-defined series.

For values of d between 0 and $R_0(1-\epsilon)$, any agreement between the two $\mathbf{S}^{(1)}$ contributions demands that

$$\Phi_{mm'} \propto \frac{J_m(n_c k d) J_{m'}(n_c k d)}{J_m(n_c k R_0) J_{m'}(n_c k R_0)} \quad . \tag{3.131}$$

However, because the exact expression for $\Phi_{mm'}$ depends on the *difference*, $m - m'$, contrary to the above requirement, agreement between the two $\mathbf{S}^{(1)}$ can not occur.

We must therefore conclude that the annular cavity is an original design with respect to geometrical deformation of an homogeneous cavity. This result applies to the whole spectrum: it may still be possible to tailor a single mode by geometrical deformation of the cavity boundary such that we would find an identical resonant wavenumber and delay for a given inclusion. It would appear that the same conclusion is true for any deformation for which $f(\phi)$ is a single valued function with respect to the geometrical center of the cavity.

Chapter 4

Application I: The annular cavity

This Chapter is the natural extension of the previous one where predictions on the annular cavity were made from a perturbation perspective. We now present a thorough numerical investigation of the annular cavity modes for different parameter sets. Emphasis is placed on the increase of anisotropic emission in the far-field from a high quality WGM with (almost) isotropic near-field as a control parameter is varied. We identify two competing escape mechanisms explaining this dichotomy. We then use semi-classical theory to determine the origin in phase space of the anisotropic far-field. Since these results do not rely on the exact position of the investigated high quality WGM, they may be used as prediction tools for very high delay resonances where numerical simulations become cumbersome and hardly possible. Finally, we investigate two phenomena that may cause difficulties in trying to achieve proper control of the far-field emission: resonant coupling and wall roughness.

It has been shown in the previous Chapter that placing a small circular inclusion in a disc cavity changes the field composition of the high quality modes. More specifically, the angular momentum composition of the incoming/outgoing characteristic modes is modified to preferentially populate states inside the domain $|m| < n_o kR_0$ instead of the immediate neighborhood of the main channel $n_c kR_0 > |m| = |m_0| > n_o kR_0$. This property is inherited from the ridge structures appearing in the scattering matrix in the form of off-diagonal horizontal and vertical bands crossing at the center of the $\mathbf{S}$ matrix.

Since the perturbation contribution of the main angular momentum $|m| = m_0$ to the delay matrix $\mathbf{Q}^{(1)}$ is proportional to $J_{m_0}(n_c kd)$, moving the inclusion beyond the semi-

classical caustic radius ($m_0/n_c k$) has a varying (oscillating) effect on the perturbed delays and the angular momentum components. On the other hand, the more monotonic behaviour of the Bessel function within the caustic radius may be exploited to provide a smooth increase of the amount of diverted field. With regards to this inner caustic scenario, the chosen application is more predictable for large inclusions, and certainly less disruptive of the main whispering gallery mode (WGM) field. Probing the inner evanescent field may then be carried out with a wide range of inclusion sizes and positions even beyond the perturbation regime while retaining a qualitative interpretation of the near-field behaviour (*i.e.* WGM-like).

These observations, derived from perturbation results of the preceding Chapter, lead naturally to consider the control of emission properties of a high quality WGM *without* sacrificing too much of its containment power (Q-factor). Moreover, owing to the simplicity of the system geometry, we should be able to provide analysis of the internal mechanisms at play in addition to direct numerical simulations.

This Chapter is separated into four Sections. The first one is dedicated to the investigation of the parametric range capable of disrupting the far-field of the WGMs, while preserving their near-field behaviour. This will be achieved by moving a constant radius inclusion toward the disc boundary along the Ox axis (see Fig. 4.1(a)). An intuitive model of the cavity dynamics will also be formulated, providing evidence of the competition of two escape mechanisms.

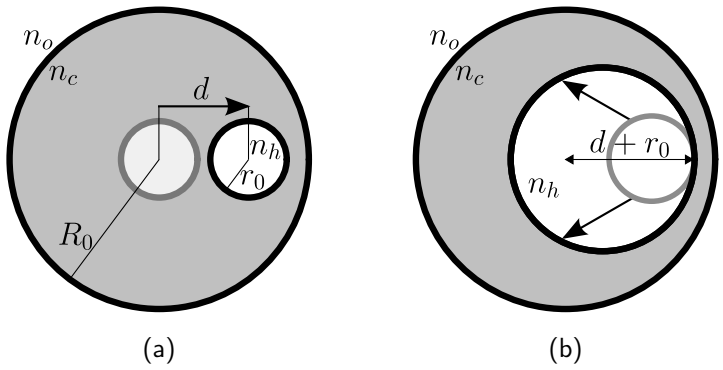


Fig. 4.1 The parametric perturbations of the disc cavity investigated in this Chapter are of two types: (a) inclusion displacement and (b) inclusion growth. In the second scenario, the inclusion radius r_0 is increased while the distance $d + r_0$ remains constant. This type of deformation is suggested from the results of the first parametric study.

Once the adequate parametric range is determined, we will proceed to exploit the inclusion size to modify the overall appearance of the far-field (again while maintaining a high delay mode). This is done in Section 4.2 through the modification of the inclusion radius (see Fig. 4.1(b)). Emphasis will be on a semi-classical analysis of the field, and

important phase space structures related to the emission properties will be identified. We will provide convincing evidence of the correspondence between wave and classical structures. We will not use the usual periodic orbit description however, but rather we will exploit a description based on classical mechanisms to cover large portions of phase space.

The following two Sections provide supplementary information. They will fill in some important details first skipped for the sake of conciseness. We will point out two aspects that could be of relevance once an experimental implementation is considered. The first topic is that of *accidental* resonant coupling between a high and a mid-size quality mode. A coupled oscillators model will be derived to illustrate the subject and will be compared to results from complete calculations from the annular cavity setup.

The second topic is inherent to all experimental realizations: manufacturing defects. We will focus on the case of outer boundary roughness, and will stress the fact that boundary roughness unfortunately provides a third way out of the cavity from the high delay WGM. For our purpose, emission control, this will demand that the phenomena leading to directional emission be of greater magnitude then the loss of uniformity in the far-field due to randomness in the geometrical configuration of the cavity.

This work was initially inspired by the one of [161]. However, we found that avoided level crossings [143, 160, 149, 121] (or *resonant couplings* on the real k axis as they are called in Section 4.3) were phenomena too special to get an appropriate workable design to manipulate the far-field. Our approach is more related to the one of [13], although we do not rely on a fictitious dynamical system [12] to model the behaviour of the light field of the annular cavity.

The original contributions of this Chapter, apart from the recourse to the scattering formalism and delay matrix to convey the computations, revolve around the control of the directional emission/reception field of a high quality annular cavity. The observation of a parametric interval supporting high quality modes with highly directional far-field, Fig. 4.7, and the model presented in Section 4.1.2 to explain this observation, ultimately leading to Fig. 4.12, are seen as novel results [101]. The classical transport mechanism domains in the chaotic part of phase space, Fig. 4.16, and their good agreement with full wave results regarding phase space distribution and far-field distribution, Figs 4.19, 4.21 and 4.22, are also original contributions [106]. The identification of resonant coupling as an issue for modal control, Section 4.3, and the investigation of the consequences of boundary roughness as leading to a third escape mechanism from the cavity Fig. 4.32 are considered novel.

4.1 The non-uniform emission from WGMs: A competition of escape mechanisms

Let us assume that a disc cavity possesses a high quality resonance in the angular momentum channel $|m| = m_0$. This angular momentum lies somewhere in the range $|m| = m_0 \in [Z_o = n_o kR_0,\, Z_c = n_c kR_0]$. A disc inclusion is then added inside the cavity such that an annular cavity is obtained. A result from perturbation theory, Eq. (3.114), informs us that the first order perturbation correction to the scattering matrix takes the form

$$S^{(1)}_{mm'} \propto \frac{J_m(n_c kd)}{\Delta_m} \frac{J_{m'}(n_c kd)}{\Delta_{m'}} \quad . \tag{4.1}$$

The matrix $\mathbf{S}^{(1)}$ is a termwise product of a first matrix composed of $J_m(n_c kd)J_{m'}(n_c kd)$ terms and of a second matrix $\Delta_m^{-1}\Delta_{m'}^{-1}$. Using the large m description of the $J_m(n_c kd)$ Bessel function (see Appendix A), we find that the first matrix is bounded by $Z_d = n_c kd$ between oscillatory ($|m| < Z_d$) and exponentially decreasing behaviours ($|m| > Z_d$). Fixing k to a constant value, the size of the oscillatory domain increases with d, delimiting a ridge (an approximately constant plateau over a given range of m values) whose extent is eventually bounded as $Z_d = Z_o$ (see Figs 4.2 and 4.3 for explanations and numerical examples). Once $Z_d = Z_o$ is reached, the ridge domain remains of the same form but increases exponentially in amplitude with d.

We insist on the growth of the ridge structure as it appears in the perturbed eigenvectors of the delay matrix as well. Since these vectors are directly responsible for the far-field appearance of the emission pattern, the control of the ridge seems, at least from a perturbation perspective, to be of central importance.

In this Section, we will provide a complete numerical computation of the characteristic delays and associated vectors of a high quality WGM supported by an annular cavity as the circular inclusion is moved toward the exterior boundary. In line with the perturbation results, we define a measure of contrast between the normal uniform emission of the disc WGM and the actual annular modes. We will also determine that it may be possible to produce a well localized WGM with a high containment power in the near-field, while observing dramatic changes in the far-field patterns.

We will also separate two escape mechanisms competing to determine the far-field appearance of the wavefield. The crossover between the d-dependent probabilities of finding the dominant mechanism happens as the delay starts to drop, signaling the lower limit (threshold) of the high containment-high anisotropic far-field parametric domain. We should stress that this result is far easier to obtain than the full numerical

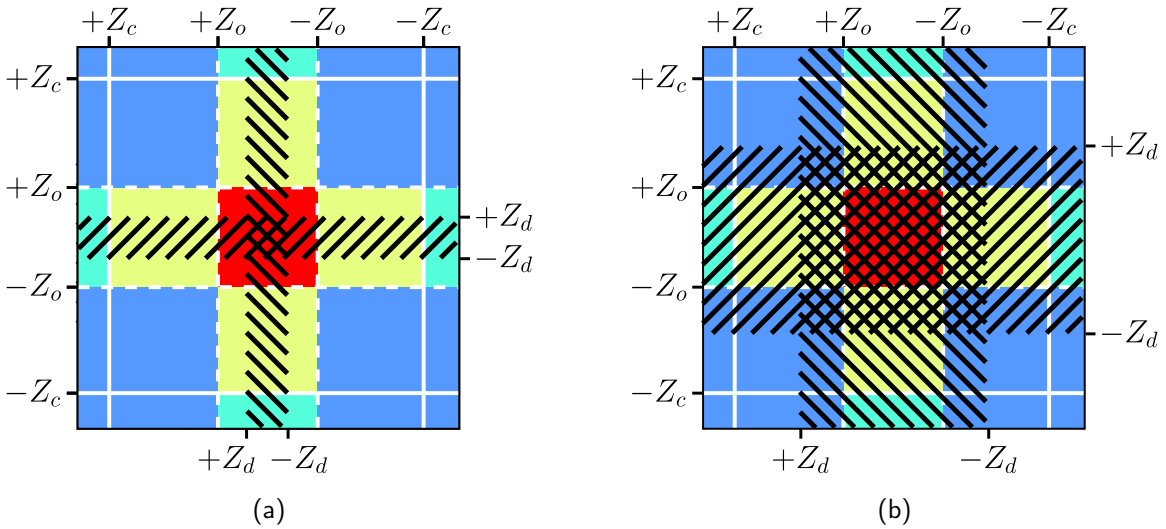


Fig. 4.2 Separation of the matrix $\mathbf{S}^{(1)}$ with regards to the respective contributions of $\Delta_m^{-1}\Delta_{m'}^{-1}$ and $J_m(n_c kd)J_{m'}(n_c kd)$. The colored areas are associated with the definitions found in Fig. 3.7(a), and the hatched areas indicate the domain of applicability of the oscillatory behavior of $J_m(Z_d)$ (single hatched: oscillatory on lines (columns), exponential decay on columns (lines); double hatched: oscillatory over lines and columns). As the inclusion position d is increased from (a) to (b), the underlying ridge region ($|m| < Z_o$) becomes completely covered by the non-decreasing terms. Given a line (or column) $m = m_0$ and $Z_c > |m_0| > Z_o$, not only is the ridge region becoming exponentially stronger with increasing d (see Eq. (A.51)), but also many more channels are being included with significant amplitude. The broadening eventually stops as Z_d reaches Z_o ($d/R_0 = n_o/n_c$): the d independent exponential decrease in m due to $\Delta_{m_0}^{-1}\Delta_m^{-1}$ remains the dominant behaviour in the region $|m| > Z_o$.

computation of a perturbed high quality WGM. In this sense, this procedure may become appealing to establish the threshold level of prohibitively large delay WGMs without actually computing them: only an approximate value of their (real) resonant wavenumbers is needed, a quantity that is readily accessible for instance through a robust semi-classical approximation of the disc cavity.

4.1.1 Effect of the displacement of the inclusion on the far-field of a WGM

We define a disc cavity having a bulk refractive index in the semiconductor range, $n_c = 3.2$, and exterior/inclusion index equals to $n_o = n_h = 1$. The cavity radius R_0 is set to 1 and is used as the length scale. The hole radius r_0 is kept constant (a number of radii are investigated) and, following the preceding discussion, we keep the center-to-center distance d along the Ox axis as a control parameter.

The delay spectrum of the homogeneous disc *without* inclusion (Fig. 4.4(a)) shows that

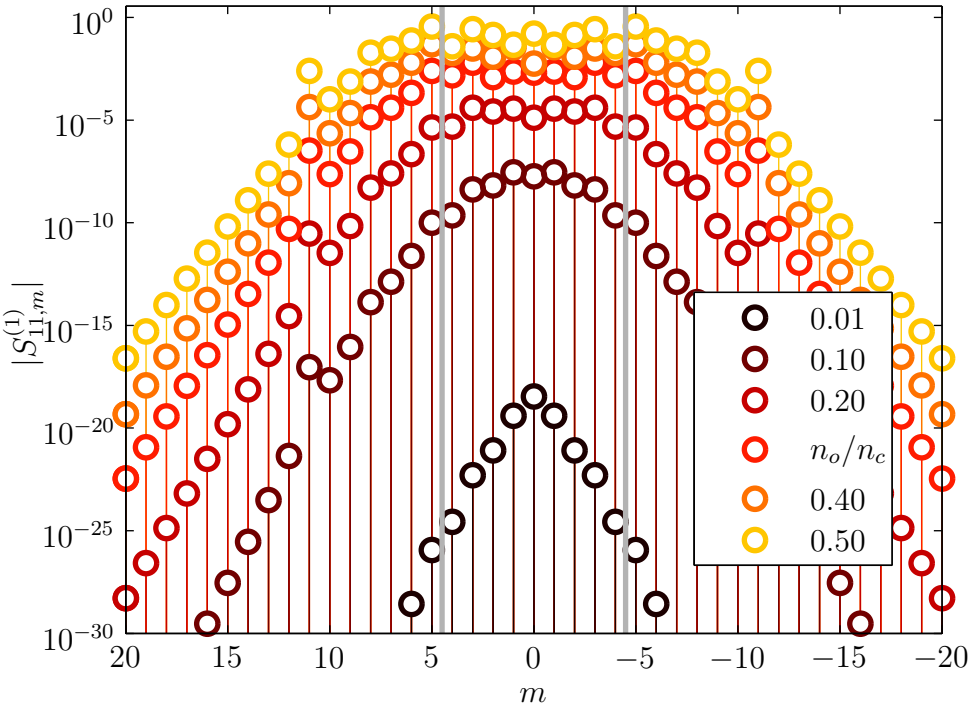
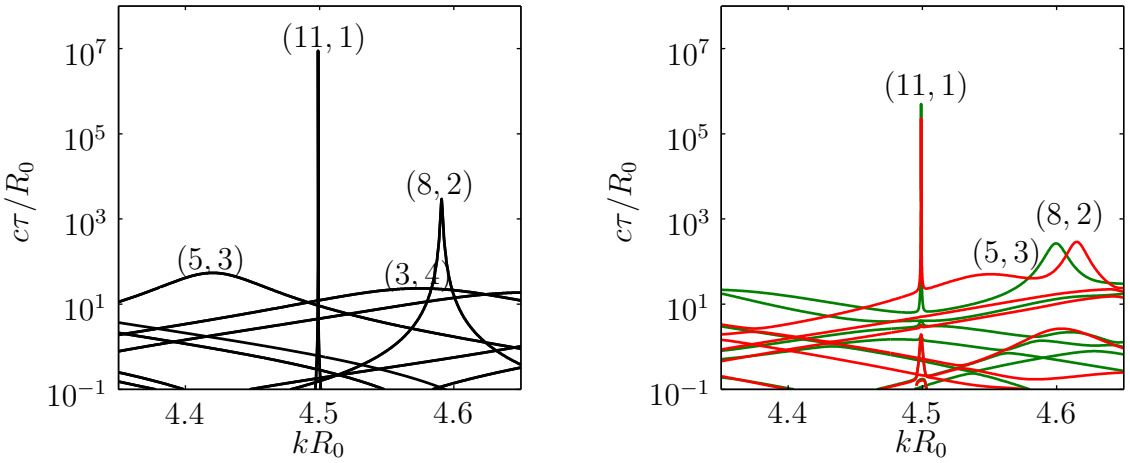


Fig. 4.3 Numerical evaluation of the line $S^{(1)}_{m_0 m}$, $m_0 = 11$, for different values of d/R_0: $n_c = 3.2$, $n_o = n_h = 1$, $kR_0 = 4.5$ and $R_0 = 1$. The vertical gray lines bound the oscillatory regime of Δ_m^{-1} (maximum size of the ridge, $\pm Z_o = \pm n_o k R_0$). The ridge domain grows in size with d until $d/R_0 = n_o/n_c$ is reached. Then a monotonic exponential increase of the whole structure follows.

a high quality degenerate $(11, 1)$ mode exist at $kR_0 \simeq 4.499$. It possesses an angular momentum $(Z_o \simeq 4.5) < |m_0| < (Z_c \simeq 14.4)$, in agreement with our prescription. We focus our attention on the even mode relative to the Ox axis. The different behaviours reported in the remainder of this Section also apply to the odd $(11, 1)$ mode, but appear at a larger perturbation (larger d and/or r_0). This agrees with Eq. (3.117) from the first order perturbation treatment of Chapter 3. Other disc cavity modes satisfying the afore-mentioned criteria (high quality having $Z_o < |m_0| < Z_c$) also behave in much the same way as our specimen mode $(11, 1)$.

In Figs 4.5 and 4.6, we record the wavenumber positions and the resonant delays of the $(11, 1) -$ even mode as a function of the center-to-center distance d over the range $d \in [0,\ R_0 - r_0]$. Five inclusion sizes (r_0) are presented.

As seen in Fig. 4.5, the resonant peak position remains roughly constant up to the semi-classical caustic radius $|m_0|/n_c k \simeq 0.76 R_0$ for all inclusion sizes. Increasing $d + r_0$ beyond that point forces the resonant modes to rearrange their amplitude distribution inside the cavity, resulting in the displacement of the position of the resonant peak to



(a) Homogeneous disc (b) Annular cavity

Fig. 4.4 Delay spectrum of (a) the homogeneous disc cavity and of (b) the annular cavity with $d/R_0 = 0.388$ and $r_0/R_0 = 0.2$. The red curves represent the delays for the Ox axis odd symmetry mode and the green curves are associated to even symmetry modes. The resonant position of modes $(5,3)$, $(11,1)$ and $(8,2)$ are shown. Note however that in the annular case, these labels have to be understood as a result of an adiabatic parametric follow-up of the disc resonances: in many instances, the effect of the inclusion may be so disruptive that the near-field looses its WGM aspect.

higher wavenumbers k. This behaviour can be verified analytically by a perturbation approach (see Fig. 3.9). Of course, the larger the size of the inclusion, the larger the displacement.

The information obtained from the resonant delay, Fig. 4.6, is qualitatively different. We observe at first the same invariance under deformation as seen in Fig. 4.5. However, before reaching the caustic radius, the delays start to drop rapidly. Moreover, the loss of 50% of the unperturbed delay value happens within a small range of $\simeq 0.2R_0$, and this for all inclusion sizes. The delay curves for different radii r_0 should actually bunch together and (exponentially) fall at a common $d + r_0$ threshold value. The premature drop of the 2 curves with $r_0/R_0 = \{0.1,\ 0.2\}$ is somewhat special and can be explained by an accidental case of resonant coupling. The explanation of this phenomenon is postponed until Section 4.3. The flat segment between $(d + r_0)/R_0 = 0$ and $\simeq 0.4$ is associated with the dominance of the tunneling through an effective cavity potential as already pointed out in [60].

In order to gauge the angular momentum content of the resonant WGM, we define a

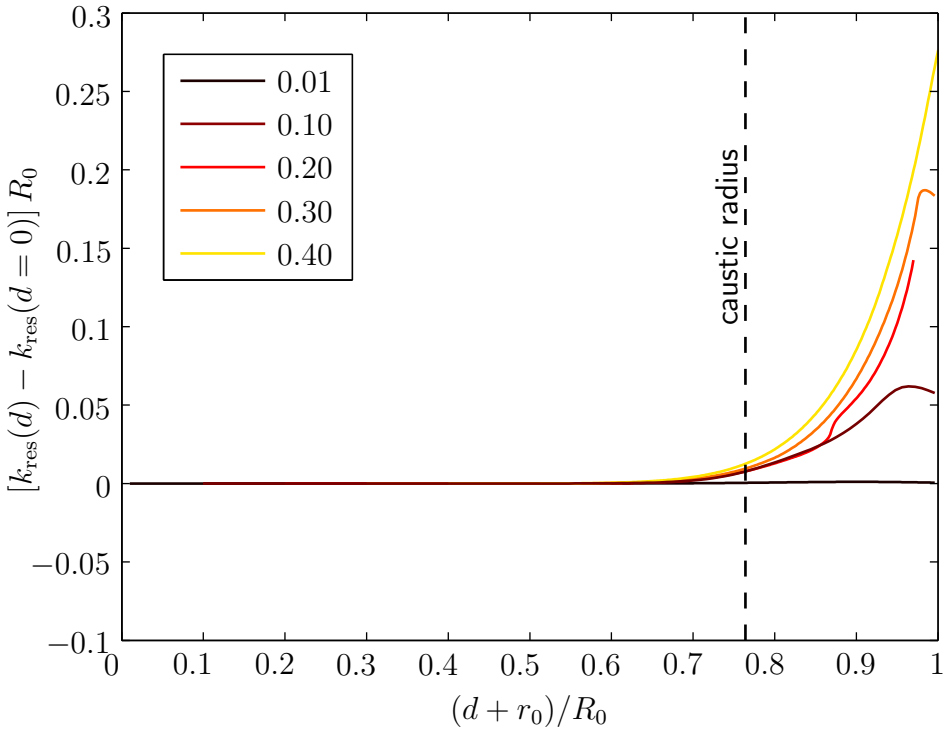


Fig. 4.5 Displacement of the resonant wavenumber position of mode $(11,1)$ relative to the corresponding one in a disc cavity with a centered ($d=0$) inclusion. Five inclusion sizes r_0/R_0 are investigated and show similar behaviours as $d+r_0$ increases. The displacement becomes especially strong as $d+r_0$ approaches the caustic radius (dashed vertical line at $\simeq 0.76$).

contrast measure for the outgoing field under parametric variations,

$$\mathcal{C}_{m_0}(r,\ \text{par}) = \frac{\sum_{|m|\neq m_0} \left|B_m H_m^{(1)}(n_o kr)\right|^2}{\sum_m \left|B_m H_m^{(1)}(n_o kr)\right|^2} \quad . \tag{4.2}$$

This measure is a function of the internal parameters (par) implicitly incorporated in the delay matrix vectors $\mathbf{B}$.

For $m_0 = 11$ and the data of Figs 4.5 and 4.6, the contrast measure evaluates the fraction of the outgoing part of the $(11,1)$ mode *that is not* the main angular component $|m| = m_0 = 11$. While $\mathcal{C}_{11}(R_0, d)$ is obviously related to the near-field aspect of the mode, the $r \to \infty$ limit will determine how much the $(11,1)$ mode has lost its uniformity in the far-field. The $r \to \infty$ limit, $\tilde{\mathcal{C}}_{m_0}$ takes the simplified form

$$\tilde{\mathcal{C}}_{m_0}(\infty, \text{par}) \equiv \lim_{r\to\infty} C_{m_0}(r,\ \text{par}) = \frac{\sum_{|m|\neq m_0} |B_m|^2}{\sum_m |B_m|^2} \quad . \tag{4.3}$$

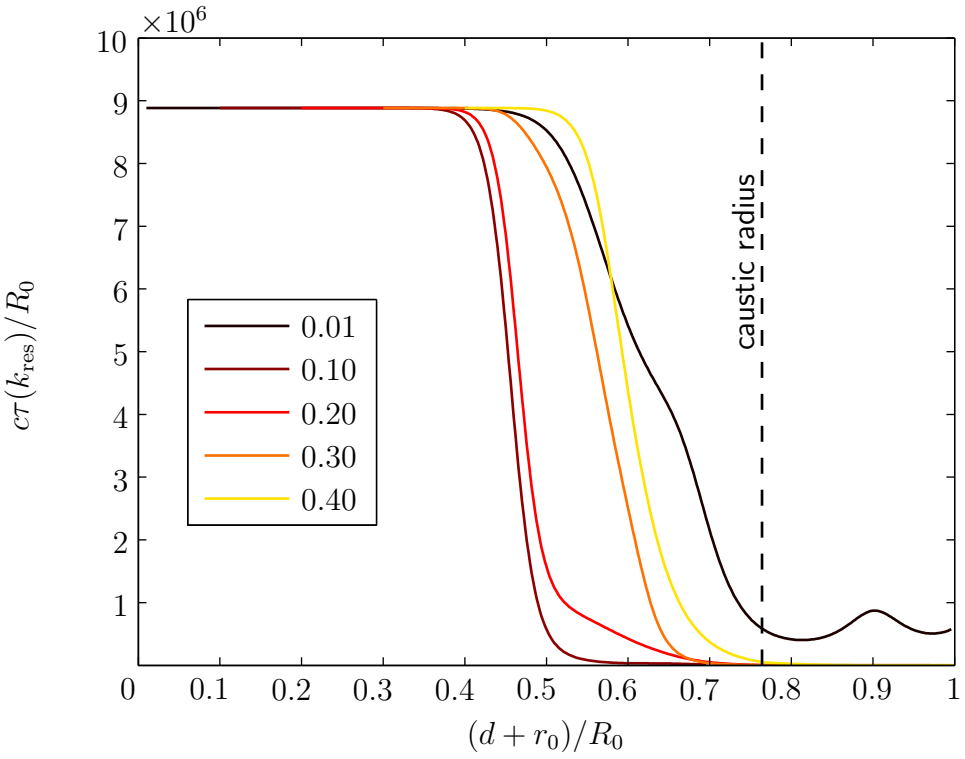


Fig. 4.6 Resonant delay value of mode $(11,1)$ relative to the center-to-center distance d for five inclusion sizes r_0/R_0. The premature drop observed for radii $r_0/R_0 = \{0.1,\ 0.2\}$ is explained by a resonant coupling with a secondary mid-size resonance. This topic is discussed in Section 4.3.

The evaluation of (4.2) is carried out for $r_0/R_0 = 0.2$ both in the near-field and the far-field regimes. In Fig. 4.7, the far-field looses its main angular momentum component early relative to the near-field. Also, $\tilde{\mathcal{C}}_{11}(\infty, d)$ reaches 0.5 near $d/R_0 = 0.27$, a position where the delay level drops to half of its unperturbed value (see Fig. 4.6). This agrees with our perturbation result that asserts that extra losses due to the perturbation of a WGM are caused primarily by lower quality angular momenta contamination, and not by an actual modification of the WGM resonance conditions. Indeed, a look at Fig. 4.5 indicates clearly that the resonant peak positions remain mostly unchanged over a large parametric range. One should also note the similarity in the expression of the contrast measure Eq. (4.3) and the general expression of the perturbed delay Eq. (3.62): it may then not come as a big surprise if the far-field contrast measure and the resonant delay are closely related.

The parametric window between $d/R_0 = 0.27$ and 0.5 where the far-field is non-uniform and the near-field remains WGM-like could be exploited as an engineering interval. The constant and predictable WGM behaviour of the near-field over this range is in sharp contrast with the non-uniform and varying far-field. This could prove to be an efficient control asset. This specific subject is the topic of Section 4.2.

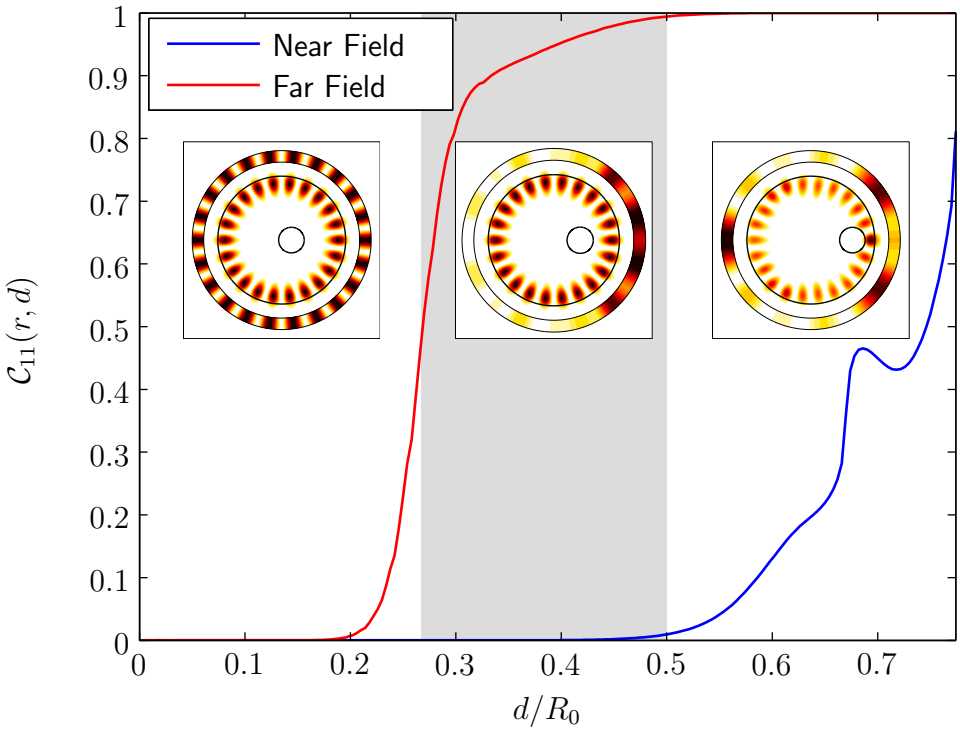


Fig. 4.7 Evaluation of Eq. (4.2) for mode $(11,1)$ at $r = R_0$ (blue curve) and $r \to \infty$ (red curve). The gray parametric region has both near-field WGM aspect ($< 1\%$ deviation) and far-field non-uniformity ($> 50\%$). Insets show the near-field ($r = R_0$, inner ring) and the outgoing far-field ($r = \infty$, outer ring) polar distribution of $|\psi(r,\phi)|^2$ for $d/R_0 = \{0.352,\ 0.602,\ 0.85\}$ (respectively, left to right).

Before moving on, it seems reasonable to address in some detail the rapid turnover of the delay curve which appears to be related to angular momenta contamination of the WGM. This can surely contribute to our understanding of the dynamical behaviour of the annular cavity. For our purpose, we develop in the next sub-section a model of the annular cavity where the loss of containment power is associated with the dominance of a secondary escape mechanism over the usual radiative escape route out of the disc cavity.

4.1.2 An iterative model of the annular cavity: Highlighting two escape mechanisms

The build-up and decay of the field of an annular cavity resonator may be constructed as a sequence of scattering and reflection events. This description of the field has already been successfully exploited for the treatment of dynamical tunneling phenomenon in *closed* cavities [45]. In this sub-section, we obtain the transition probabilities between different angular channels and confront it with the emission probability from the main

angular channel of a disc cavity.

We may define the field inside an annular region $r_0 + |d| \leq r \leq R_0$ as the result of a sequential process. Starting with an initial field condition, the corresponding wave is scattered on one hand by an effective circular boundary of radius $R_0' \geq |d| + r_0$, and reflected (and transmitted) on the other hand by the external boundary at $r = R_0$ (see Fig. 4.8). The reflected component then feeds a new round of scattering and reflection/transmission processes. In this manner, the total field $\psi_{\rm a}(\mathbf{r})$ inside the annular region can be expanded as a superposition of all incoming and outgoing *local interaction fields*

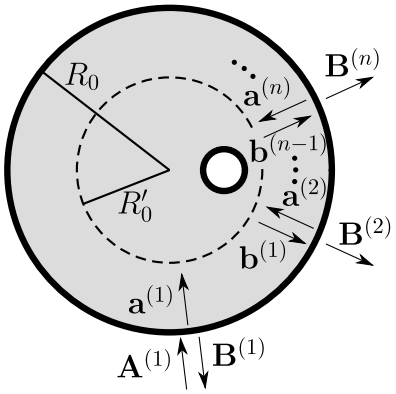


Fig. 4.8 Multiple reflections/scatterings description of the annular cavity field. The incoming and outgoing coefficients representation is used for the sake of simplicity. The total field inside the region $R_0' \leq r \leq R_0$ is decomposed as a series of scattering by the internal effective boundary at $r = R_0'$ and reflections by the external boundary at $r = R_0$.

$$\psi_{\rm a}(\mathbf{r}) = \sum_{n=1}^{\infty} \psi_{\rm a}^{(n)}(\mathbf{r}) \quad R_0' \leq r \leq R_0 \tag{4.4}$$

with the local expansions

$$\begin{array}{rcll} \psi_o^{(1)}(\mathbf{r}) & = & \sum_m A_m^{(1)} H_m^{(2)}(n_o kr)\mathrm{e}^{im\phi} + \sum_m B_m^{(1)} H_m^{(1)}(n_o kr)\mathrm{e}^{im\phi} & , \quad r > R_0 \\ \psi_o^{(n)}(\mathbf{r}) & = & \sum_m B_m^{(n)} H_m^{(1)}(n_o kr)\mathrm{e}^{im\phi} & , \quad r > R_0 \ , n > 1 \\ \psi_{\rm a}^{(n)}(\mathbf{r}) & = & \sum_m a_m^{(n)} H_m^{(2)}(n_c kr)\mathrm{e}^{im\phi} + \sum_m b_m^{(n)} H_m^{(1)}(n_c kr)\mathrm{e}^{im\phi} & , \quad R_0' \leq r \leq R_0 \ , n \geq 1. \end{array} \tag{4.5}$$

The coefficients $\mathbf{A}^{(1)}$ and $\mathbf{a}^{(n)}$ relate to the incoming waves (directed toward the geometrical center of the disc cavity) and the coefficients $\mathbf{B}^{(n)}$ and $\mathbf{b}^{(n)}$ relate to the outgoing waves. The different expansion coefficients are obtained by application of the boundary conditions (continuity of the local wavefield and its normal derivative), so that the complete superposition satisfies them as well. The only 'black-box' term in this field description is the internal scattering matrix $\mathbf{S}'$ relating the coefficients $\mathbf{a}^{(n)}$ and $\mathbf{b}^{(n)}$

$$\mathbf{b}^{(n)} = \mathbf{S}'\mathbf{a}^{(n)} \quad . \tag{4.6}$$

We illustrate in Fig. 4.9 the difference between the internal $\mathbf{S}'$ matrix and the usual 'external' $\mathbf{S}$ matrix for the annular cavity.

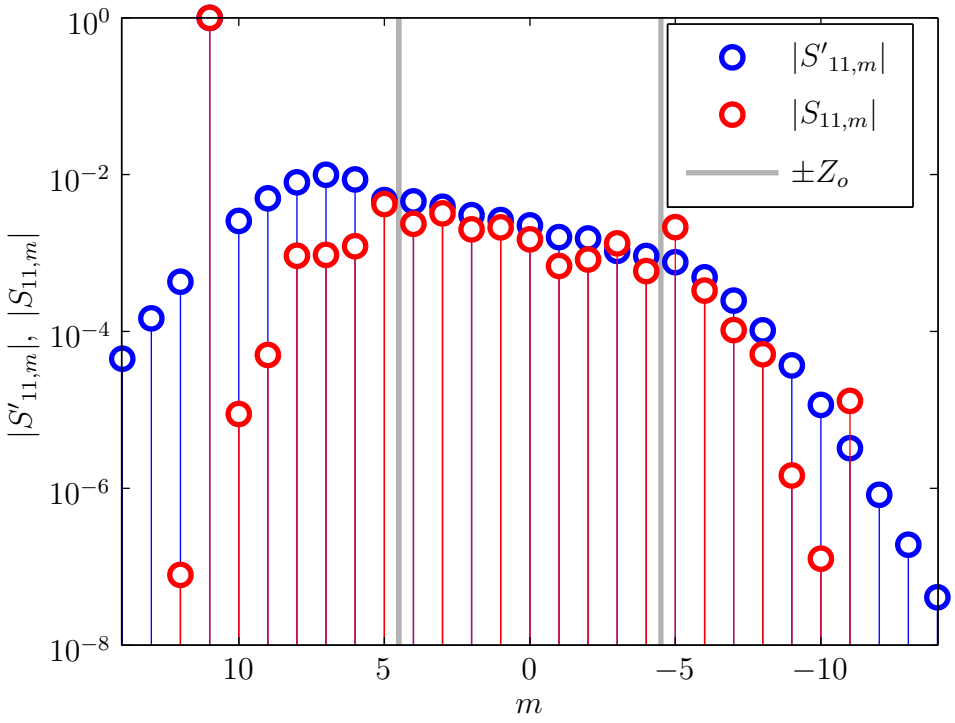


Fig. 4.9 Amplitude of the terms found on the line $m = 11$ of $\mathbf{S}'$ and $\mathbf{S}$; $n_c = 3.2$, $n_h = n_o = 1$, $R_0 = 1$, $d/R_0 = 0.4$, $r_0/R_0 = 0.2$ and $k = 4.499$. The ridge of the perturbation scattering matrix (see Fig. 4.3 for instance) is also found in both internal and external scattering matrix, but appears more asymmetrical in the former case.

The $\mathbf{S}'$ matrix can be obtained for a general internal scatterer by the numerical method presented in Chapter 2, or, in the case of the annular cavity, semi-analytically using the results from Appendix D. Moreover, fixing the geometrical aspect of the internal scatterer with the intent to displace it inside the disc cavity entitles one to use the displacement transformation on the scattering matrix, a result also found in Appendix D. This trick is useful since we only have to compute one scattering matrix through a resource intensive computation and then semi-analytically displace the object for every investigated position d.

The sequential approach is understood as a steady-state process involving an 'initial' incoming field incident on the external boundary: it begins with the field of angular momentum m incident upon the exterior boundary *only*. We obtain in a straightforward manner, by application of the local boundary conditions, the linear relations between

the different expansion coefficients

$$a_m^{(1)} = \left[\frac{H_m^{(2)}(Z_o)}{H_m^{(2)}(Z_c)}\frac{n_o F_m^{(1)}(Z_o) - n_o F_m^{(2)}(Z_o)}{n_o F_m^{(1)}(z_o) - n_c F_m^{(2)}(Z_c)}\right] A_m^{(1)} \tag{4.7}$$

$$B_m^{(1)} = -\left[\frac{H_m^{(2)}(Z_o)}{H_m^{(1)}(Z_o)}\frac{n_o F_m^{(2)}(Z_o) - n_C F_m^{(2)}(Z_c)}{n_o F_m^{(1)}(z_o) - n_c F_m^{(2)}(Z_c)}\right] A_m^{(1)} \tag{4.8}$$

with $F_m^{(1,2)}(Z) = \left[(dH_m^{(1,2)}(z)/dz)/H_m^{(1,2)}(z)\right]_Z$ and $Z_{o,c} = n_{o,c}kR_0$. Subsequent interactions with the external boundary result in the relations

$$a_m^{(n)} = \sum_{m'} \mathcal{R}_{mm'} b_{m'}^{(n-1)} \tag{4.9}$$

$$B_m^{(n)} = \sum_{m'} \mathcal{T}_{mm'} b_{m'}^{(n-1)} \quad , \tag{4.10}$$

$n \in \{\mathbb{N} \geq 1\}$ where the local *reflection* and *transmission* diagonal matrices are given by

$$\mathcal{R}_{mm'} = -\frac{H_m^{(1)}(Z_c)}{H_m^{(2)}(Z_c)}\frac{n_o F_m^{(1)}(Z_o) - n_c F_m^{(1)}(Z_c)}{n_o F_m^{(1)}(Z_o) - n_c F_m^{(2)}(Z_c)}\delta_{mm'} \tag{4.11}$$

$$\mathcal{T}_{mm'} = \frac{H_m^{(1)}(Z_c)}{H_m^{(1)}(Z_o)}\frac{n_c F_m^{(1)}(Z_c) - n_c F_m^{(2)}(Z_c)}{n_o F_m^{(1)}(Z_o) - n_c F_m^{(2)}(Z_c)}\delta_{mm'}. \tag{4.12}$$

Note that the usual Fresnel reflection coefficient [29] can be retrieved from the first expression using the appropriate asymptotic expansions for the Bessel functions (see Appendix A) [1]. The diagonal elements of these matrices are presented in Fig. 4.10 where the reflection matrix appears as a smooth version of the total internal reflection (TIR) limit [2]. Correspondingly, there is always a small non-zero transmission amplitude for

[1] For instance, in the $m < Z_o < Z_c$ regime, we use Eqs (A.37)-(A.38) (and their complex conjugate) to find the large m reflection coefficient

$$\mathcal{R}_{mm'} \simeq \frac{\sqrt{Z_c^2 - m^2} - \sqrt{Z_o^2 - m^2}}{\sqrt{Z_c^2 - m^2} + \sqrt{Z_o^2 - m^2}}\, \mathrm{e}^{i2\Theta_m(Z_c)}\delta_{mm'} \tag{4.13}$$

Using the definition of the semi-classical momentum $p_m^\alpha = \sin\chi_m^\alpha = m/n_\alpha kR_0$ (α= o, c), we retrieve the expected Fresnel coefficient (up to a phase factor),

$$\mathcal{R}_{mm'} = \frac{n_c\cos\chi_m^c - n_o\cos\chi_m^o}{n_c\cos\chi_m^c + n_o\cos\chi_m^o}\, \mathrm{e}^{i2\Theta_m(Z_c)}\delta_{mm'} \quad . \tag{4.14}$$

The Fresnel transmission coefficient however is not reobtained due to fundamental differences in the functions describing the field outside a finite size cavity and plane waves.

[2] This limit is nothing but the expression of the Snell-Descartes law which delimits the region of perfect reflection and transmission for a *planar* surface. In our present notation, it appears at $p_{\mathrm{TIR}} = n_o/n_c$.

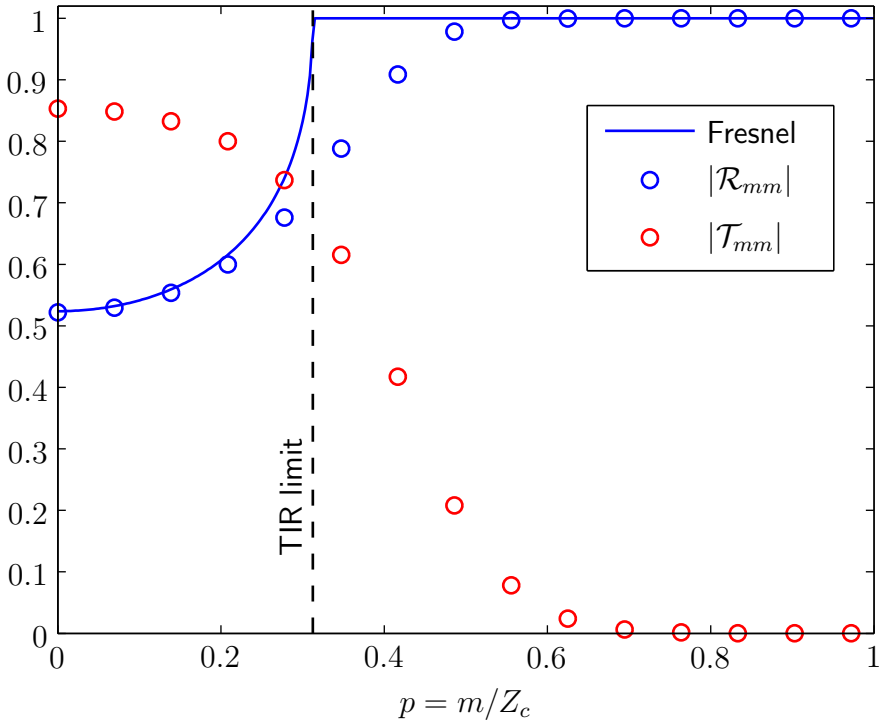


Fig. 4.10 Reflection and transmission matrices, Eqs (4.11)-(4.12), versus the semi-classical momentum $p_m = m/Z_c$. The parameters are those of the cavity under investigation $n_c = 3.2$, $n_o = 1$, $k = 4.5$ and $R_0 = 1$. As a base for comparison, the Fresnel reflection coefficient and the total internal reflection (TIR) limit ($p_{\rm TIR} = n_o/n_c$) are displayed .

all transmitted angular momentum components. For high-lying WGM having a large main angular momentum component, this means that the retention power of the cavity is very high (hence the high quality modes).

The scattering matrix $\mathbf{S}$ of the annular cavity may be deduced from the summation of all partial outgoing waves embodied in the coefficients $\{\mathbf{B}^{(n)}\}$. This iterative picture of the field is not a time step process since the angular channels do not have necessarily the same 'flight times' between two consecutive interactions with the external boundary. With this in mind, our description of the system is somewhat better related to the billiard classical map where no physical time appears on the Poincaré section of phase space.

Considering Fig. 4.7 again, it is clear that the main component of the high quality mode $(11, 1)$ *inside the cavity* for $(d + r_0)/R_0 \in [0.2,\ 0.7]$ is $|m| = m_0 = 11$. Initiating the iterative process with $a_m^{(1)} = \frac{1}{\sqrt{2}}[\delta_{m,m_0} - \delta_{m,-m_0}]$, the field is scattered and reflected through the iterative process, resulting in a superposition of what remains in the $|m| = m_0$ channels and of other angular momentum channels fed through the internal scattering. From Fig. 4.10, we expect the resonant field components $|m| = m_0$

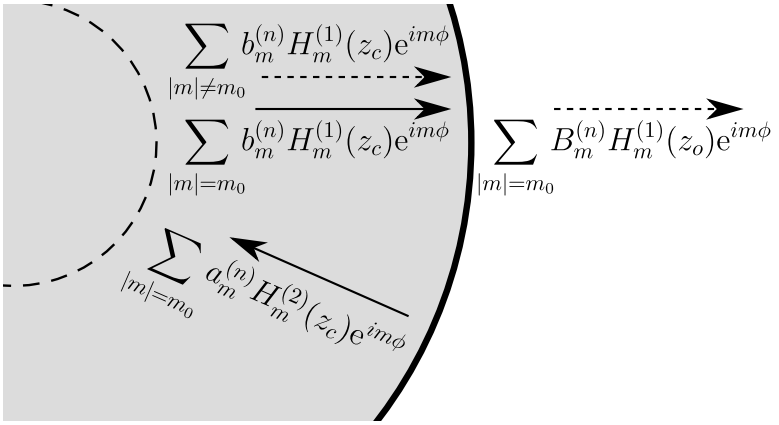


Fig. 4.11 Close-up view of escape mechanisms within a single round trip. Plain arrows are associated with portions of the field with angular momentum m_0 that remain inside the annular region $R_0' \leq r \leq R_0$. Dashed arrows represent the field that escapes the specific components $|m| = m_0$ of the field either by coupling to other angular channels through internal scattering, or by transmission to the outside.

($p_m \simeq 0.76$) to remain approximately constant inside the cavity over a large number of reflections. We further expect that the other 'contaminant' angular momentum components will be located inside the ridge portion ($|m| < Z_o$) of the internal scattering matrix (see components of matrix $\mathbf{S}'$ on Fig. 4.9), and therefore, be subject to a lower reflective power (see Fig. 4.10 for angular channels below the TIR limit). Since the main $|m| = m_0$ channels are then largely dominant over many iterates, and other components tend to escape quickly, isolating a single round trip enables one to identify the processes happening at every returning iterations without much loss of the complete dynamics. Figure 4.11 illustrates such a decomposition.

The resonance phenomenon in this iterative picture is born out of the collective (coherent) effect of all the iterations. Since only a single round trip is necessary to gather all the important features of the escape mechanisms, it matters little to accurately position the resonance for the model to be representative. Therefore, since the internal scattering matrix $\mathbf{S}'$ and the reflection matrix $\mathcal{R}$ evolve monotonically over a rather large wavenumber range in comparison to the typical width at half maximum of resonances (for $(11, 1)$, $\simeq 10^{-6} R_0^{-1}$), only an approximate value of the resonant wavenumber is needed to carry out a single iteration computation [3]. In the following, the calculations are done at $kR_0 = 4.499$.

Considering the preceding discussion, we set $a_m^{(n)} = a_m^{(1)} = \frac{1}{\sqrt{2}} [\delta_{m,m_0} - \delta_{m,-m_0}]$ so that the round-trip initial power is given by $\sum_m |a_m^{(n)}|^2 = 1$ (see Fig. 4.11). The incident

[3] The internal scatterer is assumed not to support high quality modes. In the situation where it would be the case, a precise knowledge of the resonances of $\mathbf{S}'$ is needed because of potential resonance coupling between the external annular cavity and the internal 'high quality' inclusion.

power on the external boundary *that does not* remain in the $|m| = m_0$ angular channels following the internal scattering is

$$\bar{P}'_{m_0} = \sum_{|m|\neq m_0} \left|b_m^{(n)}\right|^2 = 1 - P'_{m_0} \tag{4.15}$$

where $P'_{m_0} = \sum_{|m|=m_0} \left|b_m^{(n)}\right|^2$ is the fraction of power remaining in the $|m| = m_0$ channels after the internal scattering. The value of $\bar{P}'_{m_0}$ is a measure of the single iteration losses to angular momentum channels other than the main mode. This amount of power is considered immediately lost over the round trip.

The total scattered power transmitted outside the physical cavity through the external boundary from the $|m| = m_0$ channels is

$$\bar{P}_{m_0} = |\mathcal{T}_{m_0,m_0}|^2 P'_{m_0} = |\mathcal{T}_{m_0,m_0}|^2 \left[|b_{+m_0}^{(n)}|^2 + |b_{-m_0}^{(n)}|^2\right] \tag{4.16}$$

where we have used $\mathcal{T}_{m_0,m_0} = \mathcal{T}_{-m_0,-m_0}$.

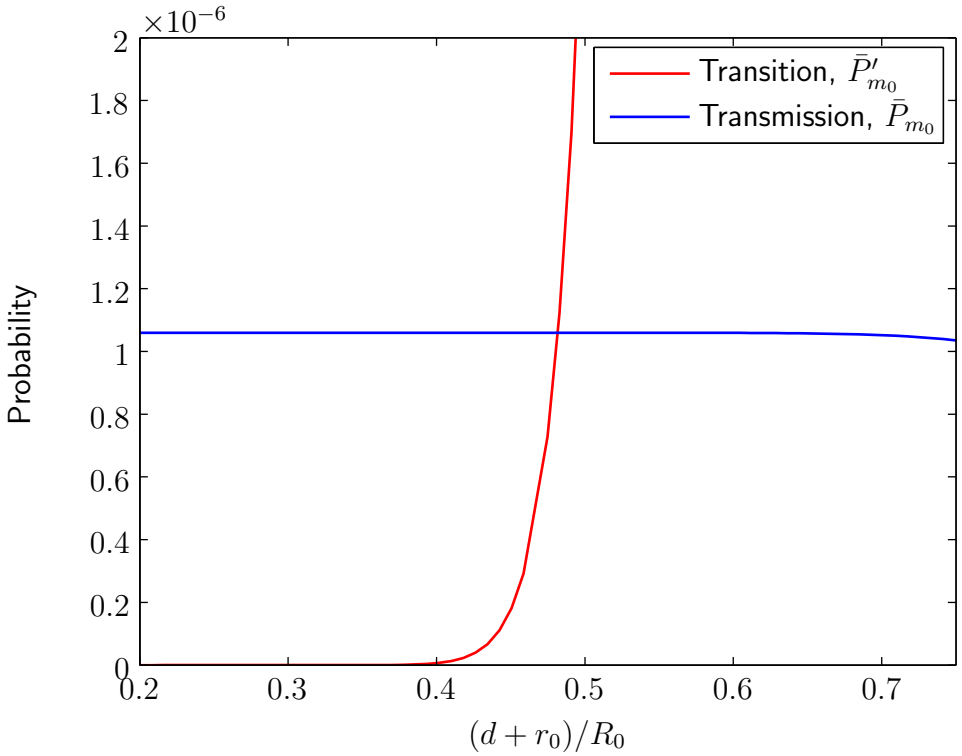


Fig. 4.12 Transition probability to other angular momenta (red) and transmission probability to the exterior of the physical cavity (blue) according to Eqs (4.15) and (4.16) respectively. Both escape probabilities reach the same value at $(d + r_0)/R_0 \simeq 0.482$: using a particle picture of the system, at this parametric position it is equally probable for a photon to escape mode $(11, 1)$ by regular potential tunneling than it is by coupling to angular momentum components different from m_0.

Since we have set the initial power to 1, we can relate Eqs (4.15) and (4.16) to actual probabilities associated to different emission mechanisms. On one hand, Eq. (4.15) is a

transition probability out of mode $(11, 1)$ to other angular momentum components, and on the other hand, Eq. (4.16) is a direct transmission probability to the exterior. Evaluating these expressions at $kR_0 = 4.499$ for values of $d/R_0 \in [0,\ 0.5]$ ($r_0 = 0.2R_0$), we find that the transmission mechanism clearly dominates at first, but that the transition mechanism quickly overcomes the former as the deformation increases: at $d/R_0 \simeq 0.33$, or $(d + r_0)/R_0 \simeq 0.53$, $\bar{P}'_{m_0}/\bar{P}_{m_0} \simeq 10$. The crossover happens at $(d + r_0)/R_0 \simeq 0.482$; this is near the position $(d + r_0)/R_0 \simeq 0.47$ where the asymptotic contrast measure $\tilde{\mathcal{C}}_{(11,1)}(\infty, d)$ equals 0.5 (Fig. 4.7) and where the nominal delay has dropped by a factor 2 (Fig. 4.6). This correspondence is quite rewarding, and of course not coincidental, as we will see.

The decomposition in these escape mechanisms is then of a great practical interest to determine the lower bound in parametric value from which to expect highly anisotropic far-field with minor deterioration of the delay value of a high quality WGM. Again, we stress that knowledge of the exact position of the resonance is not needed to successfully apply this method. This is of central importance as WGMs supporting extremely high delays, and proportionally small width, are numerically quite demanding to pinpoint accurately.

4.2 Control of the annular cavity emission output

In the preceding Section, we have presented evidences that high quality WGM and anisotropic emission far-field can be compatible in the annular cavity. The demonstration involved the displacement of a constant radius disc inclusion. Different radii were tested resulting each time in similar results (see Figs 4.5-4.6 for instance).

We have also presented that the onset of *non-uniform* emission of a high quality WGM is due to the competition between a potential barrier tunneling mechanism and an angular momentum transition mechanism. The former mechanism is inherited from the disc cavity from which the annular cavity is built upon, and the latter is due to scattering by the inner inclusion. By increasing the value of $d + r_0$, the overall probability that a WGM with angular momentum m_0 reaches any other angular momentum components $|m| \neq m_0$ eventually overcomes the intrinsic barrier tunneling probability. This results in the loss of *field uniformity* of the unperturbed WGM. The measure of the field uniformity, both in the far- and the near-field, is defined in relation to the main angular momentum m_0 of the unperturbed field. The non-uniformity increases with the fraction of a wavefield departing from the unperturbed WGM. A contrast measure $\mathcal{C}_{m_0}(r,\ \text{par})$ has been defined in Eq. (4.2) to quantify the field non-uniformity in the near-field

($r = R_0$) as well as in the far-field ($r \to \infty$). This measure allows to verify that there exists a parametric regime for high quality WGM having *near-field uniformity* ($\mathcal{C}_{m_0}(R_0,\ \text{par}) \simeq 0$) AND *far-field non-uniformity* ($\tilde{\mathcal{C}}_{m_0}(\infty,\ \text{par}) \simeq 1$).

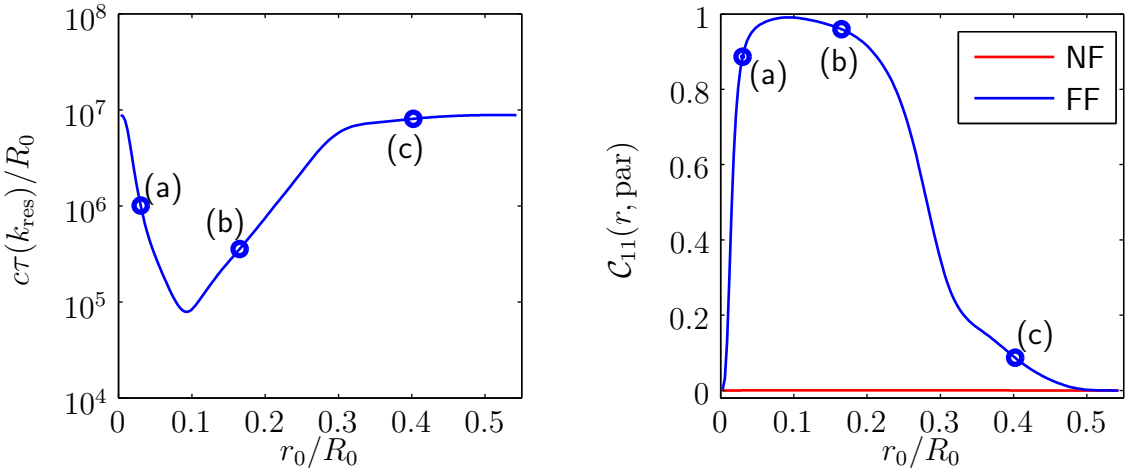
In this Section we will be concerned with the control of the output field of a high quality WGM. Moreover, we will be especially interested in a semi-classical interpretation of this control as it provides intuitive guidelines to further designs, and on a more theoretical side, evidence of particle-wave correspondence. We will first present numerical results that the far-field may change substantially by modifying the position (d) and size (r_0) of the inclusion. We will then move on to a classical interpretation of the cavity as an open billiard system in order to obtain clues regarding the emission properties of the annular cavity. Finally, using semi-classical tools, we will obtain a set of initial conditions to be inserted in the classical model.

The modification of the output of a high quality WGM demands that we find combinations (d, r_0) of the parameters at our disposal to obtain an anisotropic far-field while preserving the whispering gallery aspect of the near-field (high quality factor). Results found in Fig. 4.6 suggest that keeping the distance $d + r_0$ constant and changing the individual parameters d and r_0 may provide a way to achieve this objective.

We use again the parameters $n_c = 3.2$, $n_o = n_h = 1$ and $R_0 = 1$, and focus our attention on mode $(11, 1)$ (even symmetry) as a test subject. Reference to WGM $(11, 1)$ is purely indicative and is understood as an adiabatic deformation of the unperturbed mode found in the disc cavity. Parameter $d + r_0$ is set to a constant value of $0.55R_0$ and r_0 is increased from 0 to $0.55R_0$.

The delays and contrast values for mode $(11, 1)$ are presented on Fig. 4.13. The parameter sets $(d/R_0,\ r_0/R_0) = (0.55,\ 0)$ and $(0,\ 0.55)$ correspond to separable cases, and as such, present large delay values. Any symmetry-breaking perturbation of these limiting cases comes at the cost of decreasing the delay value (loss of quality factor). The V-shape delay profile found in Fig. 4.13(a) (log scale) between the two separable situations is associated with losses due to enhanced coupling to other available lower quality modes as is depicted by the corresponding $\mathcal{C}_{11}$ measure. Even a small inclusion, relative to the wavelength ($\lambda/n_c \sim 0.43R_0$), may produce a significant change in the far-field profile. This result is in agreement with our results from Chapter 3 as well as those of [38] where a perturbation treatment of the annular cavity is conducted.

Figures 4.14(a)-(c) present different far-field profiles at the specific locations indicated in Fig. 4.13. The far-fields switch from a narrow peak emission near $\phi = \pi$ at small r_0 to a broader, yet directional, peak in the forward direction, $\phi = 0$, at $r_0/R_0 =$



(a) Delay (b) Contrast

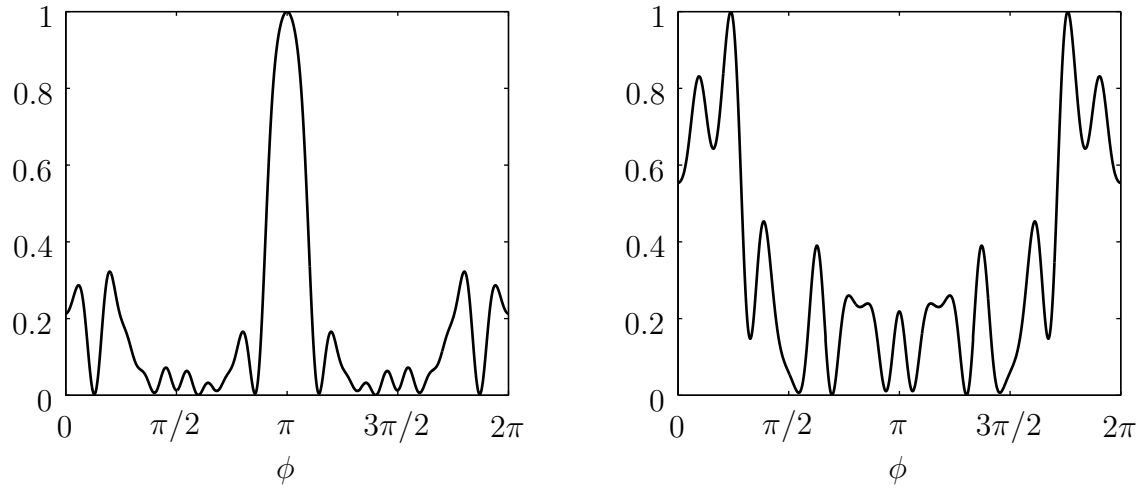
Fig. 4.13 (a) Delay value for mode $(11, 1)$ with respect to parameter r_0 ($(d + r_0)/R_0 = 0.55$). (b) Contrast measure in the far-field ($r \to \infty$) and in the near-field ($r = R_0$). According to the contrast measure, the near-field WGM aspect is unaffected by the inclusion while the far-field gets strongly modified. Blue circles mark evaluation positions of the far-field patterns of Fig. 4.14.

0.165. This is the region where the asymptotic contrast measure $\tilde{\mathcal{C}}_m(\infty, d)$ is close to 1, indicating indeed that the field has lost uniformity. In contrast, for smaller or larger r_0 outside this region, one tends towards uniformity both in the near- and the far-field ($\mathcal{C}_m(R_0, d) \simeq \tilde{\mathcal{C}}_m(\infty, d) \simeq 0$). For case (c) in Fig. 4.14, we observe an intermediate far-field profile with a carrier-envelope behaviour evolving towards uniformity.

4.2.1 Dominant structures of phase space

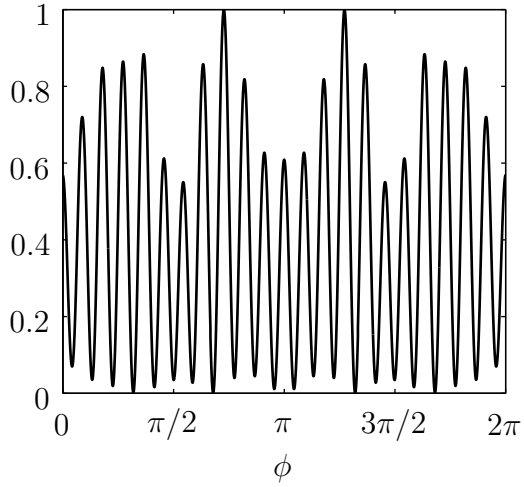
An often used approach to describe the behaviour of light in a cavity is to consider its geometrical or ray optics limit [89, 147]. This picture stems from a semi-classical Ansatz applied to the wave equation and results in equations of motion expressing the evolution of wavefronts from one point in time to another. Although the complete wavefront solution fails for systems with classical chaotic trajectories [140], it may prove rewarding precisely to focus on the propagation directions of wavefronts (the *Eikonal* equation: the gradient of constant valued wavefronts). This picture produces *photonic ray* bundles that propagate in the cavity as particles in a billiard [14].

The dynamics of the billiard systems is best represented on a *Poincaré section of phase space*, or, for the sake of simplicity, *phase space* in the remainder of this work. The phase space for billiard systems is constructed from the records of (normalized) arc



(a) (0.520, 0.030)

(b) (0.385, 0.165)



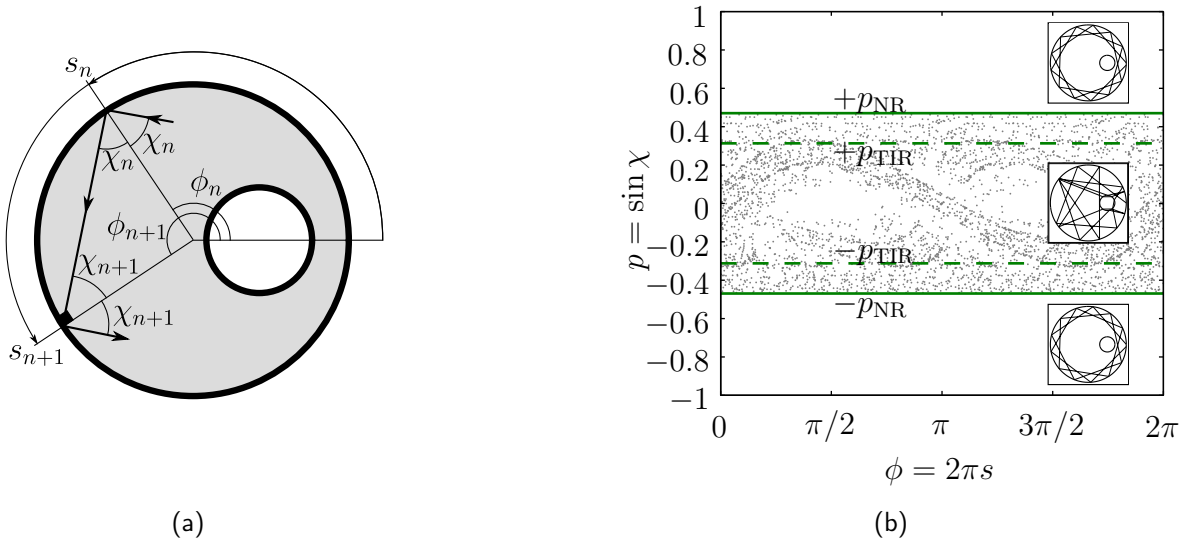
(c) (0.148, 0.402)

Fig. 4.14 Normalized far-field profile for three sets of parameters $(d/R_0,\ r_0/R_0)$.

length positions s and sine of incidence angles $p = \sin\chi$ of consecutive reflections on the external boundary, Fig. 4.15. These are *Birkhoff canonical coordinates* [16] of phase space (area preserving coordinates). The coordinate sets that are more often used for convex cavities are $(\phi,\, p)$ where ϕ is an angular position measured from an origin located inside the cavity. The specific case of the annular cavity is characterized by a well-separated phase space, Fig. 4.15(b), which consists of dynamical domains bounded by the limits

$$p = \pm p_{\rm NR} = \pm(d + r_0)/R_0 \ \forall\, \phi \quad . \tag{4.17}$$

For $|p| > p_{\rm NR}$, ray trajectories are strictly of the whispering gallery type: the caustic radius $|pR_0|$ of these trajectories is larger than the maximal radial extent of the inclusion, $d + r_0$. As such, the $|p| > p_{\rm NR}$ regions will be referred to as the *regular domains*.



(a) (b)

Fig. 4.15 (a) Representation of the canonical coordinates $(s, p = \sin\chi)$ in configuration space and (b) in phase space. The reflection of rays on the exterior boundary is specular while the internal disc inclusion permits transmission according to Fresnel coefficients [29]. Consecutive impact positions on the exterior boundary are recorded in phase space. For clarity, only trajectories within the NR region are displayed. The trajectories in the regular domain have a constant p momentum and would appear as horizontal sequences of markers in phase space.

On the other hand, the $|p| < p_{\rm NR}$ region supports only trajectories that intersect the inclusion. The immediate consequence is the random appearance of this part of phase space which is then referred to as the *Non-Regular domain* (NR). Most trajectories in the NR region are chaotic, with the exception of *marginally unstable periodic orbits* (MUPOs) [3, 4] forming continuous sets of periodic orbits closely avoiding the internal inclusion. Interestingly enough, as we will see shortly, our attention is set on trajectories that *are not* MUPOs.

At this point, the cavity is open only to rays reaching the *emission domain*, that is, trajectories having a momentum $|p| < p_{\rm TIR}$ where

$$p_{\rm TIR} = n_o/n_c \tag{4.18}$$

is the *Total Internal Reflection* (TIR) limit, mentioned earlier. For $p_{\rm NR} > p_{\rm TIR}$, only the NR domain has access to the emission region, while for $p_{\rm NR} < p_{\rm TIR}$, both regular and non-regular domains may contribute to the exiting trajectories. Because a whispering gallery trajectory formed by classical rays retains its angular momentum and corresponding semiclassical momentum (see Chapter 1)

$$p_m = \frac{m}{n_c k R_0}\ , \tag{4.19}$$

photons stored in this dynamical structure will either rapidly leave the cavity for $p_m < p_{\rm TIR}$, or will forever remain inside for $p_m > p_{\rm TIR}$. Regarding the objective of inducing

a non-uniform emission from a high quality whispering gallery type trajectory, the classical billiard picture of the cavity is a failure.

However, we know from experience (Section 4.1) that high delay WGMs do not remain confined in the cavity forever: albeit high, the associated delay is finite. Either WGMs radiate out to the exterior, or are transformed into poorly contained lower angular momentum values via a scattering process. It is tempting to transpose the loss by angular momentum transition to a classical transport mechanism towards the NR region. This is further suggested by the wave calculations that indicate a broadening of the ridge as $d + r_0$ increases (Fig. 4.3), i.e. increasing contributions of more angular channels, meaning, classically speaking, an increase of the size of the NR region. There exists a non-zero probability that a high lying WGM in phase space 'tunnels' through to the NR region. Bearing this idea in mind, we pursue our investigation.

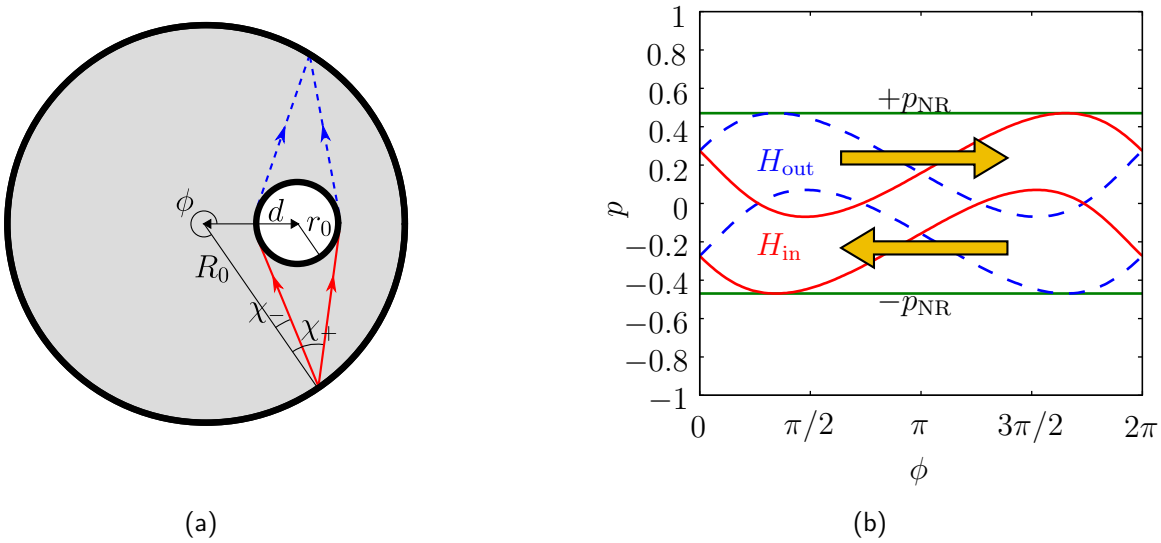
The dynamics in the NR region is governed by the trajectories impinging on the inclusion. These trajectories belong to a well-defined subdomain of the NR region [124]. We call this domain, the *incoming hole scattering region*, H_{in} (Fig. 4.16). This subdomain of phase space is bounded by

$$p_{\pm} = \sin\chi_{\pm} = -\frac{d}{h}\sqrt{1-\frac{r_0^2}{h^2}}\sin\phi \pm \frac{r_0}{h}\sqrt{1-\frac{d^2\sin^2\phi}{h^2}} \tag{4.20}$$

where $h^2 = R_0^2 + d^2 - 2R_0 d\cos\phi$. Likewise, we obtain the domain in phase space where the trajectories end up after having been scattered by the inclusion. This domain will be called the *outgoing hole scattering region*, H_{out}, and is a reflection of H_{in} relative to the $p = 0$ axis. This property stems from the time reversal dynamics in billiards.

In phase space, trajectories follow the regular dynamics of the circular billiard until they reach H_{in}. The overall dynamics in the NR region of phase space then consists in a conveyor-belt-like motion towards the H_{in} subdomain (except for MUPOs) and in mixing from H_{in} to H_{out} (Fig. 4.16(b)). Note that the trajectories in H_{in} *always* exit in H_{out}, even if the inclusion is absent: setting $n_h = n_c$ voids the effect of the inclusion, yet, the H_{out} region may still be computed.

If the classical particles are allowed to completely escape as they reach the rectangular emission domain E in phase space, bounded by the TIR limits Eq. (4.18), it is clear that the domain H_{out} provides the escape coordinates of trajectories initially inside H_{in}. This observation is especially useful if E is completely embedded in the NR dynamical region. In this case, trajectories initialized inside the region between p_{TIR} and p_{NR}



(a) (b)

Fig. 4.16 (a) Limits of the incoming scattered rays by the inclusion in configuration space (red arrows). The outgoing scattered rays (blue arrows) are obtained through time inversion (reversing the arrows) of the incoming trajectories. (b) Dynamical subdomains of phase space H_{in} (dashed blue limits) and H_{out} (plain red limits). Trajectories outside H_{in} keep their momentum p (orange arrows) until they reach H_{in} and exit through H_{out} with a different p value.

always escape through H_{out}. [4]

So far, we have obtained the following results:

- It is possible to isolate a parametric domain where the electromagnetic field remains strongly located on a WGM (*i.e.* high delay/quality factor) while exhibiting different non-uniform far-field profiles;
- The classical subdomain of phase space responsible for the escape of trajectories through internal scattering is well-defined and analytically known for the annular cavity.

The obvious question to ask next is: how are the wave results related to a strictly classical ray description of the cavity dynamics? Any success in this direction will not

[4] Even more, given the invertible *Poincaré application* $\mathcal{P}$ defining the mapping on the phase space, we may wish to identify the trajectories common to H_{out} and E that came from outside of E, say $\bar{E}$. That would define the region $\bar{E}\cap\mathcal{P}^{-1}\{H_{\mathrm{out}}\cap E\}$. The mapping of this domain, $\mathcal{P}\{\bar{E}\cap\mathcal{P}^{-1}\{H_{\mathrm{out}}\cap E\}\}$, then specifies the first escape coordinates of every trajectory leaving the cavity.

Note that, although H_{out} may not be found in all cavities, it is always possible to find a domain in E, say W, whose inverse mapping, $\mathcal{P}^{-1}\{W\}$, is in $\bar{E}$. The domain $\mathcal{P}\{\bar{E}\cap\mathcal{P}^{-1}\{W\}\}$ then contains the dominant features (first return map) of the far-field.

only lead to wave-particle correspondence[5], it will also help to design cavities having predictable emission profiles. To investigate this problem, we will first need to acquire a set of initial conditions that best represent the outcome of the dynamical tunneling from the main WGM. With this information in hand, numerical ray escape dynamics simulations will be undertaken and compared with those of full-wave simulations. The first instrument needed is a transformation that will map the wave information in coordinate space to phase space coordinates. This is discussed in the following.

4.2.2 Husimi distribution

The emission profile of the open cavity system in the ray picture is solely a matter of trajectories reaching the emission region $|p| < p_{\mathrm{TIR}}$. While strictly speaking this description does not allow whispering gallery trajectories with $p_m > p_{\mathrm{NR}} > p_{\mathrm{TIR}}$ to escape the cavity, taking into account the dynamical tunneling allow them to reach $|p| < p_{\mathrm{NR}}$. From there they get transported into the emission region through the H_{in}-H_{out} dynamics. The first objective is then to obtain a distribution of initial conditions emulating the phase space exit positions of tunneling trajectories from a WGM.

To do so, we shall rely on the Husimi quantum/wave distribution (see Appendix B),

$$F^H(s,p) = \frac{1}{2\pi\hbar} \left| \left\langle\ \beta_\kappa(s,p)\ \right|\ \psi\ \right\rangle \Big|^2 \tag{4.21}$$

where $\hbar/2 = 1/2 \times 1/nkR_0$ is the best achievable phase space area resolution on the surface of section in a cavity with a dielectric medium of refractive index n. $\left|\ \psi\ \right\rangle$ represents the electromagnetic field (to be defined in the following sub-sections) and $\left|\ \beta_\kappa(s,p)\ \right\rangle$ is a squeezed gaussian wavepacket. The use of this particular quantum distribution is justified by its correspondence to conventional probability distribution [10].

The squeezed state $\left|\ \beta_\kappa(s,p)\ \right\rangle$ in its s' coordinate representation of phase space is

$$\left\langle\ s'\ \right|\ \beta_\kappa(s,p)\ \Big\rangle = \beta_\kappa(s';s,p) = \left(\frac{\kappa}{\pi\hbar}\right)^{1/4} \mathrm{e}^{-\frac{(s'-s)^2}{(2\hbar/\kappa)}}\, \mathrm{e}^{i\frac{p}{\hbar}(s'-s)} \quad , \tag{4.22}$$

where the parameter κ sets the relative size of the dispersions $\Delta s_\kappa = \sqrt{\hbar/(2\kappa)}$ and $\Delta p_\kappa = \sqrt{\hbar\kappa/2}$. Since there is no *a priori* reason to use a different resolution for the s

[5]During the course of his research, the author found that it is actually far easier to find wave-particle *non*-correspondence, although the literature is filled with cases of *scarring* [59, 115, 75, 77, 160, 44, 120, 74], i.e. resonant modes bearing sometimes striking resemblance to classical trajectories found in phase space.

or the p coordinate, setting $\kappa = 2$ gives a square resolution to the phase space cell of area $\hbar/2^6$.

One also notes the great similarity between the kernel of the Husimi distribution Eq. (4.22) and the paraxial solution of the Helmholtz equation [148]. In a way, the Husimi distribution measures the wavefunction ψ using the best achievable confined beam at a finite wavenumber along a classical trajectory having impact coordinates (s, p).

To avoid any confusion concerning the coordinates (s, p), we restrict any representation of the Husimi distribution on a Poincaré section to the interior side of the exterior boundary (*i.e.* the phase space as seen in Fig. 4.15). We then define $\hbar = 1/n_c k R_0$.

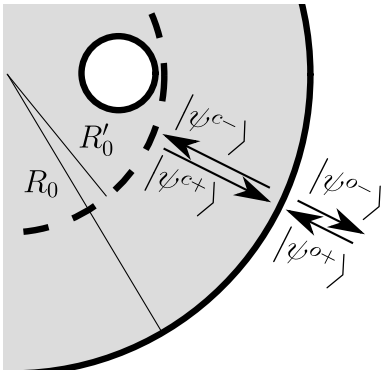


Fig. 4.17 Representation of incoming/outgoing waves relative to the external boundary.

Computing Eq. (4.21) on the Poincaré section with

$$\left\{ \begin{array}{rcl} \psi^{c+}(R_0,\phi) & = & \sum_m b_m H_m^{(1)}(n_c k R_0) \mathrm{e}^{im\phi} = \sum_m \tilde{\psi}_m^{c+} \mathrm{e}^{im\phi} \\ \psi^{c-}(R_0,\phi) & = & \sum_m a_m H_m^{(2)}(n_c k R_0) \mathrm{e}^{im\phi} = \sum_m \tilde{\psi}_m^{c-} \mathrm{e}^{im\phi} \end{array} \right. \tag{4.23}$$

as the incoming and outgoing wavefield with respect to the boundary (Fig. 4.17), we obtain the Husimi distribution (see Eq. (B.75))

$$F_{c\pm}^H(\phi, p) = \frac{1}{\sqrt{\pi\kappa\hbar}} \left| \sum_m \tilde{\psi}_m^{c\pm} \mathrm{e}^{-\frac{(p-m\hbar)^2}{2\kappa\hbar}} \mathrm{e}^{im\phi} \right|^2 \tag{4.24}$$

The Husimi distribution $F_o^H(s, p_o)$ computed on the exterior side of the cavity boundary is mapped on phase space by use of Snell-Descartes relation [62]

$$n_c p = n_o p_o, \qquad p \in [-1,\ 1] \quad . \tag{4.25}$$

Square resolution in phase space is also achievable for the field outside the cavity in the medium of index n_o by computing the Husimi distribution with $\kappa \equiv (n_c/n_o) \times 2$,

[6] The full range of s in phase space is of length 1, while the interval on p is of length 2 (from -1 to $+1$). We then demand that $\Delta s_\kappa/1 = \Delta p_\kappa/2$ for equal relative resolution and solving for κ yields $\kappa = 2$.

followed by proper p scaling using Eq. (4.25). This procedure entitles us to map in phase space the semi-classical origin of escaping fields or, alternatively, the entry domain of incoming fields. Using the same procedure as for interior waves,

$$\left\{ \begin{array}{rcl} \psi^{o+}(R_0,\phi) & = & \sum_m A_m H_m^{(2)}(n_o k R_0)\mathrm{e}^{im\phi} = \sum_m \tilde{\psi}_m^{o+}\mathrm{e}^{im\phi} \\ \psi^{o-}(R_0,\phi) & = & \sum_m B_m H_m^{(1)}(n_o k R_0)\mathrm{e}^{im\phi} = \sum_m \tilde{\psi}_m^{o-}\mathrm{e}^{im\phi} \end{array} \right. \tag{4.26}$$

we find the exterior Husimi distribution mapped on the Poincaré section through Eq. (4.25)

$$F_{o\pm}^H(\phi,p) = \frac{1}{\sqrt{\pi\kappa\hbar}} \left| \sum_m \tilde{\psi}_m^{o\pm} \mathrm{e}^{-\frac{\left(\frac{n_c}{n_o}p - m\hbar\right)^2}{2\kappa\hbar}} \mathrm{e}^{im\phi} \right|^2 \quad . \tag{4.27}$$

The Husimi distribution in the case of the annular cavity is then a superposition of $\left| \beta_\kappa(s,p) \right\rangle$ squeezed states in the p-coordinate representation centered on semiclassically quantized momenta $p_m = m\hbar$ (see Appendix B). This is a direct consequence of the angular momentum quantization of the wavefunction ψ.

Following this last observation and since the annular cavity phase space is separated in rectangular domains (Fig. 4.17), we split the wavefunction into two contributions: the *regular components* $\left| \psi^{\mathrm{R}} \right\rangle$, $|m| > p_{\mathrm{NR}}/\hbar$, and the *non-regular components* $\left| \psi^{\mathrm{NR}} \right\rangle$, $|m| < p_{\mathrm{NR}}/\hbar$. With this prescription, we finally obtain the distribution

$$\begin{array}{rcl} F^H(s,p) & = & \frac{1}{2\pi\hbar} \left| \left\langle \beta_\kappa(s,p) \right| \left. \psi^{\mathrm{R}} \right\rangle \right|^2 \\ & & + \frac{1}{2\pi\hbar} \left| \left\langle \beta_\kappa(s,p) \right| \left. \psi^{\mathrm{NR}} \right\rangle \right|^2 \\ & & + \frac{1}{\pi\hbar} \mathrm{Re}\left\{ \left\langle \psi^{\mathrm{R}} \right| \left. \beta_\kappa(s,p) \right\rangle \left\langle \beta_\kappa(s,p) \right| \left. \psi^{\mathrm{NR}} \right\rangle \right\} \ . \end{array} \tag{4.28}$$

In a strict classical limit, since the trajectories are either confined to the regular domain or to the non-regular domain of phase space, only one of the three terms composing the preceding expression would be non-zero. Hence, the last term of Eq. (4.28) is exclusively the result of wave dynamics (interference between the regular and non-regular waves) and will be discarded in our attempt to establish the semiclassical correspondence. This leaves the first two terms of Eq. (4.28) which we treat separately in the next sub-sections.

4.2.3 Initial conditions for ray optics simulations

Following the iterative approach of the dynamics of the annular cavity described in Section 4.1, we decompose the total field inside the cavity $\left| \psi^c \right\rangle$ as a series of waves $\left\{ \left| \psi^{c\pm,(j)} \right\rangle \right\}$ originating from an initial wave $\left| \psi^{c-,(1)} \right\rangle$. This initial wave $\left| \psi^{c-,(1)} \right\rangle$

is scattered by an inner effective scattering matrix of the circular domain of radius R_0' giving rise to $\left|\ \psi^{c+,(1)}\ \right\rangle$, itself being transmitted to $\left|\ \psi^{o-,(1)}\ \right\rangle$ and reflected to $\left|\ \psi^{c-,(2)}\ \right\rangle$, thus starting a new cycle (see Fig. 4.18). Again, this iterative picture has to be understood as a wave process where no physical time appears. However this is very close in spirit to the classical iterative procedure on the Poincaré section.

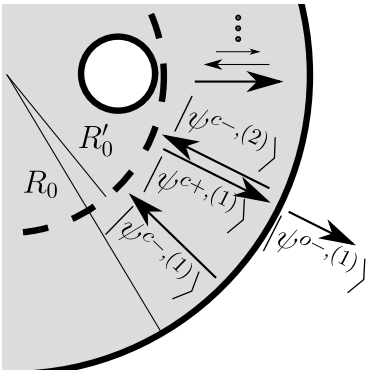


Fig. 4.18 Decomposition of the field in a series of iterates.

As in sub-section 4.1.2, we assemble a pure even symmetric WGM with angular momentum $m_0 = 11$ as an initial state $\left|\ \psi^{c-,(1)}\ \right\rangle$ inside the annular domain $R_0' < r < R_0$. The inclusion parameter $d + r_0$ is set to $0.55R_0$ so that the conditions for an anisotropic field emitting WGM are favourable. We may again focus solely on a single iteration description of the field.

With respect to Eq. (4.24), the $\left|\ \psi^{c-,(1)}\ \right\rangle$ state appears in phase space as two gaussian functions with maximum values at $p = \pm m_0\hbar$, the semi-classical momentum values of clockwise and counter-clockwise rotating WGM. According to the preceding discussion, the partial wave scattered by the inner virtual boundary at R_0' is then split into its regular and non-regular angular momentum components. Because the near-field is dominated by the main $|m| = m_0$ field components, the projection $\left|\left\langle\ \beta_\kappa(s,p)\ \right|\ \psi^{c+,(1),\mathrm{R}}\ \right\rangle\Big|^2$ is only slightly different from the Husimi distribution obtained with $\left|\ \psi^{c-,(1)}\ \right\rangle$. This is not surprising as we chose a parameter set that affects only weakly the near-field behaviour of the $(11, 1)$ mode. On the other hand, the non-regular components of the scattered state, $\left|\ \psi^{c+,(1),\mathrm{NR}}\ \right\rangle$, reveals a Husimi distribution sitting directly in the classical H_{out} region (Fig. 4.19(a) for an example).

Obtaining a Husimi distribution near the H_{out} region is a sign that escaping the main $|m| = m_0 = 11$ angular components through scattering (angular momentum transfer or 'dynamical tunneling' found in [53, 45, 146, 11, 13, 165] to cite a few) occurs preferably around the H_{in} region, especially at values of p near p_{NR}. Therefore, inspired by the Husimi distribution of the initial wave, we distribute the density of initial conditions for the classical ray simulations inside the H_{in} region according to a decreasing Gaussian

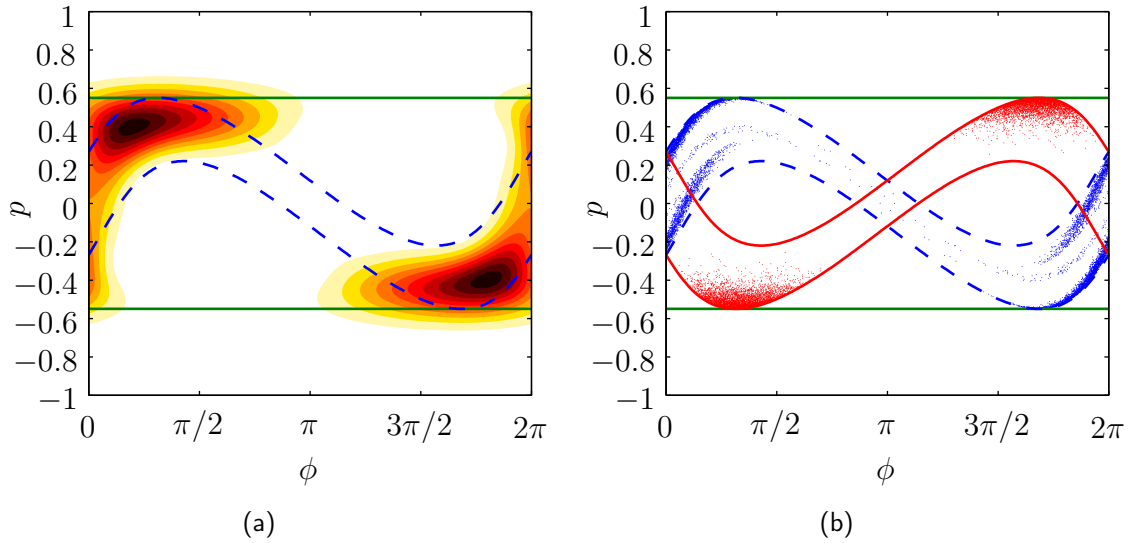


Fig. 4.19 (a) Representation in phase space of $\left|\left\langle\ \beta_\kappa(s,p)\ \right|\ \psi^{c+,(1),\mathrm{NR}}\ \right\rangle\Big|^2$ obtained after inner scattering from the initial state $\left|\ \psi^{c-,(1),\mathrm{NR}}\ \right\rangle$; $(d+r_0)/R_0 = 0.55$, $r_0/R_0 = 0.165$ and $kR_0 = 4.5$. The classical H_{out} region is shown as well as the p_{NR} limits (straight horizontal lines). The Husimi distribution resulting from the scattering by the inner virtual boundary falls within the H_{out} limits. This is to be compared with (b) where initial conditions inside H_{in} (red dots) and their first iteration to H_{out} (blue dots) are displayed.

distribution from $|p| = p_{\mathrm{NR}}$ to 0, as though they arose in the NR through dynamical tunneling. In a sense, this procedure is a sort of first order transition model where the perturbative effect is seeded proportionally to a large zeroth order distribution. An example of this distribution, corresponding to the parameter set under study, appears in Fig. 4.19(b) (red dots). The first iterate of the initial conditions (blue dots) fall inside H_{out} with a higher density right where the Husimi distribution is the largest. This observation in turn adds credibility to our choice of initial condition distribution.

4.2.4 Wave and classical simulations in phase space

Turning to the classical simulation again, we define an escape rule that differs from the simple step-function discussed in Section 4.2.1. The transmission outside the cavity does not happen through a binary mechanism: the trajectories trapped inside the cavity lose a fraction of their intensity at each boundary reflection. Also, instead of using pure Fresnel reflection and transmission coefficients [29], we allow for a fraction of the trajectory's intensity to escape *at every contact* with the Poincaré section according to a continuous k-dependent transmission coefficient $T(p)$ derived by Hentschel and Schomerus in [61]. This transmission coefficient is closely related to our discrete transmission model Eqs (4.11)-(4.12) (see also Fig. 4.10). We could have also used the

curved interface model derived by Snyder and Love [136] with similar results [7] (Fig. 4.20 for an illustration).

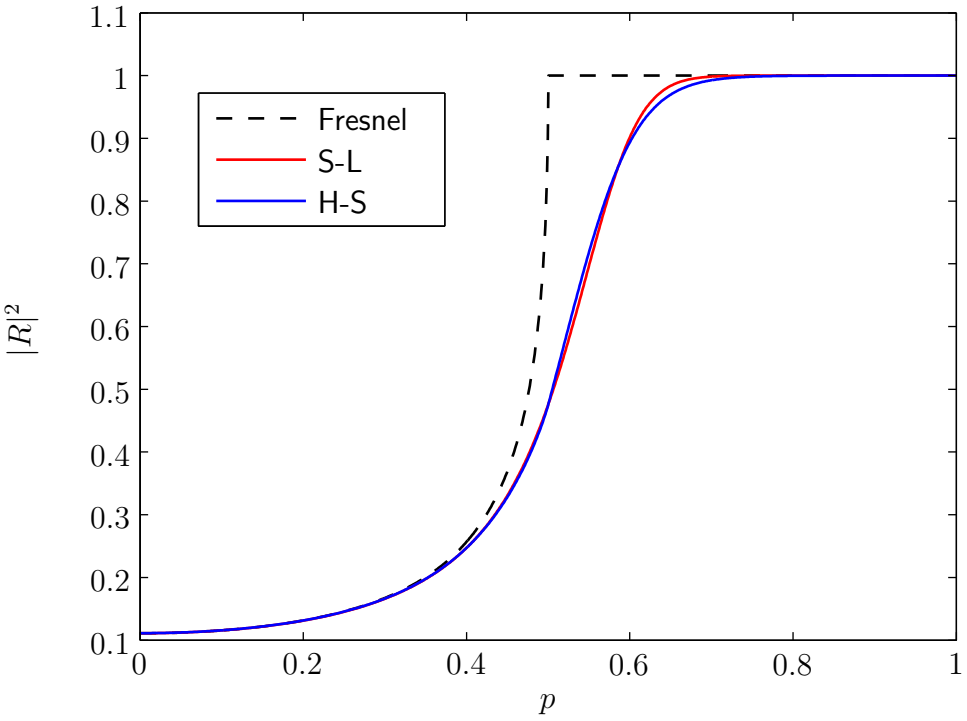


Fig. 4.20 Reflection coefficients using the infinite flat interface model (Fresnel), locally curved interface Eq. (4.29) inspired from Snyder and Love (S-L) [136] (curvature radius $\rho = 1$) and modified Fresnel laws for dielectric cavities of Hentschel and Schomerus (H-S) [61] (cavity radius $R_0 = 1$). This illustrative computation is for an incidence medium of refractive index of value 2, a transmission medium of index 1 and a wavenumber $kR_0 = k\rho = 15$.

The n-th impact position of a trajectory j on the Poincaré section is then completely defined by (s_n^j, p_n^j, I_n^j) [3] where I_n^j is the remaining intensity after $n \geq 0$ impacts with the boundary. A trajectory is assumed lost when its intensity after N_j rebounds becomes arbitrarily small relative to its initial value, $I_0^j = 1$. Note that the choice to distribute the initial conditions in phase space according to a prescribed Gaussian distribution is equivalent to a uniform distribution of initial conditions weighted with a Gaussian distribution of intensities.

[7] We have generalized the results derived in [136]. Especially for the reflection coefficient, we obtain

$$R(\chi) = \frac{in_1 \cos\chi - n_2 \left[\frac{\nu+1/2}{n_2 k\rho} - \frac{H_{\nu+1}^{(1)}(n_2 k\rho)}{H_\nu^{(1)}(n_2 k\rho)} \right]}{in_1 \cos\chi + n_2 \left[\frac{\nu+1/2}{n_2 k\rho} - \frac{H_{\nu+1}^{(1)}(n_2 k\rho)}{H_\nu^{(1)}(n_2 k\rho)} \right]} \tag{4.29}$$

where the refractive index n_1 is for the incidence medium, n_2 for the transmission medium, ρ is the local curvature radius and $\nu = \sqrt{1/4 + n_1^2 k^2 \rho^2 \sin^2\chi}$.

Trajectories are also allowed to split at the inclusion boundary, hence giving rise to multiple reflected and transmitted rays. This property results in star-like emission from the inclusion when a fraction of an impinging trajectory is transmitted inside the inclusion and gradually loses intensity at each following impacts. Again, the simulation of the trapped trajectory eventually comes to an end as the ray intensity reaches some arbitrary small value.

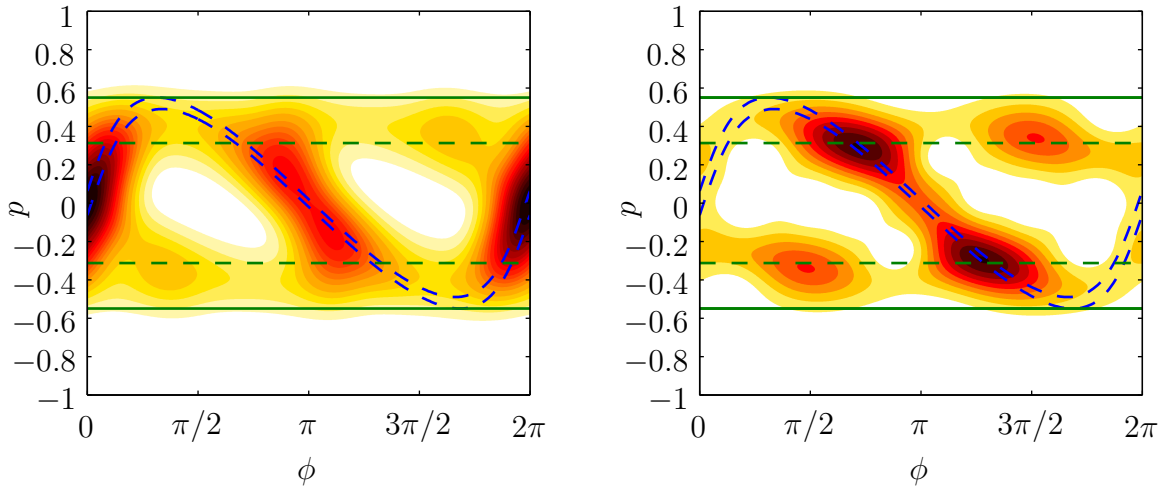
To compare the classical and wave dynamics of a characteristic mode with respect to their emission properties, we record the positions in phase space of the escaping intensity $\{T(p_n^j)I_n^j\}$ for all J trajectories. We then smooth out the recorded transmitted intensities with a Gaussian function having an effective area $\Delta s_\kappa \Delta p_\kappa = \hbar/2 = 1/(2\,n_c k R_0)$ in phase space,

$$I_{\mathrm{G}}^{\mathrm{T}}(s,p) = \sum_{j=1}^{J}\sum_{n=1}^{N_j} T(p_n^j) I_n^j \frac{1}{\pi\hbar} \mathrm{e}^{-\frac{(s_n^j-s)^2}{2\Delta s_\kappa^2} - \frac{(p_n^j-p)^2}{2\Delta p_\kappa^2}} \quad . \tag{4.30}$$

This procedure has the objective of emulating the finite resolution of the Husimi distribution. Of course, the overall ray dynamics leading to transmission remains classical and does not take into account any phase information. The smoothing process simulates only the effect of a measurement uncertainty at the emission stage and does not affect the deterministic motion of rays inside the cavity.

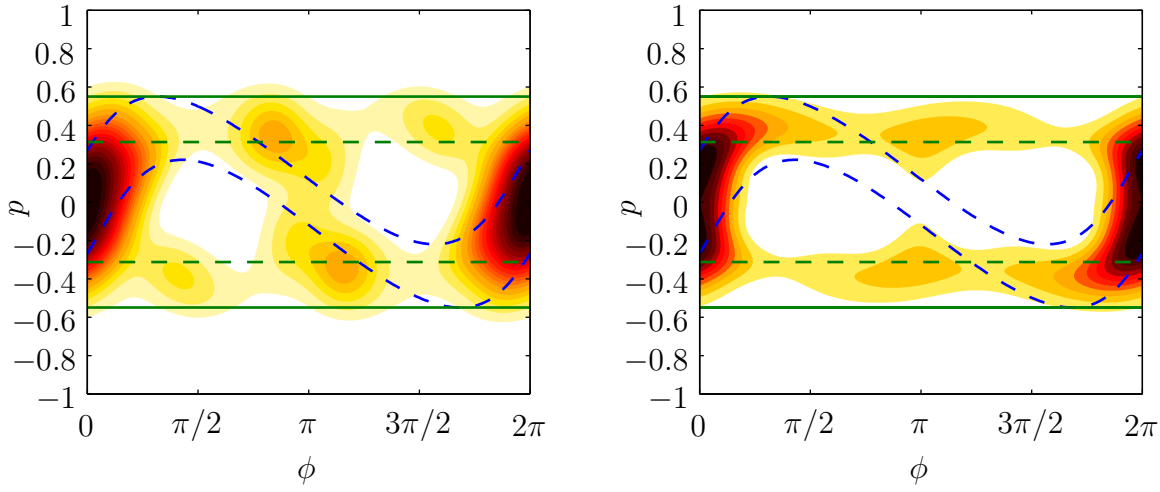
The wave emission measurements for mode $(11,1)$ [8] are reported in phase space using the wave $\left|\ \psi^{o-}\ \right\rangle$ (see Fig. 4.17 and the description in the corresponding sub-section leading to Eq. (4.27)). Because of the rapid change of behaviour from sharp directional emission around $\phi = \pi$ to a broader pattern around $\phi = 0$, we especially focus on the parameter values corresponding to markers (a) and (b) highlighted in Fig. 4.14. The distribution in phase space obtained from classical and wave simulation are displayed in Fig. 4.21.

[8] Actual characteristic modes obtained by the diagonalization of the delay matrix are used here, not the partial fields from the iterative model.



(a) Ray, $r_0/R_0 = 0.030$

(b) Wave, $r_0/R_0 = 0.030$



(c) Ray, $r_0/R_0 = 0.165$

(d) Wave, $r_0/R_0 = 0.165$

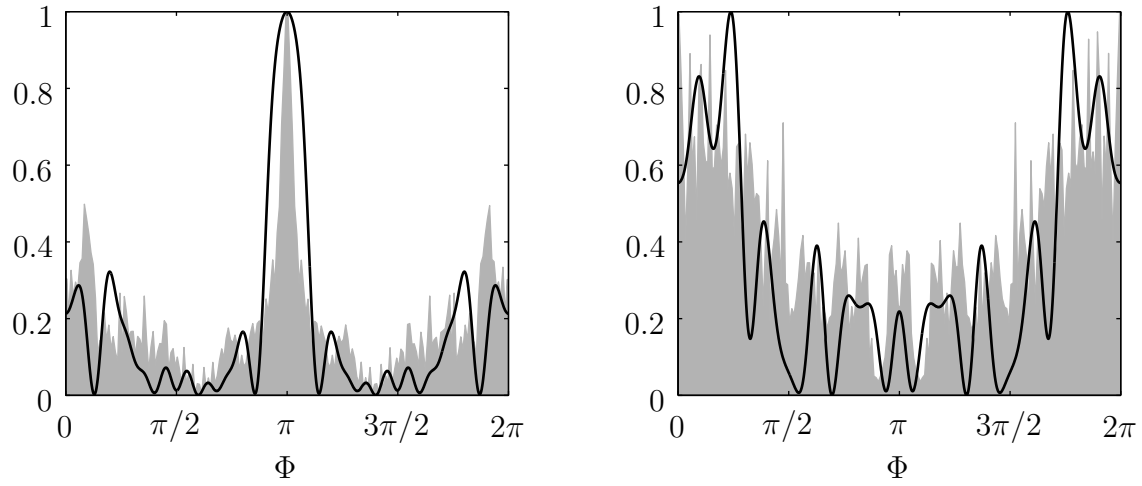
Fig. 4.21 Positions in phase space of the escaping rays/field from the non-regular region; (a)-(c) Gaussian-smoothed results from ray optics simulations and (b)-(d), outgoing Husimi distributions obtained from wave simulations for the resonant mode $(11, 1)$. The radius of the inclusion r_0 is set to $0.03R_0$ for the top figures and to $0.165R_0$ for the bottom ones, while parameter $d + r_0$ is kept constant at $0.55R_0$. Although classical and wave results appear to agree well on the distribution peaks for parameter value $r_0 = 0.165R_0$ (c)-(d), the same does not seem to hold at a smaller inclusion size (a)-(b). The inability of the wave to resolve the thin $H_{\text{in}}/H_{\text{out}}$ structures may be the cause. Note however that the 'conveyor belt' motion, Fig. 4.16, is easily identified by the sequence of spots in (b): a small inclusion may not cause the field to be strongly diverted into H_{out}, yet, it follows the conveyor belt within this resolving power.

Results from classical and wave simulations appear to agree especially well in the case of the larger inclusion position but seem to differ on the Poincaré section at smaller radii. This being said, classical interpretation is not completely lost at small r_0. As stated in sub-section 4.2.1, all trajectories entering H_{in} exit through H_{out}. The problem here is that, while the H_{in} region may be efficient at grasping some part of the WGM field, it may still be too thin to be efficiently resolved by the wavefield. In the case of small defects it seems that most of the trajectories follow the conveyor belt (see Fig. 4.21(b)) and slowly get drained out of the cavity. For instance, this explains the presence of intense 'rebound' spots located at $\phi = \pi \pm \pi/2$ in Fig. 4.21(b), and around $\phi = \pi$ in Figs 4.21(c) and (d). Similar Husimi distributions were found in [62] but underlying classical structures (H_{in} and H_{out} domains) were not identified.

Finally we compute the classical far-fields obtained by incoherently summing all the trajectory intensities propagating towards a common far-field sector. The far-field angle Φ is easily computed for trajectories escaping the circular boundary of the disc cavity,

$$\Phi = \phi - \chi_{\text{o}} \tag{4.31}$$

where ϕ is the angular origin of the escaping ray on the boundary and χ_{o} is the final refracted angle with respect to the normal vector on the exterior side of the circular boundary. The classical far-field is computed first by distributing the trajectories into N equal size far-field angular bins and then by summing up the trajectories' intensity sector-wise.



(a) (0.520, 0.030) (b) (0.385, 0.185)

Fig. 4.22 Far-field patterns from the classical simulations discussed in this Section (gray areas) and from numerical wave simulations (black curves) for two of the three sets of parameters $(d/R_0,\ r_0/R_0)$ used in Fig. 4.14. The classical far-fields are obtained by the distribution of 1.3×10^5 emitted trajectories over $N = 200$ angular bins.

To obtain the classical far-fields, the parameter sets of Fig. 4.14 are used for the sake of

comparison with known wave results. The initial values for the classical rays simulations are chosen with the technique presented earlier (see Fig. 4.19(b)). Classical results are shown in Fig. 4.22 and agree quite well with the full wave simulations. Although the near-fields do not always completely agree (see Fig. 4.21), it seems that the far-fields of wave simulations may be reproduced by an appropriate weighted subset of classical rays emerging from the H_{out} region of phase space.

Let us summarize once again the assumptions used and results obtained so far.

- Given a cavity with high delay WGMs (*i.e.* the bulk of the cavity is a disc);
- That this cavity encloses a low quality internal scatterer (*i.e* no sharp resonances in the internal scatterer alone; phase space is composed of regular regions and of a 'chaotic' domain due to the internal scatterer): a displaced 'hollow' disc in our case;
- And that we have access to geometrical parameter(s) of the inclusion: the displaced disc radius for instance.

The observations for a high delay WGM are that:

- There exists a control parameter range where anisotropic far-field and dominant WGM near-field coexist (Fig. 4.7);
  - Reaching the semi-classical caustic radius $m/n_c k$ of the perturbed WGM results in a deformation of the WGM indicating the loss of the high delay value. The semi-classical caustic radius defines an upper bound for the control parameter range (see Figs 4.5-4.6);
  - The emergence of anisotropic far-field from a high delay WGM can be approximately described by a single internal scattering model in opposition to the usual potential barrier tunneling phenomenon. As a control parameter is changed, the probability of internal scattering causing the anisotropic far-field eventually overruns the potential tunneling probability. The turning point happens as the two probabilities cross over: this defines a lower bound for the parametric range (see Fig. 4.12);
- In the control parameter range, the use of a subset of the chaotic domain in phase space, dependent on the choice of inclusion parameters, can be used to retrieve the approximate far-field behaviour of the high delay WGM;

– An appropriate choice of weighted initial values in the entry subset (H_{in}) results in a first iterate distribution resembling that obtained by the single iteration wave model (Fig. 4.19);
– While the near-field of the wave and classical simulations may not always agree (Fig. 4.21), the far-field can be well represented by classical means alone (Fig. 4.22).

We stress again that all the phenomenological models developed do not take into account any precise value of the resonant wavenumber position. The models involve functions that vary smoothly over a range of wavenumbers much larger than the actual width of the resonance of interest. This is a considerable advantage for obtaining the far-field behaviour of very high delay WGMs having resonance widths much smaller than what numerical methods may be able to resolve.

4.3 Notes on coupled resonances

It was mentioned at the beginning of this Chapter that resonances may interact when their positions cross on the real wavenumber axis. We will seek an explanation of this phenomenon with a model based on resonant coupled-damped oscillators. Specifically, we will construct a solution following a procedure similar to the one used in Chapter 2 leading to an energy based description of the system.

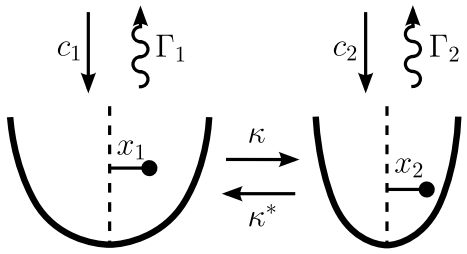


Fig. 4.23 Schematics of two coupled oscillators in their harmonic potential. These resonators possess different resonant frequencies, ω_1 and ω_2, different forcing terms, c_1 and c_2, and different environment induced damping coefficients, Γ_1 and Γ_2.

The dielectric cavity system in its scattering description may be viewed as a device providing a large collection of energy modes. At a given wavenumber, many modes coexist, but only a few are close to their resonant value. Although the analogy may not be complete, one can consider this system as a set of coupled classical oscillators, each having their own forcing strength c_j (input coefficient A_m^p), resonant frequency ω_j (wavenumber at the maximum delay), and damping (maximum delay), Γ_j, ordered as

$\Gamma_1 < \Gamma_2 < \Gamma_3 \ldots$. Under (normalized) external excitation, we focus on the amount of total energy shared by the oscillators.

A non-dimensional equation for a system of two (equal mass) coupled oscillators having normalised coordinate $x_j(t)$ can be written down simply as

$$\frac{d^2}{dt^2}\mathbf{x}(t) + \mathbf{\Gamma}\frac{d}{dt}\mathbf{x}(t) + \mathbf{\Omega}\mathbf{x}(t) = \mathbf{c}\mathrm{e}^{-i\omega\tau t} \tag{4.32}$$

with

$$\mathbf{\Gamma} = \tau \begin{pmatrix} \Gamma_1 & 0 \\ 0 & \Gamma_2 \end{pmatrix}, \qquad \mathbf{\Omega} = \tau^2 \begin{pmatrix} \omega_1^2 & \kappa \\ \kappa^* & \omega_2^2 \end{pmatrix}, \qquad \mathbf{x}(t) = \begin{pmatrix} x_1(t) \\ x_2(t) \end{pmatrix} \tag{4.33}$$

where the time scale τ is chosen as ω_1^{-1}, such that all parameters $(\mathbf{\Gamma}, \mathbf{\Omega}, \mathbf{c})$ and variables $(\mathbf{x}, t)$ are dimensionless. With this choice, keep in mind that the frequencies (ω, ω_j) and the damping coefficients (Γ_j) have a dimension of inverse time whereas the coupling term (κ) has the dimension of (inverse time)^2.

The steady-state solution to this differential system is readily obtained,

$$\mathbf{x}(t) = \left[-\omega^2\tau^2\mathbb{1} - i\omega\tau\mathbf{\Gamma} + \mathbf{\Omega}\right]^{-1}\mathbf{c}\mathrm{e}^{-i\omega\tau t} \quad . \tag{4.34}$$

In view of the open cavity system, we have essentially obtained an equivalent object to the scattering matrix: using the equation above, we can obtain the passive response of the coupled oscillators system to *any* harmonic excitation. Even if the internal mechanisms of the system are unknown (coupling, losses, resonant frequencies), we can still obtain the correct motion of the oscillators. The question that remains is of course to identify the characteristic forcing states of the system.

Much in the same line as what we have done for the extra energy stored in the cavity due to a unit power input, we consider two types of forcing (the basis of which is like the angular momentum basis),

$$\mathbf{c}^a = \begin{pmatrix} 1 \\ 0 \end{pmatrix}, \qquad \mathbf{c}^b = \begin{pmatrix} 0 \\ 1 \end{pmatrix} \quad . \tag{4.35}$$

Obviously, for $\kappa = 0$, these excitations result in the independent motion of the two oscillators. Since the overall motion of the oscillators is harmonic due to forcing, the *average energy* supported by oscillator $j = \{1, 2\}$ due to a forcing of type $\alpha = \{a, b\}$ is given by

$$\mathcal{E}_j^{\alpha\alpha} = \frac{1}{4}p_j^{\alpha *}p_j^{\alpha} + \frac{1}{4}\omega^2\tau^2 x_j^{\alpha *}x_j^{\alpha} = \frac{1}{2}\omega^2\tau^2 x_j^{\alpha *}x_j^{\alpha} \tag{4.36}$$

where p_j^α is the usual conjugate momentum to the position x_j^α. More generally, we define a complex average energy [9]

$$\mathcal{E}_j^{\alpha\alpha'} = \frac{1}{4}p_j^{\alpha*}p_j^{\alpha'} + \frac{1}{4}\omega^2\tau^2 x_j^{\alpha*}x_j^{\alpha'} = \frac{1}{2}\omega^2\tau^2 x_j^{\alpha*}x_j^{\alpha'} \quad . \tag{4.37}$$

The possible configurations are then gathered in an average energy matrix $\mathcal{E}$ enclosing all the available energy of the system,

$$\mathcal{E} = \begin{pmatrix} \mathcal{E}_{11} & \mathcal{E}_{12} \\ \mathcal{E}_{21} & \mathcal{E}_{22} \end{pmatrix} = \begin{pmatrix} \mathcal{E}_1^{aa} + \mathcal{E}_2^{aa} & \mathcal{E}_1^{ab} + \mathcal{E}_2^{ab} \\ \mathcal{E}_1^{ba} + \mathcal{E}_2^{ba} & \mathcal{E}_1^{bb} + \mathcal{E}_2^{bb} \end{pmatrix} \quad . \tag{4.38}$$

In this hermitian symmetric matrix, the off-diagonal terms are associated to the coupling energy. We wish to obtain a set of energies for which the coupling energy vanishes, so that all the energy is partitioned between oscillators 1 and 2 only. This demands an eigenvalue decomposition of the matrix $\mathcal{E}$. This is readily achieved, and two energy values are retrieved (configuration + and −)

$$\mathcal{E}_\pm = \frac{1}{2}\left(\mathcal{E}_{11} + \mathcal{E}_{22}\right) \pm \frac{1}{2}\sqrt{\left(\mathcal{E}_{11} - \mathcal{E}_{22}\right)^2 + 4|\mathcal{E}_{12}|^2} \tag{4.39}$$

with ($\tau = 1/\omega_1$)

$$\mathcal{E}_{11,22} = \frac{1}{2}\frac{\omega^2\omega_1^2}{|\Delta|^2}\left[\left(\omega^2 - \omega_{2,1}^2\right)^2 + \left(|\kappa|^2 + \omega^2\Gamma_{2,1}^2\right)\right] \tag{4.40}$$

$$\mathcal{E}_{12} = \kappa\frac{1}{2}\frac{\omega^2\omega_1^2}{|\Delta|^2}\left[\left(\omega^2 - \omega_1^2\right) + \left(\omega^2 - \omega_2^2\right) + i\omega\left(\Gamma_1 - \Gamma_2\right)\right] \tag{4.41}$$

$$\Delta = \left(\omega^2 - \omega_1^2 + i\omega\Gamma_1\right)\left(\omega^2 - \omega_2^2 + i\omega\Gamma_2\right) - |\kappa|^2 \quad . \tag{4.42}$$

Setting $\kappa = 0$ (uncoupled system), the energy of the oscillators are

$$\mathcal{E}_+\big|_{\kappa=0} = \frac{1}{2}\frac{\omega^2\omega_1^2}{\left(\omega^2 - \omega_1^2\right)^2 + \omega^2\Gamma_1^2}\ , \quad \mathcal{E}_-\big|_{\kappa=0} = \frac{1}{2}\frac{\omega^2\omega_1^2}{\left(\omega^2 - \omega_2^2\right)^2 + \omega^2\Gamma_2^2} \tag{4.43}$$

reaching a maximum of $1/2 \cdot \omega_1^2/\Gamma_{1,2}^2$ at $\omega = \omega_{1,2}$.

Since we are interested in the coupling of resonances, we set $\omega_1 = \omega_2$ in Eqs (4.40)-(4.42). This substitution leads to

$$\mathcal{E}_\pm = \frac{1}{4}\frac{\omega^2\omega_1^2}{|\Delta|^2}\left[\left(2(\omega^2 - \omega_1^2)^2 + \omega^2(\Gamma_2^2 + \Gamma_1^2) + 2|\kappa|^2\right) \pm\sqrt{\omega^4(\Gamma_2^2 - \Gamma_1^2)^2 + 4|\kappa|^2\left[2(\omega^2 - \omega_1^2)^2 + \omega^2(\Gamma_2 - \Gamma_1)^2\right]}\right] \tag{4.44}$$

[9] This procedure resembles the one of representing the operator $\hat{\mathcal{E}} = \frac{1}{2}\hat{p}^2 + \frac{1}{2}\omega^2\tau^2\hat{x}^2$ in a complete orthonormal basis $\{|\ a\ \rangle, |\ b\ \rangle\}$.

In the case where $|\kappa|$ is small,

$$|\kappa| \ll \frac{\omega^2(\Gamma_2^2 - \Gamma_1^2)}{2\sqrt{2(\omega^2 - \omega_1^2)^2 + \omega^2(\Gamma_2 - \Gamma_1)^2}} \qquad (\omega_1 = \omega_2) \ , \tag{4.45}$$

a condition found near the resonance, we may expand the square root in Eq. (4.44):

$$\sqrt{\cdot} \simeq \left[\omega^2(\Gamma_2^2 - \Gamma_1^2) + 2\left(\frac{2(\omega^2 - \omega_1^2)^2 + \omega^2(\Gamma_2 - \Gamma_1)^2}{\omega^2(\Gamma_2^2 - \Gamma_1^2)}\right)|\kappa|^2\right] \ . \tag{4.46}$$

In this approximation, the eigenvalues at the uncoupled resonance position $\omega = \omega_1$ are

$$\mathcal{E}_+ \simeq \frac{\omega_1^2}{2}\frac{\omega_1^2}{\left[\omega_1^2\Gamma_1\Gamma_2 + |\kappa|^2\right]^2}\left[\omega_1^2\Gamma_2^2 + \frac{2\Gamma_2}{\Gamma_1 + \Gamma_2}|\kappa|^2\right] \tag{4.47}$$

$$\mathcal{E}_- \simeq \frac{\omega_1^2}{2}\frac{\omega_1^2}{\left[\omega_1^2\Gamma_1\Gamma_2 + |\kappa|^2\right]^2}\left[\omega_1^2\Gamma_1^2 + \frac{2\Gamma_1}{\Gamma_1 + \Gamma_2}|\kappa|^2\right] \tag{4.48}$$

and it is verified that the uncoupled limits Eqs (4.43) are correctly recovered by setting $\kappa = 0$.

At $\omega = \omega_1$, the condition Eq. (4.45) reduces to

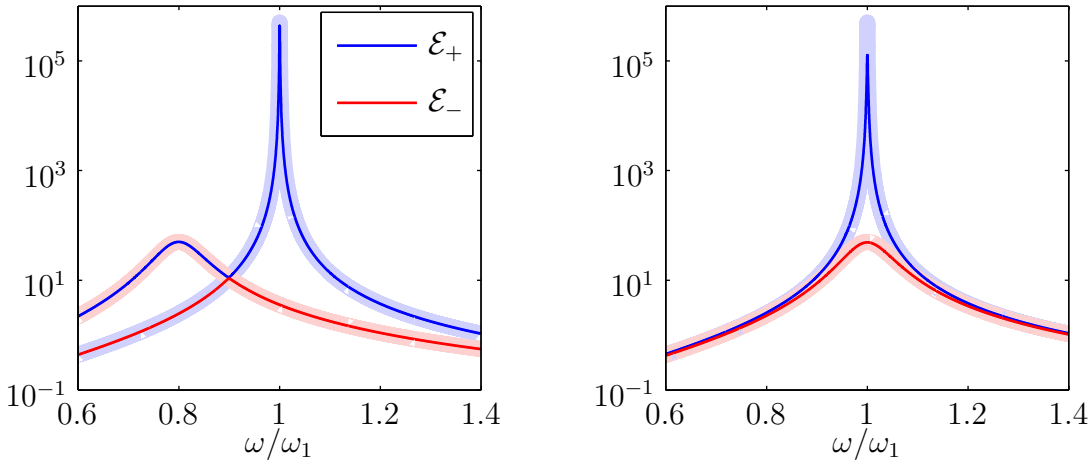
$$|\kappa| \ll \frac{\omega_1}{2}(\Gamma_2 + \Gamma_1) \quad . \tag{4.49}$$

It is instructive to compare the denominator of Eqs (4.47)-(4.48) with this condition on $|\kappa|$. For values of $\Gamma_2 \gg \Gamma_1$, it is possible to satisfy the condition on $|\kappa|$ while still having $\omega_1^2\Gamma_1\Gamma_2 \sim |\kappa|^2$. This corresponds to situations where the resonance positions remain roughly unchanged with respect to the uncoupled case, while the energy content however drops significantly.

We display on Fig. 4.24 results for two resonances having respectively $\omega_1 \neq \omega_2$ and $\omega_1 = \omega_2$. The parameters are chosen such that $\omega_1^2\Gamma_1\Gamma_2 = |\kappa|^2$. It is clearly seen that the main resonance at $\omega = \omega_1$ (blue line) loses energy compared to the uncoupled case (underlying pale blue line), the more so the closer the resonances are to each other: for $\omega_2 = \omega_1$, the loss in energy for the + configuration is almost an order of magnitude.

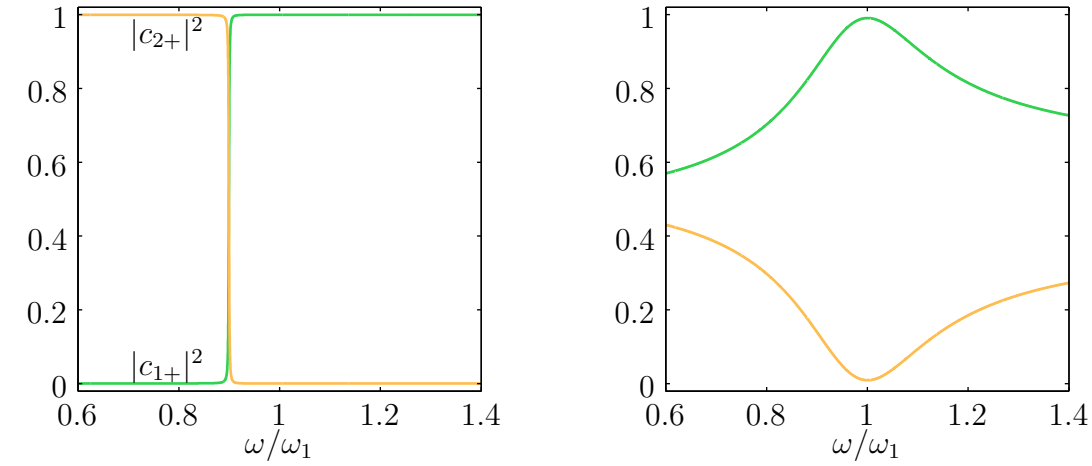
In its close-to-resonance part of the spectrum (either $\omega \sim \omega_1$ or $\omega \sim \omega_2$), the $\omega_1 \neq \omega_2$ case resembles that of the two independent oscillators system (see the forcing terms for energy level $\mathcal{E}_+$, Fig. 4.25). Although the coupling $|\kappa|$ may be 'large' with respect to the damping terms Γ_1 and Γ_2, the indirect losses due to coupling remain small because the response of the oscillator 1 at $\omega = \omega_2$ (as well as the response of the oscillator 2 at $\omega = \omega_1$) is weak.

The picture is different in the $\omega_1 = \omega_2$ case because of the $\omega_1^2\Gamma_1\Gamma_2 \sim |\kappa|^2$ condition. Focusing on oscillator 1, a strong forcing does not imply that it will get all the energy:



(a) $\omega_2/\omega_1 = 0.8$ (b) $\omega_2/\omega_1 = 1.0$

Fig. 4.24 Eigenvalues of $\mathcal{E}$, Eqs. (4.44), for parameters $\Gamma_1/\omega_1 = 10^{-3}$, $\Gamma_2/\omega_1 = 10^{-1}$ and $\kappa/\omega_1^2 = 10^{-2}$, i.e. $|\kappa|^2 = \omega_1^2\Gamma_1\Gamma_2$ and $|\kappa|/\omega_1^2 = 10^{-2} < (\Gamma_1 + \Gamma_2)/2 \simeq 5 \times 10^{-2}$. Thick pale blue and red curves serve as reference to the uncoupled oscillators energy, Eq. (4.43). Two configurations are presented: (a), non-resonant coupling; (b), resonant coupling. Note the color exchange of the $\mathcal{E}_\pm$ curves in (a): this is due to a local avoided crossing inherited from the adiabatic process of obtaining $\mathcal{E}_\pm$.



(a) $\omega_2/\omega_1 = 0.8$ (b) $\omega_2/\omega_1 = 1.0$

Fig. 4.25 Components of the eigenvector associated with the eigenvalue $\mathcal{E}_+$ for the resonance cases presented in Fig. 4.24. In both cases, at the uncoupled resonant frequency $\omega = \omega_1$, the forcing is almost completely on the first oscillator. Note the counterpart effect of the avoided crossing on the eigenvector components in (a).

the coupling term κ being large enough means that energy is shared between the two resonators. However, because of the larger damping Γ_2, the energy gained by oscillator

2 is also more easily drained, hence lowering the overall capacity of the system. From the point of view of the + configuration, oscillator 2 has a simple parasitic effect on oscillator 1.

Also, while the resonant coupling phenomenon affects strongly the + configuration, the − configuration only gets a small increment in containment power (see Fig. 4.24(b)). The reason for this is that the low damping Γ_1 of the first oscillator can't be exploited by oscillator 2 because the transferred energy keeps falling back into it due to the large coupling term.

We insist here that this phenomenon (resonant coupling between resonances) occurs because of a delicate balance between the coupling term κ and the damping coefficients $\Gamma_{1,2}$. On one hand, the coupling term must be near the damping coefficients' product ($|\kappa|^2 \simeq \omega_1^2\Gamma_1\Gamma_2$), and on the other, it still has to remain small with respect to their summation ($|\kappa| \ll \omega_1(\Gamma_1 + \Gamma_2)/2$). In these conditions, a low quality mode passing through a high quality mode will lower the overall containment power (quality) of the system.

We now return to the annular cavity system. We focus specifically on the 'abnormal' delay curve $r_0/R_0 = 0.10$ in Fig. 4.6. Looking at a semi-log graph of the maximum delay associated with mode $(11, 1)$, Fig. 4.26, a peculiar sinking is seen to occur at an early stage of the perturbation size, much before the limiting caustic radius at $d + r_0 = 0.76R_0$. This behaviour is identified by the red curve on Fig. 4.26. The computation of the delay spectrum at different values of d captures the motion of a second resonance across the main resonance $(11, 1)$, Figs 4.27(a)-(d). This secondary resonance is labeled $(5, 3)$ − even in reference to its homogeneous disc state. This observation identifies the abnormal aspect of the delay curve (Fig. 4.26) with the result of a resonant coupling.

With the results from perturbation theory, Eqs (3.62) and (3.117), we can model the expected natural delay spoiling curve as

$$\tau_{\text{mod}}(d;\, \alpha, \beta) = \frac{\tau(d=0)}{1 + \alpha\,[J_{11}(3.2 \times 4.5 \times d)]^{\beta}} \quad . \tag{4.50}$$

Assuming that the Bessel function has reached its exponential form, Eq. (A.54), this equation captures the appearance of the intended curve: a flat segment where the denominator is essentially 1, followed by a quick downward turn happening at $\alpha[J_{11}(3.2 \times 4.5 \times d)]^{\beta} \simeq 1$ [10], and finally, a straight segment having a constant slope controlled by β.

[10] A more quantitative evaluation would require the computation of the position of the maximum of the second derivative with respect to d.

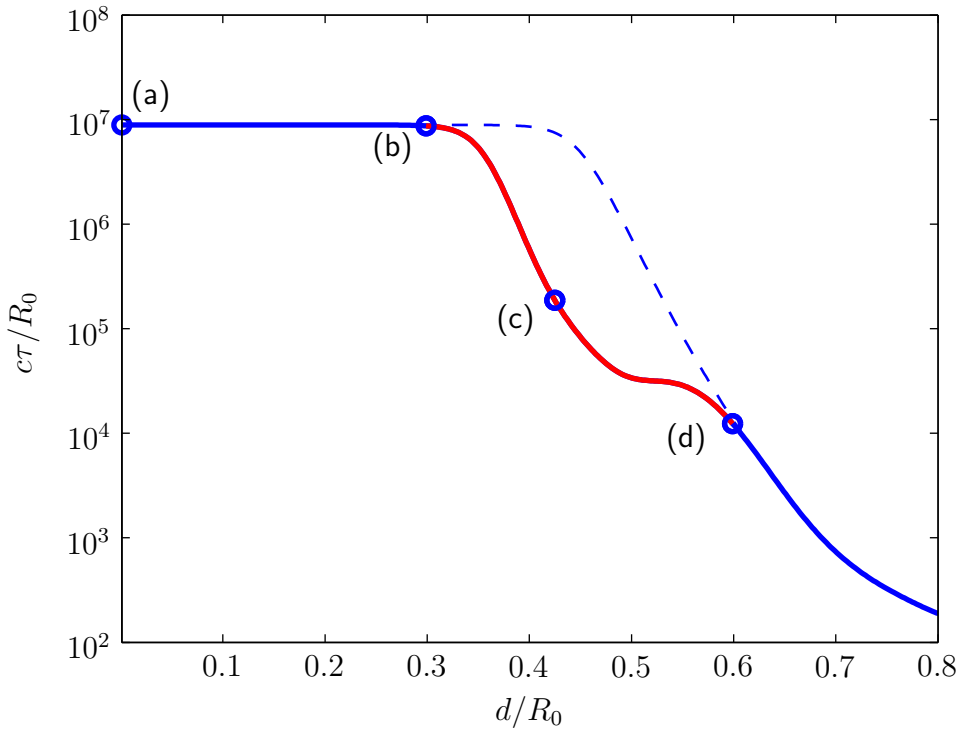
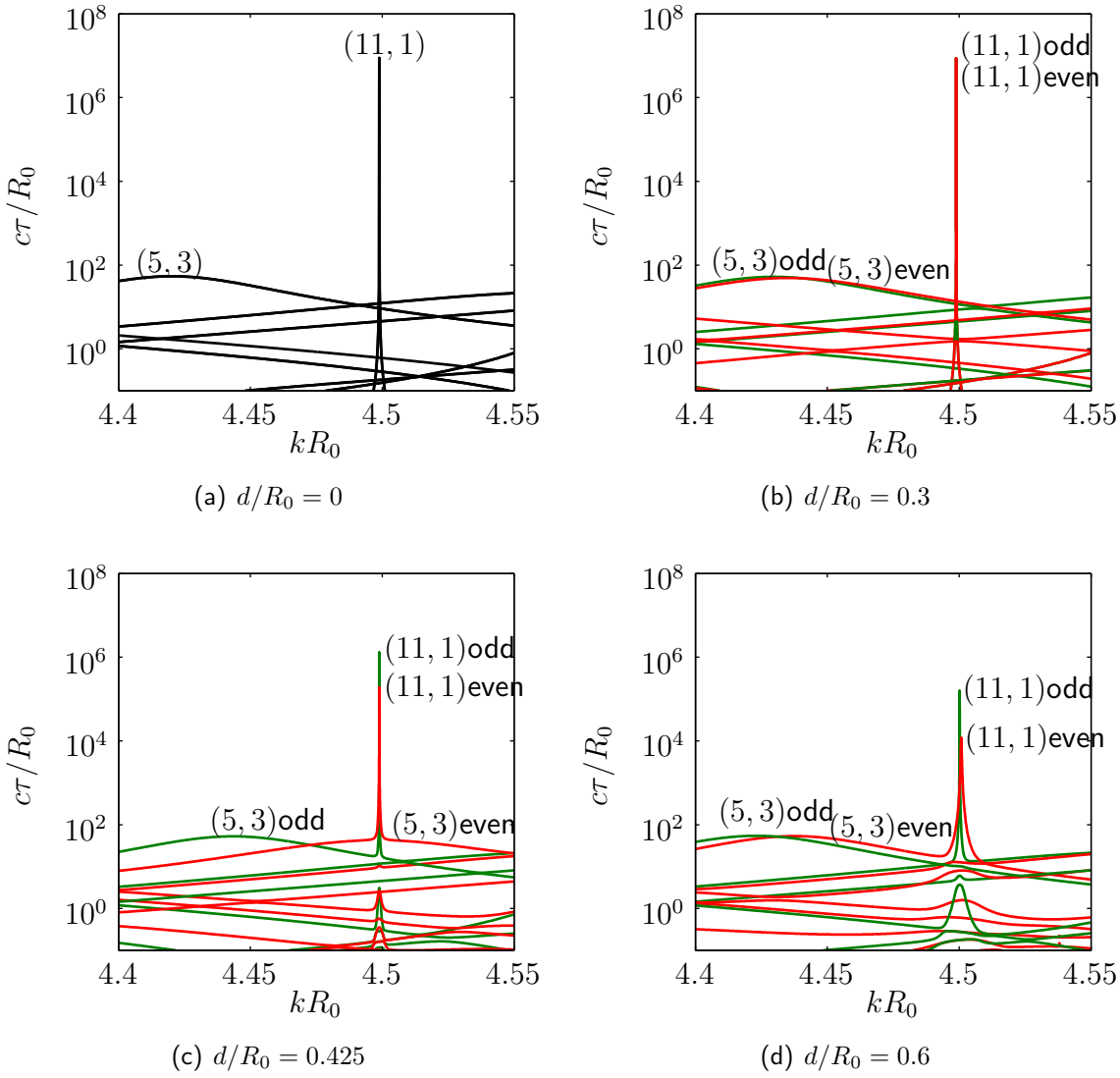


Fig. 4.26 Delay value at the peak of even mode $(11, 1)$. The semi-log graph reveals a premature fall of the delay at $d/R_0 \simeq 0.3$ and a recovery at $d/R_0 \simeq 0.6$ with respect to the monotonous delay spoiling caused by the exponentially increasing amount of field being diverted from angular momentum $m = 11$ to other channels. The markers indicate the positions at which the spectra of Fig. 4.27 are drawn. Also, the expected delay spoiling curve (dashed line) is presented (see Eq. (4.50)).

Expression (4.50) is fitted to Fig. 4.26 using a non-linear least square method [11] [107]. We used data over the range $d/R_0 = [0.62, 0.64]$. The data outside this range is unusable because it is strongly affected either by the proximity of resonance $(5, 3)$ or by the approach to the caustic radius. The parameters retrieved are $\alpha = 3.57 \times 10^6$ and $\beta_{\text{,}} = 2.8$. Interestingly, the value of β is not too far from the perturbative treatment value of 4 (see Eqs (3.62) and (3.117)). The curve computed using these parameter values is plotted in Fig. (4.26). This model curve also happens to settle close to the other 'normal' curves having $r_0/R_0 = \{0.01, 0.3, 0.4\}$ presented on Fig. 4.6.

We illustrate in Fig. 4.28(a) the data set of Fig. (4.26) with the baseline Eq. (4.50) removed. The resulting figure is compared to Fig. 4.28(b) presenting the value at the peak of $\mathcal{E}_+$ for different positions ω_2 of the secondary resonance. It is understood that the annular cavity undergoes a resonance coupling phenomenon similar to that found in coupled oscillators. The resonant coupling phenomenon described here is responsible for the high quality/high directional emission behaviour of the annular cavity as discussed

[11] The actual fitted function is the inverse of Eq. (4.50).



(a) $d/R_0 = 0$ (b) $d/R_0 = 0.3$

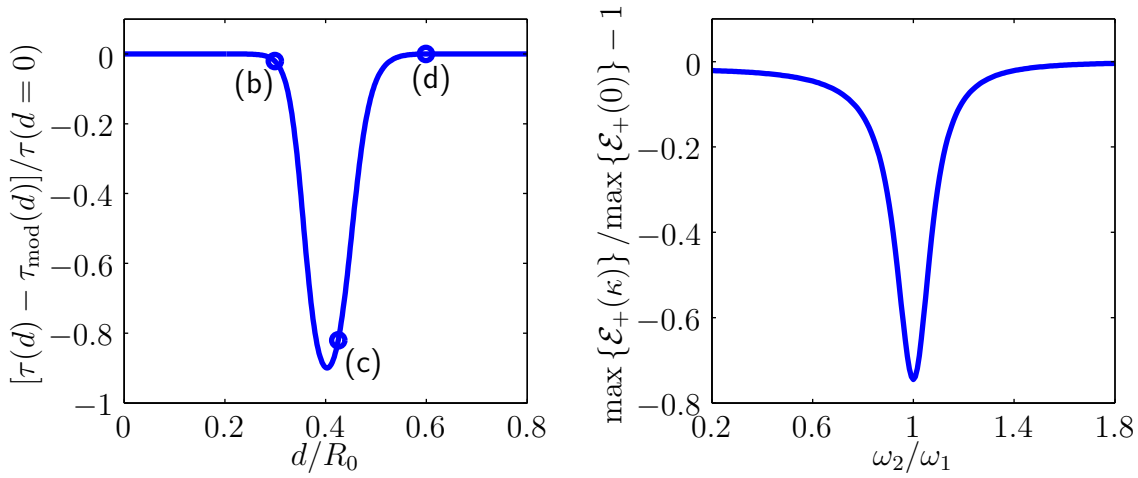
(c) $d/R_0 = 0.425$ (d) $d/R_0 = 0.6$

Fig. 4.27 Spectra for four values of the parameter d. Odd symmetry modes with respect to the Ox axis of the cavity (Fig. 4.1) appear in green, and even symmetry modes appear in red. The peak labeled $(5, 3)$even moves first across the main resonance $(11, 1)$ and nearly returns to its starting position as the parameter d is varied.

in [161].

The resonant coupling overtakes the normal delay spoiling obtained through the growth of the ridge in the scattering matrix. In a sense we may interpret the natural delay spoiling of a high quality mode as a case of *non*-resonant coupling with an infinite quantity of off-resonance modes (at a given wavenumber).

Although appealing for its theoretical interest, resonance coupling may become a problem when engineering robustness is a concern. As it appears, the hardly predictable



(a) Annular cavity

(b) Coupled oscillators

Fig. 4.28 (a) Corrected peak value of resonance $(11, 1)$ relative to the homogeneous disc peak value versus the deformation parameter d and (b) peak value of the energy $\mathcal{E}_+$ relative to the uncoupled scenario versus secondary resonance position ω_2. Markers on (a) point to Figs 4.27(b)-(d). Although we do not have direct control over the $(5, 3)$ mode resonant position, we may still force it to move across the mode $(11, 1)$ using the inclusion position d as a control parameter. The resulting effect is similar to that found in the coupled resonators system.

wandering of mid-size resonances due to the modification of a control parameter may lead to undue conclusions regarding the properties of a high quality mode. This obviously comes in opposition with our stated objective to control the output field of high quality modes.

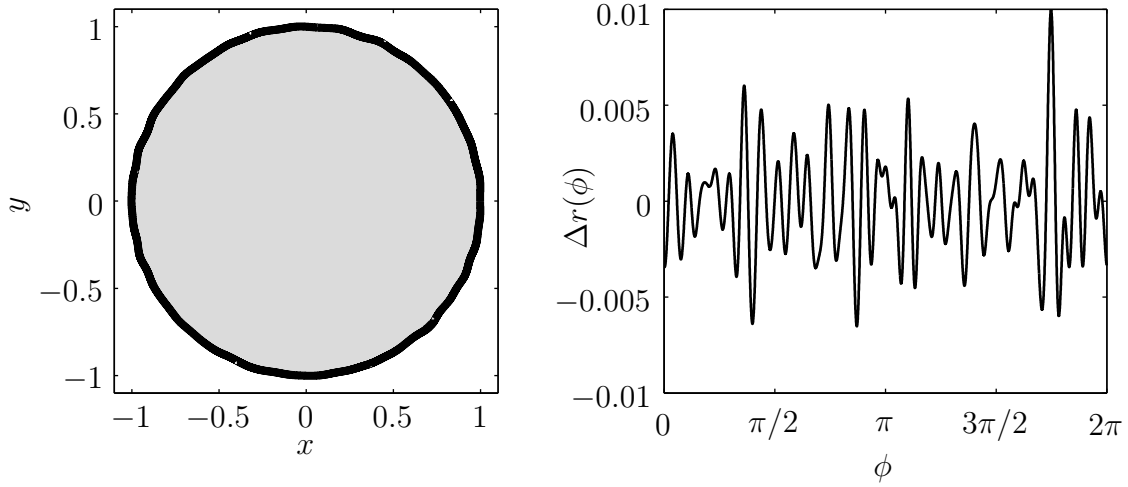
However, looking at Eqs (4.47)-(4.48), we note that it may be possible to obtain a much more constant loss of quality of a high delay mode by setting the damping Γ_2 of the secondary oscillator to a large value while keeping Γ_1 very low. The desired effect is to get $\omega_1^2\Gamma_1\Gamma_2 \ll |\kappa|^2$, so that the overall losses of the main resonance are for the most part controlled by the coupling term. In other words, we would like a cavity bearing both very high and very low quality modes. In the Conclusion of this work, we will propose a cavity design enclosing these properties.

4.4 Notes on boundary roughness

In sub-section 4.1.2, we have found out that the onset of anisotropic emission from a WGM is triggered by a competition of two escape mechanisms (see Fig. 4.12). As the probability of transition through internal scattering increases with the control param-

eter (*i.e.* the position of the inclusion), the ordinary transmission probability remains essentially constant. Because the parametric slope of the first mechanism (transition) is relatively steep in contrast to the transmission probability, the emission profile changes quickly beyond the crossover position of the two mechanisms. This position in turn defines the onset from which to expect the far-field to become anisotropic due to the inclusion. However, this situation may change dramatically with the introduction of intrinsic defects such as *boundary roughness*.

The perturbation model of Chapter 3 applied to an harmonic perturbation of the disc boundary leads to the introduction of the $\beta_{m_{0aa,bb}}$ coefficients (Eqs 3.101-3.102). Given a boundary roughness with zero mean value (*i.e* the average radius of the cavity is R_0), the perturbation model reveals that the delay value spoiling is controlled by the $\Phi_{m_0,-m_0}$ term of the roughness function Fourier series. The phase of $\Phi_{m_0,-m_0}$ determines a dominant symmetry axis of the perturbed modes Eqs (3.126)-(3.127). Assuming a perturbed resonant mode, the delay peaks of odd and even symmetry modes, formed at that point, are expected to move symmetrically in opposite directions with respect to the unperturbed peak position. The even symmetry peak is displaced toward a higher wavenumber resonant position, and the odd symmetry peak is displaced toward a lower wavenumber resonant position. This is seen by plotting the perturbed phase $\theta^{(0)}_{m_{0a,b}} + \theta^{(1)}_{m_{0a,b}}(\epsilon)$ using Eq. (3.52) and Eqs (3.101)-(3.102) (see, for instance, Fig. 3.9 which presents the phase factor for the annular cavity in the small inclusion limit).



(a) Perturbed disc cavity

(b) Boundary roughness

Fig. 4.29 (a) Disc cavity affected by (b) the boundary roughness function $\Delta r(\phi)$.

We seek a numerically exact computation of the effect of the boundary roughness on a disc cavity having a radius $R(\phi) = R_0 + \Delta r(\phi)$. As such, the numerical method presented in Chapter 2 for the computation of the scattering matrix and the delay

matrix is put to use. We set the boundary roughness function

$$\Delta r(\phi) = \sum_m F_m \mathrm{e}^{im\phi} \in \mathbb{R} \tag{4.51}$$

to possess a Gaussian noise spectrum,

$$F_m = \begin{cases} \frac{\Delta r_{\max}}{\widetilde{\Delta r}_{\max}} \mathrm{e}^{-\frac{(m-\langle m\rangle)^2}{2\sigma^2}} \mathrm{e}^{+i\chi_{|m|}} & m > 0 \\ 0 & m = 0 \\ \frac{\Delta r_{\max}}{\widetilde{\Delta r}_{\max}} \mathrm{e}^{-\frac{(m+\langle m\rangle)^2}{2\sigma^2}} \mathrm{e}^{-i\chi_{|m|}} & m < 0 \end{cases} \tag{4.52}$$

where $\Delta r_{\max} \in \mathbb{R}$ is the maximum amplitude of $\Delta r(\phi)$, $\widetilde{\Delta r}_{\max} \in \mathbb{R}$ is a normalization factor[12], $\langle m\rangle$ is the roughness central angular frequency, σ is the width of the distribution and χ_m is a random phase uniformly distributed over the interval $[0,\ 2\pi]$. With respect to the perturbation model of sub-section 3.2.1, we readily find that $\Phi_{mm'} = F_{m'-m}$.

We choose $\Delta r_{\max}/R_0 = 0.01$ (1% of the cavity radius), $\langle m\rangle = 25$ and $\sigma = 10$. The other disc cavity parameters are $n_c = 3.2$, $n_o = 1$ and $R_0 = 1$ (see Fig. 4.29 for an illustration). We seek the characteristic modes in the interval $kR_0 \in [4.35,\ 4.65]$ and pay special attention to the set of resonant peaks, in particular the modes $(11, 1)$ and $(8, 2)$. In Fig. 4.30, we present the delay spectrum obtained according to the theory and numerical implementation discussed in Chapter 2.

The delay spectrum shows an apparent splitting of the main resonances and a net deterioration of the delay value of resonant mode $(11, 1)$ and $(8, 2)$ due to boundary roughness alone. The peaks are labeled 'odd' and ' even' according to the results from perturbation theory discussed above. The near-field projections at $r = R_0$ of the 'odd' and 'even' symmetry for both resonant modes are presented in Fig. 4.31. Although the reference axis from perturbation theory seems to be lost[13], the near-fields of both modes are effectively in quadrature. Whatever the effective symmetry axis may be, the 'symmetries' of each modes appear to agree.

The comparison of the scattering matrix line at mode $(11, 1)$ resonant peak position

[12]The roughness function $\Delta r(\phi)$ is built in two steps. First, we compute $\widetilde{\Delta r}(\phi) = \sum_m \tilde{F}_m \mathrm{e}^{im\phi}$ with

$$\tilde{F}_m = \begin{cases} \mathrm{e}^{-\frac{(m-\langle m\rangle)^2}{2\sigma^2}} \mathrm{e}^{+i\chi_{|m|}} & m > 0 \\ 0 & m = 0 \\ \mathrm{e}^{-\frac{(m+\langle m\rangle)^2}{2\sigma^2}} \mathrm{e}^{-i\chi_{|m|}} & m < 0 \end{cases} . \tag{4.53}$$

Then, the normalisation factor $\widetilde{\Delta r}_{\max} = \max_\phi(\widetilde{\Delta r}(\phi))$ is found and properly substituted in $\tilde{F}_m$.

[13]We find that $F_{-22} \simeq 4.26 \times 10^{-4} \times \mathrm{e}^{i\,1.1311}$ and $F_{-16} \simeq 2.97 \times 10^{-4} \times \mathrm{e}^{i\,6.0720}$ for modes $(11, 1)$ and $(8, 2)$ respectively. This in turn gives a zeroth order symmetry axis, Eqs (3.126)-(3.127), of 0.5656 [rad] and 3.0360 [rad] for the investigated modes. These axis positions actually do not fall on a maximum (even symmetry) or a zero (odd symmetry) of any of the near-field projections.

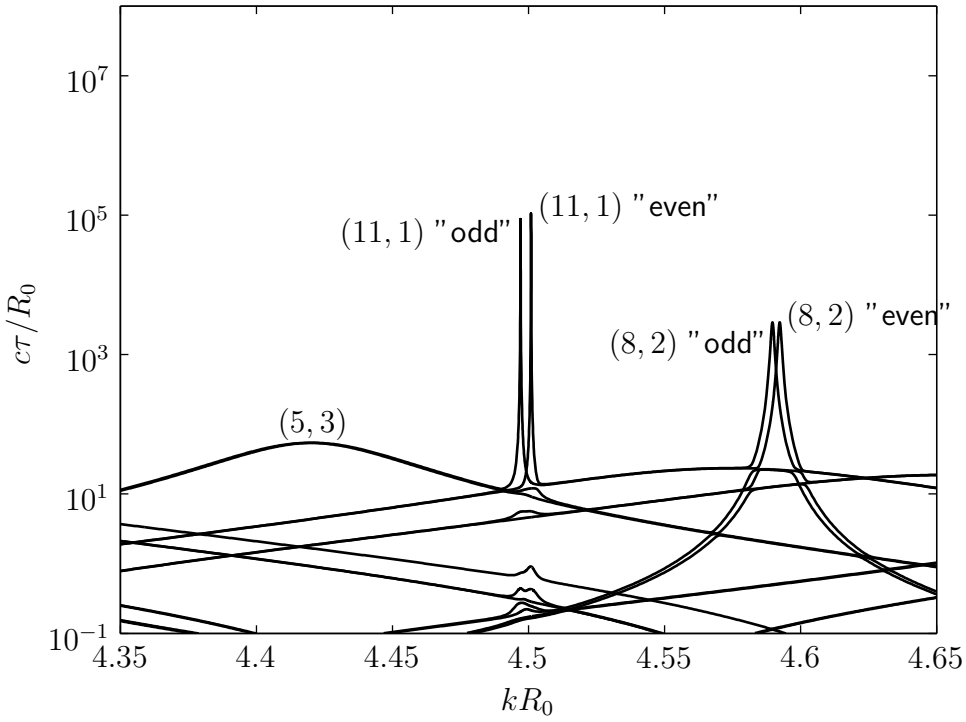
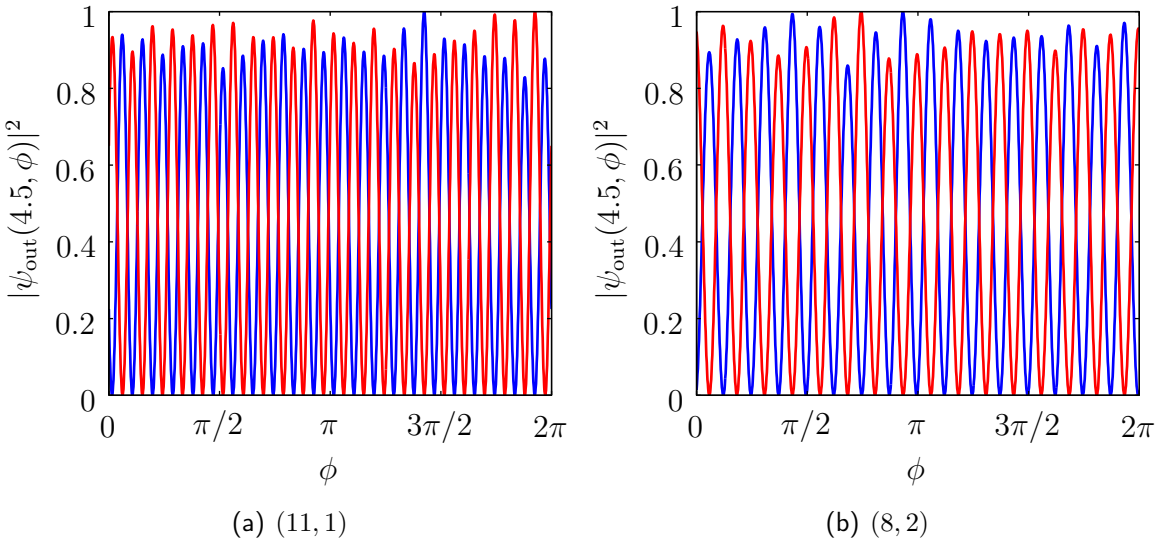


Fig. 4.30 Spectrum for the disc cavity affected by boundary roughness. The labels 'even' and 'odd' of the peaks follow the indications from perturbation theory which predicts that 'odd' symmetry modes move to lower wavenumbers and 'even' symmetry modes move to higher wavenumbers with respect to the unperturbed disc cavity. Here, $(11,1)$ 'odd' is found at $kR_0 \simeq 4.4971$ and $(11,1)$ 'even', at $kR_0 \simeq 4.5010$ (perfect disc: $kR_0 \simeq 4.4989$), and $(8,2)$ 'odd' is found at $kR_0 \simeq 4.5897$ and $(8,2)$ 'even', at $kR_0 \simeq 4.5924$ (perfect disc: $kR_0 \simeq 4.5910$).

with the one obtained for the annular cavity shows that boundary roughness could clearly run into conflict with the control scenario presented in this Chapter as the scattered amplitudes may be of the same size for both mechanisms (see Fig. 4.32). In a way, the inconvenient boundary roughness scattering supersedes the transmission mechanism as the process to overcome through controlled parametric deformation. To illustrate, instead of presenting only two curves, Fig. 4.12 would show a second flat level corresponding to the probability of escape through scattering by the exterior boundary. This third escape mechanism would quickly take over the transmission mechanism as the boundary roughness amplitude increases (here, 1% of the cavity radius) and then become the probability to beat for the controlled transition mechanism. The expected consequence is a narrowing of the window ensuring the high-delay and controlled anisotropic far-field combination (e.g. the gray domain in Fig. 4.7).

Finally, we also observe that lower quality modes seem less affected by boundary roughness than the high quality modes. For example, the unperturbed disc mode $(11,1)$ has a resonant delay $c\tau/R_0 \simeq 8.88 \times 10^6$ and perturbed delays 8.88×10^4 for 'odd' and



(a) $(11,1)$ (b) $(8,2)$

Fig. 4.31 Outgoing near-field projections at $r = R_0$ for the two 'symmetries' of resonant modes $(11,1)$ and $(8,2)$ (see the spectrum on Fig. 4.30). The two 'symmetries' (*even*, blue curves; *odd*, red curves) are seen to intertwine, expressing their quadrature with respect to some effective axis.

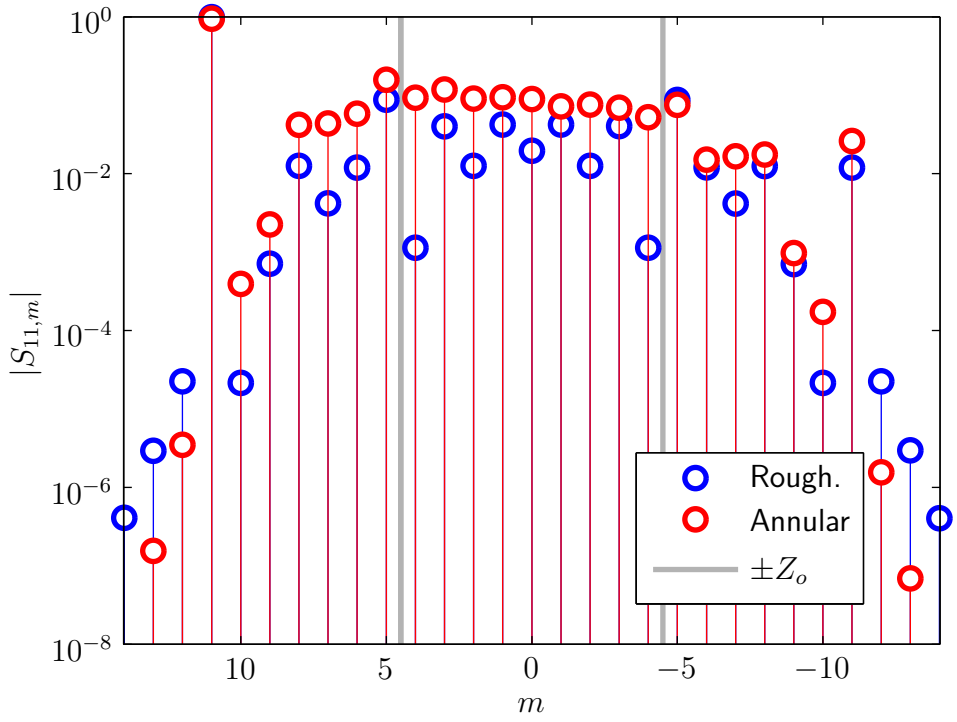


Fig. 4.32 Line $m_0 = 11$ of the scattering matrix for the annular cavity and the disc cavity affected by wall roughnesses. We used the scattering matrices located at the resonance position of odd symmetry modes $(11,1)$. The parameters used for the annular cavity are those of Fig. 4.9.

10.68×10^4 for 'even' symmetries, while mode $(8, 2)$ has an unperturbed delay value 2.95×10^3 and perturbed delays 2.8856×10^3 for 'odd' and 2.8995×10^3 for 'even' symmetries. This happens as the Fourier amplitude of component F_{-2m_0} scales only of a factor 1.4 between the two sets of modes. The rapid loss of quality of high delay modes could also add supplementary problems regarding the resonant coupling phenomenon discussed in Section 4.3 as the mid-size peaks would still wander around the spectrum due to parametric control and eventually cross the peak positions of high delay modes already weakened by boundary roughness.

This Section only scratches the surface of a topic that could cover many chapters. Surprisingly, to the author's knowledge, only the often cited paper by Rahachou and Zozoulenko [111], from which the numerical algorithm presented in this work is inspired, explores the consequences of wall roughness. In view of the dramatic consequences these can have on quality factors and effectiveness of output control, this topic definitely deserves a thorough investigation through analysis of statistical sets of cavities. Observable averages could then be deduced, and the properties of different kinds of roughness spectrum could be classified.

Chapter 5

Application II: Cavity-waveguide coupling model

In this Chapter, we present a model of electromagnetic coupling between an infinite planar waveguide and a dielectric cavity. The object of inquiry is the transmission coefficient of the guided field as it goes through the waveguide, from a continuous wave source to a fictitious broadband detector, and interacts more or less strongly with a finite size dielectric cavity. This model is inspired by the mathematical description of waveguide coupling through evanescent waves [92]. The transmission coefficient can, under certain conditions, be obtained in closed-form and makes explicit use of the scattering matrix. As illustration, the model is applied to the system composed of a waveguide and a disc cavity.

As a second major application of the formalism developed in Chapters 2 and 3, we present a novel method to analyse the electromagnetic coupling of a single mode planar waveguide with a two-dimensional cavity. This composite system is interesting as the waveguide acts simultaneously as an energy source for the cavity and as a measuring device of the cavity's activity (Fig. 5.1). The spacing between the waveguide and the cavity becomes an exchange domain where the evanescent field from the waveguide couples to the near-field components of the cavity modes, and where the modes of the cavity reconnect with the guided wave field. Of course, since the returning field will have circulated some time in the cavity, a phase offset is expected between the residual guided field inside the waveguide and the recoupled wave field from the cavity. The superposition of these components inside the waveguide is therefore prone to show interference when the field is recorded at the end of the waveguide. Since resonances of a cavity are associated with phase shifts of π radians [57, 88], the drops in transmission,

recorded over the waveguide line as the wavenumber is varied, are an indication of nearby resonances. Alternatively, one may see the resonances of the cavity as draining the wave field from the waveguide and diverting it according to the cavity's own modes.

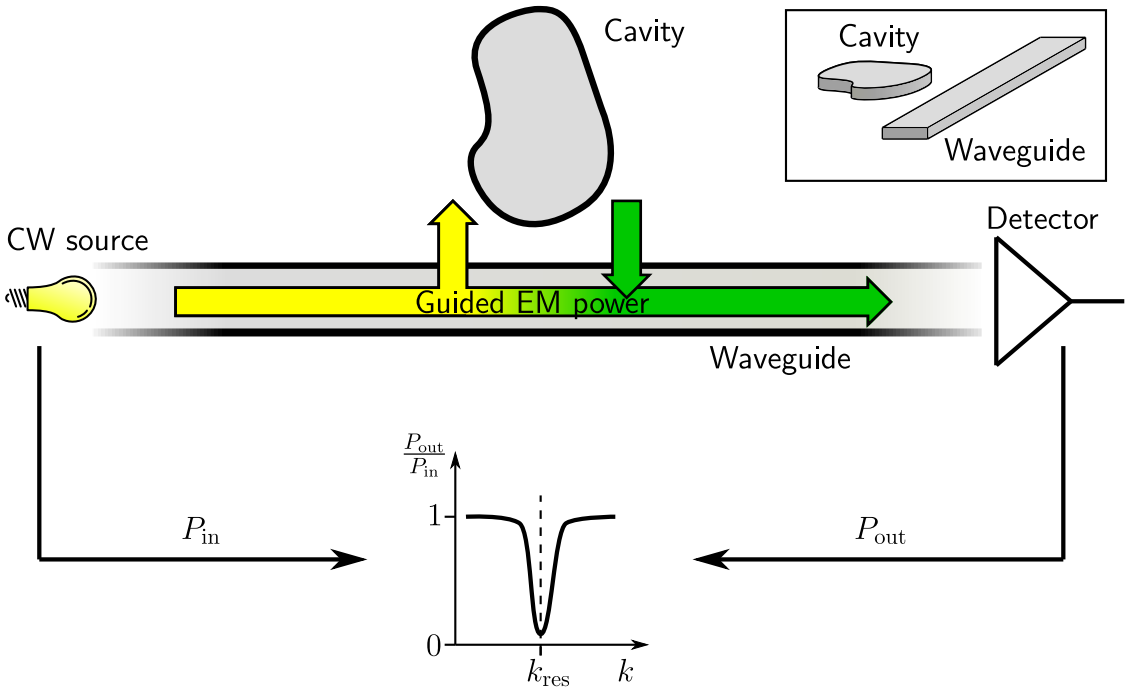


Fig. 5.1 Schematic representation of the waveguide-cavity coupling. Right-most inset presents a perspective view of the system composed of thin waveguide and cavity arranged in a common plane. The guided field is assumed to originate from a continuous wave (*i.e.* monochromatic) source and is recorded by a perfect detector. The comparison of the input and output power defines a transmission coefficient that is strongly affected by the amount of field diverted by the cavity. This is especially true around resonances of the cavity.

Although easily described through this simple phenomenological description, obtaining the transmission coefficient throughout the waveguide remains a difficult task because of the coupling of the finite cavity with the 'infinite' line through which the observable field is channeled. The computation of the electromagnetic field related to this type of setup is usually carried out numerically [22, 23, 32]. In particular cases, simplified approximations are considered, for instance near a resonance and for a single mode of the cavity [81, 49] and mostly for the disc or annular cavity [119].

Our approach is conceptually close to that of the coupling method of two planar waveguides as discussed by Okamoto [92] and turn out to be much more general than previous approximations since we make full use of the scattering matrix of the dielectric cavity. No particular resonance behaviour is assumed beforehand, and the physics of the interaction is completely encoded in the scattering matrix. An original closed-form expression for the transmission (and reflection) of the guided field is derived Eq. (5.61)

and the special case of weak coupling (large distance between waveguide and cavity) is studied in detail Eq. (5.92).

This investigation was motivated in first place by the idea of directional coupling between a non-symmetric cavity and a waveguide. The object of inquiry was to determine whether or not the rotation of an asymmetric annular cavity around its geometrical center[1] could induce a measurable effect on the recorded transmission spectrum through a waveguide. Efforts were initially put on the analytical modelisation of the system in order to isolate observable effects of the cavity orientation. Since the rotation of the cavity appears as a simple (diagonal) similarity transform on the scattering matrix (see Appendix D), we have developed a model making explicit use of the scattering matrix. Unfortunately, this study, led by a collaborating experimental research group, did not receive proper funding and was canceled early. However, because of its originality and because it somewhat 'connects' the systems discussed so far to an actual plausible setup, we feel that this model deserves its place in this work.

The first part of the analysis (Section 5.1) is concerned with the description of the interaction of the evanescent field from the waveguide with the dielectric cavity. Our treatment is similar in many respects to that of Morita [86]. Section 5.2 establishes the basic equations of the model and its general solution is presented in 5.3. The following Section 5.4 takes a new look at the previous results of Sections 5.2-5.3 and highlights anew some of the physical properties of the coupled system. Finally, the last Section 5.5 presents some calculations on the special case of coupling with a homogeneous disc. The technical details are once again relegated to an extensive Appendix (E).

5.1 Evanescent field and cylindrical harmonics

The evanescent field emerging from a single mode waveguide having refractive index n_g [2] can be written as

$$E^+(x,y) = A\cos\left(\gamma\frac{w}{2}\right)\mathrm{e}^{-\alpha(y-w/2)}\mathrm{e}^{+i\beta x} \quad , \; y \geq w/2 \quad . \tag{5.1}$$

Our intention to connect this evanescent field with the scattering matrix of the cavity demands that the right hand side of this expression be represented over an angular momentum basis in which the $\mathbf{S}$ matrix is already known.

[1] It is understood that the (small) inclusion making up the annular cavity is a distance away from the cavity center.

[2] The first Section of Appendix E reviews the principal results related to the propagation of an electromagnetic field in a dielectric slab.

With a displacement of the origin towards the center of the cavity according to Fig. 5.2, one has rather an expression of the form

$$E^+(x,y) = A\cos\left(\gamma\frac{w}{2}\right)\mathrm{e}^{-\alpha(R_0+d)}\mathrm{e}^{-\alpha y}\mathrm{e}^{+i\beta x} \quad , \; y \geq -(R_0+d) \quad . \tag{5.2}$$

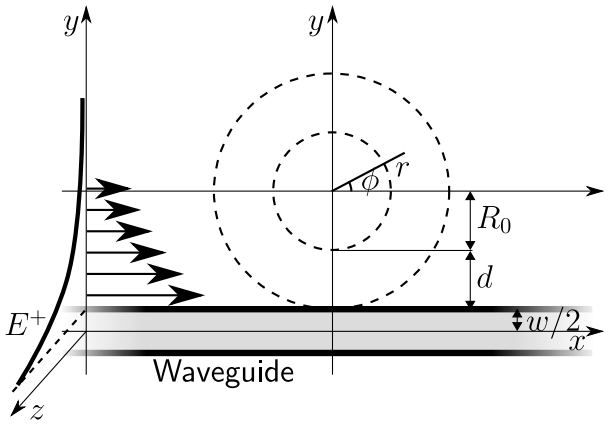


Fig. 5.2 Coordinate system for the description of the evanescent field emanating from the waveguide.

The expected evanescent field E^+ in cylindrical harmonics $J_m(n_o kr)\mathrm{e}^{im\phi}$ will have to take the form

$$E^+(x,y) = \sum_m a_m^+ J_m(n_o kr)\mathrm{e}^{im\phi} \tag{5.3}$$

and the first step in obtaining the expansion coefficients is to consider the integral ($k \in \mathbb{R}$):

$$\int d\phi \int dr\, rJ_m(n_o kr)\mathrm{e}^{-im\phi}E^+(x,y) = A\cos\left(\gamma\frac{w}{2}\right)\mathrm{e}^{-\alpha(R_0+d)}\int d\phi \int dr\, rJ_m(n_o kr)\mathrm{e}^{-im\phi}\mathrm{e}^{-\alpha y}\mathrm{e}^{+i\beta x}. \tag{5.4}$$

According to Eq. (8.511.4) of Gradshteyn and Ryzhik [50],

$$\mathrm{e}^{iz\sin(\phi+\pi/2)} = \mathrm{e}^{iz\cos\phi} = \sum_{j=-\infty}^{+\infty} i^j J_j(z)\mathrm{e}^{ij\phi} \tag{5.5}$$

and Eq. (8.411.1) [50] [3]

$$J_n(z) = \frac{1}{2\pi i^n}\int_0^{2\pi} d\theta\; \mathrm{e}^{iz\cos\theta}\mathrm{e}^{in\theta} \tag{5.6}$$

one reduces the integral to

$$\begin{aligned}\int dr \int d\phi\; rE^+J_m(n_o kr)\mathrm{e}^{-im\phi} \;&=\; A\cos\left(\gamma\frac{w}{2}\right)\mathrm{e}^{-\alpha(R_0+d)}2\pi i^{-m} \\ &\quad\times\int dr\; rJ_m(n_o kr)\sum_j i^j J_j(i\alpha r)J_{j-m}(\beta r).\end{aligned} \tag{5.7}$$

[3] This representation of the Bessel function is independent of the integration limits. They must however cover a 2π interval.

A further simplification is obtained with the use of *Graf's identity* [1] to read

$$\begin{aligned}\int dr \int d\phi\ rE^+J_m(n_okr)\mathrm{e}^{-im\phi} &= A\cos\left(\gamma\frac{w}{2}\right)\mathrm{e}^{-\alpha(R_0+d)}2\pi i^m \\ &\quad\times\left(\frac{\beta+\alpha}{\beta-\alpha}\right)^{m/2}\int dr\ rJ_m(n_okr)J_m(\sqrt{\beta^2-\alpha^2}r).\end{aligned} \tag{5.8}$$

Using appropriate normalisation, the *excitation coefficients* found in Eq. (5.3) are then calculated as

$$\begin{aligned}a_m^+ &= \frac{1}{2\pi}\frac{\int d\phi\int dr\ rJ_m(n_okr)\mathrm{e}^{-im\phi}E^+(x,y)}{\int dr\ rJ_m(n_okr)J_m(n_okr)} \\ &= A\cos\left(\gamma\frac{w}{2}\right)\mathrm{e}^{-\alpha(R_0+d)}i^m\left(\frac{\beta+\alpha}{\beta-\alpha}\right)^{m/2}\left[\frac{\int dr\ rJ_m(n_okr)J_m(\sqrt{\beta^2-\alpha^2}r)}{\int dr\ rJ_m(n_okr)J_m(n_okr)}\right].\end{aligned} \tag{5.9}$$

One then uses the fact that

$$\beta^2-\alpha^2=(n_ok)^2 \tag{5.10}$$

as defined in Appendix E (Eq. E.2) to get

$$\begin{aligned}a_m^+ &= A\cos\left(\gamma\frac{w}{2}\right)\mathrm{e}^{-\alpha(R_0+d)}i^m\left(\frac{\beta+\alpha}{\beta-\alpha}\right)^{m/2} \\ &= A\cos\left(\gamma\frac{w}{2}\right)i^m\exp\left[-\alpha(R_0+d)+\frac{m}{2}\ln\frac{\beta+\alpha}{\beta-\alpha}\right].\end{aligned} \tag{5.11}$$

The relation (5.10) implies also that $\alpha<\beta$, i.e. the $\frac{\beta+\alpha}{\beta-\alpha}$ of the preceding expression is strictly positive. If $\alpha=0$, then $\beta=n_ok$ and the evanescent wave becomes [1]

$$E^+(x,y)\xrightarrow{\alpha=0}A\cos\left(\gamma\frac{w}{2}\right)\sum_{m=-\infty}^{+\infty}i^mJ_m(n_okr)\mathrm{e}^{im\phi}=A'\mathrm{e}^{in_okr\cos\phi}=A'\mathrm{e}^{i\beta x},\ r\le R_0+d, \tag{5.12}$$

namely a plane wave.

Similarly, one derives the expansion coefficients for a field propagating towards $x\to-\infty$,

$$\begin{aligned}a_m^- &= A\cos\left(\gamma\frac{w}{2}\right)\mathrm{e}^{-\alpha(R_0+d)}i^{-m}\left(\frac{\beta+\alpha}{\beta-\alpha}\right)^{-m/2} \\ &= A\cos\left(\gamma\frac{w}{2}\right)i^{-m}\exp\left[-\alpha(R_0+d)-\frac{m}{2}\ln\frac{\beta+\alpha}{\beta-\alpha}\right].\end{aligned} \tag{5.13}$$

For a real amplitude A, one easily verifies that expressions (5.11) et (5.13) lead to the reciprocity relation $E^{+^*}(x,y)=E^-(x,y)$.

As first discussed in Chapter 2, the wave field *external* to the circular domain of radius R_0 (Fig. 5.2) can be written quite generally as

$$\tilde{E}^C = \sum_m \left[A_m H_m^{(2)}(n_o kr) + B_m H_m^{(1)}(n_o kr)\right] \mathrm{e}^{im\phi} \ , \quad r \geq R_0 \ , \tag{5.14}$$

with $B_m = \sum_{m'} S_{mm'} A_{m'}$ and $S_{mm'}$ being the scattering matrix element. The evanescent fields have a similar structure since $J_m(x) = [H^{(1)}(x) + H^{(2)}(x)]/2$ and then

$$E^{\pm}(x,y) = \sum_m \left[\frac{a_m^{\pm}}{2} H_m^{(2)}(n_o kr) + \frac{a_m^{\pm}}{2} H_m^{(1)}(n_o kr)\right] \mathrm{e}^{im\phi} \ . \tag{5.15}$$

When a scattering obstacle (e.g. a dielectric cavity) is present in this region, the coefficients of the outgoing field $\{B_m\}$ are necessarily different than those of the incoming field $\{A_m\}$. The *total field* outside the cavity produced by the evanescent exciting field moving towards $x \to +\infty$ $(+)$ or towards $x \to -\infty$ $(-)$ can then be obtained by the replacement $A_m = a^+/2$ or $A_m = a^-/2$ respectively. Since we will be interested mainly in the field *emitted by the cavity*, one must subtract from the total field the evanescent part of the exciting field from the waveguide. Hence the field induced through the evanescent excitation traveling towards $x \to +\infty$ is

$$\begin{aligned} E^{C+} &= \tilde{E}^C - E^+ \\ &= \sum_m \left[\frac{a_m^+}{2} H_m^{(2)}(n_o kr) + \left(\sum_{m'} S_{mm'} \frac{a_{m'}^+}{2}\right) H_m^{(1)}(n_o kr)\right] \mathrm{e}^{im\phi} - E^+ \end{aligned} \ . \tag{5.16}$$

This expression is simplified to

$$E^{C+} = \sum_m \left[\frac{1}{2} \sum_{m'} \left(-\delta_{mm'} + S_{mm'}\right) a_{m'}^+\right] H_m^{(1)}(n_o kr) \mathrm{e}^{im\phi} \tag{5.17}$$

or more explicitly

$$E^{C+} = A \cos\left(\gamma \frac{w}{2}\right) \mathrm{e}^{-\alpha(R_0+d)} \sum_m \left[\frac{1}{2} \sum_{m'} \left(-\delta_{mm'} + S_{mm'}\right) i^{m'} \left(\frac{\beta+\alpha}{\beta-\alpha}\right)^{m'/2}\right] H_m^{(1)}(n_o kr) \mathrm{e}^{im\phi} \ . \tag{5.18}$$

In a similar way, we obtain the cavity emitted field for an evanescent excitation traveling towards $x \to -\infty$ as

$$E^{C-} = A \cos\left(\gamma \frac{w}{2}\right) \mathrm{e}^{-\alpha(R_0+d)} \sum_m \left[\frac{1}{2} \sum_{m'} \left(-\delta_{mm'} + S_{mm'}\right) i^{-m'} \left(\frac{\beta+\alpha}{\beta-\alpha}\right)^{-m'/2}\right] H_m^{(1)}(n_o kr) \mathrm{e}^{im\phi} \ . \tag{5.19}$$

With this approach, when the scattering matrix $\mathbf{S}$ is unity (no scattering obstacle), the fields originating from the cavity $E^{C\pm}$ are equal to zero. Noteworthy is the presence of the Hankel functions of the first kind only, a further indication that $E^{C\pm}$ are strictly outgoing wave fields.

5.2 Coupling theory

The perturbative approach of coupling a waveguide to a dielectric cavity is expressed by the Ansatz

$$\mathbf{E} \simeq \mathbf{E}^C + g_+(x)\mathbf{E}^+ + g_-(x)\mathbf{E}^- \tag{5.20}$$

$$\mathbf{H} \simeq \mathbf{H}^C + g_+(x)\mathbf{H}^+ + g_-(x)\mathbf{H}^- \quad . \tag{5.21}$$

The total electric (magnetic) field $\mathbf{E}$ ($\mathbf{H}$), exact solution of the whole system (a *supermode*), is approximately written as the superposition of unperturbed fields charateristic of each component of the system: $\mathbf{E}^C$ ($\mathbf{H}^C$), the cavity electric (magnetic) field, $\mathbf{E}^\pm$ ($\mathbf{H}^\pm$), the propagating (in both directions) single mode waveguide fields (see Appendix E for a complete description of the waveguide fields). This separation is similar to that described in [92]. The functions $g_\pm(x)$ are envelops of the propagating fields and take into account the modifications (perturbations) of these fields inside the waveguide. This decomposition is illustrated in Fig. 5.3.

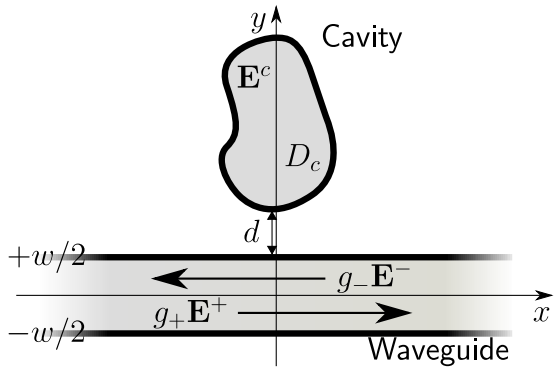


Fig. 5.3 Schematics of the coupled system (cavity + waveguide). Only the electric field is displayed. The domain occupied by the cavity is identified by D_C.

For TM polarization ($E_x = E_y = 0$), a two-dimensional system and a harmonic time dependence $\mathrm{e}^{-i\omega t}$ for the fields, the propagating waveguide fields take the form

$$\mathbf{E}^\pm = \psi(y)\mathrm{e}^{\pm i\beta x}\hat{z} \tag{5.22}$$

where β is the propagation constant and $\psi(y)$ is the transverse profile of the field (invariant with respect to the propagation direction, see Eq. (5.2) and Appendix E). This profile decreases exponentially outside the waveguide.

To first approximation, the field emanating from the cavity, $\mathbf{E}^C$ ($\mathbf{H}^C$), is produced by the excitation from the waveguide modes $\mathbf{E}^\pm$ ($\mathbf{H}^\pm$). There are therefore 2 components $\mathbf{E}^{C\pm}$ ($\mathbf{H}^{C\pm}$) to the cavity field (see Eqs. (5.18) and (5.19)). Furthermore, because of

the linear dependency of $\mathbf{E}^{C\pm}$ and $\mathbf{E}^{\pm}$, it is reasonable to modulate these contributions by the envelops $g_{\pm}(x)$ to lead to

$$\begin{aligned} \mathbf{E}^{C} &= g_{+}(x)\mathbf{E}^{C+} + g_{-}(x)\mathbf{E}^{C-} && (5.23) \\ \mathbf{H}^{C} &= g_{+}(x)\mathbf{H}^{C+} + g_{-}(x)\mathbf{H}^{C-} \ . && (5.24) \end{aligned}$$

This allows for a *local* contribution of the exciting field proportional to the value of the envelope at that position of the waveguide (the condition of equilibrium between the waveguide mode at a given position and its modification via the cavity will be discussed in further detail in Section 5.4).

All these fields must satisfy the Maxwell's equations *in their respective region of applicability* # :

$$\begin{aligned} \nabla \times \mathbf{E}^{\#} &= +i\omega\mu_0\mathbf{H}^{\#} && (5.25) \\ \nabla \times \mathbf{H}^{\#} &= -i\omega\epsilon_0 n_{\#}^2\mathbf{E}^{\#} \quad . && (5.26) \end{aligned}$$

Applying the rotational $\nabla\times$ to the expression for $\mathbf{E}$, namely [4]

$$\nabla \times \mathbf{E} \simeq \nabla \times (g_{+}\mathbf{E}^{C+}) + \nabla \times (g_{-}\mathbf{E}^{C-}) + \nabla \times (g_{+}\mathbf{E}^{+}) + \nabla \times (g_{-}\mathbf{E}^{-}) \qquad (5.28)$$

leads directly to

$$\begin{aligned} +i\omega\mu_0\mathbf{H} &= i\omega\mu_0\left(g_{+}\mathbf{H}^{C+} + g_{-}\mathbf{H}^{C-} + g_{+}\mathbf{H}^{+} + g_{-}\mathbf{H}^{-}\right) \\ &\quad + \frac{d}{dx}g_{+}\hat{x} \times \left(\mathbf{E}^{+} + \mathbf{E}^{C+}\right) + \frac{d}{dx}g_{-}\hat{x} \times \left(\mathbf{E}^{-} + \mathbf{E}^{C-}\right) \end{aligned}$$

or, after simplification, to the differential equation

$$g'_{+}\hat{x} \times \left(\mathbf{E}^{+} + \mathbf{E}^{C+}\right) + g'_{-}\hat{x} \times \left(\mathbf{E}^{-} + \mathbf{E}^{C-}\right) = \left[g'_{+}\left(E^{+} + E^{C+}\right) + g'_{-}\left(E^{-} + E^{C-}\right)\right]\hat{z} = 0. \qquad (5.29)$$

The derivative sign $'$ denotes differentiation with respect to x. The same procedure is carried out on the magnetic field $\mathbf{H}$,

$$\nabla \times \mathbf{H} \simeq \nabla \times (g_{+}\mathbf{H}^{C+}) + \nabla \times (g_{-}\mathbf{H}^{C-}) + \nabla \times (g_{+}\mathbf{H}^{+}) + \nabla \times (g_{-}\mathbf{H}^{-}) \qquad (5.30)$$

for an equivalent differential equation

$$\begin{aligned} &+i\omega\epsilon_0\left[(n^2 - n_c^2)(\mathbf{E}^{C+}g_{+} + \mathbf{E}^{C-}g_{-}) + (n^2 - n_g^2)(\mathbf{E}^{+}g_{+} + \mathbf{E}^{-}g_{-})\right] \\ &+g'_{+}\hat{x} \times \left(\mathbf{H}^{C+} + \mathbf{H}^{+}\right) + g'_{-}\hat{x} \times \left(\mathbf{H}^{C-} + \mathbf{H}^{-}\right) = 0 \qquad (5.31) \end{aligned}$$

[4] Useful identity:

$$\nabla \times (f\mathbf{F}) = f\nabla \times \mathbf{F} + \nabla f \times \mathbf{F} \quad . \qquad (5.27)$$

where n is the refractive index over the entire regions of the whole system (cavity + waveguide + surrounding), n_c is the refractive of the cavity, and n_g is the refractive index of the waveguide.

One evaluates $\hat{x} \times \mathbf{H}^{\pm,C\pm}$:

$$\hat{x} \times \mathbf{H}^{\pm,C\pm} = \hat{x} \times \frac{1}{i\omega\mu_0} \nabla \times \mathbf{E}^{\pm,C\pm} = -\frac{1}{i\omega\mu_0} \frac{\partial}{\partial x} E^{\pm,C\pm} \hat{x} \times \hat{y} = -\frac{1}{i\omega\mu_0} \frac{\partial}{\partial x} E^{\pm,C\pm} \hat{z} \ . \quad (5.32)$$

Equation (5.31) then reduces to a scalar expression

$$\begin{aligned} g'_+ \frac{\partial}{\partial x} \left(E^{C+} + E^{+} \right) + g'_- \frac{\partial}{\partial x} \left(E^{C-} + E^{-} \right) &= -(n^2 - n_c^2) k^2 (E^{C+} g_+ + E^{C-} g_-) \\ &\quad -(n^2 - n_g^2) k^2 (E^{+} g_+ + E^{-} g_-). \end{aligned} \quad (5.33)$$

In agreement with our perturbation treatment, one assumes next that the integrated contribution along the y direction of the product of the waveguide and the cavity fields is much smaller than that of the integrated product of the waveguide fields,

$$\left| \int_{-\infty}^{+\infty} dy \ E^{\pm^*} E^{C\pm,\mp} \right| \ll \left| \int_{-\infty}^{+\infty} dy \ E^{\pm^*} E^{\pm,\mp} \right| \quad . \quad (5.34)$$

This assumption has the effect of disregarding the terms $E^{C\pm}$ in (5.29),

$$g'_+ \simeq -g'_- \mathrm{e}^{-i2\beta x} \quad . \quad (5.35)$$

One considers further that this approximation is also valid for the left-hand side of Eq. (5.33),

$$\left| \int_{-\infty}^{+\infty} dy \ E^{\pm^*} \frac{\partial}{\partial x} E^{C\pm,\mp} \right| \ll \left| \int_{-\infty}^{+\infty} dy \ E^{\pm^*} \frac{\partial}{\partial x} E^{\pm,\mp} \right| \quad . \quad (5.36)$$

By multiplying (5.33) with E^{+^*} form the left, integrating over y (and over z for a thickness h: the field is considered essentially uniform over a distance $h \ll 2\pi/k$), one finds

$$i\beta P \left(g'_+ - \mathrm{e}^{-i2\beta x} g'_- \right) \simeq -k^2 \left[\kappa_+(x) g_+ + \kappa_-(x) g_- \right] \mathrm{e}^{-i\beta x} - k^2 \chi(x) \left[\mathrm{e}^{i\beta x} g_+ + \mathrm{e}^{-i\beta x} g_- \right] \mathrm{e}^{-i\beta x} \quad (5.37)$$

where

$$P = \int_{-\infty}^{+\infty} dy \ \psi^*(y) \psi(y) \quad (5.38)$$

$$\kappa_\pm(x) = \int_{-\infty}^{+\infty} dy \ (n^2 - n_c^2) \psi^*(y) E^{C\pm}(x, y) \quad (5.39)$$

$$\chi(x) = \int_{-\infty}^{+\infty} dy \ (n^2 - n_g^2) \psi^*(y) \psi(y) \quad . \quad (5.40)$$

Using Eq. (5.35), one finally obtains the system of differential equations

$$g'_+ = +i\frac{k^2}{2\beta P}\mathrm{e}^{-i\beta x}\left[(\kappa_+(x)+\chi(x)\mathrm{e}^{i\beta x})g_+ + (\kappa_-(x)+\chi(x)\mathrm{e}^{-i\beta x})g_-\right] \quad (5.41)$$

$$g'_- = -i\frac{k^2}{2\beta P}\mathrm{e}^{+i\beta x}\left[(\kappa_+(x)+\chi(x)\mathrm{e}^{i\beta x})g_+ + (\kappa_-(x)+\chi(x)\mathrm{e}^{-i\beta x})g_-\right] \quad . \quad (5.42)$$

This system of ordinary differential equations for the envelopes of forward and backward propagating guided waves are to be solved in order to retrieve the transmission and reflection coefficients.

5.3 Solution of the model

The modelisation so far has led us to a set of first order differential equations, Eqs (5.41) and (5.42), for the envelopes of the propagating guided fields. Since these envelopes control the amount of field found at the ends of the waveguide and assuming a single input field, obtaining a solution to Eqs (5.41) and (5.42) is crucial for the evaluation of the line transmission and reflection coefficients, the measurable quantities in an hypothetical experimental setup. In the following, we obtain a formal solution to this set of differential equations, then proceed to the explicit calculation of certain factors left in an integral form in the formal solution.

5.3.1 General solution

A solution of the system of differential equations (5.41)-(5.42) is readily obtained as

$$\begin{pmatrix} g_+(x) \\ g_-(x) \end{pmatrix} = \exp\left[\mathbf{G}(x)\right] \begin{pmatrix} g_+(-\infty) \\ g_-(-\infty) \end{pmatrix} \quad (5.43)$$

with

$$G_{11}(x) = G_{++}(x) = +i\frac{k^2}{2\beta P}\int_{-\infty}^{x} dx' \left(\kappa_+(x')\mathrm{e}^{-i\beta x'} + \chi(x') \right) \quad (5.44)$$

$$G_{12}(x) = G_{+-}(x) = +i\frac{k^2}{2\beta P}\int_{-\infty}^{x} dx' \left(\kappa_-(x')\mathrm{e}^{-i\beta x'} + \chi(x')\mathrm{e}^{-i2\beta x'}\right) \quad (5.45)$$

$$G_{21}(x) = G_{-+}(x) = -i\frac{k^2}{2\beta P}\int_{-\infty}^{x} dx' \left(\kappa_+(x')\mathrm{e}^{+i\beta x'} + \chi(x')\mathrm{e}^{+i2\beta x'}\right) \quad (5.46)$$

$$G_{22}(x) = G_{--}(x) = -i\frac{k^2}{2\beta P}\int_{-\infty}^{x} dx' \left(\kappa_-(x')\mathrm{e}^{+i\beta x'} + \chi(x') \right). \quad (5.47)$$

As $x \to +\infty$, the solution (5.43) becomes

$$\begin{pmatrix} g_+(+\infty) \\ g_-(+\infty) \end{pmatrix} \equiv \begin{pmatrix} g_{++} \\ g_{-+} \end{pmatrix} = \exp\left[\mathbf{G}^0\right] \begin{pmatrix} g_+(-\infty) \\ g_-(-\infty) \end{pmatrix} \equiv \exp\left[\mathbf{G}^0\right] \begin{pmatrix} g_{+-} \\ g_{--} \end{pmatrix} \quad (5.48)$$

with $G^0_{\pm\pm} = G_{\pm\pm}(+\infty)$. Since the excitation source is located at $x \to -\infty$, g_{+-} and g_{-+} are known quantities (e.g. $g_{+-} = 1$ and $g_{-+} = 0$). Moreover, because the exponential of a 2×2 matrix is also a 2×2 matrix, one can write the exit (output) terms g_{++} and g_{--} as functions of the source (input) terms g_{+-} and g_{-+}.

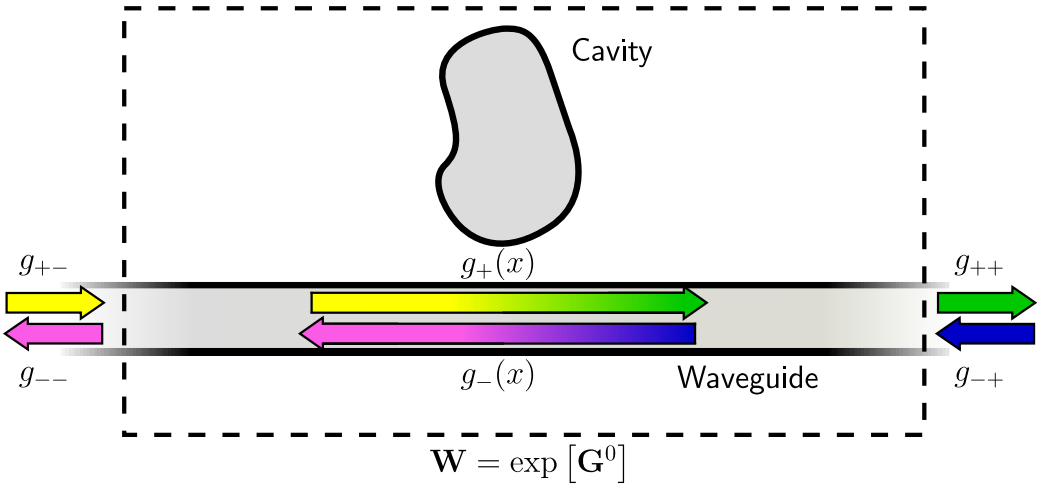


Fig. 5.4 Representation of the input and output envelopes of the guided waves. The $\mathbf{W} = \exp\left[\mathbf{G}^0\right]$ matrix is a mathematical representation of the combined waveguide-cavity system as seen from the ends of the waveguide.

An exact expression for the 2×2 matrix produced by the exponential of $\mathbf{G}^0$ is easily obtained. On calculates first the eigenvalues and eigenvectors of $\mathbf{G}^0$. Let us denote $\mathbf{\Lambda}$, the diagonal matrix of eigenvalues

$$\mathbf{\Lambda} = \begin{pmatrix} \lambda_1 & 0 \\ 0 & \lambda_2 \end{pmatrix} \quad (5.49)$$

and $\mathbf{V}$, the eigenvector matrix,

$$\mathbf{V} = \begin{pmatrix} v_{11} & v_{12} \\ v_{21} & v_{22} \end{pmatrix} \quad , \quad (5.50)$$

where v_{ij} represents the $i-$th component of the $j-$th eigenvector. We have then [5]

$$\exp\left[\mathbf{G}^0\right] = \mathbf{V}\exp\left[\mathbf{\Lambda}\right]\mathbf{V}^{-1} \tag{5.52}$$

such that

$$\begin{pmatrix} g_{++} \\ g_{-+} \end{pmatrix} = \mathbf{V}\exp\left[\mathbf{\Lambda}\right]\mathbf{V}^{-1} \begin{pmatrix} g_{+-} \\ g_{--} \end{pmatrix} \equiv \mathbf{W} \begin{pmatrix} g_{+-} \\ g_{--} \end{pmatrix} \tag{5.53}$$

where the elements of the matrix $\mathbf{W}$ are

$$\begin{aligned} W_{11} &= \frac{\mathrm{e}^{\lambda_1} v_{11}v_{22} - \mathrm{e}^{\lambda_2} v_{12}v_{21}}{\Delta_V} & W_{12} &= -\frac{(\mathrm{e}^{\lambda_1} - \mathrm{e}^{\lambda_2})v_{11}v_{12}}{\Delta_V} \\ W_{21} &= \frac{(\mathrm{e}^{\lambda_1} - \mathrm{e}^{\lambda_2})v_{22}v_{21}}{\Delta_V} & W_{22} &= -\frac{\mathrm{e}^{\lambda_1} v_{12}v_{21} - \mathrm{e}^{\lambda_2} v_{11}v_{22}}{\Delta_V} \end{aligned} \tag{5.54}$$

with $\Delta_V = \det \mathbf{V} = v_{11}v_{22} - v_{12}v_{21}$. This results in an explicit relation of g_{++} and g_{--} with respect to g_{-+} and g_{+-},

$$g_{++} = \frac{\Delta_W}{W_{22}} g_{+-} + \frac{W_{12}}{W_{22}} g_{-+} \tag{5.55}$$

$$g_{--} = -\frac{W_{21}}{W_{22}} g_{+-} + \frac{1}{W_{22}} g_{-+} \tag{5.56}$$

where $\Delta_W = \det \mathbf{W} = \det \exp\left[\mathbf{\Lambda}\right] = \mathrm{e}^{(\lambda_1+\lambda_2)}$. Furthermore, the eigenvalues $\lambda_{1,2}$ are simply expressed as

$$\lambda_{1,2} = \frac{1}{2}\left(G^0_{--} + G^0_{++}\right) \pm \frac{1}{2}\sqrt{\left(G^0_{--} - G^0_{++}\right)^2 + 4G^0_{+-}G^0_{-+}} \tag{5.57}$$

as well as the components (un-normalized) of the eigenvectors,

$$\begin{aligned} v_{11} &= 1 & v_{12} &= \frac{G^0_{+-}}{(\lambda_2 - G^0_{++})} \\ v_{21} &= \frac{(\lambda_1 - G^0_{++})}{G^0_{+-}} & v_{22} &= 1 \end{aligned} \tag{5.58}$$

Since the system of interest has a single unique source at $x \to -\infty$, one has $g_{-+} = 0$ such that the ratio of the mean power measured at infinity to the entrance power in the waveguide gives us access to the *transmission coefficient* as

$$|\mathcal{T}|^2 = \left|\frac{g_{++}}{g_{+-}}\right|^2 = \left|\frac{\Delta_W}{W_{22}}\right|^2 \quad . \tag{5.59}$$

[5] Exponential of a matrix:

$$\begin{aligned} \exp\left[\mathbf{BAB}^{-1}\right] &= \mathbb{1} + \left[\mathbf{BAB}^{-1}\right] + \frac{1}{2!}\left[\mathbf{BAB}^{-1}\right]^2 + \frac{1}{3!}\left[\mathbf{BAB}^{-1}\right]^3 + \cdots \\ &= \mathbf{B}\left[\mathbb{1} + \mathbf{A} + \frac{1}{2!}\mathbf{A}^2 + \frac{1}{3!}\mathbf{A}^3 + \cdots\right]\mathbf{B}^{-1} \\ &= \mathbf{B}\exp\left[\mathbf{A}\right]\mathbf{B}^{-1} \quad . \end{aligned} \tag{5.51}$$

and to the *reflection coefficient* as the ratio of the mean output power at $x \to -\infty$ to the entrance power as

$$|\mathcal{R}|^2 = \left|\frac{g_{--}}{g_{+-}}\right|^2 = \left|\frac{W_{21}}{W_{22}}\right|^2 \quad . \tag{5.60}$$

Using the explicit expressions (5.54) for the $\{W_{ij}\}$ matrix elements together with those of eigenvectors (5.58), the transmission and reflexion coefficients can be written as

$$\mathcal{T} = \frac{\mathrm{e}^{(\lambda_1+\lambda_2)/2}(\lambda_1-\lambda_2)}{\mathrm{e}^{(\lambda_1-\lambda_2)/2}(\lambda_1-G^0_{++}) - \mathrm{e}^{-(\lambda_1-\lambda_2)/2}(\lambda_2-G^0_{++})} \tag{5.61}$$

$$\mathcal{R} = \frac{(\mathrm{e}^{(\lambda_1-\lambda_2)/2} - \mathrm{e}^{-(\lambda_1-\lambda_2)/2})G^0_{-+}}{\mathrm{e}^{(\lambda_1-\lambda_2)/2}(\lambda_1-G^0_{++}) - \mathrm{e}^{-(\lambda_1-\lambda_2)/2}(\lambda_2-G^0_{++})} \quad . \tag{5.62}$$

Recalling that

$$\lambda_1+\lambda_2 = G^0_{--}+G^0_{++} \tag{5.63}$$

$$\lambda_1-\lambda_2 = \left[(G^0_{--}-G^0_{++})^2 + 4G^0_{+-}G^0_{-+}\right]^{1/2} \quad , \tag{5.64}$$

and if $4G^0_{+-}G^0_{-+} \ll (G^0_{--}-G^0_{++})^2$ (regime where the coupling terms between the propagating waves + et − are weak), then we may use the binomial expansion and obtain the *weak coupling* expressions for Eqs (5.61) and (5.62)

$$\mathcal{T} \simeq \mathrm{e}^{G^0_{++}} \tag{5.65}$$

$$\mathcal{R} \simeq \frac{G^0_{-+}}{G^0_{--}-G^0_{++}}\left(\mathrm{e}^{G^0_{--}-G^0_{++}}-1\right) \quad . \tag{5.66}$$

5.3.2 Evaluation of the elements of $\mathbf{G}^0$

There remains to calculate the elements of the matrix $\mathbf{G}^0$. One evaluates first the integrals (5.44)-(5.47) taken at $x \to +\infty$,

$$\int dx\, \kappa_\pm(x)\mathrm{e}^{\{\pm,\,\mp\}i\beta x} = h^{-1}(n_g^2-n_o^2)\int_{-\infty}^{+\infty} dx \int_{-w/2}^{+w/2} dy\, \psi^*(y)E^{C\pm}(x,y)\mathrm{e}^{\{\pm,\,\mp\}i\beta x}\int_0^h dz \quad . \tag{5.67}$$

Since the guided fields $E^{\pm *} = \psi^*\mathrm{e}^{\mp i\beta x}$, Eq. (5.22), are solutions of the Helmholtz equation $\left[\nabla^2 + n_g^2k^2\right]E^{\pm *} = 0$, just as $E^C \equiv E^{C\pm}$ [6] are those of $\left[\nabla^2 + n_o^2k^2\right]E^C = 0$

[6] We redefine $E^C \equiv E^{C\pm}$ for the sake of conciseness. This expression is not to be confused with $\tilde{E}^C$ defined in Eq. (5.14). We also set the coupling coefficients $\kappa \equiv \kappa_\pm$ for the same reason.

over their respective volume, we can write

$$\int d^3\mathbf{r}\; E^{\pm *}E^C = -\frac{1}{n_g^2k^2}\int d^3\mathbf{r}\; \left[\nabla^2 E^{\pm *}\right] E^C \tag{5.68}$$

$$= -\frac{1}{n_o^2k^2}\int d^3\mathbf{r}\, E^{\pm *}\left[\nabla^2 E^C\right] \tag{5.69}$$

which together with Green's second theorem [50], leads to

$$\int d^3\mathbf{r}\; \left\{E^{\pm *}\left[\nabla^2 E^C\right] - \left[\nabla^2 E^{\pm *}\right] E^C\right\} = \int_S d^2\mathbf{r}\,\hat{\nu}\; \left\{E^{\pm *}\left[\nabla E^C\right] - \left[\nabla E^{\pm *}\right] E^C\right\}\;, \tag{5.70}$$

where $\hat{\nu}$ is the unit normal vector to each surface of the volume of interest, a thin rectangular shaped infinite waveguide. Simplifying, we get

$$(n_g^2 - n_o^2)\int d^3\mathbf{r}\; E^{\pm *}E^C = \frac{1}{k^2}\int_S d^2\mathbf{r}\,\hat{\nu}\; \left\{E^{\pm *}\left[\nabla E^C\right] - \left[\nabla E^{\pm *}\right] E^C\right\} \quad . \tag{5.71}$$

Since by assumption, the field is uniform along Oz, this last equation reduces to

$$\int dx\; \kappa(x)\mathrm{e}^{\mp i\beta x} = \frac{1}{k^2}\int_C dl\,\hat{\nu}\cdot\left\{E^{\pm *}\left[\nabla E^C\right] - \left[\nabla E^{\pm *}\right] E^C\right\} \tag{5.72}$$

where C is the contour presented in Fig. 5.5. This contour integral is not closed in the usual sense since the Green's identity transforms a volume integral into a surface integral: differential *line* element dl must always be positive and any plus/minus sign appears naturally in the calculation through the normal derivative.

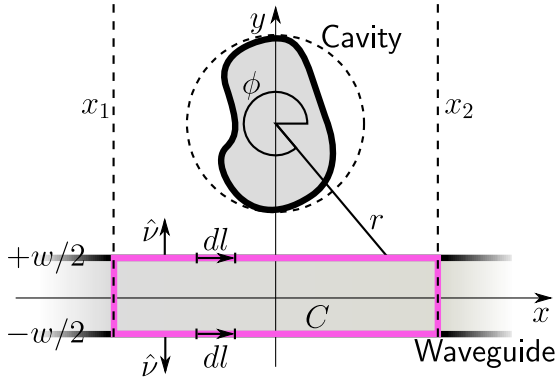


Fig. 5.5 Coordinate system for the integration over the contour C (pink rectangle). The normal vectors $\hat{\nu}$ are those of the contributing surfaces of the waveguide in regards of Eq. (5.72).

For $|x_1| = |x_2| \to \infty$, the asymptotic expansion of the Hankel function (see the expressions of the field emitted by the cavity Eqs (5.18)-(5.19)) implies that the integrals (5.72) on the transverse sections of the waveguide are zero. Two line integrals over x remain:

$$\int dx\; \kappa(x)\mathrm{e}^{\mp i\beta x} = \frac{1}{k^2}\left[\int_{-\infty}^{+\infty} dx\; \left\{E^{\pm *}\frac{\partial}{\partial y}E^C - E^C\frac{\partial}{\partial y}E^{\pm *}\right\}\Big|_{y=+w/2}\right.$$
$$\left. - \int_{-\infty}^{+\infty} dx\; \left\{E^{\pm *}\frac{\partial}{\partial y}E^C - E^C\frac{\partial}{\partial y}E^{\pm *}\right\}\Big|_{y=-w/2}\right] . \tag{5.73}$$

According to Section E.1, the waveguide field evaluated at its boundary is $\mathbf{E}^{\pm}(x, y = \pm w/2) = A\cos\gamma y\ \mathrm{e}^{\pm i\beta x}\Big|_{y=\pm w/2}$, which means that

$$\begin{aligned}\int dx\ \kappa(x)\mathrm{e}^{\mp i\beta x} &= \frac{1}{k^2}A^*\Bigg[\ \left\{\left(+\cos\left(\gamma\frac{w}{2}\right)\frac{\partial}{\partial y}+\gamma\sin\left(\gamma\frac{w}{2}\right)\right)\int_{-\infty}^{+\infty}dx\,E^C\mathrm{e}^{\mp i\beta x}\right\}\Big|_{y=+w/2}\\ &\quad+\left\{\left(-\cos\left(\gamma\frac{w}{2}\right)\frac{\partial}{\partial y}+\gamma\sin\left(\gamma\frac{w}{2}\right)\right)\int_{-\infty}^{+\infty}dx\,E^C\mathrm{e}^{\mp i\beta x}\right\}\Big|_{y=-w/2}\Bigg].\end{aligned} \tag{5.74}$$

Since the field E^C is made of cylindrical harmonics of the type $H_m^{(1)}(n_o kr)\mathrm{e}^{im\phi}$ with the polar coordinates having their origin at the center of the cavity, the integral to calculate is

$$\int_{-\infty}^{+\infty}dx\,H_m^{(1)}(n_o kr)\mathrm{e}^{im\phi}\mathrm{e}^{\mp i\beta x}=\int_{-\infty}^{+\infty}dx\,H_m^{(1)}(n_o k\sqrt{x^2+(y-y_0)^2})\mathrm{e}^{im\arctan\frac{y-y_0}{x}}\mathrm{e}^{\mp i\beta x} \tag{5.75}$$

with $y_0 = d + R_0 + w/2 > w/2 > -w/2$ and the Cartesian coordinates (x, y) centered on the waveguide (Fig. 5.5). The convergence of this integral for large values of x is verified in subsection E.2.2 of Appendix E. One rewrites the integral as

$$\int_{-\infty}^{+\infty}dx\ H_m^{(1)}(n_o kr)\mathrm{e}^{im\phi}\mathrm{e}^{\mp i\beta x}=\frac{1}{n_o k}\int_{-\infty}^{+\infty}d\xi\ H_m^{(1)}(z)\mathrm{e}^{im\alpha}\mathrm{e}^{\mp i\tilde{\beta}\xi} \tag{5.76}$$

with $z=\sqrt{\eta^2+\xi^2}$, $\xi = n_o kx$, $\eta = n_o k(y - y_0)$, $\alpha = \arctan(\eta/\xi)$ and $\tilde{\beta} = \beta/n_o k$. The system's arrangement is such that $y - y_0 < 0$. Making use of results of Appendix E, especially Eqs (E.15)-(E.18), we get [7]

$$\begin{aligned}\int_{-\infty}^{+\infty}dx\ H_m^{(1)}(n_o kr)\mathrm{e}^{im\phi}\mathrm{e}^{\mp i\beta x} &= \frac{1}{n_o k}\int_{-\infty}^{+\infty}d\xi\ \left[\int_{-\infty}^{+\infty}d\beta'\,F_m(\beta',\eta)\mathrm{e}^{i\beta'\xi}\right]\mathrm{e}^{\mp i\tilde{\beta}\xi}\\ &= \frac{1}{n_o k}\int_{-\infty}^{+\infty}d\beta'\,(-1)^m F_{-m}(\beta',|\eta|)\left[\int_{-\infty}^{+\infty}d\xi\,\mathrm{e}^{i(\beta'\mp\tilde{\beta})\xi}\right]\\ &= \frac{2\pi}{n_o k}\int_{-\infty}^{+\infty}d\beta'\,(-1)^m F_{-m}(\beta',|\eta|)\delta(\beta'\mp\tilde{\beta})\\ &= \frac{2\pi}{n_o k}(-1)^m F_{-m}(\pm\tilde{\beta},|\eta|)\quad .\end{aligned} \tag{5.77}$$

Because $\beta > n_o k$, we get that $\tilde{\beta} > 1$ which selects the evanescent parts of the representation of the Hankel functions: one recalls that the coupling between waveguide and cavity is caused by the evanescent portion of the field from the cavity. For $y < y_0$ and

[7] The principal result is derived in subsection E.2.1. A more direct integration is also presented in subsection E.2.3. A complete demonstration for all cases of signs of β and m is however not available.

$\tilde{\beta} = \beta/n_o k > 1$, one therefore has

$$\int_{-\infty}^{+\infty} dx\ H_m^{(1)}(n_o k r)\mathrm{e}^{im\phi}\mathrm{e}^{\mp i\beta x} = -\frac{2i}{n_o k}\frac{\mathrm{e}^{n_o k(y-y_0)\sqrt{\tilde{\beta}^2-1}}}{\sqrt{\tilde{\beta}^2-1}}\left[\mp i\left(\tilde{\beta}+\sqrt{\tilde{\beta}^2-1}\right)\right]^{\pm m}. \tag{5.78}$$

Hence, given (5.18), one gets

$$\begin{aligned}\int_{-\infty}^{+\infty} dx\ E^{C+}\mathrm{e}^{\mp i\beta x} &= -\frac{2i}{n_o k}\frac{1}{\sqrt{\tilde{\beta}^2-1}}\mathrm{e}^{n_o k(y-y_0)\sqrt{\tilde{\beta}^2-1}}A\cos\gamma\frac{w}{2}\ \mathrm{e}^{-\alpha(R_0+d)} \\ &\quad\times\sum_m\left[\frac{1}{2}\sum_{m'}\left(-\delta_{mm'}+S_{mm'}\right)i^{m'}\left(\frac{\beta+\alpha}{\beta-\alpha}\right)^{m'/2}\right]\left[\mp i\left(\tilde{\beta}+\sqrt{\tilde{\beta}^2-1}\right)\right]^{\pm m}\end{aligned} \tag{5.79}$$

or since $\tilde{\beta} = \beta/n_o k$ and $\alpha^2 = \beta^2 - (n_o k)^2$,

$$\begin{aligned}\int_{-\infty}^{+\infty} dx\ E^{C+}\mathrm{e}^{\mp i\beta x} &= -\frac{2i}{\alpha}\mathrm{e}^{\alpha y}\mathrm{e}^{-\alpha(2(R_0+d)+w/2)}A\cos\gamma\frac{w}{2} \\ &\quad\times\sum_m\left[\mp i\left(\frac{\beta+\alpha}{n_o k}\right)\right]^{\pm m}\cdot\frac{1}{2}\sum_{m'}\left(-\delta_{mm'}+S_{mm'}\right)\cdot\left[i\left(\frac{\beta+\alpha}{\beta-\alpha}\right)^{1/2}\right]^{+m'}.\end{aligned} \tag{5.80}$$

Similarly the contribution of E^{C-} is readily written

$$\begin{aligned}\int_{-\infty}^{+\infty} dx\ E^{C-}\mathrm{e}^{\mp i\beta x} &= -\frac{2i}{\alpha}\mathrm{e}^{\alpha y}\mathrm{e}^{-\alpha(2(R_0+d)+w/2)}A\cos\gamma\frac{w}{2} \\ &\quad\times\sum_m\left[\mp i\left(\frac{\beta+\alpha}{n_o k}\right)\right]^{\pm m}\cdot\frac{1}{2}\sum_{m'}\left(-\delta_{mm'}+S_{mm'}\right)\cdot\left[i\left(\frac{\beta+\alpha}{\beta-\alpha}\right)^{1/2}\right]^{-m'}.\end{aligned} \tag{5.81}$$

Substituting (5.80) in $\int dx\ \kappa_+(x)\mathrm{e}^{\mp i\beta x}$, one finds an elegant expression

$$\begin{aligned}+i\frac{k^2}{2\beta P}\int dx\ \kappa_+(x)\mathrm{e}^{\mp i\beta x} &= f(\alpha,\beta,\gamma;\ w) \\ &\quad\times\left[\mathbf{c}^{\pm T}(\alpha,\beta,n_o k;\ R_0,d)\cdot\left[\frac{1}{2}\left(-\mathbb{1}+\mathbf{S}\right)\right]\cdot\mathbf{v}^{+}(\alpha,\beta;\ R_0,d)\right]\end{aligned} \tag{5.82}$$

where the input power P is given by

$$P = |A|^2\left(\frac{\sin(\gamma w)}{2\gamma}+\frac{w}{2}+\frac{2\cos^2\left(\gamma\frac{w}{2}\right)}{2\alpha}\right) \quad . \tag{5.83}$$

Equation (5.82) is made up of different pieces easily recognizable: a coefficient characteristic of the waveguide

$$f(\alpha,\beta,\gamma;\ w) = +\frac{4}{\beta}\cos\left(\gamma\frac{w}{2}\right)\ \mathrm{e}^{-\alpha w/2}\ \left[\frac{\cos\left(\gamma\frac{w}{2}\right)\sinh\left(\alpha\frac{w}{2}\right)+\frac{\gamma}{\alpha}\sin\left(\gamma\frac{w}{2}\right)\cosh\left(\alpha\frac{w}{2}\right)}{\frac{1}{\gamma}\sin(\gamma w)+w+\frac{2\cos^2\left(\gamma\frac{w}{2}\right)}{\alpha}}\right]\ , \tag{5.84}$$

a vector of coupling coefficients between the field emerging from the cavity and the field of the waveguide

$$\begin{aligned}\{\mathbf{c}^{\pm}(\alpha,\beta,n_o k;\ R_0,d)\}_m &= \left[\mp i\left(\frac{\beta+\alpha}{n_o k}\right)\right]^{\pm m}\mathrm{e}^{-\alpha(R_0+d)}\\ &= (\mp i)^{\pm m}\exp\left[-\alpha(R_0+d)\pm m\ln\left(\frac{\beta+\alpha}{n_o k}\right)\right]\end{aligned} \tag{5.85}$$

a vector of the coefficients of the evanescent field from the waveguide

$$\begin{aligned}\{\mathbf{v}^{+}(\alpha,\beta;\ R_0,d)\}_{m'} &= \left[i\left(\frac{\beta+\alpha}{\beta-\alpha}\right)^{1/2}\right]^{+m'}\mathrm{e}^{-\alpha(R_0+d)}\\ &= i^{m'}\exp\left[-\alpha(R_0+d)+\frac{m'}{2}\ln\left(\frac{\beta+\alpha}{\beta-\alpha}\right)\right]\end{aligned} \tag{5.86}$$

and the identity $\mathbb{1}$ and the scattering $\mathbf{S}$ matrices. The same way, we obtain

$$\begin{aligned}-i\frac{k^2}{2\beta P}\int dx\ \kappa_-(x)\mathrm{e}^{\mp i\beta x} &= -f(\alpha,\beta,\gamma;\ w)\\ &\quad\times\left[\mathbf{c}^{\pm T}(\alpha,\beta,n_o k;\ R_0,d)\cdot\left[\frac{1}{2}\left(-\mathbb{1}+\mathbf{S}\right)\right]\cdot\mathbf{v}^{-}(\alpha,\beta;\ R_0,d)\right]\end{aligned} \tag{5.87}$$

with

$$\begin{aligned}\{\mathbf{v}^{-}(\alpha,\beta;\ R_0,d)\}_{m'} &= \left[i\left(\frac{\beta+\alpha}{\beta-\alpha}\right)^{1/2}\right]^{-m'}\mathrm{e}^{-\alpha(R_0+d)}\\ &= i^{-m'}\exp\left[-\alpha(R_0+d)-\frac{m'}{2}\ln\left(\frac{\beta+\alpha}{\beta-\alpha}\right)\right]\quad .\end{aligned} \tag{5.88}$$

One notes that the evanescent excitation vectors $\mathbf{v}^{+}$ et $\mathbf{v}^{-}$ and the coupling vectors $\mathbf{c}^{+}$ and $\mathbf{c}^{-}$ are simply related by an inversion matrix $\{\bar{\mathbf{I}}\}_{mm'}=\delta_{-mm'}$ and a parity operation $\{\mathbf{\Pi}\}_{mm'}=(-1)^m\delta_{mm'}$,

$$\mathbf{c}^{+}=\mathbf{\Pi}\bar{\mathbf{I}}\mathbf{c}^{-}\qquad,\qquad\mathbf{v}^{+}=\bar{\mathbf{I}}\mathbf{v}^{-}\ . \tag{5.89}$$

In other words $\mathbf{v}^{+}_m=\mathbf{v}^{-}_{-m}$ and $\mathbf{c}^{+}_m=(\mathbf{c}^{-}_{-m})^*=(-1)^m\mathbf{c}^{-}_{-m}$. The matrices $\bar{\mathbf{I}}$ et $\mathbf{\Pi}$ are idempotent ($\mathbf{X}^2=\mathbb{1}$), symmetric ($\mathbf{X}^T=\mathbf{X}$) and commute with each other.

The term $\chi(x)$ is made up of parts of the decreasing portions of the exponential (squared) on the surface of the cavity. Its contribution will be much smaller in magnitude than that of the coupling term. The matrix elements of $\mathbf{G}^0$ are therefore directly expressed by the integrals over the coupling coefficients already obtained

$$\begin{aligned} G^0_{++} &= +f\mathbf{c}^{+T}\frac{1}{2}(\mathbf{S}-\mathbb{1})\,\mathbf{v}^+ \qquad G^0_{+-} = +f\mathbf{c}^{-T}\frac{1}{2}(\mathbf{S}-\mathbb{1})\,\mathbf{v}^+ \\ G^0_{-+} &= -f\mathbf{c}^{+T}\frac{1}{2}(\mathbf{S}-\mathbb{1})\,\mathbf{v}^- \qquad G^0_{--} = -f\mathbf{c}^{-T}\frac{1}{2}(\mathbf{S}-\mathbb{1})\,\mathbf{v}^- \end{aligned} \tag{5.90}$$

or with the relations (5.89) ($\mathbf{v} \equiv \mathbf{v}^+$ et $\mathbf{c} \equiv \mathbf{c}^+$),

$$\begin{aligned} G^0_{++} &= +f\mathbf{c}^{T}\frac{1}{2}(\mathbf{S}-\mathbb{1})\,\mathbf{v} \qquad G^0_{+-} = +f\mathbf{c}^{T}\mathbf{\Pi}\bar{\mathbf{I}}\frac{1}{2}(\mathbf{S}-\mathbb{1})\,\mathbf{v} \\ G^0_{-+} &= -f\mathbf{c}^{T}\frac{1}{2}(\mathbf{S}-\mathbb{1})\,\bar{\mathbb{I}}\mathbf{v} \qquad G^0_{--} = -f\mathbf{c}^{T}\mathbf{\Pi}\bar{\mathbf{I}}\frac{1}{2}(\mathbf{S}-\mathbb{1})\,\bar{\mathbf{I}}\mathbf{v} \quad . \end{aligned} \tag{5.91}$$

One can finally evaluate the eigenvalues and eigenvectors of $\mathbf{G}^0$ (5.44)-(5.47) as well as the transmission and reflection coefficients (5.61)-(5.62). In the limit of weak coupling between the propagating + and − fields, Eq. (5.65), the transmission coefficient simplifies to

$$\mathcal{T} \simeq \exp\left[+f\mathbf{c}^{T}\frac{1}{2}(\mathbf{S}-\mathbb{1})\,\mathbf{v}\right] \quad . \tag{5.92}$$

This expression is the main result of this section.

5.4 Alternative development of the model

The coupling model of Okamoto, upon which we have conceptually based our description of the complete electromagnetic field, has originally been designed for the treatment of the coupling of 2 waveguides. The approach prescribes the simultaneous perturbation of the fields of both waveguides. The case of the cavity-waveguide coupling is in some sense simpler since the cavity interacts with the waveguide solely through its scattering matrix. In other words, one can assume that the field above the waveguide is correctly evaluated and concentrate uniquely on the field within the waveguide. This is what we will do in this Section.

5.4.1 Description of the electromagnetic field in the guide

In Section 5.2, we have presented the production of a cavity field excited by an evanescent continuous field from the waveguide. We argued that it was 'reasonable' to modulate the output field from the cavity with the envelopes of the guided waves following the

observation that the excitation of the cavity was linearly dependant upon the guided field. In this description, there is no further feedback with the waveguide: we seek global envelopes solving the system altogether. From the point of view of the waveguide however, the field emerging from the cavity can be seen to induce local sources of propagating field within the waveguide. In a sense, this section focuses on a 'microscopic' description of the coupling phenomenon by focusing solely on the field within the waveguide as opposed to the 'macroscopic' view of the system discussed in the preceding section.

The addition of the induced field to the existing waveguide field has two consequences. First, its superposition to the initial waveguide field (primary excitation) will produce interference without removing the initial field from the interior of the waveguide. Second, there is now the possibility of a new excitation of the cavity by the evanescent part of the induced field. A cycle of secondary excitations can now begin. Since coupling between the evanescent fields and the cavity is never perfect, as well as any further re-couplings, each new excitation will be smaller in magnitude that the preceding ones. Given that the (evanescent) power at the input is finite, this series of excitation must converge. The sequence of events is schematically presented in Fig. 5.6.

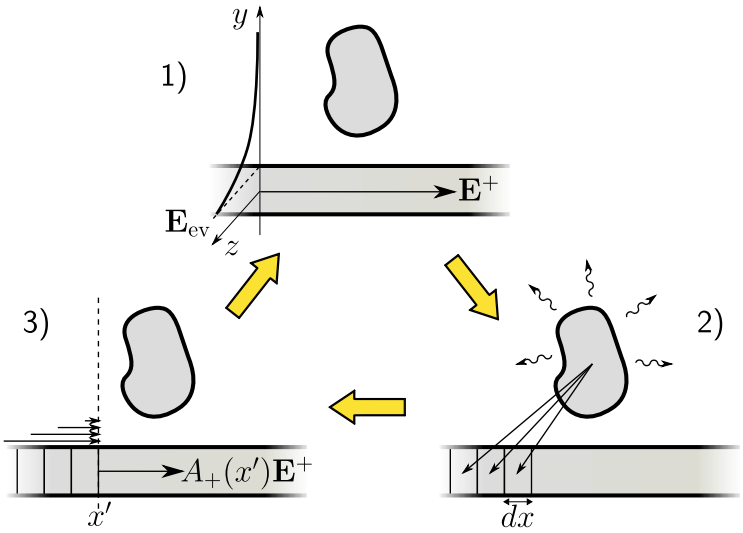


Fig. 5.6 Excitation cycle of the cavity: forward propagating '+' waves pictured. 1) An initial evanescent field excites the cavity which responds by producing a characteristic field. 2) This field in turn induces a source field in a section dx of the waveguide. 3) At x', the waveguide field is made up of a superposition of induced fields produced 'upstream'; this results in the creation of an effective amplitude $A(x')$. This waveguide field has an evanescent component that excites anew the cavity. Note that the induction phenomenon in step 2) also produces backward propagating '$-$' waves. These contribute to the reflection coefficient of the waveguide.

A mathematical formulation of the previous iterative process can be quite complex. However, one can consider a global envelope $g_{\pm}(x)$ at position x which should contain

phase and amplitude information of the superposition of induced fields to the initial waveguide mode. One thinks of $g_{\pm}(x)$ as describing the equilibrium *steady-state* situation where the field in the waveguide at x is $g_{\pm}(x)\mathbf{E}^{\pm}$ and the additional contributions from the cavity are $g_{\pm}(x)\mathrm{E}^{C\pm}$. Hence one seeks an envelope function $g_{\pm}(x)$ at x on a differential element dx such that its contribution to the excitation of the cavity shares the same envelope. Under this condition, the total electromagnetic field *inside the waveguide* can be written as

$$\begin{aligned} \mathbf{E} &\simeq g_+(x)\mathbf{E}^+ + g_+(x)\mathbf{E}^{C+} + g_-(x)\mathbf{E}^- + g_-(x)\mathbf{E}^{C-} && (5.93)\\ \mathbf{H} &\simeq g_+(x)\mathbf{H}^+ + g_+(x)\mathbf{H}^{C+} + g_-(x)\mathbf{H}^- + g_-(x)\mathbf{H}^{C-} \quad . && (5.94) \end{aligned}$$

The procedure that follows is then analogous to that of Section 5.2. Applying Maxwell's equations, one extracts our first differential equation for $g_{\pm}(x)$

$$g'_+(x)\left[E^+ + E^{C+}\right] = -g'_-(x)\left[E^- + E^{C-}\right] \tag{5.95}$$

and the second

$$\begin{aligned} g'_+(x)\frac{\partial}{\partial x}\left[E^+ + E^{C+}\right] + g'_-(x)\frac{\partial}{\partial x}\left[E^- + E^{C-}\right] &= -(n^2 - n_c^2)k^2\left(E^{C+}g_+ + E^{C-}g_-\right) \\ &\quad -(n^2 - n_g^2)k^2\left(E^+g_+ + E^-g_-\right) \ . \end{aligned} \tag{5.96}$$

The novelty of this approach is to consider that the field above the guide is modeled properly via the scattering process of Section 5.2 and is not explicitly affected by the envelope functions outside the waveguide. One justifies this method by interpreting the envelope function as the contribution to the initial waveguide mode of the superposition of all the cavity induced fields. In short, one examines only the region covered by the waveguide. Within this region of space, one has

$$\left|\int_{-w/2}^{+w/2} dy\ E^{\pm^*}E^{C\pm,\mp}\right| \ll \left|\int_{-w/2}^{+w/2} dy\ E^{\pm^*}E^{\pm,\mp}\right| \tag{5.97}$$

$$\left|\int_{-w/2}^{+w/2} dy\ E^{\pm^*}\frac{\partial}{\partial x}E^{C\pm,\mp}\right| \ll \left|\int_{-w/2}^{+w/2} dy\ E^{\pm^*}\frac{\partial}{\partial x}E^{\pm,\mp}\right| \quad . \tag{5.98}$$

Multiplying on the left with E^{+*} and integration on the section of the waveguide $y = [-w/2,\ +w/2]$, one obtains the fraction of the field from the cavity that effectively excites the waveguide. We get a new set of differential equations

$$\begin{aligned} \hat{g}'_+ &= +i\frac{k^2}{2\beta\hat{P}}\mathrm{e}^{-i\beta x}\left[\hat{\kappa}_+(x)\hat{g}_+ + \hat{\kappa}_-(x)\hat{g}_-\right] && (5.99)\\ \hat{g}'_- &= -i\frac{k^2}{2\beta\hat{P}}\mathrm{e}^{+i\beta x}\left[\hat{\kappa}_+(x)\hat{g}_+ + \hat{\kappa}_-(x)\hat{g}_-\right] \quad . && (5.100) \end{aligned}$$

with

$$\hat{P} = \int_{-w/2}^{+w/2} dy\ \psi^*(y)\psi(y) = |A|^2 \left(\frac{\sin(\gamma w)}{2\gamma} + \frac{w}{2} \right) \tag{5.101}$$

$$\hat{\kappa}_{\pm}(x) = \int_{-w/2}^{+w/2} dy\ (n^2 - n_c^2)\psi^*(y) E^{C\pm}(x,y) \quad . \tag{5.102}$$

This system of differential equations is completely *autonomous* with no forcing terms usually associated with this type of perturbation model. The boundary conditions are $\hat{g}_+(-\infty) = 1$ and $\hat{g}_-(+\infty) = 0$.

5.4.2 Solution of the alternative model

The solution of the system (5.99)-(5.100) takes the same form as the one found in Section 5.3,

$$\begin{pmatrix} \hat{g}_+(x) \\ \hat{g}_-(x) \end{pmatrix} = \exp\left[\hat{\mathbf{G}}(x)\right] \begin{pmatrix} \hat{g}_+(-\infty) \\ \hat{g}_-(-\infty) \end{pmatrix} \tag{5.103}$$

with

$$\hat{G}_{11}(x) = \hat{G}_{++}(x) = +i\frac{k^2}{2\beta\hat{P}} \int_{-\infty}^{x} dx'\ \hat{\kappa}_+(x')\mathrm{e}^{-i\beta x'} \tag{5.104}$$

$$\hat{G}_{12}(x) = \hat{G}_{+-}(x) = +i\frac{k^2}{2\beta\hat{P}} \int_{-\infty}^{x} dx'\ \hat{\kappa}_-(x')\mathrm{e}^{-i\beta x'} \tag{5.105}$$

$$\hat{G}_{21}(x) = \hat{G}_{-+}(x) = -i\frac{k^2}{2\beta\hat{P}} \int_{-\infty}^{x} dx'\ \hat{\kappa}_+(x')\mathrm{e}^{+i\beta x'} \tag{5.106}$$

$$\hat{G}_{22}(x) = \hat{G}_{--}(x) = -i\frac{k^2}{2\beta\hat{P}} \int_{-\infty}^{x} dx'\ \hat{\kappa}_-(x')\mathrm{e}^{+i\beta x'} \quad . \tag{5.107}$$

For $x \to +\infty$, Eq. (5.103) becomes

$$\begin{pmatrix} \hat{g}_+(+\infty) \\ \hat{g}_-(+\infty) \end{pmatrix} \equiv \begin{pmatrix} \hat{g}_{++} \\ \hat{g}_{-+} \end{pmatrix} = \exp\left[\hat{\mathbf{G}}^0\right] \begin{pmatrix} \hat{g}_+(-\infty) \\ \hat{g}_-(-\infty) \end{pmatrix} \equiv \exp\left[\hat{\mathbf{G}}^0\right] \begin{pmatrix} \hat{g}_{+-} \\ \hat{g}_{--} \end{pmatrix} \tag{5.108}$$

with $\hat{G}^0_{\pm\pm} = \hat{G}_{\pm\pm}(+\infty)$. Again we will need to express the 'outgoing' envelops $\hat{g}_{++}$ et $\hat{g}_{--}$ in terms of the 'incoming' ones. With the appropriate changes just indicated, we recuperate all the results of subsection 5.3.1 for the new eigenvalues $\{\hat{\lambda}_{1,2}\}$, the new eigenvectors $\{\hat{\mathbf{v}}_{1,2}\}$ and the new transmission $\hat{\mathcal{T}}$ and reflexion $\hat{\mathcal{R}}$ coefficients. A comparison with the results of Section 5.3.1 will be discussed shortly.

5.5 Results for the disc cavity

We apply the approach presented in Sections 5.2-5.4 to the case of a homogeneous disc. The parameters of the system appear in Tab. 5.1.

refractive index of the cavity	n_c	1.5
refractive index of the waveguide	n_g	1.5
refractive index of the surrounding medium	n_o	1
radius of the cavity [arb. units]	R_0	1
width of the waveguide	w/R_0	0.1
wavenumber (interval)	kR_0	$[20, 21]$

Tab. 5.1 Physical parameters of the coupled cavity-waveguide system.

For these parameters and for the wavenumber interval considered, the waveguide constants are presented in Tab. 5.2.

decay constant of evanescent field	α/R_0	[15.8570, 17.0003]
propagation constant	β/R_0	[25.5234, 27.0187]
transverse profile constant	γ/R_0	[15.7657, 16.1938]

Tab. 5.2 Waveguide physical constants.

For the homogeneous disc, the wave field is of the form

$$\sum_m \begin{cases} t_m^{\pm} J_m(n_c kr) \mathrm{e}^{im\phi} & r < R_0 \\ \left[a_m^{\pm} H_m^{(2)}(n_o kr) + b_m^{\pm} H_m^{(1)}(n_o kr) \right] \mathrm{e}^{im\phi} & r > R_0 \end{cases} \tag{5.109}$$

with $b_m^{\pm} = S_{mm} a_m^{\pm}$ and $t_m^{\pm} = T_{mm} a_m^{\pm}$,

$$S_{mm'} = -\frac{\Delta_m^*}{\Delta_m}\delta_{mm'} \quad , \quad T_{mm'} = -\frac{4i}{\pi k R_0}\frac{1}{\Delta_m}\delta_{mm'} \tag{5.110}$$

$$\Delta_m = n_c H_m^{(1)}(n_o k R_0) J_m'(n_c k R_0) - n_o H_m^{(1)'}(n_o k R_0) J_m(n_c k R_0) \ . \tag{5.111}$$

The delay spectrum of the cavity is shown in Fig. 5.7.

5.5.1 Validity of the assumptions (5.34) - (5.36) and (5.97) - (5.98)

We first seek out to verify the assumptions (5.34) and (5.36) as function of the distance d/R_0; one can always find a distance d such that the assumptions are satisfied. This step allows us to assert the validity of our approach. For (5.34), we have, with $\theta =$

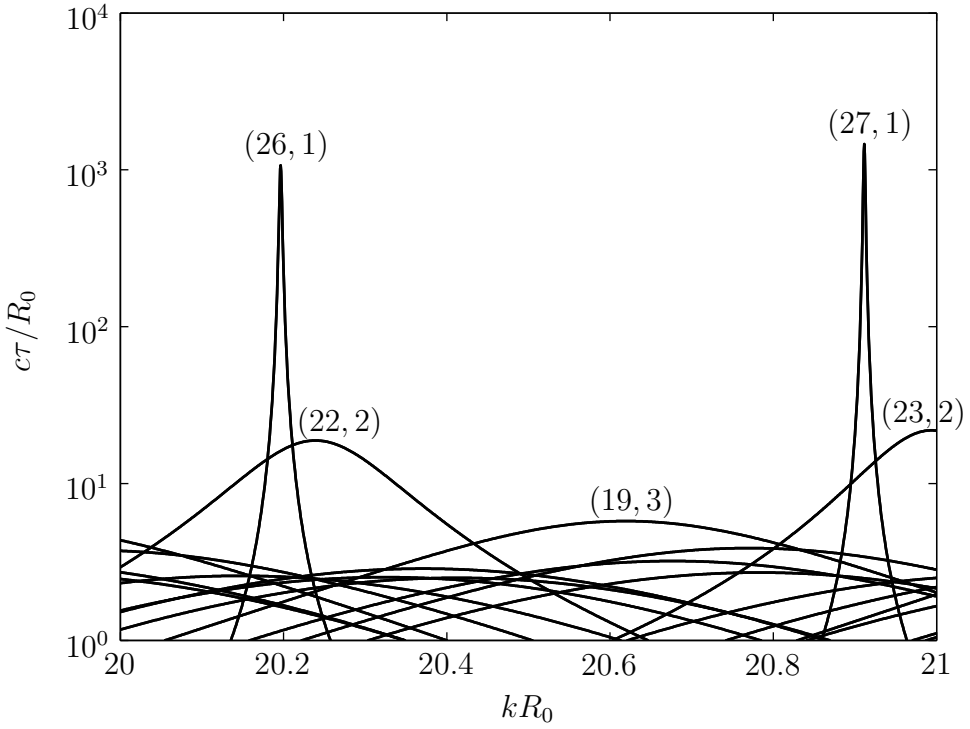


Fig. 5.7 Dealy spectrum for a homogeneous disc with parameters of Tab. 5.1. A few resonances are identified (usual notation (m,n), m: angular momentum; n: number of radial nodes).

$\arctan(y/x)$, $\xi_0 = n_o k\sqrt{x^2+y^2}$, and $\xi_c = n_c k\sqrt{x^2+y^2}$

$$
\begin{aligned}
\int_{-\infty}^{+\infty} dy\ \psi^*(y)E^{\pm}(x,y) \quad = \quad & A^* \cos\left(\gamma\frac{w}{2}\right) \mathrm{e}^{-\alpha(R_0+d)} \sum_m a_m^{\pm} \int_{\tilde{y}}^{\infty} dy\ \mathrm{e}^{-\alpha y} H_m^{(1)}(\xi_0)\mathrm{e}^{im\theta} \\
& + A^* \cos\left(\gamma\frac{w}{2}\right) \mathrm{e}^{-\alpha(R_0+d)} \sum_m a_m^{\pm} \int_{\sqrt{R_0^2-x^2}}^{\tilde{y}} dy\ \mathrm{e}^{-\alpha y} H_m^{(1)}(\xi_0)\mathrm{e}^{im\theta} \\
& + A^* \cos\left(\gamma\frac{w}{2}\right) \mathrm{e}^{-\alpha(R_0+d)} \sum_m t_m^{\pm} \int_{0}^{\sqrt{R_0^2-x^2}} dy\ \mathrm{e}^{-\alpha y} J_m(\xi_c)\mathrm{e}^{im\theta} \\
& + A^* \cos\left(\gamma\frac{w}{2}\right) \mathrm{e}^{-\alpha(R_0+d)} \sum_m t_m^{\pm} \int_{0}^{\sqrt{R_0^2-x^2}} dy\ \mathrm{e}^{+\alpha y} J_m(\xi_c)\mathrm{e}^{-im\theta} \\
& + A^* \cos\left(\gamma\frac{w}{2}\right) \mathrm{e}^{-\alpha(R_0+d)} \sum_m a_m^{\pm} \int_{\sqrt{R_0^2-x^2}}^{R_0+d} dy\ \mathrm{e}^{+\alpha y} H_m^{(1)}(\xi_0)\mathrm{e}^{-im\theta} \\
& + A^* \sum_m a_m^{\pm} \int_{R_0+d}^{R_0+d+w} dy\ \cos[\gamma(-y+R_0+d+w/2)] H_m^{(1)}(\xi_0)\mathrm{e}^{-im\theta} \\
& + A^* \cos\left(\gamma\frac{w}{2}\right) \mathrm{e}^{+\alpha(R_0+d+w)} \sum_m a_m^{\pm} \int_{R_0+d+w}^{\tilde{y}} dy\ \mathrm{e}^{-\alpha y} H_m^{(1)}(\xi_0)\mathrm{e}^{-im\theta} \\
& + A^* \cos\left(\gamma\frac{w}{2}\right) \mathrm{e}^{+\alpha(R_0+d+w)} \sum_m a_m^{\pm} \int_{\tilde{y}}^{\infty} dy\ \mathrm{e}^{-\alpha y} H_m^{(1)}(\xi_0)\mathrm{e}^{-im\theta} \quad .
\end{aligned}
\tag{5.112}
$$

The overlap integrals in the asymptotic regime ($y \in [\tilde{y},\ \infty[$) have been explicitly isolated.

The derivatives involving the cylindrical functions are easily evaluated as

$$\frac{\partial}{\partial x}H_m^{(1)}(n_o kr)\mathrm{e}^{im\phi} = \frac{n_o kx}{r}\frac{\partial}{\partial z}H_m^{(1)}(z)\Big|_{n_o kr}\mathrm{e}^{im\phi} - i\frac{my}{r^2}H_m^{(1)}(n_o kr)\mathrm{e}^{im\phi} \quad (5.113)$$

$$\frac{\partial}{\partial x}J_m(n_o kr)\mathrm{e}^{im\phi} = \frac{n_o kx}{r}\frac{\partial}{\partial z}J_m(z)\Big|_{n_o kr}\mathrm{e}^{im\phi} - i\frac{my}{r^2}J_m(n_o kr)\mathrm{e}^{im\phi} \quad . \quad (5.114)$$

At $x = 0$, the first of these expressions becomes

$$\frac{\partial}{\partial x}H^{(1)}(n_o kr)\mathrm{e}^{im\phi}\Big|_{x=0} = -i\frac{m}{y}H^{(1)}(n_o k|y|)\mathrm{e}^{i\mathrm{sign}(y)m\frac{\pi}{2}} \quad . \quad (5.115)$$

One will find a detailed evaluation of the asymptotic contributions at subsection E.2.4 of Appendix E.

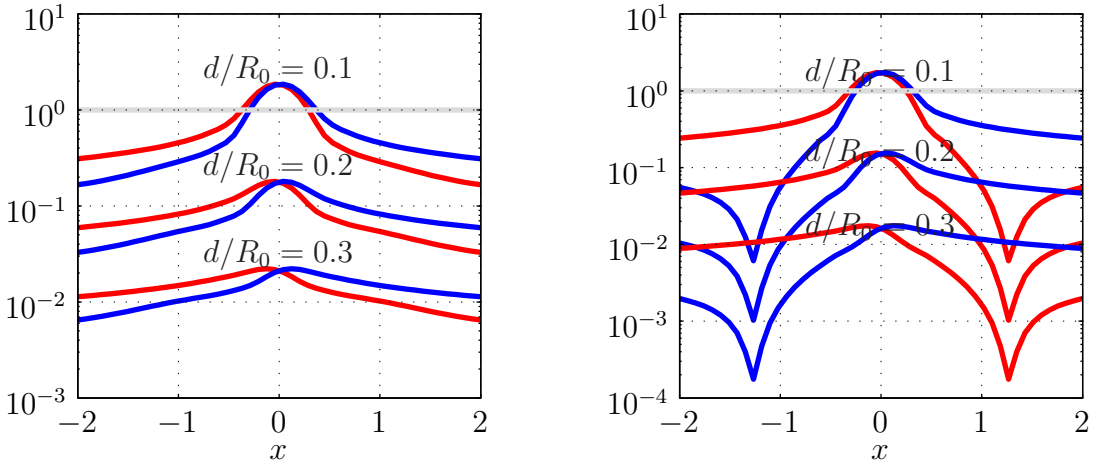
The magnitude of the exponent α of the evanescent field with respect to $n_o k$ strongly decreases the asymptotic contributions beyond say $\tilde{y} \sim 3$: we fix $\tilde{y} = 20$ for the contribution $\ll \max[|\text{integral (5.112)}|]$. The results of the calculation of the overlap are presented in Fig. 5.8 for a wavenumber k corresponding to the position of the resonance $(26, 1)$. One observes the expected symmetry between the $+$ and $-$ propagation directions. The distance $d/R_0 = 0.3$ verifies the assumptions to within approximately $\sim 2\%$ and the calculations of the following subsections will be done with this value.

We have also verified the approximations used in the alternative model of Section 5.4 and found a corresponding agreement. The equivalent verification of the assumptions (5.97)-(5.98) is presented in Fig. 5.9.

5.5.2 Transmission coefficient

While the last subsection has given us a value of $d/R_0 = 0.3$ for which the fundamental assumptions of our method are verified to within a few per cent, we are now concerned with the relative size of $\chi(x)$ and $\kappa_\pm$ in the integrals (5.44)-(5.47). Figure 5.10 shows that the contributions originating from χ may not be negligible with respect to those of $\kappa_\pm$. Note however that the spectral domain around resonances are largely dominated the $\kappa_\pm$ contributions. Since we are likely to be more interested in the impact of the resonances on the transmission, the χ contributions are dropped altogether.

Also, the cross terms G^0_{+-} and G^0_{-+} are very small with respect to the direct terms (there is only weak transfer between the $+$ and $-$ wave guide mode). So practically, one



(a) Assumption (5.34). (b) Assumption (5.36).

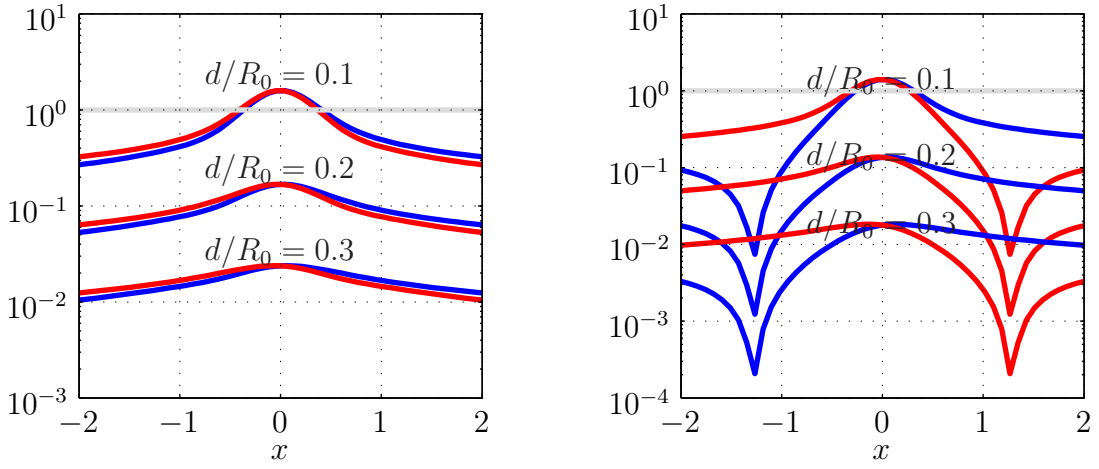
Fig. 5.8 Test of assumptions (5.34) and (5.36) as a function of x for 3 values of d; $kR_0 \simeq 20.1964$ is the position of the resonance $(26, 1)$. The blue (red) curves are associated with the overlap of the field caused by the interaction with a waveguide mode propagating towards $+\infty$ $(-\infty)$. The values are normalized to that of P and βP, Eq. (5.38), so that the light gray line at a constant value of 1 is the comparison figure.

can still use the approximate expressions (5.65)-(5.66) since the results are essentially identical to those of the more exact expressions (5.61)-(5.62). To be on the safe side, our calculations are always done with the latter equations.

Our results for the transmission and reflection coefficients are displayed in Fig. 5.11(a). One immediately sees that for the chosen parameters, transmission is essentially perfect, except around the cavity resonances $(26, 1)$ and $(27, 1)$ of Fig. 5.7 as energy is transferred to the cavity from the waveguide.

A closer look at the quantity $1 - |T(k)|^2$ (Fig. 5.11(b)) makes the correspondence with the delay spectrum even more obvious. On the right of the major peaks are bumps indicating the presence of other minor resonances (22,2) and (23,2). At the major peaks, the curves are almost lorentzian and one can evaluate their width at half-height Γ. For the peak corresponding to the resonance $(26, 1)$, we estimate a value of $\Gamma \simeq 0.0038$. This measure is equivalent to the *imaginary* part of the complex resonance position $(\Gamma/2)_{(26,1)} = k_{\mathrm{Im}} R_0$, which in turn is related to the resonance delay by $k_{\mathrm{Im}} R_0/2 = R_0/(c\tau)$, such that $c\tau/R_0 = 2/k_{\mathrm{Im}} R_0 = 4/\Gamma \simeq 1052$, a result that compares nicely with that of the theoretical spectrum of Fig. 5.7.

If we compare the results of the alternative model for the transmission coefficient, they



(a) Assumption (5.97). (b) Assumption (5.98).

Fig. 5.9 Test of assumptions (5.97) and (5.98) as a function of x for 3 values of d; $kR_0 \simeq 20.1964$ is the position of the resonance $(26, 1)$. The blue (red) curves are associated with the overlap of the field caused by the interaction with a waveguide mode propagating towards $+\infty$ $(-\infty)$. The values are normalized to that of $\hat{P}$ and $\beta\hat{P}$, Eq. (5.101), so that the light gray line at a constant value of 1 is the comparison figure.

are identical to those of Fig. 5.11 except for an overall scale factor $\simeq 1.47$ larger. This factor originates essentially from the different normalization, the incident power $\hat{P}$ in the guide versus the incident power P over all space.

Considering the results obtained with our model, it is easy to generalize our analysis to a *add-drop filter system* with two waveguides [81]. One can also remove the restrictive approximation of weak coupling within the same theoretical framework. The price to pay is the loss of our analytic results and one must resort to a full numerical solutions of the complete coupled equations. These generalizations have not been explored further in this thesis. However, these future developments would not need much new analysis and can be regarded as basically straightforward.

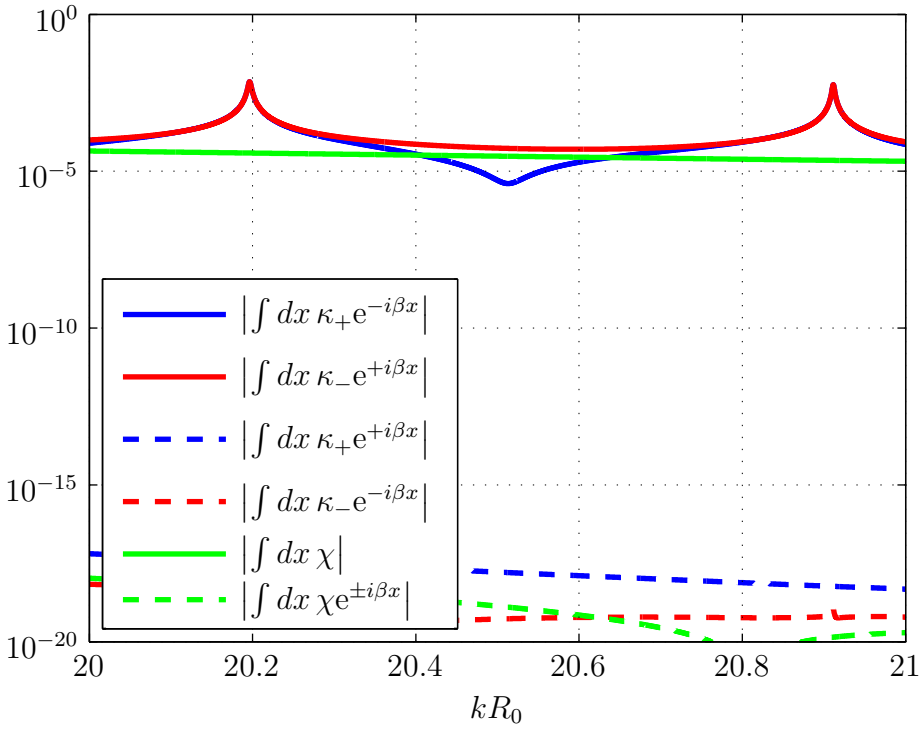
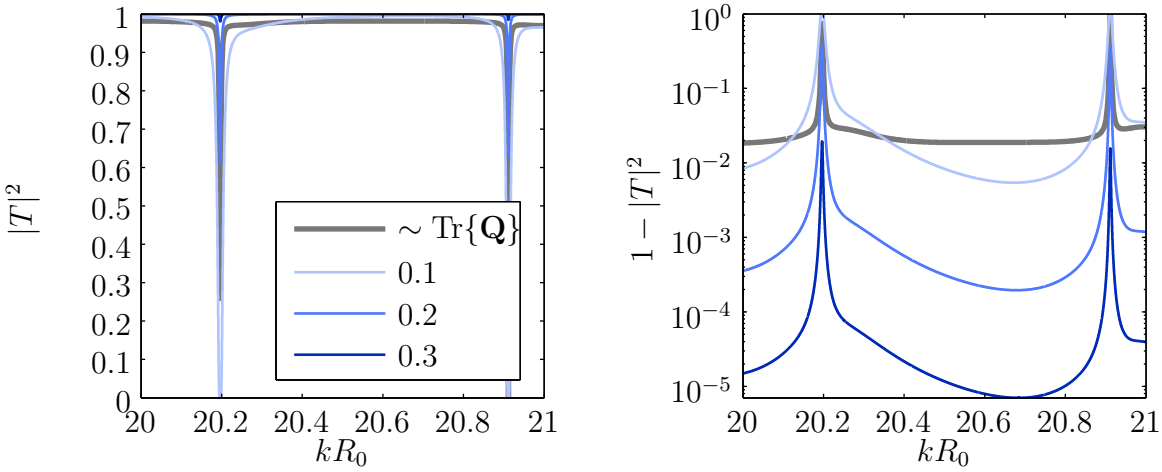


Fig. 5.10 Integrals involved in the expressions (5.44)-(5.47). One notices that the contributions of the integral over χ tot the corresponding element of the matrix $\mathbf{G}^0$ is of the same order of magnitude as the contributions of the related integral over $\kappa_\pm$.



(a) $|T|^2$ (b) $1-|T|^2$

Fig. 5.11 (a) Transmission spectrum $|T(k)|^2$ along a waveguide coupled to an homogeneous cavity. The results for three values of d/R_0 are displayed (blue lines) and the $1-\mathrm{Tr}\{\mathbf{Q}\}/\max\{\mathrm{Tr}\{\mathbf{Q}\}\}$ value is pictured as well for reference (gray line). The reflection coefficient maximum value for $d/R_0 = 0.1$ is about 10^{-31}. (b) Evaluation of $1-|T(k)|^2$ on a semi-log graph showing the secondary contributions of modes $(22,2)$ and $(23,2)$ nearby the main resonances (see delay spectrum Fig. 5.7). The graph of $\mathrm{Tr}\{\mathbf{Q}\}/\max\{\mathrm{Tr}\{\mathbf{Q}\}\}$ is also illustrated on top of this transmission spectrum to provide a useful comparison figure.

Chapter 6

Conclusions and perspectives

In this Chapter, we present a list of the main results and observations found in this work, and outline a novel dielectric cavity design that combines high delays and directional emission. This 'hybrid cavity' made of a stadium cavity embedded inside a ring cavity is designed to encapsulate the knowledge gathered throughout this work. Some early results are provided to enforce the concept, and a final discussion follows.

We present a summary of the results obtained in the preceding Chapters and a roadmap for eventual future investigations. The first Section is a list per Chapter of the main results and corresponding observations. A short discussion follows that sets the stage for the final Section of this work. This last Section is concerned with the immediate extension of the results of Chapters 4 and 5, and provides early observations of the pooling properties of an 'hybrid cavity'. This novel cavity design consists of a stadium-shaped cavity embedded into a larger high delay *ring* cavity. This original design appears to avoid the resonant coupling issue observed in the annular cavity between high delay and mid-size resonant modes by restricting the main modes to one kind of high quality WGMs only. Much like the annular cavity case, the non-uniform far-field is provided by an inner scatterer, here a stadium-shaped cavity. The stadium cavity has the property of having a 'uniform' low delays spectrum from which the high delay modes of the ring cavity find escape channels to reach the far-field. Some ideas concerning further developments are provided as well as a final word of caution.

6.1 Summary of observations and results

We review the main results obtained throughout the present work. They are presented in a list organised by Chapters. The electronic version of this document could prove

convenient for the reader as we extensively make use of *hyperlinks* for references to figures, equations and text Sections and Subsections.

- **Chapter 2** This Chapter presents the theoretical foundation upon which the rest of the document is based. Instead of using the usual **S** matrix complex k-plane description of the resonant modes of a cavity, we develop an energy-based formalism that captures the trapping effect of the cavity for real k electromagnetic fields. For every value of the wavenumber, an infinite number of characteristic modes are found. Some of these modes have especially large containment capacity: the characteristic delay spectrum of these *resonant* modes presents exceptionally high peaks. We argue that this alternative description of the behaviour of the electromagnetic field in the presence of a cavity shares many of the characteristics of the complex k-plane poles description. A numerical procedure along with early results are also presented.

  1. We devise a scattering description of the electromagnetic field based upon the use of the *delay matrix* to identify the *characteristic modes* of a two-dimensional dielectric cavity (see Eq. (2.21) and related discussion). The delay matrix **Q** itself is derived from a complex energy description of the electromagnetic field.
  2. The characteristic modes are time reversible modes in the sense that the incident wave has the same amplitude profile as the scattered wave. Only a phase factor (and an obvious complex conjugation) separates the two waves (see Eq. 2.20 and discussion in *Equivalent forms of the* **Q** *matrix* in Subsection 2.1.3).
  3. The characteristic modes appear to come from the symmetric contribution of the poles and zeros of the complex wavenumber plane scattering matrix (see Fig. 2.2 and Eq. (2.21), and the related discussion). In a sense, the time reversibility property of the characteristic modes stems from their arrangement half way from pure emission modes (poles) and pure absorbing modes (zeros).
  4. The characteristic modes bear striking similarities with conventional complex k-plane resonant modes (see Fig. 2.18 and Tab. 2.2).
  5. The discrepancies between the characteristic modes and the complex k-plane poles resonant modes are related to the complex interactions of the many characteristic modes on the real line (see discussion on delay levels anti-crossings in Subsection 2.1.3).
  6. An issue related to the delay levels anti-crossings is the reference frame dependency of the delay spectrum (see Fig. 2.4 and related discussion).

- **Chapter 3** This Chapter presents a perturbation theory of the disc cavity electromagnetic field. The approach makes use of two consecutive perturbation expansions. The first one involves a Born approximation of the perturbed field as a starting point to obtain the perturbed $\mathbf{S}$ and $\mathbf{Q}$ matrices. A second treatment revolving around the usual matrix perturbation theory is then applied to the characteristic modes. Specific analytical results on boundary and inclusion deformations are derived. These results in turn indicate some promising avenues of investigation.

    1. The scattered field associated with a small, yet undefined, variation of the refractive index of the disc cavity is expanded in a Born series (Fig. 3.1 and Eq. (3.11)). A first order correction $\mathbf{S}^{(1)}$ to the homogeneous disc cavity scattering matrix $\mathbf{S}^{(0)}$ is obtained Eq. (3.15) as well as a first order correction to the delay matrix Eqs (3.25)-(3.26).
    2. Using the delay matrix formalism for the dielectric cavity system, we establish a perturbation theory for the characteristic modes. The theory ultimately leads to a first order expansion for the delay (Eq. (3.62)) and associated incoming vectors (Eqs (3.39)-(3.40)) of the perturbed WGMs.
    3. The time reversibility property Eq. (2.20) of the characteristic modes appears twice in the perturbation treatment of the characteristic modes. First, it is *verified* on all but the two main angular momentum components ($|m| \neq m_0$) of the first order incoming vector (see Property 4, Eq. (3.100)). Second, it is *used* to determine the value of the two remaining elements ($|m| = m_0$) of the first order incoming vector (see Property 5, Eqs (3.101)-(3.102)). This last computation is central in the process of obtaining the first order correction to the phase offset and delay of characteristic modes Eqs (3.52)-(3.62).
    4. The small boundary deformation and small circular inclusion scenarios are found to have similar scattering matrices (Eqs (3.80) and (3.114)). However, further analysis shows that the annular cavity (disc+circular inclusion) is a truly original design in comparison to the perturbative boundary deformation of the disc (see Subsection 3.3.3).
    5. The refractive index perturbation has the effect of fixing the symmetry axes of the otherwise degenerate modes of the disc cavity. In the case of the boundary deformed cavity, the preferred axis appears through the Fourier series components of the boundary deformation function having the same angular momentum $|m| = m_0$ as the unperturbed WGM (Eqs (3.126)-(3.127)). Therefore, the symmetry axis may change from one mode to the other in the boundary deformation scenario.
    6. The circular inclusion cavity, on the other hand, sets its symmetry axis with respect to the disc-inclusion axis (the Ox axis). Also, the odd parity modes

($\psi(x, y = 0) = 0$) of the annular cavity have an unchanged delay value in first order perturbation (see Subsection 3.3.2). This behaviour contrasts with the even symmetry modes resonant peaks which are displaced toward higher (lower) k values for $n_h < n_c$ ($n_h > n_c$), see Figs 3.9 and 3.10.

7. A *scattering amplitude ridge* appears in the first order correction $\mathbf{S}^{(1)}$ matrix (Fig. 3.6). This ridge connects the main angular momenta $Z_o < |m| = m_0 < Z_c$ [1] of a high quality WGM to the low quality angular momenta $|m| < Z_o$ with greater amplitude than its immediate neighbors $|m| \simeq m_0$. Since $\mathbf{Q}^{(1)}$ and subsequent perturbed eigen-quantities are defined through the $\mathbf{S}^{(1)}$ matrix, they directly inherit this ridge structure (see the $\mathbf{A}^{(1)}$ perturbed incoming coefficients pictured on Fig. 3.12).

- **Chapter 4** This Chapter presents an application on the annular cavity of the theory of Chapter 2. The results obtained in Chapter 3 provide guidelines for the investigation of the main escape mechanisms of the electromagnetic field from the cavity. Semi-classical correspondence between wavefields and classical billiard trajectories is established and the dominant structures of phase space responsible for the non-uniform emission are found. We complement the Chapter with two Sections on important related topics: resonant coupling and wall roughness.

  1. The scattering probability ridge Fig. 3.6 computed from the perturbation theory of Chapter 3 is identified in the annular cavity scattering matrix ($\mathbf{S}$ on Fig. 4.9).
  2. It is found that most features of the ridge are included in the internal scattering matrix of the displaced circular scatterer/hole ($\mathbf{S}'$ on Fig. 4.9).
  3. The characteristic delay of a high quality mode of the annular cavity drops quickly as the constant radius hole is displaced towards the cavity boundary (Fig. 4.3). This happens as the resonant mode peak position on the delay spectrum remains almost stationary with respect to the unperturbed cavity resonant wavenumber (Fig. 4.5). The semi-classical caustic radius $d + r_0 = m_0/n_c k$ appears to be a parametric upper bound for this behaviour.
  4. The annular cavity high quality mode displays a parameter-dependent sequential transformation of its far-field and near-field, with a transition domain characterized by a WGM-like near-field and a strongly perturbed far-field (Fig. 4.7).
  5. A single internal scattering model of the cavity field is developed (Fig. 4.11) and is used to highlight the processes leading to the regular near-field/non-uniform far-field behaviour. The parameter-dependent probability crossover

[1] $Z_o = n_o k R_0$ and $Z_c = n_c k R_0$

of two escape mechanisms - transmission to the exterior domain and transition to angular momenta different from the main WGM channel m_0 - defines a lower parametric value from which to look for non-uniform far-field (Fig. 4.12).

6. Given a second control parameter, the inclusion radius for instance, we are able to drastically modify the far-field of a WGM located within the range bounded by the limits discussed above in points 3. and 5. (Figs 4.14(a)-(c)).

7. Since the scattering probability ridge of the internal scattering matrix $\mathbf{S}'$ (Fig. 4.9) is responsible for the perturbed aspect of the far-field and is positioned semi-classically within the non-regular domain of phase space (Fig. 4.15 along with Eq. (4.19)), we seek the dominant dynamical structures in this area of phase space. These are found to be the H_{in} and H_{out} domains, complemented with a regular 'conveyor belt' mechanism (Fig. 4.16).

8. We then compare the single scattering model (wave simulation) with the trajectories distribution (classical simulation) resulting from a single iterate from inside the H_{in} region. This comparison suggests that the Husimi distribution is an appropriate weighting function to model the output field from a 'classical' WGM situated above the non-regular limit in phase space, $(d + r_0)/R_0 < m_0/n_c kR_0$ (Fig. 4.19). While the actual characteristic modes and the classical trajectories share common features on the Poincaré section (Fig. 4.21), the resemblance is even more striking in the far-field region (Fig. 4.22).

9. The main results - existence of a WGM parametric control domain and the good agreement between classical and wave output trajectories/fields - being monotonically dependent on the wavenumber value, are of great practical interest to model the behaviour of extremely narrow resonances of the perturbed disc cavity. Only approximate values of the resonant wavenumbers are needed to carry out the computations. Such resonant wavenumbers are readily available from semi-classical approximations (Chapter 1).

10. The characteristic modes are prone to strong *resonant coupling* with each other as their resonant wavenumber positions (delay peaks) cross. A coupled oscillators model is developed to show the dramatic drop of energy containment of the system as the mid-size resonance of a low quality oscillator runs through the high energy peak of the second one (Fig. 4.24). A similar phenomenon is observed in the annular cavity (Fig. 4.28).

11. The resonant coupling is a serious issue for the parametric control of the WGMs far-field. This conclusion stems from the observation that mid-size resonant peaks move erratically over the spectrum as a control parameter is modified (Fig. 4.27).

12. The wall roughness of the disc cavity is found to lift the clockwise-counterclockwise degeneracy of WGMs. 'Even' and 'odd' modes are created with respect to an effective symmetry axis arising from the components of the boundary deformation spectrum (Fig. 4.31 and results Eqs (3.126)-(3.127) found in the perturbation theory of Chapter 3).
13. The wall roughness causes the displacement of resonant peaks of 'even' and 'odd' modes in opposite directions with respect to the unperturbed degenerate peak position (Fig. 4.30).
14. Higher quality modes are more affected by boundary roughness than low quality modes (see Fig. 4.30 and discussion in the corresponding paragraph).
15. The scattering ridge associated with the rough disc cavity may have components with sizes similar to the ones encountered in the annular cavity (Fig. 4.32). In view of our competing mechanisms description of the perturbed WGM (see Subsection 4.1.2), the boundary roughness provides the electromagnetic field a third way out of the cavity, potentially superseding the transmission mechanism as the control threshold for the anisotropic emission (see Fig. 4.12).

- **Chapter 5** This Chapter is somewhat different from the others. It presents a single (very long) calculation on the effects of connecting a cavity to a long waveguide used both as a power source and a measurement apparatus. The main interest is focused on obtaining the resonances of a cavity from the transmission spectrum of a waveguide. Closed-form expression of the waveguide transmission and reflection coefficients are obtained.

  1. For an evanescent field of the form of Eq. (5.1) impinging on a dielectric cavity, the scattered field is given by Eqs (5.18) and (5.19).
  2. Assuming the model of the complete electromagnetic field Eqs (5.20)-(5.21), we find the differential the system of equations for the envelopes of the guided waves Eqs (5.41)-(5.42).
  3. Solving Eqs (5.41)-(5.42) in a single field source scenario Fig. 5.1, we obtain simple expressions for the waveguide transmission and reflection coefficients Eqs (5.61)-(5.66).
  4. The final closed-form expression for the transmission coefficient relies only on the waveguide characteristics and the scattering matrix of the cavity (see, for instance, Eq. (5.92)).
  5. The transmission coefficient is seen to drop sharply at the positions of the high quality resonances of the disc cavity Fig. 5.11. Obtaining the transmission spectrum throughout the waveguide gives a picture of the resonance spectrum of the investigated cavity.

Out of this multitude of results, the ones concerning the possibility of controlling the output field from a high quality mode (Chapter 4) seem to be especially valuable. However, the potentially strong coupling between stationary high quality modes and wandering mid-size modes is likely to produce experimentally poorly repeatable results. For instance, accessible tolerances in mass produced annular dielectric cavities may be an issue.

As can be understood from Fig. 4.27, WGM resonances having a semi-classical caustic radius smaller than the maximum extent of the inclusion ($m_0/n_c k < d + r_0$ for the annular cavity) move erratically over the spectrum and eventually cross other high quality resonances. The ensuing strong coupling causes an accidental lowering of the containment capacity of the higher quality modes. Because of the high sensitivity of the mid-size resonances to small variations in the inclusion parameters, this coupling scenario, while appealing at first, appears to be difficult to exploit in practice. It certainly would be more interesting to reach globally all the resonances over a broad wavenumber range.

Moreover, unavoidable wall roughness affects more strongly high quality resonant modes than mid-size resonances and the severe delay decrease of the high quality modes will inevitably enhance the resonant coupling. The ensuing accidental delay spoiling through resonant coupling would then become even more dramatic.

On a different perspective, looking back at the cavity-waveguide coupling concept of Chapter 5, it appears that evanescent coupling may be an efficient route to transfer field from one dielectric structure to another. Preliminary results from the disc-waveguide coupling (see Fig. 5.11 for instance) indicate that low quality modes of the disc cavity drain significantly less field from the waveguide than their high delay counterparts. Also, since the extent of the evanescent field is defined by the propagating modes (see Appendix E), choosing a waveguide size accommodating a single mode ensures complete control over the amount of field extending from the waveguide towards the cavity. Finally, once the evanescent field is set, the magnitude of the coupling may easily be modified by changing the distance between the cavity and the waveguide.

These last observations along with the high quality/high directionality concept of Chapter 4 provide some promising avenues for the unambiguous control of the far-field output from high quality modes. In the last Section of this work, we outline the key features that an annular-like cavity should possess to achieve the control objective.

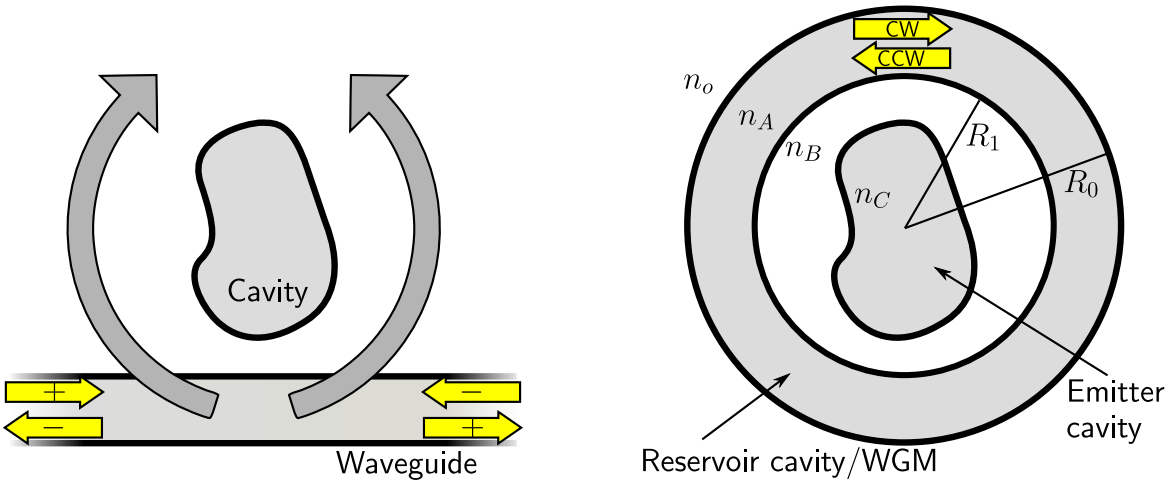
6.2 Perspectives on mode quality *vs* directionality tradeoff, and further developments

We wish to promote in this last Section the combination of the cavity-waveguide coupling concept and of the regular near-field/non-uniform far-field phenomenon. As seen in Chapter 5, the modes of a dielectric cavity may 'feed' on the propagating field of a nearby waveguide to increase their own field intensity. The amount of power drained by the cavity is governed by the presence of resonances and by the distance separating the two structures (Fig. 5.11). Suppose now that the waveguide is bent on itself, eventually completely enclosing the cavity, Fig. 6.1. It is expected that the power flow from the newly formed *ring cavity* to the thereby embedded cavity follows the same behaviour as the one observed in the waveguide-cavity coupling. What is new however, is that the closed waveguide now supports finite lifetime resonances that may share part of their circulating power with the inner cavity.

Provided that the inner cavity does not bear high quality resonances, we expect a resonant field inside the ring cavity to be only weakly affected by the presence of the embedded cavity. Since we may finely tune the amount of transferred power by changing the distance separating the embedded cavity from the ring inner radius, it is reasonable to anticipate a behaviour similar to the one depicted in Fig. 4.12: two escape mechanisms - the regular potential tunneling of the dielectric ring and the internally scattered field from the inner cavity - competing to impose their own far-field as one closes the gap separating the two dielectric structures. The difference here is that the phenomenon appears between two separate structures bounded in configuration space by a dielectric wall rather than in dynamical space through the caustic radius of a disc cavity mode. Under appropriate parametric conditions, the inner cavity may be set to drain some of the trapped field from inside the ring and to use it to impose its own far-field, Fig. 6.1(b).

Moreover, much like in the infinite waveguide case, the thickness $R_0 - R_1$, Fig. 6.1(b), of the annulus may be chosen to allow for only one kind of circulating mode. It is then possible to eliminate, for instance, all mid-size resonances having a number of radial maxima larger than 1, see Fig. 6.2. The effect on the delay spectrum is to flatten the background level, leaving only the well-separated high delay resonances, Fig. 6.3. The ring thickness as a control parameter would then appear convenient to mitigate the resonant coupling phenomenon between WGMs of different angular momenta by eliminating all mid-size resonances altogether.

As discussed above, the internal scatterer must not possess large intrinsic resonances in order to avoid depletion of the ring circulating field. This phenomenon is much like the



(a) Waveguide and cavity

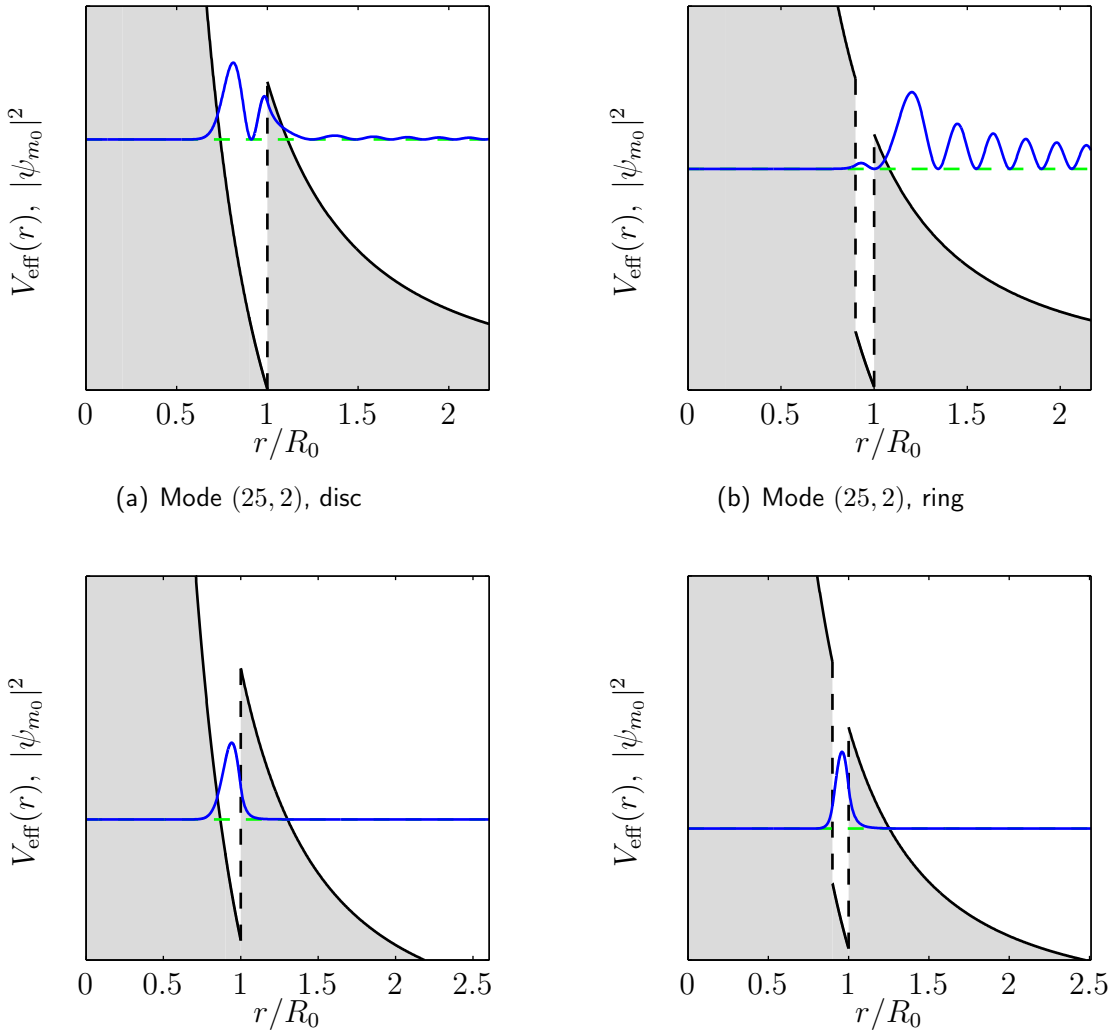
(b) Ring and inner cavities

Fig. 6.1 (a) Bending a waveguide around a nearby cavity yields (b) a composite structure inheriting the convenient properties of both dielectric sub-components. The purpose of the ring cavity is to confine large amounts of energy in a small volume while the inner cavity acts as a transformation unit converting the regular clockwise (CW) and counterclockwise (CCW) rotating near-field components into directional far-field.

resonant coupling case, but instead of coupling different modes of a single structure, it connects the modes pertaining to *different* dielectric substructures. We must then turn our attention from high delay cavities to ones bearing only low delay resonances. Of the many possible candidates, one that appears well suited for the exercise is the stadium shaped cavity [76]. This cavity has the very special property that its equivalent classical billiard counterpart is completely chaotic [25] capable of sustaining large delay modes. Thus, there are no large stable islands in its phase space [93]. Moreover, the overall dynamics is controlled by a web of unstable manifolds [129] that guide trajectories into the escape region $|p| < p_{\mathrm{TIR}} = n_B/n_C$ through specific highly directional output positions [132].

Figure 6.4(a) shows the typical phase space produced by trajectories randomly seeded into two thin rectangular sections $[1 - \Delta p < |p| < 1] \times [0 \leq \phi \leq 2\pi]$ and $\Delta p = 0.05$ (4 000 initial conditions). The trajectories impinging on the Poincaré section are colored from dark blue to white with respect to their decreasing remaining intensity[2]. Although the stadium cavity is completely chaotic, the presence of the escape domain between the TIR limits refrains the trajectories from completely filling the accessible area with high intensity trajectories. Dominant escape regions are observed and can be associated

[2]The Fresnel reflection coefficient Eq. (4.14) is used to weight the reflected intensity. Every trajectory is given a starting intensity of $I_0 = 1$. The simulation stops when the remaining intensity of a trajectory inside the billiard drops below an arbitrary level (here 10^{-10}).



(a) Mode $(25, 2)$, disc

(b) Mode $(25, 2)$, ring

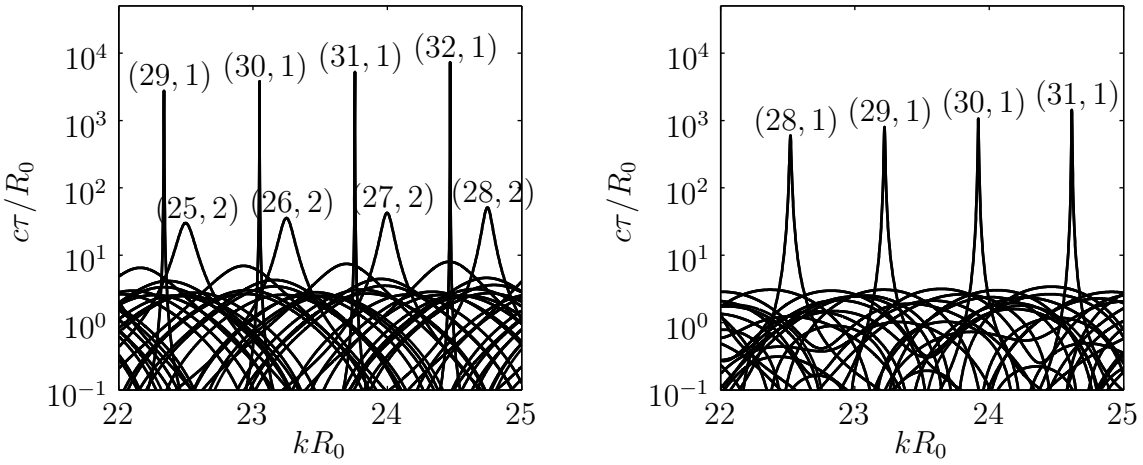
(c) Mode $(30, 1)$, disc

(d) Mode $(30, 1)$, ring

Fig. 6.2 Effect of the introduction of an inner boundary on the resonant modes of a disc cavity represented by the effective potential model (see Chapter 1 and [67]). For the disc cavity, $R_0 = 1$, $n_o = 1$ and $n_A = n_B = n_C = 1.5$, and for the ring cavity, $R_0 = 1$, $R_1 = 0.9R_0$, $n_o = 1$, $n_A = 1.5$ and $n_B = n_C = 1$, see Fig. 6.1(b) for the definitions. Under certain combinations of physical parameters such as the one selected here, it may be possible to diminish the low quality modes of the disc cavity (a)-(b) and to retain only their high delay counterparts (c)-(d).

with the corresponding classical near-field Fig. 6.4(b) and far-field Fig. 6.4(c). Notice that due to statistical sampling, the far-field shown in Fig. 6.4(c) is built from a set of 40 000 initial conditions instead of just 4 000 for the 'qualitative' needs of Figs 6.4(a) and 6.4(b).

After these preliminaries, we may now turn our attention to the full-wave results. Combining the ring cavity (delay spectrum of Fig. 6.3(b)) with a well chosen stadium cavity



(a) Disc (b) Ring

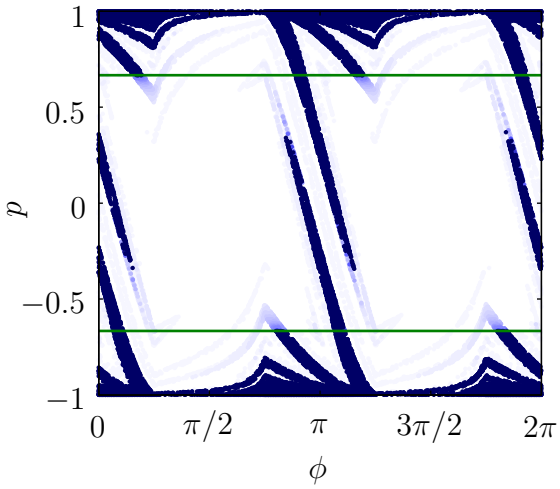
Fig. 6.3 Spectra from the disc and ring cavities. The resonant modes of the disc cavity are forced to settle at different wavenumbers by the ring inner boundary. Given adequate parametric conditions (here $R_0 = 1$, $R_1 = 0.9R_0$, $n_o = 1$, $n_A = 1.5$ and $n_B = n_C = 1$, see Fig. 6.2), the disc spectrum (a) may be modified to leave only the high delay modes to stand out (b). Notice that the peaks of lower quality resonant modes $(25, 2)$, $(26, 2)$, ... do not actually disappear: they are relocated somewhere out of this selected wavenumber window.

(delay spectrum of Fig. 6.5(a)), we arrive at an hybrid spectrum encompassing both the high delays of the ring cavity and the low quality/directional modes of the stadium cavity, Fig. 6.5(b)[3]. The results for the resonant delays - the eight peaks of Fig. 6.5(b) - are summarized in Tab. 6.1.

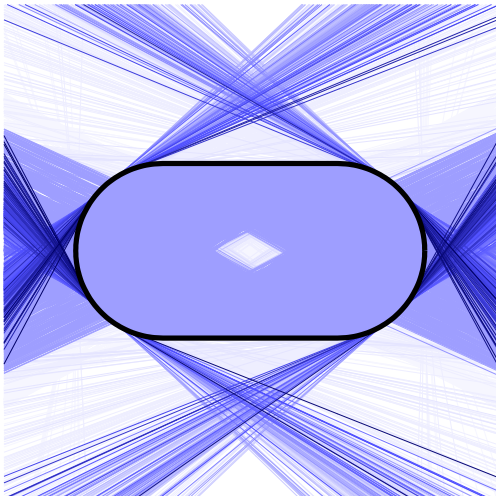
Table 6.1 informs us that the delay of all modes is reduced by a *common* factor of $60 - 70\%$ (in contrast to many orders of magnitude as is often found in geometrically deformed cavities). This is an indication that our attempt to uniformize delay spoiling through the use of a low quality scatterer has been successful. Small variations in the spoiling level may be due to local resonant coupling with modes of the stadium cavity, see for instance the resonant modes $(28, 1) - ee$ (purple) and $(29, 1) - oe$ (green) of Fig. 6.5(b).

It also appears that the field from the WGMs is drained more efficiently by modes of the stadium with the highest delay values (essentially, the upper layers of the 'background level' of Fig. 6.5(a) having delay values around $4 - 7$). In a sense, this is much like the resonant coupling phenomenon but with very broad overlapping resonances. An

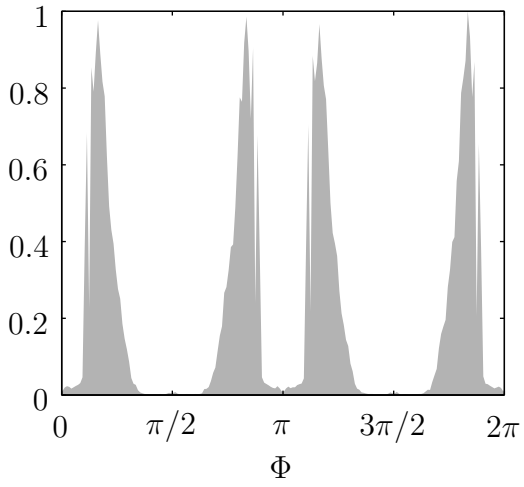
[3]Referring to Fig. 6.3, the definitions of the symmetry types are: For an odd symmetry (o) with respect to a given axis, the field shows a line of nodes (zero-value field); for an even symmetry (e) with respect to a given axis, the field shows a line of extrema (minima and/or maxima alternating).



(a) Phase space



(b) Near-field

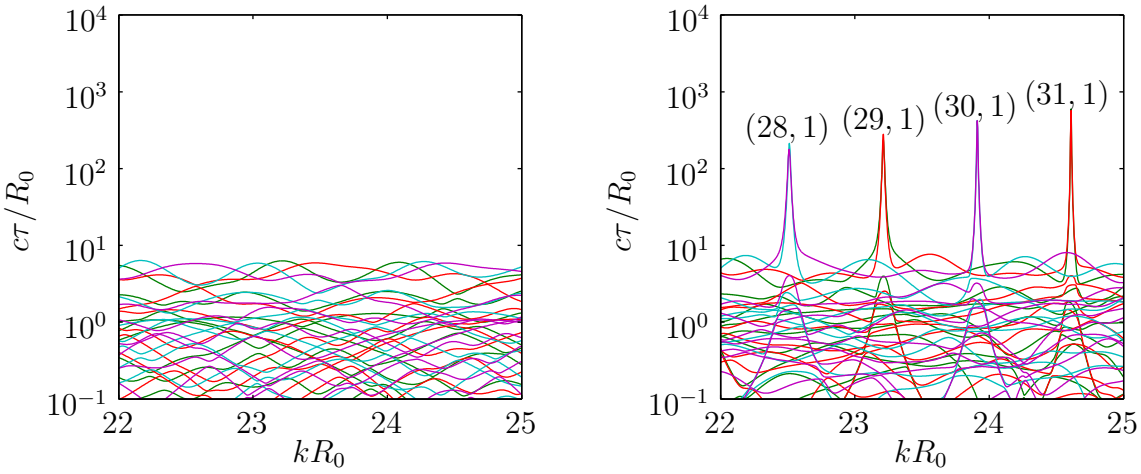


(c) Far-field

Fig. 6.4 (a) Representation of the phase space of the stadium cavity for a set of initial conditions randomly selected inside thin rectangles $[0.95 < |p| < 1] \times [0 \leq \phi \leq 2\pi]$ (4 000 initial conditions). The linear side walls of the stadium have a length of $2r_s$, $r_s = 0.425$ being the radius of its semi-circular sections. Thus, the full length of the stadium is $4r_s$ and its full width is $2r_s$. The refractive index inside the stadium is 1.5 (glass) and 1.0 outside. These values specify the Fresnel reflection coefficient Eq. (4.14) that progressively decreases the circulating intensity I of the trajectories (dark blue: $I = 1$; white: $I = 0$). The green horizontal lines are the TIR limits, $p_{\mathrm{TIR}} = 2/3$. (b) An overview of the near-field corresponding to the phase space (a) is also presented. Notice that the color of the trajectories scales from dark blue to white with the decreasing intensity (normal irradiance over unit area). (c) The classical far-field of the stadium cavity for a set of $40\,000$ randomly chosen initial conditions. The far-field is built from the distribution of the escaping intensity of all trajectories into 200 far-field angular bins.

example of this behaviour is displayed in Fig. 6.6.

As Fig. 6.5(b) suggests, some of the highest quality modes of the stadium found in



(a) Stadium (b) Hybrid ring+stadium

Fig. 6.5 (a) Delay spectrum computed for the stadium cavity of Fig. 6.4 alone and (b) delay spectrum of the combined ring and stadium cavity. The geometrical center of the stadium cavity is fixed at the center of the ring cavity. This setup forces the expression of the $Ox - Oy$ symmetry axes of the stadium into the modes of the ring cavity: light blue is $Ox - Oy$=odd-odd (oo), purple is even-even (ee), red is even-odd (eo) and green is odd-even (oe).

the upper layers of the spectrum of Fig. 6.5(a) get promoted to somewhat higher values. This phenomenon is caused by the exterior ring with acts as a reflector to the otherwise escaping field, which consequently enhances the effective trapping capacity of the stadium modes.

Finally, the comparison of the far-field computed through classical means (using the Husimi distribution as a weighting function for the initial conditions as described in Chapter 4) and full wave simulations shows again that a large part of the far-field is well modeled by geometric optics, Fig. 6.7. The dominant features of the far-fields are the four narrow peaks resembling those of the isolated stadium billiard Fig. 6.4(c). Although the far-field is not completely similar to the one from the stadium cavity, it appears reasonable to suppose that slight modifications of the parametric layout of the stadium cavity could improve the directional emission properties of the field.

The choice of the stadium cavity was made because of the 4 known peaks in the emission far-field [132]. The properties of the composite system just investigated are not exclusive to this particular choice of embedded cavity. In a sense, this comes back to the initial investigation of geometrical deformations of cavities with dominant chaotic phase space [90, 91, 89, 147, 128]. However now, the roles associated with large delay and high directionality do not rest on a single structure but on two components having their own distinct functional purpose.

Mode $(m_0, 1)$	Symmetry	Resonant delay $c\tau/R_0$		
		Ring	Hybrid	Variation [%]
$(28, 1)$	oo (ee)	598	213 (178)	-65 (-70)
$(29, 1)$	eo (oe)	800	280 (234)	-65 (-71)
$(30, 1)$	oo (ee)	1071	424 (422)	-60 (-61)
$(31, 1)$	eo (oe)	1436	569 (598)	-60 (-58)

Tab. 6.1 Summary of the computed resonant delays for the hybrid ring+stadium cavity Fig. 6.5(b) *vs* the plain ring cavity 6.3(b). Values in parentheses indicate the results for the corresponding symmetries. The overall variation of the peak delays caused by the stadium cavity is approximately $60 - 70\%$ of the nominal ring cavity resonant delays. Notice that the modes having an even m_0 number separate into $(Ox - Oy)$ even-even and odd-odd symmetries and that the modes having an odd m_0 number separate into even-odd and odd-even symmetries. This is a consequence of the number of times it may be possible for a given m_0 to separate both the nodes and extrema (minima and maxima) of the ring field distribution with respect to the symmetry axes imposed by the inner scatterer.

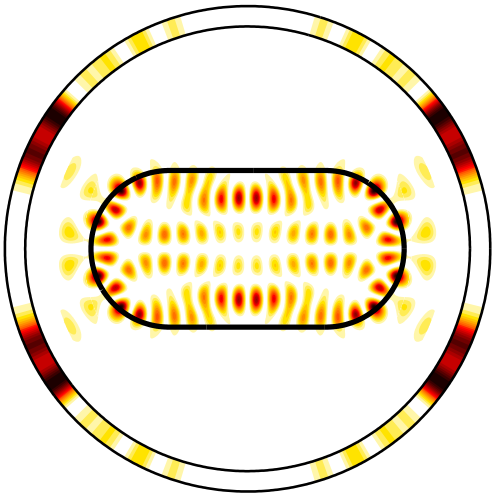
It could also prove rewarding to exploit the ring cavity as a lens device for the escaping field. This is very much in line with recent work in the microcavity field [155, 55].

An extension of the present proposal may be foreseen in the area of microlaser modeling. Since the intensity of the field is mainly concentrated in the ring domain of the cavity, it appears reasonable to suppose that the laser action will be confined to this part of the cavity. Free of coupling between the radial and angular coordinates, the lasing system will then be spatially separable and we may focus solely on the solution of the Maxwell-Bloch equations [54]. The output laser field for sharp resonances is then scattered by the inner cavity (short-lived modes: no laser effect) and the corresponding far-field is recorded.

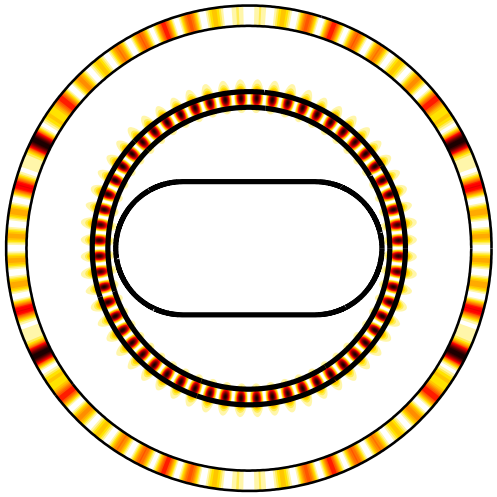
One also notes that one could also consider the incoming/outgoing reciprocal relation of the characteristic modes discussed in Chapter 2 to propose a device that could concentrate the field coming from a narrow angular domain of the far-field into the dielectric ring. In this application, the dielectric cavity could be regarded as a sensor/absorbing device working in the reverse direction of that of the laser system discussed in the previous paragraph.

These scenarios rely on a perturbation model of the ring field. In contrast with the small refractive index deformations of Chapter 3, it may be worthwhile to develop a perturbation theory of the high quality ring modes by known *low quality modes* of the inner cavity.

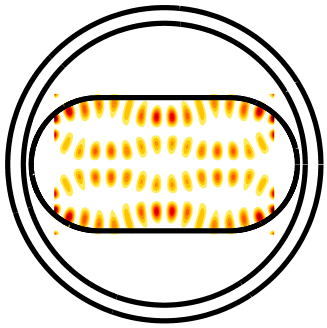
Another interesting avenue of research for the hybrid ring-scatterer system could be the explicit utilization of the resonant coupling for high quality sensors. The frequency



(a) Stadium, $c\tau/R_0 = 6.2$ and $kR_0 = 24.27$ (top layer of Fig. 6.5(a))



(b) Hybrid ring+stadium cavity $c\tau/R_0 = 424$ and $kR_0 = 23.91$



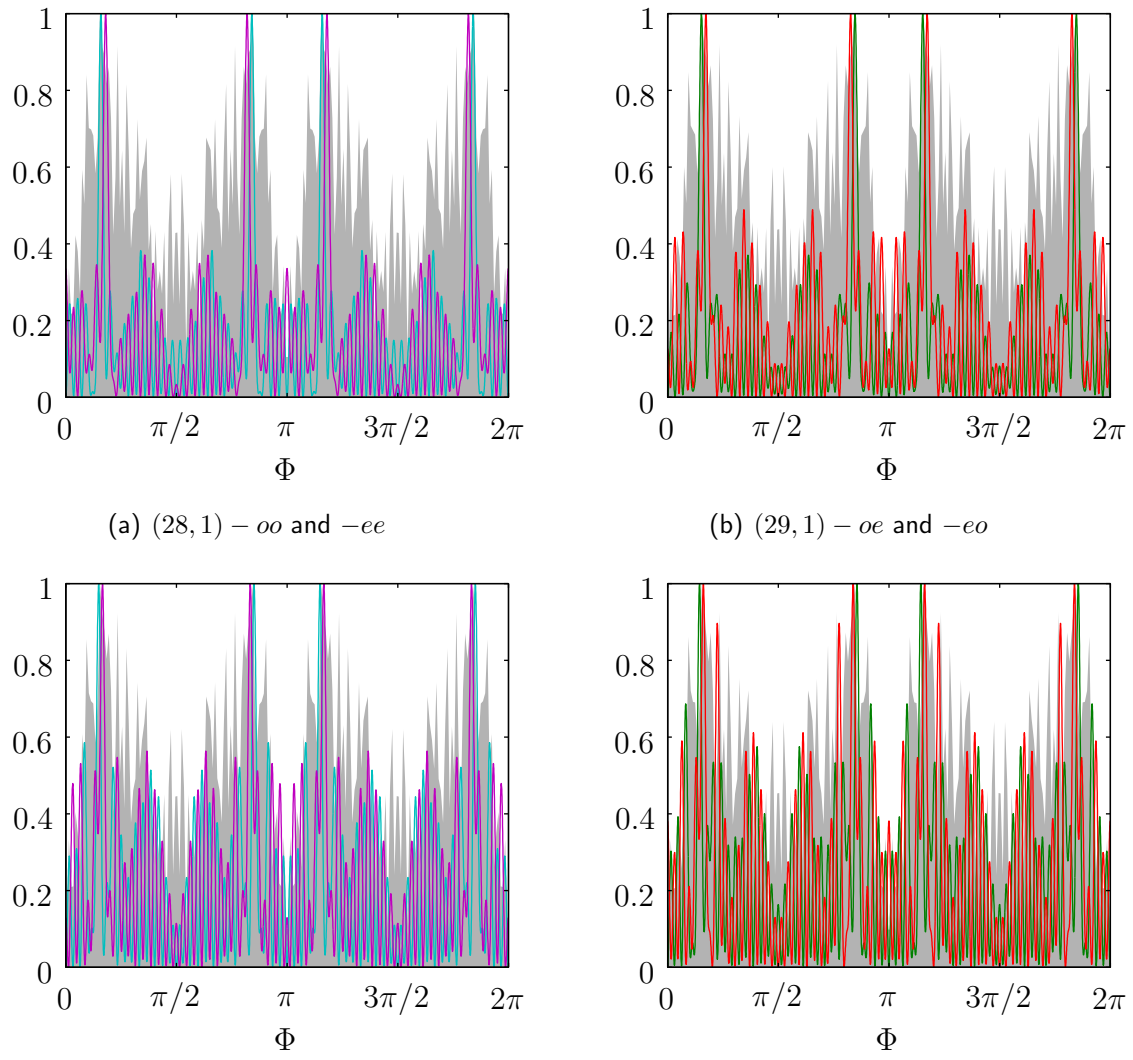
(c) Detail of (b)

Fig. 6.6 (a) A resonant mode of the stadium cavity is found to be dominant in (b)-(c) the near-field of the ring and stadium hybrid cavity mode $(30, 1) - oo$. Figure (c) is produced by masking all but a rectangular section of the field presented in (b). Notice the similarity in the far-field for the stadium and the hybrid cavities (outer ring of (a) and (b)).

detuning between two spectrally overlapping high quality modes of the ring cavity and the inner scatterer cavity[4], as a third perturbative object passes through the gap area, could enhance the probability of detection of the said object.

The heuristic semi-classical description of the transition from an evanescent field source

[4]One could think of the inner scatterer as a disc cavity with a higher refractive index than the ring cavity.



(a) $(28,1) - oo$ and $-ee$

(b) $(29,1) - oe$ and $-eo$

(c) $(30,1) - oo$ and $-ee$

(d) $(31,1) - oe$ and $-eo$

Fig. 6.7 Classical far-fields (grey areas) and wave simulated far-fields $|\psi(\infty,\phi)|^2$ (colored lines) for the resonant modes of Fig. 6.5(b) . The color code for the symmetries is the same as the one employed for the spectra. The initial conditions for the classical simulations are selected from the $H_{\rm in}$ domain of phase space with a decreasing gaussian distribution (Husimi distribution of the circulating WGMs) as in Chapter 4. Among the key features of the classical far-field are the 4-points peaks of Fig. 6.4(c) directly inherited from the stadium sub-structure.

to a scatterer currently done through the use of the Husimi distribution in Chapter 4 could be modified to be more 'physical'. The weighting function used to seed the initial conditions in the emission domain of phase space is essentially a decreasing exponential function. Since this function is typical of any evanescent field, the investigation of the imprint of such evanescent field in phase space could be useful to model the actual transition probability. In view of the hybrid ring-scatterer configuration discussed in this Section, special attention could be given to the study of frustrated waves between

dielectric interfaces not necessarily parallel to each other.

There are also some technical improvements that could be carried out. For instance, one would like to eliminate the numerical derivative of the **S** matrix for the computation of the delay matrix[5] and it would be worthy to explicitly extend the method to the transverse electric (TE) modes. The last few paragraphs are mostly speculative and are laid out only to demonstrate some of the possibilities remaining. Finally, a word of personal advice to anyone wishing to tackle this research theme ('microcavities' in a broad sense): define well beforehand the scope of the field he/she wants to cover, and stick to it at any cost. The main issue with this domain is that it stands over both engineering and applied science (bio-sensors, optical couplers or laser devices for instance), and more fundamental science (wave-particle duality, 'quantum chaos' or quantum 'open systems'). From my experience, the risk associated with the vastness of the field is that one's efforts may easily get scattered into many different directions - pun intended - resulting in overall low outcomes.

[5]This could be achieved by introducing the wavenumber derivative inside the numerical method of Appendix C and to carry out explicitly the operation at the level where the basis expansion is done, see Section C.1.

Annexe A

Fonctions de Bessel: Relations exactes et approximations

Cette annexe rassemble quelques résultats des sections 9.1, 9.2 et 9.3 de l'ouvrage de Abramowitz et Stegun [1] portant sur les fonctions de Bessel. Bien qu'elles soient assez courantes, il demeure pratique de résumer ici les expressions qui sont utilisées fréquemment dans le présent document, et d'ajuster la notation en conséquence. Des relations exactes pour les fonctions de Bessel $J_m(z)$ et $Y_m(z)$ et les fonction de Hankel $H_m^{(1)}(z)$ et $H_m^{(2)}(z)$ sont présentées dans un premier temps. Suivent des développements approximatifs de ces mêmes fonctions pour différents cas d'ordre m et d'argument z. Puisque les fonctions de Hankel peuvent être définies par les fonctions de Bessel, l'expression "fonctions de Bessel" désigne l'ensemble de ces fonctions spéciales.

A.1 Relations exactes de fonctions de Bessel

Il existe une bonne quantité d'expressions exactes utilisant les fonctions de Bessel (voir [1, 50]). Quelques-unes provenant de la section 9.1 de Abramowitz et Stegun [1] sont regroupées ici. L'ordre noté m est un entier alors que ν désigne un nombre réel ou complexe. Si aucune restriction supplémentaire ne s'applique, l'argument z est complexe. La notation $F_\nu(z)$ (ou encore, $F_m(z)$) identifie une des fonctions spéciales $J_\nu(z)$, $Y_\nu(z)$, $H_\nu^{(1)}(z)$ ou $H_\nu^{(2)}(z)$ (ou $J_m(z)$, $Y_m(z)$, $H_m^{(1)}(z)$ ou $H_m^{(2)}(z)$ respectivement).

Équation de Bessel :

$$z^2\frac{d^2F_\nu(z)}{dz^2} + z\frac{dF_\nu(z)}{dz} + \left(z^2 - \nu^2\right)F_\nu(z) = 0 \tag{A.1}$$

Construction des fonctions de Hankel :

$$H_\nu^{(1)}(z) = J_\nu(z) + iY_\nu(z) \quad (A.2)$$
$$H_\nu^{(2)}(z) = J_\nu(z) - iY_\nu(z) \quad (A.3)$$

Identités sur le signe de l'ordre :

$$J_{-m}(z) = (-1)^m J_m(z) \quad (A.4)$$
$$Y_{-m}(z) = (-1)^m Y_m(z) \quad (A.5)$$
$$H_{-\nu}^{(1)}(z) = \mathrm{e}^{+i\nu\pi} H_\nu^{(1)}(z) \quad (A.6)$$
$$H_{-\nu}^{(2)}(z) = \mathrm{e}^{-i\nu\pi} H_\nu^{(2)}(z) \quad (A.7)$$

Identités sur la conjugaison complexe ($\nu \in \mathbb{R}$) :

$$[J_\nu(z)]^* = J_\nu(z^*) \quad (A.8)$$
$$[Y_\nu(z)]^* = Y_\nu(z^*) \quad (A.9)$$
$$\left[H_\nu^{(1)}(z)\right]^* = H_\nu^{(2)}(z^*) \quad (A.10)$$
$$\left[H_\nu^{(2)}(z)\right]^* = H_\nu^{(1)}(z^*) \quad (A.11)$$

Règles de récurrence et de dérivation :

$$F_{\nu+1}(z) = -F_{\nu-1}(z) + \frac{2\nu}{z} F_\nu(z) \quad (A.12)$$
$$\frac{d}{dz} F_\nu(z) = -F_{\nu+1}(z) + \frac{\nu}{z} F_\nu(z) \quad (A.13)$$

Particulièrement, $\frac{d}{dz} J_0(z) = -J_1(z)$ et $\frac{d}{dz} Y_0(z) = -Y_1(z)$. Il peut être avantageux d'utiliser directement l'équation différentielle (A.1) pour évaluer la dérivée seconde.

Théorème de déplacement de Graf : Le théorème de déplacement de Graf se montre d'une grande utilité pour modifier le référentiel d'une fonction de Bessel associée à une exponentielle complexe (harmonique cylindrique). Un cas spécial est celui où les origines O et O' de deux référentiels sont séparés d'une distance u (voir schéma Fig. A.1). On définit les coordonnées polaires (z, ϕ) et (z', ϕ') attachées respectivement à ces deux référentiels. L'harmonique cylindrique $F_m(z)\mathrm{e}^{im\phi}$ s'exprime donc dans les coordonnées primées comme

$$F_m(z)\mathrm{e}^{im\phi} = \sum_{m'} J_{m'-m}(u) F_{m'}(z')\mathrm{e}^{im'\phi'} \ , \quad u < z' \quad (A.14)$$
$$F_m(z)\mathrm{e}^{im\phi} = \sum_{m'} F_{m'-m}(u) J_{m'}(z')\mathrm{e}^{im'\phi'} \ , \quad u > z' \quad (A.15)$$

La transformation des coordonnées (z', ϕ') vers les coordonnées (z, ϕ) est obtenue par simple remplacement $(z', \phi') \leftrightarrow (z, \phi)$ dans les expressions précédentes.

Les mêmes expressions s'appliquent pour des arguments z, z' et u complexes sous certaines contraintes [1].

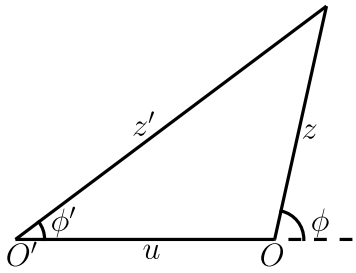


Fig. A.1 Interprétation géométrique des éléments constitutifs du théorème de déplacement de Graf. Cette représentation ne s'applique que lorsque les arguments des fonctions de Bessel sont réels et positifs.

Wronskiens : Wronskien $W\left[f(z), g(z)\right] = f(z)\frac{d}{dz}g(z) - g(z)\frac{d}{dz}f(z)$ pour différentes combinaisons de fonctions de Bessel:

$$W\left[J_\nu(z), Y_\nu(z)\right] = J_{\nu+1}(z)Y_\nu(z) - J_\nu(z)Y_{\nu+1}(z) \tag{A.16}$$

$$= \frac{2}{\pi z} \tag{A.17}$$

$$W\left[H_\nu^{(1)}(z), H_\nu^{(2)}(z)\right] = H_{\nu+1}^{(1)}(z)H_\nu^{(2)}(z) - H_\nu^{(1)}(z)H_{\nu+1}^{(2)}(z) \tag{A.18}$$

$$= -\frac{4i}{\pi z} \tag{A.19}$$

Les Wronskiens sont indépendants de l'ordre ν.

A.2 Développements des fonctions de Bessel

Les développements des fonctions de Bessel présentés ici sont tronqués à l'ordre correspondant à l'utilisation préconisée dans ce travail. Le lecteur intéressé aux développements complets (le plus souvent, des séries infinies) est invité à consulter directement la référence principale de cette section [1]. Dans ce qui suit, la variable x est réelle. Les développements pour un argument complexe existent sous restriction [1].

A.2.1 Développements pour m fixe et $x \ll m$

- $J_m(x)$:
  La limite des petits arguments de la fonction de Bessel $J_m(x)$ pour $m \geq 0$ prend la forme

$$J_m(x) = \left(\frac{1}{2}x\right)^m \left[\frac{1}{m!} - \frac{1}{(m+1)!}\left(\frac{1}{2}x\right)^2\right] + \mathcal{O}(x^{m+4}) \ . \tag{A.20}$$

Les ordres négatifs sont traités par la relation (A.4). Seule la fonction d'ordre 0 est non-nulle à l'origine.

- $Y_m(x)$:
  La limite des petits arguments de la fonction de Bessel $Y_m(x)$ pour $m \geq 0$ est singulière à l'origine:

$$Y_0(x) = \frac{2}{\pi}\ln\left(\frac{1}{2}x\right) + \frac{2}{\pi}\gamma + \mathcal{O}(x^2) \tag{A.21}$$

$$Y_m(x) = -\frac{(m-1)!}{\pi}\left(\frac{1}{2}x\right)^{-m} + \mathcal{O}(x^{-m+2}) \ , \quad m > 0 \tag{A.22}$$

  avec $\gamma = 0.577\,215\,664\,901\,532\ldots$, la constante d'Euler-Mascheroni [1]. Les ordres négatifs sont traités par la relation (A.5).

- $H_m^{(1)}(x)$ et $H_m^{(2)}(x)$:
  Le développement des fonctions de Hankel suit essentiellement celui des fonctions de Bessel $Y_m(x)$,

$$H_0^{(1)}(x) = \left[1 + i\frac{2}{\pi}\gamma\right] + i\frac{2}{\pi}\ln\left(\frac{1}{2}x\right) + \mathcal{O}(x^2) \tag{A.23}$$

$$H_m^{(1)}(x) = -i\frac{(m-1)!}{\pi}\left(\frac{1}{2}x\right)^{-m} + \mathcal{O}(x^{-m+2}) \ , \quad m > 0 \tag{A.24}$$

  Les ordres négatifs sont traités par la relation (A.6), et les développements des fonctions de Hankel $H_m^{(2)}(x)$ sont obtenus par le remplacement $i \to -i$ dans les expressions précédentes.

A.2.2 Développements pour m fixe et $x \gg m$

Pour la limite des grand arguments x devant l'ordre $m > 0$, on définit

$$\tilde{\Theta}_m(x) = x - m\frac{\pi}{2} - \frac{\pi}{4} \quad . \tag{A.25}$$

Tout comme les développements pour les petits arguments x, on utilisera les expressions (A.4)-(A.7) pour accomoder les ordres m négatifs. Les dérivées par rapport à l'argument x sont indiquées par la notation primée, $F'_\nu(x)$.

[1] Cette constante est définie formellement comme une limite de la différence entre la série harmonique et le logarithme naturel, $\gamma = \lim_{n\to\infty}\left[\sum_{j=1}^{n}\frac{1}{j} - \ln n\right]$.

- $J_m(x)$:
  La fonction de Bessel $J_m(x)$ dans la limite des grands arguments prend une forme oscillante et faiblement décroissante

$$J_m(x) \approx \sqrt{\frac{2}{\pi x}}\left[+\cos\tilde{\Theta}_m(x) - \left(\frac{4m^2-1}{8x}\right)\sin\tilde{\Theta}_m(x)\right] + \mathcal{O}(x^{-2-1/2}) \quad \text{(A.26)}$$

$$J'_m(x) \approx \sqrt{\frac{2}{\pi x}}\left[-\sin\tilde{\Theta}_m(x) - \left(\frac{4m^2+3}{8x}\right)\cos\tilde{\Theta}_m(x)\right] + \mathcal{O}(x^{-2-1/2}) \quad \text{(A.27)}$$

- $Y_m(x)$:
  La fonction de Bessel $Y_m(x)$ dans la limite des grands arguments prend une forme oscillante et faiblement décroissante

$$Y_m(x) \approx \sqrt{\frac{2}{\pi x}}\left[\sin\tilde{\Theta}_m(x) + \left(\frac{4m^2-1}{8x}\right)\cos\tilde{\Theta}_m(x)\right] + \mathcal{O}(x^{-2-1/2}) \quad \text{(A.28)}$$

$$Y'_m(x) \approx \sqrt{\frac{2}{\pi x}}\left[\cos\tilde{\Theta}_m(x) - \left(\frac{4m^2+3}{8x}\right)\sin\tilde{\Theta}_m(x)\right] + \mathcal{O}(x^{-2-1/2}) \quad \text{(A.29)}$$

- $H_m^{(1)}(x)$ et $H_m^{(2)}(x)$:
  Les fonctions de Hankel $H_m^{(1)}(x)$ et $H_m^{(2)}(x)$ dans la limite des grands arguments prennent une forme oscillante complexe et faiblement décroissante

$$H_m^{(1)}(x) \approx \sqrt{\frac{2}{\pi x}}\mathrm{e}^{+i\tilde{\Theta}_m(x)}\left[1 + i\left(\frac{4m^2-1}{8x}\right)\right] + \mathcal{O}(x^{-2-1/2}) \quad \text{(A.30)}$$

$$H_m^{(1)\prime}(x) \approx \sqrt{\frac{2}{\pi x}}\mathrm{e}^{+i\tilde{\Theta}_m(x)}\left[i - \left(\frac{4m^2+3}{8x}\right)\right] + \mathcal{O}(x^{-2-1/2}) \quad \text{(A.31)}$$

  Les développements des fonctions de Hankel $H_m^{(2)}(x)$ sont obtenus par le remplacement $i \to -i$.

A.2.3 Développements pour m grand

Pour l'ordre $m > 0$ grand, les expressions des fonctions de Bessel prennent des formes différentes selon le rapport de l'argument x et de l'ordre m (voir les développements de Debye, section 9.3 de [1]). Tout comme les développements pour les petits et grands arguments x, on utilisera les expressions (A.4)-(A.7) pour accomoder les ordres m négatifs. Les développements des fonctions de Bessel qui suivent sont des approximations au moins d'ordre $\mathcal{O}(m^{-1})$.

Cas $m + m^{-1/3} < x$:

Pour des arguments x supérieurs à l'ordre m, on définit l'expression

$$\Theta_m(x) = x\sqrt{1-(m/x)^2} - m\arccos(m/x) - \frac{\pi}{4} \quad . \tag{A.32}$$

Notons que $\lim_{x \gg m} \Theta_m(x) \to \tilde{\Theta}_m(x)$, où $\tilde{\Theta}_m(x)$ est présentée à l'équation (A.25).

- $J_m(x)$:
  La fonction de Bessel $J_m(x)$ suit une lente décroissance oscillante

$$J_m(x) \approx +\sqrt{\frac{2}{\pi x\sqrt{1-(m/x)^2}}}\cos\Theta_m(x) \tag{A.33}$$

$$J'_m(x) \approx -\sqrt{\frac{2\sqrt{1-(m/x)^2}}{\pi x}}\sin\Theta_m(x) \quad . \tag{A.34}$$

  La limite $x \gg m$ de ces expressions permet de retrouver les expressions (A.26) et (A.27).

- $Y_m(x)$:
  La fonction de Bessel $J_m(x)$ suit une lente décroissance oscillante

$$Y_m(x) \approx +\sqrt{\frac{2}{\pi x\sqrt{1-(m/x)^2}}}\sin\Theta_m(x) \tag{A.35}$$

$$Y'_m(x) \approx +\sqrt{\frac{2\sqrt{1-(m/x)^2}}{\pi x}}\cos\Theta_m(x) \tag{A.36}$$

  La limite $x \gg m$ de ces expressions permet de retrouver les expressions (A.28) et (A.29).

- $H_m^{(1)}(x)$ et $H_m^{(2)}(x)$:

$$H_m^{(1)}(x) \approx +\sqrt{\frac{2}{\pi x\sqrt{1-(m/x)^2}}}\mathrm{e}^{+i\Theta_m(x)} \tag{A.37}$$

$$H_m^{(1)'}(x) \approx +\sqrt{\frac{2\sqrt{1-(m/x)^2}}{\pi x}}\mathrm{e}^{+i[\Theta_m(x)+\pi/2]} \tag{A.38}$$

  La limite $x \gg m$ de ces expressions permet de retrouver les expressions (A.30) et (A.31). Les développements pour la seconde fonction de Hankel et sa dérivée sont obtenus par le remplacement $i \to -i$.

Cas $m - m^{-1/3} < x < m + m^{-1/3}$:

Les développements des fonctions de Bessel dans le domaine de transition ($x \sim m$) fait intervenir des fonctions de Airy, Ai$(\cdot)$ et Bi$(\cdot)$ [1],

$$J_m(x) \approx \frac{2^{1/3}}{m^{1/3}}\mathrm{Ai}(-2^{1/3}m^{-1/3}(x-m)) \tag{A.39}$$

$$Y_m(x) \approx -\frac{2^{1/3}}{m^{1/3}}\mathrm{Bi}(-2^{1/3}m^{-1/3}(x-m)) \tag{A.40}$$

Puisque les fonctions de Airy tombent rapidement dans un régime asymptotique exponentiel (croissant ou décroissant) ou oscillant, autrement bien modélisés par d'autres approximations des fonctions de Bessel, on sera intéressé au comportement linéaire dans le voisinage de $x = m$. Pour les petits arguments, les fonctions de Airy prennent la forme (à l'ordre $\mathcal{O}(m^{-1}(x-m)^3)$, section 10.4 de [1])

$$\mathrm{Ai}(-2^{1/3}m^{-1/3}(x-m)) \approx \frac{1}{3^{2/3}\Gamma(2/3)} + \frac{2^{1/3}}{3^{1/3}\Gamma(1/3)}\frac{(x-m)}{m^{1/3}} \tag{A.41}$$

$$\mathrm{Bi}(-2^{1/3}m^{-1/3}(x-m)) \approx \frac{3^{1/2}}{3^{2/3}\Gamma(2/3)} - \frac{3^{1/2}2^{1/3}}{3^{1/3}\Gamma(1/3)}\frac{(x-m)}{m^{1/3}} \ . \tag{A.42}$$

Puisqu'il est désirable de conserver une approximation des fonctions de Bessel au moins à l'ordre m^{-1}, on restreint l'approximation au domaine $m - m^{-1/3} < x < m + m^{-1/3}$. On a donc une forme approximative des fonctions de Bessel au moins de cet ordre pour l'intervalle $m - m^{-1/3} < x < m + m^{-1/3}$.

- $J_m(x)$:
  L'approximation locale de la fonction de Bessel $J_m(x)$ pour l'intervalle de transition prend la forme

$$J_m(x) \approx +\frac{2^{1/3}}{3^{2/3}\Gamma(2/3)}\frac{1}{m^{1/3}} + \frac{2^{2/3}}{3^{1/3}\Gamma(1/3)}\frac{(x-m)}{m^{2/3}} \tag{A.43}$$

$$J'_m(x) \approx +\frac{2^{2/3}}{3^{1/3}\Gamma(1/3)}\frac{1}{m^{2/3}} \tag{A.44}$$

- $Y_m(x)$:
  L'approximation locale de la fonction de Bessel $Y_m(x)$ pour l'intervalle de transition prend la forme

$$Y_m(x) \approx -\frac{2^{1/3}3^{1/2}}{3^{2/3}\Gamma(2/3)}\frac{1}{m^{1/3}} + \frac{2^{2/3}3^{1/2}}{3^{1/3}\Gamma(1/3)}\frac{(x-m)}{m^{2/3}} \tag{A.45}$$

$$Y'_m(x) \approx +\frac{2^{2/3}3^{1/2}}{3^{1/3}\Gamma(1/3)}\frac{1}{m^{2/3}} \quad . \tag{A.46}$$

- $H_m^{(1)}(x)$ et $H_m^{(2)}(x)$:
  L'approximation locale de la fonction $H_m^{(1)}(x)$ pour l'intervalle de transition prend la forme

$$H_m^{(1)}(x) \approx +\frac{2^{1/3}(1-i3^{1/2})}{3^{2/3}\Gamma(2/3)}\frac{1}{m^{1/3}} + \frac{2^{2/3}(1+i3^{1/2})}{3^{1/3}\Gamma(1/3)}\frac{(x-m)}{m^{2/3}} \quad (A.47)$$

$$H_m^{(1)'}(x) \approx +\frac{2^{2/3}(1+i3^{1/2})}{3^{1/3}\Gamma(1/3)}\frac{1}{m^{2/3}} \quad . \quad (A.48)$$

  Les développements pour la seconde fonction de Hankel et sa dérivée sont obtenus par remplacement $i \to -i$.

Cas $x < m - m^{-1/3}$:

Pour ce qui suit,

$$\Lambda_m(x) = -m\sqrt{1-(x/m)^2} + m\,\mathrm{arccosh}(m/x) \quad . \quad (A.49)$$

Puisque les fonctions $\sqrt{1-(x/m)^2}$ et $\mathrm{arccosh}(m/x)$, croissantes pour le domaine d'intérêt, se confondent vers $x \to m$, mais que la pente de la seconde est toujours plus grande que celle de la première, la fonction $\Lambda_m(x)$ est donc strictement positive,

$$\Lambda_m(x) > 0 \quad \forall\ x \in [0,\ m - m^{-1/3}[\quad . \quad (A.50)$$

De plus, comme $\mathrm{arccosh}(m/a) < \mathrm{arccosh}(m/b)$ pour $a > b$, alors

$$\Lambda_m(a) < \Lambda_m(b) \quad ,\ a > b \quad . \quad (A.51)$$

Finalement, pour $\alpha = m'/m$ et $m' > x$

$$\Lambda_{m'}(x) = \alpha\Lambda_m(x/\alpha) \quad . \quad (A.52)$$

Ces dernières relations impliquent à leur tour que

$$\Lambda_{m'}(x) > \Lambda_m(x) \quad \forall \quad m' > m \quad . \quad (A.53)$$

- $J_m(x)$:
  Pour des arguments x inférieurs à l'ordre m, la fonction $J_m(x)$ prend la forme

$$J_m(x) \approx +\frac{1}{\sqrt{2\pi m\sqrt{1-(x/m)^2}}}\mathrm{e}^{-\Lambda_m(x)} \quad (A.54)$$

$$J'_m(x) \approx +\sqrt{\frac{m\sqrt{1-(x/m)^2}}{2\pi x^2}}\mathrm{e}^{-\Lambda_m(x)} \quad (A.55)$$

- $Y_m(x)$:
  Pour des arguments x inférieurs à l'ordre m, la fonction $Y_m(x)$ prend la forme

$$Y_m(x) \approx -\sqrt{\frac{2}{\pi m\sqrt{1-(x/m)^2}}}\mathrm{e}^{+\Lambda_m(x)} \tag{A.56}$$

$$Y'_m(x) \approx +\sqrt{\frac{2m\sqrt{1-(x/m)^2}}{\pi x^2}}\mathrm{e}^{+\Lambda_m(x)} \tag{A.57}$$

- $H_m^{(1)}(x)$ et $H_m^{(2)}(x)$:

$$H_m^{(1)}(x) \approx +\frac{1}{\sqrt{\pi m\sqrt{1-(x/m)^2}}}\left[\frac{1}{\sqrt{2}}\mathrm{e}^{-\Lambda_m(x)} - i\sqrt{2}\mathrm{e}^{+\Lambda_m(x)}\right] \tag{A.58}$$

$$H_m^{(1)'}(x) \approx +\sqrt{\frac{m\sqrt{1-(x/m)^2}}{\pi x^2}}\left[\frac{1}{\sqrt{2}}\mathrm{e}^{-\Lambda_m(x)} + i\sqrt{2}\mathrm{e}^{+\Lambda_m(x)}\right] \tag{A.59}$$

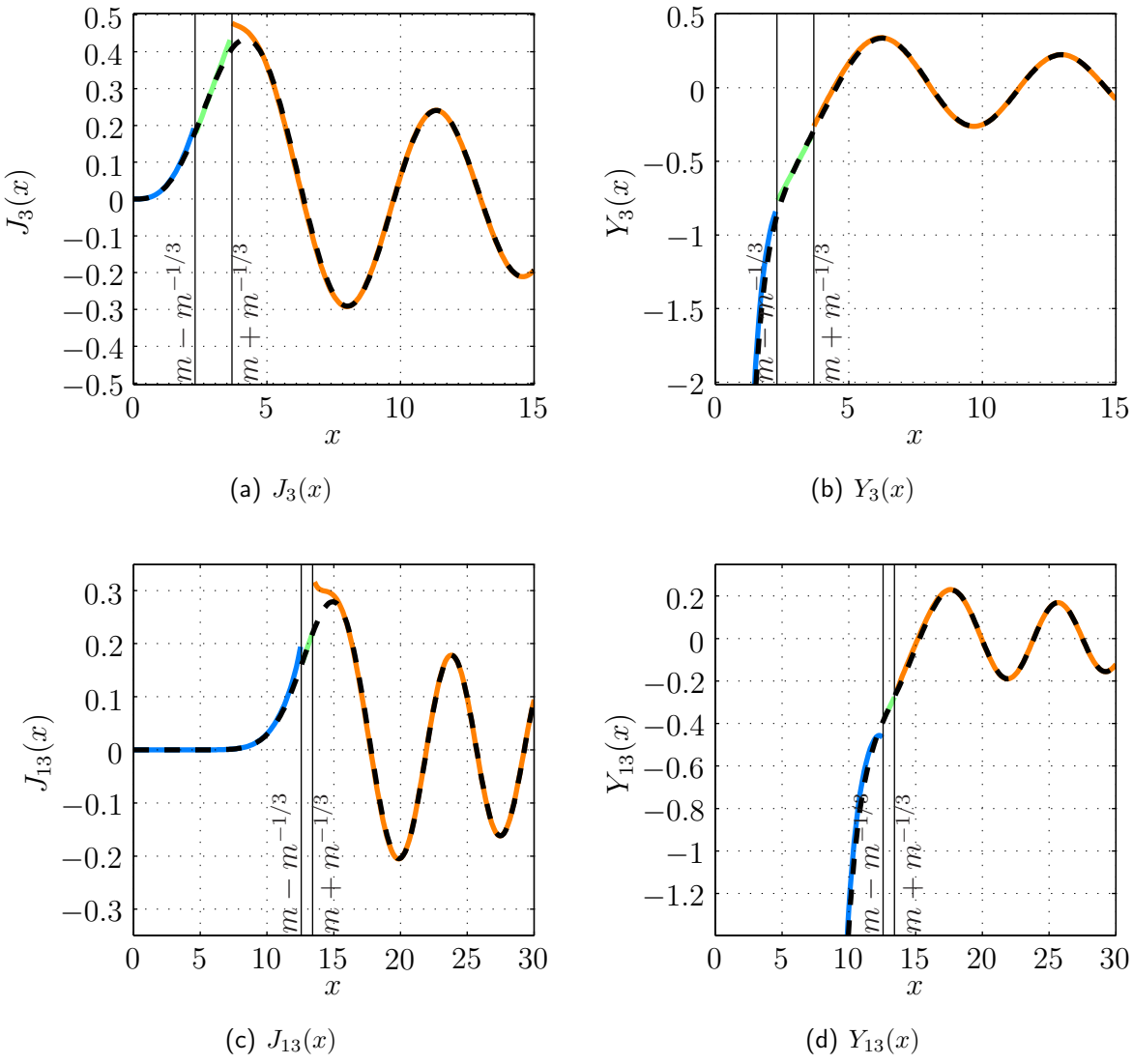
  Les développements pour la seconde fonction de Hankel et sa dérivée sont obtenus par remplacement $i \to -i$.

On retrouve les approximations des petits arguments (A.20), (A.22) et (A.24) en employant d'abord l'identité $\operatorname{arccosh}(a) = \ln\left(a+\sqrt{a^2-1}\right)$ dans l'expression de $\exp\left[\pm\Lambda_m(x)\right]$, et en appliquant la limite $x \ll m$,

$$\exp\left[\pm\Lambda_m(x)\right] \approx \mathrm{e}^{\mp m} m^{\pm m}\left(\frac{x}{2}\right)^{\mp m} \quad . \tag{A.60}$$

Comme les développements de cette section sont consacrés aux grands m, on identifie directement la formule de Stirling pour les grands factoriels, $m! \approx \sqrt{2\pi}\mathrm{e}^{-m}m^{m+1/2}$.

Puisque les limites des petits et grands arguments peuvent être retrouvées à l'aide des développements aux grands ordres, ces derniers revêtent une importance toute spéciale pour l'analyse d'expressions utilisant les fonctions de Bessel. Quelques exemples de l'utilisation des développements aux grands ordres sont présentés à la Fig. A.2.



(a) $J_3(x)$ (b) $Y_3(x)$

(c) $J_{13}(x)$ (d) $Y_{13}(x)$

Fig. A.2 Évaluation numérique de $J_m(x)$ and $Y_m(x)$ pour $m = 3$ et $m = 13$ (trait noir discontinu) et évaluation des développements approximatifs aux grands ordres correspondants: trait plein bleu, $x < m - m^{-1/3}$; trait plein vert, $m - m^{-1/3} < x < m + m^{-1/3}$; trait plein orangé, $m + m^{-1/3} < x$. Les développements aux grands ordres obtenus sont remarquablement précis, même pour $m = 3$.

Annexe B

Oscillateurs, états comprimés et distribution de Husimi

Cette annexe regroupe des résultats bien connus associés aux oscillateurs harmoniques classique et ondulatoire, aux états cohérents et à leur généralisation sous la forme d'états comprimés, ainsi qu'aux distributions quantiques. Ce dernier volet se concentre particulièrement sur la distribution de Husimi, distribution possédant un rôle central dans l'étude des systèmes à dynamique complexe.

B.1 Oscillateur harmonique classique: Rappels

Pour le Hamiltonien de l'oscillateur harmonique classique

$$H = \frac{1}{2m}p^2 + \frac{1}{2}m\omega^2 q^2 \tag{B.1}$$

les équations du mouvement sont

$$\frac{d}{dt}q = \frac{1}{m}p \quad , \quad \frac{d}{dt}p = -m\omega^2 q \quad . \tag{B.2}$$

En combinant ces deux expressions, on obtient l'équation différentielle ordinaire du deuxième ordre

$$\frac{d^2}{dt^2}q + \omega^2 q = 0 \tag{B.3}$$

qui se solutionne directement

$$q(t) = q(0)\mathrm{e}^{\pm i\omega t} \quad , \quad p(t) = \pm im\omega q(0)\mathrm{e}^{\pm i\omega t} \quad . \tag{B.4}$$

On peut aussi utiliser la quantité

$$\alpha = \frac{1}{\sqrt{2m\omega}} \left(m\omega q + ip\right) \tag{B.5}$$

pour obtenir un système simplifié

$$\frac{d}{dt}\alpha = \frac{1}{\sqrt{2m\omega}} \left(m\omega \frac{d}{dt}q + i\frac{d}{dt}p\right) = -i\omega\alpha \tag{B.6}$$

qui implique une solution de forme

$$\alpha(t) = \alpha(0)\mathrm{e}^{-i\omega t} \quad . \tag{B.7}$$

On retrouve les quantités $q(t)$ et $p(t)$ en inversant $\alpha(t)$ et son complexe conjugué

$$q(t) = \frac{1}{\sqrt{2m\omega}} \left(\alpha(0)\mathrm{e}^{-i\omega t} + \alpha^*(0)\mathrm{e}^{+i\omega t}\right) \tag{B.8}$$

$$p(t) = -i\sqrt{\frac{m\omega}{2}} \left(\alpha(0)\mathrm{e}^{-i\omega t} - \alpha^*(0)\mathrm{e}^{+i\omega t}\right) \quad . \tag{B.9}$$

B.2 Oscillateur harmonique ondulatoire: Rappels

L'oscillateur harmonique à une dimension de la mécanique quantique est décrit par l'opérateur hamiltonien[1]

$$\hat{H} = \frac{1}{2m}\hat{p}^2 + \frac{1}{2}m\omega^2\hat{q}^2 \tag{B.10}$$

où m est la masse de la particule d'intérêt, $\hat{q}$ et $\hat{p}$, les opérateurs position et impulsion, et ω, la fréquence angulaire de l'oscillation. Les opérateurs hermitiques position et impulsion satisfont la règle de commutation postulée de la mécanique quantique

$$[\hat{q}, \hat{p}] = i\hbar \quad . \tag{B.11}$$

La construction d'opérateurs de création $\hat{a}^\dagger$ et d'annihilation $\hat{a}$

$$\hat{a} = \frac{1}{\sqrt{2m\hbar\omega}} \left(m\omega\hat{q} + i\hat{p}\right) \tag{B.12}$$

$$\hat{a}^\dagger = \frac{1}{\sqrt{2m\hbar\omega}} \left(m\omega\hat{q} - i\hat{p}\right) \tag{B.13}$$

permet de réécrire le Hamiltonien (B.10)

$$\hat{H} = \left(\hat{a}^\dagger\hat{a} + \frac{1}{2}\right)\hbar\omega \quad . \tag{B.14}$$

[1] Les résultats de cette section sont bien connus et on en retrouve le développement, par exemple, chez [36].

Les valeurs propres de cet Hamiltonien sont

$$E_n = \left(n + \frac{1}{2}\right)\hbar\omega, \ \forall\ n \in \mathbb{N} \tag{B.15}$$

et les états propres associés, $\left|\ n\ \right\rangle$, dans la représentation $\left|\ q\ \right\rangle$ sont exprimés en terme du produit d'une gaussienne et d'un polynôme d'Hermite $H_n(z)$

$$\left\langle\ q\ \middle|\ n\ \right\rangle = \psi_n(q) = \frac{1}{(2\pi\Delta q^2)^{1/4}}\frac{1}{\sqrt{2^n n!}}\mathrm{e}^{-\frac{1}{4}\frac{q^2}{\Delta q^2}} H_n\left(\frac{q}{\sqrt{2}\Delta q}\right) \tag{B.16}$$

où $\Delta q = \sqrt{\hbar/2m\omega}$. Les niveaux d'énergie de l'oscillateur harmonique unidimensionnel ne sont pas dégénérés. Ces états $\left\{\left|\ n\ \right\rangle\right\}$ forment une base complète et orthonormale. On écrit donc la relation de fermeture

$$\mathbb{1} = \sum_{n=0}^{\infty} \left|\ n\ \right\rangle\left\langle\ n\ \right| \quad . \tag{B.17}$$

Parmi les résultats intermédiaires menant aux expressions des valeurs propres de l'Hamiltonien, on retient l'application des opérateur $\hat{a}$ et $\hat{a}^\dagger$ sur les états propres $\left|\ n\ \right\rangle$,

$$\hat{a}\left|\ n\ \right\rangle = \sqrt{n}\left|\ n-1\ \right\rangle \tag{B.18}$$

$$\hat{a}^\dagger\left|\ n\ \right\rangle = \sqrt{n+1}\left|\ n+1\ \right\rangle \tag{B.19}$$

et

$$\hat{a}^\dagger\hat{a}\left|\ n\ \right\rangle = n\left|\ n\ \right\rangle \tag{B.20}$$

$$\hat{a}\left|\ 0\ \right\rangle = 0 \tag{B.21}$$

ainsi que la valeur du commutateur

$$\left[\hat{a}, \hat{a}^\dagger\right] = \mathbb{1} \quad . \tag{B.22}$$

B.3 États cohérents

B.3.1 Représentation des états cohérents sur la base $\left\{\left|\ n\ \right\rangle\right\}$

On définit l'état cohérent comme le vecteur propre de $\hat{a}$,

$$\hat{a}\left|\ \alpha\ \right\rangle = \alpha\left|\ \alpha\ \right\rangle \quad . \tag{B.23}$$

On obtient l'état cohérent $\left|\ \alpha\ \right\rangle$ en terme des états propres de l'oscillateur harmonique $\left\{\left|\ n\ \right\rangle\right\}$ à l'aide de l'expression (B.18). Partant de la projection sur $\left|\ n=0\ \right\rangle$, la projection successive des états $\left|\ n=1\ \right\rangle$, $\left|\ n=2\ \right\rangle$... sur le côté gauche de (B.18) permet de dégager, par récurrence, la relation

$$\left\langle\ n\ \right|\left.\ \alpha\ \right\rangle = \frac{\alpha^n}{\sqrt{n!}}\left\langle\ 0\ \right|\left.\ \alpha\ \right\rangle \quad . \tag{B.24}$$

On trouve une relation semblable pour $\left\langle\ \alpha\ \right|$,

$$\left\langle\ \alpha\ \right|\left.\ n\ \right\rangle = \frac{(\alpha^*)^n}{\sqrt{n!}}\left\langle\ \alpha\ \right|\left.\ 0\ \right\rangle \quad . \tag{B.25}$$

À l'aide de la relation de fermeture (B.17), on explicite $\left|\ \alpha\ \right\rangle$ dans la représentation $\left\{\left|\ n\ \right\rangle\right\}$

$$\left|\ \alpha\ \right\rangle = \sum_{n=0}^{\infty}\left|\ n\ \right\rangle\left\langle\ n\ \right|\left.\ \alpha\ \right\rangle = \left\langle\ 0\ \right|\left.\ \alpha\ \right\rangle\sum_{n=0}^{\infty}\frac{\alpha^n}{\sqrt{n!}}\left|\ n\ \right\rangle \quad . \tag{B.26}$$

Le terme $\left\langle\ 0\ \right|\left.\ \alpha\ \right\rangle$ est obtenu par normalisation de $\left\langle\ \alpha\ \right|\left.\ \alpha\ \right\rangle$, encore une fois, par le biais de (B.17),

$$\left\langle\ 0\ \right|\left.\ \alpha\ \right\rangle = \mathrm{e}^{-\frac{1}{2}|\alpha|^2} \quad . \tag{B.27}$$

L'expression complète de $\left|\ \alpha\ \right\rangle$ dans la base $\left|\ n\ \right\rangle$ est donc, à une phase près,

$$\left|\ \alpha\ \right\rangle = \mathrm{e}^{-\frac{1}{2}|\alpha|^2}\sum_{n=0}^{\infty}\frac{\alpha^n}{\sqrt{n!}}\left|\ n\ \right\rangle \quad . \tag{B.28}$$

Parmi les résultats intermédiaires importants, on considère la projection de l'état cohérent sur la base des positions. Partant de l'équation aux valeurs propres (B.23), on obtient une équation différentielle sur la position q

$$\left\langle\ q\ \right|\left|\hat{a}\right|\left.\ \alpha\ \right\rangle = \alpha\left\langle\ q\ \right|\left.\ \alpha\ \right\rangle = \frac{1}{\sqrt{2m\hbar\omega}}\left\langle\ q\ \right|\left.(m\omega\hat{q}+i\hat{p})\right|\left.\ \alpha\ \right\rangle \tag{B.29}$$

$$= \frac{1}{\sqrt{2m\hbar\omega}}\left(m\omega q+\hbar\frac{d}{dq}\right)\left\langle\ q\ \right|\left.\ \alpha\ \right\rangle \quad . \tag{B.30}$$

La solution normalisée pour $\left\langle\ q\ \right|\left.\ \alpha\ \right\rangle$ prend finalement la forme

$$\left\langle\ q\ \right|\left.\ \alpha\ \right\rangle = \left(\frac{m\omega}{\pi\hbar}\right)^{1/4}\mathrm{e}^{-\mathrm{Im}\{\alpha\}^2}\mathrm{e}^{+i\mathrm{Re}\{\alpha\}\mathrm{Im}\{\alpha\}}\exp\left[-\left(\sqrt{\frac{m\omega}{2\hbar}}q-\alpha\right)^2\right] \quad . \tag{B.31}$$

On obtient directement par transformée de Fourier la représentation en impulsion,

$$\left\langle\ p\ \right|\left.\ \alpha\ \right\rangle = \frac{1}{(\pi m\hbar\omega)^{1/4}}\mathrm{e}^{-\mathrm{Re}\{\alpha\}^2}\mathrm{e}^{-i\mathrm{Re}\{\alpha\}\mathrm{Im}\{\alpha\}}\exp\left[-\left(\frac{1}{\sqrt{2m\hbar\omega}}p+i\alpha\right)^2\right] \quad . \tag{B.32}$$

Le choix de la phase à l'expression (B.32) est alors justifié par soucis de symétrie entre les représentations en position et en impulsion de l'état cohérent.

Suivant (B.5), on définit la quantité $\alpha(q_0, p_0) = \frac{1}{\sqrt{2m\hbar\omega}}\,(m\omega q_0 + ip_0)$, ce qui renvoie aux expressions

$$\left\langle\ q\ \right|\ \alpha(q_0,p_0)\ \left\rangle = \left(\frac{m\omega}{\pi\hbar}\right)^{1/4} \mathrm{e}^{+i\frac{1}{2}\frac{p_0 q_0}{\hbar}} \mathrm{e}^{+i\frac{p_0(q-q_0)}{\hbar}} \exp\left[-\frac{1}{2}\frac{(q-q_0)^2}{(\hbar/m\omega)}\right] \tag{B.33}$$

et

$$\left\langle\ p\ \right|\ \alpha(q_0,p_0)\ \left\rangle = \frac{1}{(\pi m\hbar\omega)^{1/4}} \mathrm{e}^{-i\frac{1}{2}\frac{p_0 q_0}{\hbar}} \mathrm{e}^{-i\frac{q_0(p-p_0)}{\hbar}} \exp\left[-\frac{1}{2}\frac{(p-p_0)^2}{(m\hbar\omega)}\right] \tag{B.34}$$

Les états cohérents $\left|\ \alpha\ \right\rangle$ ne sont pas orthogonaux entre eux,

$$\left|\left\langle\ \alpha'\ \right|\ \alpha\ \right\rangle\right|^2 = \mathrm{e}^{-|\alpha'-\alpha|^2} \quad . \tag{B.35}$$

On obtient cependant une relation de fermeture dans l'espace complexe des α ($d^2\alpha = d\mathrm{Re}\{\alpha\}d\mathrm{Im}\{\alpha\}$ est un élément d'aire d'un tel espace),

$$\frac{1}{\pi}\int d^2\alpha \left|\ \alpha\ \right\rangle\left\langle\ \alpha\ \right| = \mathbb{1} \quad . \tag{B.36}$$

Ce résultat est obtenu en utilisant deux fois la relation de fermeture (B.17) et en posant ensuite $\alpha = r\mathrm{e}^{i\theta}$ ($d^2\alpha = r\ dr\ d\theta$).

B.3.2 L'état cohérent comme état quasi classique

Le propagateur $\exp(-i\frac{1}{\hbar}\hat{H}t)$ est utilisé pour expliciter la dépendance temporelle de l'état cohérent $\left|\ \alpha\ \right\rangle$. Dans le cas de l'oscillateur harmonique, si à $t = 0$ l'état cohérent $\left|\ \alpha_0\ \right\rangle$ est défini, alors, suivant la représentation (B.28) puis l'expression des énergies propres de l'oscillateur harmonique (B.15), on obtient

$$\left|\ \alpha(t)\ \right\rangle = \mathrm{e}^{-i\frac{1}{2}\omega t}\left|\ \alpha_0 \mathrm{e}^{-i\omega t}\ \right\rangle \quad . \tag{B.37}$$

L'état $\left|\ \alpha(t)\ \right\rangle$ vérifie la normalisation $\left\langle\ \alpha(t)\ \right|\ \alpha(t)\ \left\rangle = 1\right.$.

L'application de l'opérateur $\hat{a}$ sur l'état cohérent $\left|\ \alpha(t)\ \right\rangle$ retourne

$$\hat{a}\left|\ \alpha(t)\ \right\rangle = \alpha_0 \mathrm{e}^{-i\omega t}\left|\ \alpha(t)\ \right\rangle \tag{B.38}$$

identifiant $\left|\ \alpha(t)\ \right\rangle$ comme vecteur propre de $\hat{a}$ (i.e. un état cohérent demeure un état cohérent sous évolution temporelle dans le potentiel harmonique).

Suivant la définition des opérateurs $\hat{a}$ et $\hat{a}^\dagger$, les opérateurs position et impulsion prennent la forme

$$\hat{q} \;=\; \sqrt{\frac{\hbar}{2m\omega}}\left(\hat{a}^\dagger + \hat{a}\right) \tag{B.39}$$

$$\hat{p} \;=\; i\sqrt{\frac{m\hbar\omega}{2}}\left(\hat{a}^\dagger - \hat{a}\right) \quad . \tag{B.40}$$

$$\begin{array}{lrcl} J=0: & \langle \hat{q}^0(t) \rangle_\alpha & = & 1 \\ J=2: & \langle \hat{q}^2(t) \rangle_\alpha & = & \left[\langle \hat{q}(t) \rangle_\alpha\right]^2 + \left[\Delta \hat{q}_\alpha\right]^2 \\ J=3: & \langle \hat{q}^3(t) \rangle_\alpha & = & \left[\langle \hat{q}(t) \rangle_\alpha\right]^3 + 3\left[\Delta \hat{q}_\alpha\right]^2 \left[\langle \hat{q}(t) \rangle_\alpha\right] \end{array}$$

Les valeurs moyennes de position et d'impulsion sur l'état cohérent $\left|\ \alpha(t)\ \right\rangle$ sont donc

$$\langle \hat{q}(t) \rangle_\alpha = \left\langle\ \alpha(t)\ \left|\hat{q}\right|\ \alpha(t)\ \right\rangle = \sqrt{\frac{\hbar}{2m\omega}}\left(\alpha_0 \mathrm{e}^{-i\omega t} + \alpha_0^* \mathrm{e}^{+i\omega t}\right) \tag{B.41}$$

$$\langle \hat{p}(t) \rangle_\alpha = \left\langle\ \alpha(t)\ \left|\hat{p}\right|\ \alpha(t)\ \right\rangle = -i\sqrt{\frac{m\hbar\omega}{2}}\left(\alpha_0 \mathrm{e}^{-i\omega t} - \alpha_0^* \mathrm{e}^{+i\omega t}\right) \tag{B.42}$$

ou encore, suivant la description $\alpha_0 = \alpha(q_0, p_0)$ de la section précédente,

$$\langle \hat{q}(t) \rangle_\alpha = q_0 \cos\omega t + \frac{p_0}{m\omega}\sin\omega t \tag{B.43}$$

$$\langle \hat{p}(t) \rangle_\alpha = p_0 \cos\omega t - m\omega q_0 \sin\omega t \quad . \tag{B.44}$$

La dispersion $\Delta\hat{O}_\alpha(t) = \sqrt{\left\langle \hat{O}^2(t) \right\rangle_\alpha - \left\langle \hat{O}(t) \right\rangle_\alpha^2}$ se calcule directement à partir de (B.39) et (B.40),

$$\Delta \hat{q}_\alpha = \sqrt{\frac{\hbar}{2m\omega}} \tag{B.45}$$

$$\Delta \hat{p}_\alpha = \sqrt{\frac{m\hbar\omega}{2}} \quad . \tag{B.46}$$

D'après ces résultats, l'état cohérent d'un potentiel harmonique est un état d'incertitude minimale pour tout temps, $\Delta\hat{q}_\alpha(t) \times \Delta\hat{p}_\alpha(t) = \hbar/2$. De plus, sa forme gaussienne prescrite par les représentations (B.33) et (B.34) ne change pas au cours de son évolution temporelle. Par ailleurs, on montre [2] que tous les moments de l'état cohérent ne sont définis que par ses deux premiers moments ($J \in \mathbb{N}$),

$$\left\langle \hat{q}^J(t) \right\rangle_\alpha = \left[\langle \hat{q}(t) \rangle_\alpha\right]^J + \sum_{j=1}^{\lfloor J/2 \rfloor} \left(\begin{array}{c} J \\ 2j \end{array} \right) (2j-1)!! \left[\Delta \hat{q}_\alpha\right]^{2j} \left[\langle \hat{q}(t) \rangle_\alpha\right]^{J-2j} \tag{B.47}$$

$$\left\langle \hat{p}^J(t) \right\rangle_\alpha = \left[\langle \hat{p} \rangle_\alpha(t)\right]^J + \sum_{j=1}^{\lfloor J/2 \rfloor} \left(\begin{array}{c} J \\ 2j \end{array} \right) (2j-1)!! \left[\Delta \hat{p}_\alpha\right]^{2j} \left[\langle \hat{p}(t) \rangle_\alpha\right]^{J-2j} \tag{B.48}$$

où $\lfloor a \rfloor$ signifie la plus petite partie entière de a (e.g. $\lfloor 0.5 \rfloor = 0$, $\lfloor 2.9 \rfloor = 2$), et $(2a-1)!! = 1 \cdot 3 \cdot 5 \cdot \ldots \cdot (2a-1)$ est la double factorielle. On obtient par exemple

L'évolution temporelle de l'état cohérent s'apparente donc à celle obtenue pour une particle classique, comme en témoigne la comparaison des expressions (B.8) et (B.9) et (B.41) et (B.42). Dans ce contexte, l'épithète quasi classique conférée à l'état cohérent est donc justifiée.

[2] On utilise alors les représentations en p et en q (B.33) et (B.34) de l'état cohérent.

B.3.3 États comprimés

Pour l'Hamiltonien

$$\hat{H}' = \frac{1}{2m}\hat{p}^2 + \frac{1}{2}m\Omega^2\hat{q}^2 \tag{B.49}$$

on définit les opérateurs de création et d'annihilation comprimés $\hat{b}$ et $\hat{b}^\dagger$ en terme des opérateurs de position et d'impulsion

$$\hat{b} = \frac{1}{\sqrt{2m\hbar\Omega}}\left(m\Omega\hat{q} + i\hat{p}\right) \tag{B.50}$$

$$\hat{b}^\dagger = \frac{1}{\sqrt{2m\hbar\Omega}}\left(m\Omega\hat{q} - i\hat{p}\right) \tag{B.51}$$

avec $\Omega = \kappa\omega$ la fréquence angulaire d'oscillation de l'oscillateur harmonique quantique et κ, une constante positive. L'état comprimé $\left|\ \beta\ \right\rangle$ est défini comme le vecteur propre de l'opérateur d'annihilation comprimé,

$$\hat{b}\left|\ \beta\ \right\rangle = \beta\left|\ \beta\ \right\rangle \quad . \tag{B.52}$$

Moyennant le changement de fréquence prescrit, l'ensemble des résultats obtenus pour l'état cohérent s'appliquent alors directement à l'état comprimé.

On note que les opérateurs comprimés s'expriment en terme des opérateurs $\hat{a}$ et $\hat{a}^\dagger$ suivant les expressions (B.12) et (B.13),

$$\hat{b} = \nu\hat{a}^\dagger + \mu\hat{a} \tag{B.53}$$

$$\hat{b}^\dagger = \mu\hat{a}^\dagger + \nu\hat{a} \tag{B.54}$$

avec

$$\nu = \frac{1}{2}\left(\sqrt{\kappa} - \frac{1}{\sqrt{\kappa}}\right) \tag{B.55}$$

$$\mu = \frac{1}{2}\left(\sqrt{\kappa} + \frac{1}{\sqrt{\kappa}}\right) \quad . \tag{B.56}$$

Par rapport à l'état cohérent, le changement de fréquence a pour effet de diminuer la taille de la dispersion sur une coordonnée au détriment de la seconde coordonnée,

$$\Delta\hat{q}_\beta = \frac{1}{\sqrt{\kappa}}\Delta\hat{q}_\alpha \tag{B.57}$$

$$\Delta\hat{p}_\beta = \sqrt{\kappa}\Delta\hat{p}_\alpha \quad . \tag{B.58}$$

La notion d'état comprimé prend tout son sens pour un état cohérent soumis à une variation du potentiel harmonique d'un facteur κ^2 [130]. Le paquet d'onde suit alors une séquence de contractions et de dilatations dont l'amplitude en position et en impulsion suit les expressions précédentes.

B.4 Distribution de Husimi

B.4.1 Distributions quantiques

La représentation des trajectoires d'un système classique dans son espace des phases permet l'interprétation globale de la dynamique sous-jacente. C'est un outil puissant qui est cependant perdu dans le cadre de la physique ondulatoire dû à l'impossibilité de représenter simultanément une fonction d'onde à la fois en position et en impulsion. On parvient au mieux à construire une distribution quantique, qui, bien qu'entachée d'une certaine arbitrarité, permet d'apprécier qualitativement la correspondance entre une fonction d'onde et les structures dominantes de l'espace des phases.

Pour un opérateur $\hat{O}(\hat{q},\hat{p})$ et la fonction classique $O(q,p)$ obtenue par remplacement direct des opérateurs position et impulsion par leur équivalent scalaire, il serait désirable d'établir l'égalité sur la mesure de $\hat{O}(\hat{q},\hat{p})$ par l'état ψ et la valeur moyenne de $O(q,p)$. Autrement dit, pour une fonction de distribution quantique $F(q,p)$, on pose

$$\left\langle \hat{O}(\hat{q},\hat{p}) \right\rangle_{\psi} = \left\langle \ \psi \ \left| \hat{O}(\hat{q},\hat{p}) \right| \ \psi \ \right\rangle = \int dqdp \ O(q,p) F(q,p) \quad . \tag{B.59}$$

Cependant, la non-commutativité des opérateurs position et impulsion implique que $F(q,p)$ n'est pas uniquement définie. Cohen [35] a montré que l'utilisation de l'opérateur

$$\hat{O}(\hat{q},\hat{p}) = \mathrm{e}^{i\xi\hat{q}+i\eta\hat{p}} f(\xi,\eta) \tag{B.60}$$

permet d'accéder à un grand nombre de fonctions de distribution quantique par le simple choix de la fonction d'association $f(\xi,\eta)$ [35, 73, 63]. Cette fonction d'association est choisie de sorte qu'elle compense l'effet de la non-commutativité des opérateurs position et impulsion. Du point de vue classique cependant, l'expression (B.60) demeure égale à $\mathrm{e}^{i\xi q+i\eta p}$ et (B.59) est toujours satisfaite. Dans le cadre de ce travail, l'attention est portée sur la distribution de Husimi $F^H(q,p)$.

B.4.2 Une distribution particulière: La distribution de Husimi

La distribution quantique de Husimi est obtenue en distribuant sur (B.60) les opérateurs comprimés $\hat{b}$ et $\hat{b}^\dagger$ suivant l'ordre antinormal. On cherche donc à écrire

$$\left\langle \mathrm{e}^{-v^*\hat{b}} \mathrm{e}^{+v\hat{b}^\dagger} \right\rangle_{\psi} = \int dqdp \ \mathrm{e}^{i\xi q+i\eta p} F^H(q,p) \quad . \tag{B.61}$$

Les définitions (B.50) et (B.51) renvoient directement à

$$\mathrm{e}^{i\xi\hat{q}+i\eta\hat{p}} = \mathrm{e}^{v\hat{b}^\dagger - v^*\hat{b}} \tag{B.62}$$

avec

$$v(\xi,\eta) = -\sqrt{\frac{m\hbar\Omega}{2}}\eta + i\sqrt{\frac{\hbar}{2m\Omega}}\xi \quad . \tag{B.63}$$

Puisque $[\hat{b},\hat{b}^\dagger] = \mathbb{1}$, la formule de Baker-Campbell-Hausdorf [130] se simplifie[3] et l'expression (B.62) devient

$$\mathrm{e}^{i\xi\hat{q}+i\eta\hat{p}} = \mathrm{e}^{+\frac{1}{2}|v|^2}\mathrm{e}^{-v^*\hat{b}}\mathrm{e}^{+v\hat{b}^\dagger} \quad . \tag{B.64}$$

En regard à (B.60), on définit alors la fonction d'association $f(\xi,\eta) = f^H(\xi,\eta)$,

$$f^H(\xi,\eta) = \mathrm{e}^{-\frac{1}{2}|v(\eta,\xi)|^2} \quad . \tag{B.65}$$

La distribution quantique de Husimi $F^H(q,p)$ est ensuite obtenue par transformée de Fourier,

$$F^H(q,p) = \frac{1}{(2\pi)^2}\int d\xi d\eta \left\langle \mathrm{e}^{-v^*\hat{b}}\mathrm{e}^{+v\hat{b}^\dagger}\right\rangle_\psi \mathrm{e}^{-i\xi q - i\eta p} \quad . \tag{B.66}$$

On voit bien que la fonction d'association n'apparaît finalement que de façon formelle dans les expressions précédentes puisque les coordonnées de l'espace des phases (classique) commutent toujours.

L'identité (B.36) est insérée entre les opérateurs de l'expression (B.66),

$$F^H(q,p) = \frac{1}{\pi}\frac{1}{(2\pi)^2}\int d\xi d\eta \int d^2\beta' \left|\langle\ \psi\ |\ \beta'\ \rangle\right|^2 \mathrm{e}^{-v^*\beta'}\mathrm{e}^{+v\beta'^*}\mathrm{e}^{-i\xi q - i\eta p} \tag{B.67}$$

puis, à l'aide de (B.63) et puisque $d^2\beta' = d\mathrm{Re}\{\beta'\}d\mathrm{Im}\{\beta'\}$, l'expression finale pour la distribution de Husimi est obtenue

$$F^H(q,p) = \frac{1}{2\pi\hbar}\left|\langle\ \beta\ |\ \psi\ \rangle\right|^2 \quad . \tag{B.68}$$

La distribution de Husimi est calculée explicitement sur la coordonnée q (coordonnée pour laquelle la fonction ψ est généralement connue) en utilisant (B.33),

$$F^H(q,p) = \frac{1}{(2\pi)^{3/2}\hbar}\left|\int_{-\infty}^{+\infty} dq'\ \psi(q')\cdot\frac{1}{\sqrt{\Delta\hat{q}_\beta}}\mathrm{e}^{-i\frac{1}{\hbar}p(q'-q)}\exp\left[-\frac{1}{4}\frac{(q'-q)^2}{(\Delta\hat{q}_\beta)^2}\right]\right|^2 \quad . \tag{B.69}$$

Dans la limite où $\Delta\hat{q}_\beta \to 0$, la distribution de Husimi devient proportionnelle au module carré de la fonction d'onde sur q,

$$\lim_{\Delta\hat{q}_\beta\to 0} F^H(q,p) \propto |\psi(q)|^2 \quad . \tag{B.70}$$

[3] $\mathrm{e}^{\hat{A}+\hat{B}} = \mathrm{e}^{-[\hat{A},\hat{B}]/2}\mathrm{e}^{\hat{A}}\mathrm{e}^{\hat{B}}$ si $[[\hat{A},\hat{B}],\hat{A}] = 0$ et $[[\hat{A},\hat{B}],\hat{B}] = 0$

Une relation semblable est obtenue pour $\Delta\hat{p}_\beta \to 0$,

$$\lim_{\Delta\hat{p}_\beta \to 0} F^H(q,p) \propto |\psi(p)|^2 \quad . \tag{B.71}$$

Puisque l'expression (B.69) possède la forme d'une convolution, on utilise avantageusement le théorème de convolution pour l'évaluation numérique de la distribution de Husimi,

$$F^H(q,p) = \frac{1}{(2\pi)^{1/2}\hbar} \left| \mathcal{F}_y^{-1} \left\{ \frac{1}{\sqrt{\pi}} \frac{1}{\sqrt{1/\Delta\hat{q}_\beta}} \exp\left[-\frac{(y-p/\hbar)^2}{1/\left(\Delta\hat{q}_\beta\right)^2} \right] \cdot \mathcal{F}_x\left\{\psi(x)\right\}(y) \right\}(q) \right|^2 \tag{B.72}$$

où

$$\mathcal{F}_x\left\{g(x)\right\}(y) = \frac{1}{2\pi}\int_{-\infty}^{+\infty} dx\ \mathrm{e}^{-iyx} g(x) \tag{B.73}$$

$$\mathcal{F}_y^{-1}\left\{G(y)\right\}(x) = \int_{-\infty}^{+\infty} dy\ \mathrm{e}^{+iyx} G(y) \quad . \tag{B.74}$$

De plus, si $\psi(q+mQ) = \psi(q)$, $m = ...-2,-1,0,1,2...$, alors $\psi(q)$ est périodique en Q et la distribution de Husimi devient

$$F_Q^H(q,p) = \frac{1}{\sqrt{2\pi}} \frac{1}{4\Delta\hat{p}_\beta} \left| \sum_m c_m \exp\left[-\frac{\left(p - m\frac{2\pi}{Q}\hbar\right)^2}{4\left(\Delta\hat{p}_\beta\right)^2} \right] \mathrm{e}^{im\frac{2\pi}{Q}q} \right|^2 \tag{B.75}$$

avec $\{c_m\}$, les coefficients de la série de Fourier de $\psi(q)$.

La distribution de Husimi se rapproche d'une distribution de probabilité habituelle (normalisable, réelle, positive). Pour $\left|\ \psi\ \right\rangle$ normalisé, cette distribution est bornée supérieurement à $1/2\pi\hbar$. Elle possède l'avantage d'adoucir les fluctuations rapides de ψ, en contraste avec la distribution de Wigner [63], ce qui a contribué à sa popularité pour l'étude de systèmes présentant les signes du "chaos quantique" [73]. D'autre part, la distribution de Husimi ne permet pas d'obtenir les distributions marginales,

$$\int dq\ F^H(q,p) \neq \psi(p) \tag{B.76}$$

$$\int dp\ F^H(q,p) \neq \psi(q) \tag{B.77}$$

contrairement à la distribution de Wigner conçue spécifiquement pour satisfaire l'égalité de ces équations.

B.4.3 Exemple: Application à l'oscillateur harmonique

Le Hamiltonien de l'oscillateur harmonique classique (B.1) affecté d'une énergie $(n+1/2)\hbar\omega$ est réécrit en fonction des dispersions de l'état cohérent (B.45) et (B.46),

$$n + \frac{1}{2} = \frac{1}{4}\frac{p^2}{\left(\Delta\hat{p}_\alpha\right)^2} + \frac{1}{4}\frac{q^2}{\left(\Delta\hat{q}_\alpha\right)^2} \quad . \tag{B.78}$$

Pour $\kappa = 1$, un cas spécial de la distribution de Husimi (B.68) est évalué à l'aide de (B.28),

$$F^H_{\kappa=1}(q,p) = \frac{1}{2\pi\hbar}\frac{1}{n!}\mathrm{e}^{-|\alpha|^2}|\alpha|^{2n} \quad . \tag{B.79}$$

Il s'agit là en fait de la distribution Q de Glauber-Sudarshan [73]. En utilisant $\alpha = \frac{1}{2}\frac{q}{\Delta\hat{q}_\alpha} + i\frac{1}{2}\frac{p}{\Delta\hat{p}_\alpha}$, on vérifie que

$$F^H_{\kappa=1}(q,p) = \frac{1}{2\pi\hbar}\frac{1}{4^n n!}\left(\frac{q^2}{(\Delta\hat{q}_\alpha)^2} + \frac{p^2}{(\Delta\hat{p}_\alpha)^2}\right)^n \cdot \exp\left[-\frac{1}{4}\left(\frac{q^2}{(\Delta\hat{q}_\alpha)^2} + \frac{p^2}{(\Delta\hat{p}_\alpha)^2}\right)\right] \quad . \tag{B.80}$$

L'expression générale de la distribution de Husimi prend plutôt la forme

$$\begin{aligned} F^H(q,p) &= \frac{1}{2\pi\hbar}\frac{2\sqrt{\kappa}}{\kappa+1}\frac{1}{2^n n!}\left(\frac{\kappa-1}{\kappa+1}\right)^n \left|H_n\left[\frac{1}{\sqrt{2}\sqrt{\kappa^2-1}}\left(\frac{q}{\Delta\hat{q}_\alpha/\kappa} - i\frac{p}{\Delta\hat{p}_\alpha}\right)\right]\right|^2 \\ &\quad \cdot \exp\left[-\frac{1}{2}\frac{1}{\kappa+1}\left(\frac{q^2}{(\Delta\hat{q}_\alpha)^2/\kappa} + \frac{p^2}{(\Delta\hat{p}_\alpha)^2}\right)\right] \end{aligned} \tag{B.81}$$

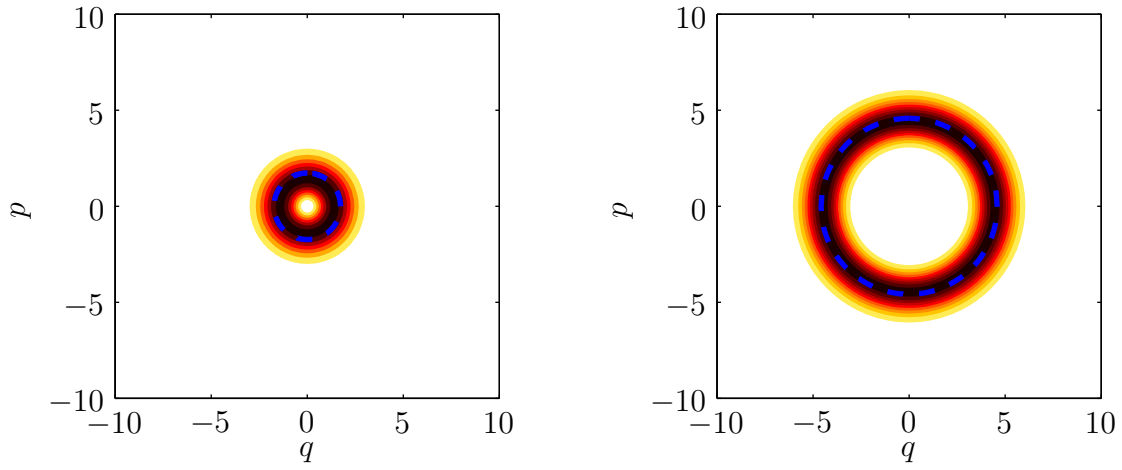
où l'intégrale 7.374.8 de [50] a été utilisée. Puisque dans la limite des grands arguments le polynôme d'Hermite devient $H_n(z) \sim (2z)^n$, on vérifie que $\lim_{\kappa\to 1} F^H(q,p)$ tend bien vers (B.80).

Des exemples d'application de la distribution de Husimi sont présentés pour $\kappa = 1$ et deux niveaux d'énergie $n = 1$ et $n = 10$ (figure B.1). La constante d'action $\hbar$ est fixée à 1 et la dispersion sur q est numériquement égale à celle sur p ($\Delta\hat{q}_\alpha = \Delta\hat{p}_\alpha = 1/\sqrt{2}$). La trajectoire classique correspondant à l'énergie du niveau n apparaît aussi pour fin de comparaison. De toute évidence, par rapport à la taille de l'orbite, la distribution quantique se resserre autour de la trajectoire classique avec l'augmentation de l'énergie. Ce résultat est évidemment attendu pour un système quantique dont l'énergie devient importante par rapport à l'espacement entre les niveaux d'énergie.

Deux autres exemples montrent l'effet du choix de κ sur la distribution calculée pour le niveau $n = 10$ (figure B.2). La valeur de $\kappa = \kappa_0$ (ou $\kappa = 1/\kappa_0$) est fixée de sorte que la dispersion de l'état comprimé sur p (ou q) soit égale à la valeur maximale atteinte en p (ou q) par la trajectoire classique,

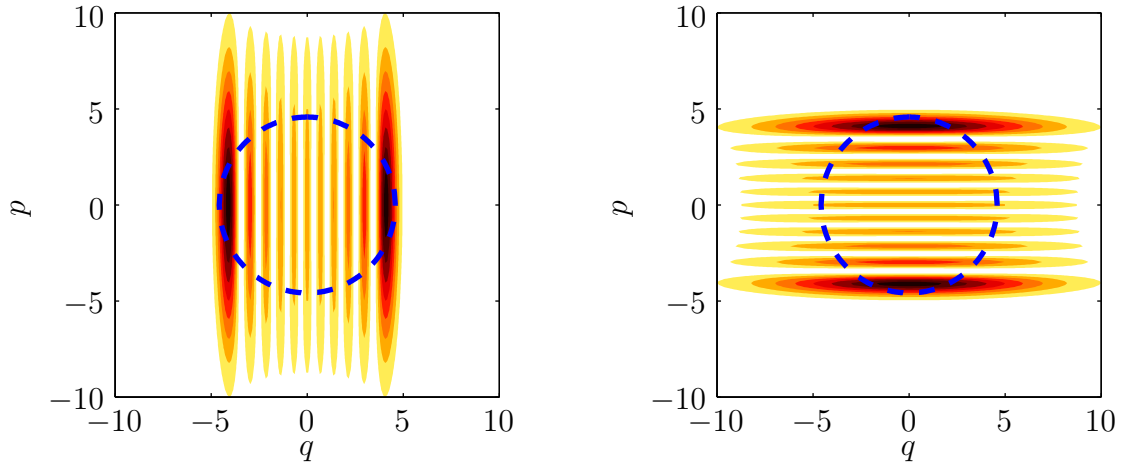
$$\Delta\hat{p}_\beta = \sqrt{\kappa_0}\Delta\hat{p}_\alpha = 2\Delta\hat{p}_\alpha\sqrt{n+1/2} \quad . \tag{B.82}$$

Pour $n = 10$ et les autres paramètres fixés aux valeurs utilisées pour produire la figure B.1, on obtient $\kappa_0 = 42$. La distribution obtenue correspond à la situation où $\Delta\hat{q}_\beta$ (ou $\Delta\hat{p}_\beta$) est numériquement petit, la limite formelle étant exprimée par (B.70) (ou (B.71)). En ce sens, une coupe à $p = 0$ de la distribution de Husimi obtenue pour la compression en q ainsi que le module carré de la fonction d'onde de l'oscillateur harmonique (B.16) sont présentés à la figure B.3.



(a) $n = 1$ (b) $n = 10$

Fig. B.1 Distribution de Husimi pour $\kappa = 1$ en amplitude linéairement croissante de jaune à noir, et trajectoire classique dans l'espace des phases pour l'oscillateur harmonique (trait bleu discontinu); $\Delta\hat{q}_\alpha = 1/\sqrt{2}$, $\hbar = 1$. (a) Niveau d'énergie $n = 1$ de l'oscillateur quantique. (b) Niveau d'énergie $n = 10$ de l'oscillateur quantique.



(a) $\kappa_0 = 42$ (b) $\kappa_0 = 1/42$

Fig. B.2 Distribution de Husimi (B.81) pour le niveau $n = 10$ de l'oscillateur harmonique. (a) Distribution comprimée sur q ($\Delta\hat{q}_\beta = 1/\sqrt{42} \cdot \Delta\hat{q}_\alpha = 1/\sqrt{84} \approx 0.11$, $\Delta\hat{p}_\beta \approx 4.58$). (b) Distribution comprimée sur p ($\Delta\hat{p}_\beta = 1/\sqrt{42} \cdot \Delta\hat{p}_\alpha = 1/\sqrt{84} \approx 0.11$, $\Delta\hat{q}_\beta \approx 4.58$).

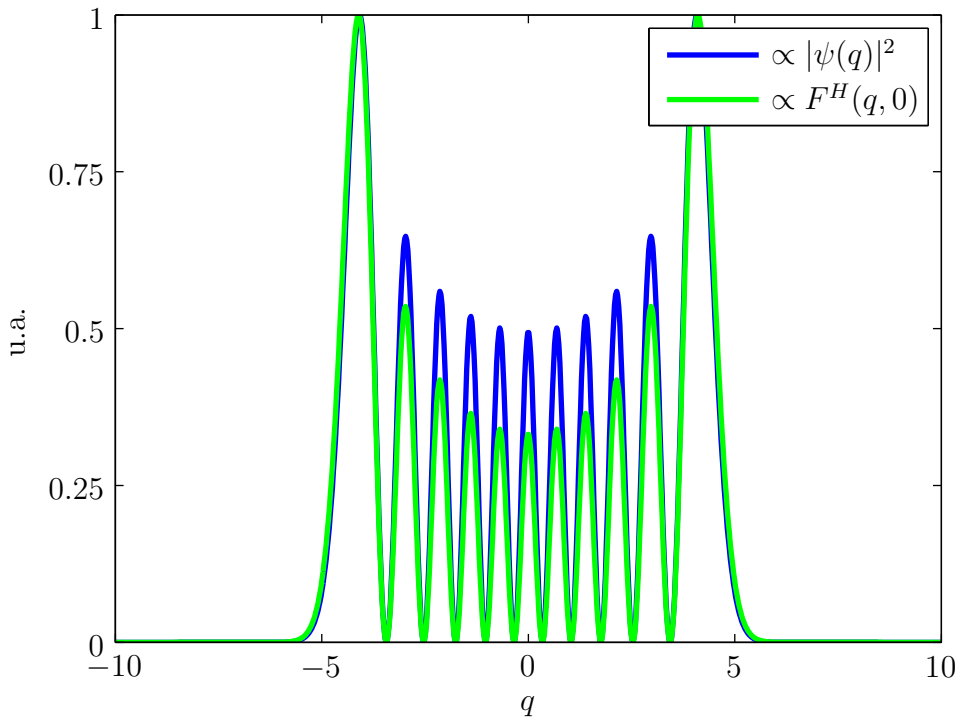


Fig. B.3 Coupe à $p = 0$ de la distribution de Husimi présentée à la figure B.2(a) et fonction d'onde $|\psi_{10}(q)|^2$ de l'oscillateur harmonique. Les courbes sont normalisées à leur valeur maximale respective. Une coupe semblable peut être obtenue pour la distribution en p.

Annexe C

Calcul numérique de la matrice S

Cette annexe explicite la méthode numérique permettant le calcul de la matrice de diffusion **S** présentée au chapitre 2. L'approche préconisée consiste en une séparation de la section d'une cavité diélectrique en une série de N anneaux concentriques minces sur lesquels l'indice de réfraction est supposé dépendre uniquement de la position angulaire. La séquence d'anneaux est limitée à l'intérieur par un disque d'indice de réfraction constant, et à l'extérieur, par un domaine d'indice constant s'étendant potentiellement jusqu'à l'infini. La continuité de la fonction d'onde est ensuite établie en connectant les anneaux successifs à leur frontière commune. Le domaine central étant un disque d'indice constant, plusieurs simplifications importantes peuvent être obtenues. On extrait ainsi un algorithme de mise à jour d'une simple matrice $\mathcal{S}_{22}^{0,N+1}$ permettant ultimement le calcul de **S**.

C.1 Développement de l'équation angulaire locale sur une base de Fourier

On cherche à solutionner le problème aux limites périodiques

$$\left\{ \frac{d^2}{d\phi^2} + \left[n^2(r_j, \phi) k^2 r_j^2 + \xi_\mu^j \right] \right\} \Phi_\mu^j(\phi) = 0 \quad , \; \Phi_\mu^j(\phi + 2\pi) = \Phi_\mu^j(\phi) \quad . \tag{C.1}$$

Une solution permettant de satisfaire automatiquement la condition périodique consiste en un développement en série de Fourier,

$$\Phi_\mu^j(\phi) = \frac{1}{2\pi} \sum_{m=-\infty}^{+\infty} c_{m\mu}^j \mathrm{e}^{im\phi} \quad . \tag{C.2}$$

Le remplacement de cette solution dans l'équation différentielle et la projection sur un élément de la base de Fourier $\mathrm{e}^{-im'\phi}$ permet d'obtenir

$$\sum_m \left\{ -m^2\delta_{mm'} + \xi_\mu^j \delta_{mm'} + k^2 r_j^2 \frac{1}{2\pi} \int_0^{2\pi} d\phi \; n^2(r_j,\phi) \mathrm{e}^{i(m-m')\phi} \right\} c_{m\mu}^j = 0 \qquad \text{(C.3)}$$

soit l'expression d'un système aux valeurs propres

$$\mathbf{L}^j \cdot \mathbf{c}_\mu^j = \xi_\mu^j \mathbf{c}_\mu^j \qquad \text{(C.4)}$$

avec

$$\mathbf{L}_{mm'}^j = m^2\delta_{mm} - k^2 r_j^2 \frac{1}{2\pi} \int_0^{2\pi} d\phi \; n^2(r_j,\phi) \mathrm{e}^{i(m-m')\phi} \quad . \qquad \text{(C.5)}$$

Puisque pour k et $n(r_j,\phi)$ réels, la matrice $\mathbf{L}$ est hermitique, la base de vecteurs $\{\mathbf{c}_\mu^j\}$ est orthogonale et normalisable, et les valeurs propres $\{\xi_\mu^j\}$ sont réelles. Sous ces conditions, les fonctions $\{\Phi_\mu^j(\phi)\}$ sont alors déclarées orthonormées.

Selon (C.5), la matrice $\mathbf{L}$ est composée d'une matrice diagonale réelle et d'une seconde matrice dite de *Toeplitz* dont toutes les diagonales sont constantes. L'application numérique demandant la troncature de $\mathbf{L}^j$ en une matrice carrée $(2M+1)\times(2M+1)$, on parvient à construire cette matrice par la permutation d'un simple vecteur de taille $4M+1$ contenant les termes de la série de Fourier

$$\tilde{n}_\nu^j = \frac{1}{2\pi} \int_0^{2\pi} d\phi \; n^2(r_j,\phi) \mathrm{e}^{i\nu\phi} \quad . \qquad \text{(C.6)}$$

Puisque les fréquences négatives $\nu < 0$ de la série de Fourier s'obtiennent par la conjugaison complexe des fréquences positives, un gain supplémentaire en nombre de calculs peut être réalisé. Si $\mathbf{M}_{mm'} = {m'}^2\delta_{mm'}$, alors pour les éléments de la matrice $\mathbf{L}^j$ arrangés sur les colonnes de $m' > 0$ à gauche vers $m' < 0$ à droite et les lignes de $m > 0$ en haut vers $m < 0$ en bas, on a

$$\mathbf{L}^j = \mathbf{M} - k^2 r_j^2 \begin{pmatrix} \ddots & \ddots & & & & \\ \ddots & \tilde{n}_0^j & \tilde{n}_1^j & \tilde{n}_2^j & \tilde{n}_3^j & \\ & \tilde{n}_1^{j*} & \tilde{n}_0^j & \tilde{n}_1^j & \tilde{n}_2^j & \\ & \tilde{n}_2^{j*} & \tilde{n}_1^{j*} & \tilde{n}_0^j & \tilde{n}_1^j & \\ & \tilde{n}_3^{j*} & \tilde{n}_2^{j*} & \tilde{n}_1^{j*} & \tilde{n}_0^j & \ddots \\ & & & & \ddots & \ddots \end{pmatrix} \quad . \qquad \text{(C.7)}$$

Lorsque l'intégrale (C.6) ne possède par de solution analytique, l'algorithme de transformée de Fourier rapide (*Fast Fourier Transform*, FFT) permet d'obtenir simultanément l'ensemble des fréquences nécessaires à la composition de $\mathbf{L}^j$ par un échantillonnage de l'indice de réfraction.

Les termes de la diagonale de $\mathbf{L}^j$ croissent comme le carré de l'ordre vers ses extrémités. Étant donnée la forme de $\mathbf{L}$, les termes diagonaux prennent éventuellement des valeurs bien supérieures aux termes non diagonaux, isolant numériquement la diagonale du "coeur" de la matrice. Suivant le théorème de Parseval, le module carré du plus grand terme de la série de Fourier $\tilde{n}_\nu^j$ est égale ou inférieur à l'intégrale sur le cercle du module carré de l'indice de réfraction. Ce dernier est évidemment lui-même inférieur au carré du maximum sur ϕ de l'indice de réfraction carré,

$$\max_\nu\{|\tilde{n}_\nu^j|^2\} \leq \frac{1}{2\pi}\int_0^{2\pi} d\phi \ \left|n^2(r_j,\phi)\right|^2 \leq \left[\max\left\{n^2(r_j,\phi)\right\}_\phi\right]^2 \quad . \tag{C.8}$$

En considérant la limite $\max\{n^2(r_j,\phi)\}_\phi k^2 r_j^2$ définissant la plus grande fréquence efficace du système (*i.e.* sa largeur de bande efficace au-delà de laquelle la diagonale devient dominante), un choix de troncature de $\mathbf{L}^j$ satisfaisant le critère de Nyquist [107] est $M = 2\sqrt{\max\{n^2(r_j,\phi)\}_\phi} k r_j$.

C.2 Définition des matrices intermédiaires

Pour ce qui suit, on utilisera la notation opérationnelle des fonctions $\Phi_\mu^j(\phi) = \langle\ \phi\ |\ \Phi_\mu^j\ \rangle$ pour simplifier l'écriture des intégrales de recouvrement des fonctions. Notez que les matrices $\mathcal{S}$ utilisées ici sont différentes des matrices $\mathbf{S}$ du chapitre 2: ces dernières relient effectivement les coefficients $\mathbf{a}$ et $\mathbf{b}$ d'une couche à ceux de la couche suivante, alors que les matrices $\mathcal{S}$ sont des versions modifiées des $\mathbf{S}$ où des facteurs dépendant de la position des interfaces pour la couche inférieure sont retirés et passés à la couche supérieure. Les matrices $\mathcal{S}$ sur les anneaux intermédiaires présentent alors des puissances du ratio $(r_j - \epsilon)/(r_j + \epsilon)$ comme seule dépendance à la position des interfaces.

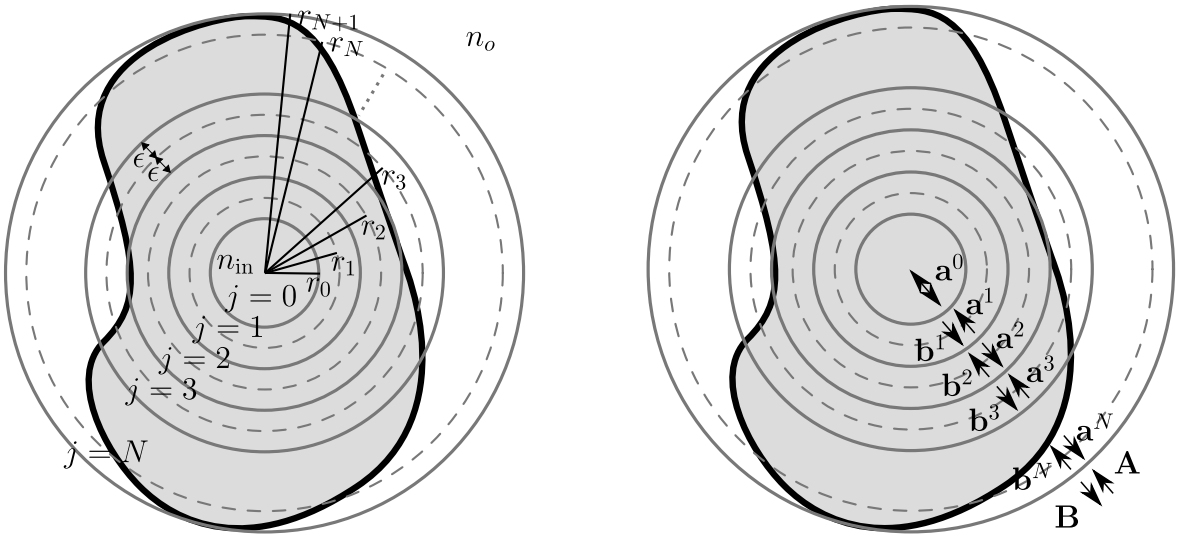
La notation primée $'$ indique la dérivée par rapport à l'argument de la fonction sur laquelle elle s'applique. Les rayons sont ordonnées suivant $r_j < r_{j+1}$. Toutes les matrices sont carrées.

Une représentation schématique de l'approche par séparation en anneaux concentriques apparaît à la figure C.1.

C.2.1 Domaine intérieur et couplage au premier anneau ($j = 0$)

La fonction d'onde à l'intérieur du domaine circulaire de rayon $r = r_0$ et d'indice de réfraction n_{in} constant est

$$\left|\ \psi^0(r)\ \right\rangle = \sum_m a_m^0 J_m(n_{\text{in}} kr)\left|\ \Phi_m^0\ \right\rangle \tag{C.9}$$



(a) Domaines concentriques (b) Coefficients de développement

Fig. C.1 (a) Représentation schématique de la séparation de la surface de la cavité en domaines annulaires. L'indice de réfraction constant à l'intérieur du disque intérieur est $n_{\rm in}$ et à l'extérieur, n_o. Notez que le rayon intérieur r_0 est situé à ϵ (et non 2ϵ) du rayon r_1, tout comme le rayon $R_{\max}$ par rapport à r_N. (b) Coefficients de développement $\mathbf{a}^j$ et $\mathbf{b}^j$ sur des couches successives.

avec $\Phi^0_m(\phi) = \left\langle\ \phi\ \right|\ \Phi^0_m\ \left\rangle = \mathrm{e}^{im\phi}\right.$.

La fonction d'onde à l'intérieur du permier anneau dont l'indice de réfraction est approximativement $n(r_1,\phi)$ s'écrit quant à elle

$$\left|\ \psi^1(r)\ \right\rangle = \sum_\mu \left[a^1_\mu\ \rho_1^{+\sqrt{\xi^1_\mu}} + b^1_\mu\, \rho_1^{-\sqrt{\xi^1_\mu}}\right] \left|\ \Phi^1_\mu\ \right\rangle \tag{C.10}$$

où $\rho_1 = r/r_1$ est la coordonnée radiale normalisée au rayon médian de l'anneau, et $\{\xi^1_\mu\}$ et $\{\Phi^1_\mu(\phi)\}$ sont obtenus par solution du système aux valeurs propres (C.5).

Les matrices suivantes sont formées pour le domaine intérieur

$$\mathbf{J}_{mm'} = J_m(n_{\rm in}kr_0)\delta_{mm'} \tag{C.11}$$

$$\mathbf{DJ}_{mm'} = J'_m(n_{\rm in}kr_0)\delta_{mm'} \tag{C.12}$$

et pour le domaine annulaire,

$$\mathbf{\Lambda}^1_{\mu\mu'} = \sqrt{\xi^1_\mu}\,\delta_{\mu\mu'} \quad . \tag{C.13}$$

Les termes de couplage entre les domaines sont représentés par la matrice

$$\mathbf{U}^{0,1}_{\mu\mu'} = \left\langle\ \Phi^0_\mu\ \right|\ \Phi^1_{\mu'}\ \left\rangle \quad . \right. \tag{C.14}$$

On définit deux matrices intermédiaires

$$\mathbf{F}^{0,1} = +\left[\mathbf{U}^{0,1}\mathbf{\Lambda}^{1}\mathbf{U}^{0,1\dagger} - \mathbf{D}\mathbf{J}\,\mathbf{J}^{-1}\right] \tag{C.15}$$

$$\mathbf{G}^{0,1} = -\left[\mathbf{U}^{0,1}\mathbf{\Lambda}^{1}\mathbf{U}^{0,1\dagger} + \mathbf{D}\mathbf{J}\,\mathbf{J}^{-1}\right] \quad . \tag{C.16}$$

La matrice $\mathcal{S}_{22}^{0}$ s'écrit donc

$$\mathcal{S}_{22}^{0} = -\mathbf{U}^{0,1}\left\{\mathbf{F}^{0,1}\right\}^{-1}\mathbf{G}^{0,1}\mathbf{U}^{0,1\dagger} \tag{C.17}$$

et on définit

$$\mathcal{S}_{22}^{0,1} = \mathcal{S}_{22}^{0} \quad . \tag{C.18}$$

C.2.2 Anneaux intermédiaires ($j = 1, 2, 3, \ldots N-1$)

La fonction d'onde à l'intérieur du domaine annulaire de rayon médian $r = r_j$ et de largeur 2ϵ, et dont l'indice de réfraction est approximativement $n(r_j, \phi)$ est

$$\mid \psi^{j}(r) \rangle = \sum_{\mu}\left[a_{\mu}^{j}\,\rho_{j}^{+\sqrt{\xi_{\mu}^{j}}} + b_{\mu}^{j}\,\rho_{j}^{-\sqrt{\xi_{\mu}^{j}}}\right] \mid \Phi_{\mu}^{j} \rangle \tag{C.19}$$

alors que la fonction d'onde à l'intérieur de l'anneau voisin de rayon médian $r = r_{j+1}$ et de largeur 2ϵ, et dont l'indice de réfraction est approximativement $n(r_{j+1}, \phi)$ est

$$\mid \psi^{j+1}(r) \rangle = \sum_{\mu}\left[b_{\mu}^{j+1}\rho_{j+1}^{+\sqrt{\xi_{\mu}^{j+1}}} + a_{\mu}^{j+1}\rho_{j+1}^{-\sqrt{\xi_{\mu}^{j+1}}}\right] \mid \Phi_{\mu}^{j+1} \rangle \tag{C.20}$$

où $\rho_j = r/r_j$ et $\rho_{j+1} = r/r_{j+1}$ sont les coordonnées radiales normalisées au rayon médian des anneaux, et $\{\xi_{\mu}^{j}\}$ et $\{\Phi_{\mu}^{j}(\phi)\}$ ainsi que $\{\xi_{\mu}^{j+1}\}$ et $\{\Phi_{\mu}^{j+1}(\phi)\}$ sont obtenus par solution du système aux valeurs propres (C.5) dans leur domaine d'application respectif [1].

La matrice suivante est formée pour le domaine annulaire intérieur

$$\mathbf{\Lambda}_{\mu\mu'}^{j} = \sqrt{\xi_{\mu}^{j}}\,\delta_{\mu\mu'} \tag{C.21}$$

et pour le domaine annulaire extérieur,

$$\mathbf{\Lambda}_{\mu\mu'}^{j+1} = \sqrt{\xi_{\mu}^{j+1}}\,\delta_{\mu\mu'} \quad . \tag{C.22}$$

Les termes de couplage entre les domaines sont représentés par la matrice

$$\mathbf{U}_{\mu\mu'}^{j,j+1} = \langle\ \Phi_{\mu}^{j} \mid \Phi_{\mu'}^{j+1}\ \rangle \quad . \tag{C.23}$$

[1] On notera que, selon cette convention d'alternance du caractère des coefficients $\{a_{\mu}^{j}\}$ et $\{b_{\mu}^{j}\}$, N doit être un nombre *impair*.

On définit deux matrices intermédiaires

$$\mathbf{F}^{j,j+1} = \mathbf{U}^{j,j+1}\mathbf{\Lambda}^{j+1}\mathbf{U}^{j,j+1\dagger} + \Lambda^j \tag{C.24}$$

$$\mathbf{G}^{j,j+1} = -\mathbf{U}^{j,j+1}\mathbf{\Lambda}^{j+1}\mathbf{U}^{j,j+1\dagger} + \Lambda^j \tag{C.25}$$

ce qui permet d'écrire succintement les matrices de connexion suivantes

$$\mathcal{S}_{11}^{j+1} = -\mathbb{1} + 2\left\{\mathbf{F}^{j,j+1}\right\}^{-1}\mathbf{\Lambda}^j \tag{C.26}$$

$$\mathcal{S}_{12}^{j+1} = \left[\mathbb{1} - \left\{\mathbf{F}^{j,j+1}\right\}^{-1}\mathbf{G}^{j,j+1}\right]\mathbf{U}^{j,j+1} \tag{C.27}$$

$$\mathcal{S}_{21}^{j+1} = 2\mathbf{U}^{j,j+1\dagger}\left\{\mathbf{F}^{j,j+1}\right\}^{-1}\mathbf{\Lambda}^j \tag{C.28}$$

$$\mathcal{S}_{22}^{j+1} = -\mathbf{U}^{j,j+1\dagger}\left\{\mathbf{F}^{j,j+1}\right\}^{-1}\mathbf{G}^{j,j+1}\mathbf{U}^{j,j+1} \quad . \tag{C.29}$$

Finalement, on calcule la matrice

$$\mathbf{K}^{j,j+1} = \left[\left(\frac{r_j-\epsilon}{r_j+\epsilon}\right)^{\mathbf{\Lambda}^j} - \mathcal{S}_{11}^{j+1}\left(\frac{r_j+\epsilon}{r_j-\epsilon}\right)^{\mathbf{\Lambda}^j}\mathcal{S}_{22}^{0,j}\right]^{-1} \tag{C.30}$$

qui permet d'évaluer la matrice de transfert $\mathcal{S}_{22}^{0,j+1}$,

$$\mathcal{S}_{22}^{0,j+1} = \left[\mathcal{S}_{21}^{j+1}\left(\frac{r_j+\epsilon}{r_j-\epsilon}\right)^{\mathbf{\Lambda}^j}\right]\mathcal{S}_{22}^{0,j}\left[\mathbf{K}^{j,j+1}\mathcal{S}_{12}^{j+1}\right] + \mathcal{S}_{22}^{j+1} \quad . \tag{C.31}$$

Cette dernière matrice est identifiée au chapitre 2 comme étant celle qui permettera ultimement le calcul de la matrice de diffusion $\mathbf{S}$.

C.2.3 Dernier anneau et couplage au domaine extérieur ($j = N$)

La fonction d'onde à l'intérieur du dernier anneau de rayon médian r_N et de largeur 2ϵ dont l'indice de réfraction est approximativement $n(r_N, \phi)$ s'écrit

$$\mid \psi^N(r) \rangle = \sum_\mu \left[a_\mu^N \rho_N^{+\sqrt{\xi_\mu^N}} + b_\mu^N \rho_N^{-\sqrt{\xi_\mu^N}}\right] \mid \Phi_\mu^N \rangle \tag{C.32}$$

où $\rho_N = r/r_N$ est la coordonnée radiale normalisée au rayon médian de l'anneau, et $\{\xi_\mu^N\}$ et $\{\Phi_\mu^N(\phi)\}$ sont obtenus par solution du système aux valeurs propres (C.5).

La fonction d'onde à l'extérieur du domaine circulaire de rayon $r_{N+1} = r_N + \epsilon$ et d'indice de réfraction n_o constant est

$$\mid \psi(r) \rangle = \sum_m \left[A_m H_m^{(2)}(n_o k r) + B_m H_m^{(1)}(n_o k r)\right] \mid \Phi_m^{N+1} \rangle \tag{C.33}$$

avec $\Phi_m^{N+1}(\phi) = \left\langle\ \phi\ \middle|\ \Phi_m^{N+1}\ \right\rangle = \mathrm{e}^{im\phi}$.

La matrice suivante est formée pour le domaine annulaire

$$\mathbf{\Lambda}^N_{\mu\mu'} \ = \ \sqrt{\xi_\mu^N}\,\delta_{\mu\mu'} \quad . \tag{C.34}$$

et pour le domaine extérieur

$$\mathbf{H^1}_{mm'} \ = \ H_m^{(1)}(n_o k r_{N+1})\delta_{mm'} \tag{C.35}$$
$$\mathbf{DH^1}_{mm'} \ = \ H_m^{(1)'}(n_o k r_{N+1})\delta_{mm'} \tag{C.36}$$
$$\mathbf{H^2}_{mm'} \ = \ H_m^{(2)}(n_o k r_{N+1})\delta_{mm'} \tag{C.37}$$
$$\mathbf{DH^2}_{mm'} \ = \ H_m^{(2)'}(n_o k r_{N+1})\delta_{mm'} \quad . \tag{C.38}$$

Les termes de couplage entre les domaines sont représentés par la matrice

$$\mathbf{U}^{N,N+1}_{\mu\mu'} = \left\langle\ \Phi_\mu^N\ \middle|\ \Phi_{\mu'}^{N+1}\ \right\rangle \quad . \tag{C.39}$$

On définit comme précédemment deux matrices intermédiaires

$$\mathbf{F}^{N,N+1} \ = \ \mathbf{U}^{N,N+1}\mathbf{DH^1}\left\{\mathbf{H^1}\right\}^{-1}\mathbf{U}^{N,N+1\dagger} + \mathbf{\Lambda}^N \tag{C.40}$$
$$\mathbf{G}^{N,N+1} \ = \ \mathbf{U}^{N,N+1}\mathbf{DH^2}\left\{\mathbf{H^2}\right\}^{-1}\mathbf{U}^{N,N+1\dagger} + \mathbf{\Lambda}^N \tag{C.41}$$

ce qui permet d'écrire succintement les matrices suivantes

$$\mathcal{S}_{11}^{N+1} \ = \ -\mathbb{1} + 2\left\{\mathbf{F}^{N,N+1}\right\}^{-1}\mathbf{\Lambda}^N \tag{C.42}$$
$$\mathcal{S}_{12}^{N+1} \ = \ \left[\mathbb{1} - \left\{\mathbf{F}^{N,N+1}\right\}^{-1}\mathbf{G}^{N,N+1}\right]\mathbf{U}^{N,N+1} \tag{C.43}$$
$$\mathcal{S}_{21}^{N+1} \ = \ 2\mathbf{U}^{N,N+1\dagger}\left\{\mathbf{F}^{N,N+1}\right\}^{-1}\mathbf{\Lambda}^N \tag{C.44}$$
$$\mathcal{S}_{22}^{N+1} \ = \ -\mathbf{U}^{N,N+1\dagger}\left\{\mathbf{F}^{N,N+1}\right\}^{-1}\mathbf{G}^{N,N+1}\mathbf{U}^{N,N+1} \quad . \tag{C.45}$$

Finalement, on calcule la matrice

$$\mathbf{K}^{N,N+1} = \left[\left(\frac{r_N-\epsilon}{r_N+\epsilon}\right)^{\mathbf{\Lambda}^N} - \mathcal{S}_{11}^{N+1}\left(\frac{r_N+\epsilon}{r_N-\epsilon}\right)^{\mathbf{\Lambda}^N}\mathcal{S}_{22}^{0,N}\right]^{-1} \tag{C.46}$$

qui permet d'évaluer $\mathcal{S}_{22}^{0,N+1}$,

$$\mathcal{S}_{22}^{0,N+1} = \left[\mathcal{S}_{21}^{N+1}\left(\frac{r_N+\epsilon}{r_N-\epsilon}\right)^{\mathbf{\Lambda}^N}\right]\mathcal{S}_{22}^{0,N}\left[\mathbf{K}^{N,N+1}\mathcal{S}_{12}^{N+1}\right] + \mathcal{S}_{22}^{N+1} \quad . \tag{C.47}$$

On obtient finalement la matrice de diffusion numérique, $\bar{\mathbf{S}}$, comme

$$\bar{\mathbf{S}} \equiv \mathbf{S}_{22}^{0,N+1} = \left\{\mathbf{H^1}\right\}^{-1}\mathcal{S}_{22}^{0,N+1}\mathbf{H^2} \quad . \tag{C.48}$$

Annexe D

Forme analytique de la matrice S en cavité annulaire

Dans cette annexe, on obtiendra la forme analytique de la matrice de diffusion $\mathbf{S}$ pour un système composé d'une cavité homogène dans laquelle on a introduit une inclusion. Il s'agit de la *cavité annulaire*. Pour ce faire, nous aurons besoin d'un certain nombre d'outils mathématiques qui seront présentés en premier lieu. La matrice $\mathbf{S}$ s'obtient en plusieurs étapes dont les principales sont: construction de la matrice de diffusion $\tilde{\mathbf{S}}_c$ due à la présence de l'inclusion dans un système de coordonnées centré à l'inclusion, obtention d'une matrice de déplacement $\mathbf{T}$ permettant l'écriture de la matrice $\mathbf{S}_c = \mathbf{T}\,\tilde{\mathbf{S}}_c\,\mathbf{T}^\dagger$ propre au référentiel centré à l'origine de la cavité, et finalement combinaison des éléments développés pour obtenir la matrice $\mathbf{S}$ et la matrice des délais $\mathbf{Q}$ du système composé.

Deux identités tirées de [1] seront centrales aux développements analytiques, nous les rappelons ici.

AS (9.1.79): **théorème d'addition / déplacement de Graf**

$$Z_\nu(w)\,\mathrm{e}^{i\nu\chi} = \sum_{k=-\infty}^{\infty} Z_{\nu+k}(u)J_k(v)\mathrm{e}^{ik\alpha} \qquad (v<u) \tag{D.1}$$

où $Z_\nu = \{H_\nu^{(1,2)}, J_\nu, Y_\nu\}$, $w^2 = u^2 + v^2 - 2uv\cos\alpha$, i.e. que $\mathbf{u}$, $\mathbf{v}$ et $\mathbf{w}$ forment les côtés d'un triangle avec $\mathbf{u} = \mathbf{v} + \mathbf{w}$, χ est l'angle opposé au côté v et α est l'angle opposé à w (voir Eqs. (A.14)-(A.15) et schéma correspondant). On note que la restriction $v < u$ ne s'applique pas si $Z_\nu = J_\nu$ et ν est un entier ou zéro.

AS (9.1.75): **théorème d'addition de Neumann**

$$Z_\nu(u \pm v) = \sum_{k=-\infty}^{\infty} Z_{\nu\mp k}(u)J_k(v) \qquad (v<u). \tag{D.2}$$

Ici aussi la restriction $v < u$ n'est pas nécessaire si $Z_\nu = J_\nu$ et ν est un entier ou zéro.

D.1 Matrice de déplacement T et effet du déplacement de l'origine sur la matrice de diffusion

On établit dans ce qui suit l'expression des transformations nécessaires pour exprimer nos fonctions d'onde dans 2 référentiels différents, dont les origines O et O' sont séparées par un vecteur $\mathbf{d}$, *i.e.* $\mathbf{r} = \mathbf{r}' + \mathbf{d}$.

D.1.1 Cas $r > d$

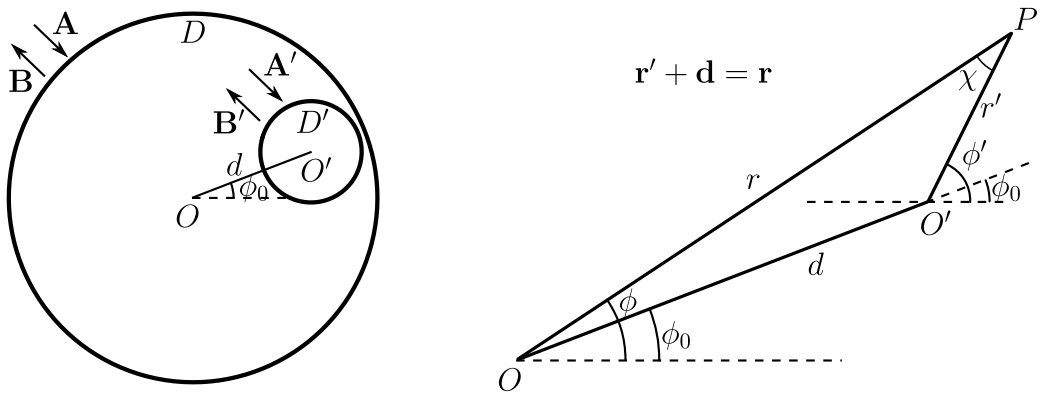


Fig. D.1 (a) L'objet de cette section est de transformer une fonction d'onde décrite par rapport à une origine en O' et connue à l'extérieur d'un domaine circulaire D', en une nouvelle forme possédant des coordonnées centrées sur l'origine O. On cherchera donc à écrire les coefficients $\mathbf{A}$ et $\mathbf{B}$ des ondes partielles valides à l'extérieur d'un disque D en fonction des coefficients $\mathbf{A}'$ et $\mathbf{B}'$ autour du domaine D'. (b) Construction géométrique de la translation pour $r > d$.

Considérons une fonction d'onde à l'extérieur d'un domaine circulaire D', Fig. D.1(a), et exprimée sur les coordonnées (r', ϕ')

$$\psi'(r', \phi') = \sum_m \left[A'_m H_m^{(2)}(nkr') + B'_m H_m^{(1)}(nkr')\right] \mathrm{e}^{im\phi'} \quad , \ (r', \phi') \notin D' \quad . \tag{D.3}$$

On change ensuite le référentiel de cette onde pour le transporter vers les coordonnées (r, ϕ) sur une distance d en gardant $r > d$ (Fig. D.1(b)). La fonction de Hankel s'écrit

alors à l'aide de l'identité de Graf (D.1)

$$\begin{aligned} H_m^{(1,2)}(nkr')\mathrm{e}^{im\phi'} &= \mathrm{e}^{im\phi}\left[H_m^{(1,2)}(nkr')\mathrm{e}^{im\chi}\right] \\ &= \mathrm{e}^{im\phi}\sum_\nu H_{m+\nu}^{(1,2)}(nkr)J_\nu(nkd)\mathrm{e}^{i\nu(\phi-\phi_0)} \quad , \ r>d \\ &= \sum_\nu \left[\mathrm{e}^{-i(\nu-m)\phi_0}J_{\nu-m}(nkd)\right] H_\nu^{(1,2)}(nkr)\,\mathrm{e}^{i\nu\phi} \quad . \end{aligned} \tag{D.4}$$

La fonction d'onde s'écrit pour $(r,\phi)\notin D'$

$$\begin{aligned} \psi(r,\phi) &= \sum_\nu \left\{ \left[\sum_m \mathrm{e}^{-i(\nu-m)\phi_0}J_{\nu-m}(nkd)A'_m\right] H_\nu^{(2)}(nkr) \right. \\ &\qquad \left. + \left[\sum_m \mathrm{e}^{-i(\nu-m)\phi_0}J_{\nu-m}(nkd)B'_m\right] H_\nu^{(1)}(nkr)\right\}\mathrm{e}^{i\nu\phi} \quad , \end{aligned} \tag{D.5}$$

$$\equiv \sum_\nu \left[A_\nu H_\nu^{(2)}(nkr)+B_\nu H_\nu^{(1)}(nkr)\right]\mathrm{e}^{i\nu\phi}. \tag{D.6}$$

Posant

$$\{\mathbf{J}(nkd)\}_{\nu m}\equiv J_{\nu-m}(nkd) \qquad , \qquad \{\mathbf{R}(\phi_0)\}_{\nu\nu'}\equiv \mathrm{e}^{i\nu\phi_0}\delta_{\nu\nu'}, \tag{D.7}$$

on obtient une *matrice de déplacement* prenant la forme

$$\mathbf{T}(nkd,\phi_0)\equiv \mathbf{R}^\dagger(\phi_0)\,\mathbf{J}(nkd)\,\mathbf{R}(\phi_0). \tag{D.8}$$

Pour un argument réel[1], la matrice $\mathbf{J}(nkd)$ est réelle et orthogonale, $\mathbf{J}(nkd)\,\mathbf{J}(nkd)^T=\mathbb{1}$, ce qui implique que $\mathbf{T}(nkd,\phi_0)$ est unitaire. Ce résultat est déduit directement du théorème d'addition de Neumann (D.2) et du résultat $J_{a-b}(0)=\delta_{ab}$. En vue de l'application que nous ferons de la matrice $\mathbf{T}(nkd,\phi_0)$, on remarque que si $\mathbf{B}'$ et $\mathbf{A}'$ sont reliées par

$$\mathbf{B}'=\mathbf{S}'\mathbf{A}' \tag{D.9}$$

alors

$$\mathbf{B}=\mathbf{T}(nkd,\phi_0)\,\mathbf{S}'\,\mathbf{T}^\dagger(nkd,\phi_0)\mathbf{A}\equiv\mathbf{S}\mathbf{A}. \tag{D.10}$$

D.1.2 Cas $r<d$

On répète les opérations précédentes, mais cette fois le déplacement des origines est tel que $r<d$ (Fig. D.2). La fonction de Hankel s'écrit maintenant suivant (D.1)

$$\begin{aligned} H_m^{(1,2)}(nkr')\mathrm{e}^{im\phi'} &= \mathrm{e}^{im(\pi+\phi_0)}(-1)^m\left[H_{-m}^{(1,2)}(nkr')\mathrm{e}^{-im\chi}\right] \\ &= \mathrm{e}^{im\phi_0}\sum_\nu H_{-m+\nu}^{(1)}(nkd)J_\nu(nkr)\mathrm{e}^{i\nu(\phi-\phi_0)} \quad , \ r<d \\ &= \sum_\nu \left[\mathrm{e}^{i(m-\nu)\phi_0}H_{\nu-m}^{(1)}(nkd)\right]J_\nu(nkr)\mathrm{e}^{i\nu\phi} \quad . \end{aligned} \tag{D.11}$$

[1]Dans le cas général où l'argument pourrait être complexe, il faudra distinguer entre l'opération de transposée simple $\mathbf{M}^T$ d'une matrice $\mathbf{M}$ de l'opération transposée complexe $\mathbf{M}^\dagger$. Nos résultats s'adressent aux cas où les arguments sont réels.

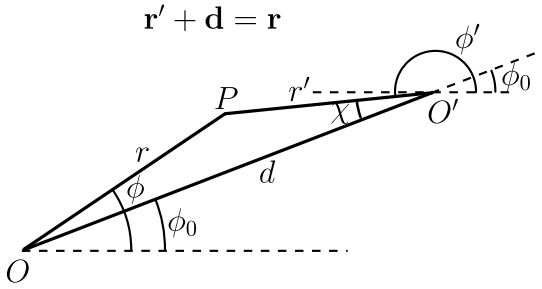


Fig. D.2 Construction géométrique de la translation pour $r < d$.

La fonction d'onde s'écrit alors pour (r, ϕ)

$$\begin{aligned} \psi(r,\phi) &= \sum_{\nu} \left\{ \sum_{m} \mathrm{e}^{i(m-\nu)\phi_0} \left[H^{(2)}_{\nu-m}(nkd) A'_m + H^{(1)}_{\nu-m}(nkd) B'_m \right] \right\} J_\nu(nkr) \mathrm{e}^{i\nu\phi}, \\ &\equiv \sum_{\nu} A_\nu J_\nu(nkr) \mathrm{e}^{i\nu\phi}. \end{aligned} \tag{D.12}$$

Il n'existe pas de matrice de déplacement comme au cas précédent. On écrit cependant de façon plus synthétique une *matrice de transformation* $\tau(nkd, \phi_0)$

$$\tau(nkd, \phi_0) \equiv \left[\mathbf{R}^\dagger(\phi_0) \mathbf{H}^\dagger(nkd) \mathbf{R}(\phi_0) + \mathbf{R}^\dagger(\phi_0) \mathbf{H}(nkd) \mathbf{R}(\phi_0) \mathbf{S}' \right] \tag{D.13}$$

avec

$$\{\mathbf{H}(nkd)\}_{\nu m} \equiv H^{(1)}_{\nu-m}(nkd) \qquad , \qquad \{\mathbf{R}(\phi_0)\}_{\nu\nu'} \equiv \mathrm{e}^{i\nu\phi_0} \delta_{\nu\nu'} \tag{D.14}$$

de sorte que

$$\mathbf{A} \equiv \tau(nkd, \phi_0)\, \mathbf{A}'. \tag{D.15}$$

Nous avons considérer ce cas par souci de généralité, mais il n'apparaîtra pas dans la construction des matrices de diffusion.

D.2 Effet du déplacement de l'origine sur la matrice des délais d'une cavité

Le résultat (D.10) présente l'effet de la translation sur la matrice de diffusion: pour la matrice de diffusion connue $\mathbf{S}'$ obtenue pour une cavité centrée à l'origine O' (Fig. D.1), on exprime la matrice de diffusion $\mathbf{S}$ sur un domaine circulaire comprenant la cavité

diélectrique, mais dont l'origine O est différente de O', en termes d'une transformation de similarité sur $\mathbf{S}'$. Puisqu'une quantité d'intérêt menant à la caractérisation des modes d'une cavité est la matrice hermitique des délais,

$$\mathbf{Q} = -i\mathbf{S}^\dagger \frac{\partial \mathbf{S}}{\partial k} = +i\left(\frac{\partial \mathbf{S}^\dagger}{\partial k}\right)\mathbf{S} = \mathbf{Q}^\dagger, \tag{D.16}$$

relevant elle-même de la matrice de diffusion, il est légitime de s'interroger de l'effet qu'aurait un tel changement d'origine sur les délais de la cavité déplacée. On se concentre ici strictement sur le cas $r > d$ de la section précédente.

En utilisant le résultat (D.10) et la définition de la matrice des délais, on obtient directement une expression de la matrice des délais déplacée $\mathbf{Q}$,

$$\mathbf{Q} = \mathbf{T}\left[-i\left(\mathbf{S}'^\dagger \mathbf{T}^\dagger \frac{\partial \mathbf{T}}{\partial k}\mathbf{S}' - \mathbf{T}^\dagger \frac{\partial \mathbf{T}}{\partial k}\right) - i\mathbf{S}'\frac{\partial \mathbf{S}'}{\partial k}\right]\mathbf{T}^\dagger \tag{D.17}$$

avec $\mathbf{T} = \mathbf{T}(nkd, \phi_0)$ tel que défini à Eq. (D.8). On cherche donc dans un premier temps à obtenir une forme simplifiée du terme $\mathbf{T}^\dagger \partial\mathbf{T}/\partial k$.

D.2.1 Calcul de $\mathbf{T}^\dagger(nkd, \phi_0)\frac{\partial}{\partial k}\mathbf{T}(nkd, \phi_0)$

Pour la matrice de déplacement $\mathbf{T}(nkd, \phi_0)$ définie en (D.8), on calcule la dérivée par rapport à k

$$\frac{\partial}{\partial k}\mathbf{T}(nkd, \phi_0) = \mathbf{R}^\dagger(\phi_0)\left(\frac{\partial}{\partial k}\mathbf{J}(nkd)\right)\mathbf{R}(\phi_0) \quad . \tag{D.18}$$

On a donc le produit

$$\begin{aligned}
\{\mathbf{T}^\dagger(nkd, \phi_0)\frac{\partial}{\partial k}\mathbf{T}(nkd, \phi_0)\}_{\nu\mu} &= \{\mathbf{R}^\dagger(\phi_0)\mathbf{J}(nkd)\left(\frac{\partial}{\partial k}\mathbf{J}(nkd)\right)\mathbf{R}(\phi_0)\}_{\nu\mu} \\
&= nd\sum_m \mathrm{e}^{-i\nu\phi_0} J_{\nu-m}(z)\left(\frac{\partial}{\partial z}J_{\mu-m}(z)\right)\mathrm{e}^{i\mu\phi_0} \\
&= \frac{1}{2}nd\sum_m \mathrm{e}^{-i\nu\phi_0} J_{\nu-m}(z)\left[J_{\mu-m-1}(z) - J_{\mu-m+1}(z)\right]\mathrm{e}^{i\mu\phi_0} \\
&= \frac{1}{2}nd\,\mathrm{e}^{-i\nu\phi_0}\left[\sum_m J_{\nu-m}(z)\left[J_{\mu-m-1}(z) - J_{\mu-m+1}(z)\right]\right]\mathrm{e}^{i\mu\phi_0} \\
&= \frac{1}{2}nd\,\mathrm{e}^{-i\nu\phi_0}\left[\sum_m J_m(z)\left[J_{(\mu-\nu-1)+m}(z) - J_{(\mu-\nu+1)+m}(z)\right]\right]\mathrm{e}^{i\mu\phi_0}
\end{aligned} \tag{D.19}$$

où, à la seconde étape, l'identité (9.1.27) de [1] a été utilisée (Eqs. (A.12)-(A.13) de ce document).

Aussi, puisque $J_{a-b}(0) = \delta_{ab}$ et suivant l'identité (D.2), on a

$$\{\mathbf{T}^\dagger(nkd,\phi_0)\frac{\partial}{\partial k}\mathbf{T}(nkd,\phi_0)\}_{\nu\mu} = \frac{1}{2}nd\,\mathrm{e}^{-i\nu\phi_0}\left(\delta_{\nu,\mu-1}-\delta_{\nu,\mu+1}\right)\mathrm{e}^{i\mu\phi_0} \tag{D.20}$$

ou encore avec la définition[2]

$$\{\mathbf{\Sigma}\}_{mm'} \equiv \delta_{m,m'-1} \tag{D.22}$$

alors

$$\mathbf{T}^\dagger(nkd,\phi_0)\frac{\partial}{\partial k}\mathbf{T}(nkd,\phi_0) = \frac{1}{2}nd\,\mathbf{R}^\dagger(\phi_0)\left(\mathbf{\Sigma}-\mathbf{\Sigma}^T\right)\mathbf{R}(\phi_0) \quad . \tag{D.23}$$

Lorsque $\phi_0 = 0$ comme dans la Fig. D.1, cette dernière relation devient plus simplement

$$\mathbf{J}^T(nkd)\frac{\partial}{\partial k}\mathbf{J}(nkd) = \frac{1}{2}nd\,\left(\mathbf{\Sigma}-\mathbf{\Sigma}^T\right) \quad . \tag{D.24}$$

D.2.2 Matrice des délais déplacée Q

La substitution de Eq. (D.23) dans l'expression de la matrice $\mathbf{Q}$ Eq. (D.17) permet d'obtenir le résultat final en termes de la matrice des délais de la cavité dans son référentiel d'origine, $\mathbf{Q'} = -i\mathbf{S'}^\dagger\partial\mathbf{S'}/\partial k$, et d'une seconde matrice $\mathbf{D}(\mathbf{S'};\,nd,\phi_0)$,

$$\mathbf{Q} = \mathbf{T}(nkd,\phi_0)\left[\mathbf{D}(\mathbf{S'};\,nd,\phi_0)+\mathbf{Q'}\right]\mathbf{T}^\dagger(nkd,\phi_0) = \mathbf{T}\left[\mathbf{D}+\mathbf{Q'}\right]\mathbf{T}^\dagger \tag{D.25}$$

avec

$$\mathbf{D}(\mathbf{S}';\,nd,\phi_0) = -i\frac{1}{2}nd\left[\mathbf{S}'^\dagger\mathbf{R}^\dagger(\phi_0)\left(\mathbf{\Sigma}-\mathbf{\Sigma}^T\right)\mathbf{R}(\phi_0)\mathbf{S}' - \mathbf{R}^\dagger(\phi_0)\left(\mathbf{\Sigma}-\mathbf{\Sigma}^T\right)\mathbf{R}(\phi_0)\right] \tag{D.26}$$

On remarque immédiatement que l'effet du déplacement d sur $\mathbf{D}$ est linéaire, le paramètre d n'apparaissant nulle part ailleurs dans son expression. On vérifie directement que $\mathbf{D}$ est bien hermitique en distribuant l'imaginaire i sur la matrice $\left(\mathbf{\Sigma}-\mathbf{\Sigma}^T\right)$ qui devient alors elle-même hermitique.

Par ailleurs, les valeurs propres de la matrice $\frac{1}{2}\left(i\mathbf{\Sigma}-i\mathbf{\Sigma}^T\right)$ forment un ensemble

$$\left\{\cos\left(\frac{j}{M+1}\frac{\pi}{2}\right)\right\}\ ,\ j = 1,2,3,...,2M+1 \tag{D.27}$$

[2]La matrice $\mathbf{\Sigma}-\mathbf{\Sigma}^T$ apparaît donc comme une matrice possédant une diagonale d'éléments 1 *en-dessous* de la diagonale principale et une diagonale d'éléments -1 *au-dessus* de la diagonale principale, et 0 partout ailleurs,

$$\mathbf{\Sigma}-\mathbf{\Sigma}^T = \begin{pmatrix} \ddots & & & & & \\ & 0 & -1 & 0 & 0 & \\ & +1 & 0 & -1 & 0 & \\ & 0 & +1 & 0 & -1 & \\ & 0 & 0 & +1 & 0 & \\ & & & & & \ddots \end{pmatrix} \quad . \tag{D.21}$$

dont le rayon spectral est inférieur à 1 [3]. Les valeurs propres apparaissent donc en paires réelles opposées en signe, et on trouve une valeur propre égale à 0.

Puisque $\mathrm{Tr}\{\mathbf{XY}\} = \mathrm{Tr}\{\mathbf{YX}\}$ et $\mathrm{Tr}\{\mathbf{X}+\mathbf{Y}\} = \mathrm{Tr}\{\mathbf{X}\} + \mathrm{Tr}\{\mathbf{Y}\}$, que $\mathbf{S}'$ est unitaire et que $\mathbf{\Sigma}$ ne possède aucun élément sur sa diagonale principale, on a directement que $\mathrm{Tr}\{\mathbf{Q}'\} = \mathrm{Tr}\{\mathbf{Q}\}$, i.e. la somme des délais des modes propres de la cavité non-déplacée demeure inchangée. Ce résultat s'accorde aussi avec l'observation que les valeurs propres de $\frac{1}{2}\left(i\mathbf{\Sigma} - i\mathbf{\Sigma}^T\right)$ apparaissent en paires opposées de signe.

On s'attend cependant à ce que les délais moyens individuels de ces modes varient puisque, ayant déplacé la cavité, on retarde certaines portions du champ alors que d'autres sont avancées. Le rayon spectral des matrices composant $\mathbf{D}$ étant strictement inférieur à 1, le rayon spectral de $\mathbf{D}$ devrait donc être de l'ordre du déplacement optique nd. Pour $nd \ll q'_\nu$, avec q'_ν un délai propre de $\mathbf{Q}'$, l'effet du déplacement sur le délai propre déplacé q_ν sera donc typiquement perturbatif. Les modes présentant des densités d'énergie élevées à l'intérieur de la cavité sont ainsi moins affectés par le déplacement de la cavité que les modes de plus faible qualité pour lesquels $q'_\nu \sim nd$.

---

[3] La matrice $\frac{1}{2}\left(i\mathbf{\Sigma} - i\mathbf{\Sigma}^T\right)$ est hermitique et tridiagonale. Pour une matrice de taille finie, $2M+1$, le système aux valeurs propres

$$\frac{1}{2}\left(i\mathbf{\Sigma} - i\mathbf{\Sigma}^T\right)\mathbf{x} = \lambda\mathbf{x} \tag{D.28}$$

peut sécrire comme un problème aux différences

$$\frac{1}{2}ix_{m+1} - \frac{1}{2}ix_{m-1} = \lambda x_m \ , \tag{D.29}$$

$$+\frac{1}{2}ix_{-M+1} = \lambda x_{-M} \quad , \quad -\frac{1}{2}ix_{+M-1} = \lambda x_{+M} \quad . \tag{D.30}$$

D'emblée, on détermine que le cas $\lambda = 1$ pour $x_m = 1 \ \forall \ m$ est impossible.

La solution générale de l'équation aux différences est $x_m = c_+ r_+^m + c_- r_-^m$ avec $r_\pm = -i\left(\lambda \pm \sqrt{\lambda^2 - 1}\right)$. En appliquant les conditions aux limites, on obtient les coefficients $c_\pm$ puis l'expression auxiliaire permettant d'obtenir les valeurs propres,

$$\left(\frac{r_+}{r_-}\right)^{2M+2} = 1 \quad . \tag{D.31}$$

D'après cette expression, le rapport des racines r_+/r_- est $\mathrm{e}^{i\frac{2\pi j}{2M+2}}$ avec $j = 1, 2, 3..., 2M+1$. On explique la limitation sur j par la condition $\lambda \neq 1$ mentionnée plus haut. En remplaçant les racines $r_\pm$, on obtient que les valeurs propres satisfont

$$\lambda_j = \cos\left(\frac{j}{M+1}\frac{\pi}{2}\right) \ , \ j = 1, 2, 3..., 2M+1 \quad . \tag{D.32}$$

D.3 Matrice de diffusion S de la cavité annulaire

Soit la cavité diélectrique annulaire présentée à la Fig. D.3. On écrit les développements en ondes partielles pour les différentes régions et les 2 référentiels, l'un au centre de l'inclusion et l'autre au centre de la cavité,

$$\tilde{\psi}_h(\rho,\theta) = \sum_m \tilde{a}_{hm} J_m(n_h k\rho) \mathrm{e}^{im\theta} \tag{D.33}$$

$$\tilde{\psi}_c(\rho,\theta) = \sum_m \left[\tilde{a}_{cm} H_m^{(2)}(n_c k\rho) + \tilde{b}_{cm} H_m^{(1)}(n_c k\rho)\right] \mathrm{e}^{im\theta} \tag{D.34}$$

$$\psi_c(r,\phi) = \sum_m \left[a_{cm} H_m^{(2)}(n_c kr) + b_{cm} H_m^{(1)}(n_c kr)\right] \mathrm{e}^{im\phi} \tag{D.35}$$

$$\psi_o(r,\phi) = \sum_m \left[a_{om} H_m^{(2)}(n_o kr) + b_{om} H_m^{(1)}(n_o kr)\right] \mathrm{e}^{im\phi} \quad . \tag{D.36}$$

Les 4 développements s'appliquent respectivement sur l'intérieur de l'inclusion ($\rho \leq r_0$, index n_h), sur l'extérieur immédiat de l'inclusion ($r_0 \leq \rho \leq R_0 - d - r_0$, index n_c), sur l'intérieur de la cavité jusqu'à sa frontière extérieure ($d + r_0 \leq r \leq R_0$), et finalement sur l'extérieur de la cavité ($r \geq R_0$, index n_o). Autrement dit, un coup d'oeil à la Fig. D.3(b) nous indique que le développement (D.34) sera adéquat dans l'anneau formé par les zones jaune et verte et le développement (D.35) conviendra à l'anneau formé des zones bleue et verte. La fonction d'onde sera exprimée sur la totalité du domaine D_c par l'union des développements (D.34) et (D.35) lorsque

$$r_0/R_0 \leq 1 - 3d/R_0 \quad . \tag{D.37}$$

Cette condition géométrique assure que la restriction imposée sur les développements en ondes partielles soit satisfaite. La zone rouge de la Fig. D.1 disparaît si (D.37) est valide. On notera par ailleurs que la restriction est sur la représentation point-par-point de la fonction d'onde et non sur la construction de la matrice de diffusion qui pourra être obtenue même pour des cavités annulaires ne satisfaisant pas (D.37) .

Si la matrice de diffusion $\tilde{\mathbf{S}}_c$ associée au domaine D_h est connue ($\tilde{\mathbf{b}}_c = \tilde{\mathbf{S}}_c\, \tilde{\mathbf{a}}_c$), alors on peut écrire la fonction d'onde (D.35) évaluée sur la frontière de rayon $r = r_0 + d$ avec des coefficients exprimés au moyen de la matrice de déplacement (D.8) (évaluée sans perte de généralité à $\phi_0 = 0$)

$$a_{c\nu} = \sum_m J_{\nu-m}(n_c kd)\tilde{a}_{cm} \quad , \quad b_{c\nu} = \sum_m J_{\nu-m}(n_c kd)\tilde{b}_{cm} \quad , \tag{D.38}$$

ou encore sous forme matricielle

$$\mathbf{a}_c = \mathbf{J}(n_c kd)\tilde{\mathbf{a}}_c \quad , \quad \mathbf{b}_c = \mathbf{J}(n_c kd)\tilde{\mathbf{b}}_c. \tag{D.39}$$

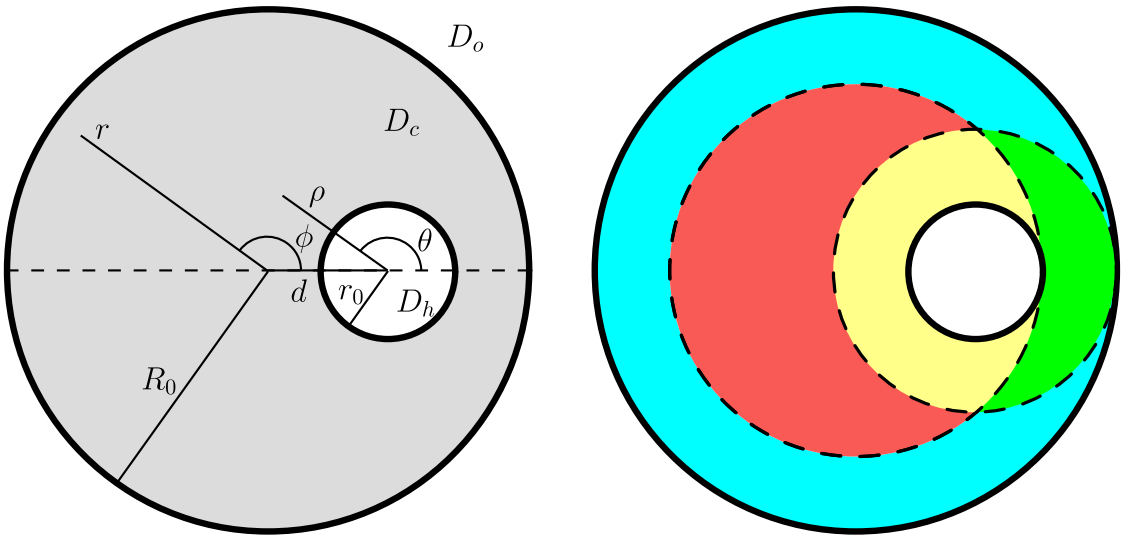


Fig. D.3 (a) Schéma de la cavité annulaire, ses paramètres et coordonnées, et (b) présentation des différents domaines de développement en ondes partielles de la fonction d'onde. Le domaine D_h (disque blanc) d'indice n_h repésente l'inclusion de la cavité annulaire, le domaine D_c (gris sur (a); vert, jaune, bleu et rouge sur (b); indice n_c) est le corps de la cavité et D_o (blanc) est le milieu extérieur (indice n_o). La fonction d'onde peut être développée en ondes partielles sur les coordonnées (ρ, θ) dans les zones jaune et verte et sur (r, ϕ) dans les zones verte, bleue ainsi que sur la totalité de D_o. La zone rouge n'est pas toujours couverte par le développement en ondes partielles entrantes et sortantes autour de l'origine de ces deux systèmes de coordonnées: les paramètres de construction doivent satisfaire (D.37) afin que le développement en ondes partielles recouvre totalement D_c.

On obtient donc la matrice de diffusion modifiée $\mathbf{S}_c$ en fonction de la matrice de diffusion $\tilde{\mathbf{S}}_c$ obtenue par diffusion sur D_h

$$\mathbf{S}_c = \mathbf{J}(n_c k d)\, \tilde{\mathbf{S}}_c\, \mathbf{J}^T(n_c k d). \tag{D.40}$$

L'application des conditions aux frontières (polarisation TM, continuité de la fonction et de sa dérivée) mène au système linéaire d'équations

$$H_m^{(2)}(Z_c) a_{cm} + H_m^{(1)}(Z_c) \sum_{m'} (\mathbf{S}_c)_{mm'} a_{cm'} = H_m^{(2)}(Z_o) a_{om} + H_m^{(1)}(Z_o) b_{om} \tag{D.41}$$

$$n_c \left[H_m^{(2)\prime}(Z_c) a_{cm} + H_m^{(1)\prime}(Z_c) \sum_{m'} (\mathbf{S}_c)_{mm'} a_{cm'} \right] = n_o \left[H_m^{(2)\prime}(Z_o) a_{om} + H_m^{(1)\prime}(Z_o) b_{om} \right] \tag{D.42}$$

avec $Z_c = n_c k R_0$ et $Z_o = n_o k R_0$.

Solutionnant (D.41) et (D.42) par élimination des coefficients $\mathbf{a}_c$, on obtient finalement la matrice de diffusion de la cavité annulaire, $\mathbf{S}_{ac}$, reliant les coefficients $\mathbf{b}_o = \mathbf{S}_{ac}\, \mathbf{a}_o$

comme

$$\mathbf{S}_{ac} = -\left[n_c \mathbf{G}\mathbf{F}^{-1}\mathbf{H}^1(Z_o) - n_o \mathbf{H}^{1'}(Z_o)\right]^{-1}\left[n_c \mathbf{G}\mathbf{F}^{-1}\mathbf{H}^2(Z_o) - n_o \mathbf{H}^{2'}(Z_o)\right] \qquad \text{(D.43)}$$

avec

$$\mathbf{F} = \mathbf{H}^2(Z_c) + \mathbf{H}^1(Z_c)\,\mathbf{S}_c \qquad , \qquad \mathbf{G} = \mathbf{H}^{2'}(Z_c) + \mathbf{H}^{1'}(Z_c)\,\mathbf{S}_c \quad , \qquad \text{(D.44)}$$

$$\{\mathbf{H}^{1,2}(z)\}_{mm'} = H_m^{(1,2)}(z)\delta_{mm'} \qquad , \qquad \{\mathbf{H}^{1',2'}(z)\}_{mm'} = \frac{d}{dz}H_m^{(1,2)}(z)\delta_{mm'}. \qquad \text{(D.45)}$$

Ce résultat est une forme alternative, mais équivalente [4], à celui obtenu par [60]. Par contre, la limite de convergence (D.37) de l'approche n'est pas aussi bien définie chez [60]. On complétera les opérations par le calcul de la matrice des délais grâce à l'expression

$$\mathbf{Q} = -i\,\mathbf{S}^\dagger \frac{\partial \mathbf{S}}{\partial k} \quad . \qquad \text{(D.50)}$$

[4] On peut en effet obtenir une expression identique à celle de [60] par les manipulations suivantes. On écrit d'abord le système d'équations (D.41-D.42) sous forme matricielle

$$\begin{pmatrix} \mathbf{H}^2 & \mathbf{H}^1 \\ n_o\mathbf{H}^{2'} & n_o\mathbf{H}^{1'} \end{pmatrix}\begin{pmatrix} \mathbf{a}_o \\ \mathbf{b}_o \end{pmatrix} = \begin{pmatrix} \mathbf{F}\,\mathbf{a}_c \\ n_c\mathbf{G}\,\mathbf{a}_c \end{pmatrix} \qquad \text{(D.46)}$$

En général, on ne peut inverser facilement la matrice du côté gauche de cette équation. Par contre, certaines observations nous permettrons de le faire. D'abord, la matrice est composée de blocs contenant des matrices diagonales qui commutent entre elles. De plus ces matrices ne contiennent que des fonctions de Hankel et leurs dérivées premières avec une propriété fondamentale que leur Wronskien, $W[H_m^{(1)}(z), H_m^{(2)}(z)] = H_m^{(1)}(z)H_m^{(2)'}(z) - H_m^{(1)'}(z)H_m^{(2)}(z) = -4i/(\pi z)$, est égal à une constante indépendante de m. Ceci est suffisant pour pouvoir écrire

$$\begin{pmatrix} \mathbf{a}_o \\ \mathbf{b}_o \end{pmatrix} = \frac{1}{\Delta}\begin{pmatrix} n_o\mathbf{H}^{1'} & -\mathbf{H}^1 \\ -n_o\mathbf{H}^{2'} & \mathbf{H}^2 \end{pmatrix}\begin{pmatrix} \mathbf{F}\,\mathbf{a}_c \\ n_c\mathbf{G}\,\mathbf{a}_c \end{pmatrix}. \qquad \text{(D.47)}$$

où Δ est le déterminant de toute la matrice. On notera avec un certain étonnement que cette procédure est identique à l'inversion d'une matrice 2 x 2! On inverse ensuite la première ligne de (D.47) pour isoler $\mathbf{a}_c$ en fonction de $\mathbf{a}_o$

$$\mathbf{a}_c = \Delta\left[n_o\mathbf{H}^{1'}\mathbf{F} - n_c\mathbf{H}^1\mathbf{G}\right]^{-1}\mathbf{a}_o\ . \qquad \text{(D.48)}$$

Résultat qu'on introduit dans la seconde ligne de (D.47) pour finalement obtenir

$$\begin{aligned} \mathbf{b}_o &= -\left[n_o\mathbf{H}^{2'}\mathbf{F} - n_c\mathbf{H}^2\mathbf{G}\right]\left[n_o\mathbf{H}^{1'}\mathbf{F} - n_c\mathbf{H}^1\mathbf{G}\right]^{-1}\mathbf{a}_o \\ &= -\left[n_o\mathbf{H}^{2'} - n_c\mathbf{H}^2\mathbf{G}\mathbf{F}^{-1}\right]\left[n_o\mathbf{H}^{1'} - n_c\mathbf{H}^1\mathbf{G}\mathbf{F}^{-1}\right]^{-1}\mathbf{a}_o. \end{aligned} \qquad \text{(D.49)}$$

Cette expression correspond à celle de [60] .

Annexe E

Modes d'un guide d'onde plan

En premier lieu, cette annexe présente la méthode de calcul des modes propagatoires d'une plaque diélectrique d'épaisseur w sur l'axe Oy, et infinie sur le plan $OxOz$. La condition permettant d'obtenir un guide monomode est obtenue et utilisée pour évaluer l'évolution de l'indice effectif en fonction de l'épaisseur d'un guide d'onde. Ensuite, une série de résultats analytiques, en partie inédits, complète le chapitre 5 où le modèle de couplage cavité-guide d'onde est décrit en détails.

E.1 Modes d'un guide d'onde plan

Cette première partie recueille les équations principales de la section 2.1 de l'ouvrage de K. Okamoto [92] dédiée au calcul des modes propres d'un guide d'onde planaire infini. Les différents paramètres suivent la notation:

n_g	:	indice de réfraction du guide (réel)
n_o	:	indice de réfraction de l'environnement (réel, $n_g > n_o$)
w	:	largeur du guide d'onde
k	:	nombre d'onde (réel)

Pour le guide d'onde plan (*slab waveguide*) représenté à la Fig. E.1 et un champ électrique (magnétique) orienté selon l'axe Oz, on obtient une solution générale aux équations de Maxwell pour le champ électrique (magnétique) scalaire

$$\left.\begin{matrix} E_z(x,y) \\ H_z(x,y) \end{matrix}\right\} = \begin{cases} A\cos(\gamma w/2 - \phi)\mathrm{e}^{-\alpha(y-w/2)+i\beta x} & y \geq +w/2 \\ A\cos(\gamma y - \phi)\mathrm{e}^{i\beta x} & -w/2 \leq y \leq +w/2 \\ A\cos(\gamma w/2 + \phi)\mathrm{e}^{+\alpha(y+w/2)+i\beta x} & y \leq -w/2 \end{cases} \quad \text{(E.1)}$$

et

$$\gamma \equiv \sqrt{(n_g k)^2 - \beta^2} \qquad , \qquad \alpha \equiv \sqrt{\beta^2 - (n_o k)^2} \ . \tag{E.2}$$

Ces expressions sont posées en Ansatz. Elles décrivent un champ transverse stationnaire à l'intérieur du guide et un champ exponentiellement décroissant à l'extérieur. Il s'agit de la solution physique au modèle de propagation dans le guide. Pour ce qui suit, on nommera TE (Transverse Électrique) la polarisation où le champ électrique est transverse au plan $OxOy$, et TM (Transverse Magnétique) la polarisation où le champ magnétique est transverse au plan $OxOy$.

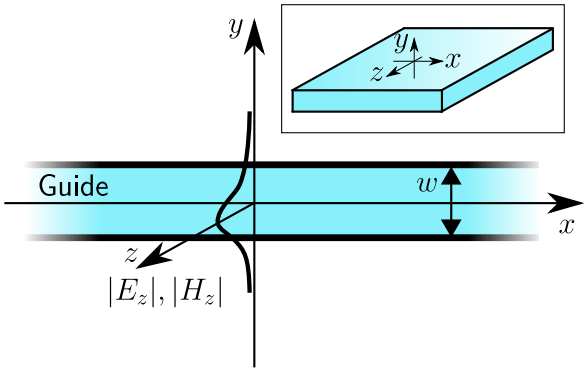


Fig. E.1 Représentation de la section du guide d'onde plan et de l'amplitude du champ. Il s'agit d'une coupe sur le plan $OxOy$ de la plaque diélectrique infinie apparaissant dans le coin supérieur droit de la Fig.

L'application des conditions aux frontières[1] permet d'isoler une expression reliant $u = \gamma w/2 > 0$, $s = \alpha w/2 > 0$ et ϕ:

$$\text{(TE)} \quad s = u \tan(u \pm \phi) \quad , \quad \text{(TM)} \quad s = \frac{n_o^2}{n_g^2} u \tan(u \pm \phi) \tag{E.3}$$

$$\phi \ = \ j\frac{\pi}{2} \quad , \ j \in \mathbb{N} \quad . \tag{E.4}$$

Pour un nombre d'onde k fixe, on doit aussi avoir la relation

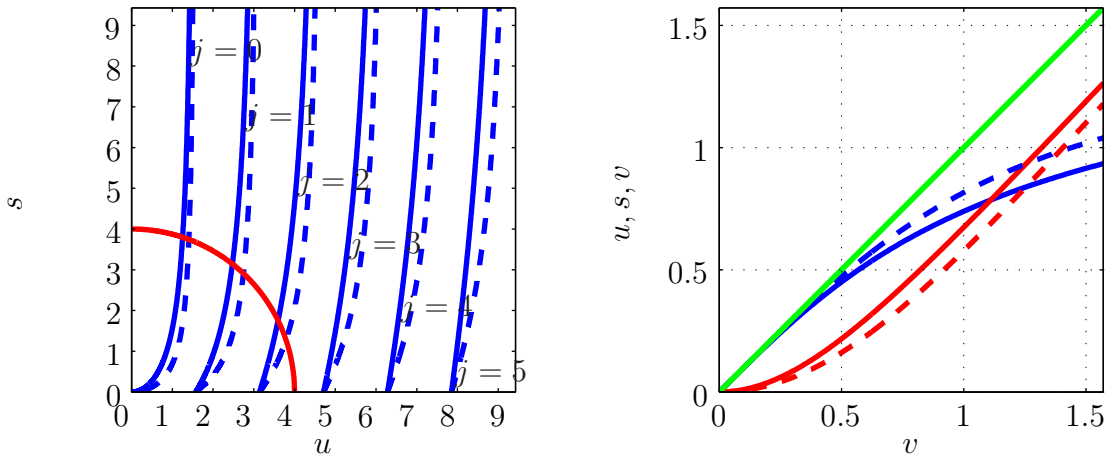
$$s^2 + u^2 = v^2 \equiv (kw/2)^2 (n_g^2 - n_o^2) \quad . \tag{E.5}$$

Les expressions (E.3) et (E.5) doivent être satisfaites simultanément (Fig. E.2(a)).

[1]Conditions aux frontières pour le guide plan:

$$\text{TE} \ : \ \begin{cases} E_z(x, \pm w/2)_{\text{in}} & = & E_z(x, \pm w/2)_{\text{out}} \\ \frac{d}{dy} E_z(x, \pm w/2)_{\text{in}} & = & \frac{d}{dy} E_z(x, \pm w/2)_{\text{out}} \end{cases}$$

$$\text{TM} \ : \ \begin{cases} H_z(x, \pm w/2)_{\text{in}} & = & H_z(x, \pm w/2)_{\text{out}} \\ \frac{1}{n_g^2} \frac{d}{dy} H_z(x, \pm w/2)_{\text{in}} & = & \frac{1}{n_o^2} \frac{d}{dy} H_z(x, \pm w/2)_{\text{out}} \end{cases}$$



(a) (b)

Fig. E.2 (a) Solution graphique du système d'équations (E.3)-(E.5): en bleu, Eq. (E.3) pour les différents modes du guide et en rouge, l'espression de la conservation du nombre d'onde Eq. (E.5) pour $v = 4$. Les modes TE sont représentés en traits continus et les modes TM, en traits discontinus. Un espace paramétrique continu d'indices de réfraction, de nombres d'onde et d'épaisseurs de guide satisfont cette égalité. Dans ce cas d'espèce, le guide supporte trois modes propagatoires et le mode TM est calculé pour un ratio d'indices $n_o/n_g = 2/3$. (b) Solution du système d'équations (E.3)-(E.5) pour un intervalle de v allant de 0 jusqu'à la fréquence de coupure du mode $j = 1$ pour les deux polarisations (TE: trait continu; TM: trait discontinu, $n_o/n_g = 2/3$). On obtient ainsi les solutions s (rouge) et u (bleu) pour le guide monomode. La ligne verte est le résultat de $\sqrt{u^2 + s^2}$, soit v.

Pour chaque mode, il existe une fréquence de coupure v_{cutoff} en deçà de laquelle le mode n'existe pas:

$$v_{\text{cutoff}} = j\frac{\pi}{2} \quad . \tag{E.6}$$

Comme nous sommes intéressés à la solution monomode du guide (Fig. E.2(b)), on demande

$$(kw/2) < \frac{1}{\sqrt{n_g^2 - n_o^2}}\frac{\pi}{2} \quad . \tag{E.7}$$

Techniquement, une fois $\gamma = u/(w/2)$ obtenu, on trouve directement la constante de propagation $\beta = \sqrt{n_g^2 k^2 - \gamma^2}$. L'indice effectif n_{eff} [19] d'un guide plan s'obtient alors directement,

$$n_{\text{eff}} = \sqrt{n_g^2 - \gamma^2/k^2} = \sqrt{n_g^2 - 4\frac{u^2}{k^2 w^2}} \quad . \tag{E.8}$$

Cette quantité revêt avant tout un intérêt expérimental: pour une source de longueur d'onde connue (grandeur du nombre d'onde), on obtient directement la composante du nombre d'onde se propageant dans la direction de l'axe Ox par une multiplication avec l'indice effectif. Un résultat typique pour un guide monomode est présenté à la Fig. (E.3).

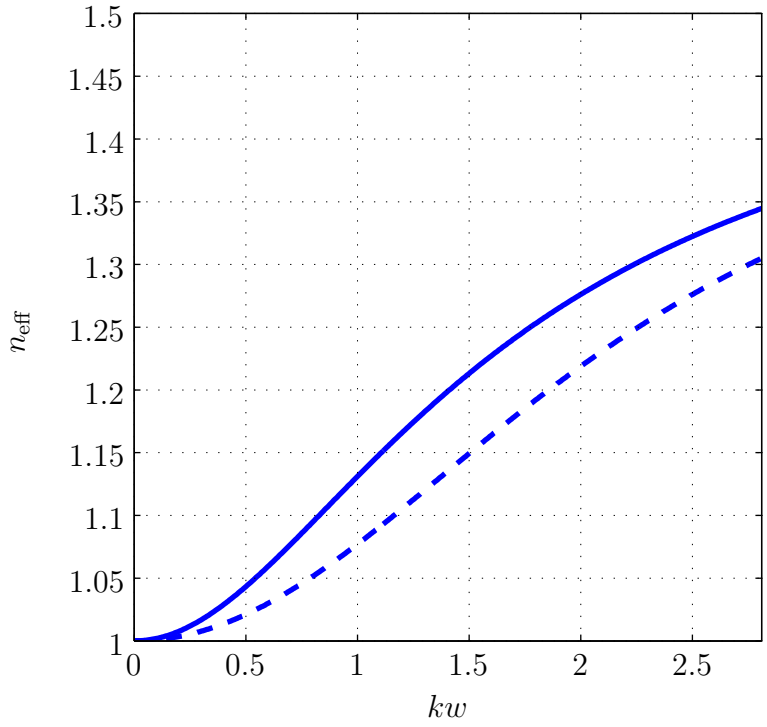


Fig. E.3 Indice effectif tel que défini par Eq. (E.8) en fonction de l'épaisseur normalisée au nombre d'onde pour le premier mode (TE: trait continu; TM: trait discontinu). Les constantes utilisées sont $n_g = 1.5$ (verre), $n_o = 1.0$ et $k = 1$. L'indice effectif pour une épaisseur nulle est n_o, mais n'atteint qu'asymptotiquement la valeur n_g pour un guide infiniment épais.

E.2 Modèle de couplage cavité-guide d'onde: Analyse

E.2.1 Représentation en ondes planes de $H_m^{(1)}(z)\mathrm{e}^{im\phi}$

On reprend ici le développement de l'harmonique cylindrique $H_m^{(1)}(z)\mathrm{e}^{im\phi}$ présenté chez Cincotti *et al.* [34]. Le but à atteindre est de représenter cette harmonique cylindrique comme une superposition d'onde planes.

Suivant [50], la fonction de Hankel peut s'écrire

$$H_m^{(1)}(z) = -\frac{1}{\pi}\int_C d\theta\ \mathrm{e}^{-iz\sin\theta+im\theta} = -\frac{(-i)^m}{\pi}\int_{C'} d\theta\ \mathrm{e}^{iz\cos\theta+im\theta}\ ,\ m\in\mathbb{Z} \qquad \text{(E.9)}$$

où C' est présentée à la Fig. E.4. La forme exacte de ce parcours est arbitraire mais doit se plier aux exigences suivantes:

- C' passe par l'origine

- $\mathrm{Im}\{C'\}$ rejoint $+i\infty$ dans la région $-\pi \leq u \leq 0$

- $\mathrm{Im}\{C'\}$ rejoint $-i\infty$ dans la région $0 \leq u \leq +\pi$.

- la projection de C' sur l'axe réel doit être égale à $-\pi$

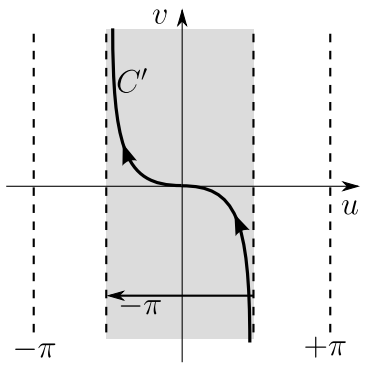


Fig. E.4 Parcours C' de la représentation (E.9) de la fonction de Hankel $H^{(1)}(z)$; $\theta = u + iv$.

On peut donc déformer ce contour de sorte à obtenir trois intégrales distinctes (voir Fig. E.5):

$$H_m^{(1)}(z) = -\frac{(-i)^m}{\pi}\left[\int_{\pi-\alpha-i\infty}^{\pi-\alpha} d\theta \ \ldots + \int_{\pi-\alpha}^{-\alpha} d\theta \ \ldots + \int_{-\alpha}^{-\alpha+i\infty} d\theta \ \ldots\right] \quad \text{(E.10)}$$

$$= -\frac{(-i)^m}{\pi}\left[\ (-1)^m i\mathrm{e}^{-im\alpha}\int_{-\infty}^{0} dv \ \mathrm{e}^{-iz\cos(iv-\alpha)-mv} \right.$$
$$- \mathrm{e}^{-im\alpha}\int_0^{\pi} du \ \mathrm{e}^{iz\cos(u-\alpha)+imu}$$
$$\left. + i\mathrm{e}^{-im\alpha}\int_0^{+\infty} dv \ \mathrm{e}^{iz\cos(iv-\alpha)-mv}\right] \quad \text{(E.11)}$$

où $0 \leq \alpha \leq \pi$.

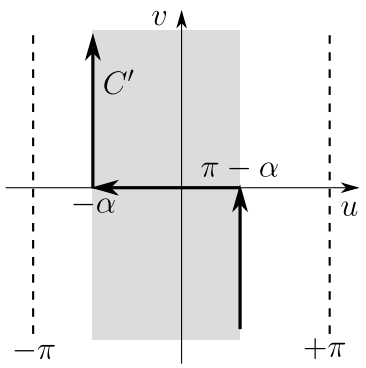


Fig. E.5 Parcours C' modifié en fonction de l'expression (E.10).

On peut donc écrire

$$\begin{aligned} H_m^{(1)}(z)\mathrm{e}^{im\alpha} &= -\frac{(-i)^m}{\pi}\left[\; (-1)^m i \int_{-\infty}^{0} dv \; \mathrm{e}^{-iz\cos(iv-\alpha)-mv} \right. \\ &\qquad - \int_0^{\pi} du \; \mathrm{e}^{iz\cos(u-\alpha)+imu} \\ &\qquad \left. + i\int_0^{+\infty} dv \; \mathrm{e}^{iz\cos(iv-\alpha)-mv} \right] \\ &= -\frac{(-i)^m}{\pi}\left[\; (-1)^m i \int_{-\infty}^{0} dv \; \mathrm{e}^{-iz(\cosh v\cos\alpha + i\sinh v\sin\alpha)-mv} \right. \\ &\qquad - \int_0^{\pi} du \; \mathrm{e}^{iz(\cos u\cos\alpha+\sin u\sin\alpha)+imu} \\ &\qquad \left. + i\int_0^{+\infty} dv \; \mathrm{e}^{iz(\cosh v\cos\alpha + i\sinh v\sin\alpha)-mv} \right] \quad . \end{aligned} \tag{E.12}$$

Si on exprime cette équation en coordonnées cartésiennes $\xi \equiv z\cos\alpha$, $\eta \equiv z\sin\alpha$, on obtient

$$\begin{aligned} H_m^{(1)}(z)\mathrm{e}^{im\alpha} &= -\frac{(-i)^m}{\pi}\left[\; (-1)^m i \int_{0}^{+\infty} dv \; \mathrm{e}^{-i(\xi\cosh v - i\eta\sinh v)+mv} \right. \\ &\qquad - \int_0^{\pi} du \; \mathrm{e}^{i(\xi\cos u+\eta\sin u)+imu} \\ &\qquad \left. + i\int_0^{+\infty} dv \; \mathrm{e}^{i(\xi\cosh v + i\eta\sinh v)-mv} \right] \quad . \end{aligned} \tag{E.13}$$

Puisque les intervalles d'intégration sont tous positifs, on substitue

$$\begin{aligned} v &= \ln\left(\beta + \sqrt{\beta^2-1}\right) \quad \text{si} \qquad \beta = \cosh v \\ u &= \arccos\beta \qquad\qquad\quad \text{si} \qquad \beta = \cos u \end{aligned}$$

et on obtient

$$\begin{aligned} H_m^{(1)}(z)\mathrm{e}^{im\alpha} &= -\frac{(-i)^m}{\pi}\Bigg[(-1)^m i\int_{-\infty}^{-1} d\beta \left(\frac{\left(-\beta+\sqrt{\beta^2-1}\right)^m}{\sqrt{\beta^2-1}}\,\mathrm{e}^{-\eta\sqrt{\beta^2-1}}\right)\mathrm{e}^{+i\xi\beta} \\ &\quad -\int_{-1}^{+1} d\beta \left(\frac{\left(\beta+i\sqrt{1-\beta^2}\right)^m}{\sqrt{1-\beta^2}}\,\mathrm{e}^{i\eta\sqrt{1-\beta^2}}\right)\mathrm{e}^{+i\xi\beta} \\ &\quad +i\int_{1}^{+\infty} d\beta \left(\frac{1}{\sqrt{\beta^2-1}\left(\beta+\sqrt{\beta^2-1}\right)^m}\,\mathrm{e}^{-\eta\sqrt{\beta^2-1}}\right)\mathrm{e}^{+i\xi\beta}\Bigg] \quad . \end{aligned} \tag{E.14}$$

Plus succintement, on écrira

$$H_m^{(1)}(z)\mathrm{e}^{im\alpha} = \int_{-\infty}^{+\infty} d\beta\; F_m(\beta,\eta)\mathrm{e}^{i\beta\xi} \tag{E.15}$$

avec

$$F_m(\beta,\eta) = \begin{cases} -\frac{(-i)^m}{\pi}(-1)^m i\left(\frac{\left(-\beta+\sqrt{\beta^2-1}\right)^m}{\sqrt{\beta^2-1}}\,\mathrm{e}^{-\eta\sqrt{\beta^2-1}}\right) & -\infty < \beta \leq -1 \\ +\frac{(-i)^m}{\pi}\left(\frac{\left(\beta+i\sqrt{1-\beta^2}\right)^m}{\sqrt{1-\beta^2}}\,\mathrm{e}^{i\eta\sqrt{1-\beta^2}}\right) & -1 \leq \beta \leq +1 \\ -\frac{(-i)^m}{\pi} i\left(\frac{1}{\sqrt{\beta^2-1}\left(\beta+\sqrt{\beta^2-1}\right)^m}\,\mathrm{e}^{-\eta\sqrt{\beta^2-1}}\right) & +1 \leq \beta < +\infty \end{cases} \quad . \tag{E.16}$$

L'intégrale sur $[-1,\ +1]$ caractérise les modes propagatoires en η alors que les deux autres sont associées aux ondes évanescentes. On trouve facilement l'extension du développement précédent pour $-\pi \leq \alpha \leq 0$ ($\eta < 0$) en considérant

$$H_{-m}^{(1)}(z)\mathrm{e}^{i(-m)\alpha} = (-1)^m H_m^{(1)}(z)\mathrm{e}^{im(-\alpha)} \quad . \tag{E.17}$$

On a donc

$$F_m(\beta,-|\eta|) = (-1)^m F_{-m}(\beta,|\eta|) \quad . \tag{E.18}$$

E.2.2 Résultat asymptotique de l'intégrale $\int_{x_0}^{+\infty} dx\; H_m^{(1)}(n_o kr)\mathrm{e}^{im\phi}\mathrm{e}^{\mp i\beta x}$ pour $x_0/y \gg |m|$

On présente le calcul de l'intégrale

$$I_{1\mp} \equiv \int_{x_0}^{+\infty} dx\; H_m^{(1)}(n_o kr)\mathrm{e}^{im\phi}\mathrm{e}^{\mp i\beta x} \tag{E.19}$$

pour la situation où $x_0/y \gg m$ et $y \neq 0$. Le résultat est obtenu dans un premier temps pour $x_0 > 0$ et $m \geq 0$ puis est étendu aux autres cas. Ce calcul est motivé de deux façons:

- L'évaluation numérique de l'intégrale sur l'ensemble de l'axe réel requiert un domaine d'intégration fini,
- Comme l'intégrale sur $[-x_0, x_0]$ est finie pour $y \neq 0$, un résultat asymptotique convergeant implique que l'intégrale sur l'axe réel converge elle aussi.

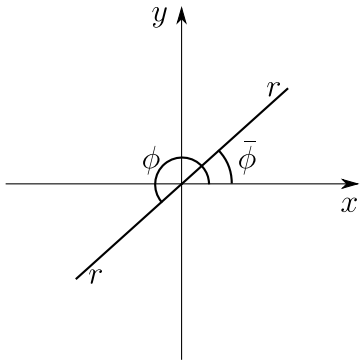


Fig. E.6 Convention de coordonnées pour le développement asymptotique de l'intégrale (E.19).

On pose $\eta = x/y$, $|y| > 0$ et $\xi = n_o k y$. Pour $|1/\eta_0| = |y/x_0| \ll 1$ ($\phi \approx 2\pi$), on a

$$\mathrm{e}^{im\phi} = (\cos\phi + i\sin\phi)^m \sim \left(1 + i\frac{1}{\eta}\right)^m = \sum_{j=0}^{m} \left(\begin{array}{c} m \\ j \end{array}\right) \left(i\frac{1}{\eta}\right)^j = 1 + im\frac{1}{\eta} + \mathcal{O}(\eta^{-2}) \quad . \tag{E.20}$$

De plus, comme on suppose $\xi\eta_0 \gg |m|$, on a

$$\begin{aligned}
H_m^{(1)}(n_o kr) &\sim \sqrt{\frac{2}{\pi\xi\eta\sqrt{1+\frac{1}{\eta^2}}}}\mathrm{e}^{-im\pi/2 - i\pi/4}\mathrm{e}^{i\xi\eta\sqrt{1+\frac{1}{\eta^2}}}\left(1 + i\frac{4m^2-1}{8\xi\eta\sqrt{1-\frac{1}{\eta^2}}}\right) + \mathcal{O}(\eta^{-(2+1/2)}) \\
&= \sqrt{\frac{2}{\pi|\xi|}}\mathrm{e}^{-im\pi/2 - i\pi/4}\frac{1}{\sqrt{|\eta|}}\mathrm{e}^{i\xi\eta}\mathrm{e}^{i\xi\frac{1}{2}\frac{1}{\eta}}\left(1 + i\frac{4m^2-1}{8\xi\eta\sqrt{1-\frac{1}{\eta^2}}}\right) + \mathcal{O}(\eta^{-(2+1/2)}) \\
&= \sqrt{\frac{2}{\pi|\xi|}}\mathrm{e}^{-im\pi/2 - i\pi/4}\frac{1}{\sqrt{|\eta|}}\mathrm{e}^{i\xi\eta}\left(1 + i\xi\frac{1}{2}\frac{1}{\eta}\right)\left(1 + i\frac{4m^2-1}{8\xi\eta\sqrt{1-\frac{1}{\eta^2}}}\right) + \mathcal{O}(\eta^{-(2+1/2)}) \\
&= \sqrt{\frac{2}{\pi|\xi|}}\mathrm{e}^{-im\pi/2 - i\pi/4}\frac{1}{\sqrt{|\eta|}}\mathrm{e}^{i\xi\eta}\left[1 + i\left(\xi\frac{1}{2} + \frac{4m^2-1}{8\xi}\right)\frac{1}{\eta}\right] + \mathcal{O}(\eta^{-(2+1/2)})
\end{aligned}$$

puis

$$H_m^{(1)}(n_o kr)\mathrm{e}^{im\phi}\mathrm{e}^{\mp i\beta x} \sim \sqrt{\frac{2}{\pi|\xi|}}\mathrm{e}^{-im\pi/2-i\pi/4}\frac{1}{\sqrt{|\eta|}}\left[1+i\left(\xi\frac{1}{2}+\frac{4m^2-1}{8\xi}+m\right)\frac{1}{\eta}\right]\mathrm{e}^{i(\xi\mp\tilde{\xi})\eta}+\mathcal{O}(\eta^{-(2+1/2)})$$

où $\tilde{\xi}=\beta y$. L'intégrale prend donc la forme

$$\begin{aligned} I_{1\mp} &\sim y\int_{\eta_0}^{\mathrm{sign}(y)\infty} d\eta\ \sqrt{\frac{2}{\pi|\xi|}}\mathrm{e}^{-im\pi/2-i\pi/4}\frac{1}{\sqrt{|\eta|}}\left[1+i\left(\xi\frac{1}{2}+\frac{4m^2-1}{8\xi}+m\right)\frac{1}{\eta}\right]\mathrm{e}^{i(\xi\mp\tilde{\xi})\eta}+\mathcal{O}(|\eta_0|^{-(1+1/2)}) \\ &\sim |y|\sqrt{\frac{2}{\pi|\xi|}}\mathrm{e}^{-im\pi/2-i\pi/4}\left[\int_{\eta_0=\mathrm{sign}(y)\times x_0/y}^{+\infty} d\eta\ \frac{1}{\sqrt{\eta}}\mathrm{e}^{\mathrm{sign}(y)i(\xi\mp\tilde{\xi})\eta}\right. \\ &\quad \left.+\mathrm{sign}(y)i\left(\xi\frac{1}{2}+\frac{4m^2-1}{8\xi}+m\right)\int_{\eta_0=\mathrm{sign}(y)\times x_0/y}^{+\infty} d\eta\ \frac{1}{\eta^{3/2}}\mathrm{e}^{\mathrm{sign}(y)i(\xi\mp\tilde{\xi})\eta}\right]+\mathcal{O}(|\eta_0|^{-(1+1/2)}) \quad \text{(E.21)} \end{aligned}$$

Il y a donc deux intégrales à calculer. On procède au changement de variable

$$\eta'=\sqrt{\frac{(|\tilde{\xi}|\mp|\xi|)}{\pi/2}}\ \eta^{1/2}=\sqrt{\frac{(\beta\mp n_o k)x}{\pi/2}} \quad \text{(E.22)}$$

de sorte que

$$\begin{aligned} \int_{\eta_0}^{+\infty} d\eta\ \frac{1}{\eta^{1/2}}\mathrm{e}^{\mp i(|\tilde{\xi}|\mp|\xi|)\eta} &= \sqrt{\frac{2\pi}{(|\tilde{\xi}|\mp|\xi|)}}\int_{\eta_0'}^{+\infty} d\eta'\ \mathrm{e}^{\mp i\frac{\pi}{2}\eta'^2} \\ &= \sqrt{\frac{2\pi}{(|\tilde{\xi}|\mp|\xi|)}}\left[\left(\frac{1}{2}-C(\eta_0')\right)\mp i\left(\frac{1}{2}-S(\eta_0')\right)\right] \quad \text{(E.23)} \end{aligned}$$

et

$$\begin{aligned} &\int_{\eta_0}^{+\infty} d\eta\ \frac{1}{\eta^{3/2}}\mathrm{e}^{\mp i(|\tilde{\xi}|\mp|\xi|)\eta} = \\ &\qquad 2\left\{\frac{1}{\eta_0^{1/2}}\mathrm{e}^{\mp i(|\tilde{\xi}|\mp|\xi|)\eta_0}+\sqrt{2\pi(|\tilde{\xi}|\mp|\xi|)}\left[\mp i\left(\frac{1}{2}-C(\eta_0')\right)-\left(\frac{1}{2}-S(\eta_0')\right)\right]\right\} \quad \text{(E.24)} \end{aligned}$$

où

$$\eta_0'=\sqrt{\frac{(|\tilde{\xi}|\mp|\xi|)}{\pi/2}}\eta_0^{1/2}=\sqrt{\frac{(\beta\mp n_o k)x_0}{\pi/2}} \quad \text{(E.25)}$$

et

$$C(x) = \int_0^x dt\ \cos\frac{\pi}{2}t^2 \le \frac{1}{2} \quad \text{(E.26)}$$

$$S(x) = \int_0^x dt\ \sin\frac{\pi}{2}t^2 \le \frac{1}{2} \quad \text{(E.27)}$$

sont les intégrales de Fresnel [1]. Finalement

$$\begin{aligned} I_{1\mp} &\sim \mathrm{e}^{-im\pi/2-i\pi/4}\left\{\frac{2}{\sqrt{n_o k(\beta\mp n_o k)}}\left[\left(\frac{1}{2}-C(\eta_0')\right)\mp i\left(\frac{1}{2}-S(\eta_0')\right)\right]\right\} \\ &+2iy\sqrt{\frac{2}{\pi n_o k|y|}}\mathrm{e}^{-im\pi/2-i\pi/4}\left(n_o k y\frac{1}{2}+\frac{4m^2-1}{8n_o k y}+m\right)\times \\ &\left\{\frac{1}{(x_0/|y|)^{1/2}}\mathrm{e}^{\mp i(\beta\mp n_o k)x_0}+\sqrt{2\pi(\beta\mp n_o k)|y|}\left[\mp i\left(\frac{1}{2}-C(\eta_0')\right)-\left(\frac{1}{2}-S(\eta_0')\right)\right]\right\} \\ &+\mathcal{O}(|\eta_0|^{-(1+1/2)}) \end{aligned} \tag{E.28}$$

Pour un intervalle d'intégration $]-\infty,\ -x_0]$, $x_0\gg 0$, on a (voir la Fig. E.6)

$$I_{2\mp}\equiv\int_{-\infty}^{-x_0}dx\ H_m^{(1)}(n_o kr)\mathrm{e}^{im\phi}\mathrm{e}^{\mp i\beta x}=\int_{-\infty}^{-x_0}dx\ H_m^{(1)}(n_o kr)\mathrm{e}^{im(\bar{\phi}+\pi)}\mathrm{e}^{\mp i\beta x}\quad . \tag{E.29}$$

On développe l'exponentielle autour de $\bar{\phi}=0$:

$$\mathrm{e}^{im\bar{\phi}}=\left(\cos\bar{\phi}+i\sin\bar{\phi}\right)^m\approx\left(1+i\frac{-y}{-x}\right)^m=1+im\frac{-y}{-x}+\mathcal{O}((y/x)^2) \tag{E.30}$$

de sorte que

$$\begin{aligned} I_{2\mp} &= (-1)^m\int_{-\infty}^{-x_0}dx\ H_m^{(1)}(n_o kr)\left(1+im\frac{-y}{-x}+\mathcal{O}((y/x)^2)\right)\mathrm{e}^{\mp i\beta x} \\ &= (-1)^m\int_{x_0}^{+\infty}dx\ H_m^{(1)}(n_o kr)\left(1-im\frac{y}{x}+\mathcal{O}((y/x)^2)\right)\mathrm{e}^{\pm i\beta x}\ . \end{aligned} \tag{E.31}$$

Le résultat de l'intégrale est donc similaire à celui obtenu précédemment pour un intervalle d'intégration positif:

$$\begin{aligned} I_{2\mp} &\sim (-1)^m\mathrm{e}^{-im\pi/2-i\pi/4}\left\{\frac{2}{\sqrt{n_o k(\beta\pm n_o k)}}\left[\left(\frac{1}{2}-C(\eta_0')\right)\pm i\left(\frac{1}{2}-S(\eta_0')\right)\right]\right\} \\ &+(-1)^m 2iy\sqrt{\frac{2}{\pi n_o k|y|}}\mathrm{e}^{-im\pi/2-i\pi/4}\left(n_o k y\frac{1}{2}+\frac{4m^2-1}{8n_o k y}-m\right)\times \\ &\left\{\frac{1}{(x_0/|y|)^{1/2}}\mathrm{e}^{\pm i(\beta\pm n_o k)x_0}+\sqrt{2\pi(\beta\pm n_o k)|y|}\left[\pm i\left(\frac{1}{2}-C(\eta_0')\right)+-\left(\frac{1}{2}-S(\eta_0')\right)\right]\right\} \\ &+\mathcal{O}(|\eta_0|^{-(1+1/2)}). \end{aligned} \tag{E.32}$$

Puisque les intégrales de Fresnel sont finies, le régime asymptotique des intégrales sur la fonction de Hankel l'est aussi. Ces intégrales doivent donc converger.

On a calculé l'erreur quadratique moyenne

$$\mathrm{Err}(\eta_0) = \left[\frac{1}{N} \sum_{j=1}^{N} \left| \int_{\text{analytique, } \beta_j} - \int_{\text{numerique, } \beta_j} \right|^2 \right]^{1/2} \tag{E.33}$$

entre la forme fermée de l'intégrale sur l'intervalle de $-\infty$ à $+\infty$ et une intégration numérique partielle complétée par le développement asymptotique présenté plus haut. Pour $m = +4$, $n_o k = 5$, $y = -1$ et $N = 100$ valeurs de β entre $n_o k + 0.1$ et $n_o k + 5$ pour chaque valeur de η_0, le résultat de la comparasion est présenté à la Fig. E.7.

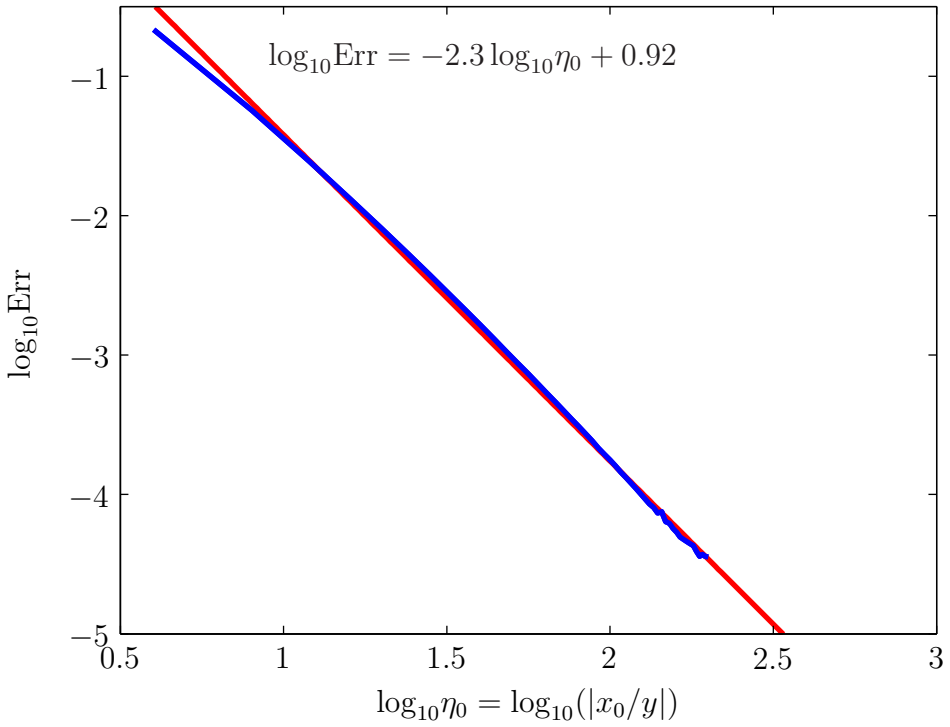


Fig. E.7 $\log_{10}(\mathrm{Err})$ en fonction de $\log_{10}(\eta_0)$. Une régression linéaire a été calculée. La pente obtenue est de -2.3 ce qui est plus élevé que prévu par le développement asymptotique (~ -1.5). Nous n'avons pas poussé l'investigation plus loin mais il se peut qu'une symétrie dans l'intégrale du terme d'ordre $-(2 + 1/2)$ augmente la convergence en η_0. Un résultat semblable a été obtenu pour $m = 3$ (pente ~ -2.5). Il faut probablement voir $\mathcal{O}(|\eta|^{-(1+1/2)})$ comme une borne supérieure.

E.2.3 Intégration de $\int_{-\infty}^{+\infty} dx\ H_m^{(1)}(n_o k r)\mathrm{e}^{im\phi}\mathrm{e}^{\mp i\beta x}$

Nous désirons calculer l'intégrale

$$I_{3\mp} \equiv \int_{-\infty}^{+\infty} dx\ H_m^{(1)}(n_o k r)\mathrm{e}^{im\phi}\mathrm{e}^{\mp i\beta x} \tag{E.34}$$

sur la ligne par une intégrale de contour dans le plan complexe. On procède tout d'abord au changement de variable $\eta \equiv x/y$, puis $\eta \to \mathrm{sign}(y)\eta$:

$$\begin{aligned} I_{3\mp} &= y \int_{-\infty\cdot y/|y|}^{+\infty\cdot y/|y|} d\eta\ H_m^{(1)}(n_o k|y|(1+\eta^2)^{1/2}) \mathrm{e}^{im \arctan 1/\eta} \mathrm{e}^{\mp i\beta y\eta} \\ &= |y| \int_{-\infty}^{+\infty} d\eta\ H_m^{(1)}(n_o k|y|(1+\eta^2)^{1/2}) \mathrm{e}^{im\,\mathrm{sign}(y) \arctan 1/\eta} \mathrm{e}^{\mp i\beta|y|\eta}\ . \end{aligned} \tag{E.35}$$

On pose $\xi \equiv n_o k|y|$ et $\tilde{\xi} \equiv \beta|y|$. D'après le développement réalisé à la section E.1, on a que $\xi < \tilde{\xi}$. De plus, puisque

$$\arctan 1/\eta = \frac{1}{2i} \ln \frac{\eta + i}{\eta - i} \tag{E.36}$$

on a

$$I_{3\mp} = |y| \int_{-\infty}^{+\infty} d\eta\ H_m^{(1)}(\xi(1+\eta^2)^{1/2}) \left(\frac{\eta+i}{\eta-i}\right)^{\mathrm{sign}(y)\frac{m}{2}} \mathrm{e}^{\mp i\tilde{\xi}\eta}\ . \tag{E.37}$$

Le calcul à effectuer est donc

$$I_{4\mp} \equiv \int_{-\infty}^{+\infty} d\eta\ H_m^{(1)}(\xi(1+\eta^2)^{1/2}) \left(\frac{\eta+i}{\eta-i}\right)^{\mathrm{sign}(y)\frac{m}{2}} \mathrm{e}^{\mp i\tilde{\xi}\eta} \quad . \tag{E.38}$$

On remarque dans un premier temps que

$$I_{4\mp} = \int_{-\infty}^{+\infty} d\eta\ H_m^{(1)}(\xi(1+\eta^2)^{1/2}) \left(\frac{\eta-i}{\eta+i}\right)^{\mathrm{sign}(y)\frac{m}{2}} \mathrm{e}^{\pm i\tilde{\xi}\eta}\ , \tag{E.39}$$

une relation qui peut être utile s'il était nécessaire d'inverser la fraction. On définit en ce sens deux fonctions

$$f_\mp(z) = H_m^{(1)}(\xi(1+z^2)^{1/2}) \left(\frac{z+i}{z-i}\right)^{\mathrm{sign}(y)\frac{m}{2}} \mathrm{e}^{\mp i\tilde{\xi}z}\ ,\ z \in \mathbb{C} \tag{E.40}$$

et

$$\tilde{f}_\pm(z) = H_m^{(1)}(\xi(1+z^2)^{1/2}) \left(\frac{z-i}{z+i}\right)^{\mathrm{sign}(y)\frac{m}{2}} \mathrm{e}^{\pm i\tilde{\xi}z}\ ,\ z \in \mathbb{C} \quad . \tag{E.41}$$

Comme ces fonctions possèdent le même comportement sur l'axe réel, on pourra en choisir une plutôt que l'autre si la situation demande une condition de convergence particulière. On pose

$$r_+ \mathrm{e}^{i\theta_+} = z - i \qquad , \qquad r_- \mathrm{e}^{i\theta_-} = z + i$$

(voir Fig. E.8) de sorte que

$$f_\mp(r_+, r_-, \theta_+, \theta_-) = H_m^{(1)}(\xi\sqrt{r_+ r_-}\mathrm{e}^{i\frac{1}{2}(\theta_+ + \theta_-)}) \left(\frac{r_-}{r_+}\right)^{\mathrm{sign}(y)\frac{m}{2}} \mathrm{e}^{i\mathrm{sign}(y)\frac{m}{2}(\theta_- - \theta_+)} \mathrm{e}^{\mp i\tilde{\xi}\left(r_+ \mathrm{e}^{i\theta_+} + i\right)} \quad . \tag{E.42}$$

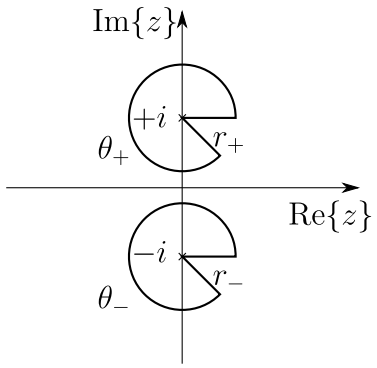


Fig. E.8 Convention des coordonnées polaires locales autour des points $z = \{\pm i\}$.

Une rotation complète autour de $z = +i$ renvoie

$$f_{\mp}(r_+, r_-, \theta_+ + 2\pi, \theta_-) = H_m^{(1)}(\xi\sqrt{r_+ r_-}\mathrm{e}^{i\frac{1}{2}(\theta_+ + \theta_-)}\mathrm{e}^{i\pi})\left(\frac{r_-}{r_+}\right)^{\mathrm{sign}(y)\frac{m}{2}} \times \mathrm{e}^{i\mathrm{sign}(y)\frac{m}{2}(\theta_- - \theta_+)}\mathrm{e}^{-i\mathrm{sign}(y)m\pi}\mathrm{e}^{\mp i\tilde{\xi}\left(r_+\mathrm{e}^{i\theta_+}+i\right)} \quad . \tag{E.43}$$

D'après [1], on a

$$H_m^{(1)}(z\mathrm{e}^{i\pi}) = -\mathrm{e}^{-im\pi}H_m^{(2)}(z) \tag{E.44}$$

et donc $f_{\mp}(z)$ est une fonction multiforme autour de $z = +i$. On montre de la même façon qu'un comportement semblable existe autour de $z = -i$. Les points $z = \{\pm i\}$ sont des *points de branchement* de $f_{\mp}(z)$.

La fonction $\tilde{f}_{\pm}(z)$ possède les mêmes points de branchement.

Lorsque $|m/\xi| \ll r_+ \approx r_- \to R \to \infty$ ($r_+\mathrm{e}^{i\theta_+} \approx r_-\mathrm{e}^{i\theta_-} \to R\mathrm{e}^{i\theta}$), la fonction de Hankel prend la forme asymptotique [50]

$$H^{(1)}(\xi\sqrt{r_+ r_-}\mathrm{e}^{i\frac{1}{2}(\theta_+ + \theta_-)}) \to \left[\sqrt{\frac{2}{\pi R}}\mathrm{e}^{-i\frac{1}{2}\theta}\mathrm{e}^{-im\pi/2 - i\pi/4}\right]\mathrm{e}^{i\xi R\mathrm{e}^{i\theta}} \tag{E.45}$$

de sorte que le régime asymptotique de $f_{\mp}(z)$ est

$$f_{\mp}(z) \sim \mathrm{e}^{i(\xi\mp\tilde{\xi})R\mathrm{e}^{i\theta}} \sim \mathrm{e}^{-(\xi\mp\tilde{\xi})R\sin\theta} \quad . \tag{E.46}$$

Puisque $\tilde{\xi} > \xi$,

- $f_-(z) \to 0$ pour $|z| \to \infty$ lorsque $-\pi < \theta < \quad 0$,
- $f_+(z) \to 0$ pour $|z| \to \infty$ lorsque $\quad 0 < \theta < +\pi$.

La situation est l'opposée pour la fonction $\tilde{f}_{\pm}(z)$:

- $\tilde{f}_-(z) \to 0$ pour $|z| \to \infty$ lorsque $-\pi < \theta < \quad 0$,
- $\tilde{f}_+(z) \to 0$ pour $|z| \to \infty$ lorsque $\quad 0 < \theta < +\pi$.

La forme des parcours retenus pour effectuer l'intégration est présentée aux Figs E.9 et E.10. Notons qu'une coupure a été introduite sur l'axe imaginaire pour uniformiser la fonction. Il reste cependant à obtenir le comportement de $f(z)$ près des points de branchement. On utilise dans ce but le développement des petits arguments de la fonction de Hankel:

$$H_m^{(1)}(\xi\sqrt{r_+r_-}\mathrm{e}^{i\frac{1}{2}(\theta_++\theta_-)}) \sim -i\frac{(|m|-1)!2^{|m|}}{\pi}\frac{1}{(r_+r_-)^{|m|/2}}\mathrm{e}^{-i\frac{|m|}{2}(\theta_++\theta_-)}\times\left\{\begin{array}{ll}1 & m\geq 0\\ (-1)^m & m<0\end{array}\right. . \tag{E.47}$$

On obtient les cas où $f_\mp$ ou $\tilde{f}_\pm$ sont constants autour de $\pm i$ selon chacun des domaines de convergence asymptotique:

- $\mathrm{sign}(y)m > 0$:
  - $f_-(z \to -i) \to -i\frac{(|m|-1)!}{\pi}\mathrm{e}^{+i|m|\pi/2}\mathrm{e}^{-\tilde{\xi}} \times \left\{\begin{array}{ll}1 & m\geq 0\\ (-1)^m & m<0\end{array}\right.$
  - $\tilde{f}_+(z \to +i) \to -i\frac{(|m|-1)!}{\pi}\mathrm{e}^{-i|m|\pi/2}\mathrm{e}^{-\tilde{\xi}} \times \left\{\begin{array}{ll}1 & m\geq 0\\ (-1)^m & m<0\end{array}\right.$

- $\mathrm{sign}(y)m < 0$:
  - $f_+(z \to +i) \to -i\frac{(|m|-1)!}{\pi}\mathrm{e}^{-i|m|\pi/2}\mathrm{e}^{-\tilde{\xi}} \times \left\{\begin{array}{ll}1 & m\geq 0\\ (-1)^m & m<0\end{array}\right.$
  - $\tilde{f}_-(z \to -i) \to -i\frac{(|m|-1)!}{\pi}\mathrm{e}^{+i|m|\pi/2}\mathrm{e}^{-\tilde{\xi}} \times \left\{\begin{array}{ll}1 & m\geq 0\\ (-1)^m & m<0\end{array}\right.$

Considérons le parcours de la Fig. E.9 pour $f_+(z)$ et $\mathrm{sign}(y)m < 0$. D'après le théorème intégrale de Cauchy, on a pour ce parcours

$$\oint = 0 = \int_{C_{R_1}} + \int_{C_{R_2}} + \int_{C_\epsilon} + \int_{C_1} + \int_{C_2} + \int_{\mathbb{R}} \quad . \tag{E.48}$$

Suivant l'analyse asymptotique et le comportement autour de $z = +i$ de $f_+(z)$, on

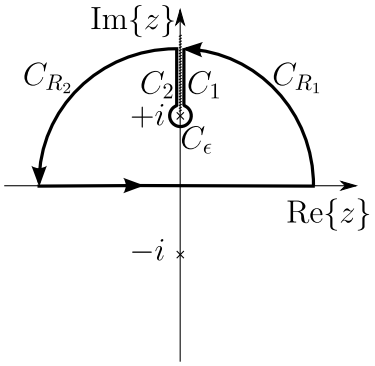


Fig. E.9 Parcours d'intégration pour $f_+(z)$ et $\tilde{f}_+(z)$.

déduit que les trois premières intégrales sont nulles. Reste alors (voir [1], équations 9.1.39 (fonction de Hankel) et 9.6.3 et 9.6.6 (fonction de Bessel modifiée $I_m(z)$))

$$\begin{aligned}
\int_{\mathbb{R}} dz\ f_+(z) &= -\left[\int_{C_1} + \int_{C_2}\right] \\
&= -\left[\ \int_{+i\infty}^{+i} dz\ H_m^{(1)}(\xi\sqrt{1+z^2}) \left(\frac{z+i}{z-i}\right)^{\mathrm{sign}(y)\frac{m}{2}} \mathrm{e}^{+i\tilde{\xi}z}\right. \\
&\qquad \left. + \int_{+i}^{+i\infty} dz\ -H_m^{(2)}(\xi\sqrt{1+z^2}) \left(\frac{z+i}{z-i}\right)^{\mathrm{sign}(y)\frac{m}{2}} \mathrm{e}^{+i\tilde{\xi}z}\right] \\
&= +i\left[\ \int_{+1}^{+\infty} du\ H_m^{(1)}(i\xi\sqrt{u^2-1}) \left(\frac{u-1}{u+1}\right)^{-\mathrm{sign}(y)\frac{m}{2}} \mathrm{e}^{-\tilde{\xi}u}\right. \\
&\qquad \left. + \int_{+1}^{+\infty} du\ H_m^{(2)}(i\xi\sqrt{u^2-1}) \left(\frac{u-1}{u+1}\right)^{-\mathrm{sign}(y)\frac{m}{2}} \mathrm{e}^{-\tilde{\xi}u}\right] \\
&= 2i\int_{+1}^{+\infty} du\ J_m(i\xi\sqrt{u^2-1}) \left(\frac{u-1}{u+1}\right)^{-\mathrm{sign}(y)\frac{m}{2}} \mathrm{e}^{-\tilde{\xi}u} \\
&= 2i\mathrm{e}^{im\pi/2}\int_{+1}^{+\infty} du\ I_m(\xi\sqrt{u^2-1}) \left(\frac{u-1}{u+1}\right)^{-\mathrm{sign}(y)\frac{m}{2}} \mathrm{e}^{-\tilde{\xi}u} \\
&= 2i\mathrm{e}^{im\pi/2}\int_{+1}^{+\infty} du\ I_{-\mathrm{sign}(y)m}(\xi\sqrt{u^2-1}) \left(\frac{u-1}{u+1}\right)^{-\mathrm{sign}(y)\frac{m}{2}} \mathrm{e}^{-\tilde{\xi}u} \qquad \text{(E.49)}
\end{aligned}$$

D'après le résultat 6.646.2 de Gradshteyn et Ryzhik [50], cette dernière intégrale est égale à

$$\int_{\mathbb{R}} dz\ f_+(z) = 2i\mathrm{e}^{+im\pi/2}\frac{\mathrm{e}^{-\sqrt{\tilde{\xi}^2-\xi^2}}}{\sqrt{\tilde{\xi}^2-\xi^2}}\left(\frac{\xi}{\tilde{\xi}+\sqrt{\tilde{\xi}^2-\xi^2}}\right)^{-\mathrm{sign}(y)m} \qquad \text{(E.50)}$$

expression valide pour $\mathrm{sign}(y)m < 0$.

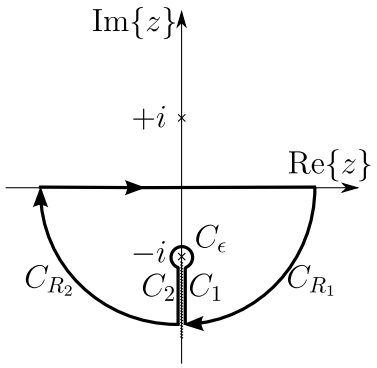


Fig. E.10 Parcours d'intégration pour $f_-(z)$ et $\tilde{f}_-(z)$.

On trouve aussi que pour $\text{sign}(y)m > 0$

$$\int_{\mathbb{R}} dz\ f_-(z) = 2i\mathrm{e}^{-im\pi/2}\frac{\mathrm{e}^{-\sqrt{\tilde{\xi}^2-\xi^2}}}{\sqrt{\tilde{\xi}^2-\xi^2}}\left(\frac{\xi}{\tilde{\xi}+\sqrt{\tilde{\xi}^2-\xi^2}}\right)^{\text{sign}(y)m} \quad . \tag{E.51}$$

E.2.4 Calcul de $\int_{\tilde{x}}^{+\infty} dx\ \mathrm{e}^{-\alpha x}H_m^{(1)}(\kappa x)$ pour $\tilde{x} \gg |m|/\kappa$

On s'intéresse au calcul de

$$I_5 = \int_{\tilde{x}}^{+\infty} dx\ \mathrm{e}^{-\alpha x}H_m^{(1)}(\kappa x) \tag{E.52}$$

pour $\tilde{x} \gg |m|/\kappa$ avec $\alpha > 0$ et $\kappa > 0$.

Le développement asymptotique de la fonction de Hankel $H_m^{(1)}(\kappa x)$ pour $\tilde{x} \gg |m|/\kappa$ s'écrit [1]

$$H_m^{(1)}(\kappa x) \sim \sqrt{\frac{2}{\pi\kappa}}\mathrm{e}^{-i\left(m\frac{\pi}{2}+\frac{\pi}{4}\right)}\left[\frac{1}{x^{1/2}}\mathrm{e}^{i\kappa x} + \left(i\frac{4m^2-1}{8\kappa}\right)\frac{1}{x^{3/2}}\mathrm{e}^{i\kappa x}\right] + \mathcal{O}((\kappa x)^{-5/2}) \tag{E.53}$$

ce qui permet la forme asymptotique de l'intégrale

$$I_5 \sim \sqrt{\frac{2}{\pi\kappa}}\mathrm{e}^{-i\left(m\frac{\pi}{2}+\frac{\pi}{4}\right)}\left[\int_{\tilde{x}}^{+\infty} dx\ x^{-1/2}\mathrm{e}^{-(\alpha-i\kappa)x} + \left(i\frac{4m^2-1}{8\kappa}\right)\int_{\tilde{x}}^{+\infty} dx\ x^{-3/2}\mathrm{e}^{-(\alpha-i\kappa)x}\right] + \epsilon_5(\tilde{x}) \tag{E.54}$$

où

$$\epsilon_5(\tilde{x}) = \sqrt{\frac{2}{\pi\kappa}}\mathrm{e}^{-i\left(m\frac{\pi}{2}+\frac{\pi}{4}\right)}\left(\frac{(4m^2-1)(4m^2-9)}{2(8\kappa)^2}\right)\int_{\tilde{x}}^{+\infty} dx\ x^{-5/2}\mathrm{e}^{-(\alpha-i\kappa)x} \tag{E.55}$$

est le terme d'erreur sur l'intégrale I_5. Le développement de la fonction de Hankel est poussé à un ordre supérieur à 2 afin d'obtenir un terme d'erreur au moins linéairement décroissant. Puisqu'on vérifie par intégration par parties que

$$\begin{aligned}\int_{\tilde{x}}^{+\infty} dx\ x^{-1/2}x^{-n}\mathrm{e}^{-(\alpha-i\kappa)x} &= -\mathrm{e}^{-(\alpha-i\kappa)\tilde{x}}\sum_{j=1}^{n}\left(\prod_{p=1}^{j}\frac{1}{p-n-\frac{1}{2}}\right)(\alpha-i\kappa)^{j-1}\tilde{x}^{j-n-\frac{1}{2}} \\ &\quad + \left(\prod_{j=1}^{n}\frac{1}{j-n-\frac{1}{2}}\right)(\alpha-i\kappa)^{n}\int_{\tilde{x}}^{+\infty} dx\ x^{-1/2}\mathrm{e}^{-(\alpha-i\kappa)x}\end{aligned} \tag{E.56}$$

avec $n \in \mathbb{N}$, on s'attardera à l'intégrale

$$F(\tilde{x}) = \int_{\tilde{x}}^{+\infty} dx\ x^{-1/2}\mathrm{e}^{-(\alpha-i\kappa)x} = 2\int_{\sqrt{\tilde{x}}}^{+\infty} d\eta\ \mathrm{e}^{-(\alpha-i\kappa)\eta^2} \quad . \tag{E.57}$$

Considérons l'intégrale

$$\int_C dz\ \mathrm{e}^{-\mu z^2} \tag{E.58}$$

avec $\arg(\mu) = -\theta_0$, $-\pi < -\theta_0 < 0$ suivant le parcours C présenté à la Fig. E.11.

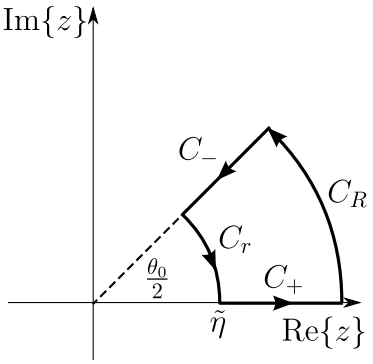


Fig. E.11 Parcours d'intégration C composé des segments droits C_+ et C_- ainsi que des arcs de cercle C_r et C_R d'angle $\theta_0/2$ centrés sur l'origine. On considère C_R dans sa limite à l'infini.

On a donc

$$\oint_C = \int_{C_+} + \int_{C_R} + \int_{C_-} + \int_{C_r} \quad . \tag{E.59}$$

Puisque l'intégrande de (E.58) ne possède pas de pôles à l'intérieur de C, l'intégrale fermée sur C est nulle. Comme $-\pi < -\theta_0 < 0$, l'intégrale sur C_R ne contribue pas non plus, et donc,

$$\int_{\tilde{\eta}}^{+\infty} dz\ \mathrm{e}^{i\mu z^2} = +\int_{\mathrm{e}^{i\theta_0/2}\tilde{\eta}}^{\mathrm{e}^{i\theta_0/2}\cdot\infty} dz\ \mathrm{e}^{-\mu z^2} + \int_{\tilde{\eta}}^{\tilde{\eta}\mathrm{e}^{i\theta_0/2}} dz\ \mathrm{e}^{-\mu z^2} \quad . \tag{E.60}$$

Le changement de variable

$$z \to \mathrm{e}^{-i\frac{\theta_0}{2}}\ z \tag{E.61}$$

dans la première intégrale et

$$z = \mathrm{e}^{+i\frac{\theta}{2}}\ \tilde{\eta} \tag{E.62}$$

dans la seconde renvoie

$$\int_{\tilde{\eta}}^{+\infty} dz\ \mathrm{e}^{i\mu z^2} = \mathrm{e}^{i\theta_0/2}\int_{\tilde{\eta}}^{\infty} dz\ \mathrm{e}^{-|\mu|z^2} + i\frac{\tilde{\eta}}{2}\mathrm{e}^{i\theta_0/2}\int_0^{\theta_0} d\theta\ \exp\left[-i\frac{\theta}{2} - |\mu|\tilde{\eta}^2\mathrm{e}^{-i\theta}\right] \tag{E.63}$$

ou encore

$$\int_{\tilde{\eta}}^{+\infty} dz\ \mathrm{e}^{i\mu z^2} = \mathrm{e}^{i\theta_0/2}\frac{1}{2}\sqrt{\frac{\pi}{|\mu|}}\mathrm{erfc}(\sqrt{|\mu|}\tilde{\eta}) + i\frac{\tilde{\eta}}{2}\mathrm{e}^{i\theta_0/2}\int_0^{\theta_0} d\theta\ \exp\left[-i\frac{\theta}{2} - |\mu|\tilde{\eta}^2\mathrm{e}^{-i\theta}\right] \tag{E.64}$$

avec la fonction d'erreur complémentaire [1]

$$\mathrm{erfc}(z) = \frac{2}{\sqrt{\pi}}\int_z^{\infty} dt\ \mathrm{e}^{-t^2} \quad . \tag{E.65}$$

Si $\tilde{\eta} = \sqrt{\tilde{x}}$, $\mu = \alpha - i\kappa$ et $\theta_0 = \arg(\alpha - i\kappa)$, alors

$$F(\tilde{x}) = \mathrm{e}^{i\theta_0/2}\left[\sqrt{\frac{\pi}{|\alpha - i\kappa|}}\mathrm{erfc}(\sqrt{|\alpha - i\kappa|\tilde{x}}) + i\sqrt{\tilde{x}}\int_0^{\theta_0} d\theta\ \exp\left(-i\frac{\theta}{2} - |\alpha - i\kappa|\tilde{x}\mathrm{e}^{-i\theta}\right)\right] \quad . \tag{E.66}$$

On peut maintenant évaluer l'expression (E.56) pour quelques cas particuliers:

$$\int_{\tilde{x}}^{+\infty} dx\ x^{-3/2}\mathrm{e}^{-(\alpha-i\kappa)x} = 2\tilde{x}^{-1/2}\mathrm{e}^{-(\alpha-i\kappa)\tilde{x}} - 2(\alpha - i\kappa)F(\tilde{x}) \tag{E.67}$$

$$\int_{\tilde{x}}^{+\infty} dx\ x^{-5/2}\mathrm{e}^{-(\alpha-i\kappa)x} = \left[\frac{2}{3}\tilde{x}^{-3/2} - \frac{4}{3}(\alpha - i\kappa)\tilde{x}^{-1/2}\right]\mathrm{e}^{-(\alpha-i\kappa)\tilde{x}} + \frac{4}{3}(\alpha - i\kappa)^2 F(\tilde{x}) \tag{E.68}$$

$$\int_{\tilde{x}}^{+\infty} dx\ x^{-7/2}\mathrm{e}^{-(\alpha-i\kappa)x} = \left[\frac{2}{5}\tilde{x}^{-5/2} - \frac{4}{15}(\alpha - i\kappa)\tilde{x}^{-3/2} + \frac{8}{15}(\alpha - i\kappa)^2\tilde{x}^{-1/2}\right]\mathrm{e}^{-(\alpha-i\kappa)\tilde{x}} - \frac{8}{15}(\alpha - i\kappa)^3 F(\tilde{x}) \quad . \tag{E.69}$$

On obtient ainsi

$$I_5 \sim \sqrt{\frac{2}{\pi\kappa}}\mathrm{e}^{-i\left(m\frac{\pi}{2}+\frac{\pi}{4}\right)}\left[F(\tilde{x}) + i\frac{4m^2-1}{8\kappa}\left(2\tilde{x}^{-1/2}\mathrm{e}^{-(\alpha-i\kappa)\tilde{x}} - 2(\alpha - i\kappa)F(\tilde{x})\right)\right] + \epsilon_5(\tilde{x}) \tag{E.70}$$

et

$$\epsilon_5(\tilde{x}) = \sqrt{\frac{2}{\pi\kappa}}\mathrm{e}^{-i\left(m\frac{\pi}{2}+\frac{\pi}{4}\right)}\left(-\frac{(4m^2-1)(4m^2-9)}{2(8\kappa)^2}\right)\times \left[\left(\frac{2}{3}\tilde{x}^{-3/2} - \frac{4}{3}\tilde{x}^{-1/2}(\alpha - i\kappa)\right)\mathrm{e}^{-(\alpha-i\kappa)\tilde{x}} + \frac{4}{3}(\alpha - i\kappa)^2 F(\tilde{x})\right] \quad . \tag{E.71}$$

De même manière, on peut examiner le comportement asymptotique de

$$I_6 = \int_{\tilde{x}}^{+\infty} dx\ x^{-1}\mathrm{e}^{-\alpha x}H_m^{(1)}(\kappa x) \quad , \tag{E.72}$$

soit

$$\begin{aligned} I_6 \ \sim\ & \sqrt{\frac{2}{\pi\kappa}}\mathrm{e}^{-i\left(m\frac{\pi}{2}+\frac{\pi}{4}\right)}\left\{2\tilde{x}^{-1/2}\mathrm{e}^{-(\alpha-i\kappa)\tilde{x}} - 2(\alpha-i\kappa)F(\tilde{x})\right. \\ & \left. + \left(i\frac{4m^2-1}{8\kappa}\right)\left[\left(\frac{2}{3}\tilde{x}^{-3/2} - \frac{4}{3}\tilde{x}^{-1/2}(\alpha-i\kappa)\right)\mathrm{e}^{-(\alpha-i\kappa)\tilde{x}} + \frac{4}{3}(\alpha-i\kappa)^2F(\tilde{x})\right]\right\} + \epsilon_6(\tilde{x}) \end{aligned} \tag{E.73}$$

avec

$$\begin{aligned} \epsilon_6(\tilde{x}) \ =\ & \sqrt{\frac{2}{\pi\kappa}}\mathrm{e}^{-i\left(m\frac{\pi}{2}+\frac{\pi}{4}\right)}\left(-\frac{(4m^2-1)(4m^2-9)}{2(8\kappa)^2}\right)\times \\ & \left[\left(\frac{2}{5}\tilde{x}^{-5/2} - \frac{4}{15}(\alpha-i\kappa)\tilde{x}^{-3/2} + \frac{8}{15}(\alpha-i\kappa)^2\tilde{x}^{-1/2}\right)\mathrm{e}^{-(\alpha-i\kappa)\tilde{x}} - \frac{8}{15}(\alpha-i\kappa)^3F(\tilde{x})\right] \quad . \end{aligned} \tag{E.74}$$

Les expressions approximatives de $|I_5|/\sqrt{2/(\kappa\pi)}$ et $|I_6|/\sqrt{2/(\kappa\pi)}$ sont maintenant tracées en fonction de $\xi = \kappa\tilde{x}$ pour $\kappa = 1$, $\alpha/\kappa = 0.2$. Le premier terme du membre de droite des expressions (E.70), I_{50}, et (E.73), I_{60}, (trait plein) et le terme d'erreur associé (trait discontinu) sont présentés aux Figs E.12(a)-E.12(d). On remarque que le terme de correction ϵ_5 (ϵ_6) croise la contribution principale I_{50} (I_{60}) plus loin en ξ avec l'augmentation de m. Aussi, la convergence de I_6 est plus lente que I_5. Typiquement, en choisissant $\xi = \kappa\tilde{x} = 8m$ on parvient à obtenir une différence de 10% entre la contribution principale et le terme de correction pour I_{50}. En valeur absolue, la valeur de I_{60} est de quelques ordres de grandeur inférieure à I_{50} pour une même valeur ξ. La correction sur I_{60} est cependant plus importante, 50%, pour $\xi = 8m$.

E.2.5 Calcul de $\int dx'\ \chi(x')\mathrm{e}^{+i2\beta x'}$ pour le disque homogène et la cavité annulaire

Cette dernière sous-section présente le calcul de l'intégrale de $\chi(x)$ pour le disque homogène et la cavité annulaire. On obtient tout d'abord le résultat de l'intégrale

$$I_7(u,v;\ x_0,y_0) = \int_0^R \int_0^{2\pi} drrd\phi\ \mathrm{e}^{iu[y(r,\phi)+y_0]}\mathrm{e}^{iv[x(r,\phi)+x_0]} \tag{E.75}$$

avec u et v des quantités complexes et $(x_0,\ y_0)$ le centre du domaine circulaire. Suivant une représentation en terme d'harmoniques cylindriques [1], on a

$$\begin{aligned} I_7(u,v;\ x_0,y_0) &= \mathrm{e}^{iuy_0}\mathrm{e}^{ivx_0}\int_0^R\int_0^{2\pi} drrd\phi\ \mathrm{e}^{iur\sin\phi}\mathrm{e}^{ivr\cos\phi} \\ &= \mathrm{e}^{iuy_0}\mathrm{e}^{ivx_0}\int_0^R\int_0^{2\pi} drrd\phi\ \sum_{j=-\infty}^{+\infty} J_j(ur)\mathrm{e}^{j\phi}\sum_{j'=-\infty}^{+\infty} i^{j'}J_{j'}(vr)\mathrm{e}^{j'\phi} \\ &= 2\pi\mathrm{e}^{iuy_0}\mathrm{e}^{ivx_0}\int_0^R drr\ \sum_{j=-\infty}^{+\infty} i^{-j}J_j(ur)J_j(vr) \quad . \end{aligned} \tag{E.76}$$

Ensuite, suivant l'identité de Graf [1], on a directement

$$\begin{aligned} I_7(u,v;\ x_0,y_0) &= 2\pi\mathrm{e}^{iuy_0}\mathrm{e}^{ivx_0}\int_0^R drr\ J_0(\sqrt{u^2+v^2}r) \\ &= 2\pi\mathrm{e}^{iuy_0}\mathrm{e}^{ivx_0}\frac{1}{u^2+v^2}\int_0^{\sqrt{u^2+v^2}R} d\rho\rho\ J_0(\rho) \\ &= 2\pi\mathrm{e}^{iuy_0}\mathrm{e}^{ivx_0}\frac{R}{\sqrt{u^2+v^2}}J_1(\sqrt{u^2+v^2}R) \end{aligned} \tag{E.77}$$

où la relation de récurrence $J_1'(z) = J_0(z) - z^{-1}J_1(z)$ a été utilisée [1]. Pour le disque homogène de rayon R_0 et d'indice n_c centré à $(x_0,y_0) = (0, d+R_0)$ dans un milieu d'indice n_o, on a

$$\begin{aligned} \int_{-\infty}^{+\infty} dx'\ \chi(x')\mathrm{e}^{i2\beta x'} &= |A|^2\cos^2\left(\gamma\frac{w}{2}\right)(n_c^2-n_o^2)\int_0^{R_0}\int_0^{2\pi} drrd\phi\ \mathrm{e}^{-2\alpha[y(r,\phi)+(d+R_0)]}\mathrm{e}^{i2\beta x(r,\phi)} \\ &= |A|^2\cos^2\left(\gamma\frac{w}{2}\right)(n_c^2-n_o^2)I_7(i2\alpha,2\beta;\ 0,d+R_0) \\ &= |A|^2\cos^2\left(\gamma\frac{w}{2}\right)(n_c^2-n_o^2)\mathrm{e}^{-2\alpha(R_0+d)}\frac{2\pi R_0}{\xi}J_1(\xi R_0) \quad . \end{aligned} \tag{E.78}$$

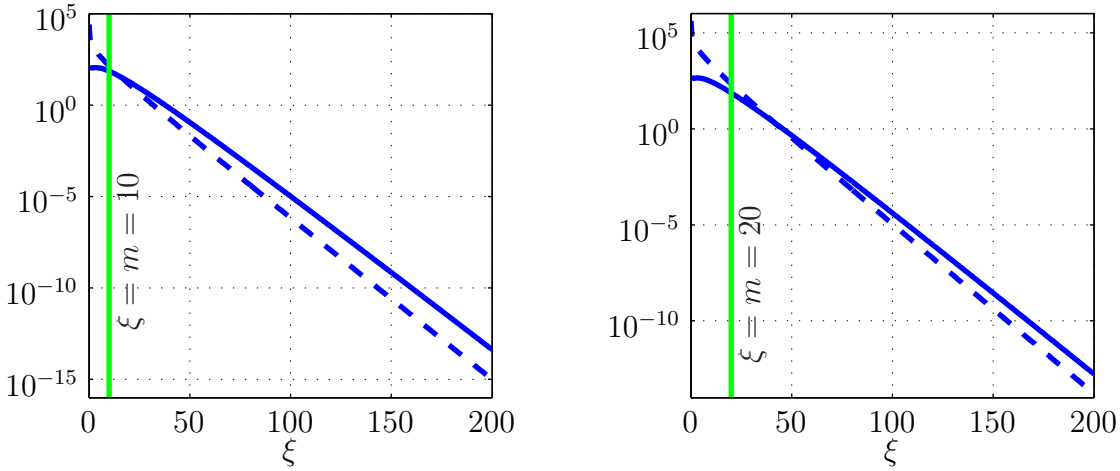
avec $\xi = 2\sqrt{-\alpha^2+\beta^2}$.

Lorsque $\beta = 0$, alors $J_1(\pm iz) = iI_1(\pm z)$, et comme $I_1(\pm z) = \pm I_1(z)$, le choix de la

branche de la racine n'a pas d'importance et le résultat de l'intégrale est réel et positif ($n_c > n_o$). $I_1(z)$ dénote la fonction de Bessel modifiée [1].

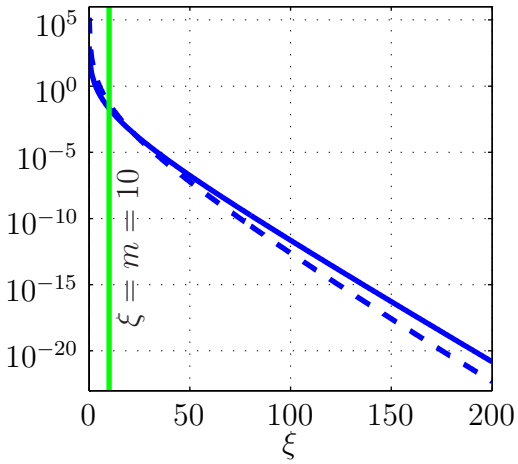
Pour une cavité annulaire dont le défaut circulaire de rayon r_0 et d'indice n_h est situé à (x_h, y_h) (le défaut est inclus à l'intérieur du disque décrit plus haut), on a

$$\begin{aligned}\int_{-\infty}^{+\infty} dx'\ \chi(x')\mathrm{e}^{i2\beta x'} &= |A|^2\cos^2\left(\gamma\frac{w}{2}\right)(n_c^2-n_o^2)2\pi\mathrm{e}^{-2\alpha(R_0+d)}\frac{R_0}{\xi}J_1(\xi R_0)\\ &\quad -|A|^2\cos^2\left(\gamma\frac{w}{2}\right)(n_c^2-n_h^2)2\pi\mathrm{e}^{-2\alpha y_h}\mathrm{e}^{i2\beta x_h}\frac{r_0}{\xi}J_1(\xi r_0)\\ &= |A|^2\cos^2\left(\gamma\frac{w}{2}\right)\frac{2\pi}{\xi}\times\\ &\quad \big[(n_c^2-n_o^2)R_0\mathrm{e}^{-2\alpha(R_0+d)}J_1(\xi R_0)\\ &\quad -(n_c^2-n_h^2)r_0\mathrm{e}^{-2\alpha y_h}\mathrm{e}^{i2\beta x_h}J_1(\xi r_0)\big] \quad . \end{aligned} \tag{E.79}$$

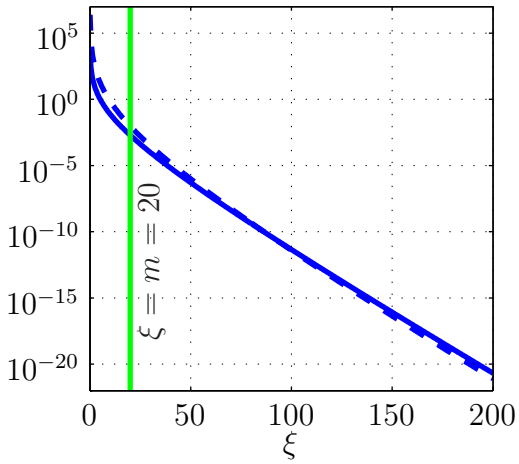


(a) I_{50} et ϵ_5; $m = 10$

(b) I_{50} et ϵ_5; $m = 20$



(c) I_{60} et ϵ_6; $m = 10$



(d) I_{60} et ϵ_6; $m = 20$

Fig. E.12 Convergence de I_5 et I_6 en fonction de $\xi = \kappa\tilde{x}$ pour deux valeurs de m. Les traits bleus continus sont associés à I_{50} et I_{60} alors que les traits bleus discontinus correspondent aux termes correctifs ϵ_5 et ϵ_6. La ligne verte verticale indique la position $\xi = m$.

Annexe F

Fonctions de Green

Cette annexe présente le calcul de la fonction de Green libre de l'équation de Helmholtz 2D, et les différentes fonctions de Green sortantes pour le disque diélectrique homogène. On utilise la propriété de symmétrie de la fonction de Green sous inversion des positions de la source et du point d'observation pour réduire le nombre de cas à considérer pour le disque homogène.

F.1 Fonction de Green libre en 2D

La fonction de Green libre en 2D de l'équation de Helmholtz pour un milieu diélectrique satisfait

$$\nabla^2_{\mathbf{r}} G_0(\mathbf{r}, \mathbf{r}'; k) + n^2 k^2 G_0(\mathbf{r}, \mathbf{r}'; k) = \delta(\mathbf{r} - \mathbf{r}') \tag{F.1}$$

où $\delta(\mathbf{r} - \mathbf{r}')$ agit en tant que point source de courant à $\mathbf{r}'$ et n^2 est la constante diélectrique. Sous transformation de coordonnées, $\mathbf{R} = \mathbf{r} - \mathbf{r}'$, l'équation de Helmholtz devient

$$\nabla^2_{\mathbf{R}} G_0(\mathbf{R}, 0; k) + n^2 k^2 G_0(\mathbf{R}, 0; k) = \delta(\mathbf{R}) \quad . \tag{F.2}$$

On suppose maintenant qu'il soit possible de développer $G_0(\mathbf{R}, 0; k)$ en tant que transformée de Fourier de $\tilde{G}_0(\mathbf{q}, 0; k)$

$$G_0(\mathbf{R}, 0; k) = \frac{1}{(2\pi)^2} \int d^2\mathbf{q} \ \exp\left[-i\mathbf{q} \cdot \mathbf{R}\right] \tilde{G}_0(\mathbf{q}, 0; k) \quad . \tag{F.3}$$

Par conséquent, on a

$$\left(\nabla^2_{\mathbf{R}} + n^2 k^2\right) \int d^2\mathbf{q} \ \exp\left[-i\mathbf{q} \cdot \mathbf{R}\right] \tilde{G}_0(\mathbf{q}, 0; k) = \int d^2\mathbf{q} \ \exp\left[-i\mathbf{q} \cdot \mathbf{R}\right] \ \delta(\mathbf{R}) \tag{F.4}$$

d'où l'on tire

$$\tilde{G_0}(\mathbf{q}, 0; k) = \frac{1}{-\mathbf{q}^2 + n^2k^2}, \tag{F.5}$$

pour la transformée de Fourier de la fonction de Green.

La transformée inverse s'écrit alors

$$\begin{aligned} G_0(\mathbf{R}, 0; k) &= \frac{1}{(2\pi)^2} \int d^2\mathbf{q} \ \exp\left[-i\mathbf{q}\cdot\mathbf{R}\right] \frac{1}{-\mathbf{q}^2 + n^2k^2} \\ &= \frac{1}{(2\pi)^2} \int_0^\infty dq \ \frac{q}{-q^2 + n^2k^2} \int_0^{2\pi} d\theta \ \exp\left[-iqR\cos\theta\right] \quad . \end{aligned} \tag{F.6}$$

D'après l'équation (8.411.1) de [50], l'intégrale sur l'angle polaire est simplement une représentation de la fonction de Bessel $J_0(qR)$. Ainsi,

$$G_0(\mathbf{R}, 0; k) = \frac{1}{2\pi} \int_0^\infty dq \ \frac{qJ_0(qR)}{-q^2 + n^2k^2} \quad . \tag{F.7}$$

L'intégrande est singulier à $q = nk$, de sorte que l'intégrale comme telle soit mal définie. En définissant $i\beta_\epsilon = i(-ink + \epsilon)$ sous la limite $\epsilon \to 0^+$ (la singularité est déplacée de l'axe réel positif vers le premier quadrant du plan complexe), on obtient

$$G_0(\mathbf{R}, 0; k) = \lim_{\epsilon\to 0^+} -\frac{1}{2\pi} \int_0^\infty dq \ \frac{qJ_0(qR)}{q^2 + \beta_\epsilon^2} \quad . \tag{F.8}$$

Selon l'équation (6.532.4) de [50] (sous la condition $\mathrm{Re}\{\beta_\epsilon > 0\}$), l'intégrale (F.8) est la fonction de Bessel modifiée $K_0(\beta_\epsilon R)$. Finalement, suite à l'identité (8.407.1) de [50] ($K_0(z) = i\pi/2 \ H_0^{(1)}(iz), \ -\pi < \arg z \leq \pi/2$) et l'évaluation de la limite, on trouve

$$G_0^+(\mathbf{r}, \mathbf{r}'; k) = -\frac{i}{4} H_0^{(1)}(nk|\mathbf{r} - \mathbf{r}'|). \tag{F.9}$$

Cette solution est définie pour $\epsilon > 0$ et est représentative d'une onde sortante au champ lointain (partant de la source comme origine).

Si $-i\beta_\epsilon = -i(+ink+\epsilon)$ pour $\epsilon \to 0^+$, alors la singularité est déplacée vers le 4e quadrant du plan complexe, mais l'équation (F.8) demeure vraie. Comme $\epsilon > 0$, la solution de l'intégrale demeure la même, mais l'identité entre la fonction de Bessel modifiée et les fonctions de Hankel renvoie plutôt

$$G_0^-(\mathbf{r}, \mathbf{r}'; k) = +\frac{i}{4} H_0^{(2)}(nk|\mathbf{r} - \mathbf{r}'|) \tag{F.10}$$

qui correspond cette fois, au champ lointain, à une onde entrante au "puits" à $\mathbf{r}'$.

F.2 Fonctions de Green du disque homogène

A l'aide de l'identité de Graf [1] pour développer la fonction de Hankel d'ordre 0,

$$H_0^{(1)}(nk|\mathbf{r}-\mathbf{r}'|) = \begin{cases} \sum_{m=-\infty}^{+\infty} J_m(nkr')H_m^{(1)}(nkr)\mathrm{e}^{im(\phi-\phi')} & , \quad r' < r \\ \sum_{m=-\infty}^{+\infty} J_m(nkr)H_m^{(1)}(nkr')\mathrm{e}^{im(\phi'-\phi)} & , \quad r' > r \end{cases} , \tag{F.11}$$

on pourra exprimer la fonction de Green sortante (F.9) dans les différentes régions de l'espace possédant un indice de réfraction constant.

Le système d'intérêt est un disque diélectrique de rayon R_0 et d'indice n_c plongé dans un milieu d'indice n_o. On se rappelle que la source ponctuelle est située en $\mathbf{r}'$. Tout dépendant de la position de cette source (à l'intérieur ou à l'extérieur du disque) et de sa position relative au point d'observation $\mathbf{r}$, six cas différents peuvent être identifiés (Fig. F.1) dont deux seront par contre identiques sous échange simultané de $r \leftrightarrow r'$.

Pour une source localisée à l'intérieur du disque, $r' < R_0$, on aura une fonction de Green intérieure pour $r \leq R_0$

$$G_{cc}(\mathbf{r},\mathbf{r}') = \sum_m a_{cm}\left[J_m(n_c kr')\mathrm{e}^{-im\phi'}\right] J_m(n_c kr)\mathrm{e}^{im\phi} + G_0^+(\mathbf{r},\mathbf{r}') \tag{F.12}$$

et une fonction de Green extérieure pour $r \geq R_0$

$$G_{co}(\mathbf{r},\mathbf{r}') = \sum_m b_{cm}\left[J_m(n_c kr')\mathrm{e}^{-im\phi'}\right] H_m^{(1)}(n_o kr)\mathrm{e}^{im\phi} \quad . \tag{F.13}$$

Pour une source localisée à l'extérieur de la cavité, $r' > R_0$, on aura une fonction de Green intérieure pour $r \leq R_0$

$$G_{oc}(\mathbf{r},\mathbf{r}') = \sum_m a_{om}\left[H_m^{(1)}(n_o kr')\mathrm{e}^{-im\phi'}\right] J_m(n_c kr)\mathrm{e}^{im\phi} \tag{F.14}$$

et une fonction de Green extérieure pour $r \geq R_0$

$$G_{oo}(\mathbf{r},\mathbf{r}') = \sum_m b_{om}\left[H_m^{(1)}(n_o kr')\mathrm{e}^{-im\phi'}\right] H_m^{(1)}(n_o kr)\mathrm{e}^{im\phi} + G_0^+(\mathbf{r},\mathbf{r}'). \tag{F.15}$$

Puisque de façon tout à fait générale [116], les fonctions de Green $G(\mathbf{r},\mathbf{r}')$ seront symétriques sous interchange de $\mathbf{r} \leftrightarrow \mathbf{r}'$, en autant que $\mathbf{r}$ et $\mathbf{r}'$ sont dans les mêmes

régions de l'espace, on s'attend donc que $G_{cc}(\mathbf{r},\mathbf{r}') = G_{cc}(\mathbf{r}',\mathbf{r})$ et $G_{oo}(\mathbf{r},\mathbf{r}') = G_{oo}(\mathbf{r}',\mathbf{r})$. Ceci élimine, tel que mentionné, 2 cas de positions relatives de la source et du point d'observation, i.e. les cas $r < r'$ et $r > r'$ mènent à des expressions identiques pour $r \leq R_0$ et $r \geq R_0$ respectivement. De plus, l'échange de la source et du point d'observation doit mener au même résultat physique pour une source et un point d'observation situés de part et d'autre de la frontière du disque, i.e. que $G_{co}(\mathbf{r},\mathbf{r}') = G_{oc}(\mathbf{r}',\mathbf{r})$. Ces conditions imposent nécessairement des relations entre les coefficients des développements (F.12-F.15). On vérifiera explicitement qu'il en est bien ainsi une fois les expressions des coefficients obtenues.

Les coefficients $\{a_{c,om}\}$ et $\{b_{c,om}\}$ sont obtenus par l'application des conditions aux frontières habituelles. Pour la polarisation TM (continuité de la fonction et de sa première dérivée) et pour $r' < R_0$, on obtient directement [1]

$$\text{(TM)} \quad a_{cm} = -\frac{1}{4i}\left[\frac{n_c H_m^{(1)}(Z_o) H_m^{(1)'}(Z_c) - n_o H_m^{(1)'}(Z_o) H_m^{(1)}(Z_c)}{n_c H_m^{(1)}(Z_o) J'_m(Z_c) - n_o H_m^{(1)'}(Z_o) J_m(Z_c)}\right] \tag{F.16}$$

$$\text{(TM)} \quad b_{cm} = +\frac{1}{4i}\left[\frac{n_c H_m^{(1)}(Z_c) J'_m(Z_c) - n_c H_m^{(1)'}(Z_c) J_m(Z_c)}{n_c H_m^{(1)}(Z_o) J'_m(Z_c) - n_o H_m^{(1)'}(Z_o) J_m(Z_c)}\right] \tag{F.17}$$

$$= -\frac{1}{2\pi k R_0}\left[\frac{1}{n_c H_m^{(1)}(Z_o) J'_m(Z_c) - n_o H_m^{(1)'}(Z_o) J_m(Z_c)}\right] \tag{F.18}$$

alors que pour $r' > R_0$, on a

$$\text{(TM)} \quad a_{om} = +\frac{1}{4i}\left[\frac{n_o H_m^{(1)}(Z_o) J'_m(Z_o) - n_o H_m^{(1)'}(Z_o) J_m(Z_o)}{n_c H_m^{(1)}(Z_o) J'_m(Z_c) - n_o H_m^{(1)'}(Z_o) J_m(Z_c)}\right] \tag{F.19}$$

$$= -\frac{1}{2\pi k R_0}\left[\frac{1}{n_c H_m^{(1)}(Z_o) J'_m(Z_c) - n_o H_m^{(1)'}(Z_o) J_m(Z_c)}\right] \tag{F.20}$$

$$\text{(TM)} \quad b_{om} = -\frac{1}{4i}\left[\frac{n_c J_m(Z_o) J'_m(Z_c) - n_o J_m(Z_c) J'_m(Z_o)}{n_c H_m^{(1)}(Z_o) J'_m(Z_c) - n_o H_m^{(1)'}(Z_o) J_m(Z_c)}\right] \tag{F.21}$$

avec $Z_c = n_c k R_0$, $Z_o = n_o k R_0$.

Pour la polarisation TE (continuité de la fonction et de sa dérivée normale pondérée

[1] Le Wronskien suivant est utile lors des simplifications

$$W[H_m^{(1)}(z), J_m(z)] = iW[Y_m(z), J_m(z)] = -\frac{2i}{\pi z} \quad .$$

par l'indice de réfraction) et pour $r' < R_0$, on obtient de même manière

$$\text{(TE)} \quad a_{cm} = -\frac{1}{4i}\left[\frac{n_c^{-1}H_m^{(1)}(Z_o)H_m^{(1)'}(Z_c) - n_o^{-1}H_m^{(1)'}(Z_o)H_m^{(1)}(Z_c)}{n_c^{-1}H_m^{(1)}(Z_o)J'_m(Z_c) - n_o^{-1}H_m^{(1)'}(Z_o)J_m(Z_c)}\right] \tag{F.22}$$

$$\text{(TE)} \quad b_{cm} = +\frac{1}{4i}\left[\frac{n_c^{-1}H_m^{(1)}(Z_c)J'_m(Z_c) - n_c^{-1}H_m^{(1)'}(Z_c)J_m(Z_c)}{n_c^{-1}H_m^{(1)}(Z_o)J'_m(Z_c) - n_o^{-1}H_m^{(1)'}(Z_o)J_m(Z_c)}\right] \tag{F.23}$$

$$= -\frac{1}{2\pi n_c^2 k R_0}\left[\frac{1}{n_c^{-1}H_m^{(1)}(Z_o)J'_m(Z_c) - n_o^{-1}H_m^{(1)'}(Z_o)J_m(Z_c)}\right] \tag{F.24}$$

alors que pour $r' > R_0$, on a

$$\text{(TE)} \quad a_{om} = +\frac{1}{4i}\left[\frac{n_o^{-1}H_m^{(1)}(Z_o)J'_m(Z_o) - n_o^{-1}H_m^{(1)'}(Z_o)J_m(Z_o)}{n_c^{-1}H_m^{(1)}(Z_o)J'_m(Z_c) - n_o^{-1}H_m^{(1)'}(Z_o)J_m(Z_c)}\right] \tag{F.25}$$

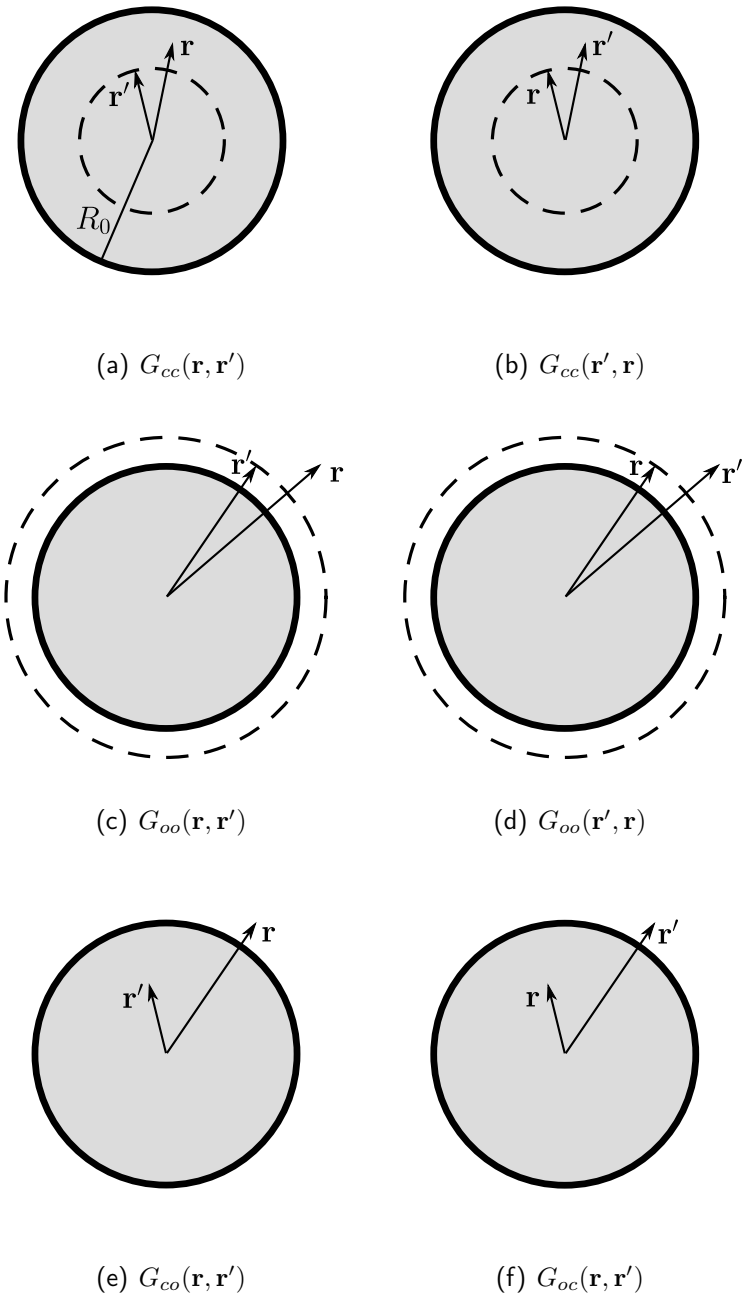
$$= -\frac{1}{2\pi n_o^2 k R_0}\left[\frac{1}{n_c^{-1}H_m^{(1)}(Z_o)J'_m(Z_c) - n_o^{-1}H_m^{(1)'}(Z_o)J_m(Z_c)}\right] \tag{F.26}$$

$$\text{(TE)} \quad b_{om} = -\frac{1}{4i}\left[\frac{n_c^{-1}J_m(Z_o)J'_m(Z_c) - n_o^{-1}J_m(Z_c)J'_m(Z_o)}{n_c^{-1}H_m^{(1)}(Z_o)J'_m(Z_c) - n_o^{-1}H_m^{(1)'}(Z_o)J_m(Z_c)}\right] \quad . \tag{F.27}$$

Grâce aux relations

$$H_m^{(1)}(z) = (-1)^m H_{-m}^{(1)}(z) \qquad \text{et} \qquad J_m(z) = (-1)^m J_{-m}(z), \tag{F.28}$$

on conclut d'abord que $a_{c,om} = a_{c,o-m}$ et $b_{c,om} = b_{c,o-m}$, et ensuite que les relations de symétrie énoncées plus haut pour les fonctions de Green sont bien respectées. Finalement, la relation de réciprocité $G_{co}(\mathbf{r}, \mathbf{r}') = G_{oc}(\mathbf{r}', \mathbf{r})$ est aussi satisfaite puisque $b_{cm} = a_{om}$.



(a) $G_{cc}(\mathbf{r}, \mathbf{r}')$ (b) $G_{cc}(\mathbf{r}', \mathbf{r})$

(c) $G_{oo}(\mathbf{r}, \mathbf{r}')$ (d) $G_{oo}(\mathbf{r}', \mathbf{r})$

(e) $G_{co}(\mathbf{r}, \mathbf{r}')$ (f) $G_{oc}(\mathbf{r}, \mathbf{r}')$

Fig. F.1 Représentation des positions de la source $\mathbf{r}'$ et du point d'observation $\mathbf{r}$ des six cas de fonction de Green pour le disque homogène (disque gris). Sous échange des positions $\mathbf{r}$ et $\mathbf{r}'$, les situations présentées aux figures (a) et (b), et (c) et (d) sont équivalentes pour les fonctions de Green. La même équivalence peut être établie entre $G_{co}(\mathbf{r}, \mathbf{r}')$, (e), et $G_{oc}(\mathbf{r}, \mathbf{r}')$, (f).

Bibliography

[1] M. Abramowitz and I. A. Stegun, *Handbook of Mathematical Functions*, Dover, 1964.

[2] W. Ahn, S. V. Boriskina, Y. Hong, and B. M. Reinhard, *Photonic plasmonic mode coupling in on-chip integrated optoplasmonic molecules*, ACS Nano **6** (2012), 951–960.

[3] E. G. Altmann, *Emission from dielectric cavities in terms of invariant sets of the chaotic ray dynamics*, Phys. Rev. A **79** (2009), 013830 (1–9).

[4] E. G. Altmann, A. E. Motter, and H. Kantz, *Stickiness in Hamiltonian systems: From sharply divided to hierarchical phase space*, Phys. Rev. E **73** (2006), 026207 (1–10).

[5] G. B. Arfken, H. J. Weber, and F. Harris, *Mathematical Methods for Physicists*, Academic Press, 2000.

[6] S. Arnold, D. Keng, S. I. Shopova, S. Holler, W. Zurawsky, and F Vollmer, *Whispering gallery mode carousel - a photonic mechanism for enhanced nanoparticle detection in biosensing*, Opt. Express **17** (2009), 6230–6238.

[7] S. Arnold, M. Noto, and F. Vollmer, *Consequences of extreme photon confinement in micro-cavities: Ultra-sensitive detection of perturbations by bio-molecules*, Frontiers of Optical Spectroscopy (B. Di Bartolo and O. Forte, eds.), 2005, pp. 337–357.

[8] Various authors, *Integrated optics: From single photon sources to complex photonic circuits*, Laser & Photon. Rev **6** (2012), 1–143.

[9] V. M. Babič and V. S. Buldyrev, *Short-Wavelength Diffraction Theory: Asymptotic Methods*, Springer, 1991.

[10] A. Bäcker, S. Fürsberger, and R. Schubert, *Poincaré Husimi representation of eigenstates in quantum billiards*, Phys. Rev. E **70** (2004), 036204 (1–10).

[11] A. Bäcker, R. Ketzmerick, S. Löck, M. Robnik, G. Vidmar, R. Höhmann, U. Kuhl, and H.-J. Stöckmann, *Dynamical tunneling in mushroom billiards*, Phys. Rev. Lett. **100** (2008), 174103 (1–4).

[12] A. Bäcker, R. Ketzmerick, S. Löck, and L. Schilling, *Regular-to-chaotic tunneling rates using a fictitious integrable system*, Phys. Rev. Lett. **100** (2008), 104101 (1–4).

[13] A. Bäcker, R. Ketzmerick, S. Löck, J. Wiersig, and M. Hentschel, *Quality factors and dynamical tunneling in annular microcavities*, Phys. Rev. A **79** (2009), 063804 (1–6).

[14] M. V. Berry, *Regularity and chaos in classical mechanics, illustrated by three deformations of circular 'billiard'*, Eur. J. Phys. **2** (1981), 91–102.

[15] R. Bhatia, *Graduate Texts in Graduate Mathematics: Matrix Analysis*, Springer, 1996.

[16] G. D. Birkhoff, *On the periodic motions of dynamical systems*, Acta Math. **50** (1927), 359–379.

[17] S. Bittner, E. Bogomolny, B. Dietz, M. Miski-Oglu, P. Oria Iriarte, A. Richter, , and F. Schäfer, *Experimental test of a trace formula for two-dimensional dielectric resonators*, Phys. Rev. E **81** (2010), 066215 (1–12).

[18] S. Bittner, E. Bogomolny, B. Dietz, M. Miski-Oglu, and A. Richter, *Application of a trace formula to the spectra of flat three-dimensional dielectric resonators*, Phys. Rev. E **85** (2012), 026203 (1–12).

[19] S. Bittner, B. Dietz, M. Miski-Oglu, P. Oria Iriarte, A. Richter, and F. Schäfer, *Experimental test of a two-dimensional approximation for dielectric microcavities*, Phys. Rev. A **80** (2009), 023825 (1–9).

[20] R. Blümel and W. P. Reinhardt, *Chaos in Atomic Physics*, Cambridge University Press, 1997.

[21] E. Bogomolny, R. Dubertrand, and C. Schmit, *Trace formula for dielectric cavities: General properties*, Phys. Rev. E **78** (2008), 056202 (1–14).

[22] S. Boriskina, T. M. Benson, P. Sewell, and A. I. Nosich, *Tuning of elliptic whispering-gallery-mode microdisk waveguide filters*, J. Light. Tech. **21** (2003), 1987–1995.

[23] S. V. Boriskina, T. M. Benson, P. Sewell, and A. I. Nosich, *Effect of a layered environment on the complex natural frequencies of two-dimensional WGM dielectric-ring resonators*, J. Lightwave Tech. **20** (2002), 1563–1572.

[24] J. P. Boyd, *Chebyshev and Fourier Spectral Methods*, Dover, 2000.

[25] L. A. Bunimovich, *On the ergodic properties of nowhere dispersing billiards*, Comm. Math. Phys. **65** (1979), 295–312.

[26] C. A. A. de Carvalho and H. M. Nussenzveig, *Time Delay*, Phys. Rep. **364** (2002), 83–174.

[27] R. K. Chang and A. J. Campillo, *Optical Processes in Microcavities*, World Scientific, Singapore, 1996.

[28] S. J. Chapman, J. M. H. Lawry, J. R. Ockendon, and R. H. Tewz, *On the Theory of Complex Rays*, SIAM Review **41** (1999), 417–509.

[29] D. K. Cheng, *Field and Wave Electromagnetics*, Addison-Wesley, 1992.

[30] A. Chiasera, Y. Dumeige, P. Féron, M. Ferrari, Y. Jestin, G. N. Conti, S. Pelli, S. Soria, and G. C. Righini, *Spherical Whispering-Gallery-Mode Microresonators*, Laser & Photon. Rev **64** (2010), 457–482.

[31] Y. D. Chong, L. Ge, and A. D. Stone, PT*-symmetry breaking and laser-absorber modes in optical scattering systems*, Phys. Rev. Lett. **106** (2011), 093901 (1–4).

[32] I. D. Chremmos and N. K. Uzunoglu, *Transmission and radiation in a slab waveguide coupled to a whispering-gallery resonator: volume-integral-equation analysis*, J. Opt. Soc. Am. A **21** (2004), 839–846.

[33] K. M. Christoffel and P. Brumer, *Quantum and classical dynamics in the stadium billiard*, Phys. Rev. A **33** (1986), 1309–1321.

[34] G. Cincotti, F. Gori, and M. Santarsiero, *Plane wave expansion of cylindrical functions*, Opt. Comm. **95** (1993), 192–198.

[35] L. Cohen, *Generalized phase-space distribution functions*, J. Math. Phys **7** (1966), 781–787.

[36] C. Cohen-Tannoudji, B. Diu, and F. Laloe, *Mécanique Quantique*, Hermann, 1998.

[37] COMSOLAB, *COMSOL Multiphysics User's Guide v3.2*, COMSOLAB, 2005.

[38] C. P. Dettmann, G. V. Morozov, M. Sieber, and H. Waalkens, *Directional emission from an optical microdisk resonator with a point scatterer*, Europhys. Lett. **82** (2008), 34002 (1–5).

[39] ———, *Unidirectional emission from circular dielectric microresonators with a point scatterer*, Phys. Rev. A **80** (2009), 063813 (1–11).

[40] N. Djellali, I. Gozhyk, D. Owens, S. Ozenko, M. Lebental, J. Lautru, C. Ulysse, B. Kippelen, and J. Zyss, *Controlling the directional emission of holey organic microlasers*, Appl. Phys. Lett. **95** (2009), 101108 (1–3).

[41] R. Dubertrand, E. Bogomolny, N. Djellali, M. Lebental, and C. Schmit, *Circular dielectric cavity and its deformation*, Phys. Rev. A **77** (2008), 013804 (1–16).

[42] S.M. Dutra and G. Nienhuis, *What Is a Quantized Mode of a Leaky Cavity?*, Springer Berlin Heidelberg, 2001, pp. 338–354.

[43] X. Fan, I. M. White, S. I. Shopova, H. Zhu, J. D. Suter, and Y. Sun, *Sensitive optical biosensors for unlabeled targets: A review*, Anal. Chimica Acta **620** (2008), 8–26.

[44] D. S. L. Figueira and Frateschi N. C., *Evidences of the simultaneous presence of bow-tie and diamond scars in rare-earth doped amorphous silicon microstadium resonators*, J. Appl. Phys. **103** (2008), 063106 (1–4).

[45] S. Frischat and E. Doron, *Dynamical tunneling in mixed systems*, Phys. Rev. E **57** (1998), 1421–1443.

[46] T. Fukushima, T. Harayama, and J. Wiersig, *Ray-wave correspondence in an unstable quasistadium laser resonator*, Phys. Rev. A **73** (2006), 023816 (1–4).

[47] T. Fukushima, T. Tanaka, and T. Harayama, *Unidirectional beam emission from strained InGaAsP multiple-quantum-well quasistadium laser diodes*, Appl. Phys. Lett. **86** (2005), 171103 (1–3).

[48] U. Gerland, *Spectral statistics and dynamical localization: Sharp transition in a generalized Sinai billiard*, Phys. Rev. Lett. **83** (1999), 1139–1142.

[49] M. I. Gorodetsky and V. S. Ilchenko, *Optical microsphere resonators: optimal coupling to high-Q whispering-gallery modes*, J. Opt. Soc. Am. B **16** (1999), 147–154.

[50] I. S. Gradshteyn and J. M. Ryzhik, *Table of Integrals, Series, and Products*, Academic Press, 1993.

[51] M. C. Gutzwiller, *Chaos in Classical and Quantum Mechanics*, Springer, 1990.

[52] F. Haake, *Quantum Signatures of Chaos*, Springer, 2010.

[53] G. Hackenbroich and J. U. Nöckel, *Dynamical tunneling in optical cavities*, Europhys. Lett. **39** (1997), 371–376.

[54] T. Harayama, P. Davis, and K. S. Ikeda, *Whispering gallery mode lasers*, Prog. Theo. Phys. Supp. **139** (2000), 363–374.

[55] T. Harayama and Shinohara, *Designing coupled microcavity lasers for high-Q modes with unidirectional light emission*, Opt. Lett. **36** (2011), 1116–1118.

[56] T. Harayama and S. Shinohara, *Two-dimensional microcavity lasers*, Laser Photonics Rev. **5** (2011), 247–271.

[57] A. U. Hazi, *Behaviour of the eigenphase sum near a resonance*, Phys. Rev. A **19** (1979), 920–922.

[58] E. Hecht, *Optics*, Addison-Wesley, 2001.

[59] E. J. Heller, *Bound-state eigenfunctions of classically chaotic Hamiltonian systems: Scars of periodic orbits*, Phys. Rev. Lett. **53** (1984), 1515–1518.

[60] M. Hentschel and K. Richter, *Quantum chaos in optical systems: The annular billiard*, Phys. Rev. E **66** (2002), 056207 (1–13).

[61] M. Hentschel and H. Schomerus, *Fresnel laws at curved dielectric interfaces of microresonators*, Phys. Rev. E **65** (2002), 045603 (1–4).

[62] M. Hentschel, H. Schomerus, and R. Schubert, *Husimi functions at dielectric interfaces: Inside-outside duality for optical systems and beyond*, Europhys. Lett. **62** (2003), 636–642.

[63] M. Hillery, R. F. O'Connell, M. O. Scully, and E. P. Wigner, *Distribution functions in Physics: Fundamentals*, Phys. Rep. **106** (1984), 121–167.

[64] H.-S. Hsu, C. Cai, and A. M. Armani, *Ultra-low-threshold Er:Yb sol-gel microlaser on silicon*, Opt. Express **17** (2009), 23265–23271.

[65] K. F. Huang, Y. F. Chen, H. C. Lai, and Y. P. Lan, *Observation of the wave function of a quantum billiard from the transverse patterns of vertical cavity surface emitting lasers*, Phys. Rev. Lett. **89** (2002), 224102 (1–4).

[66] John D. Jackson, *Classical electrodynamics*, third edition ed., Wiley, 1998.

[67] B. R. Johnson, *Theory of morphology-dependent resonances: Shape resonances and width formulas*, J. Opt. Soc. Am. A **10** (1993), 343–352.

[68] J. B. Keller and S. I. Rubinow, *Asymptotic solution of eigenvalue problems*, Ann. Phys **9** (1960), 24–75.

[69] Joseph B. Keller, *Rays, waves and asymptotics*, Bull. Amer. Math. Soc. **84** (1978), 727–750.

[70] M. G. Krein, *On perturbation determinants and the trace formula*, Dokl. Akad. Nauk. SSSR Sr. Mat. **144** (1962), 268.

[71] M. Kuznetsov, *VECSEL Semiconductor Lasers: A Path to High-Power, Quality Beam and UV to IR Wavelength by Design, in Semiconductor Disk Lasers: Physics and Technology*, Wiley-VCH Verlag GmbH & Co. KGaA, 2010.

[72] K.-J. Langenberg, R. Marklein, and K. Mayer, *Ultrasonic Nondestructive Testing of Materials: Theoretical Foundations*, CRC Press, 2012.

[73] H.-W. Lee, *Theory and application of the quantum phase-space distribution functions*, Phys. Rep. **259** (1995), 147–211.

[74] J. Lee, S. Rim, J. Cho, and C.-M. Kim, *Unidirectional resonance modes supported by secondary islands in a microcavity comprised of two half-ellipses*, Phys. Rev. A **83** (2011), 033815 (1–4).

[75] S. B. Lee, J. H. Lee, J. S. Yang, H. J. Moon, S. W. Kim, and K. An, *Observation of scared modes in an asymmetrically deformed microcylinder lasers*, Phys. Rev. Lett. **88** (2002), 033903 (1–4).

[76] S. Y. Lee, M. S. Kurdoglyan, S. Rim, and C. M. Kim, *Resonance patterns in a stadium-shaped microcavity*, Phys. Rev. A **70** (2004), 023809 (1–8).

[77] S. Y. Lee, S. Rim, J. W. Ryu, T. Y. Kwon, M. Choi, and C. M. Kim, *Quasiscarred resonances in a spiral-shaped microcavity*, Phys. Rev. Lett. **93** (2004), 164102 (1–4).

[78] Q. Ma, T. Rossmann, and Z. Guo, *Whispering-gallery mode silica microsensors for cryogenic to room temperature measurement*, Meas. Sci. Technol. **21** (2010), 025310 (1–7).

[79] H. Makino, T. Harayama, and Y. Aizawa, *Effects of bifurcations on the energy level statistics for oval billiards*, Phys. Rev. E **59** (1999), 4026–4035.

[80] S. Mandal, J. M. Goddard, and D. Erickson, *A multiplexed optofluidic biomolecular sensor for low mass detection*, Lab on a Chip **9** (2009), 2924–2932.

[81] C. Manolatou, M. J. Khan, S. Fan, P. R. Villeneuve, H. A. Haus, and J. D. Joannopoulos, *Coupling of modes analysis of resonant channel add-drop filters*, IEEE J. Quantum Electronics **35** (1999), 1322–1331.

[82] L. Marchildon, *Mécanique Quantique*, De Boeck, 2000.

[83] S.W. McDonald and A.N. Kaufman, *Spectrum of eigenfunctions for a Hamiltonian with stochastic trajectories*, Phys. Rev. Lett. **42** (1979), 1189–1191.

[84] ———, *Wave chaos in the stadium: Statistical properties of short-wave solutions of the Helmholtz equation*, Phys. Rev. A **37** (1988), 3067–3086.

[85] C. D. Meyer, *Matrix Analysis and Applied Linear Algebra. Book and Solutions Manual*, SIAM: Society for Industrial and Applied Mathematics, 2001.

[86] N. Morita, *Scattering and mode conversion of guided modes of a slab waveguide by a circular cylinder*, IEEE Proc. **127** (1980), 263–269.

[87] M. E. Motamedi, *MOEMS: Micro-Opto-Electro-Mechanical Systems*, SPIE, 2005.

[88] R. G. Newton, *Scattering Theory of Waves and Particles (2nd edition)*, Springer Verlag, 1982.

[89] J. U. Nöckel, *Resonances in nonintegrable open systems*, Ph.D. thesis, Yale University, 1997.

[90] J. U. Nöckel and A. D. Stone, *Chaotic light: A theory of asymmetric resonant cavities*, Optical Processes in Microcavities (R. K. Chang and A. J. Campillo, eds.), World Scientific, Singapore, 1996.

[91] J. U. Nöckel, A. D. Stone, G. Chen, H. L. Grossman, and R. K. Chang, *Directional emission from asymmetric resonant cavities*, Opt. Lett.. **21** (1996), 1609–1611.

[92] K. Okamoto, *Fundamentals of Optical Waveguides*, Academic Press, 2006.

[93] E. Ott, *Chaos in Dynamical Systems*, Cambridge University Press, 1993.

[94] G. Painchaud-April and L. J. Dubé, *Scattering Description of the Resonant Modes of Open 2D Dielectric Cavities*, 2nd International Workshop on Microcavities and their Applications (WOMA 2011), 2011.

[95] G. Painchaud-April, J. Dumont, D. Gagnon, and L. J. Dubé, *S and Q matrices reloaded: Applications to open, inhomogeneous, and complex cavities*, Transparent Optical Networks (ICTON), 2013 15th International Conference on, 2013, pp. 1–4.

[96] ———, *S and Q Matrices Reloaded: Applications to open, inhomogeneous, and complex cavities*, 15th International Conference on Transparent Optical Networks, 2013.

[97] G. Painchaud-April, J. Poirier, and L. J. Dubé, *Transport Mechanisms in Dielectric Optical Microcavities*, 63rd Canadian Association of Physicists Annual Congress, 2008.

[98] ———, *Controlling Transport Properties in Dielectric Billiards*, 10th SIAM Conference on Applications of Dynamical Systems, 2009.

[99] ———, *Phase Space as an Optical Engineering Tool in Open Microcavity Designs*, 10th SIAM Conference on Applications of Dynamical Systems, 2009.

[100] G. Painchaud-April, J. Poirier, D. Gagnon, and L. J. Dubé, *Phase Space Engineering in Optical Microcavities I: Preserving near-field uniformity while inducing far-field directionality*, 12th International Conference on Transparent Optical Networks, 2010.

[101] G. Painchaud-April, J. Poirier, D. Gagnon, and L.J. Dubé, *Phase space engineering in optical microcavities I: Preserving near-field uniformity while inducing far-field directionality*, Transparent Optical Networks (ICTON), 2010 12th International Conference on, 2010, pp. 1–4.

[102] G. Painchaud-April, J. Poirier, S. Saïdi, Y-A. Peter, E. Brasselet, and L. J. Dubé, *Highly Directional Emission from Inhomogeneous Dielectric Microcavities*, 63rd Canadian Association of Physicists Annual Congress, 2008.

[103] G. Painchaud-April, J. Poirier, P-Y. St-Louis, J. Lépine, S. Saïdi, and L. J. Dubé, *Wave Chaos in a New Class of Optical Microcavity*, 9th SIAM Conference on Applications of Dynamical Systems, 2007.

[104] R. Paschotta, *Encyclopedia of Laser Physics and Technology*, Wiley, 2008.

[105] J. Poirier, G. Painchaud-April, D. Gagnon, and L. J. Dubé, *Phase Space Engineering in Optical Microcavities II: Controlling the far-field*, 12th International Conference on Transparent Optical Networks, 2010.

[106] J. Poirier, G. Painchaud-April, D. Gagnon, and L.J. Dube, *Phase space engineering in optical microcavities II. controlling the far-field*, Transparent Optical Networks (ICTON), 2010 12th International Conference on, 2010, pp. 1–4.

[107] W. H. Press, S. A. Teukolsky, W. T. Vetterling, and B. P. Flannery, *Numerical Recipes 3rd edition: The Art of Scientific Computing*, Cambridge University Press, 2007.

[108] T. Prosen, *Berry-Robnik level statistics in a smooth billiard system*, J. Phys. A **31** (1998), 7023–7029.

[109] J. Ptasinski, S. W. Kim, L. Pang, I.-C. Khoo, and Y. Fainman, *Optical tuning of silicon photonic structures with nematic liquid crystal claddings*, Opt. Lett. **38** (2013), 2008–2010.

[110] H. Quan and Z. Guo, *Simulation of whispering-gallery-mode resonance shifts for optical miniature biosensors*, J. Quant. Spec. Rad. Transfer **93** (2005), 231–243.

[111] A. I. Rahachou and I. V. Zozoulenko, *Effects of boundary roughness on a Q factor of whispering-gallery-mode lasing microdisk cavities*, J. Appl. Phys. **94** (2003), 7929–7931.

[112] ———, *Elastic scattering of surface electron waves in quantum corrals: Importance of the shape of the adatom potential*, Phys. Rev. B **70** (2004), 233409 (1–4).

[113] ———, *Scattering matrix approach to the resonant states and Q values of microdisk lasing cavities*, Appl. Opt **43** (2004), 1761–1772.

[114] H.-C. Ren, F. Vollmer, S. Arnold, and A. Libchaber, *High-Q microsphere biosensor - analysis from absorption of rodlike bacteria*, Opt. Express **15** (2007), 17410–17423.

[115] N. B. Rex, H. E. Tureci, H. G. L. Schwefel, R. K. Chang, and A. D. Stone, *Fresnel filtering in lasing emission from scarred modes of wave-chaotic optical resonators*, Phys. Rev. Lett. **88** (2002), 094102 (1–4).

[116] L. S. Rodberg and R. M. Thaler, *Introduction to the Quantum Theory of Scattering*, Academic Press, 1967.

[117] I. Rotter, *A continuum shell model for the open quantum mechanical nuclear system*, Rep. Prog. Phys. **54** (1991), 635–682.

[118] S. Rotter, P. Ambichl, and F. Libisch, *Generating particlelike scattering states in wave transport*, Phys. Rev. Lett. **106** (2011), 120602 (1–4).

[119] D. R. Rowland and J. D. Love, *Evanescent wave coupling of whispering gallery modes of a dielectric cylinder*, IEEE Proc. J **140** (1993), 177–188.

[120] J. W. Ryu, S. Y. Lee, C. M. Kim, and Y. J. Park, *Quasiscarred modes and their branching behavior at an exceptional point*, Phys. Rev. E **83** (2011), 015203 (1–4).

[121] J.-W. Ryu, S.-Y. Lee, and S. W. Kim, *Coupled nonidentical microdisks: Avoided crossing of energy levels and unidirectional far-field emission*, Phys. Rev. A **79** (2009), 053858 (1–7).

[122] S. Saidi, *Etude d'une nouvelle classe de billards inhomogènes et son apport aux microcavités laser*, Ph.D. thesis, Université Pierre et Marie Curie, 2005.

[123] S. Saïdi, G. Painchaud-April, J. Poirier, P-Y. St-Louis, J. Lépine, and L. J. Dubé, *Classical Chaos in a Novel Inhomogeneous Photonic Billiard*, 9th SIAM Conference on Applications of Dynamical Systems, 2007.

[124] N. Saito, H. Hirooka, J. Ford, F. Vivaldi, and G. H. Walker, *Numerical study of billiard motion in an annulus bounded by non-concentric circles*, Physica D **5** (1982), 273–286.

[125] M. A. Santiago-Cordoba, S. Boriskina, F. Vollmer, and M. C. Demirel, *Nanoparticle-based protein detection by optical shift of a resonant microcavity*, Appl. Phys. Lett. **99** (2011), 073701 (1–3).

[126] R. Schäfer, U. Kuhl, and H. J. Stöckmann, *Directed emission from a dielectric microwave billiard with quadrupolar shape*, New J. Phys. **8** (2006), 46 (1–17).

[127] H. Schomerus, *Quantum noise and self-sustained radiation of PT-symmetric systems*, Phys. Rev. Lett. **104** (2010), 233601 (1–4).

[128] H. G. L. Schwefel, *Directionality and vector resonances of regular and chaotic dielectric microcavities*, Ph.D. thesis, Yale University, 2004.

[129] H. G. L. Schwefel, N. B. Rex, E. Tureci, R. K. Chang, A. D. Stone, T. Ben-Messaoud, and J. Zyss, *Dramatic shape sensitivity of directional emission patterns from similarly deformed cylindrical polymer lasers*, J. Opt. Soc. Am. B **21** (2004), 923–934.

[130] M. O. Scully and M. S. Zubairy, *Quantum Optics*, Cambridge, 1997.

[131] I. Shimamura, *Complete separation of resonance and nonresonance channel spaces*, J. Phys. B **44** (2011), 201002 (1–4).

[132] S. Shinohara, T. Harayama, H. E. Tureci, and A. D. Stone, *Ray-wave correspondence in the nonlinear description of stadium-cavity lasers*, Phys. Rev. A **74** (2006), 033820 (1–5).

[133] S. I. Shopova, R. Rajmangal, S. Holler, and S. Arnold, *Plasmonic enhancement of a whispering-gallery-mode biosensor for single nanoparticle detection*, Appl. Phys. Lett. **98** (2011), 243104 (1–3).

[134] M. Simonius, *Overlapping resonances and unitarity of the scattering matrix*, Nucl. Phys. A **218** (1974), 53–60.

[135] F. T. Smith, *Lifetime matrix in collision theory*, Phys. Rev. **118** (1960), 349–356.

[136] A. W. Snyder and J. D. Love, *Reflection at a curved dielectric interface - Electromagnetic tunneling*, IEEE Trans. Microwave Theory and Techniques **23** (1975), 134–141.

[137] S. M. Spillane, T. J. Kippenberg, and K. J. Vahala, *Ultralow-threshold Raman laser using a spherical dielectric microcavity*, Nature **415** (2002), 621–623.

[138] B. Z. Steinberg and A. Boag, *Splitting of microcavity degenerate modes in rotating photonic crystals-the miniature optical gyroscopes*, J. Opt. Soc. Am. B **24** (2007), 142–151.

[139] H.-J. Stöckmann, *Quantum Chaos: An Introduction*, Cambridge University Press, 1999.

[140] A. D. Stone, *Einstein's unknown insight and the problem of quantizing chaos*, Physics Today **58 (10)** (2005), 37–43.

[141] S. Sunada and T. Harayama, *Sagnac effect in resonant microcavities*, Phys. Rev. A **74** (2006), 021801 (1–4).

[142] _____, *Design of resonant microcavities: Application to optical gyroscopes*, Opt. Express **15** (2007), 16245–16254.

[143] T. Takami, *Semiclassical interpretation of avoided crossings for classically non-integrable systems*, Phys. Rev. Lett. **68** (1992), 3371–3374.

[144] I. Teraoka and S. Arnold, *Theory of resonance shifts in TE and TM whispering gallery modes by nonradial perturbations for sensing applications*, J. Opt. Soc. Am. B **23** (2006), 1381–1389.

[145] _____, *Resonance shifts of counterpropagating whispering-gallery modes: degenerate perturbation theory and application to resonator sensors with axial symmetry*, J. Opt. Soc. Am. B **26** (2009), 1321–1329.

[146] S. Tomsovic, *Tunneling and chaos*, Physica Scripta **T90** (2001), 162–165.

[147] H. E. Tureci, *Wave chaos in dielectric resonators: Asymptotic and numerical approaches*, Ph.D. thesis, Yale University, 2003.

[148] H. E. Tureci, H. G. L. Schwefel, A. D. Stone, and E. E. Narimanov, *Gaussian-optical approach to stable periodic orbit resonances of partially chaotic dielectric micro-cavities*, Opt. Express **10** (2002), 752–776.

[149] J. Unterhinninghofen, J. Wiersig, and M. Hentschel, *Goos-hänchen shift and localization of optical modes in deformed microcavities*, Phys. Rev. E **78** (2008), 016201 (1–8).

[150] D. W. Vernooy, V. S. Ilchenko, H. Mabuchi, E. W. Streed, and H. J. Kimble, *High-Q measurements of fused-silica microspheres in the near infrared*, Opt. Lett. **23** (1998), 247–249.

[151] F. Vollmer, *Taking detection to the limit. Label-free, high-sensitivity detection of biomolecules using optical resonance*, B.I.F. Futura **20** (2005), 239–244.

[152] F. Vollmer and S. Arnold, *Whispering-gallery-mode biosensing: label free detection down to single molecules*, Nature Methods **5** (2008), 591–596.

[153] F. Vollmer, S. Arnold, D. Braun, I. Teraoka, and Al. Libchaber, *Multiplexed DNA quantification by spectroscopic shift of two microsphere cavities*, Biophys. J. **85** (2003), 1974–1979.

[154] H. Wallkens, J. Wiersig, and H. R. Dullin, *Elliptic quantum billiards*, Ann. Phys. (NY) **260** (1997), 50–90.

[155] Q. J. Wang, C. Yan, N. Yu, J. Unterhinninghofen, J. Wiersig, C. Pflügl, L. Diehl, T. Edamura, M. Yamanishi, H. Kan, , and F. Capasso, *Whispering-gallery mode resonators for highly unidirectional laser action*, Proceedings of the National Academy of Sciences **52** (2010), 22407–22412.

[156] A. L. Washburn, L. C. Gunn, and R. C. Bailey, *Label-free quantitation of a cancer biomarker in complex media using silicon photonic microring resonators*, Anal. Chem. **81** (2009), 9499–9506.

[157] A. L. Washburn, M. S. Luchansky, A. L. Bowman, and R. C. Bailey, *Quantitative, label-free detection of five protein biomarkers using multiplexed arrays of silicon photonic microring resonators*, Anal. Chem. **82** (2010), 69–72.

[158] J. Wiersig, *Boundary element method for resonances in dielectric microcavities*, J. Opt. Soc. Am. A **5** (2003), 53–60.

[159] ———, *Hexagonal dielectric resonators and microcrystal lasers*, Phys. Rev. A **67** (2003), 023807 (1–12).

[160] ———, *Formation of long-lived, scarlike modes near avoided resonance crossings in optical microcavities*, Phys. Rev. Lett. **97** (2006), 253901 (1–4).

[161] J. Wiersig and M. Hentschel, *Unidirectional light emission from high-Q modes in optical microcavities*, Phys. Rev. A **73** (2006), 031802 (1–4).

[162] Y.-F. Xiao, C.-H. Dong, C.-I. Zou, Z.-F. Han, L. Yang, and G.-C. Guo, *Low-threshold microlaser in a high Q asymmetrical microcavity*, Opt. Lett.. **34** (2009), 509–511.

[163] Y. Yamamoto and R. E. Slusher, *Optical processes in microcavities*, Phys. Today **46** (1993), 66–73.

[164] C. Yan, Q. J. Wang, L. Diehl, M. Hentschel, J. Wiersig, N. Yu, C. Pflügl, F. Capasso, M. A. Belkin, T. Edamura, M. Yamanishi, and H. Kan, *Directional emission and universal far-field behavior from semiconductor lasers with limaçon-shaped microcavity*, Appl. Phys. Lett. **94** (2009), 251101 (1–3).

[165] J. Yang, S.-B. Lee, S. Moon, S.-Y. Lee, S. W. Kim, T. T. A. Dao, J.-H. Lee, , and K. An, *Pump-induced dynamical tunneling in a deformed microcavity laser*, Phys. Rev. Lett. **104** (2010), 243601 (1–4).

[166] J. Zakrzewski and D. Delande, *Parametric motion of energy levels in quantum chaotic systems. I. curvature distributions*, Phys. Rev. E **47** (1993), 1650–1664.

[167] J. Zakrzewski, D. Delande, and M. Kuś, *Parametric motion of energy levels in quantum chaotic systems. II. avoided-crossing distributions*, Phys. Rev. E **47** (1993), 1665–1676.

[168] C. Zener, *Non-Adiabatic Crossing of Energy Levels*, Proc. R. Soc. Lond. A **137** (1932), 696–702.

[169] H. Zhu, I. M. White anad J. D. Suter, J. Gohring, and X. Fan, *A universal label-free biosensing platform based on opto-fluidic ring resonators*, Proc. of SPIE **7167** (2009), 71670I (1–13).

[170] H. Zhu, I. M. White, J. D. Suter, and X. Fan, *Phage-based label-free biomolecule detection in an opto-fluidic ring resonator*, Biosens. Bioelectron. **24** (2008), 461–466.